Kemal Hanjalić and Brian Launder

Modelling Turbulence in Engineering and the Environment

Rational Alternative Routes to Closure

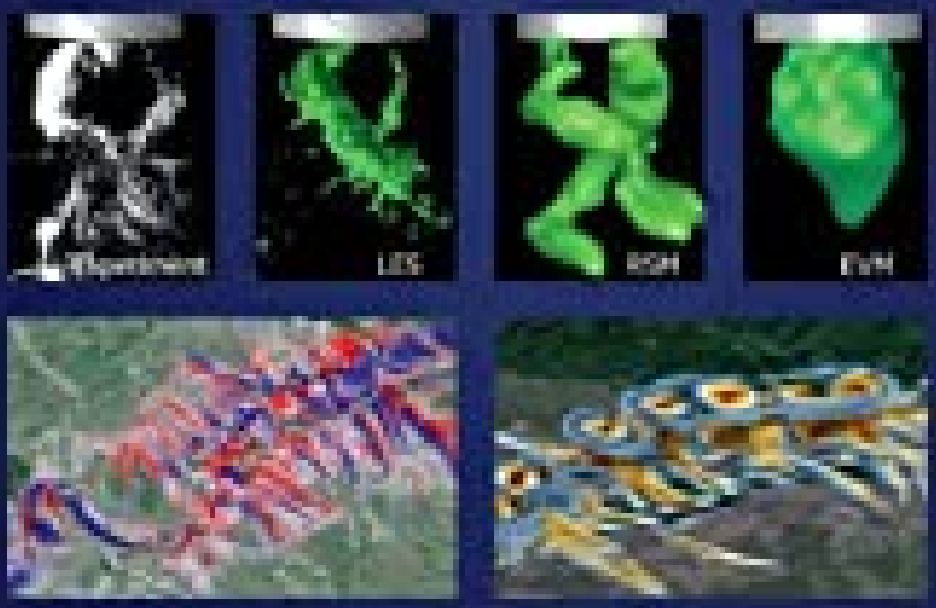

Second Edition

CAMBRIDGE

MODELLING TURBULENCE IN ENGINEERING AND THE ENVIRONMENT

Rational Alternative Routes to Closure

Modelling transport and mixing by turbulence in complex flows are huge challenges for computational fluid dynamics (CFD). This highly readable book introduces readers to modelling levels that respect the physical complexity of turbulent flows. It examines the hierarchy of Reynolds-averaged Navier–Stokes (RANS) closures in various situations ranging from fundamental flows to three-dimensional industrial and environmental applications. The general second-moment closure is simplified to linear eddy-viscosity models, demonstrating how to assess the applicability of simpler schemes and the conditions under which they give satisfactory predictions.

The principal changes for the second edition reflect the impact of computing power: a new chapter devoted to unsteady RANS and another on how large-eddy simulation, LES, and RANS strategies can be effectively combined for particular applications.

This book will remain the standard for those in industry and academia seeking expert guidance on the modelling options available, and for graduate students in physics, applied mathematics and engineering entering the world of turbulent flow CFD.

KEMAL HANJALIĆ is Professor Emeritus at the Delft University of Technology and an international fellow of the UK's Royal Academy of Engineering and the Russian Academy of Science. His innovative and sustained contributions to turbulence-model development, including heat transfer and environmental flows, have been recognized by the Max Planck and Nusselt–Reynolds Research Prizes.

BRIAN LAUNDER, Emeritus Professor at the University of Manchester, has enjoyed more than a half-century of turbulence-modelling projects with his co-author. Widely cited for his two-equation eddy-viscosity modelling, his main focus has been stress-transport and non-linear eddy-viscosity closures. He was elected FRS and FREng for his turbulence research with honorary doctorates from three European universities.

MODELLING TURBULENCE IN ENGINEERING AND THE ENVIRONMENT

Rational Alternative Routes to Closure

Second Edition

KEMAL HANJALIĆ and BRIAN LAUNDER
Delft University of Technology *University of Manchester*

Chapter 10 co-authored with

ALISTAIR J. REVELL
University of Manchester

CAMBRIDGE UNIVERSITY PRESS

CAMBRIDGE
UNIVERSITY PRESS

University Printing House, Cambridge CB2 8BS, United Kingdom

One Liberty Plaza, 20th Floor, New York, NY 10006, USA

477 Williamstown Road, Port Melbourne, VIC 3207, Australia

314–321, 3rd Floor, Plot 3, Splendor Forum, Jasola District Centre, New Delhi – 110025, India

103 Penang Road, #05–06/07, Visioncrest Commercial, Singapore 238467

Cambridge University Press is part of the University of Cambridge.

It furthers the University's mission by disseminating knowledge in the pursuit of education, learning, and research at the highest international levels of excellence.

www.cambridge.org
Information on this title: www.cambridge.org/9781108835060
DOI: 10.1017/9781108875400

First published 2011

Second edition 2023

Printed in the United Kingdom by TJ Books Limited, Padstow Cornwall

A catalogue record for this publication is available from the British Library.

Library of Congress Cataloging-in-Publication Data
Names: Hanjalić, Kemal, author. | Launder, B. E. (Brian Edward), author.
Title: Modelling turbulence in engineering and the environment : rational alternative routes to closure / Kemal Hanjalić, Technische Universiteit Delft, The Netherlands and Brian Launder, University of Manchester; Chapter 10 co-authored by Alistair Revell, University of Manchester.
Description: Second edition. | Cambridge, United Kingdom ; New York, NY : Cambridge University Press, 2022. | Includes bibliographical references and index.
Identifiers: LCCN 2021059599 (print) | LCCN 2021059600 (ebook) | ISBN 9781108835060 (hardback) | ISBN 9781108875400 (ebook)
Subjects: LCSH: Turbulence–Mathematical models. | BISAC: SCIENCE / Mechanics / Fluids
Classification: LCC TA357.5.T87 H367 2022 (print) | LCC TA357.5.T87 (ebook) | DDC 532/.0527–dc23/eng/20220217
LC record available at https://lccn.loc.gov/2021059599
LC ebook record available at https://lccn.loc.gov/2021059600

ISBN 978-1-108-83506-0 Hardback

Contents

Preface

Over the decade since the first edition of *Modelling Turbulence in Engineering and the Environment* made its appearance, the wider topic of computational fluid dynamics – or CFD as it is now universally known – has become even more firmly established as the route to resolving important and possibly challenging questions of fluid motion in the turbulent flow regime. As the reader may judge from the Preface to that first edition (which follows), our view was that the progressive shift, then underway, from using the Reynolds-averaged Navier–Stokes (RANS) equations as the basis for accounting for turbulent transport (so-called RANS modelling) to large-eddy simulation (LES) was not assuredly the preferred practice for many applications.

The notion that, to improve the reliability of one's CFD computations, one needed to upgrade the modelling strategy from a RANS-based closure to LES largely arose from the presumption that RANS-based modelling was invariably associated with the use of a linear eddy-viscosity approximation. That presumption we emphatically rejected. Our emphasis in the first edition was rather at a closure level where turbulent momentum, heat and mass fluxes were found not from such quasi-laminar constitutive concepts but rather by approximation of their own transport equations, a path formally known as 'second-moment closure'. Indeed, the subheading to the book's title was *Second-Moment Routes to Closure*. This overall philosophy is one that we retain in the present edition, though, for reasons that will shortly become clear, the subtitle has been changed to recognize the broader range of modelling now included.

It is not argued that second-moment closure is *always* the best RANS approach to follow, however. In simple shear flows where turbulence transport is small, second-moment closures amount to what is tantamount to an eddy-viscosity model (EVM) of turbulence. There are then clear advantages to making simplifications to the physical model in order to achieve major savings in computational time, whether from solving fewer equations or from faster rates of convergence – or,

https://doi.org/10.1017/9781108875400.001 Published online by Cambridge University Press

more usually, from both. Readers familiar with the first edition will thus find that Chapters 1–7, where the key analysis and simplifications are made, are largely unchanged apart from modifications to the wording to simplify or otherwise clarify the meaning. Chapter 8, while presenting the same four alternative approaches for bridging the near-wall viscous layer, includes a challenging application relating to the urban environment to underline the applicability of the approaches beyond engineering.

The principal changes in the second edition are the two additional final chapters. The continuing rapid expansion in cheap computing power has stimulated two major areas of growth. The first is the solution of the transport equations in time-dependent mode, the *unsteady* RANS or URANS approach. This strategy was included in the first edition as a section of a chapter, but the number and complexity of the applications that have appeared in recent years now merit its figuring as a major chapter in its own right. Overall, the considerable success of the URANS approach, especially when adopted with a full or truncated form of second-moment closure, raises fundamental questions vis-à-vis LES in modelling the large-scale turbulence structures. Not all of those questions are yet resolved, but they are at least given a preliminary airing in Chapter 9.

Finally, Chapter 10 brings a collaboration between what are sometimes seen as opposing strategies. In many engineering or environmental problems, there are flow regions where LES is clearly the best approach (or even the only viable scheme) to employ. In many others, however, such as in flows bounded by solid walls, the solution of the relatively thin but important wall-adjacent areas can be entrusted to a RANS or URANS model. This practice mitigates the formidable grid density required in the wall region by the usual LES approach and equally, even with a URANS solution, enables substantially greater time steps. Then again, in some flow types, a RANS or URANS approach can perhaps cover the bulk of the flow while LES is employed only in critical regions involving complex physis not adequately accounted for by common RANS models. The final chapter thus considers how the two approaches may be brought effectively together within a single numerical solver, particularly considering the role and importance of the RANS model in different applications and the issues of interfacing between the two approaches.

As for the new subtitle to this second edition, by ‘Rational Alternative Routes to Closure’ we simply mean that the different approaches to modelling are based on a mixture of rigorous analysis, experimental inferences and, hopefully, sound physical insight while (echoing the first edition) giving particular emphasis to second-moment approaches to closure.

In bringing this edition to publication, the authors have benefitted from many individuals for information or advice, most of whom are already acknowledged in the first edition’s preface. In addition, we would here mention particularly

helpful interactions with Branislav Basara, Domenico Borello, Bruno Chaouat, Sharath Girimaji, Muhamed Hadziabdic, Michale Hrebtov, Rustam Mullyadzanov and Danesh Tafti. Finally, we are pleased to acknowledge a substantial contributor to the present edition, Professor Alistair Revell from Manchester University. As a specialist in the development and application of hybrid RANS-LES methods, he has made major contributions to the shape and scope of the final chapter and his name is, therefore, included on the title page.

Preface to the First Edition

Scientific papers on how to represent in mathematical form the types of fluid motion we call *turbulent flow* have been appearing for over a century while, for the last sixty years or so, a sufficient body of knowledge has been accumulated to tempt a succession of authors to collect, systematize and distil a proportion of that knowledge into textbooks. From the start, a bewildering variety of approaches has been advocated: thus, even in the 1970s, the algebraic mixing-length models presented in the book by Cebeci and Smith (1974) jostled on the bookshelves with Leslie's (1973) manful attempt to make comprehensible to a less specialized readership the direct-interaction approach developed by Kraichnan and colleagues. As the progressive advance in computing power made it possible to apply the emerging strategy of CFD to an ever-widening array of industrially important flows, however, EVMs based on the solution of two transport equations for scalar properties of turbulence (essentially, length and time scales of the energy-containing eddies) emerged as the modelling strategy of choice and, correspondingly, have been the principal focus in several textbooks on the modelling of turbulent flows (e.g. Launder and Spalding, 1972; Piquet, 1999; Wilcox, 2000).

Today, two-equation EVMs remain the workhorse of industrial CFD and are applied through commercially marketed software to flows of a quite bewildering complexity, though often with uncertain accuracy. However, there has been a major shift among the modelling research community to abandon approaches based on the RANS equations in favour of LES, where the numerical solution for any flow adopts a three-dimensional, time-dependent discretization of the Navier–Stokes equations using a model to account simply for the effects of turbulent motions too fine in scale to be resolved with the mesh adopted – that is, a *sub-grid-scale* (or *sgs*) model. While acknowledging that LES offers the prospects of tackling turbulence problems beyond the scope of RANS, a further major driver for this changeover has been the manifold inadequacies of the stress–strain hypothesis adopted by linear EVMs. While such a simple linkage between mean strain rate and turbulent

https://doi.org/10.1017/9781108875400.002 Published online by Cambridge University Press

stress seemed adequate for a large proportion of two-dimensional, nearly parallel flows, its weaknesses became abundantly clear as attention shifted to recirculating, impinging and three-dimensional shear flows. Although an LES approach will, most probably, also adopt an sgs model of eddy-viscosity type, the consequences are less serious for two reasons. First, the majority of the transport caused by the turbulent motion will be directly resolved by the large eddies, and second, the finer scale eddies that must still be resolved by the sgs model of turbulence will arguably be a good deal closer to isotropy. Thus, adopting an isotropic eddy viscosity as the sgs model may not significantly impair the accuracy of the solution.

However, to overcome many of the weaknesses of linear EVMs used within a RANS framework, it is quite unnecessary to upgrade one's modelling to LES level. Rather than adopting a linear algebraic relation to link stress and strain, one can obtain the turbulent stresses by solving closed forms of the exact Reynolds stress equations. It is this approach that represents the main focus of the present book, a modelling strategy known formally as *second-moment closure*, a label that also embraces the corresponding modelling of turbulent heat and species fluxes. This closure level, first advocated in the early 1950s (Rotta, 1951), has in principle a far greater capacity than EVMs for capturing the diverse influences of complex strain fields, body forces or substantial transport on the evolution of the turbulent stresses. This is because the direct effects of strain field, body forces and convective transport on the turbulent stresses appear directly in the second-moment equations in forms requiring no approximation! It is true that modelling is still needed, both in the second-moment equations and in the scale-determining equation, the latter of which must also be solved to complete closure. But, at the second-moment level, one can proceed further by way of analysis while several additional invariant parameters become available to help shape compliance with limiting states of turbulence.

Admittedly, even with a well-constructed code explicitly designed for second-moment closure (as many commercial solvers are not), such schemes require typically twice as much computational resource as corresponding EVMs. But this is a very small price to pay for predicting the flow correctly, while the computational costs will still usually be one or two orders of magnitude less than the cost of obtaining an LES of the same flow.

Why, the reader may legitimately ask, if second-moment closure represents such a major advance over eddy-viscosity approaches, has this situation not become evident and widely accepted by potential users? The present authors can offer no certain answer to that question. To those working at that closure level it *is* well known. Indeed, in the more comprehensive current textbooks, one will at least find signposts to modern forms of second-moment closures. But perhaps such broad-coverage treatments, while of inestimable value as reference sources, are

unable to justify the space for providing a detailed examination of particular modelling forms or for showing a broad coverage of the successes and weaknesses of particular models. Perhaps, we concluded, one needed a textbook that focussed principally on second-moment closure, that provided the background in sufficient depth, bringing to light strategies from earlier decades that are still useful and also including the latest models available. Finally, one needed a textbook that discussed in detail a comprehensive range of applications so that potential users could judge the likely utility of the schemes in the flows that interest them. It has been our aim, in the pages that follow, to provide such a coverage.

The writers themselves began working together on second-moment closure in the late 1960s and over the ensuing forty-odd years have repeatedly interacted on research strategy in this field, both in specific collaborative research projects and through the ERCOFTAC[1] special interest group in turbulence modelling. Our views on closure modelling, if not identical, are sufficiently closely aligned that, when we learned that each of us was contemplating preparing a textbook on the subject, we quickly decided that we should pool our efforts and produce a joint volume. Throughout, this has been an equal partnership and, as in all our joint papers, our names are sequenced alphabetically.

To a neutral and knowledgeable reader, the material presented may well be seen as giving too great an emphasis to the authors' own work. In part this 'bias' arises from wanting to show the performance of particular models for a wide range of test cases that (we have learned from experience) are sensitive to the modelling assumptions. We trust, however, that the cited references make the connection to (and the dependence on) the work of others plainly evident. Indeed, our hope would be that having had their enthusiasm for second-moment closure stimulated or reawakened by the present text, many readers will be encouraged to plunge into at least some of the other recent textbooks in turbulence modelling and, thereafter, to read the original journal papers that are cited.

In fact, one of the choices made in producing this book is directly aimed at encouraging the reader to progress into the original research literature. In presenting different models, while the main ideas and underlying principles have been included (along with examples of a model's performance), in many cases, we have not given a complete mathematical statement still less the boundary conditions or other essential numerical aspects of handling the equations appropriate to different classes of flow.

While, in some respects, the book is more comprehensive in its coverage of second-moment closure than most (perhaps all) alternative volumes on turbulence modelling, there are also omissions about which some brief explanation needs to be given. Although we make early reference to situations where the density fluctuations in the convective transport term need to be acknowledged and modelled, the

[1] European Research Community on Flow Turbulence and Combustion.

https://doi.org/10.1017/9781108875400.002 Published online by Cambridge University Press

reader will find that this is not a subject to which we return. The reason is simple: we have ourselves done little work in the area, so our position statement could only be arrived at by borrowing conclusions from what others have written. It would, we felt, be better for the interested reader, instead, to digest directly the views of those with greater experience. In fact, two such individuals, Tom Gatski and Jean-Paul Bonnet (2009), have recently collaborated to produce a textbook specifically focussed on compressibility in high-speed flow, which we commend to the reader. Equally, while both of us have made proposals for obtaining the turbulent thermal timescale by solving an equation for the dissipation rate of temperature fluctuations, we nevertheless nowadays prefer to adopt simpler practices ourselves. Thus, here we leave Nagano's (2002) review to summarize the painstaking research and optimization in this area carried out by Nagano and his colleagues. A final important area where we offer no contribution is that of how to embed the concepts of turbulent intermittency within the closure. Long ago, Libby (1975) proposed a transport equation for intermittency that has been used and developed over the ensuing decades by numerous workers, especially those working in combustion and, more recently, those attempting to predict transition from laminar to turbulent flow. In the latter area, the review by Savill (2002b) gives an indication of the directions being followed to broaden the range of such flows that can be tackled.

Despite the care we have tried to apply in checking the typescript, we know there will inevitably be errors in what is written, whether just typographical slips or interpretational errors on our part. Readers are warmly invited to draw these to our attention (in writing, please) so that in any future reprinting they may be corrected.

In closing, we express our thanks to our host institutions for the infrastructure support they have provided. In the case of one of us (KH), this also includes La Sapienza University, Rome, where, as the holder of an EU-funded Marie Curie Chair, he spent much of the period during the book's preparation. Finally, we are especially conscious that the task of preparing this book would not have been realizable without the contributions of many past and present colleagues. In particular, we offer our thanks and appreciation to Tim Craft, Song Fu, Hector Iacovides, Suad Jakirlić, Saša Kenjereš, Remi Manceau, Kazuhiko Suga and the late Ibrahim Hadžić. We have also benefitted greatly over the years from inputs on various aspects of modelling from Peter Bradshaw, Paul Durbin, Tom Gatski, Bill Jones, Nobu Kasagi, Hiroshi Kawamura, Dominique Laurence, Michael Leschziner, John Lumley, Yasu Nagano, Steve Pope, Bill Reynolds, Wolfgang Rodi, Roland Schiestel, Ronald So, Dave Wilcox and Micha Wolfshtein. Finally, we extend a special thank you to the research students and postdoctoral researchers – too numerous to name individually – with whom we have shared the occasional frustrations but, ultimately, the pleasurable satisfactions of turbulence-modelling research.

Principal Nomenclature

Symbol	Meaning
A	Lumley's two-component stress ('flatness') parameter, $A \equiv 1 - \frac{9}{8}(A_2 - A_3)$
A_2	second invariant of stress anisotropy, $A_2 \equiv a_{ij}a_{ji}$
A_3	third invariant of stress anisotropy, $A_3 \equiv a_{ij}a_{jk}a_{ki}$
A_θ	scalar flux correlation function, $A_\theta \equiv (\overline{\theta u_i})^2/(\overline{\theta^2}\,\overline{u_k u_k})$, Eq. (3.32)
A^+	coefficient in van Driest's near-wall form of mixing-length hypothesis
a_{ij}	Reynolds stress anisotropy tensor, $a_{ij} \equiv \overline{u_i u_j}/k - 2\delta_{ij}/3$
B_i, $\mathbf{B}$	magnetic flux density
b_{ij}	$b_{ij} \equiv a_{ij}/2$
b^i_{lj}	third-order tensor in the model for $\Phi_{\theta j_2}$, Eq. (4.49)
b^{mi}_{lj}	fourth-order tensor in the model for Φ_{ij_2}, Eq. (4.39)
C	species concentration
C_p	pressure coefficient, $C_p \equiv 2(P_w - P_\infty)/\rho U_\infty^2$
C_κ	constant in Kolmogorov's $-5/3$ law for energy variation with wave number, Eq. (3.6)
C_{DES}, C_{DDES}, ...	coefficients in DES, DDES, IDDES
C_{ij}	cross (mixed) stress, Eqs. (9.9, 10.12)
$\mathcal{C}_{ij}$	convection of the Reynolds stress tensor, $\overline{u_i u_j}$
$\mathcal{C}_{\theta i}$	convection of the turbulent scalar flux, $\overline{\theta u_i}$
$\mathcal{C}_{\theta\theta}$	convection of scalar variance, $\overline{\theta^2}$
$\mathcal{C}_\phi$	convection of a turbulence variable, ϕ
c_μ	coefficient in eddy-viscosity formula
c_p	specific heat at constant pressure
$c_{\varepsilon 1}$, $c_{\varepsilon 2}$, ...	coefficients of source/sink terms in the modelled ε equation
c_1, c_2, ...	coefficients in the models of the pressure-strain term

c_S	Smagorinsky coefficient, Eq. (10.14)
D	diameter, channel width
D_{ij}	complementary stress production tensor $D_{ij} \equiv -(\overline{u_i u_k}\partial U_k/\partial x_j + \overline{u_j u_k}\partial U_k/\partial x_i)$
$\mathcal{D}_{ij}$	total diffusion of the Reynolds stress tensor
$\mathcal{D}^p_{ij}$	turbulent diffusion of the Reynolds stress tensor $\overline{u_i u_j}$ by pressure fluctuations, Eq. (2.20)
$\mathcal{D}^t_{ij}$	turbulent diffusion of the Reynolds stress tensor $\overline{u_i u_j}$ by velocity fluctuations, Eq. (2.18)
$\mathcal{D}^\nu_{ij}$	molecular diffusion of the Reynolds stress tensor $\overline{u_i u_j}$, Eq. (2.18)
$\mathcal{D}_{\theta i}$	total diffusion of scalar flux $\overline{\theta u_i}$, Eq. (2.25)
$\mathcal{D}^p_{\theta i}$	turbulent diffusion of scalar flux $\overline{\theta u_i}$ by pressure fluctuations, Eqs. (2.22, 2.25)
$\mathcal{D}^t_{\theta i}$	turbulent diffusion of scalar flux $\overline{\theta u_i}$ by velocity fluctuations, Eqs. (2.22, 2.25)
$\mathcal{D}^\alpha_{\theta i}$	thermal molecular diffusion of scalar flux $\overline{\theta u_i}$, Eqs. (2.22, 2.25)
$\mathcal{D}^\nu_{\theta i}$	viscous diffusion of scalar flux $\overline{\theta u_i}$, Eqs. (2.22, 2.25)
$\mathcal{D}_{\theta\theta}$	total diffusion of scalar variance $\overline{\theta^2}$, Eq. (3.20)
$\mathcal{D}_\phi$	total diffusion of a turbulence variable ϕ
$\mathcal{D}^p_\phi$	turbulent diffusion of variable ϕ by pressure fluctuations
$\mathcal{D}^t_\phi$	turbulent diffusion of variable ϕ by velocity fluctuations
$\mathcal{D}^\nu_\phi$	molecular diffusion of variable ϕ
$\tilde{d}$ $(\equiv L_{DES})$	effective length scale in DES, $\tilde{d} = \min(d_w, C_{DES}\Delta)$, Eq. (10.42)
d_w	distance to the nearest wall in Eq. (10.42)
E	two-component-limit parameter for dissipation tensor, $E \equiv 1 - \frac{9}{8}(E_2 - E_3)$
E	integration constant in log-law, $E \approx 8.4$ for a smooth wall
E_2	second invariant of e_{ij}, $E_2 \equiv e_{ij}e_{ji}$
E_3	third invariant of e_{ij}, $E_3 \equiv e_{ij}e_{jk}e_{ki}$
$E(\kappa)$	contribution by the Fourier-mode wavenumber κ to the turbulent kinetic energy
e_i	fluctuating electric potential
e_{ij}	stress dissipation-rate anisotropy tensor, $e_{ij} \equiv \varepsilon_{ij}/\varepsilon - \frac{2}{3}\delta_{ij}$
$\mathcal{F}_{ij}$	turbulent stress production due to all body forces, Eq. (2.23)
$\mathcal{F}_{\theta i}$	turbulent scalar flux production due to all body forces, Eq. (2.23)

Symbol	Meaning
$\mathcal{F}_\phi$	production of a turbulence variable ϕ by all body forces
f	scalar variable in Durbin's elliptic relaxation EVM
f	natural shed frequency
f_D	van Driest wall damping function, Eq. (10.15)
f_i	fluctuating body force
f_k	ratio of unresolved to total turbulent kinetic energy in PANS, $f_k = k_u/k$
$f_L\ (\equiv \alpha)$	RANS/LES switching function, Eqs. (10.31, 10.34) $f_L = \max(1, L_{RANS}/L_{LES})$
f_w	wall damping function in GL and HJ low-Re RSM
f_Δ	blending function in VLES, Eq. (10.33)
G	spatial filter function, Eqs. (10.8, 10.9)
$\mathcal{G}_{ij}$	turbulent stress production due to gravitational force, Eqs. (2.19, 4.74)
g	gravitational acceleration constant
g_i, $\mathbf{g}$	gravitational vector
H	height of the step in flow over a backward-facing step
Ha	Hartmann number
H, H_{12}	boundary-layer shape factor, δ^*/θ (note $\delta_1 \equiv \delta^*$, $\delta_2 \equiv \theta$, $H_{12} \equiv H$)
h	half width of a plane channel
h	enthalpy, $h \equiv \int c_p dT$
h	heat transfer coefficient, $h \equiv q''_w/(\Theta_w - \Theta_{ref})$
II	alternative notation for the second invariant of stress anisotropy, $II \equiv b_{ij}b_{ji}/2 = A_2/8$
III	alternative notation for the third invariant of stress anisotropy, $III \equiv b_{ij}b_{jk}b_{ki}/3 = A_3/24$
J	Jayatilleke function (relative resistance of sublayer to heat and momentum transfer from a smooth wall), Eq. (8.5)
K	acceleration parameter, $K \equiv (\nu/U_\infty^2)(dU_\infty/dx)$
K	mean flow kinetic energy, $K \equiv \frac{1}{2}U_i^2$
k	turbulent kinetic energy, $k \equiv \frac{1}{2}\overline{u_i u_i}$
k^*	sub-grid-scale turbulence energy normalized by total (sgs plus resolved) k, Eq. (10.40)
k_{ssv}	'scale-supplying variable' in PANS (resolved k), Eq. (10.63)
L, $\mathcal{L}$	characteristic flow dimension
L	integral turbulent length scale (usually defined as $k^{3/2}/\varepsilon$; for definitions of bounded length scale in elliptic relaxation models see Eqs. (6.74, 7.45))

l	turbulence length scale, $k^{3/2}/\varepsilon$
ℓ	alternative turbulence length scale (used in Wilcox–Rubesin model), $\ell = c_\mu l$
L_{DDES}	effective length scale in DDES, Eq. (10.45)
L_{IDDES}	effective length scale in IDDES, Eq. (10.48)
L_K	von Karman length scale, Eq. (10.36)
L_{ij}	Leonard stress, Eqs. (9.9, 10.12)
$\mathcal{M}_{ij}$	stress production due to fluctuating (electro)-magnetic (Lorenz) force, Eq. (4.95)
N	bulk-flow Stuart number, $N \equiv \sigma B_0^2 L/\rho U_b$
Nu	Nusselt number, $\mathrm{Nu} \equiv hD/\lambda$, D denotes relevant length dimension, for example, pipe diameter
n_i, $\mathbf{n}$	wall-normal unit vector
$\hat{P}$, P, p	instantaneous, mean and fluctuating pressure
P^+	non-dimensional pressure gradient, $P^+ = \nu(\partial P/\partial x)/\rho U_\tau^3$
P	wall-adjacent grid node
$\mathcal{P}_{ij}$	stress production due to mean velocity gradient, Eq. (2.18)
$\mathcal{P}_{\theta i}$	production of turbulent scalar flux $\overline{\theta u_i}$, Eq. (2.22)
$\mathcal{P}_k$	production of turbulent kinetic energy k, $\mathcal{P}_k = \mathcal{P}_{ii}/2$, Eq. (1.5)
$\mathcal{P}_{\theta\theta}$	production of the mean-square scalar variance $\overline{\theta^2}$, Eq. (3.20)
$\mathcal{P}_\phi$	production of a turbulence variable ϕ by gradients of mean and fluctuating properties
Pr	molecular Prandtl/Schmidt number
Q	criterion for eduction of coherent vortical structures, $Q \equiv -(S_{ij}S_{ij} - W_{ij}W_{ij})/2$
$\dot{q}$	internal heat source
$q_w^{''}$	wall heat flux
q_w	kinematic wall heat flux, $q_w = q_w^{''}/\rho c_p$
R	pipe radius
R, r	thermal-to-mechanical timescale ratio, $R = \overline{\theta^2}\varepsilon/k\varepsilon_{\theta\theta}$; $r = 1/R$
R_{ij}	Reynolds stress, Eqs. (9.8, 10.12)
Ra	Rayleigh number, $\mathrm{Ra} \equiv \beta g(\Theta_w - \Theta_{ref})L^3/\alpha\nu$, where L is a characteristic flow dimension, Θ_w and Θ_{ref} denote the wall and reference temperatures, respectively
Re_L	Reynolds number based on a characteristic flow dimension, L and velocity, U_0, $\mathrm{Re}_L \equiv U_0 L/\nu$
Re_m	channel flow Reynolds number based on the mean (bulk) velocity, $\mathrm{Re}_m \equiv U_m 2h/\nu$

Symbol	Meaning
Re_H	Reynolds number of flow behind a backward-facing step of height H
Re_M	magnetic Reynolds number, $\mathrm{Re}_M \equiv \mu_0 \sigma U L$, [$(\mu_0\sigma)^{-1}$ is known as the *magnetic diffusivity*]
Re_t	turbulent Reynolds number, $\mathrm{Re}_t \equiv k^2/(\nu\varepsilon)$
Re_{δ_s}	Reynolds number based on Stokes thickness and maximum free-stream velocity
Re_θ	Reynolds number based on momentum thickness, $\mathrm{Re}_\theta \equiv U_\infty \theta/\nu$
Re_τ	Reynolds number based on friction velocity and channel half width, $\mathrm{Re}_\tau = U_\tau h/\nu$
Re_λ	Taylor microscale Reynolds number, $\mathrm{Re}_\lambda \equiv \sqrt{\overline{u_1^2}}\lambda/\nu$
R_f	flux Richardson number, $\mathrm{R}_f \equiv -\mathcal{G}_k/\mathcal{P}_k$
Ri	gradient Richardson number, $\mathrm{Ri} \equiv R_f \sigma_\theta$
$\mathcal{R}_{ij}$	stress production due to system rotation, Eqs. (2.19, 4.68)
R_{ij}	Reynolds stress, Eqs. (9.8, 10.12)
$R_{ij}(\mathbf{x},\mathbf{x}')$	two-point correlation tensor, $R_{ij}(\mathbf{x},\mathbf{x}') \equiv \overline{u_i(\mathbf{x})u_j(\mathbf{x}')}$
Ro	bulk rotation number (various definitions according to specific application comprising rotating velocity divided by some other reference velocity)
r	radial coordinate
r_i, $\mathbf{r}$	position vector
r	mechanical-to-scalar timescale ratio, $r \equiv k\varepsilon_{\theta\theta}/(\overline{\theta^2}\varepsilon) \equiv 1/R$
S	salt concentration ('salinity')
S_w	swirl intensity, a dimensionless ratio of the axial fluxes of angular to axial momentum, $S_w \equiv 2\pi \int_0^R UWr^2 dr/\pi R^3 U_b^2$ or $S_w = \int_0^R UWr^2 dr/R\int_0^R U^2 r dr$
S	invariant of the non-dimensional mean strain tensor, $\mathrm{S} \equiv \sqrt{\tilde{S}_{mn}\tilde{S}_{nm}}$
$\mathcal{S}$	invariant of the strain rate tensor, $\mathcal{S} \equiv \sqrt{S_{ij}S_{ji}}$
S^*	alternative invariant of mean strain tensor used by Yakhot's group, $\mathrm{S}^* = \sqrt{2}\mathrm{S}$, Eq. (5.4)
S	dimensionless mean strain (in simple shear), $\mathsf{S} \equiv 2(k/\varepsilon)(S_{12}S_{12})^{1/2} = (k/\varepsilon)dU/dy$
Sr	Strouhal number, $\mathrm{Sr} \equiv fL/U$, dimensionless vortex shedding frequency

St	Stanton number, $\mathrm{St} \equiv h/\rho U_\infty c_p$
S_{ij}	mean rate of strain tensor, $S_{ij} \equiv \frac{1}{2}(\partial U_i/\partial x_j + \partial U_j/\partial x_i)$
$\tilde{S}_{ij}$	non-dimensional mean rate of strain, $\tilde{S}_{ij} \equiv S_{ij}k/\varepsilon$
$\mathcal{S}_{\varepsilon 1}$,$\mathcal{S}_{\varepsilon 2}$,$\mathcal{S}_{\varepsilon 3}$	general symbols for the source and sink terms in the ε equation, respectively
s_{ij}	fluctuating rate of strain, $s_{ij} \equiv \frac{1}{2}(\partial u_i/\partial x_j + \partial u_j/\partial x_i)$
T	temperature [°K]
$\mathcal{T}$	characteristic turbulence timescale, (usually $\mathcal{T}$ is taken as k/ε, but not in Eq. (5.23)); for definitions of bounded time-scale in elliptic relaxation models see Eqs. (6.74, 7.35 and 7.44)
$\mathcal{T}(\kappa)$	spectral energy transfer rate
$\mathbb{T}_{ij}^{(n)}$	tensor integrity bases
t	time
U	streamwise mean velocity component
$\overline{U}$	filtered velocity in LES
$U,\ V,\ W$	Cartesian components of mean velocity
$\hat{U}_i,\ U_i,\ u_i$	instantaneous, mean and fluctuating velocity vector
$\tilde{U}$	local time-averaged velocity, Eq. (9.1)
$\widetilde{U}$	phase/ensemble averaged velocity, Eqs. (2.8, 2.9, 9.7)
$U_m, U_b,\ \bar{U}$	bulk velocity
U_q	buoyancy velocity, $U_q \equiv (\beta g q_w \alpha^2/\nu)^{1/4}$
U_w	wall velocity
U_∞	free-stream velocity
U_τ	friction velocity, $\sqrt{\tau_w/\rho}$
U^+	mean velocity non-dimensionalized with friction velocity, $U^+ \equiv U/U_\tau$
U^*	mean velocity for use in wall functions, $U^* \equiv Uk^{1/2}/U_\tau^2 \equiv \rho U k^{1/2}/\tau_w$
ΔU	streamwise velocity change across free shear flow
$-\overline{u_i u_j}$	kinematic Reynolds-stress tensor
$u,\ v,\ w$	Cartesian representation of turbulent velocities
V	mean velocity component in direction y
Va	Valensi number, $\mathrm{Va} \equiv R^2\omega/\nu$
W	invariant of the non-dimensional rotation rate, $\mathrm{W} \equiv \sqrt{\tilde{W}_{ij}\tilde{W}_{ij}}$
W	spanwise and circumferential velocity component
Wo	Womersley number, $\mathrm{Wo} \equiv R\sqrt{\omega/\nu} = \sqrt{\mathrm{Va}}$
W_{wall}	circumferential velocity of rotating wall

Symbol	Meaning
W_{ij}	mean rate-of-rotation tensor, $W_{ij} = 1/2(\partial U_i/\partial x_j - \partial U_j/\partial x_i)$
$\tilde{W}_{ij}$	non-dimensional mean rate-of-rotation tensor, $\tilde{W}_{ij} \equiv W_{ij}k/\varepsilon$
w_{ij}	fluctuating rate-of-rotation tensor, $w_{ij} = 1/2(\partial u_i/\partial x_j - \partial u_j/\partial x_i)$
x_i, $\mathbf{x}$	Cartesian coordinates in index and vector notation
x, y, z	Cartesian coordinates
y	wall distance,
y^+	non-dimensionalized wall distance, $y^+ = U_\tau y/\nu$
y^*	alternative normalized wall distance, $y^* \equiv k^{1/2}y/\nu$
$y_{1/2}$	half width of plane jet or wake

Greek Symbols	Meaning
α	thermal diffusivity, $\alpha = \lambda/(\rho c_p)$
β	thermal expansion coefficient, $\beta = -(1/\rho)(\partial\rho/\partial\Theta)\big\vert_{C,P}$
γ	molecular diffusivity of a scalar
γ	concentration (salinity) expansion coefficient, $\gamma = (1/\rho)(\partial\rho/\partial C)\big\vert_{\Theta,P}$
Δ	characteristic mesh size in direct and large-eddy simulations
δ	boundary layer thickness
δ_1, δ^*	displacement thickness, $\delta_1 = \int_0^\infty (1 - U/U_\infty)dy$ for a uniform density
δ_2, θ	momentum thickness $\delta_2 = \int_0^\infty \frac{U}{U_\infty}\left(1 - \frac{U}{U_\infty}\right)dy$ for uniform density
δ_s	Stokes thickness, $\delta_s = \sqrt{2\nu/\omega}$
δ_ν	viscous length scale, $\delta_\nu = \nu/U_\tau$
δ_{ij}	Kronecker unit symbol
ε	dissipation rate of the turbulence kinetic energy k, $\varepsilon = \nu\overline{(\partial u_i/\partial x_j)^2}$
ε^h	homogeneous dissipation rate of k, $\varepsilon^h = \varepsilon - {}^1\!/_2\mathcal{D}_k^\nu$
ε_P	turbulence energy transfer rates from production region in multi-scale model
ε_T	turbulence energy transfer rates across the transfer region in multi-scale model

ε_w	wall value of the kinetic energy dissipation rate
$\tilde{\varepsilon}$	'quasi-homogeneous' dissipation rate of k, $\tilde{\varepsilon} = \varepsilon - \mathcal{D}_k^{\nu} \equiv \varepsilon - 2\nu(\partial k^{1/2}/\partial x_n)^2$
ε^+	dimensionless dissipation rate (in wall units), $\varepsilon^+ \equiv \varepsilon\nu/U_\tau^4$
ε_{ij}	stress dissipation rate tensor, $\varepsilon_{ij} \equiv 2\nu\overline{(\partial u_i/\partial x_k)(\partial u_j/\partial x_k)}$
ε_{ij}^h	homogeneous stress dissipation rate tensor, $\varepsilon_{ij}^h = \varepsilon_{ij} - {}^1\!/_2\mathcal{D}_{ij}^{\nu}$
ε_{ijk}	viscous dissipation of triple velocity moments, Eqs. (4.102, 4.103)
$\varepsilon_{\theta\theta}$	dissipation rate of the scalar variance, $\varepsilon_{\theta\theta} = 2\alpha\overline{(\partial\theta/\partial x_j)^2}$
ϵ_{ijk}	third rank alternating unit symbol (= +1 for *i, j, k* all different and in cyclic order; −1 for *i, j, k* all different in anti-cyclic order; 0 in other cases)
ζ	normalized effective wall-normal velocity $\overline{v^2}/k$ in ζ- f EVM
ζ	enstrophy (mean square of the vorticity fluctuations), $\zeta = \overline{\omega_i\omega_i}$
η	Kolmogorov length scale, $\eta \equiv (\nu^3/\varepsilon)^{1/4}$,
Θ	mean scalar property in general (primarily used for mean temperature)
θ	momentum thickness
θ	scalar property fluctuations
$\overline{\theta^2}$	mean-square scalar fluctuations (scalar variance)
ϑ	Kolmogorov timescale, $\vartheta \equiv (\nu/\varepsilon)^{1/2}$
κ	wave number, $\kappa \equiv 2\pi/\lambda$
κ	von Karman constant in log-law, $\kappa \approx 0.41$
κ^*	von Karman constant in the velocity log-law normalized with $k^{1/2}$, $\kappa^* = c_\mu^{1/4}\kappa$
$\tilde{\kappa}$	von Karman constant in the log-law for temperature, $\tilde{\kappa} \approx 0.38$
$\tilde{\kappa}^*$	von Karman constant in the temperature log-law normalized with $k^{1/2}$, $\tilde{\kappa}^* = c_\mu^{1/4}\tilde{\kappa}$
λ	Taylor microscale, $\lambda^2 \equiv \overline{u_1^2}/\overline{(\partial u_1/\partial x_1)^2}$, Eq. (3.11)
λ	thermal conductivity
λ	wave length
λ	ratio of shear stress at wall to that at edge of viscous layer, Eq. (8.27)
λ_α	eigenvalue of mean strain rate
μ	molecular viscosity of a fluid

Greek Symbols	**Meaning**
μ_t	turbulent (eddy) viscosity of a fluid
μ_0	magnetic permeability
ν	kinematic molecular viscosity of a fluid, $\nu \equiv \mu/\rho$
ν_t	kinematic turbulent viscosity of a fluid, $\nu_t \equiv \mu_t/\rho$
ν_t^+	non-dimensional turbulent viscosity, $\nu_t^+ \equiv \nu_t/\nu$
ν_{sgs}	sub-grid-scale eddy viscosity
$\tilde{\nu}$	kinematic turbulent viscosity in the SA model
Π_{ij}	velocity–pressure-gradient correlation, $\Pi_{ij} \equiv (1/\rho)[\overline{u_i(\partial p/\partial x_j)} - \overline{u_j(\partial p/\partial x_i)}]$
$\hat{\rho},\ \rho,\ \rho'$	instantaneous, mean and fluctuating fluid density
σ	electrical conductivity of fluid
σ_φ	turbulent Prandtl–Schmidt number for diffusion of φ
τ	total shear stress (viscous plus turbulent)
τ^+	non-dimensional shear stress, $\tau^+ \equiv \tau/\tau_w$
τ_{ij}	stress tensor
τ_{ij}^t	turbulent stress tensor, $\tau_{ij}^t \equiv -\rho\overline{u_i u_j}$
τ_{ij}^v	viscous stress tensor, $\tau_{ij}^v = 2\mu(S_{ij} - \frac{1}{3}S_{kk}\delta_{ij})$
τ_w	wall shear stress
$\hat{\Phi},\ \Phi,\ \varphi$	general variable: instantaneous, mean/filtered and fluctuation
$\tilde{\Phi}$	local time-averaged general variable, Eq. (9.1)
Φ_{ij}	pressure-strain correlation in the $\overline{u_i u_j}$ equation, $\Phi_{ij} \equiv (1/\rho)\ \overline{p(\partial u_i/\partial x_j + \partial u_j/\partial x_i)}$
$\Phi_{\theta j}$	pressure-scalar gradient correlation in $\overline{\theta u_j}$equation, $\Phi_{\theta j} \equiv (1/\rho)\overline{p\partial\theta}/\partial x_j$
$\overline{\varphi u_i}$	scalar flux vector
ϕ	general symbol for a turbulence variable
Ψ	generalized turbulent scale variable, $\Psi \equiv k^m \varepsilon^n$,
ψ	parameter in SAWF scheme accounting for departures from equilibrium, Eq. (8.31)
Ω	angular velocity
Ω	magnitude of the mean vorticity
Ω_k	system rotation vector, angular velocity vector
Ω_i, $\boldsymbol{\Omega}$	mean vorticity vector, $\Omega_i \equiv \epsilon_{ijk}\partial U_k/\partial x_j$, ($\boldsymbol{\Omega} \equiv \nabla \times \mathbf{V}$)
ω_i, $\boldsymbol{\omega}$	fluctuating vorticity vector, $\omega_i \equiv \epsilon_{ijk}\partial u_k/\partial x_j$, ($\boldsymbol{\omega} \equiv \nabla \times \mathbf{v}$)
ω	turbulence 'frequency' or specific dissipation rate, ε/k

Superscripts, subscripts	
+	quantity normalized by wall units ν and U_τ
*	quantity normalized by wall units ν and $k^{1/2}$ (but note U^* definition above)
$\hat{}$	instantaneous value of variable
$'$	turbulent fluctuating value of variable
$\sim$	root-mean-square value of turbulence variable (e.g. $\tilde{u}_1 \equiv \sqrt{\overline{u_1^2}}$)
c	centre-line value (of a symmetric free shear flow)
c	coherent
h	homogeneous
int	RANS/LES interface
mod	modelled
n	normal-to-the-wall direction
res	resolved
s	stochastic
sgs	sub-grid-scale
u	unresolved
v	evaluated at edge of viscous sublayer
w	wall value
∞	free-stream conditions

Abbreviations and acronyms (subjects)	
AWF	analytic wall functions
APG	adverse pressure gradient
ASM	algebraic second-moment (closure)
A(R)SM	algebraic (Reynolds) stress model
AFM	algebraic flux model
BWT	blended wall treatment
CFD	computational fluid dynamics
CFL	Courant, Friedrichs and Lewy number, Eq. (10.18)
CV	control volume
DDES	delayed DES

DES	detached eddy simulation
DIHRL	dynamically interfaced HRL
DNS	direct numerical simulation
DSM	differential second-moment closure
EA(R)SM	explicit algebraic (Reynolds) stress model
EB	elliptic blending
ELES	embedded LES
ER	elliptic relaxation
ER	expansion ratio
EVM	eddy-viscosity model
Exp.	experiment
FPG	favourable pressure gradient
GGD(H)	generalized gradient diffusion (hypothesis)
GWF	generalized wall functions
HRL	hybrid RANS-LES
HTM	hybrid turbulence model
IP	isotropization of production
LES	large eddy simulation
NWF	numerical wall functions
NLEVM	non-linear EVM
PANS	partially averaged Navier–Stokes
PITM	partially integrated transport model
QI	quasi-isotropic
RANS	Reynolds-averaged Navier–Stokes
RDT	rapid distortion theory
RNG	renormalization group theory
RSM	Reynolds stress model
SA	Spalart–Allmaras
SAWF	simplified analytical wall functions
SMC	second-moment closure
SST	shear-stress transport (model)
TRANS	time-resolved (triple-decomposition based) RANS
URANS	unsteady RANS
VLES	very large eddy simulation
WF	wall function(s)
WIN	wall integration (model)
WMLES	wall-modelled LES
ZPG	zero pressure gradient

Author abbreviations	
CLS	Craft, Launder, Suga
CKL	Craft, Kidger, Launder
DFJ	Dianat, Fairweather, Jones
FLT	Fu, Launder, Tselepidakis
GL	Gibson, Launder
GS	Gatski, Speziale
HJ	Hanjalić, Jakirlić
HL	Hanjalić, Launder
JM	Jones, Musonge
JMG	Jongen, Mompean, Gatski
LRR	Launder, Reece, Rodi
LS	Launder, Sharma
LT	Launder, Tselepidakis
SA	Spalart, Allmaras
SL	Shih, Lumley
SSG	Speziale, Sarkar, Gatski
WJ	Wallin, Johansson

1

Introduction

1.1 The fact of turbulent flow

Man has evolved within a world where air and water are, by far, the most common fluids encountered. The scales of the environment around him and of the machines and structures his ingenuity has created mean that, given their relatively low kinematic viscosities, the relevant global Reynolds number, Re, associated with the motion of both fluids is, in most cases, sufficiently high that the resultant flow is of the continually time-varying, spatially irregular kind we call *turbulent*.

If, however, our Reynolds number is chosen not by the overall physical dimension of the body of interest – an aircraft wing, say – and the fluid velocity past it but by the smallest distance over which the velocity found within a turbulent eddy changes appreciably and the time over which such a velocity change will occur, its value then turns out to be of order unity. Indeed, one might observe that if this last Reynolds number, traditionally called the micro-scale Reynolds number, Re_η, were significantly greater than unity, the rate at which the turbulent kinetic energy is destroyed by viscous dissipation could not balance the overall rate at which turbulence 'captures' kinetic energy from the mean flow.

This immutable fact of turbulence life lies at the heart of the problem of computing turbulent flows. Any complete numerical solution of the Navier–Stokes equations must resolve accurately these fine-scale motions as well as the large-scale overall flow picture in which we are interested. Because of the range of scales to be resolved, from the fine-scale dissipative motions to the complete flow field, it is only feasible at present to carry out such a *direct numerical simulation* (DNS) of turbulent flow for relatively simple shear flows for overall Reynolds numbers typically of order 10^5 and then only with 'supercomputer' scales of hardware. If one is, thus, to embark on the computation of practically interesting turbulent flows reasonably cheaply (recognizing that in most cases one needs to make tens or even hundreds of computations of the same geometric configuration to obtain

https://doi.org/10.1017/9781108875400.003 Published online by Cambridge University Press

a sufficiently full picture), some form of modelling is essential to compensate for being unable to resolve directly all the turbulence scales as well as the mean flow.

1.2 Broad options in modelling

Two broad strategies for modelling are commonly employed.

- Large-eddy simulation (LES), where one resolves as large a proportion of the turbulent fluctuations as one judges necessary (or can afford) and applies a model – a sub-grid-scale (sgs) model – to account for the effects of those motions of a finer scale than can be resolved with the adopted mesh. The principal needs, so far as the dynamic field is concerned, are to account for momentum transfer by the unresolved motions and to ensure that kinetic energy is removed from the simulation at the appropriate rate (which amounts to modelling the effective sgs stresses created in the fluid).
- Reynolds-averaged Navier–Stokes (RANS) equations, in which the effects of *all* the turbulent fluctuations are subsumed within the model – generally termed *the turbulence model*. As with LES, the non-linearity of the convective transport means that models are needed to account for the effective turbulent fluxes of momentum, enthalpy and chemical species in their respective transport equations. These are termed the turbulent (or Reynolds) stresses and the turbulent heat or mass fluxes; they emerge naturally in Chapter 2 and are shown symbolically as $\overline{u_i u_j}$ and $\overline{\theta u_j}$, where u_i and θ denote turbulent fluctuations of velocity and the scalar in question about their mean value and the overbar implies time averaging.

It is this second approach to modelling turbulence that is the principal focus of the present book. There are also strategies that are, effectively, a blend of these two approaches. Such schemes form the subject of the book's final chapter; but, for the present, they are not considered further, except to remark that the development of such hybrid approaches reflects, in part, the inadequacies of the RANS models that are most commonly used in engineering computations. Thus, if more generally applicable approaches to RANS closure are adopted, that, on the one hand, reduces the need to resort to such hybrid LES-RANS schemes while, on the other, also provides a more secure RANS component in situations where such combined approaches are necessary or desirable.

A comparative illustration of the numerical resolution of turbulent flow in a pipe or channel required by these different numerical approaches – DNS, LES and RANS – is shown in Fig. 1.1. A random-like oscillating signal with sharp peaks (top figure, left) provides a snapshot of the true instantaneous velocity, $\hat{U}$, in a vertical cross plane. A properly resolved DNS (with the computational cells

https://doi.org/10.1017/9781108875400.003 Published online by Cambridge University Press

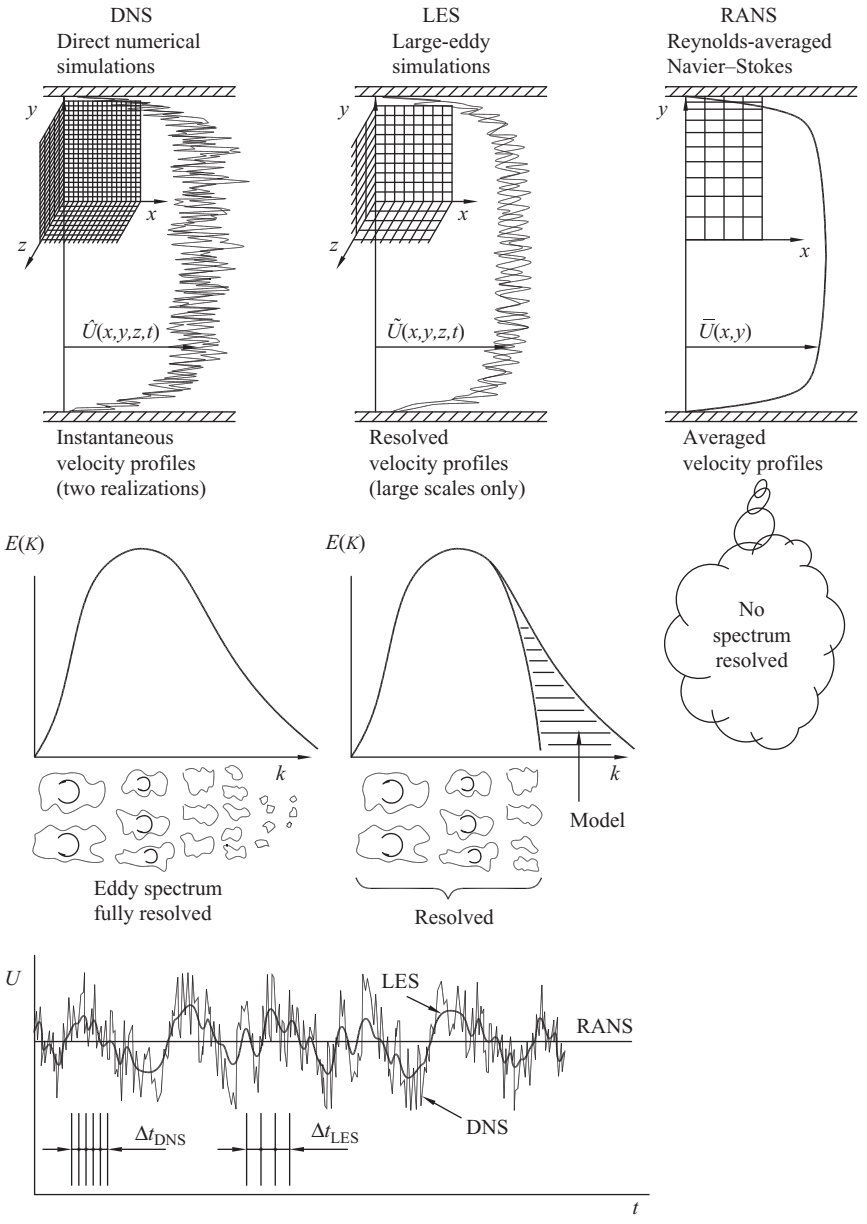

Fig. 1.1 Illustrative comparison of DNS, LES and RANS simulations of a fully developed, steady turbulent flow in a pipe or a plane channel. Top: typical computational grids and sketches of a set of instantaneous velocity profiles ($\hat{U}$) from DNS, filtered velocity profiles ($\tilde{U}$) from LES, and the time-averaged profile ($\bar{U}$) obtained by RANS. Centre: a sketch of the resolved energy spectrum $E(\kappa)$ for DNS and LES (note: RANS is also called 'one-point closure' because it computes the averaged turbulence properties at a point in space with no information on the turbulence spectrum). Bottom: time signal at a point in the flow and typical time steps for DNS and LES. The RANS solution, by definition, gives a constant velocity at a point in a steady flow.

https://doi.org/10.1017/9781108875400.003 Published online by Cambridge University Press

smaller than the smallest important eddy size) will provide the complete range of wavelengths of velocity fluctuations. The instantaneous velocity profile obtained by LES (top figure, middle) also shows a range of wavelengths, but because the computational mesh is coarser, the signal is somewhat smoother, representing the filtered velocity $\tilde{U}$. High frequencies, i.e. those with a wavelength smaller than the computational cells, are absent because they have been filtered out. The top-right figure shows the time-averaged velocity $\bar{U}$ which exhibits a smooth profile that can be obtained with a much coarser grid and which, for a simple shear flow such as considered here, may be just two dimensional.

The second row of figures illustrates the *resolved* energy spectrum $E(\kappa)$ determined using each of the methods. Here $E(\kappa)$ represents the contribution to the turbulence kinetic energy from all Fourier modes in the range from κ to $\kappa + d\kappa$, where $\kappa = 2\pi/\lambda$ is the wavenumber modulus and λ is the wavelength. Naturally, DNS should provide the complete spectrum, while LES excludes only the high wavenumber portion (beyond $\kappa_c = 2\pi/\Delta$, where Δ is the characteristic mesh size). In contrast, RANS can provide *no information* about the turbulence spectrum, but simply the value of the turbulence energy that would be obtained by integrating over the whole wavenumber range for any point in space.

The bottom figure illustrates the three methods in a different way: here a time record of fluid velocity is shown at a point in space in a steady flow. Again, the strongly oscillating peaky signal (such as would be recorded by a hot-wire anemometer) is representative of a typical DNS of velocity fluctuations at a point. The smoother oscillating signal is a typical LES result, whereas the RANS record would simply give a constant value. Resolving the DNS signal requires very small time steps, whereas LES tolerates a somewhat larger time step corresponding with the coarser computational mesh.

Both LES and RANS have particular strengths and dedicated proponents. Because, using LES, with the numerical solver one resolves directly a large proportion of the energy-containing turbulent motions, the model is less crucial to the computed behaviour of the flow than it is with RANS. Thus, a far from accurate sgs model may nevertheless lead to satisfactory numerical simulations. Just how important the sgs model is naturally depends on how large a proportion of the total effect of the turbulence it is required to carry. Currently, the most common strategy in sgs modelling is to assume that the magnitude of the components of the sgs stresses is directly proportional to the corresponding components of the resolved strain, the coefficient of proportionality being what is termed the sgs kinematic viscosity. The computational cost of an LES calculation naturally depends greatly on the fineness of the computational mesh chosen.

With a RANS approach, to a far greater extent than with LES, the fidelity of the computed flow hinges on a wise choice of model. The great majority of computations at present, particularly those for industrial applications for

https://doi.org/10.1017/9781108875400.003 Published online by Cambridge University Press

complex-shaped configurations, still employ a linear eddy-viscosity model where the local value of the turbulent (or eddy) kinematic viscosity, υ_t, is computed in the course of the solution, usually by way of supplementary transport equations for what amount to representative length and time scales for the energy-containing turbulent motions.

Within RANS there is, however, a hierarchy of alternative, more elaborate modelling strategies available, ranging from non-isotropic turbulent viscosity models to schemes which provide modelled transport equations of the individual turbulent stresses (or second moments) as well as their diffusion (the third moments). The focus of this book is on such alternative strategies with our primary attention being on modelling the second moments. The reason for this choice is simply that turbulent shear flows are not in any general sense describable by a model based on a linear eddy-viscosity model, while a well-crafted second-moment closure extends greatly the range of flows and phenomena that can be captured. Merely considering the stress-generation processes, as is done briefly in Section 1.3, allows one to appreciate why turbulent flows respond, qualitatively, as they do to the application of mean flow deformations of various types.

The discussion on modelling via second-moment closure has so far considered simply the turbulent stresses. If the processes of interest involve heat or mass transport, the averaged forms of the thermal energy and species transport equations likewise contain unknown turbulent second-moment correlations: the turbulent heat and species fluxes. Within a linear eddy-viscosity scheme these rates of transfer in any direction are taken directly proportional to the corresponding spatial gradient of mean temperature and mean species concentration, respectively. Such an assumption has similar shortcomings to that of the eddy viscosity approximation for momentum transport. Solving transport equations for these other second moments brings corresponding benefits to those for the turbulent stresses, especially where buoyant force fields are significant.

1.3 A preview of the mean-strain generation processes in the stress-transport equation

One of the attractions of second-moment closure compared with simpler approaches to modelling is that the second-moment generation terms are exactly represented and thus require no further approximation. This fact means that, where these terms are major contributors to the budget for the second moment in question, one is half-way to closure without having to make any approximations. Moreover, without completing a model for the remaining processes, one can often infer the character of a turbulent flow just by simply noting how the generation

https://doi.org/10.1017/9781108875400.003 Published online by Cambridge University Press

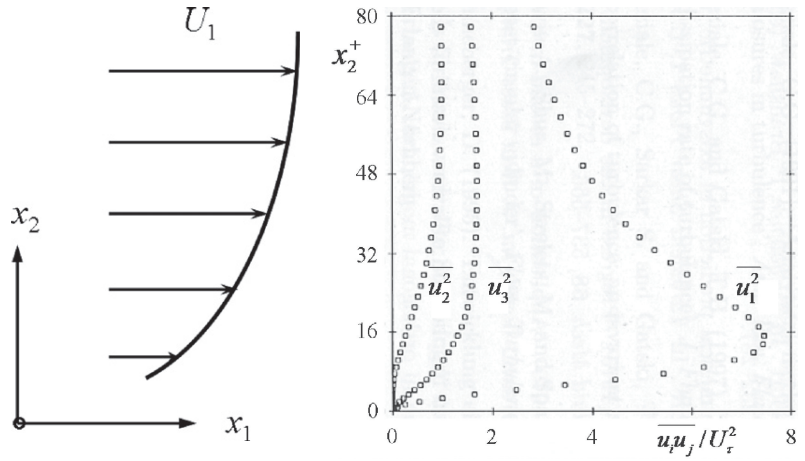

Fig. 1.2 A simple shear flow: (a) typical mean velocity profile; (b) turbulent normal stress components in a plane channel flow, as a function of the non-dimensional wall distance $x_2^+ \equiv x_2 U_\tau/\nu$ (where U_τ is the wall friction velocity and ν is fluid kinematic viscosity). From the DNS of Kim *et al.* (1987).

is distributed among the turbulent stresses or heat fluxes for different externally applied conditions.

A formal derivation of the second-moment equations is deferred to Chapter 2 but here, to convey in advance some impression of the insight gained from a knowledge of the mean-strain generation process, we examine a few examples for commonly arising strain fields. In the absence of force fields, the interaction between the mean strain and the existing turbulence provides the source for further stress creation. Thus, in most circumstances, once a flow becomes turbulent it remains turbulent. The turbulent stress-generation tensor, $\mathcal{P}_{ij}$, in a uniform density flow will be shown in §2.3 to be given by

$$\mathcal{P}_{ij} = -\left(\overline{u_i u_k}\frac{\partial U_j}{\partial x_k} + \overline{u_j u_k}\frac{\partial U_i}{\partial x_k}\right) \tag{1.1}$$

where $\overline{u_i u_j}$ denotes the turbulent stress and $\partial U_i/\partial x_k$ is the gradient of the mean-velocity component in direction x_k.

Let us first see how these generation terms are distributed among the different Reynolds-stress components for the case of a simple shear flow where the mean flow is purely in direction x_1 and varies only in the x_2 direction, Fig. 1.2a. This is very nearly the situation that applies in a two-dimensional boundary layer. The resultant values of $\mathcal{P}_{ij}$ for each of the six stress components are obtained by assigning appropriate values to i and j. The repeated subscript k signals that elements carrying that subscript are to be summed with k taking successively the values 1, 2

https://doi.org/10.1017/9781108875400.003 Published online by Cambridge University Press

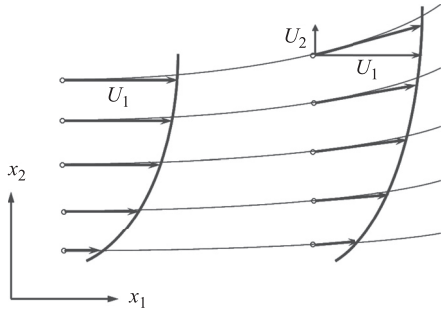

Fig. 1.3 Example of a mildly curved turbulent shear flow.

and 3. In the present case, however, the mean velocity varies only in direction x_2, so only $k = 2$ makes a contribution to $\mathcal{P}_{ij}$. The reader may thus readily verify that:

$$\begin{aligned}
\overline{u_1^2} \quad & \mathcal{P}_{11} = -2\,\overline{u_1 u_2}\frac{\partial U_1}{\partial x_2} \\
\overline{u_2^2} \quad & \mathcal{P}_{22} = 0 \\
\overline{u_3^3} \quad & \mathcal{P}_{33} = 0 \\
\overline{u_1 u_3} \quad & \mathcal{P}_{13} = 0 \\
\overline{u_2 u_3} \quad & \mathcal{P}_{23} = 0 \\
\overline{u_1 u_2} \quad & \mathcal{P}_{12} = -\overline{u_2^2}\frac{\partial U_1}{\partial x_2}.
\end{aligned} \tag{1.2}$$

It is noted from the last of these results that the generation rate of the shear stress, $\overline{u_1 u_2}$, is opposite in sign from the mean velocity gradient, a fact which explains why the shear stress itself normally has a sign opposite from the velocity gradient. Note, too, that turbulent velocity fluctuations in the direction of the mean velocity gradient are instrumental in creating that shear stress (or momentum transfer). Regarding the normal stresses, it is perhaps surprising that the only component in which there is a generation is the streamwise component, $\overline{u_1^2}$. As reference to thin shear flow data readily confirms, Fig. 1.2b, this component is by far the largest stress though turbulent fluctuations do occur in all directions. Where, in practice, the source of the fluctuating energy (or normal stresses) in directions x_2 and x_3 comes from will become clear in Chapter 2.

Let us next add a small degree of complexity to the strain field by imagining a weak streamline curvature in the x_1–x_2 plane, Fig. 1.3. We retain Cartesian coordinates so the curvature manifests itself by a non-zero value of $\partial U_2/\partial x_1$. Thus, from Eq. (1.1) the shear-stress generation becomes:

$$\mathcal{P}_{12} = -\left(\overline{u_2^2}\frac{\partial U_1}{\partial x_2} + \overline{u_1^2}\frac{\partial U_2}{\partial x_1}\right). \tag{1.3}$$

https://doi.org/10.1017/9781108875400.003 Published online by Cambridge University Press

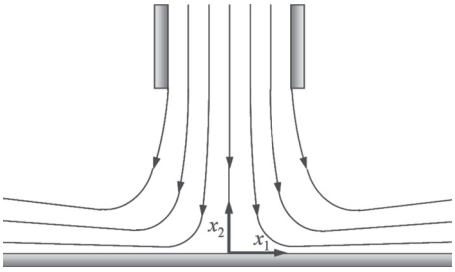

Fig. 1.4 Sketch of the stagnation region in a jet impinging normally on a flat wall.

It is evident from Fig. 1.2b that even far from the wall $\overline{u_1^2}$ is at least twice as large as $\overline{u_2^2}$, a situation that also pertains in strong free shear flows, like a jet. In a flow past a solid surface, however, as one progressively approaches the wall, the disparity between the two normal stresses becomes progressively greater, Fig. 1.2b. Thus, the effect of the curvature term in Eq. (1.3) becomes greatly amplified. Indeed, the great sensitivity of boundary layers to wall curvature has been known for many years (Bradshaw, 1973). If, however, one were to assume turbulent stresses were represented by an isotropic turbulent viscosity, ν_t, one would conclude:

$$\overline{u_1 u_2} = -\nu_t \left(\frac{\partial U_1}{\partial x_2} + \frac{\partial U_2}{\partial x_1} \right). \tag{1.4}$$

In this representation, the weighting of the two strain components is equal, each being multiplied by the scalar turbulent viscosity.[1] The above example provides the first illustration of the over-simplification produced by the eddy viscosity formula alluded to in §1.2.

An even sharper example is provided in the case of impinging flow. Let us consider the rate at which turbulent kinetic energy is being produced by virtue of the mean-flow straining along the centre-line of a plane, symmetric stagnation flow, Fig. 1.4. The turbulence energy, k, is just half the sum of the normal stresses and its production rate, $\mathcal{P}_k$, is thus:

$$\mathcal{P}_k = -\overline{u_i u_j} \frac{\partial U_i}{\partial x_j}. \tag{1.5}$$

Along the symmetry plane the turbulence energy generation arises purely from the normal strains, which, we assume, are adequately represented by the potential flow solution for plane stagnation flow: $\partial U_1/\partial x_1 = -\partial U_2/\partial x_2 = C$, a constant.

[1] It should be recognized that Eq. (1.3) expresses the *production rate* of the shear stress, while Eq. (1.4) refers to the shear stress itself. However, as will be seen later, at least in stress components with major stress generation terms, the stress production rate is indeed closely related to the magnitude of the stress.

https://doi.org/10.1017/9781108875400.003 Published online by Cambridge University Press

Thus:

$$\mathcal{P}_k = -\left(\overline{u_1^2}\frac{\partial U_1}{\partial x_1} + \overline{u_2^2}\frac{\partial U_2}{\partial x_2}\right) = C\left(\overline{u_2^2} - \overline{u_1^2}\right). \tag{1.6}$$

From Eq. (1.6) it is evident that for this flow the rate of production of turbulent kinetic energy depends on the difference between the normal stresses, i.e. on the anisotropy of the turbulent stress field. The value of $\mathcal{P}_k$ may be positive, negative or zero depending on the relative levels of the two normal stresses. If, however, the turbulence energy generation had been represented by a turbulent viscosity, it is easily verified that the following form would be obtained:

$$\mathcal{P}_k = 4\nu_t C^2. \tag{1.7}$$

Equation (1.7) implies no such sensitivity to anisotropy; indeed, in all circumstances it returns an erroneously high energy generation rate. Computations of impinging flows with eddy viscosity models thus lead to quite spurious peaks of turbulence energy in the vicinity of a stagnation point unless problem-specific corrections are adopted (Taulbee and Tran, 1988; Craft *et al.*, 1993; Durbin, 1996). A similar anomalous outcome of using eddy-viscosity models has also been observed in other flows where normal straining plays an important role. For example, both the analytical and numerical solutions for confined homogeneous turbulence subjected to cyclic compressive/dilatational strain show that depending on the sign of the strain the turbulence production takes alternately positive and negative values, resulting in zero net production over a cycle (Hadžić *et al.*, 2001). Because of the continuous dissipation, however, both the turbulent kinetic energy and the characteristic turbulence frequency (the reciprocal of the turbulent time scale) eventually decay, irrespective of the initial turbulence level, anisotropy of the stress field or Reynolds number. In contrast, eddy viscosity models predict an erroneous continual increase of the turbulent kinetic energy because of the incorrect positive generation of turbulence during the compression phase. Other examples where the broad character of a turbulent flow can be inferred from considering the stress generation terms may be found in flows affected by body forces whether due to system rotation (Coriolis force), density stratification (buoyant force) or magnetic field (Lorentz force). Such cases are discussed in detail in §4.5.

1.4 Some consequences of the no-slip boundary condition at a wall

At a rigid, stationary wall the velocity goes to zero, at least in the continuum regime to which attention is limited. This condition applies to the turbulent fluctuations as well as to the mean velocity. Thus the turbulent stresses all vanish at the wall and wall friction is exerted through purely viscous effects just as in laminar flow.

https://doi.org/10.1017/9781108875400.003 Published online by Cambridge University Press

As is evident from Fig. 1.2b, however, the turbulent velocity components do not all increase at the same rate as one moves away from the wall. There are several reasons for this, as will emerge in Chapters 4 and 6, but one that is examined here briefly is the constraint applied by mass conservation. For a uniform density flow, as will be shown formally in §2.3, the turbulent velocity fluctuations as well as the mean flow are divergence free:

$$\frac{\partial u_1}{\partial x_1} + \frac{\partial u_2}{\partial x_2} + \frac{\partial u_3}{\partial x_3} = 0. \tag{1.8}$$

This equation applies everywhere, including the fluid–wall interface $x_2 = 0$. But on this surface $\partial u_1/\partial x_1 = \partial u_3/\partial x_3 = 0$ since u_1 and u_3 are zero throughout the $x_1 \sim x_3$ plane. It follows that $\partial u_2/\partial x_2$ must also be identically zero there. Thus, we deduce that, while the root-mean-square values of u_1 and u_3 initially increase linearly with distance from the wall, x_2, the corresponding value of u_2 can only increase as x_2^2, while the shear stress $\overline{u_1 u_2}$ can at most increase as x_2^3. These inferred exponents of the different stress-component variations will be seen in Chapter 6 to be fully in accord with DNS data.

The fact that $\overline{u_1 u_2}$ increases as the cube of the distance from the wall implies that initially, for small x_2, this turbulent shear stress will be negligible compared with viscous shear stress. As one proceeds further from the wall, however, one enters a region where there is a rapid changeover to a regime where the turbulent stress becomes the dominant contributor to momentum transfer. Since the total shear stress (viscous plus turbulent) is very nearly constant over what is a very thin layer (compared with the shear flow as a whole), there will inevitably be a rapid reduction in the slope of the mean velocity. That is, one moves from a region where viscous action ($\nu \partial U_1/\partial x_2$) is the principal mechanism for momentum transfer to one where most of the momentum transport is by turbulence. This rapid changeover is clearly evident from the mean velocity profiles in Fig. 1.1, top right (denoted as RANS), and in more detail in Fig. 6.1.

In fact, in a simple shear flow, the maximum generation rate of turbulent kinetic energy occurs right in this changeover region. For, this will occur where

$$\frac{d}{dx_2}\left(\overline{u_1 u_2}\frac{dU_1}{dx_2}\right) = 0, \tag{1.9}$$

or, on expanding the differential, where:

$$\overline{u_1 u_2}\,\frac{d^2 U_1}{dx_2^2} + \frac{dU_1}{dx_2}\frac{d\,\overline{u_1 u_2}}{dx_2} = 0. \tag{1.10}$$

On the assumption that the total shear stress ($(\nu dU_1/dx_2) - \overline{u_1 u_2}$) is changing much less rapidly than its constituent parts, we can replace the turbulent shear-stress derivative in Eq. (1.10) by the corresponding derivative of viscous stress. With this

https://doi.org/10.1017/9781108875400.003 Published online by Cambridge University Press

substitution and after cancelling the common factor d^2U_1/dx_2^2, it emerges that the maximum turbulence energy generation rate occurs where $-\overline{u_1u_2} = \nu dU_1/dx_2$, i.e. where the turbulent and viscous stresses are equal!

The discussion above has brought out a few of the challenges posed by the near-wall sublayer where viscous as well as turbulent transport is important. Although the region usually occupies much less that 1% of the total flow volume, it is a vitally important, albeit complex region to model. Indeed, the question of how the flow within this sublayer is modelled is examined explicitly in Chapter 6.

1.5 Sequencing of the material

Following this brief glimpse of the potential and one of the major areas of difficulty in modelling at second-moment level, Chapter 2 begins the formal journey by developing the exact set of equations that needs to be modelled and then solved within second-moment closure. These equations are 'un-closed', meaning that they contain terms whose value is not directly knowable and for which closure approximations must be provided. It also discusses some of the physical features of turbulent flow that need to be borne in mind when devising closure approximations. Chapter 3, while not directly concerned with closure, explores a number of issues relating to turbulence characterization and introduces certain invariant parameters that will be of great help in modelling.

Chapter 4 is the first chapter on turbulence modelling itself and it covers many of the key aspects of closing the second-moment equations. Three types of process are considered: the roles of pressure-containing products, triple and higher order products and the dissipative actions of viscosity. Different levels of approximation are proposed, usually proceeding from the simplest to the most complex. This chapter includes cases where force fields exert a substantial effect on the turbulence structure. While buoyancy and rotation are the most common and important of these, electromagnetic force fields are also important in a number of geophysical flows and also, potentially, in engineering where the emphasis is on turbulence control. Chapter 5 explores routes for determining the turbulence energy dissipation rate and thus turbulent time and length scales of the energetic motions. To complete this modelling trilogy, Chapter 6 develops the important modifications to the closure model that are required if it is necessary or desirable to carry the second-moment computations through the viscosity-affected sublayer to the wall itself.

Not all practically interesting flows require a modelling strategy as comprehensive as second-moment closure, however. Thus, in Chapter 7 various types of simplification are introduced that are applicable in particular types of flow. By including a few examples where the approximations in question are manifestly

unsuccessful, however, we hope to provide a reminder that such simplified schemes always need to be applied with caution and with a broad qualitative understanding of how the prevailing flow conditions are likely to affect the second moments of interest. Provided that is done, the eddy-viscosity model, referred to disparagingly above, may reappear as a simple yet viable approach for many nearly two-dimensional thin shear flows where gradients normal to the wall far outweigh those in other directions. Chapter 8 applies further modelling simplifications to the wall-adjacent sublayer region. Even if one simplifies the model in this region to an eddy-viscosity form, the requirements for an extra-fine mesh to resolve accurately the complex variation of both the turbulence-field variables and the source and sink processes that determine their level can mean that the great majority of computer resources are consumed in resolving this region. Sometimes that is the inevitable price to pay for reliable predictions; but in many others, simpler strategies are possible. Chapter 8 presents the strategy commonly used in CFD software and four much newer approaches developed by the authors and their colleagues that provide more comprehensive and reliable schemes.

Chapter 9 explores the additional possibilities that arise in certain types of flow from treating the flow as unsteady – even if to an observer the flow may appear steady. Such situations arise especially, though not exclusively, in conditions where destabilizing force fields play a dominant role. Then the adoption of a time-dependent solution of the mean and turbulent flow equations frequently leads to the large-scale unsteadiness of the turbulent motion being rather well resolved. Indeed, the faithful capturing of the turbulence macro-structure is particularly striking when second-moment-closure approaches are adopted. The scope and limitations of this unsteady RANS (or URANS) mode of analysis is still the subject of research though, from the examples presented, it clearly has a substantial role to play in the hierarchy of approaches to capturing turbulent flows.

It is not implied, however, that a RANS or URANS approach to modelling is always the best option. The greater detail and the greater assured accuracy of an LES will, for particular flows, make the added computational cost and time worth spending, especially if the region of flow where such an approach is adopted can be limited. In Chapter 10, the concept of hybrid RANS–LES schemes is introduced, where some of the most promising approaches are presented, in what is still a rapidly evolving field. The aim of this hybrid strategy is to insert a more accurate LES modelling just in a limited region where the RANS approach is particularly liable to error. The most important issue in implementing such a strategy is how one handles the interface conditions or the blending strategy between these two modelling approaches.

2

The exact equations

2.1 The underpinning conservation equations

It is presumed that the reader is familiar with the basic laws of mass, momentum and energy conservation, which describe fluid motion and thermal transport. Nevertheless, it is instructive to outline the basic equations, their physical interpretation and principles of averaging as used in RANS methods for computing turbulent flows and associated transport phenomena. This short section will also introduce the nomenclature and the assumptions adopted throughout the book.

2.1.1 Navier–Stokes equations of fluid motion

The instantaneous velocity field in a turbulent flow is described by the continuity and the momentum (Navier–Stokes) equations expressing the conservation of mass and momentum (Newton's second law) for an infinitesimal control volume ('a point') in space, which in conservative form may be written as:

$$\frac{\partial \hat{\rho}}{\partial t} + \frac{\partial (\hat{\rho}\hat{U}_i)}{\partial x_i} = 0, \tag{2.1}$$

$$\frac{\partial (\hat{\rho}\hat{U}_i)}{\partial t} + \frac{\partial (\hat{\rho}\hat{U}_j\hat{U}_i)}{\partial x_j} = \sum_n \hat{F}_i^n - \frac{\partial \hat{P}}{\partial x_i} + \frac{\partial}{\partial x_j}\left[\hat{\mu}\left(\frac{\partial \hat{U}_i}{\partial x_j} + \frac{\partial \hat{U}_j}{\partial x_i} - \frac{2}{3}\frac{\partial \hat{U}_k}{\partial x_k}\delta_{ij}\right)\right], \tag{2.2}$$

where $\hat{P}$ denotes pressure, $\hat{\rho}$ and $\hat{\mu}$ are the density and dynamic viscosity of the fluid, respectively, and $\hat{F}_i$ denotes body force per unit volume. The term in square brackets is in fact the viscous stress, τ_{ij}, for a Newtonian fluid. Together with the pressure it represents the total stress, i.e. the force per unit area acting on the surface of an elementary fluid control volume. When spatial gradients of density are

https://doi.org/10.1017/9781108875400.004 Published online by Cambridge University Press

unimportant, the analysis in later chapters will generally employ kinematic stresses, τ_{ij}/ρ, and the corresponding kinematic viscosity ν.

The circumflexes appearing above all quantities serve as a reminder that each, potentially, will display fluctuations due to turbulence. In the majority of situations of practical relevance (excluding flows affected by buoyancy and combusting flows), density and viscosity fluctuations at a point will be sufficiently small to have negligible direct effect on turbulence and will therefore be disregarded. Furthermore, in many cases of interest the fluid can be assumed to be incompressible at any time instant, i.e. one where $\partial \hat{U}_i/\partial x_i = 0$.

2.1.2 Scalar transport

The transport of some instantaneous scalar property $\hat{\Theta}$ by the turbulent motion can be derived from the scalar conservation equation, which is expressed as:

$$\frac{\partial(\hat{\rho}\hat{\Theta})}{\partial t} + \frac{\partial(\hat{\rho}\hat{U}_j\hat{\Theta})}{\partial x_j} = \hat{S}_\Theta + \frac{\partial}{\partial x_j}\left(\hat{\gamma}\frac{\partial\hat{\Theta}}{\partial x_j}\right), \tag{2.3}$$

where $\hat{\gamma}$ is the appropriate molecular diffusivity and $\hat{S}_\Theta$ is the source, i.e. the rate of creation of the property per unit volume. As in Eq. (2.2), for many flows, the turbulent fluctuations of density and molecular diffusivity can be neglected, though their variation over the flow due to significant variation of temperature, chemical composition and pressure must be accounted for.

The scalar property most frequently considered in engineering and environmental flows is the specific enthalpy of the fluid $\hat{h}$ for which case Eq. (2.3) denotes the instantaneous energy conservation (the first law of thermodynamics). However, it will be convenient to choose the temperature as the subject of Eq. (2.3), in which case the instantaneous temperature, $\hat{\Theta}$, is related to the instantaneous enthalpy, $\hat{h}$, via $d\hat{h} = c_p d\hat{\Theta}$, where c_p is the specific heat at constant pressure. $\hat{S}_\Theta$ is then the internal source of energy per unit volume (heat generation by Joule heating, chemical or nuclear reaction) divided by c_p and $\gamma = \lambda/c_p$, where λ is the thermal conductivity of the fluid. For convective heat transfer, with $\hat{\Theta}$ denoting temperature, when the density is uniform, Eq. (2.3) is usually divided by ρ, in which case γ becomes the thermal diffusivity $\alpha \equiv \lambda/(\rho c_p)$. Likewise, $\hat{\Theta}$ can stand for mass concentration of a species, with $\hat{S}_\Theta$ denoting the reaction rate (if any) for that species.

Besides conventional sources or sinks, we can conveniently imagine the term $\hat{S}_\Theta$ absorbing any terms that, for a particular transported scalar property, do not fit elsewhere. For example, the molecular diffusion process can be governed by a more elaborate law than supposed by the simple gradient-diffusion relation while, if $\hat{\Theta}$ stands for temperature, the time-dependent term in the equation should strictly

https://doi.org/10.1017/9781108875400.004 Published online by Cambridge University Press

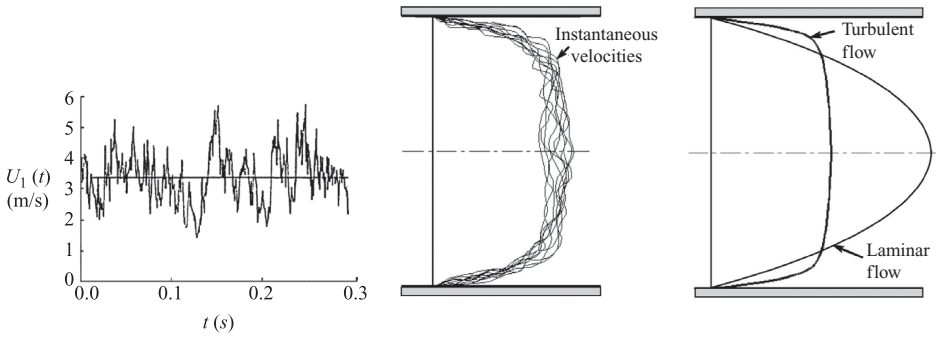

Fig. 2.1 Left: measured axial velocity fluctuations at a point in a steady turbulent flow. Centre and right: a selection of time realizations and mean velocity profiles across a cross section of a pipe.

be multiplied by the specific heat at constant volume divided by that at constant pressure, a difference that can be absorbed into $\hat{S}_\Theta$.

2.2 The Reynolds equations

As observed in Chapter 1, the numerical solution of Eqs. (2.1) to (2.3) is the target of direct numerical simulations (DNS). Because of the non-stationary, three-dimensional character of turbulence, the equations must always be solved in time and in all three space coordinates, thus inevitably requiring huge computing resources. Large-eddy simulations (LES) are less demanding because a coarser grid and larger time increments are employed, with the effects of the unresolved sub-grid-scale motion being accounted for by an empirical model for the sub-grid-scale stress. Nevertheless, a large portion of the spectrum still needs to be resolved numerically in time and three-dimensional space so that the computing resources, especially for high Reynolds number, wall-bounded flows, remain formidable for most industrial applications.

Thus, for the great majority of flows relevant to industry or the environment, the RANS approach is at present the only practicable option. Not only does it tolerate a much coarser computational grid, but, in many practical situations, the flow may be regarded as steady in the mean; the problem then reduces to one involving only spatial variations. Indeed, it even reduces to two space coordinates if the flow is homogeneous in one direction or possesses axial symmetry.

An illustration of the instantaneous and averaged velocity field in a pipe is provided in Fig. 2.1. A time history of velocity at a point in a turbulent flow shows irregular, non-repeating fluctuations, despite the fact that the average flow rate is constant (a steady flow), Fig. 2.1, left. Likewise, a sequence of instantaneous distributions of velocity across the pipe cross section shows a collection of

https://doi.org/10.1017/9781108875400.004 Published online by Cambridge University Press

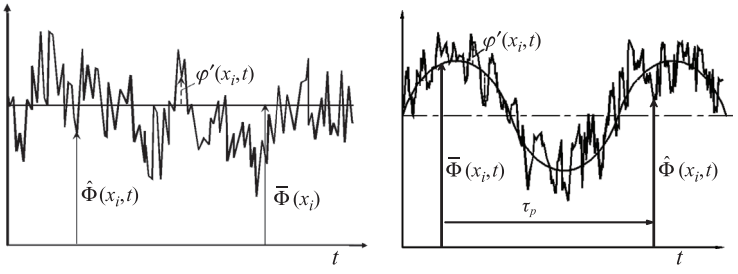

Fig. 2.2 Illustration of time and phase averaging, respectively.

non-repeatable irregular curves (velocity field realizations) with only one common value: zero at the wall, Fig. 2.1, centre. However, we are usually not interested in the instantaneous values of velocity but rather in the averaged field and its effects and consequences – forces on structures, friction, drag, heat and mass transfer. The mean velocity profile for turbulent flow through a pipe, obtained by averaging a large number of instantaneous realizations, is shown in Fig. 2.1, right. For comparison, the laminar (parabolic) velocity profile for the same flow rate is also shown.

2.2.1 Reynolds decomposition and averaging

The averaging of a fluctuating field can be accomplished in various ways, but most methods make use of the *Reynolds decomposition* by which an instantaneous variable $\hat{\Phi}$ (velocity, pressure, temperature, etc.) is expressed as the sum of the average or mean value, $\bar{\Phi}$, and fluctuation around that mean, φ'

$$\hat{\Phi} = \bar{\Phi} + \varphi'. \tag{2.4}$$

The RANS approach necessarily implies time averaging over a sufficient time interval for an unambiguous mean value to be established, and it is, strictly speaking, applicable only to *stationary* flows, Fig. 2.2, left,

$$\bar{\Phi}(x_i) = \lim_{\tau\to\infty} \frac{1}{\tau} \int_0^\tau \hat{\Phi}(x_i, t)dt = \overline{\hat{\Phi}}(x_i). \tag{2.5}$$

It follows from applying this averaging strategy to each side of Eq. (2.4) that

$$\overline{\varphi'} = \lim_{\tau\to\infty} \frac{1}{\tau} \int_0^\tau \varphi'(x_i, t)dt = 0. \tag{2.6}$$

Thus, for stationary turbulence, the decomposition can be expressed in terms of the independent variables as

$$\hat{\Phi}(x_i, t) = \bar{\Phi}(x_i) + \varphi'(x_i, t). \tag{2.7}$$

https://doi.org/10.1017/9781108875400.004 Published online by Cambridge University Press

The time averaging can also be applied to unsteady flows if the characteristic timescale of the mean flow is much larger than that of turbulence. Of course, the integration time interval τ should always be sufficiently large to make it possible to define uniquely the mean values of the turbulent fluctuations, but sufficiently small for the mean value to be independent of τ.

If the bulk flow varies significantly with time, and with a timescale not much larger than those of the lowest frequency turbulent fluctuations, the time average has no meaning and we need to use other ways of averaging. In cases where the flow exhibits a periodicity (not necessarily sinusoidal or regular in any other way) with an identifiable period τ_p, it is convenient to adopt the *phase averaging* over n_p periods, Fig. 2.2, right

$$\bar{\Phi}(x_i) = \lim_{n_p \to \infty} \frac{1}{n_p} \sum_{n=0}^{n_p} \hat{\Phi}(x_i, t + n\tau_p). \tag{2.8}$$

Practical examples of periodic flows are found not only in internal combustion engines, reciprocating pumps and compressors and turbomachinery but also in vortex shedding behind bluff bodies or certain natural convection flows in enclosures.

For unsteady flows of a more general kind, the only option is the *ensemble averaging* over n_e independent realizations ('samples') of the same event,

$$\bar{\Phi}(x_i) = \lim_{n_e \to \infty} \frac{1}{n_e} \sum_{n=1}^{n_e} \hat{\Phi}^n(x_i, t). \tag{2.9}$$

In fact, ensemble averaging is the most appropriate way of obtaining the mean value in a fluctuating field, where each realization should come from an independent measurement or computation. As such, however, ensemble averaging is highly impractical and time consuming, and often simply not possible. In stationary and periodic flows, it is reasonable to assume that both time and phase averaging are equivalent to ensemble averaging.

In certain research studies of unsteady flows, ensemble averaging has been applied to a series of time realizations of a characteristic flow structure, identified by some predefined structure parameter (e.g. a two-point correlation of a property); this is known as a *conditional averaging*. An example of such an approach is shown in Fig. 2.3, where a symmetry-accounting ensemble averaging is applied to process the DNS results in order to identify the averaged motion ('the wind') in Rayleigh–Bénard convection (thermal buoyancy-driven fluid motion between two infinite horizontal planes, where the lower wall is warmer than the upper one). Note that in this example conventional time averaging over a sufficiently long time interval gives zero mean velocity over the complete domain.

Further types of averaging can also be defined and used where convenient. For example, in numerical simulations, the averaging is often applied over a surface or

https://doi.org/10.1017/9781108875400.004 Published online by Cambridge University Press

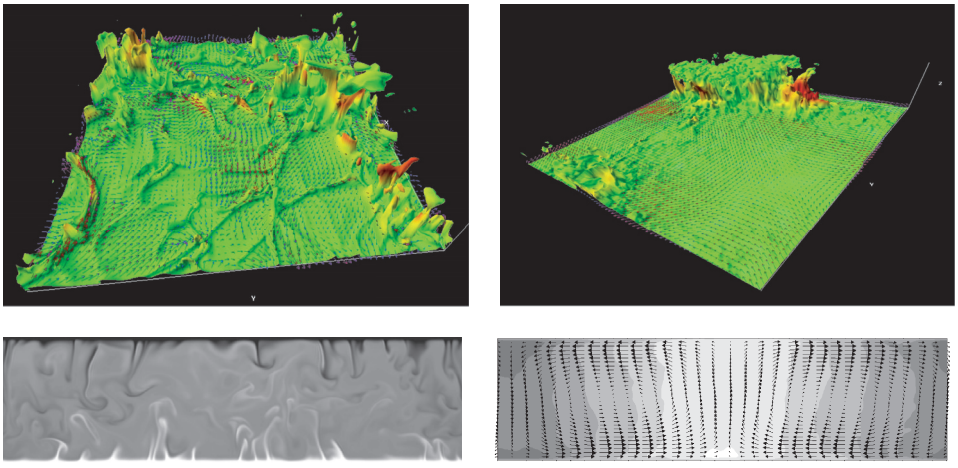

Fig. 2.3 Instantaneous (left) and symmetry-accounting ensemble-averaged (right) fields in Rayleigh–Bénard convection. Top: temperature iso-surface coloured by the kinetic energy. Bottom: temperature iso-contours with ensemble-averaged velocity profiles. From DNS data of van Reeuwijk *et al.* (2005, 2008).

a line along which the mean flow is expected to be homogeneous, thus enabling the desired number of realizations to be achieved for a relatively short computational time instead of collecting a large number of time realizations at a single point.

Finally, for flows where density variations are large (requiring the retention of density fluctuations), some form of mass-weighted averaging is usually adopted. The most widely used strategy is that alluded to by Reynolds (1895) but first formally proposed by Favre (1965) in which the instantaneous velocity is decomposed into a density-weighted average velocity and the fluctuations about that average

$$\hat{U}_i(x_i, t) = V_i + v_i, \tag{2.10}$$

where $V_i = \hat{\rho}\hat{U}_i/\rho$ and $v_i = \hat{\rho}u_i/\rho$. Note that now $\overline{\hat{\rho}v_i} = 0$, but $\bar{v}_i \neq 0$.

Some rules on Reynolds decomposition

Irrespective of the averaging method, some common rules apply to all averaging operators. Consider two instantaneous variables in a turbulent fluid flow

$$\hat{\Phi} = \bar{\Phi} + \varphi' \quad \text{and} \quad \hat{\Psi} = \bar{\Psi} + \psi'$$

and note the following rules:

- multiplication by a constant c has no effect on averaging

$$\overline{c\hat{\Phi}} = c\overline{\hat{\Phi}} = c\bar{\Phi};$$

https://doi.org/10.1017/9781108875400.004 Published online by Cambridge University Press

- addition and subtraction also have no effect on averaging

$$\overline{\hat{\Phi} \pm \hat{\Psi}} = \overline{\hat{\Phi}} \pm \overline{\hat{\Psi}} = \bar{\Phi} \pm \bar{\Psi};$$

- differentiation and integration obey commutation rules (s denotes a time or space coordinate)

$$\overline{\frac{\partial \hat{\Phi}}{\partial s}} = \frac{\partial \overline{\hat{\Phi}}}{\partial s} = \frac{\partial \bar{\Phi}}{\partial s}, \quad \overline{\int \hat{\Phi} ds} = \int \overline{\hat{\Phi}} ds = \int \bar{\Phi} ds;$$

- multiplication is an exception to these rules because of the likely interaction between fluctuations of different velocity components as well as with those of a scalar property at a point; thus, the averaged product of the two fluctuations is likely to be non-zero (i.e. the signals should be presumed to be correlated)

$$\overline{\varphi' \psi'} \neq 0 \quad \text{even though} \quad \overline{\varphi'} = 0 \quad \text{and} \quad \overline{\psi'} = 0.$$

Hence, the averaged product of the two instantaneous signals is

$$\overline{\hat{\Phi}\hat{\Psi}} = \overline{(\bar{\Phi} + \varphi')(\bar{\Psi} + \psi')} = \overline{\bar{\Phi}\bar{\Psi}} + \underbrace{\overline{\bar{\Phi}\psi'}}_{=0} + \underbrace{\overline{\varphi'\bar{\Psi}}}_{=0} + \overline{\varphi'\psi'} = \bar{\Phi}\bar{\Psi} + \overline{\varphi'\psi'}. \quad (2.11)$$

For convenience, overbars and primes will hereafter be omitted (except where needed to avoid ambiguity) so that capital letters will denote the mean, i.e. $\Phi \equiv \bar{\Phi}$, and lower-case letters the turbulent fluctuations $\varphi \equiv \varphi'$, i.e. $\hat{\Phi} = \Phi + \varphi$.

2.2.2 Averaged conservation equations

The Reynolds decomposition of the instantaneous variables into mean and fluctuating parts and averaging can now be applied to each term in the equations of motion and scalar transport, Eqs. (2.1) to (2.3). Habitually the averaging, denoted with a bar over the variable symbol, is performed in time, but apart from the interpretation, the same form of equation is recovered if one applies other averaging procedures such as phase or ensemble averaging.

For every term except that involving the product of fluctuating velocities, the averaging process simply leads to the instantaneous value being replaced by the average. For the exceptional term, the convective transport of x_i-momentum or of some scalar quantity, the non-linearity of the term ensures a more complex result.

For the momentum equation

$$\begin{aligned} \overline{\hat{U}_j \hat{U}_i} &= \overline{(U_j + u_j)(U_i + u_i)} = \overline{U_j U_i} + \overline{U_j u_i} + \overline{u_j U_i} + \overline{u_j u_i} \\ &= U_j U_i + \overline{u_j u_i}. \end{aligned} \quad (2.12)$$

https://doi.org/10.1017/9781108875400.004 Published online by Cambridge University Press

Thus, after some rearrangement and assuming density fluctuations at a point are negligible, the averaged equations of motion are obtained as

$$\frac{\partial \rho}{\partial t} + \frac{\partial (\rho U_i)}{\partial x_i} = 0, \tag{2.13}$$

$$\frac{\partial (\rho U_i)}{\partial t} + \frac{\partial (\rho U_j U_i)}{\partial x_j} = \sum_n F_i^n - \frac{\partial P}{\partial x_i} + \frac{\partial}{\partial x_j}\left[\mu\left(\frac{\partial U_i}{\partial x_j} + \frac{\partial U_j}{\partial x_i}\right) - \rho\overline{u_i u_j}\right]. \tag{2.14}$$

These equations, generally known as the *Reynolds equations*, differ from those describing a laminar flow only by the presence of the final term containing averaged products ('one-point correlations') of fluctuating velocities. The process it represents is the additional transfer rate of x_i-momentum due to turbulent fluctuations. While originating from an averaging of the convective transport on the left side of the equation, habitually, it is brought to the right side, as in Eq. (2.14). Since the first term within square brackets is the viscous stress, the second, $-\rho\overline{u_i u_j}$, has naturally been interpreted as a *turbulent stress* or, more formally, the *Reynolds stress tensor*. As this tensor is symmetric, there are in general six independent components of the Reynolds stress. They are unknown elements in the averaged equations of motion, and the major theme of this book is developing a satisfactory, albeit approximate, route for obtaining their values in order to close the Reynolds equations.

In the case of a flow with substantial density fluctuations, one cannot avoid considering the instantaneous density, and the averaging needs to be applied to the original equations of motion, Eqs. (2.1) and (2.2). The decomposition of the instantaneous density into mean and fluctuation parts, $\hat{\rho} = \bar{\rho} + \rho'$, and averaging would, however, generate several additional terms containing averaged products of fluctuating variables: $U_i\overline{\rho' u_j}$, $U_j\overline{\rho' u_i}$, $\overline{\rho' u_i u_j}$. These terms need to be approximated in addition to the stress tensor $\rho\overline{u_i u_j}$, thus adding further complexity to the task of closing the Reynolds equations. The problem can be formally avoided by using mass-weighted averaging, Eq. (2.10). In that case, the convection term in (2.2) becomes

$$\begin{aligned}\overline{\hat{\rho}\hat{U}_j\hat{U}_i} &= \overline{\hat{\rho}(V_j + v_j)(V_i + v_i)} = \rho\overline{V_j V_i} + \overline{\hat{\rho} v_i} V_j + \overline{\hat{\rho} v_j} V_i + \overline{\hat{\rho} v_i v_j} \\ &= \rho V_j V_i + \overline{\hat{\rho} v_i v_j}.\end{aligned} \tag{2.15}$$

The quantity $\overline{\hat{\rho} v_i v_j}$ is known as the mass-weighted Reynolds stress. Notice that, contrary to 'volume' averaging, the number of turbulent correlations arising from averaging the convective terms is just one – as in an incompressible flow. This is the feature that has made the use of mass-weighted quantities in variable density flow so popular. However, while the averaged equations retain the same form as for incompressible flow, the interpretation of the Reynolds stress is different. This issue becomes of importance when attempting to compare the computed

https://doi.org/10.1017/9781108875400.004 Published online by Cambridge University Press

Reynolds stress with measurements which, depending on the technique used, may provide either volume-weighted or mass-weighted averages, or even some mixed average.

It should also be noted that while density-weighted averaging removes the extra *mathematical* complexity associated with large density fluctuations, it does not necessarily follow that the physical processes are adequately accounted for with uniform-density models.

Applying averaging to the scalar-transport equation, Eq. (2.3), leads to the following rate equation for the mean level of the scalar

$$\frac{\partial(\rho\Theta)}{\partial t} + \frac{\partial(\rho U_j \Theta)}{\partial x_j} = \bar{S}_\Theta + \frac{\partial}{\partial x_j}\left(\gamma \frac{\partial \Theta}{\partial x_j} - \rho\overline{\theta u_j}\right). \tag{2.16}$$

An overbar has been placed on S_Θ to serve as a reminder that the source term may be non-linear and, in that event, its mean value may differ considerably from that obtained by inserting just the mean values of the separate constituent terms. Having drawn attention to this possibility, however, we shall not consider it further in the present treatment, attention being limited to cases where the source or sink term is effectively zero. Just as with the averaged momentum equation, the additional convective flux of the scalar due to the turbulent velocity fluctuations is conveniently interpreted as a supplementary diffusional process, which is why the term $\rho\overline{\theta u_j}$ has been transferred to the right side of the equation. Like the Reynolds stresses, this turbulent scalar flux is an unknown and will correspondingly require approximation.

2.2.3 The modelling framework and rationale

In all practically interesting problems the mean momentum and continuity equations, together, in many cases, with one or more equations of the type (2.16) for transported scalars, are to be solved numerically. The solving procedure will, in all probability, be of fairly general construction designed to cope with different flow problems ranging from some geometrically or physically simple flows (for testing modelling ideas and concepts) to real-life three-dimensional flows of great complexity. Ideally, the *turbulence model* – the scheme for determining $\overline{u_i u_j}$ and $\overline{\theta u_j}$ – should enjoy a range of applicability comparable with that of the numerical procedure and should fit comfortably within it.

Schemes discussed in this book are *one-point* closures. As remarked earlier, in such approaches, the only averaged products of fluctuating quantities that appear are those in which the two or more quantities in question are evaluated at the *same* point. 'Two-point' and spectral approaches have also been proposed and developed (an extensive account can be found in the book of Schiestel (2008) and earlier in Mathieu and Jeandel (1984) and Leslie (1973)). Models of this type are seen more

https://doi.org/10.1017/9781108875400.004 Published online by Cambridge University Press

as helping to reveal the underlying physics than as models for use in computational procedures for engineering flows.

Within the single-point framework, there is a wide range of modelling approaches. At present, most applied computational work on turbulent flows still adopts the idea that the turbulent fluxes and stresses can be represented in terms of effective turbulent diffusion coefficients for momentum, heat, chemical species and other transportable quantities of interest. Approaches of this type range from simple mean-field closure (where the turbulent viscosity is expressed in terms of the mean velocity field and flow topography) to the widely used *two-equation models* where the effective diffusion coefficients are determined from local values of two scalar properties of the turbulence (and which may or may not have a direct measurable physical significance). These in turn are obtained from transport equations similar to those describing mean flow quantities save that source and sink terms always play an important role.

In some respects, it makes sense to consider models based on the idea of a turbulent viscosity first before proceeding to the more advanced second-moment treatments. The authors believe, however, that it is preferable to go directly to a more comprehensive treatment from which 'turbulent viscosity' models emerge as special cases under particular circumstances. Such an approach reveals more clearly the shortcomings and limitations of the turbulent viscosity models. The term 'second-moment' applies to models based on the exact transport equations for the second moments, i.e. for $\overline{u_i u_j}$ and $\overline{\theta u_j}$, etc. These equations, while exact, are unclosed: they contain correlations that are not exactly determinable and which must therefore be approximated or 'modelled' in terms of quantities that *are*.

Most of the chapters that follow consider in detail the strategies and issues in the approaches to closure at this level and the application of the resultant models to a diversity of flow problems. Before considering the closure questions, however, it will be instructive to examine the exact second-moment equations and, in particular, the processes causing these quantities to depart from the levels found in isotropic turbulence. These topics are developed in the next sections.

2.3 The second-moment equations

2.3.1 Stress-transport equation

An exact equation describing the transport of the kinematic Reynolds stress $\overline{u_i u_j}$ is derived from the equation for the velocity fluctuations u_i. That equation is readily obtained by subtracting the averaged momentum equation (2.14) from that for the instantaneous velocity (Eq. 2.2)

https://doi.org/10.1017/9781108875400.004 Published online by Cambridge University Press

$$\frac{Du_i}{Dt} \equiv \frac{\partial u_i}{\partial t} + U_k \frac{\partial u_i}{\partial x_k} = -u_k \frac{\partial U_i}{\partial x_k} + \frac{1}{\rho} \sum_n f_i^n - \frac{1}{\rho} \frac{\partial p}{\partial x_i} + \frac{\partial}{\partial x_k} \left[\nu \frac{\partial u_i}{\partial x_k} - u_i u_k + \overline{u_i u_k} \right] \tag{2.17}$$

in which we now use k rather than j as the repeated suffix. Multiplying Eq. (2.17) by u_j and averaging, then adding to it the mirror equation in which suffices i and j are interchanged leads, after some manipulation, to

$$\frac{D\overline{u_i u_j}}{Dt} \equiv \underbrace{\frac{\partial \overline{u_i u_j}}{\partial t}}_{\mathcal{L}_{ij}} + \underbrace{U_k \frac{\partial \overline{u_i u_j}}{\partial x_k}}_{\mathcal{C}_{ij}} = \underbrace{-\left(\overline{u_i u_k} \frac{\partial U_j}{\partial x_k} + \overline{u_j u_k} \frac{\partial U_i}{\partial x_k} \right)}_{\mathcal{P}_{ij}} + \underbrace{\frac{1}{\rho} \sum_n \left(\overline{f_i^n u_j} + \overline{f_j^n u_i} \right)}_{\mathcal{F}_{ij}} \boxed{\underbrace{-\frac{1}{\rho} \left(\overline{u_i \frac{\partial p}{\partial x_j}} + \overline{u_j \frac{\partial p}{\partial x_i}} \right)}_{\Pi_{ij}}} - \boxed{\underbrace{2\nu \overline{\frac{\partial u_i}{\partial x_k} \frac{\partial u_j}{\partial x_k}}}_{\varepsilon_{ij}}} + \underbrace{\frac{\partial}{\partial x_k} \left[\nu \frac{\partial \overline{u_i u_j}}{\partial x_k} \boxed{-\overline{u_i u_j u_k}} \right]}_{\mathcal{D}_{ij}^{\nu} + \mathcal{D}_{ij}^{t}}. \tag{2.18}$$

The left side of the equation expresses the total rate of change of the quantity $\overline{u_i u_j}$ for a small identified packet of fluid. The rate of change arises from an imbalance of the terms on the right. Here the terms have been grouped, following well-established practice, to allow physical interpretation of the processes. One line is given to each process and, beneath each term, a shorthand label appears for the process in question; *that* will be used to simplify the appearance of later equations.

The first two processes represent rates of creation of $\overline{u_i u_j}$, in one case by the action of mean strain, $\mathcal{P}_{ij}$, and in the other by body forces $\mathcal{F}_{ij}$. The first of these, comprising products of Reynolds stresses and mean velocity gradients, can clearly be treated exactly in a second-moment closure. If the body force is linear, as when one examines the flow in a rotating coordinate frame, that too can be handled without further approximation.

https://doi.org/10.1017/9781108875400.004 Published online by Cambridge University Press

Each of the terms represents a physical process contributing to the stress budget at a point in space. Identifying the physical character of each is a prerequisite for its modelling and thus for closing the equation. This physical identification is particularly important for modelling the terms containing higher order moments and derivatives of the fluctuating velocity and pressure (placed within boxes for emphasis), which cannot be computed from the available set of equations. For this purpose some terms need to be expanded or reformulated to display their physical meaning more transparently.

First, it is noted that the second term on the right is the sum of contributions to the stress-transport balance by all (active) fluctuating body forces. Here attention will be limited to buoyancy arising from thermal and/or concentration fluctuations creating density fluctuations, electromagnetic (Lorentz) and rotation (Coriolis) forces:

$$\begin{aligned}\mathcal{F}_{ij} &\equiv \frac{1}{\rho}\sum_n \overline{f_i^n u_j} + \overline{f_j^n u_i} \\ &= \underbrace{\left(\overline{\rho' u_j} g_i + \overline{\rho' u_i} g_j\right)/\rho}_{\mathcal{G}_{ij}} + \underbrace{\left(\overline{f_i^L u_j} + \overline{f_j^L u_i}\right)/\rho}_{\mathcal{M}_{ij}} \underbrace{-2\Omega_k\left(\overline{u_j u_m}\epsilon_{ikm} + \overline{u_i u_m}\epsilon_{jkm}\right)}_{\mathcal{R}_{ij}},\end{aligned} \tag{2.19}$$

where f_i^L stands for the fluctuating Lorentz force, and Ω_k represents the system rotation rate (angular velocity).[1]

Clearly, the production of the turbulent stress by the Coriolis force can be treated exactly, but the other two contributions require the correlation between the fluctuating body force and velocity to be modelled, a topic dealt with in §4.5.

The physical meaning of the term involving the gradient of fluctuating pressure, Π_{ij}, is not so obvious and it is helpful to rewrite it as the sum of two parts: the divergence of the pressure-velocity product $\mathcal{D}_{ij}^p$ and what (for incompressible flows) is a traceless part since $\partial u_k/\partial x_k = 0$, denoted as Φ_{ij},

$$\underbrace{-\frac{1}{\rho}\left(\overline{u_i\frac{\partial p}{\partial x_j}} + \overline{u_j\frac{\partial p}{\partial x_i}}\right)}_{\Pi_{ij}} = \underbrace{-\frac{\partial}{\partial x_k}\left(\frac{1}{\rho}\overline{p(u_i\delta_{jk} + u_j\delta_{ik})}\right)}_{\mathcal{D}_{ij}^p} + \underbrace{\frac{1}{\rho}\overline{p\left(\frac{\partial u_i}{\partial x_j} + \frac{\partial u_j}{\partial x_i}\right)}}_{\Phi_{ij}}. \tag{2.20}$$

[1] The Coriolis force per unit mass, $-2\boldsymbol{\Omega}\times\hat{\mathbf{U}}$, written in index notation for a Cartesian coordinate system as $-\epsilon_{ijk}2\Omega_k U_j$ (where ϵ_{ijk} is the third-rank alternating symbol) appears in the instantaneous momentum equation (2.2) when it is transformed into a non-inertial frame rotating with angular velocity Ω_k. The Reynolds decomposition results in splitting the Coriolis force into its average, $-\epsilon_{ijk}2\Omega_k U_j$, and its fluctuations, $-\epsilon_{ijk}2\Omega_k u_j$, which appear in Eqs. (2.14) and (2.17), respectively. However, the transformation to the rotating frame also results in a centrifugal force (originating from the frame acceleration), $-\boldsymbol{\Omega}\times(\boldsymbol{\Omega}\times\mathbf{x}) \equiv -\nabla\left[1/2(\boldsymbol{\Omega}\times\mathbf{x})^2\right] = -\boldsymbol{\Omega}^2\mathbf{x}$, or $\Omega_k\Omega_k x_i$. Since no fluid flow parameters appear in the centrifugal force, it exerts no effect on turbulence. Indeed, because the centrifugal force is irrotational and conservative (i.e. it can be represented as a potential), it can be absorbed into the pressure gradient term as a modified pressure $P^* = P - \rho(\boldsymbol{\Omega}\times\mathbf{x})^2/2$, where x is the radius vector of the point under consideration.

https://doi.org/10.1017/9781108875400.004 Published online by Cambridge University Press

The term $\mathcal{D}^p_{ij}$ can be recognized as a process that leads to a spatial transport of $\overline{u_i u_j}$, that is a *diffusion* of the stress by pressure fluctuations.[2]

The stress-transport equation can now be conveniently represented in symbolic form:

$$\mathcal{L}_{ij} + \mathcal{C}_{ij} = \mathcal{P}_{ij} + \underbrace{\mathcal{G}_{ij} + \mathcal{M}_{ij} + \mathcal{R}_{ij}}_{\mathcal{F}_{ij}} + \Phi_{ij} - \varepsilon_{ij} + \underbrace{(\mathcal{D}^v_{ij} + \mathcal{D}^t_{ij} + \mathcal{D}^p_{ij})}_{\mathcal{D}_{ij}}. \quad (2.21)$$

A pictorial representation of the various terms and their physical meanings is shown in Fig. 2.4. The correlation between fluctuating pressure and fluctuating strain, Φ_{ij}, is a very important one. As mentioned above, its trace is zero, and if one forms the transport equation for the turbulent kinetic energy by taking half the sum of the equations for the three normal-stress components (i.e. those for which i and j take the same value, $\overline{u_k u_k}/2$), this term is zero for incompressible fluid flow. Thus, in an incompressible flow the pressure-strain process makes no direct contribution to the overall level of turbulence energy but serves, inter alia, to redistribute energy among the normal-stress components.

The terms comprising $\mathcal{D}_{ij}$ are easily recognized as diffusive in character since we see from integrating them across a thin shear flow bounded by non-turbulent fluid that they make no contribution to the average level of $\overline{u_i u_j}$ at any section even though, within the shear flow, the correlations themselves are non-zero. Their effect is thus to promote a spatial redistribution. Note that the total diffusion term $\mathcal{D}_{ij}$ consists of viscous diffusion $\mathcal{D}^v_{ij}$ and turbulent transport by fluctuating velocity $\mathcal{D}^t_{ij}$ and by fluctuating pressure $\mathcal{D}^p_{ij}$. The term $\mathcal{D}^v_{ij}$ describing diffusive transport by molecular action is negligible over all or nearly all the flow. However, it is invariably important within the viscous layer next to a solid wall.

Finally, the term ε_{ij} represents (very nearly) the destruction rate of $\overline{u_i u_j}$ by viscous action. Unlike viscous diffusion, the dissipation terms cannot in general be ignored. We can see this is so by contracting Eq. (2.18) to produce an equation for the transport of kinetic energy. Then, for the thin shear flow discussed above,

[2] Other decompositions of Π_{ij} have been considered. Lumley (1975b) proposed

$$-\Pi_{ij} = \left[\frac{1}{\rho}\left(\overline{u_i \frac{\partial p}{\partial x_j}} + \overline{u_j \frac{\partial p}{\partial x_i}}\right) - \frac{2}{3}\rho \frac{\partial \overline{p u_n}}{\partial x_n}\delta_{ij}\right] + \frac{2}{3\rho}\frac{\partial \overline{p u_n}}{\partial x_n}\delta_{ij}$$

and Mansour *et al.* (1988) suggested

$$-\Pi_{ij} = \left[\frac{1}{\rho}\left(\overline{u_i \frac{\partial p}{\partial x_j}} + \overline{u_j \frac{\partial p}{\partial x_i}}\right) - \frac{1}{\rho}\frac{\overline{u_i u_j}}{k}\frac{\partial \overline{p u_n}}{\partial x_n}\right] + \frac{1}{\rho}\frac{\overline{u_i u_j}}{k}\frac{\partial \overline{p u_n}}{\partial x_n}.$$

In both cases the first term on the right is traceless, thus redistributive, whereas the second term has a character of turbulent transport by pressure fluctuations. However, both decompositions lead to non-physical solutions in some generic flows (Groth, 1991). For example, in a flow that is homogeneous in direction x_3, $\mathcal{D}^p_{33}$ is identically zero, whereas both expressions will give erroneous non-zero turbulent transport also in the homogeneous directions.

https://doi.org/10.1017/9781108875400.004 Published online by Cambridge University Press

The exact equations

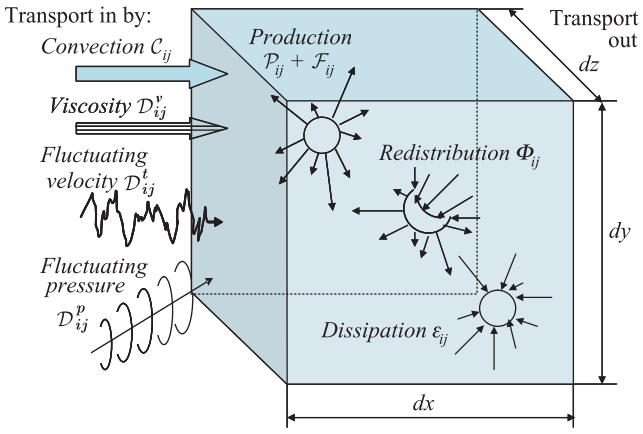

Fig. 2.4 Pictorial representation of the physical meanings of terms in the $\overline{u_i u_j}$ equation (after Bradshaw, 1976).

$\mathcal{D}_{kk}$ makes no contribution to the overall level of turbulence energy at any section, while Φ_{kk} vanishes identically at all points. The term $\mathcal{P}_{kk}$will be positive, representing the continual removal of energy from the mean flow by the action of the Reynolds stress on the mean shear. Thus, if ε_{kk} were negligible, there would be a limitless growth in the turbulent kinetic energy of the flow. Such a scenario is contrary to both intuition and observation. The crucial difference between ε_{ij} and the viscous diffusion term $\mathcal{D}^v_{ij}$ is that the former comprises correlations of fluctuating *velocity derivatives* and, in the finest scales of motion present, turbulent velocity derivatives are very large.

The role of stress generation

Further consideration of Φ_{ij}, $\mathcal{D}_{ij}$ and ε_{ij} is deferred to Chapter 4. It will, however, be instructive to explore in a little greater depth the glimpse provided in Chapter 1 into specific forms that the production tensors take in a few cases. In most practical flows, the production terms firmly stamp the character of the resultant turbulent stress tensor. First, consider the case of *simple shear*, with $dU_1/dx_2 = \lambda$, where λ is assumed positive and all other components of mean velocity and their derivatives are zero. From the stress transport equation (2.18) applied to individual components we see that stress production is non-zero only for the $\overline{u_1^2}$ and $\overline{u_1 u_2}$ components, as summarized in Table 2.1. From the upper row of Table 2.1, $\mathcal{P}_{12}$, the production rate of $\overline{u_1 u_2}$ is negative (since $\overline{u_2^2}$ is undoubtedly positive); though short of a proof, the reader will accept the likelihood that $\overline{u_1 u_2}$ is consequently negative (i.e. of the same sign as its production rate), which in turn gives the 'sensible' result

https://doi.org/10.1017/9781108875400.004 Published online by Cambridge University Press

Table 2.1 *Stress production rates due to primary and secondary shear*

$\mathcal{P}_{ij}$	$\mathcal{P}_{11}$	$\mathcal{P}_{22}$	$\mathcal{P}_{33}$	$\mathcal{P}_{12}$
Due to primary shear $\dfrac{\partial U_1}{\partial x_2} = \lambda$	$-2\overline{u_1u_2}\lambda$	0	0	$-\overline{u_2^2}\lambda$
Due to curvature perturbation $\dfrac{\partial U_2}{\partial x_1} = \delta$	0	$-2\overline{u_1u_2}\delta$		$-\overline{u_1^2}\delta$

that the generation of $\overline{u_1^2}$ is positive. There is no direct production of either $\overline{u_2^2}$ or $\overline{u_3^2}$. This does not mean that there will be no turbulent fluctuations in the x_2 and x_3 directions for we have already noted that the pressure-strain correlation Φ_{ij} serves to redistribute energy among the various normal stresses. Nevertheless, we should expect – and this is amply confirmed by experiment – that $\overline{u_1^2}$ would be the largest of the normal-stress components in simple shear (see, for example, Fig. 1.2).

Figure 2.5 illustrates, for this case, the flow of kinetic energy from the mean motion to turbulence, its exchange among components and ultimate destruction by viscosity. This same budget applies very nearly to other thin shear flows (provided $\partial U_1/\partial x_1$ and $\partial U_2/\partial x_2 \ll \partial U_1/\partial x_2$). We focus for the moment on the interaction among stress components. The self-sustaining character of turbulence in a simple shear is emphasized by the clockwise circular arrow connecting the stresses in Fig. 2.5: turbulent velocity fluctuations in the direction of the mean-velocity gradient ($\overline{u_2^2}$) promote a growth in shear stress, which, in turn, serves to augment the intensity of streamwise fluctuations. Pressure interactions deflect some of this energy to fluctuations in the direction of the velocity gradient – and so the sequence repeats itself. It is what we might call turbulence's eternal triangle.

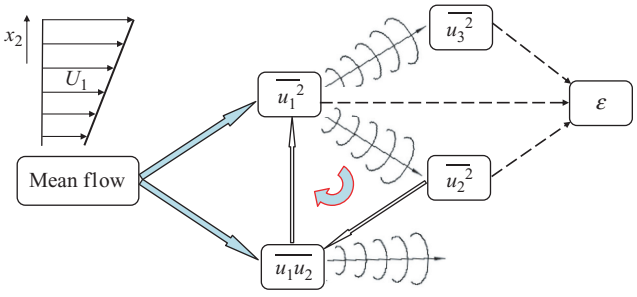

Fig. 2.5 A schematic diagram of energy flow and stress interactions in a thin shear flow. Pressure interactions are indicated symbolically by 'waves'.

https://doi.org/10.1017/9781108875400.004 Published online by Cambridge University Press

The lower line in Table 2.1 shows the effects of superimposing on the primary shear a weak (but not negligible) secondary strain δ ($\delta = \partial U_2/\partial x_1$), which represents a curving of the mean-flow streamlines. The shear stress and the normal stress in the direction of the velocity gradient are directly modified and their effects reinforce one another. That is to say, if δ is positive, the extra contribution to $\mathcal{P}_{12}$ will tend to enlarge the (negative) magnitude of $\overline{u_1 u_2}$, while the contribution to $\mathcal{P}_{22}$ leads to an enhancement of $\overline{u_2^2}$, which in turn helps amplify $\overline{u_1 u_2}$ through the principal contribution to $\mathcal{P}_{12}$. It is this mutual reinforcement property of $\mathcal{P}_{ij}$, represented in Fig. 2.6 by the broken lines, that makes turbulent shear flows so sensitive to weak streamline curvature.

2.3.2 Transport equation for turbulent scalar flux

Buoyancy has an effect on turbulence generation that in some respects is akin to streamline curvature. It is more complicated, however, for it involves a coupling of the Reynolds stress and scalar flux fields $\overline{\theta u_i}$. The corresponding equation for $\overline{\theta u_i}$ is obtained by multiplying Eq. (2.3) by u_i, then adding it to Eq. (2.2) multiplied by θ and averaging. The result may be expressed as

$$\begin{aligned}\frac{D\overline{\theta u_i}}{Dt} \equiv \underbrace{\frac{\partial \overline{\theta u_i}}{\partial t}}_{\mathcal{L}_{\theta i}} + \underbrace{U_k \frac{\partial \overline{\theta u_i}}{\partial x_k}}_{\mathcal{C}_{\theta i}} &= \underbrace{-\left(\overline{u_i u_k}\frac{\partial \Theta}{\partial x_k} + \overline{\theta u_k}\frac{\partial U_i}{\partial x_k}\right)}_{\mathcal{P}_{\theta i}=\mathcal{P}^{\Theta}_{\theta i}+\mathcal{P}^{U}_{\theta i}} \\ &\quad \underbrace{+\frac{1}{\rho}\sum_n \overline{\theta f_i^n}}_{\mathcal{F}_{\theta i}} \\ &\quad \boxed{\underbrace{-\frac{1}{\rho}\overline{\theta \frac{\partial p}{\partial x_i}}}_{\Pi_{\theta i}}} \\ &\quad - \boxed{\underbrace{(\alpha+\nu)\overline{\frac{\partial \theta}{\partial x_k}\frac{\partial u_i}{\partial x_k}}}_{\varepsilon_{\theta i}}} \\ &\quad + \underbrace{\frac{\partial}{\partial x_k}\left[\alpha u_i \overline{\frac{\partial \theta}{\partial x_k}} + \nu\theta\overline{\frac{\partial u_i}{\partial x_k}} \boxed{-\overline{\theta u_i u_k}}\right]}_{\mathcal{D}^{\alpha}_{\theta i}+\mathcal{D}^{\nu}_{\theta i}+\mathcal{D}^{t}_{\theta i}}\end{aligned} \tag{2.22}$$

where

$$\mathcal{F}_{\theta i} \equiv \frac{1}{\rho}\sum_n \overline{\theta f_i^n} = \underbrace{\overline{\rho'\theta} g_i/\rho}_{\mathcal{G}_{\theta i}} + \underbrace{\overline{\theta f_i^L}/\rho}_{\mathcal{M}_{\theta i}} \underbrace{-2\Omega_k \overline{\theta u_j}\epsilon_{ijk}}_{\mathcal{R}_{\theta i}} \tag{2.23}$$

https://doi.org/10.1017/9781108875400.004 Published online by Cambridge University Press

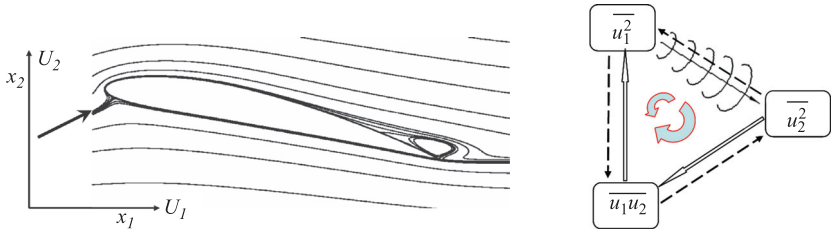

Fig. 2.6 Stress couplings in weakly curved shear flows: full arrows indicate the production due to primary strain and broken arrows indicate production due to secondary (curvature) strain. The pressure-strain effect is indicated symbolically by 'waves'.

represents the sum of the production of scalar flux by fluctuations of different body forces – gravitation, Lorentz force and Coriolis force.

Just as in the stress equation, the correlation containing the fluctuating pressure gradient, $\Pi_{\theta i}$, is conveniently decomposed into a divergence part representing the turbulent diffusion of the scalar by pressure fluctuations, $\mathcal{D}^p_{\theta i}$, and the remaining term $\Phi_{\theta i}$ interpreted as 'pressure scrambling' of the fluctuating scalar field, i.e.

$$\underbrace{-\frac{1}{\rho}\overline{\theta\frac{\partial p}{\partial x_i}}}_{\Pi_{\theta i}} = \underbrace{-\frac{\partial}{\partial x_k}\left(\frac{1}{\rho}\overline{p\theta}\delta_{ik}\right)}_{\mathcal{D}^p_{\theta i}} + \underbrace{\frac{1}{\rho}\overline{p\frac{\partial\theta}{\partial x_i}}}_{\Phi_{\theta i}}. \tag{2.24}$$

The scalar flux transport equation can now be written in symbolic form,

$$\begin{aligned}\mathcal{L}_{\theta i} + \mathcal{C}_{\theta i} = {} & \underbrace{\mathcal{P}^{\Theta}_{\theta i} + \mathcal{P}^{U}_{\theta i}}_{\mathcal{P}_{\theta i}} + \underbrace{\mathcal{G}_{\theta i} + \mathcal{M}_{\theta i} + \mathcal{R}_{\theta i}}_{\mathcal{F}_{\theta i}} \\ & + \Phi_{\theta i} - \varepsilon_{\theta i} + \underbrace{(\mathcal{D}^{\alpha}_{\theta i} + \mathcal{D}^{\nu}_{\theta i} + \mathcal{D}^{t}_{\theta i} + \mathcal{D}^{p}_{\theta i})}_{\mathcal{D}_{\theta i}}.\end{aligned} \tag{2.25}$$

The emerging equation is similar in structure to that describing the transport of Reynolds stress. The generation terms $\mathcal{P}_{\theta i}$ comprise products of second-moment correlations and mean-field gradients and will not require approximation. Diffusive transport of $\overline{\theta u_i}$, i.e. $\mathcal{D}_{\theta i}$, is caused by velocity and pressure fluctuations and by molecular transport. The last of these consists of two terms: one associated with scalar conductivity/diffusivity and the other with fluid viscosity. Pressure fluctuations also play a non-dispersive role ($\Phi_{\theta i}$), which we shall later see is of vital importance. Note that, unlike Φ_{ij}, since $\Phi_{\theta i}$ is a vector, it cannot be contracted to show its redistributive character, but nevertheless one can expect that it contributes to diminishing both the magnitude of and the differences between components of the scalar flux by 'scrambling' turbulent eddies.

https://doi.org/10.1017/9781108875400.004 Published online by Cambridge University Press

Table 2.2 *Heat-flux generation rates due to a temperature gradient* $\partial\Theta/\partial x_2$

$\mathcal{P}_{\theta i}$	$\mathcal{P}_{\theta 1}$	$\mathcal{P}_{\theta 2}$	$\mathcal{P}_{\theta 3}$
Due to shear $\dfrac{\partial U_1}{\partial x_2}$	$-\overline{u_1u_2}\dfrac{\partial\Theta}{\partial x_2} - \overline{\theta u_2}\dfrac{\partial U_1}{\partial x_2}$	$-\overline{u_2^2}\dfrac{\partial\Theta}{\partial x_2}$	0
Due to shear $\dfrac{\partial U_1}{\partial x_3}$	0	$-\overline{u_2^2}\dfrac{\partial\Theta}{\partial x_2}$	0

The role of flux generation

The unknown processes in Eq. (2.25) will be approximated in Chapter 4. Here we consider briefly the form taken by the generation terms under a simple temperature gradient $d\Theta/dx_2$ in a fluid moving in direction x_1. If the background Reynolds stress field is isotropic ($\overline{u_iu_j} = \delta_{ij}\overline{u_mu_m}/3$), the only direction in which a heat flux is generated is that of the temperature gradient x_2, and the sign of $\mathcal{P}_{\theta 2}$ is opposite from that of the temperature gradient. This is also the case in a non-isotropic stress field if the mean shear lies entirely in a plane normal to the temperature gradient (i.e. dU_1/dx_3, see the last line of Table 2.2). When the direction of mean velocity gradient coincides with that of the temperature gradient, however, a streamwise scalar flux is generated, contributions arising from both $\mathcal{P}_{\theta i}^{\Theta}$ and $\mathcal{P}_{\theta i}^{U}$. If one accepts the idea that the stresses and fluxes will be of the same sign as the generation terms, we can see that the two contributions to the generation reinforce one another, both being of the same sign as the product $(d\Theta/dx_2)(dU_1/dx_2)$.

With the above information, it is now possible to infer the effect of a buoyantly stable stratification of fluid on the stress generation rates. Turbulent fluctuations in density, ρ', give rise to a fluctuating body force per unit mass $-\rho' g/\rho$ in the vertical direction, g being the gravitational acceleration. Thus, in the Reynolds stress equations, with x_2 vertically up so that the gravitational vector is defined as $g_k = (0, -g, 0)$, we find non-zero buoyant generation components as follows

$$\mathcal{G}_{22} = -2\overline{\rho' u_2}g/\rho, \qquad \mathcal{G}_{12} = -\overline{\rho' u_1}g/\rho. \tag{2.26}$$

If the fluid in question is a perfect gas, $\rho'/\rho = -\theta/\Theta$ (where Θ stands for temperature and the origin on its scale is absolute zero), and so the generation rates can be written as

$$\mathcal{G}_{22} = +2\overline{\theta u_2}g/\Theta, \qquad \mathcal{G}_{12} = +\overline{\theta u_1}g/\Theta. \tag{2.27}$$

In a stably stratified medium, $\partial\Theta/\partial x_2$ is positive. To fix ideas let us suppose that $\partial U_1/\partial x_2$ is also positive. So, $\mathcal{P}_{\theta 2}$ and thus (we suppose) $\mathcal{G}_{22}$ are negative.

https://doi.org/10.1017/9781108875400.004 Published online by Cambridge University Press

Likewise, from the above discussion, $\mathcal{P}_{\theta 1}$ and hence $\mathcal{G}_{\theta 1}$ will be positive. Thus, there is a double-edged effect of buoyancy on the Reynolds shear stress: $\mathcal{G}_{22}$ will tend to reduce $\overline{u_2^2}$, thus diminishing $\mathcal{P}_{12}$ (see Table 2.1), while $\mathcal{G}_{12}$, being of the opposite sign from $\mathcal{P}_{12}$, will also act to reduce the vertical transport of streamwise momentum by turbulence.

2.3.3 A 'model' without modelling

In the foregoing subsections we obtained the exact transport equation for $\overline{u_i u_j}$ and $\overline{\theta u_i}$ and examined the form that the generation terms in these equations take in a few situations. As noted, these generation terms are exact. Of course, before the transport equations can be used to find the stress and flux levels, models must be devised for the unknown processes – the task of Chapter 4. To round off this section, however, we can make some qualitative estimates without resorting to mathematical modelling, by simply making the simplistic assumption that

$$\text{Value of second moment} \propto \text{Generation rate of second moment} \times \text{Turbulence time scale}.$$

Thus:

$$\overline{\theta u_i} = c_\theta \mathcal{T}_t (\mathcal{P}_{\theta i} + \mathcal{G}_{\theta i}). \tag{2.28}$$

The choice of turbulent time scale $\mathcal{T}_t$ and how to compute it is deferred to Chapter 5. However, the basic idea can readily be tested by looking at *ratios* of the scalar fluxes.

Thus:

$$\frac{\overline{\theta u_1}}{\overline{\theta u_2}} = \frac{\mathcal{P}_{\theta 1} + \mathcal{G}_{\theta 1}}{\mathcal{P}_{\theta 2} + \mathcal{G}_{\theta 2}}. \tag{2.29}$$

In a mildly heated shear flow without body forces, in which $\partial\Theta/\partial x_2$ and $\partial U_1/\partial x_2$ are the only non-zero temperature and velocity components, one finds from experiment that the left side of Eq. (2.29) is approximately -1.3 in an equilibrium free flow, and the right side is about -1.6. Near a wall the ratio of the turbulent heat fluxes is larger, about -2.2, as is correspondingly the ratio of the generation terms (about -2.1). Thus, there does indeed seem to be more than a casual connection between the left and right sides of Eq. (2.29). The success is particularly striking when set against the background of results given by simple eddy-diffusivity models. Such schemes would predict that, because there are no x_1 gradients in mean temperature, the turbulent flux in that direction would be zero!

When considering the Reynolds stresses one needs to apply this simple concept to *departures* from the isotropic state (the deviatoric part of the stress tensor $\overline{u_i u_j}$).

https://doi.org/10.1017/9781108875400.004 Published online by Cambridge University Press

This is not inconsistent with (2.28); the isotropic value of a vector is of course zero. Accordingly:

$$\overline{u_i u_j} - \frac{1}{3}\delta_{ij}\overline{u_k u_k} = c\mathcal{T}_t\left(\mathcal{P}_{ij} - \frac{1}{3}\delta_{ij}\mathcal{P}_{kk}\right). \tag{2.30}$$

In fact, this formula, arrived at by a much less direct route, has formed the basis of many successful predictions of turbulent free shear flows as discussed in §7.3.1.

https://doi.org/10.1017/9781108875400.004 Published online by Cambridge University Press

3

Characterization of stress and flux dynamics: elements required for modelling

3.1 Introduction

Before embarking on the primary topic of this book, the modelling of turbulence via second-moment and partially time-resolved closures, it is appropriate, briefly, to review some of the features of real turbulence that will have to be accounted for or, at least, acknowledged. Such a survey could be an extensive one for there is a great deal that is known and documented on the subject. Attention is limited here, however, to what are seen as *essentials* to modelling. Those wishing to equip themselves with a fuller background than is provided herein will find extensive coverage in the broader-based textbooks on turbulent flows, for example, those by Pope (2000) or Schiestel (2008) or, indeed, the earlier treatises by Hinze (1975) and Monin and Yaglom (1975).

The present chapter covers two main themes. The first is an examination of two vitally important scalar properties of turbulence, the turbulent kinetic energy, k, and the corresponding mean-square scalar variance, $\overline{\theta^2}$, together with their respective rates of dissipation by molecular action. This occupies §3.2–§3.6. The second theme is an examination of some intrinsic properties of the Reynolds-stress tensor and scalar-flux vector that provide powerful aids in modelling these quantities.

3.2 Energy flow processes in turbulence

Equation (2.18) provided the Reynolds-stress transport equation whose closure (i.e. conversion to a closed, soluble form) will be the primary focus of later chapters. For present purposes, however, the equation is undesirably complex. Thus, here we examine, instead, the equation for the turbulent kinetic energy, k, i.e. half the sum of the normal stresses: $k \equiv [\overline{u_1^2} + \overline{u_2^2} + \overline{u_3^2}]/2 \equiv \overline{u_i^2}/2$. While, clearly, the transport equation for k can be deduced straightforwardly by contracting Eq. (2.18), it can also be obtained directly by multiplying the instantaneous momentum equation for

https://doi.org/10.1017/9781108875400.005 Published online by Cambridge University Press

$\hat{U}_i \equiv (U_i + u_i)$ by u_i and averaging. Here it is assumed that body forces are absent and that the physical properties of the fluid are constant:

$$\overline{u_i\left(\frac{\partial(U_i+u_i)}{\partial t}+\frac{\partial\left[(U_j+u_j)(U_i+u_i)\right]}{\partial x_j}\right)} = -\overline{\frac{u_i\partial(P+p)}{\partial x_i}}+\overline{\frac{u_i\partial}{\partial x_j}\left(\frac{\nu\partial(U_i+u_i)}{\partial x_j}\right)}. \tag{3.1}$$

After discarding vanishing terms in Eq. (3.1) and taking all but the convective transport terms to the right-hand side, the required equation for k may be expressed as:

$$\frac{Dk}{Dt}\equiv\frac{\partial k}{\partial t}+U_j\frac{\partial k}{\partial x_j}=\underbrace{\frac{\partial}{\partial x_j}\left(\nu\frac{\partial k}{\partial x_j}-\overline{\frac{pu_j}{\rho}}-\overline{u_jk'}\right)}_{\mathcal{D}_k}\underbrace{-\overline{u_iu_j}\frac{\partial U_i}{\partial x_j}}_{\mathcal{P}_k}\underbrace{-\nu\overline{\left(\frac{\partial u_i}{\partial x_j}\right)^2}}_{\varepsilon} \tag{3.2}$$

where k' denotes the instantaneous turbulence energy, $\frac{1}{2}u_iu_i$. In words, the equation expresses the fact that, as a small fluid element is carried along, its turbulent kinetic energy changes as a result of a net imbalance among the processes on the right-hand side, namely, diffusive transport, $\mathcal{D}_k$, due to viscosity and turbulence (associated with both velocity and velocity–pressure interactions), production of turbulence by deformation of the mean velocity field, $\mathcal{P}_k$, and dissipation of k by viscous action, ε.

The corresponding *mean* kinetic energy equation may likewise be obtained by multiplying the momentum equation by the mean velocity and averaging:

$$\overline{U_i\left(\frac{\partial(U_i+u_i)}{\partial t}+\frac{\partial\left[(U_j+u_j)(U_i+u_i)\right]}{\partial x_j}\right)} = -\overline{\frac{U_i\partial(P+p)}{\partial x_i}}+\overline{\frac{U_i\partial}{\partial x_j}\left(\frac{\nu\partial(U_i+u_i)}{\partial x_j}\right)}$$

which can be manipulated to the following transport equation for $K\equiv U_i^2/2$:

$$\frac{DK}{Dt}=\underbrace{-\frac{\partial(PU_i)}{\rho\partial x_i}}_{a}+\underbrace{\nu\frac{\partial^2K}{\partial x_j^2}}_{b}\underbrace{-\nu\left(\frac{\partial U_i}{\partial x_j}\right)^2}_{c}\underbrace{-\frac{\partial}{\partial x_j}(U_i\overline{u_iu_j})}_{d}+\underbrace{\overline{u_iu_j}\frac{\partial U_i}{\partial x_j}}_{e}. \tag{3.3}$$

Thus, the mean kinetic energy of a particle will change through a net imbalance in the contributions from the following:

(a) reversible working by mean pressure gradients,
(b) viscous diffusion of K,

https://doi.org/10.1017/9781108875400.005 Published online by Cambridge University Press

(c) viscous dissipation,
(d) reversible working by the Reynolds stresses on the flow field,
(e) loss of mean kinetic energy to turbulence.

The attribution of the last of the above processes is self-evident since the same term appears in the turbulence energy budget, Eq. (3.2), but with an opposite sign.

It is worth noting that both the turbulent and the mean kinetic energy equations were first presented by Osborne Reynolds in his 'Reynolds averaging' paper (Reynolds, 1895) that provided the starting point for all RANS work. Although the turbulent kinetic energy is a scalar quantity, noting its response in various situations has proved very helpful in guiding modelled forms of both the stress and scale-determining equations. Specifically, five particular cases are noted:

(i) energy decay in homogeneous turbulence $U_1 \dfrac{dk}{dx_1} = -\varepsilon$
(ii) rapid distortion $U_j \dfrac{\partial k}{\partial x_j} = \mathcal{P}_k$
(iii) diffusion-dissipation equilibrium $0 = \mathcal{D}_k - \varepsilon$
(iv) local (turbulence energy) equilibrium $0 = \mathcal{P}_k - \varepsilon$
(v) convection-diffusion equilibrium $U_1 \dfrac{\partial k}{\partial x_1} = \mathcal{D}_k$.

These reduced forms of the turbulence energy equation provide pivotal test cases for modelling turbulence and are thus frequently used for choosing at least some of the empirical coefficients in the models. While examined in more detail in later chapters, the following briefly serves to explain the relevance of each case.

(i) In the absence of production agencies (no strain rate, no body forces), homogeneous turbulence will freely decay through viscous dissipation. This process is irreversible. Experiments show (and DNS studies confirm) that, provided the turbulent Reynolds number (of which more shortly) is sufficiently high, the turbulence energy exhibits a power-law decay with time (or equivalently in space): $k \propto t^{-n}$ (or $k \propto x^{-n}$) with $n \approx 1.2$, trianagular symbols in Fig. 3.1. Matching that exponent allows the empirical coefficient associated with the sink term in the scale-determining equation to be fixed.
(ii) In a turbulent flow suddenly subjected to a strong mean rate of strain, the dissipation can, for a time, be neglected compared with the imposed production. Such a situation arises, for example, when turbulence is passed through a duct whose cross-sectional dimensions are changing rapidly. Various test data have been provided by experiment and DNS. Indeed, for the latter, viscous dissipation can be 'switched off' to provide a pure test case. Equally, *rapid distortion theory* (RDT), a linear, analytical treatment of turbulence, is specifically designed to be applicable in such extreme deformations.

https://doi.org/10.1017/9781108875400.005 Published online by Cambridge University Press

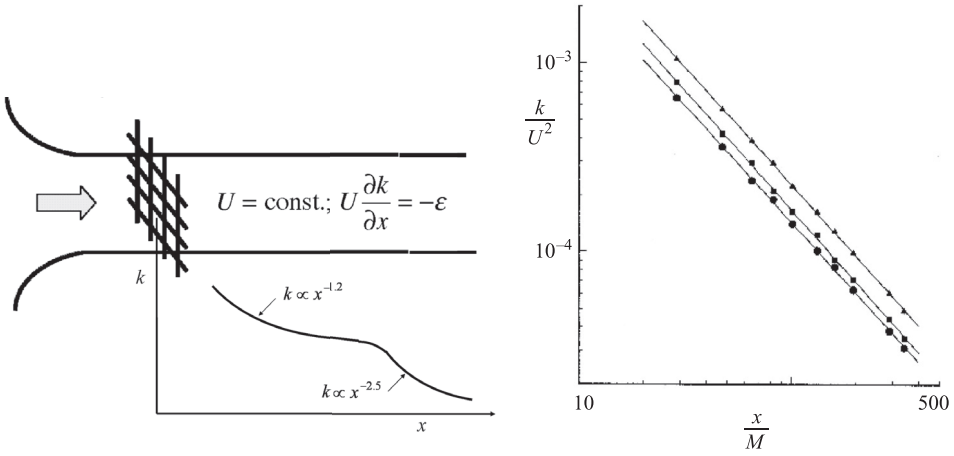

Fig. 3.1 Decay of isotropic turbulence generated by a grid in a wind tunnel. Left: a sketch of the experiment and decay of kinetic energy along the tunnel. Right: experimental results for the initial ('inertial') period. From Pope (2000), adapted from Comte-Bellot and Corrsin (1966).

(iii) For the case of fully developed flow through a pipe or plane channel, the production of energy is negligible near the axis while convection is zero by definition. Then, the dissipative loss of turbulence energy is made good by a diffusive inflow of energy from regions nearer the duct or pipe wall. A similar situation may arise in stagnant, separated flow regions, for example behind a blunt obstacle. It is essential to account correctly for the resultant turbulence energy levels in order to predict accurately the turbulent heat transfer rates from the obstacle. This diffusion-dissipation balance is also the limiting form of the k-equation in the viscous layer adjacent to a smooth wall; however, in this case, the diffusive mechanism is predominantly viscous.

(iv) For a shear flow along a wall, within the fully turbulent near-wall region, provided streamwise pressure gradients are weak, convection and diffusion terms will be negligible compared with the production and dissipation processes. This situation is illustrated in Fig. 3.2, which shows the energy budget for flow through a plane channel.

(v) At the free edge of a turbulent flow both production and dissipation can often be neglected compared with convection and diffusion, which are roughly in balance.

In free shear flows and, indeed, in most real flows in engineering and the environment, *all* the terms in the energy budget are important. Figure 3.3 shows, for example, the different terms in the budget for the case of a round jet in stagnant surroundings. In this flow, like the boundary layer, turbulence energy

https://doi.org/10.1017/9781108875400.005 Published online by Cambridge University Press

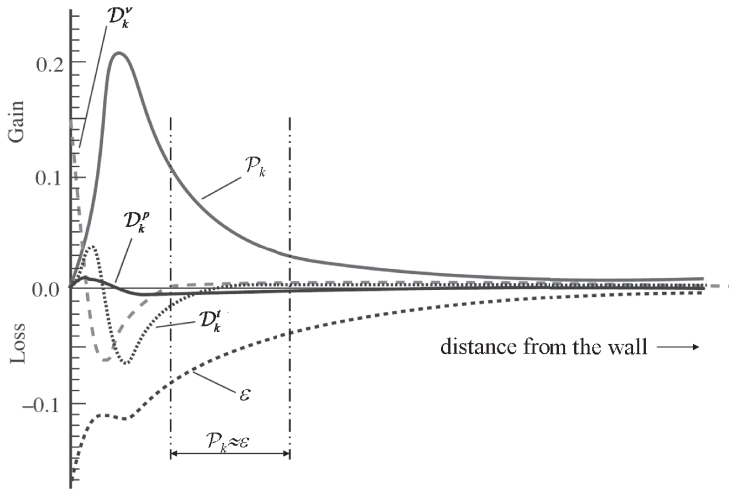

Fig. 3.2 Budget of turbulent kinetic energy in a fully developed plane-channel flow, normalized with the friction velocity, U_τ, and kinematic viscosity, ν.

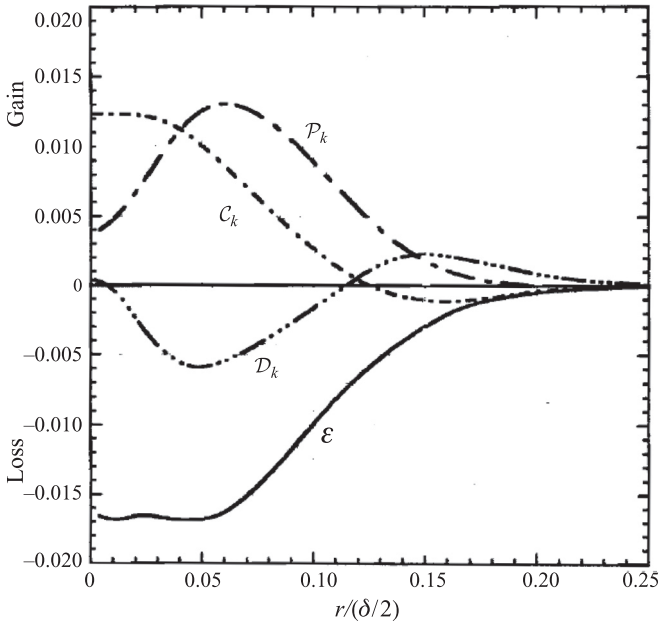

Fig. 3.3 Budget of turbulence kinetic energy in a fully developed round jet normalized with $U_c^3(x - x_0)$, where x is the streamwise coordinate, x_0 is the location of the virtual jet origin and U_c is the jet centre-line velocity (only half of the jet is shown). From experiments of Panchapakesan and Lumley (1993).

production is provided by the transverse mean velocity gradient, here $\partial U/\partial r$. However, the absence of a constraining wall means that the jet can expand freely and, consequently, the convection and diffusion terms play a more important role than

https://doi.org/10.1017/9781108875400.005 Published online by Cambridge University Press

in the wall boundary layer. It is noted also that there remains a significant energy production even on the jet axis where the mean radial velocity gradient is zero. There the generation is due to *streamwise* gradients of mean velocity.

3.3 The spectral character of turbulence

The figures of energy budgets considered above make it clear that the energy dissipation rate is nearly always a significant term in the turbulence energy equation. Yet, those encountering this fact for the first time may well feel that the mathematical form of the energy equation suggests otherwise. For example, to make a rudimentary assessment of the relative magnitudes of the production and dissipation processes in the round jet, one might suppose that the characteristic turbulent velocity is one order of magnitude smaller than the centre-line mean velocity, U_c, and that the characteristic length scale for both production and dissipation processes is the radius of the jet, δ_r. One would thus conclude that:

$$\langle \mathcal{P}_k \rangle \approx \left\langle -\overline{u v} \frac{\partial U}{\partial r} \right\rangle \approx U_c^2 \times 10^{-2} \frac{U_c}{\delta_r} = 10^{-2} \frac{U_c^3}{\delta_r},$$

$$\langle \varepsilon \rangle \equiv \left\langle \nu \overline{\left(\frac{\partial u_i}{\partial x_j} \right)^2} \right\rangle \approx \frac{\nu}{U_c \delta_r} \frac{U_c^3 \times 10^{-2}}{\delta_r}$$

where the angular brackets simply indicate an averaging across the shear layer, and u and v denote velocity fluctuations in the axial (x) and radial (r) directions as usual for two-dimensional flows. The above result thus suggests that $\langle \varepsilon \rangle / \langle \mathcal{P}_k \rangle \approx (U_c \delta_r / \nu)^{-1}$. On the basis of this analysis one would not hesitate to conclude that the dissipation contribution was negligible since the Reynolds number, $U_c \delta_r / \nu$, of a turbulent round jet is at least measured in thousands (usually tens of thousands and sometimes hundreds of thousands)! Even if one notes that the dissipation term shown actually consists of nine contributing components (so the above order-of-magnitude analysis would have underestimated its value), the conclusion remains the same: the dissipation term is negligible!

However, *the 'analysis' above is defective and should be entirely disregarded!* There are two serious errors in the assumptions made about the scales, both associated with the dissipation term. The first is the presumption that the appropriate velocity scale to assign to u_i is the same as that assigned for the turbulent shear stress, $\overline{uv}$. The second and even more serious error is that the characteristic length scale for the dissipation be taken as the local radius of the shear flow. As is clearly visible in the instantaneous fluctuating velocity trace shown in Fig. 2.1, there is a wide range of time scales present in a turbulence signal and, correspondingly,

https://doi.org/10.1017/9781108875400.005 Published online by Cambridge University Press

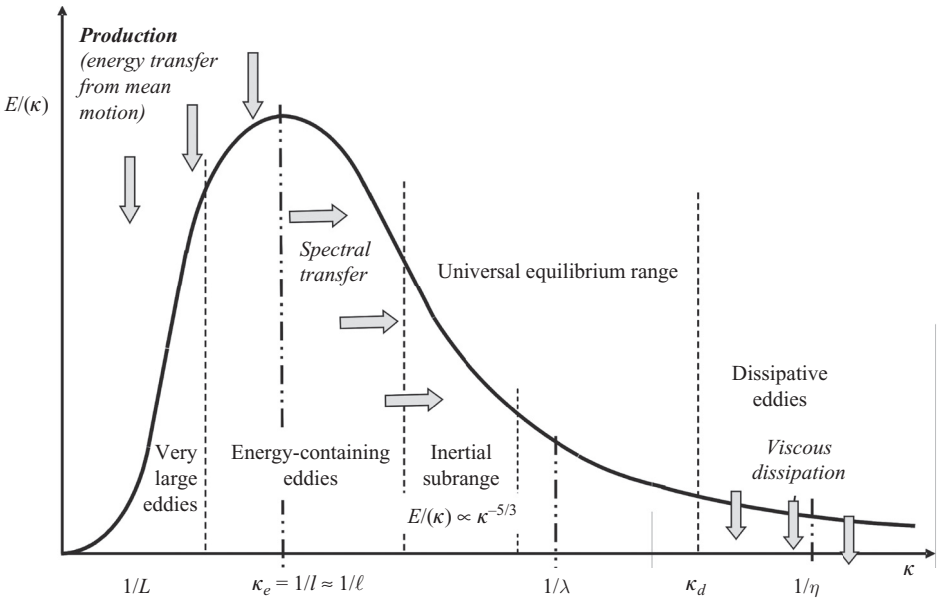

Fig. 3.4 A schematic diagram of the energy spectrum for high Reynolds number turbulence. Here λ denotes the Taylor microscale, Eq. (3.11), and η the Kolmogorov length scale (defined below, p. 45).

a wide range of length scales. The dissipation of turbulence energy always takes place predominantly in the very finest scales present for that is where the steepest velocity gradients occur. Indeed, *the size of those length scales adjusts so as to destroy energy at just the rate that energy is fed to them by the continual breakdown of larger scale eddies into smaller and smaller scales of motion!*

Thus, the view that emerges is that turbulence energy is 'captured' from the mean flow by successive engulfment by the large-scale eddies. Thereafter, by a process of eddy stretching and distortion, such newly captured turbulence energy is progressively broken down, inviscidly, to finer and finer scales until eventually the scales of motion are so fine (and thus the mean velocity gradients so steep) that the kinetic energy is dissipated to thermal energy by viscous action. The turbulent eddies that are too small to be involved significantly in the energy-capture process yet too large to be responsible for significant dissipation thus play the role of energy carriers, transferring energy from larger eddies to successively smaller ones. These intermediate eddies form what is known as the *inertial subrange*, Fig. 3.4.

This spectral view of turbulence can be expressed mathematically by taking the Fourier transform of the two-point velocity correlation[1] (cf. Hinze, 1975;

[1] The two-point velocity correlation is defined as $R_{ij}(\mathbf{x}, \mathbf{x}') \equiv \overline{u_i(\mathbf{x})u_j(\mathbf{x}')}$, where $\mathbf{x}$ and $\mathbf{x}' \equiv \mathbf{x} + \mathbf{r}$ denote the position vectors (denoted for clarity in bold) of two points in space. Clearly, when $\mathbf{r} = 0$, $R_{ij} = \overline{u_i u_j}$ and as $\mathbf{r} \to \infty$, $R_{ij} \to 0$. Such two-point correlations provide a possible basis for determining length scales

https://doi.org/10.1017/9781108875400.005 Published online by Cambridge University Press

Monin, 1975; Pope, 2000), which brings into prominence the wave number κ (with dimension length^{-1}) as the appropriate independent variable (rather than, say, length scale or frequency). In a homogeneous flow the equation can be written as:

$$\frac{\partial E(\kappa)}{\partial t} = \mathcal{P}_k(\kappa) - \frac{\partial}{\partial \kappa}\mathcal{T}(\kappa) - 2\nu\kappa^2 E(\kappa) \tag{3.4}$$

where $E(\kappa)$ is the kinetic energy per unit wave number, $\mathcal{P}_k(\kappa)$is the turbulence energy production rate per unit wave number and $\mathcal{T}(\kappa)$ is the spectral energy transfer rate. Note that $\int_0^\infty E(\kappa)d\kappa = k$ and $\int_0^\infty 2\nu\kappa^2 E(\kappa)d\kappa = \varepsilon$.

In a strictly equilibrium flow where $E(\kappa)$ is invariant with time, the spectral energy transfer rate at any wave number is equal to:

$$\mathcal{T}(\kappa) = \int_0^\kappa \left[\mathcal{P}_k(\kappa) - 2\nu\kappa^2 E(\kappa)\right] d\kappa. \tag{3.5}$$

For these mid-range wave numbers where neither production nor dissipation is significant, $\mathcal{T}(\kappa) = \mathcal{P}_k = \varepsilon$. Figure 3.4 provides an impression of the distribution of $E(\kappa)$ with wave number. Its variation within the inertial subrange is readily inferred by dimensional considerations[2] if one supposes that it should depend simply on the wave number and the energy throughput rate, which can be taken to be equal to ε:

$$E(\kappa) = C_\kappa \varepsilon^{2/3}\kappa^{-5/3}. \tag{3.6}$$

This is Kolmogorov's 'minus-five-thirds' law (Kolmogorov, 1941). Experimental data suggest a value of 1.5 for the coefficient C_κ. In making measurements of spectra using hot-wire anemometry (or other fast-response instruments) one only records a one-dimensional slice of the spectrum. Provided the turbulent Reynolds number is high enough, however, the minus-five-thirds law is plainly evident, as seen in Fig. 3.5, which shows data collected by Saddoughi and Veeravalli (1994).

A further important spectral feature of turbulence is that as energy is conveyed to higher and higher wave numbers, in the process of being stretched, twisted and buffeted, the anisotropy of the velocity fluctuations of such eddies decreases. Lumley (1967), for example, has analysed the case of a simple shear flow and concluded in that situation that the spectral decay of turbulent shear stress in the inertial subrange should follow a $-7/3$ power law compared with the minus-five-thirds law for the turbulence energy. Indeed, in modelling it is commonly supposed that by the time energy has reached the dissipation range, the dissipation tensor is effectively

of the large-scale motion; for example, $L_{11} \equiv \int_0^\infty R_{11}dr_1/\overline{u_1^2}$, a quantity known as an *integral length scale*. In this work, the scalar quantity $k^{3/2}/\varepsilon$ is used throughout as the length scale representative of the large-scale energy-containing eddies, but that varies through the turbulence field in a similar way to the integral length scales.

[2] In dimensional analysis, the possibly contributing quantities that are *omitted* are just as important as those which are included. Thus, here, mean strain is excluded because the eddies in the inertial subrange are too small to notice mean velocity gradients, while viscosity is dropped because their eddy Reynolds number is too high for viscous stresses to constrain their motion significantly.

https://doi.org/10.1017/9781108875400.005 Published online by Cambridge University Press

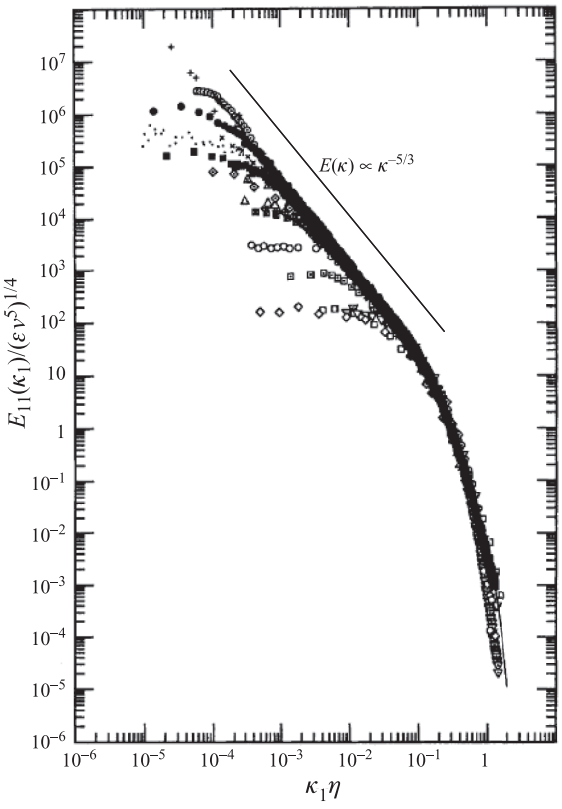

Fig. 3.5 A collection of measured one-dimensional spectra in different flows at different Reynolds numbers Re_λ (ranging from 23 to 3180). From Saddoughi and Veeravalli (1994).

isotropic. For a homogeneous flow, that situation implies that the product of two velocity derivatives can be expressed as follows:

$$\overline{\frac{\partial u_i}{\partial x_j}\frac{\partial u_k}{\partial x_l}} = \frac{\varepsilon}{30\nu}\left[4\delta_{ik}\delta_{jl} - \delta_{ij}\delta_{kl} - \delta_{il}\delta_{kj}\right] \tag{3.7}$$

(from which the reader may verify, by contracting the equation for $i = k$ and $j = l$, that it simply reverts to the definition of ε). For the component terms of ε one finds, by making all the indices equal in Eq. (3.7), that

$$\overline{\left(\frac{\partial u_1}{\partial x_1}\right)^2} = \overline{\left(\frac{\partial u_2}{\partial x_2}\right)^2} = \overline{\left(\frac{\partial u_3}{\partial x_3}\right)^2} = \frac{\varepsilon}{15\nu} \tag{3.8}$$

while for the other components of ε:

$$\overline{\left(\frac{\partial u_1}{\partial x_2}\right)^2} = \overline{\left(\frac{\partial u_1}{\partial x_3}\right)^2} = \overline{\left(\frac{\partial u_2}{\partial x_1}\right)^2} = \cdots = \frac{2\varepsilon}{15\nu}. \tag{3.9}$$

https://doi.org/10.1017/9781108875400.005 Published online by Cambridge University Press

A non-isotropic turbulent flow in which the dissipation rate is nevertheless isotropic (by virtue of the stretching that produces the very fine scales of motion in which dissipation takes place) is said to be *locally isotropic*. It is still a matter of significant controversy within the turbulence community whether local isotropy does indeed prevail in commonly encountered fully turbulent shear flows. The assumption will usually be made in the modelling chapters that it *does* but whether or not that is strictly correct is usually not of great significance. Of greater importance is the problem of characterizing correctly the large departures from local isotropy as one approaches a wall.

It is finally relevant to note that Eq. (3.8) can be inverted to obtain an expression for ε, which, in terms of the first of the mean-square velocity derivatives, can be written as:

$$\varepsilon = 15\nu\overline{\left(\frac{\partial u_1}{\partial x_1}\right)^2}. \tag{3.10}$$

In flows where the turbulence level is low and the translational velocity uniform (and in the direction x_1), it is possible to obtain a reasonably accurate estimate of the above spatial velocity derivative from the (simpler to measure) rate of velocity variation with time at the point in question, a strategy known as Taylor's hypothesis (Taylor, 1935). Moreover, Taylor introduced a turbulent length scale λ (now known as the *Taylor microscale*) defined as

$$\lambda^2 \equiv \overline{u_1^2}/\overline{(\partial u_1/\partial x_1)^2} \tag{3.11}$$

in terms of which:

$$\varepsilon = 15\nu\frac{\overline{u_1^2}}{\lambda^2}. \tag{3.12}$$

Although Taylor linked the length scale λ with that of the finest-scale eddies responsible for turbulence energy dissipation *that* has long been recognized as incorrect. Nevertheless, the Taylor microscale and the associated Reynolds number, $\mathrm{Re}_\lambda \equiv \sqrt{\overline{u_1^2}}\lambda/\nu$, are firmly embedded in the turbulence lexicon. In isotropic turbulence $\overline{u_1^2} = (2/3)k$ so, in terms of k and ε:

$$\mathrm{Re}_\lambda = \sqrt{\frac{2}{3}k\frac{15\nu(2k/3)}{\varepsilon\nu^2}} = \sqrt{\frac{20}{3}\frac{k^2}{\varepsilon\nu}} \equiv \sqrt{\frac{20}{3}\mathrm{Re}_t}. \tag{3.13}$$

The quantity Re_t is a Reynolds number representative of the energy-containing turbulent eddies and will recur frequently in the turbulence models presented in Chapters 6–8.

https://doi.org/10.1017/9781108875400.005 Published online by Cambridge University Press

3.4 The ε-equation

The energy dissipation rate is a major unknown in the k-equation. Although, to close the stress-transport equations, one needs to model the *Reynolds-stress* dissipation rate, ε_{ij}, providing a path to find ε is clearly a major step in that direction. Moreover, in modelling other processes in the stress-transport equations, a turbulent time scale is needed to characterize the rate at which the processes proceed. That time scale is conveniently provided by the quantity k/ε, which will be denoted hereafter as $\mathcal{T}$.

In this latter role, some have argued that ε is an inappropriate choice for the scale-determining variable. However, the fact remains that it has been (and continues to be) the preferred variable over a range of turbulence models of differing degrees of complexity. One obvious benefit of solving an equation for ε is that one then determines directly the sink term in the k-equation without the need for further explicit modelling. The reasons advanced for *not* choosing ε as the scale-determining variable turn on the fact that its exact transport equation describes the dynamics of the fine-scale dissipative eddies which are not representative of the large-scale turbulence principally responsible for momentum and heat transport. While this is certainly true for high-Reynolds-number turbulence not too close to a rigid boundary, in the immediate proximity of a wall there are no large eddies and viscous interactions exert an increasingly important effect on large-scale turbulence transport. The main difficulty, however, is that few of the terms in the exact equation for ε can be used without further modelling in any closed form of that equation. This problem is, however, one that is shared by all the alternatives and may be considered one of the endemic difficulties in developing a modelled scale equation.

The exact transport equation for $\varepsilon \equiv \overline{\nu(\partial u_i/\partial x_j)^2}$ can be derived by taking the spatial derivative of the equation for the rate of change of the instantaneous velocity, multiplying that by $2\,\nu\partial u_i/\partial x_j$ and, finally, time averaging the product. Thus, the left side of the transport equation becomes:

$$2\nu\overline{\frac{\partial u_i}{\partial x_j}\frac{\partial}{\partial x_j}\left(\frac{Du_i}{Dt}\right)} = \frac{D\varepsilon}{Dt}. \tag{3.14}$$

It is noted that the quantity ε is not, strictly, the energy dissipation rate though in regions where Re_t is high, it differs negligibly from it.[3]

A substantial algebraic manipulation of the corresponding right-hand side of the equation is needed to clarify the physical processes contained in the mathematics.

[3] The true kinematic dissipation rate is $\overline{\tau_{ij}s_{ij}}/\rho$, where $\tau_{ij} = 2\mu(s_{ij} - \delta_{ij}s_{kk}/3)$ is the fluctuating viscous stress and $s_{ij} \equiv (\partial u_i/\partial x_j + \partial u_j/\partial x_i)/2$ is the fluctuating strain rate, so that:

$$\varepsilon = \frac{1}{2}\nu\overline{\left(\frac{\partial u_i}{\partial x_j} + \frac{\partial u_j}{\partial x_i}\right)^2} \equiv \nu\left[\overline{\left(\frac{\partial u_i}{\partial x_j}\right)^2} + \overline{\frac{\partial u_i}{\partial x_j}\frac{\partial u_j}{\partial x_i}}\right] = \nu\left[\overline{\left(\frac{\partial u_i}{\partial x_j}\right)^2} + \frac{\partial^2\overline{u_i u_j}}{\partial x_i \partial x_j}\right].$$

https://doi.org/10.1017/9781108875400.005 Published online by Cambridge University Press

That is done by expanding and re-grouping terms in a similar fashion to that applied to the equation for the second moments. The resultant complete equation for ε can then be written as:

$$\begin{aligned}\frac{D\varepsilon}{Dt} &\equiv \underbrace{\frac{\partial \varepsilon}{\partial t}}_{\mathcal{L}_\varepsilon} + \underbrace{\frac{\partial U_k \varepsilon}{\partial x_k}}_{\mathcal{C}_\varepsilon} \\ &= \boxed{\underbrace{-2\nu\left(\overline{\frac{\partial u_i}{\partial x_l}\frac{\partial u_k}{\partial x_l}} + \overline{\frac{\partial u_l}{\partial x_i}\frac{\partial u_l}{\partial x_k}}\right)\frac{\partial U_i}{\partial x_k}}_{\mathcal{P}_{\varepsilon 1}+\mathcal{P}_{\varepsilon 2}}} \quad \boxed{\underbrace{-2\nu\overline{u_k\frac{\partial u_i}{\partial x_l}\frac{\partial^2 U_i}{\partial x_k \partial x_l}}}_{\mathcal{P}_{\varepsilon 3}}} \\ &\quad \boxed{\underbrace{-2\nu\overline{\frac{\partial u_i}{\partial x_k}\frac{\partial u_i}{\partial x_l}\frac{\partial u_k}{\partial x_l}}}_{\mathcal{P}_{\varepsilon 4}}} + \boxed{\underbrace{\sum_n \frac{2\nu}{\rho}\overline{\frac{\partial f_i^n}{\partial x_k}\frac{\partial u_i}{\partial x_k}}}_{\mathcal{F}_\varepsilon}} - \boxed{\underbrace{2\overline{\left(\nu\frac{\partial^2 u_i}{\partial x_k \partial x_l}\right)^2}}_{\Upsilon}} \\ &\quad \underbrace{\underbrace{+\frac{\partial}{\partial x_k}\left(\nu\frac{\partial \varepsilon}{\partial x_k}\right)}_{\mathcal{D}_\varepsilon^\nu} + \boxed{\underbrace{\frac{\partial}{\partial x_k}(-\overline{u_k\varepsilon'})}_{\mathcal{D}_\varepsilon^t}} + \boxed{\underbrace{\frac{\partial}{\partial x_k}\left(-\frac{2\nu}{\rho}\overline{\frac{\partial p}{\partial x_i}\frac{\partial u_k}{\partial x_i}}\right)}_{\mathcal{D}_\varepsilon^p}}}_{\mathcal{D}_\varepsilon},\end{aligned} \tag{3.15}$$

where, ε' stands for the instantaneous value, $\nu(\partial u_i/\partial u_j)^2$. The terms in boxes all need to be modelled and their physical interpretation is not immediately obvious.

However, some insight may be gained by comparing this equation with the similar but substantially simpler equation for the enstrophy (the mean square of the fluctuating vorticity) $\zeta \equiv \overline{\omega_i \omega_i}$, where:

$$\omega_i \equiv \epsilon_{ijk}\frac{\partial u_k}{\partial x_j} \text{ (or } \boldsymbol{\omega} \equiv \boldsymbol{\nabla} \times \mathbf{u}) \,. \tag{3.16}$$

The enstrophy, ζ, like the energy dissipation rate, consists of the averaged squares of fluctuating velocity gradients. Indeed, from the general quadratic velocity-derivative tensor, Eq. (3.7), it is readily deduced that in isotropic, homogeneous turbulence:

$$\zeta = \varepsilon/\nu. \tag{3.17}$$

Indeed, even in a low Reynolds number channel flow, Gorski and Bernard (1996) have shown from comparing the two sides of Eq. (3.17) (obtained from their DNS data of this flow) that the equality expressed by that equation is very nearly

Because the derivatives of the fluctuating velocity are associated with the finest eddy scales, which are expected to be isotropic at high Reynolds numbers, the second term in the two expressions on the right is usually negligible.

https://doi.org/10.1017/9781108875400.005 Published online by Cambridge University Press

completely satisfied all the way to the wall despite the very strong inhomogeneity present in the near-wall region.

The transport equation for ζ can be obtained in an analogous fashion to that for ε (see Eq. (3.14)) by taking the curl of the fluctuating velocity transport equation and multiplying each side of it by the right-hand side of Eq. (3.16). After manipulation this leads to the following equation for the transport of ζ (e.g. Gorski and Bernard, 1996):

$$\begin{aligned}\frac{\partial \zeta}{\partial t}+\frac{\partial U_k \zeta}{\partial x_k} = & \underbrace{2\overline{\omega_i \omega_j}\frac{\partial U_i}{\partial x_j}+2\overline{\omega_i \frac{\partial u_i}{\partial x_j}}\Omega_j}_{\mathcal{P}_{\zeta 1}+\mathcal{P}_{\zeta 2}} \underbrace{-2\overline{u_j \omega_i}\frac{\partial \Omega_i}{\partial x_j}}_{\mathcal{P}_{\zeta 3}} \\ & \underbrace{-\frac{\partial}{\partial x_j}(\overline{u_j \zeta'})+\nu\frac{\partial^2 \zeta}{\partial x_i^2}}_{\mathcal{D}_\zeta} \underbrace{+2\overline{\omega_i \omega_j \frac{\partial u_i}{\partial x_j}}}_{\mathcal{P}_{\zeta 4}} \underbrace{-2\nu\overline{\frac{\partial \omega_i}{\partial x_j}\frac{\partial \omega_i}{\partial x_j}}}_{\Upsilon_\zeta},\end{aligned} \tag{3.18}$$

where $\Omega_i \equiv \epsilon_{ijk}(\partial U_k/\partial x_j)$ and ζ' is the instantaneous value of ζ, i.e. $\omega_i \omega_i$. In the above equation, the terms $\mathcal{P}_{\zeta 1}$, $\mathcal{P}_{\zeta 2}$ and $\mathcal{P}_{\zeta 3}$ represent the enstrophy production due to the stretching and bending of vortex filaments by, respectively, the mean flow deformation $(\partial U_i/\partial x_j)$, the mean vorticity, Ω_j, and its gradient. The final production term $\mathcal{P}_{\zeta 4}$ is analogous to $\mathcal{P}_{\zeta 1}$ except that now it is the fluctuating strain that is responsible for the (self-) stretching of the vortex filaments. The terms grouped under $\mathcal{D}_\zeta$ have a recognizable divergence form and represent the diffusion of ζ by turbulent velocity fluctuations and molecular action. The last term, Υ_ζ, is the viscous destruction of enstrophy. It is finally noted that the enstrophy equation contains no pressure fluctuations, which might indicate that, even near a wall, the pressure-diffusion term in the ε equation was insignificant.

Returning to the ε equation, Eq. (3.15), we note first, from Eq. (3.7), that if the dissipating eddies are isotropic, the fluctuating velocity-derivative products in $\mathcal{P}_{\varepsilon 1}$ and $\mathcal{P}_{\varepsilon 2}$ are both proportional to $\varepsilon \delta_{ik}$; so, on multiplication by $\partial U_i/\partial x_k$, it is evident from continuity that the terms are zero in an incompressible flow. The term $\mathcal{P}_{\varepsilon 3}$ is also zero where the mean velocity gradient is uniform. Except possibly within the 'buffer' region next to a wall where there is a very rapid changeover from viscous to turbulent transport (with the associated rapid variation in slope of the mean velocity discussed in §1.4), the process generally makes a negligible contribution to the ε budget. That leaves simply two remaining source terms, $\mathcal{P}_{\varepsilon 1}$ and Υ_ε, whose magnitudes can be estimated by way of the Kolmogorov velocity and length scales representative of the dissipative eddies:[4] $\upsilon_K \equiv (\varepsilon \nu)^{1/4}$, $\eta \equiv (\nu^3/\varepsilon)^{1/4}$. From

[4] The forms of the dissipative scales emerge directly from assuming that their magnitudes are determined simply by the viscous dissipation rate and the kinematic viscosity. Note that, in consequence, the Reynolds number of the dissipative scales is of order unity.

https://doi.org/10.1017/9781108875400.005 Published online by Cambridge University Press

inserting these scales for the velocities and lengths appearing in the two source terms we find:

$$\mathcal{P}_{\varepsilon 4} \approx \Upsilon_\varepsilon \sim \mathcal{O}\left(\frac{\varepsilon^{3/2}}{\nu^{1/2}}\right) \sim \mathcal{O}\left(\frac{\varepsilon}{\mathcal{T}}\mathrm{Re}_t^{1/2}\right) \tag{3.19}$$

where, as a reminder, the time scale $\mathcal{T}$ is k/ε. The Reynolds number formed from the Kolmogorov scales is always unity irrespective of the bulk flow Reynolds number. The term $\mathrm{Re}_t \equiv k^2/\nu\varepsilon$, introduced in Eq. (3.13), is, as already remarked, a Reynolds number representative of the energy-containing turbulence and will usually simply be termed the turbulent Reynolds number. It is a key dimensionless parameter in modelling and will recur repeatedly throughout the book, especially in Chapters 6 and 8. Its maximum value in different turbulent flows typically ranges from several hundred to several million though evidently the no-slip condition means that it falls to zero at a wall. Equation (3.19) implies that each of the source terms is larger than the convective transport terms by the factor $\mathrm{Re}_t^{1/2}$ but their difference must evidently be of magnitude $\mathcal{O}(\varepsilon/\mathcal{T})$. How to characterize that difference in terms of calculable parameters is seen as one of the principal challenges in turbulence modelling and will be a major topic of Chapter 5 with further considerations in Chapter 6.

3.5 Transport equation for the mean-square scalar variance, $\overline{\theta^2}$

The mean-square scalar variance, $\overline{\theta^2}$, has already been introduced to characterize the intensity of scalar fluctuations as well as to define a turbulence scale for a scalar field. This variable plays the same role in characterizing a scalar field as does k for the velocity field. Moreover, in stratified flows, $\overline{\theta^2}$ appears directly in the buoyant source term in the vertical scalar flux equation (i.e. in the direction of the gravitational vector), thus its modelling is essential in flows substantially affected by buoyancy whether the stratification be caused by thermal or concentration gradients.

The transport equation for $\overline{\theta^2}$, first presented by Corrsin (1952), is readily obtained by multiplying Eq. (2.3) for the transport of a scalar, $\hat{\Theta}$, by twice the fluctuating scalar, 2θ, and averaging:[5]

$$\frac{D\overline{\theta^2}}{Dt} \equiv \underbrace{\frac{\partial\overline{\theta^2}}{\partial t}}_{\mathcal{L}_{\theta\theta}} + \underbrace{U_j\frac{\partial\overline{\theta^2}}{\partial x_j}}_{\mathcal{C}_{\theta\theta}} = \underbrace{-2\overline{\theta u_j}\frac{\partial\Theta}{\partial x_j}}_{\mathcal{P}_{\theta\theta}} \underbrace{-2\alpha\overline{\left(\frac{\partial\theta}{\partial x_j}\right)^2}}_{\varepsilon_{\theta\theta}} + \underbrace{\frac{\partial}{\partial x_j}\left(\alpha\frac{\partial\overline{\theta^2}}{\partial x_j} - \overline{\theta^2 u_j}\right)}_{\mathcal{D}_{\theta\theta}}. \tag{3.20}$$

[5] By analogy with k, some workers take $\overline{\theta^2}/2$ as the key turbulence scalar variable, and indeed have designated it k_θ (e.g. Nagano, 2002). It is important to be alert as to which choice has been made when comparing, for example, the ratio of dynamic and thermal time scales.

https://doi.org/10.1017/9781108875400.005 Published online by Cambridge University Press

The equation closely resembles the turbulence energy equation save for the absence of pressure diffusion (since pressure does not appear in the $\hat{\Theta}$ transport equation). The terms thus have a familiar physical meaning: $\mathcal{L}_{\theta\theta}$, the local time rate of change; $\mathcal{C}_{\theta\theta}$, the convective transport; $\mathcal{D}_{\theta\theta}$, the (molecular plus turbulent) diffusion; $\mathcal{P}_{\theta\theta}$, production caused by mean scalar gradients; $\varepsilon_{\theta\theta}$, the molecular destruction (the rate of 'scalar dissipation').

For passive scalars with a Prandtl–Schmidt number close to unity and comparable boundary conditions, the relative magnitude of the various terms in the $\overline{\theta^2}$ budget is also broadly similar to the corresponding terms in the turbulence energy equation. Thus, just as for the k-equation considered in §3.2, one can devise several generic flows where only two of the terms in the complete $\overline{\theta^2}$ equation are significant, which assists in the task of devising models of the unknown processes. For example, for a boundary layer in the fully turbulent region close to a uniformly heated or cooled wall, the production and dissipation terms far outweigh transport, so the thermal field is very close to a state of local equilibrium in which $\mathcal{P}_{\theta\theta} \approx \varepsilon_{\theta\theta}$, the implications of which contribute, in Chapter 7, to modelling the mean temperature distribution. The decay of turbulence energy behind a grid, as noted in §3.2, provides the primary test case for calibrating the sink term in the ε-equation. The corresponding decay of thermal fluctuations downstream of a heated grid (so that convective transport simply arises from the dissipation rate of temperature fluctuations associated with conduction in the finest scales) might thus be expected to provide vital information on how to model the decay of temperature fluctuations.

In a way it *does*, but probably not of the kind a modeller would be hoping to find. From a broad consensus of experiments (e.g. Lin and Lin, 1973; Warhaft and Lumley, 1978; Warhaft, 2000) it is clear that the decay exponent m in the expression $\overline{\theta^2} \propto t^{-m}$ depends greatly on initial conditions – effectively on the ratios of the length scales of the energy-containing parts of the dynamic and thermal turbulence fields, Fig. 3.6. While the causes of this behaviour remain inadequately understood, as Warhaft (2000) indicates, in flows where mean thermal gradients are present (thus creating a source of temperature fluctuations) the time-scale ratio for the thermal and dynamic turbulence heads towards a constant value irrespective of its initial value.

In general, the budget for $\overline{\theta^2}$, like that for k, varies from one particular flow to another even within the same broad class of flows. For example, in two-dimensional free shear flows, mixing layers developing between two streams of unequal temperatures display an overall excess of production over dissipation, whereas in axisymmetric wakes, the average level of production is much less than the average dissipation, resulting in an appreciable convective loss as the flow develops downstream, Fig. 3.7.

https://doi.org/10.1017/9781108875400.005 Published online by Cambridge University Press

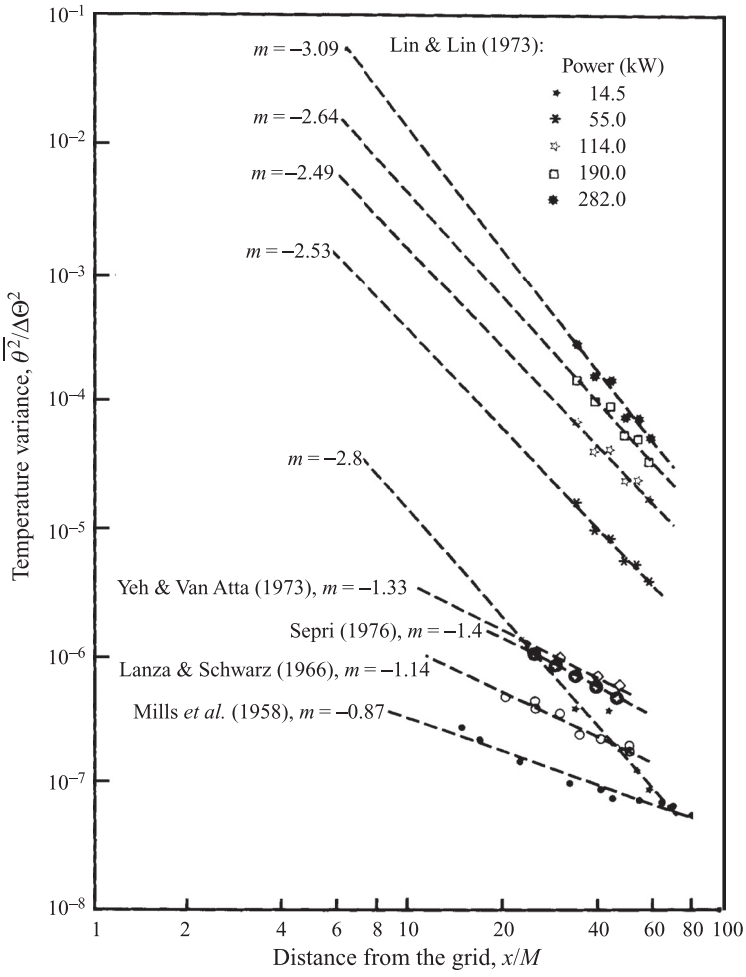

Fig. 3.6 Decay of grid turbulence downstream from heated grids. Reprinted with permission from Warhaft and Lumley (1978). ©1978, American Institute of Physics.

3.6 Transport equation for dissipation of scalar variance, $\varepsilon_{\theta\theta}$

Just as with the dynamic field, the dissipation rate of scalar variance, $\varepsilon_{\theta\theta} \equiv 2\,\alpha\overline{(\partial\theta/\partial x_j)^2}$, is the predominant choice for a second variable for the scalar turbulence. This is used to obtain time and length scales representative of the thermal turbulence and, of course, to determine the sink term in Eq. (3.20). This variable turns out to be especially important in modelling reacting or combusting flows (topics outside the scope of the present book). An exact transport equation for $\varepsilon_{\theta\theta}$ can be derived by a path analogous to that followed to obtain the ε-equation: first take the derivative with respect to x_j of each side of the transport equation for

https://doi.org/10.1017/9781108875400.005 Published online by Cambridge University Press

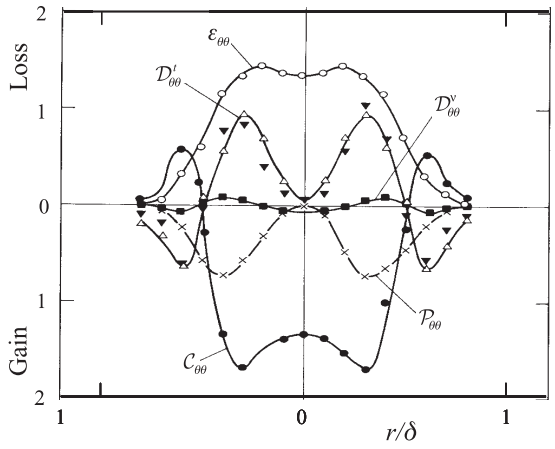

Fig. 3.7 Dimensionless budget of mean square temperature variance in the wake of a sphere. Reprinted with permission from Freymuth and Uberoi (1973). ©1973, American Institute of Physics.

the instantaneous scalar $(\Theta + \theta)$ and then multiply each term by $4\alpha\partial\theta/\partial x_j$ and average each term. After some algebraic manipulation, one obtains:

$$\frac{D\varepsilon_{\theta\theta}}{Dt} \equiv \underbrace{\frac{\partial \varepsilon_{\theta\theta}}{\partial t}}_{\mathcal{L}_{\varepsilon_{\theta\theta}}} + \underbrace{\frac{\partial (U_k \varepsilon_{\theta\theta})}{\partial x_k}}_{\mathcal{C}_{\varepsilon_{\theta\theta}}}$$

$$= \underbrace{-4\alpha \left(\overline{\frac{\partial\theta}{\partial x_l}\frac{\partial u_k}{\partial x_l}} \right) \frac{\partial \Theta}{\partial x_k}}_{\mathcal{P}_{\varepsilon_{\theta\theta}1}} \underbrace{-4\alpha \left(\overline{\frac{\partial\theta}{\partial x_i}\frac{\partial\theta}{\partial x_k}} \right) \frac{\partial U_i}{\partial x_k}}_{\mathcal{P}_{\varepsilon_{\theta\theta}2}} \underbrace{-4\alpha \overline{u_k \frac{\partial\theta}{\partial x_l}\frac{\partial^2 \Theta}{\partial x_k \partial x_l}}}_{\mathcal{P}_{\varepsilon_{\theta\theta}3}}$$

$$\underbrace{-4\alpha \overline{\frac{\partial\theta}{\partial x_k}\frac{\partial\theta}{\partial x_l}\frac{\partial u_k}{\partial x_l}}}_{\mathcal{P}_{\varepsilon_{\theta\theta}4}} - \underbrace{4\overline{\left(\alpha \frac{\partial^2\theta}{\partial x_k \partial x_l}\right)^2}}_{\Upsilon_{\theta\theta}}$$

$$\underbrace{\underbrace{+\frac{\partial}{\partial x_k}\left(\alpha \frac{\partial \varepsilon_{\theta\theta}}{\partial x_k}\right)}_{\mathcal{D}^v_{\varepsilon_{\theta\theta}}} + \underbrace{\frac{\partial}{\partial x_k}(-\overline{\varepsilon'_{\theta\theta} u_k})}_{\mathcal{D}^t_{\varepsilon_{\theta\theta}}}}_{\mathcal{D}_{\varepsilon_{\theta\theta}}}. \tag{3.21}$$

Just as for the corresponding ε-equation, the source terms containing the mean-field gradients are zero if the double products of temperature derivatives (or temperature and velocity derivatives) are locally isotropic. The term $\mathcal{P}_{\varepsilon_{\theta\theta}3}$ is also negligible

https://doi.org/10.1017/9781108875400.005 Published online by Cambridge University Press

except possibly very close to the wall where there is a rapid changeover from molecular to turbulent transport. The remaining source and sink terms, $\mathcal{P}_{\varepsilon_{\theta\theta}4}$ and $\Upsilon_{\theta\theta}$, can be shown to be the dominant terms by making an order-of-magnitude estimate in terms of the Kolmogorov scales.[6] When it comes to modelling these terms, however, one needs to allow both scalar and dynamic time scales to exert an effect – certainly, if one requires the modelled equation to mimic the non-universal decay of $\overline{\theta^2}$ shown in Fig. 3.6. As discussed in Chapter 5, therefore, many workers (including the present authors) have usually preferred to prescribe the relevant turbulent scalar time scale (and thus the local level of $\varepsilon_{\theta\theta}$) by other means.

3.7 Turbulence anisotropy, invariants and realizability

A primary aim of this book is to provide a path for determining the second moments in a turbulent flow, namely the kinematic Reynolds stresses, $\overline{u_i u_j}$, and the scalar fluxes, $\overline{\theta u_j}$. Because the stress tensor is symmetric, it will in general comprise six distinct terms: three diagonal components ($i = j$), which stretch or compress a fluid element (the *normal* stresses, $\overline{u_1^2}, \overline{u_2^2}, \overline{u_3^2}$), and three off-diagonal components ($i \neq j$), i.e. $\overline{u_1 u_2} = \overline{u_2 u_1}, \overline{u_1 u_3} = \overline{u_3 u_1}$ and $\overline{u_2 u_3} = \overline{u_3 u_2}$. At any point in a fluid, the magnitudes of the different stress components necessarily depend on the orientation of the coordinate system. Indeed, we can align the orthogonal coordinates so that the shear stresses are all zero – the so-called *principal coordinates* – in which case the normal stresses take their extreme values. These matters and some consequences are examined in the following sections.

3.7.1 Turbulent stress anisotropy

In flows of practical interest the turbulent stress tensor is non-isotropic, a state created partly by the deformation of the large eddies by mean strain or body forces, partly by flow inhomogeneities and partly by boundary conditions. If the stress tensor *were* isotropic, all the normal stresses would be equal and there would be no shear stresses (for otherwise reorienting the axes would then cause the normal stresses to be unequal). Thus, in isotropic turbulence, $\overline{u_i u_j} = 2\delta_{ij}k/3$. A departure from the isotropic state provides a measure of the stress anisotropy which can be expressed in terms of the deviatoric part of the stress tensor, i.e.

$$\overline{u_i u_j} = \underbrace{\left(\overline{u_i u_j} - \frac{2}{3}k\delta_{ij}\right)}_{\text{anisotropic}} + \underbrace{\frac{2}{3}k\delta_{ij}}_{\text{isotropic}} . \tag{3.22}$$

[6] This necessarily requires that the molecular Prandtl–Schmidt number should be not too different from unity (i.e. probably acceptable for gases and many liquids but not for liquid metals).

https://doi.org/10.1017/9781108875400.005 Published online by Cambridge University Press

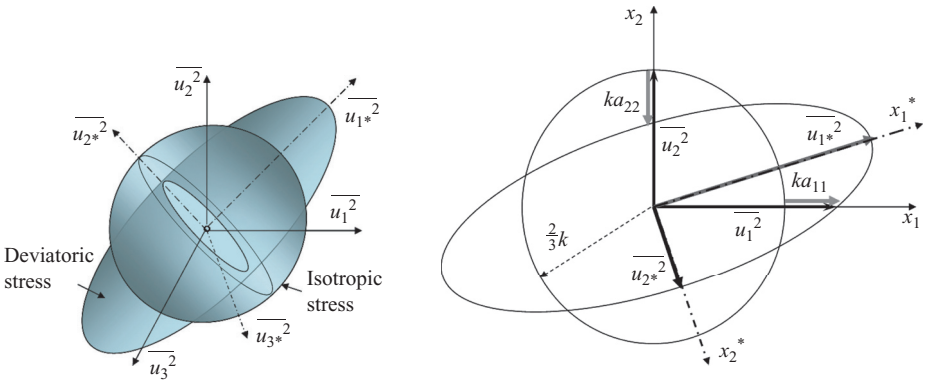

Fig. 3.8 Stress ellipsoid (left) and a two-dimensional cut for $x_3 = 0$ (right) for a point in the selected coordinate system (x_1, x_2, x_3) showing components of stress anisotropy (deviatoric part of the stress tensor), a_{11} and a_{22}. The principal stress coordinate axes are denoted by $x_1^*,\ x_2^*$.

The deviatoric part, made non-dimensional by dividing by k, is referred to as the *stress-anisotropy tensor*, a_{ij}:

$$a_{ij} \equiv \frac{\overline{u_i u_j}}{k} - \frac{2}{3}\delta_{ij.} \tag{3.23}$$

Note that the diagonal components of a_{ij} must fall within the range

$$-\frac{2}{3} \leq a_{\beta\beta} \leq \frac{4}{3} \tag{3.24}$$

(where no summation is implied on repeated Greek subscripts).[7]

It is only the anisotropic part of the stress tensor that transports momentum, while the isotropic part is 'inactive'. In treating the momentum equation, it can be lumped with the mean pressure. The normal stresses at a point can be represented by a 'stress ellipsoid' shown in Fig. 3.8. The magnitudes of the normal stresses in the chosen coordinate system (x_1, x_2, x_3) correspond to the intersection points of the axes with the ellipsoid surface, while the isotropic stress corresponds to the sphere of radius $2k/3$. The principal coordinates correspond with the major and minor axes of the stress ellipsoid, and the (normal) stress components – the *principal stresses* – are the eigenvectors of the stress tensor.

[7] An alternative anisotropy tensor, usually identified by the symbol b_{ij}, is also found in the literature, where the deviatoric stress is normalized by the sum of the normal stresses rather than k:

$$b_{ij} \equiv \frac{\overline{u_i u_j}}{2k} - \frac{1}{3}\delta_{ij} = \frac{a_{ij}}{2}.$$

https://doi.org/10.1017/9781108875400.005 Published online by Cambridge University Press

3.7.2 Turbulent stress invariants and limiting states

For any second-rank tensor one can define a number of invariants, comprising scalar products of the components which are thus independent of the coordinate system. For the stress-anisotropy tensor there are three basic invariants, defined as follows:

$$A_1 \equiv a_{ii} = 0, \quad A_2 \equiv a_{ji}a_{ij}, \quad A_3 \equiv a_{ij}a_{jk}a_{ki} \tag{3.25}$$

or, in expanded form:

$$\begin{aligned} A_2 &= a_{11^*}^2 + a_{22^*}^2 + a_{33^*}^2 \\ &= a_{11}^2 + a_{22}^2 + a_{33}^2 + 2(a_{12}^2 + a_{13}^2 + a_{23}^2) \end{aligned} \tag{3.26}$$

$$\begin{aligned} A_3 &= a_{11^*}^3 + a_{22^*}^3 + a_{33^*}^3 \\ &= a_{11}^3 + a_{22}^3 + a_{33}^3 + 3a_{12}^2(a_{11} + a_{22}) + 3a_{13}^2(a_{11} + a_{33}) \\ &\quad + 3a_{23}^2(a_{22} + a_{33}) + 6a_{12}a_{13}a_{23}. \end{aligned} \tag{3.27}$$

Clearly, higher order invariants can be defined, but these can all be expressed (from the Cayley–Hamilton theorem, see Chapter 4) in terms of A_2 and A_3. The invariants provide, in a compact way, information about the character of the stress anisotropy. This is most clearly illustrated by considering them in principal coordinate axes. The second invariant, A_2, is always positive and gives a direct measure of the stress anisotropy: the larger A_2, the more anisotropic is the stress field. The third invariant comprises cubic products and thus can be positive (if two of the anisotropy components are negative), thus producing a cigar-shaped stress ellipsoid, or negative (i.e. with only one negative component) when, in the limit, the stress ellipsoid deforms to a pancake-shaped disc.[8] Thus, A_3 gives more subtle information about the nature of the stress anisotropy.

The anisotropy invariants can of course be combined in various ways to produce further invariants that will have different characteristics. One that is especially helpful in modelling is what is known as Lumley's flatness parameter (Lumley, 1978):

$$A \equiv 1 - 9\,[A_2 - A_3]\,/8. \tag{3.28}$$

What makes this parameter so useful is that, while it evidently equals unity in isotropic turbulence, when the turbulence is so non-isotropic that one of the normal-stress components is zero (what is known as *two-component turbulence*), A is equal to zero. This surprising result is readily verified by working in principal axes (though the * symbol will no longer be applied). If, say, $\overline{u_1^2} = 0$, then, quite generally, the stress-anisotropy components can be written as: $a_{11} = -\frac{2}{3}$,

[8] The deformation of an idealized turbulent eddy shape goes in the opposite manner from the deformation of the stress ellipsoid: a cigar-shaped ellipsoid usually corresponds to a disc-shaped eddy and vice versa.

https://doi.org/10.1017/9781108875400.005 Published online by Cambridge University Press

$a_{22} = (\frac{1}{3} + \delta)$, $a_{33} = (\frac{1}{3} - \delta)$, where δ is a constant lying in the range $-1 \leq \delta \leq 1$. Then, it is readily verified from Eqs. (3.26) and (3.27) that $(A_2 - A_3)$ is equal to 8/9 irrespective of the value of δ.

In an analogous way, one can define an anisotropy tensor and its invariants for the stress dissipation rate:

$$e_{ij} \equiv \frac{\varepsilon_{ij}}{\varepsilon} - \frac{2}{3}\delta_{ij}, \quad E_1 \equiv e_{ii} = 0, \quad E_2 \equiv e_{ij}e_{ji}, \quad E_3 \equiv e_{ij}e_{jk}e_{ki}. \tag{3.29}$$

In a high Reynolds number flow away from the vicinity of a wall the stress-dissipation invariants are all negligible, but close to a solid wall where there are no large eddies they exhibit non-zero values, apparently irrespective of Reynolds number (though smaller than the corresponding values of the stress invariants), indicating an endemic departure from local isotropy.

The above stress invariants find many uses in second-moment modelling. First, they help to define possible states of the stress tensor – sometimes termed *realizable* states. Even some of the most successful models of turbulence can generate non-realizable states (usually during iteration of an unconverged stress field) and, if such an occurrence arises, it may shortly thereafter wreck convergence. It may thus be desirable to build in checks to ensure that, even during progress to a solution, the turbulence field can only pass through a succession of realizable states achieved, conveniently, by placing bounds on the stress invariants. Another role for the invariants is just as parameters in modelling a process, a topic on which much more will be written in later chapters.

To complete this examination of stress invariants we note three limiting states. The first, which hardly needs mentioning, is that of isotropic turbulence where A_2 and A_3 are zero and, as noted above, $A = 1$. The other two states of particular fundamental interest are *two-component* turbulence and *one-component* turbulence. Both can be reached, in principle, through the action of a force field or by applying an axisymmetric deformation to an idealized turbulence field where slip is permitted on the surfaces of the axisymmetric nozzle or diffuser. In such a deformation, if the streamwise strain is $\partial U_1/\partial x_1$, then from continuity and axisymmetry considerations: $\partial U_2/\partial x_2 = \partial U_3/\partial x_3 = -\frac{1}{2}\partial U_1/\partial x_1$. The stress field will also remain axisymmetric through the deformation; thus, $a_{22} = a_{33} = -a_{11}/2$. The two stress-anisotropy invariants thus take the following form for axisymmetric flow:

$$A_2 = \frac{3}{2}a_{11}^2, \quad A_3 = \frac{3}{4}a_{11}^3. \tag{3.30}$$

https://doi.org/10.1017/9781108875400.005 Published online by Cambridge University Press

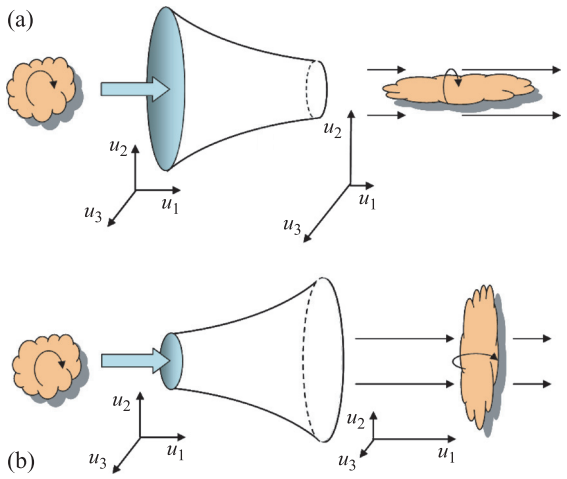

Fig. 3.9 Axisymmetric turbulence created by passing initially isotropic turbulence through an area contraction (a) and expansion (b), leading ultimately to the two-component and one-component limits, respectively.

Eliminating a_{11} between the two parts of (3.30) gives the following interrelation among the invariants for axisymmetric, shearless flow:

$$A_3 = \pm\frac{3}{4}\left(\frac{2}{3}A_2\right)^{3/2} \tag{3.31}$$

where the positive sign refers to an area expansion and the negative sign to an area contraction. In the case of a converging passage, the acceleration will stretch eddies in the streamwise direction, Fig. 3.9a, but note that since the production rate of streamwise normal stress, $\mathcal{P}_{11} = -2\overline{u_1^2}\left(\partial U_1/\partial x_1\right)$, is negative, the streamwise normal stress will fall, while, correspondingly, the production of the normal stresses in the duct's cross-sectional plane is positive, and thus those stresses will increase. In the extreme limit one finds $\overline{u_1^2} \to 0$ and $\overline{u_2^2} = \overline{u_3^2} \to k$.

If, in contrast, isotropic turbulence is passed through a diverging axisymmetric duct,[9] Fig. 3.9b, the flow deceleration compresses the eddies in the streamwise direction, which leads to an augmentation of the streamwise normal stress since the production of that component is now positive, while that of $\overline{u_2^2}$ and $\overline{u_3^2}$ is negative. Thus in the extreme limit one now finds $\overline{u_2^2} = \overline{u_3^2} \to 0$ and $\overline{u_1^2} \to 2k$.

While the limiting states described above cannot in practice be achieved in actual experiments, there are real-life situations where the turbulence *is* constrained to the two-component state. At a phase interface in the presence of a body force – the most common example of which arises at the free (water–air) surface in a lake –

[9] Imagining an inviscid flow with slip occurring at the walls, thus avoiding separation, an effect that would certainly arise in a real flow.

https://doi.org/10.1017/9781108875400.005 Published online by Cambridge University Press

turbulent velocity fluctuations normal to the interface are suppressed, while those parallel to it are effectively unconstrained. Similar effects caused by body forces can arise in other situations such as the electromagnetic Lorentz force, which again dampens velocity fluctuations in the direction of the force. An even more important example is the limiting form of the anisotropy tensor very close to a smooth wall. As shown in Chapter 1, the normal-stress components parallel to the wall then vary as x_2^2, while the component normal to the wall varies as x_2^4; thus, in the limit as the wall is approached $\overline{u_2^2}$ becomes negligible compared with the other normal-stress components. This behaviour is well illustrated in Fig. 3.10, from the early DNS channel flow data of Kim *et al.* (1987). Figure 3.10, left, shows the non-zero Reynolds-stress components on a linear scale, while Fig 3.10, right, presents the Reynolds stresses normalized by the turbulence energy, the logarithmic abscissa scale giving especial prominence to the near-wall region. From the latter it is clear that the stress field does reach a two-component state deep in the viscous sublayer. The flatness parameter A thus also falls to zero in the vicinity of the wall, as seen in Fig. 3.14.

As a final 'canonical' flow we consider the development of an idealized flow through a rectangular-sectioned duct that gradually changes its shape but with its cross-sectional area remaining constant, Fig. 3.11. Thus, the streamwise velocity remains constant, there being neither stretching nor compression in that direction, but the initially isotropic turbulence is subject to a plane-strain distortion. The mean velocity field is thus: $U_1 = \text{const}$; $U_2 = -U_3 = -cx_1$. Consequently, $\mathcal{P}_{11} = 0$ and, initially, $\mathcal{P}_{22} = -\mathcal{P}_{33}$ since the stress field at the start is isotropic. Thus, the initial development of the stress tensor will be one where $a_{11} = 0$, $a_{22} = -a_{33}$,[10] which results in $A_2 = 2a_{22}^2$ and $A_3 = 0$.

We can now summarize the above examination of types of homogeneous turbulent flows subjected to a variety of irrotational strains by plotting the limiting processes and the resultant states of the stress field on the *invariant map* shown in Fig. 3.12, a presentation first provided by Lumley (1978). The important conclusion is that realizable turbulence must have values of the invariants that place them within or on the boundaries of the triangular area shown.

Somewhat different shapes of the domain of realizable turbulence can be obtained by choosing alternative invariants. For example, Pope (2000) uses the quantities $(1/24\ A_2)^{1/2}$ and $(1/48\ A_3)^{1/3}$, while Craft and Launder (2002b) adopt A as an alternative to A_3, thus confining the region of realizable turbulence to the first quadrant, Fig. 3.13.

[10] Although, when the distortion is first applied and the turbulence is isotropic, $\mathcal{P}_{33} = -\mathcal{P}_{22}$, the consequent increase in $\overline{u_2^2}$ and decrease in $\overline{u_3^2}$ reduces the magnitude of $\mathcal{P}_{33}$ relative to $\mathcal{P}_{22}$ and consequently both a_{11} and A_3 will slowly become non-zero as the flow develops through the distortion.

https://doi.org/10.1017/9781108875400.005 Published online by Cambridge University Press

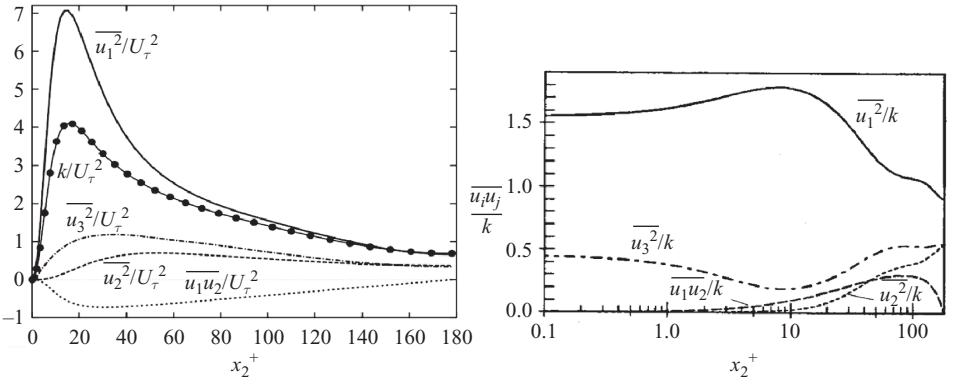

Fig. 3.10 Distribution of turbulent stress components very close to the wall in a plane channel flow, normalized with the wall friction velocity (left) and with the kinetic energy k (right). Evaluated from DNS results of Kim *et al.* (1987).

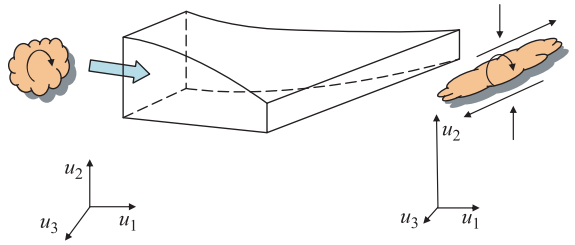

Fig. 3.11 Plane distortion created by passing initially isotropic turbulence through a constant-area duct with a gradual change of its form.

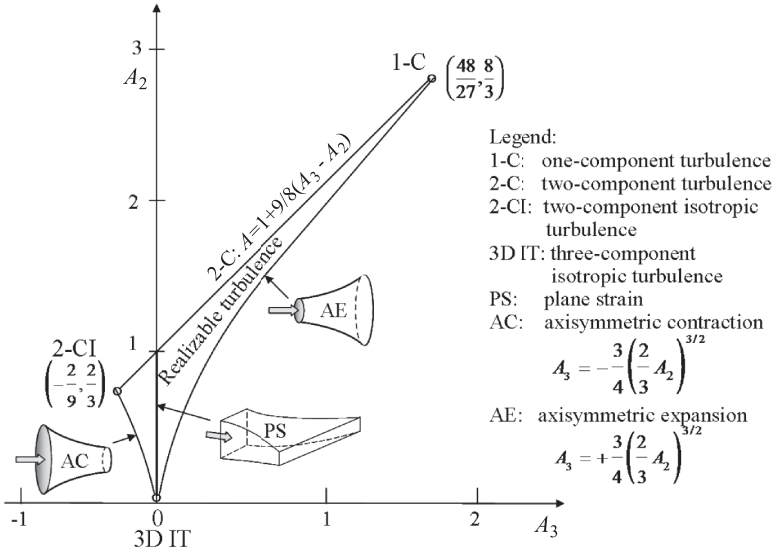

Fig. 3.12 Stress-invariant map, summarizing the realizable region of turbulence and its limits.

https://doi.org/10.1017/9781108875400.005 Published online by Cambridge University Press

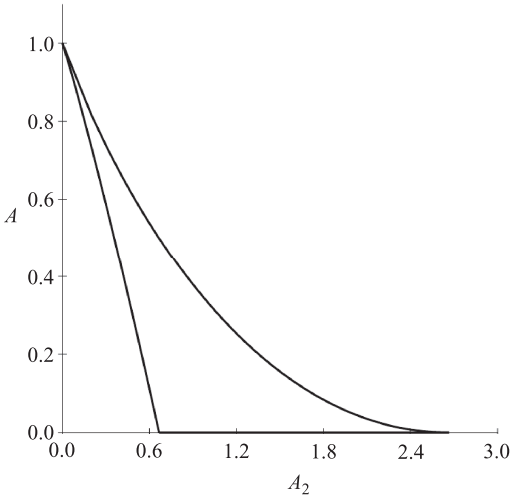

Fig. 3.13 Anisotropy map in the $A - A_2$ domain (Craft and Launder, 2002b).

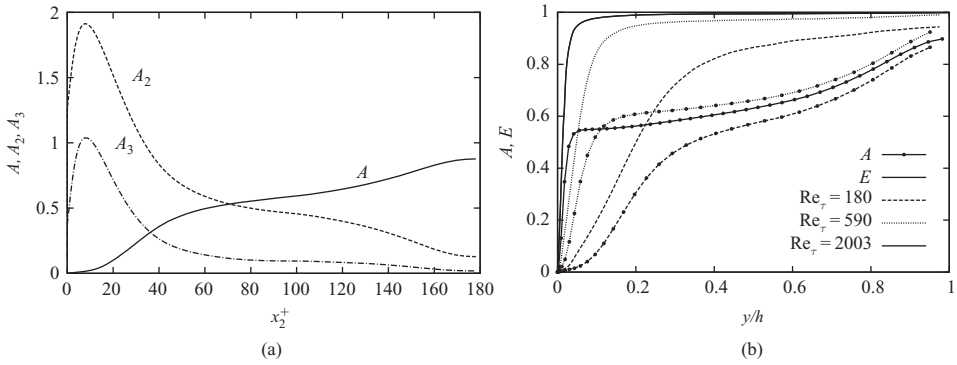

Fig. 3.14 Stress-anisotropy invariants (a) and comparison of the stress and dissipation-rate flatness parameters (b) in a fully developed plane channel flow (evaluated from DNS results of Kim *et al.*, 1987; Moser *et al.*, 1999 and Hoyas and Jimenez, 2006).

To give some impression of how the invariants may be distributed across a wall-bounded shear flow, Fig. 3.14 shows their variation in channel flow obtained from the available DNS data. The peak values of the invariants A_2 and A_3 actually occur a little way from the wall though, as remarked above, A vanishes at the wall itself. We note that while the dissipation flatness parameter, E, (Fig. 3.14b) also vanishes at the wall, it rises more rapidly than A (increasingly so as the bulk Reynolds number is raised) and approaches unity (its isotropic value) over the central half of the channel.

https://doi.org/10.1017/9781108875400.005 Published online by Cambridge University Press

3.7.3 Anisotropy of the scalar field

The scalar flux is a vector and thus a strict scalar-flux analogue of the stress-invariant map and realizability constraints on the stress invariants does not exist. A variable that *can* serve as a measure of the anisotropy of a scalar field is the scalar-flux correlation function:

$$A_\theta \equiv \frac{(\overline{\theta u_j})^2}{\overline{\theta^2}\,\overline{u_k u_k}}. \tag{3.32}$$

One can, in fact, go further in pursuing an analogy with the stress field by defining a mixed second-rank anisotropy tensor (Shih *et al.*, 1990):

$$a_{ij}^\theta \equiv \frac{\overline{\theta^2}\,\overline{u_i u_j} - \overline{\theta u_i}\cdot\overline{\theta u_j}}{\overline{\theta^2}\cdot\overline{u_k^2} - (\overline{\theta u_k})^2}. \tag{3.33}$$

It is readily appreciated that from this one can construct invariants in just the same way as for the stress tensor. Thus:

$$A_2^\theta \equiv a_{ij}^\theta a_{ji}^\theta, \quad A_3^\theta \equiv a_{ij}^\theta a_{jk}^\theta a_{ki}^\theta, \quad A^\theta \equiv 9[1-3A_2^\theta+2A_3^\theta]/2.$$

As discussed in later chapters, the invariant A_θ has been found to be a useful parameter in correlating variations of the scalar-to-mechanical time scale. However, attempts to use one or more of the mixed scalar-dynamic invariants to refine the empirical coefficients in the scalar flux equations (analogous to what is successfully done for the stress-transport equations) has not met with significant success.

https://doi.org/10.1017/9781108875400.005 Published online by Cambridge University Press

4

Approaches to closure

4.1 General remarks and basic guidelines

The aim of turbulence modelling is to mimic those processes not exactly determinable at the chosen level of closure in terms of mean and turbulence properties that *are*. The challenge is sometimes referred to as the *turbulence closure problem*. It is recalled that the focus is on the second moments, $\overline{\varphi u_j}$, which appear as the unknown variables in the Reynolds-averaged mean momentum and scalar transport equations. The processes in question are the turbulent transport of momentum and any scalar of interest, represented by the turbulent stress, $\overline{u_i u_j}$, and scalar flux, $\overline{\theta u_j}$, respectively. These second moments are always tensors of a higher order than the variables for which the mean-flow transport equations are solved. For example, if φ is a scalar, $\overline{\varphi u_j}$ is a vector (a first-order tensor), and if φ is a vector, $\overline{\varphi u_j}$ is a second-order tensor. This complicates the closure task because, first, with closure at second-moment level, one needs to solve many more additional equations to determine these unknown variables than for the corresponding laminar flow. Moreover, to close the second-moment equations one has to devise approximations for third moments for which experimental data are relatively scarce.

At a practical level, one naturally wishes to adopt the simplest closure consistent with achieving the desired accuracy and width of applicability. This goal clearly affects the importance that different workers have attached to different closure principles. As a first requirement, any surrogate form must have the same dimensions as the correlation it replaces; there is no controversy on this point. Next, the mathematical character of the model should conform in various respects with the original. For example, if the process requiring approximation is a second-rank, symmetric tensor with zero trace, the search for a model should be limited to forms possessing these properties. Although this principle is usually adhered to at second-moment level, it is frequently ignored in modelling the third moments.

https://doi.org/10.1017/9781108875400.006 Published online by Cambridge University Press

This can be regarded as the application of a further fundamental concept: *the principle of receding influence*. Broadly, the idea is that the nth-moment correlations have markedly less effect on the mean flow than those of $(n-1)$th order. So, rules that are held inviolate for second moments are sometimes dispensed with in the interests of algebraic and computational convenience in dealing with third moments. It is clearly a matter of taste, and of the flows to be calculated, how freely one invokes this principle. Everyone developing models at this level makes some use of it, however, for it is that idea which ultimately legitimizes second-moment closure.

Two further principles of mathematical physics have commonly been invoked in determining modelling approaches. First, it is generally accepted that the approximate forms should exhibit the same response to translations, accelerations and reflections of the coordinate frame as the real processes (e.g. Donaldson, 1971). The second constraint is that the modelled set of transport equations should be rendered physically incapable of generating impossible or 'unrealizable' values such as negative normal stresses or correlation coefficients (such as $\overline{u_1 u_2}/\sqrt{\overline{u_1^2}\,\overline{u_2^2}}$ greater than unity, Schumann, 1977). Here the work of André *et al.* (1979) is also mentioned: they devised a scheme for overwriting or 'clipping' the values of triple moments whenever they reached physically unattainable values in comparison with other double and triple moments. Although Schumann suggested ways of securing 'realizability', the interested reader is referred to the far more detailed treatment by Lumley (1978). Unfortunately, although the principle of realizability is sound, its adoption adds considerably to the complexity of the turbulence closure and only the later generations of modelling proposals have employed realizable forms in computations of inhomogeneous flows, for example Shih and Lumley (1985), and Craft and Launder (1989). Models which, in principle, are capable of generating impossible values of second moments may, in practice, do so for flows which are of only academic interest. Indeed, second-moment closure studies of recirculating, swirling and other complex flows have been made with forms that do not guarantee realizability. However, employing fully realizable closures often increases the convergence rates in flows requiring an iterative solution, while certain features of turbulence that consistently eluded the simpler models (such as the observed reduction of turbulent mixing at high strain rates) emerge naturally without specific empirical tuning.

The next concept is self-evident but because it is key to a successful turbulence model it is still worth emphasizing. The model should always be a physically plausible substitute for the real process. This statement includes the choice of contributing physical quantities; for example, whether the model should comprise exclusively turbulence correlations or include terms containing mean-field

elements – and the way they are combined together. It is often helpful to explore different ways of expressing the correlation of interest; one form might give much more insight than another.

The above considerations can be summarized in a set of mathematical and physical rules with which every term in the equations defining a turbulence model should ideally comply:

- dimensional coherence
- tensorial (vector) order consistency
- coordinate frame indifference (frame and index invariance)
- realizability
- limiting properties (which may also be a corollary of realizability, for example, two-component turbulence)
- physical coherence, implying that turbulence correlations should be modelled in terms of turbulence parameters instead of, for example, global mean-flow characteristics such as the bulk-flow Reynolds number or pressure gradient.

A considerable simplification to the task of turbulence modelling results from applying the *high Reynolds number hypothesis*. Simply stated, the proposal contains two complementary ideas:

(i) that the large-scale interactions predominantly responsible for momentum and scalar transport are unaffected by the viscosity of the fluid;
(ii) that the fine-scale motions responsible for viscous dissipation are unaware of the nature of the mean flow and the large-scale turbulence; their structure is similar to that found in isotropic turbulence.

It is, in fact, well established that the fine-scale motion, particularly in regard to higher moment correlations, is not exactly like isotropic turbulence, but nevertheless, if judiciously applied, both aspects of the high Reynolds number hypothesis are very useful in turbulence modelling.

In the following sections we consider the principles and practice of modelling the terms in Eq. (2.18) and (2.22) contained in boxes. First, exact (but unusable) expressions for the important pressure-containing correlations will be obtained. Then, in §4.3 what we term the *basic models* of each term will be presented. Despite being largely based on intuition and heuristic arguments and being 50 years or more old, because of their simplicity, these models are still widely used in industrial practice. Moreover, the basic closures are often the leading terms of more elaborate, higher order models, which are then extensively considered in §4.4. The

https://doi.org/10.1017/9781108875400.006 Published online by Cambridge University Press

effects of various force fields on the pressure-containing correlations are the subject of §4.5, while finally the role of triple moments and their modelling is considered in §4.6.

4.2 Pressure interactions, Φ_{ij} and $\Phi_{\theta j}$: the Poisson equation

Modelling the terms involving fluctuating pressure interactions in Eqs. (2.18) and (2.22) is the most challenging task in second-moment closure. Before considering arguments and routes for modelling these interactions, it is noted that pressure fluctuations have a profound effect on turbulence dynamics. Pressure perturbations travel in all directions through the fluid as waves, at a propagation speed which in an incompressible fluid is infinite. Thus, the effect is by no means local, but is felt instantly over the whole flow domain, as may be seen below from the Poisson equation that governs the fluctuating pressure. By taking the divergence of the Navier–Stokes equations (2.2) and subtracting its mean part, a Poisson equation is produced with the fluctuating pressure as its subject:

$$\frac{1}{\rho}\frac{\partial^2 p}{\partial x_l^2} = -\frac{\partial^2}{\partial x_l \partial x_m}(u_l u_m - \overline{u_l u_m}) - 2\frac{\partial U_l}{\partial x_m}\frac{\partial u_m}{\partial x_l} + \frac{\partial f_l}{\partial x_l}. \tag{4.1}$$

The equation can be integrated over volume V bounded by the surface A, using Green's theorem, to yield the fluctuating pressure at a point defined by the position vector $\mathbf{x}$, Fig. 4.1:[1]

$$\begin{aligned} p(\mathbf{x}) = {} & \underbrace{\frac{\rho}{4\pi}\int_V \frac{\partial^2}{\partial x_l' \partial x_m'}(u_l' u_m' - \overline{u_l' u_m'})\frac{dV(\mathbf{x}')}{r}}_{p_{(1)}} + \underbrace{\frac{\rho}{2\pi}\int_V \frac{\partial U_l'}{\partial x_m'}\frac{\partial u_m'}{\partial x_l'}\frac{dV(\mathbf{x}')}{r}}_{p_{(2)}} \\ & \underbrace{-\frac{\rho}{4\pi}\int_V \frac{\partial f_l'}{\partial x_l'}\frac{dV(\mathbf{x}')}{r}}_{p_{(3)}} + \underbrace{\frac{1}{4\pi}\int_V \left[\frac{1}{r}\frac{\partial p'}{\partial n} - p'\frac{\partial}{\partial n}\left(\frac{1}{r}\right)\right] dA}_{p_{(w)}} \end{aligned} \tag{4.2}$$

where $r \equiv |\mathbf{x}' - \mathbf{x}|$. All variables under the integral sign (denoted by primes) are evaluated at the point P' with position vector $\mathbf{x}'$, Fig. 4.1.

As noted above, Eq. (4.2) is elliptic, implying that the resulting field is non-local, i.e. it extends beyond the location of its source. Terms on the right of the equation can be regarded as sources of pressure fluctuations. The first three terms,

[1] Green's identity states that $\nabla(G\nabla p) = \nabla G \nabla p + G\nabla^2 p$, where G and p are continuous functions. Taking a volume integral and converting the first term into a surface integral using Green's theorem, leads to $\int_A G\nabla p dA = \int_V (\nabla G \nabla p + G\nabla^2 p) dV$. By assigning the Dirac delta function for the Green function, $G = 1/r$, one obtains:

$$p(\mathbf{x}) = -\frac{1}{4\pi}\int_V \nabla^2 p' \frac{dV(\mathbf{x}')}{r} + \frac{1}{4\pi}\int_A \left[\frac{1}{r}\frac{\partial p'}{\partial n} - p'\frac{\partial}{\partial n}\left(\frac{1}{r}\right)\right] dA.$$

https://doi.org/10.1017/9781108875400.006 Published online by Cambridge University Press

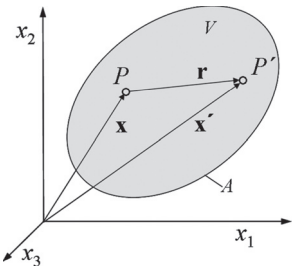

Fig. 4.1 Sketch relating to the integration of the Poisson equation.

$p_{(1)}$, $p_{(2)}$, $p_{(3)}$ are the particular solutions of the Poisson equation for unconfined space, whereas the last term, $p_{(w)}$, becomes significant only in the proximity of a solid wall. It is noted that $p_{(1)}$ is non-linear in velocity fluctuations, whereas $p_{(2)}$ is linear both in mean velocity gradient and in velocity fluctuations. The term $p_{(3)}$ arises from fluctuating body forces. It is to be expected that any comprehensive model for the turbulent pressure-containing correlations (Φ_{ij} and $\Phi_{\theta j}$) will comprise terms corresponding to the different sources in Eq. (4.2).

By multiplying Eq. (4.2) by $(\partial u_i/\partial x_j + \partial u_j/\partial x_i)$ and averaging, the pressure-strain process can be written as:

$$
\begin{aligned}
\Phi_{ij} &= \overline{\frac{p}{\rho}\left(\frac{\partial u_i}{\partial x_j}+\frac{\partial u_j}{\partial x_i}\right)} \\
&\equiv \underbrace{-\frac{1}{4\pi}\int_V \overline{\left(\frac{\partial^2 u_l u_m}{\partial x_l \partial x_m}\right)'\left(\frac{\partial u_i}{\partial x_j}+\frac{\partial u_j}{\partial x_i}\right)}\frac{dV(\mathbf{x}')}{r}}_{\Phi_{ij_1}} \\
&\quad \underbrace{-\frac{1}{2\pi}\int_V \left(\frac{\partial U_l}{\partial x_m}\right)'\overline{\left(\frac{\partial u_m}{\partial x_l}\right)'\left(\frac{\partial u_i}{\partial x_j}+\frac{\partial u_j}{\partial x_i}\right)}\frac{dV(\mathbf{x}')}{r}}_{\Phi_{ij_2}} \\
&\quad \underbrace{+\frac{1}{4\pi}\int_V \overline{\left(\frac{\partial f_m}{\partial x_m}\right)'\left(\frac{\partial u_i}{\partial x_j}+\frac{\partial u_j}{\partial x_i}\right)}\frac{dV(\mathbf{x}')}{r}}_{\Phi_{ij_3}} \\
&\quad \underbrace{+\frac{1}{4\rho\pi}\int_A \left[\frac{1}{r}\frac{\partial}{\partial n}\left(\overline{p'\left(\frac{\partial u_i}{\partial x_j}+\frac{\partial u_j}{\partial x_i}\right)}\right)-\overline{p'\left(\frac{\partial u_i}{\partial x_j}+\frac{\partial u_j}{\partial x_i}\right)}\frac{\partial}{\partial n}\left(\frac{1}{r}\right)\right]dA}_{\Phi_{ij}^{w}}
\end{aligned}
\tag{4.3}
$$

https://doi.org/10.1017/9781108875400.006 Published online by Cambridge University Press

where the primes denote that the quantity in question is evaluated at a distance r from where Φ_{ij} is determined (indicated by point P' in Fig. 4.1). It is convenient to write the above equation in the short-hand form:[2]

$$\Phi_{ij} = \Phi_{ij_1} + \Phi_{ij_2} + \Phi_{ij_3} + \Phi_{ij}^{w}. \tag{4.4}$$

The constituents in the above expression are known by names that reflect the content of the corresponding integrand in Eq. (4.3) and the physical process it represents. It is recalled that the wave nature of pressure fluctuations tends to destroy the coherence of eddy structures and to diminish any correlations that might exist between different fluctuating variables. In free space, the first three terms represented by volume integrals will usually act, directly or indirectly, to reduce the turbulent stress anisotropy. The last term, originating from the surface integral, will generally counteract the isotropization trend through the induced inviscid blocking of velocity fluctuations in the vicinity of a solid wall or phase interface.

In the absence of any mean strain or body forces and away from a wall or interface the only non-zero term is the *non-linear* Φ_{ij_1}, which will redistribute energy among the components and diminish any shear stress, causing turbulence *slowly* to approach its isotropic state. If, however, isotropic turbulence is subjected to a sudden rate of strain, the dominant action will be through the term Φ_{ij_2}, which is *linear* (in the velocity gradient) and which acts *rapidly* to modify the preferential feeding (production) of turbulence energy into particular coordinate direction(s) by the active components of the mean rate of strain. A simple (though incomplete) characterization of the process is that of reducing the anisotropy of the stress production. Term Φ_{ij_3} will generally act in the same spirit if, instead of mean strain, a body force is applied suddenly to isotropic turbulence. Finally, we may expect a wall to modify the fluctuating pressure field in its vicinity by virtue of its blocking effect.

Thus, to summarize the physical meaning and labelling of the constituents of the pressure redistribution term Φ_{ij}:

[2] Instead of considering the pressure-strain correlation Φ_{ij}, one may focus on the velocity–pressure-gradient correlation Π_{ij} as it appeared in the original Eq. (2.18) before being split into pressure-diffusion and pressure-strain parts, $\Pi_{ij} \equiv \mathcal{D}_{ij}^{p} + \Phi_{ij}$, Eq. (2.20). Differentiating Eq. (4.2) with respect to x_i, multiplying it by u_j and averaging, and then adding it to the same equation with the indices i and j interchanged gives an integral equation for Π_{ij} which is very similar to Eq. (4.3) except that all terms in the integrand which are evaluated at point $P(\mathbf{x})$ are differentiated by x_i. Π_{ij} can then be split into parts corresponding to the different terms in the integral equation: $\Pi_{ij} = \Pi_{ij_1} + \Pi_{ij_2} + \Pi_{ij_3} + \Pi_{ij}^{w}$ and the component parts modelled separately just as for Φ_{ij}. The apparent advantage of this approach is that Π_{ij} (and all its constituents) are zero at a solid wall, whereas $\mathcal{D}_{ij}^{p}$ and Φ_{ij} are finite and of opposite sign at a wall. This should make the modelling easier in the region very close to a wall, where $\mathcal{D}_{ij}^{p}$ (and thus Φ_{ij}) can be quite significant. It is recalled, however, that Π_{ij} is not redistributive (it has a finite trace even in incompressible turbulence). This is, in principle, an unattractive feature because it invalidates the use of the redistribution constraint in modelling the component parts of Π_{ij}. However, because one needs to resort to a good deal of empiricism in closing the elements of either Π_{ij} or Φ_{ij}, both approaches eventually lead to the same model, except that, when choosing Φ_{ij}, one needs to provide a separate model for the pressure diffusion. The latter issue is important only for near-wall modelling and for certain cases of force-field-driven flows. These issues are considered further in Chapter 6.

https://doi.org/10.1017/9781108875400.006 Published online by Cambridge University Press

- Φ_{ij_1} – return to isotropy of non-isotropic turbulence (the *slow* or *non-linear* term)
- Φ_{ij_2} – isotropization of strain production (the *rapid* or *linear* term)
- Φ_{ij_3} – isotropization of force production (the *rapid* or *linear* term)
- Φ_{ij}^w – wall blocking (the wall *echo* term).

An analogous equation for $\Phi_{\theta j}$ can be obtained by replacing $(\partial u_i/\partial x_j + \partial u_j/\partial x_i)$ by $(\partial\theta/\partial x_j)$ in Eq. (4.3):

$$\begin{aligned}\Phi_{\theta j} \equiv \overline{\frac{p}{\rho}\left(\frac{\partial\theta}{\partial x_j}\right)} = &\underbrace{-\frac{1}{4\pi}\int_V \overline{\left(\frac{\partial^2 u_l u_m}{\partial x_l \partial x_m}\right)'\left(\frac{\partial\theta}{\partial x_j}\right)}\frac{dV(\mathbf{x}')}{r}}_{\Phi_{\theta j_1}} \\ &\underbrace{-\frac{1}{2\pi}\int_V \left(\frac{\partial U_l}{\partial x_m}\right)'\overline{\left(\frac{\partial u_m}{\partial x_l}\right)'\left(\frac{\partial\theta}{\partial x_j}\right)}\frac{dV(\mathbf{x}')}{r}}_{\Phi_{\theta j_2}} \\ &\underbrace{+\frac{1}{4\pi}\int_V \overline{\left(\frac{\partial f_m}{\partial x_m}\right)'\left(\frac{\partial\theta}{\partial x_j}\right)}\frac{dV(\mathbf{x}')}{r}}_{\Phi_{\theta j_3}} \\ &\underbrace{+\frac{1}{4\pi}\int_A \left[\frac{1}{r}\frac{\partial}{\partial n}\left(\overline{p'\left(\frac{\partial\theta}{\partial x_j}\right)}\right) - \overline{p'\left(\frac{\partial\theta}{\partial x_j}\right)}\frac{\partial}{\partial n}\left(\frac{1}{r}\right)\right]dA}_{\Phi_{\theta j}^w}\end{aligned} \tag{4.5}$$

or, in short-hand notation,

$$\Phi_{\theta j} = \Phi_{\theta j_1} + \Phi_{\theta j_2} + \Phi_{\theta j_3} + \Phi_{\theta j}^w \tag{4.6}$$

where the component terms have similar physical meanings and labels to those in Φ_{ij}.

In principle, approximations for the constituent processes in (4.3) and (4.5) can be developed starting from the solution of the Poisson equation for the pressure fluctuations. Analyses of this type have been presented by Naot *et al.* (1973); Lin and Wolfshtein (1979) and others (in which it is assumed that the two-point velocity-correlation tensor appearing in the kernel retains the exact, axisymmetric form found in isotropic turbulence, thus permitting analytical integration). A less formal approach is usually favoured, however. General surrogate forms are assumed for the different component parts of Φ_{ij} and $\Phi_{\theta j}$. Then, by insisting that the model possesses certain symmetry and contraction properties of the original process and that it should comply with some or all of the other physical constraints noted above (while also conforming with certain experimental data or direct numerical simulations), the various constants in the model are determined.

https://doi.org/10.1017/9781108875400.006 Published online by Cambridge University Press

While such analytical approaches will form the main focus of this chapter, in what follows, as indicated above, an even simpler, heuristic approach will be presented next based on intuition and experimental observations. This leads to simple models of each of the constituents of the complete terms Φ_{ij} and $\Phi_{\theta j}$.

4.3 The basic second-moment closure for high-Re_t flow regions

4.3.1 Rotta–Monin return-to-isotropy models of Φ_{ij_1} and $\Phi_{\theta j_1}$

To model the parts of Φ_{ij} and $\Phi_{\theta j}$ arising from $p_{(1)}$, we seek forms containing only turbulent quantities. Experiments indicate that grid turbulence made strongly non-isotropic by passing it through a duct of rapidly changing cross-sectional shape will gradually revert towards isotropy once the mean strain is removed. If the dissipation process remains isotropic (i.e. local isotropy applies), we must conclude that Φ_{ij_1} (which, like the other parts of Φ_{ij}, is traceless) is the agency promoting this reversion. The process occurs gradually due to non-linear turbulence self-interactions. The simplest approach, and one that accords with intuition, is Rotta's (1951) *linear* return model. It assumes that Φ_{ij} will act as a sink or source of the stress component $\overline{u_i u_j}$ directly in proportion to its deviation from the isotropic state scaled with an appropriate time scale which we take to be the turnover time, $\mathcal{T}$ ($\mathcal{T} \equiv k/\varepsilon$):

$$\Phi_{ij_1} = -c_1 \left(\overline{u_i u_j} - \frac{1}{3} \overline{u_k u_k} \delta_{ij} \right) \Big/ \mathcal{T} = -c_1 \varepsilon \left(\frac{\overline{u_i u_j}}{k} - \frac{2}{3} \delta_{ij} \right) = -c_1 \varepsilon a_{ij}. \quad (4.7)$$

By applying this model to the decay of anisotropic turbulence (in the absence of mean strain or body forces), the requirement that all normal-stress components ($i = j$) should remain positive, implies that, if the stress dissipation remains isotropic (i.e. $\varepsilon_{ij} = \frac{2}{3}\delta_{ij}\varepsilon$), the coefficient c_1 must be greater than unity. Different values have been suggested in the course of model development, depending upon the scheme used to represent the *rapid term* (see below); the values commonly used nowadays lie in the range $1.5 \leq c_1 \leq 1.8$.

The corresponding process, $\Phi_{\theta j_1}$, in the $\overline{\theta u_j}$ equation is modelled, following Monin (1965), as:

$$\Phi_{\theta j_1} = -c_{1\theta} \frac{\varepsilon}{k} \overline{\theta u_j}. \quad (4.8)$$

However, the value of the empirical coefficient, $c_{1\theta}$, normally adopted (around 3.5) is roughly twice as large as the value of c_1. Part of the reason for this disparity is the use of the dynamic time scale, k/ε, to characterize the process rather than a time scale involving both the dynamic and scalar intensities. Several research groups have used $[(k/\varepsilon)(\overline{\theta^2}/\varepsilon_{\theta\theta})]^{1/2}$, a choice that brings the two coefficients closer together.

https://doi.org/10.1017/9781108875400.006 Published online by Cambridge University Press

4.3.2 The isotropization-of-production (IP) model of Φ_{ij_2} and $\Phi_{\theta j_2}$

It is evident from Eq. (4.3) that since this term is multiplied by a mean velocity gradient, the term will be non-zero only in the presence of a mean rate of strain. If isotropic turbulence is subjected to a suddenly imposed velocity gradient, Φ_{ij_2} will instantly become non-zero. An early analytical strategy for predicting the changes to the stress field in this type of situation is known as *rapid-distortion theory*, reinforcing the descriptor *rapid term*. Although the process was entirely neglected in some of the early closure proposals (e.g. Donaldson *et al.*, 1972; Lumley and Khajeh Nouri, 1974), today it represents a vital ingredient of all second-moment closures. Its effects will tend to redistribute the action of the imposed strain, reducing the effective mean-strain generation in the components where the production term is large and deflecting it in some proportion to other components. It is thus supposed that the principal effect of the mean-strain part of the pressure-strain process is, effectively, to *reduce the anisotropy of the production tensor*, leading to a model analogous to Rotta's model of the slow term, i.e.

$$\Phi_{ij_2} = -c_2 \left(\mathcal{P}_{ij} - \frac{1}{3}\mathcal{P}_{kk}\delta_{ij} \right). \tag{4.9}$$

Equation (4.9) is known as the *isotropization-of-production (IP)* model (Naot *et al.*, 1970). It combines simplicity with at least qualitative accuracy and has been used in many computations of complex flows. Moreover, though inspired by intuition, it is noted that if, as is often the case, the value of c_2 is taken as 0.6, in isotropic turbulence subjected to a rapid distortion, one obtains the exact result obtained by Crow (1968):

$$\Phi_{ij_2}^{iso} = 0.4k \left(\frac{\partial U_i}{\partial x_j} + \frac{\partial U_j}{\partial x_i} \right) \equiv 0.8\, k\, S_{ij}. \tag{4.10}$$

Equation (4.9) can be regarded as a simplification of a more general non-linear model discussed in §4.4, in which simply the leading linear term is retained. It has been widely applied in a diversity of flows and has been found to be conclusively better than the superficially more general 'quasi-isotropic' form, to be considered in §4.4.3, at least when used in conjunction with the simple linear model of Φ_{ij_1}.

The idea underlying the IP model is readily applied to the force-field part of Φ_{ij} (as will be considered in §4.5) and, moreover, to the mean-strain contribution of the pressure-scalar gradient to $\Phi_{\theta j_2}$. Thus, for the latter:

$$\Phi_{\theta i_2} = -c_{2\theta}\mathcal{P}_{\theta i}^{U} = +c_{2\theta}\overline{\theta u_k}\frac{\partial U_i}{\partial x_k} \tag{4.11}$$

where the coefficient has been given values in the range $0.4 \leq c_{2\theta} \leq 0.55$. Notice that only the part of production of the $\overline{\theta u_i}$ transport equation arising from $\overline{\theta\, Du_i}/Dt$

https://doi.org/10.1017/9781108875400.006 Published online by Cambridge University Press

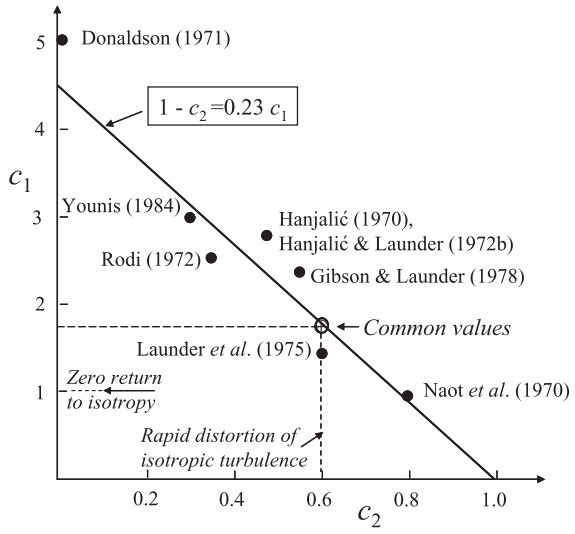

Fig. 4.2 Map of proposals for coefficients in the Basic Model for Φ_{ij}.

is included in Eq. (4.11) since it is only that part of the equation that contains the pressure-fluctuation term. That has been the usual choice in modelling though Jones and Musonge (1988) have argued that the mean-scalar-gradient part of the generation also gets modified in some way by the pressure fluctuations (see §4.4.2). With the coefficient $c_{2\theta}$ set to about 0.5, Eq. (4.11) is distinctly more successful than the formally more general linear quasi-isotropic form (c.f. §4.4) at least if the proposal of Monin (1965) for $\Phi_{i\theta 1}$ is adopted.

4.3.3 Optimum choice of coefficients in the basic pressure-strain model

Equations (4.7) and (4.9) have been included as part of many different modelling proposals and have been incorporated into several commercial software packages. For this reason the pair of equations (including, where appropriate, wall-reflection terms and other closure elements discussed below) is often referred to as the *Basic Model*.

The question arises, however, as to what values should be assigned to the coefficients c_1 and c_2. Values proposed for c_1 range[3] from 1 to 5, while recommendations for c_2 cover the range from zero to 0.8, Fig. 4.2. This array of different values suggests, at first glance, that since such disparate pairings have been put forward, the whole approach is worthless. Looked at with an experimentalist's eye, however,

[3] In fact, Naot *et al.* (1970) neglected entirely the slow, turbulence part of the pressure-strain process but also assumed $\varepsilon_{ij} = \varepsilon\overline{u_i u_j}/k$ in place of the more usual local isotropy ($\varepsilon_{ij} = 2\delta_{ij}\varepsilon/3$). Their assumptions are equivalent to taking $c_1 = 1$ (rather than zero) together with $\varepsilon_{ij} = 2\delta_{ij}\varepsilon/3$. That is, $-\varepsilon\overline{u_i u_j}/k = -c_1(\varepsilon/k)[\overline{u_i u_j} - 2\delta_{ij}k/3] - 2\delta_{ij}\varepsilon/3$ if $c_1 = 1$.

https://doi.org/10.1017/9781108875400.006 Published online by Cambridge University Press

one might be tempted to fit a straight line through the 'data points'. Now, in the case of a simple shear flow in local equilibrium (i.e. where turbulence generation and dissipation processes are in balance) and where the dissipation is isotropic, it is readily shown that, with these models, the resultant stress tensor depends not on the individual values of c_1 and c_2 but rather on the single parameter $(1 - c_2)/c_1$. The line in Fig. 4.2 is simply that corresponding to $(1 - c_2)/c_1 = 0.23$, which evidently does rather a good job of fitting the various proposals. What we conclude is that, for simple shear flows in local equilibrium, the very different pairs of c_1 and c_2 lead to nearly the same results. In order to pick the 'best' pairing one needs to look at *non-equilibrium* cases. It was noted above that a value of c_2 of 0.6 exactly describes the case of isotropic turbulence subjected to rapid distortion, while direct simulations of the return of anisotropic turbulence towards isotropy suggest a level of c_1 from 1.5 to 2.0 if the level of stress anisotropy is similar to that found in a typical free shear flow. The pairing usually adopted nowadays for c_1 and c_2 of 1.8 and 0.6 is fully compatible with these extreme cases and is marked by a circle in Fig. 4.2.

Before leaving this topic, mention should be made of the pairing of Younis (1984) (see Gibson and Younis, 1986). His proposal arose from the failure to predict swirling jets correctly when larger values of c_2 were adopted. However, it is noted that $\mathcal{P}_{ij}$ is not an objective tensor (i.e. not frame invariant) and, thus, with the IP model, neither is Φ_{ij_2}. If the model of Φ_{ij} is made objective (as it should be) by including the stress-convection tensor $\mathcal{C}_{ij}$, Eq. (2.18) (which, while usually small in regions where $\mathcal{P}_{ij}$ is important, can, nevertheless be large in a swirling flow), then it is found that reasonably satisfactory predictions of the swirling jet are obtained with the 'standard' values of c_1 and c_2 noted above (Fu *et al.*, 1987a). Further discussion on this topic may be found in §4.5.

4.3.4 Wall corrections to Φ_{ij} and $\Phi_{\theta j}$ with the basic model

While the combination of Eqs. (4.7) and (4.9) produces approximately the correct relative levels of the Reynolds stresses in many free shear flows, it fails to do so as one approaches a wall. The difference is brought out clearly in Table 4.1, which compares stress ratios in a local-equilibrium homogeneous free shear flow (Champagne *et al.*, 1970) with those found in a fully turbulent, high Reynolds number flow near a wall, also in local equilibrium.

The values in the latter case are not strictly constant (the anisotropy increasing steadily as the wall is approached) but the table suffices to show that there is a much greater difference among the normal stresses than is observed in the homogeneous, equilibrium free shear flow. It is not just rigid walls where surface effects on Φ_{ij} and $\Phi_{\theta j}$ are important. In free-surface flows the resultant pressure

https://doi.org/10.1017/9781108875400.006 Published online by Cambridge University Press

Table 4.1 *Comparison of stress-anisotropy components in homogeneous and near-wall shear flows*

	a_{11}	a_{22}	a_{33}	a_{12}
Homogeneous shear, Champagne *et al.* (1970)	0.30	−0.18	−0.12	−0.33
Near-wall region of a boundary layer	0.55	−0.45	−0.11	−0.24

'reflections' from the free surface are also significant[4] – indeed, indirectly, through the secondary motions created by the resulting stress anisotropy near the free surface, they are the underlying cause of why the maximum velocity in a river often lies below the free surface. There is thus clearly something important missing from the pressure-strain approximation adopted with the Basic Model.

The main effect of the wall on Φ_{ij} is to dampen the level of $\overline{u_2^2}$ (the normal stress perpendicular to the wall) to less than half the level found in a free shear flow. (It is mainly this reduction that makes the two-dimensional wall jet in stagnant surroundings spread at only two-thirds of the rate of the free jet despite the contribution of wall friction which, on its own, would act to augment the spreading rate relative to that of the free jet.) The nature of the wall effect on the pressure interaction is defined by the surface integral in Eq. (4.3), but this gives barely a hint of how to account for this effect in the model of the pressure-containing terms. However, common everyday experience tells us that a solid wall will 'splat' neighbouring eddies, causing higher turbulence anisotropy broadly as indicated in Table 4.1. One is led to infer that a wall or free surface impedes the isotropizing action of the pressure fluctuations. The outcome has sometimes been referred to as an *echo effect* caused by pressure reflections from the wall or free surface. However, this early interpretation is not strictly correct since a pressure wave reflecting from a solid surface will retain the same character as the incoming wave, which means that, in a near-wall region, the pressure-scrambling effect and the consequent isotropization of the stress field and its generation process will be enhanced by pressure reflection and not diminished.[5] Rather, the major effect originates from non-viscous kinematic blocking due to the impermeability of the wall or free surface, i.e. from the continuity constraint, which suppresses velocity fluctuations in the wall-normal direction. Because the effect is not dissipative, energy remains conserved,

[4] Strictly, the free surface is at a uniform pressure. But turbulent agitations cause the free surface to be slightly 'crinkled', i.e. the surface is not quite plane and is continually changing. However, if the free surface is imagined to be replaced by an undeformable but frictionless lid, as is habitually done in free-surface studies, then pressure fluctuations *will* exist at the lid surface.

[5] Indeed, this is seen by converting the surface integral in Eq. (4.3) into a volume integral by considering the wall surface as a symmetry plane and accounting for the pressure field in the image volume on the other side of the virtual plane around point $P^*(\mathbf{x}^*)$ mirroring point $P(\mathbf{x})$ in Fig. 4.1, so that the complete Φ_{ij} can be written as a volume integral over $dV(1/r + 1/r^*)$.

https://doi.org/10.1017/9781108875400.006 Published online by Cambridge University Press

resulting in a larger proportion in the streamwise and, to a lesser extent, spanwise components. Whatever the physical explanation, accounting for these effects is an essential step in the accurate modelling of wall-bounded inhomogeneous flows with the Basic Model.

But can these wall effects be automatically accounted for as one approaches the wall, effectively through the boundary conditions? There has certainly been a great deal of research aimed at developing models of Φ_{ij} that *do* automatically respond to the proximity of the wall. Later sections in this chapter will consider more elaborate models of Φ_{ij} that do not suffer this wall-proximity problem, at least not to the same extent. However, the 'basic' model presented above requires rather substantial correction close to a wall to return accurate relative levels of the stress components. This is usually achieved by introducing the unit vector normal to the wall, n (so, for example, if the wall lies in the x_1-x_3 plane n will have components (0,1,0)), and applying a correction proportional to the turbulent length scale $k^{3/2}/\varepsilon$ divided by the distance from the wall. The total correction is normally split into two parts: one associated with the slow and the other with the rapid term.

The first practical proposal for handling near-wall effects was made by Shir (1973), who assumed that the 'turbulence' or 'slow' part of the pressure-strain term was the only part affected by the proximity of the wall:

$$\Phi^w_{ij_1} = c_1^w \left[\overline{u_k u_m} n_k n_m \delta_{ij} - \tfrac{3}{2}(\overline{u_k u_i} n_k n_j + \overline{u_k u_j} n_k n_i)\right] f_w(l/n_p r_p) \qquad (4.12)$$

where l is the turbulent length scale, $k^{3/2}/\varepsilon$, and $n_i r_i$ implies the normal distance from the wall, while f_w is an empirical function that varies from unity near the wall to zero far enough from it for no wall influence to be felt. So, if x_2 is the direction normal to the wall, the model applies the following corrections to the individual components:

$$\Phi^w_{11_1} = c_1^w \overline{u_2^2} f_w, \quad \Phi^w_{22_1} = -2c_1^w \overline{u_2^2} f_w, \quad \Phi^w_{33_1} = c_1^w \overline{u_2^2} f_w, \quad \Phi^w_{12_1} = -\tfrac{3}{2} c_1^w \overline{u_1 u_2} f_w. \qquad (4.13)$$

Later workers (e.g. Gibson and Launder, 1978) have assumed that the wall affects all parts of the pressure-strain process, an assumption that was later confirmed by the analysis of DNS data by Brasseur and Lee (1987). They showed that the distance over which the two-point correlations in the pressure-strain integrals (cf. Eq. (4.3)) were active was greater for those associated with Φ_{ij_2} than for Φ_{ij_1}. Following the structure suggested by Eq. (4.12), an additional term was thus proposed in the form:

$$\Phi^w_{ij_2} = c_2^w \left[\Phi_{km_2} n_k n_m \delta_{ij} - \tfrac{3}{2}(\Phi_{ik_2} n_k n_j + \Phi_{jk_2} n_k n_i)\right] f_w(l/n_p r_p). \qquad (4.14)$$

The function f_w is usually (but not universally, see for example Naot and Rodi, 1982b) taken directly proportional to $0.4k^{3/2}/\varepsilon x_n$ (where x_n is used to denote the normal distance from the wall instead of the more general form $n_p r_p$) with

https://doi.org/10.1017/9781108875400.006 Published online by Cambridge University Press

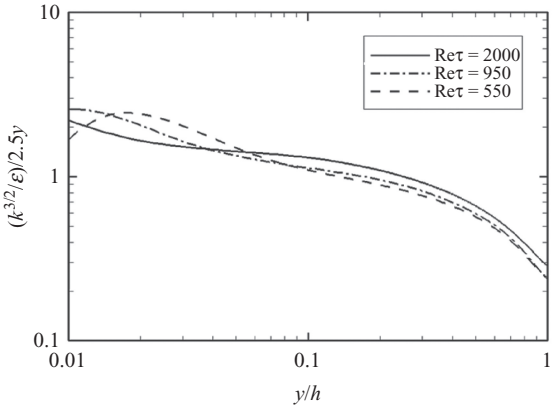

Fig. 4.3 Variation of the function $f_w = l/x_n$ over a half-channel of width h, where $l = k^{3/2}/c_l\varepsilon$ and $c_l = \kappa/c_\mu^{3/4} \approx 2.5$. Computed from DNS data of Hoyas and Jimenez (2006).

a constant of proportionality chosen such that the function equals unity in an equilibrium near-wall flow. The variation of the function f_w in a channel flow for three Reynolds numbers, Fig. 4.3, shows that the effect decays with distance from the wall but, nevertheless, it is not entirely negligible even at the channel centre (implying effects from *both* walls should be included in computing that flow). The above pair of wall corrections, Eqs. (4.12) and (4.14) in conjunction with Rotta's return-to-isotropy and IP models, has been widely used in practice. Indeed, for two-dimensional wall-attached flows (for which they were tuned) they return broadly acceptable results, as illustrated in Fig. 4.4, showing the distribution of stress components in a flat-plate boundary layer.

If transport equations are to be solved for the turbulent heat or mass fluxes, corresponding corrective terms to account for wall-proximity effects on the pressure-temperature gradient correlation have also been proposed of the form (Gibson and Launder, 1978; McGuirk and Papadimitriou, 1988):

$$\Phi^w_{\theta j_1} = -c^w_{1\theta}(\varepsilon/k)\overline{u_k\theta}n_j n_k f(l/n_p r_p), \quad \Phi^w_{\theta j_2} = -c^w_{2\theta}\Phi_{\theta k_2} n_j n_k f(l/n_p r_p). \tag{4.15}$$

In practice, $\Phi^w_{\theta j_2}$ is zero if the velocity normal to the wall vanishes so, while $c^w_{1\theta}$ has been taken as 0.5 in both the above studies, no recommendation[6] has been made for $c^w_{2\theta}$.

[6] In fact, (Dol, 2001) (also Dol *et al.* (1999), although concluding from the DNS data of Versteegh and Nieuwstadt (1998) for an infinite side-heated vertical channel that the wall correction $\Phi^w_{\theta j}$ is much smaller than the sum of the slow and rapid terms, did propose a model for both the 'slow' and 'rapid' processes in Eq. (4.15) with a single coefficient $c^w_{1\theta} = c^w_{2\theta} = \max(0, 0.58 - 0.69A^{1/2})$. Apart from the flow considered, however, no further testing has been reported in the literature.

https://doi.org/10.1017/9781108875400.006 Published online by Cambridge University Press

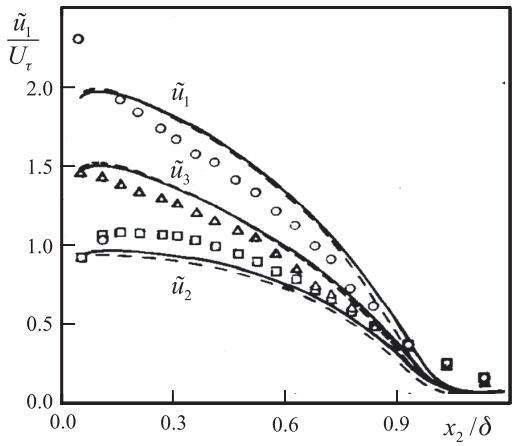

Fig. 4.4 Turbulence intensities in the flat-plate boundary layer: effects of wall-correction models. Broken line: Gibson and Launder (1978), Eq. (4.14); Continuous line: Craft and Launder (1992), Eq. (4.30); Symbols experimental data. From Launder (1993).

4.3.5 *The dissipative correlations* ε_{ij} *and* $\varepsilon_{\theta j}$

As noted in §2.3.1 and §3.3, the dissipative correlations ε_{ij} and $\varepsilon_{\theta j}$ arise from the fine-scale motion for it is in these eddies that instantaneous gradients of velocity, temperature, etc. are steepest. We assume, therefore, from the high Reynolds number hypothesis, that the motions contributing predominantly to ε_{ij} and $\varepsilon_{\theta j}$ are isotropic. Now, the term $\overline{(\partial u_j/\partial x_k)(\partial\theta/\partial x_k)}$ changes sign if the coordinate direction x_j is reversed; but the properties of isotropic turbulence are unaffected by such reflections of axes. The only value that $\overline{(\partial u_j/\partial x_k)(\partial\theta/\partial x_k)}$ can take, therefore, and be consistent with isotropic turbulence is zero. That is:

$$\varepsilon_{\theta j} = 0. \tag{4.16}$$

Likewise ε_{ij} must be expressible as proportional to the product of the contraction $\varepsilon \equiv \nu\overline{(\partial u_i/\partial x_j)^2}$ and the isotropic unit tensor δ_{ij}. Thus:

$$\varepsilon_{ij} = \tfrac{2}{3}\varepsilon\,\delta_{ij} \tag{4.17}$$

where the constant of proportionality is obtained by contracting each side of the equation. An implication of (4.17) is that there is no viscous sink of shear stress. The process Φ_{ij} is thus the only mechanism for preventing the unlimited growth of the off-diagonal components of $\overline{u_i u_j}$.

There is still little agreement in the literature on whether the dissipative correlations can be adequately approximated by the isotropic relations. Measurements are not usually sufficiently accurate to allow conclusions to be drawn. Direct numerical simulations show significant and systematic departures from local isotropy but even

https://doi.org/10.1017/9781108875400.006 Published online by Cambridge University Press

today these simulations are still at relatively low Reynolds number; so, they may not reflect the situation in practical applications which occur at Reynolds numbers orders of magnitude higher. In practice, in applying second-moment closure, it is difficult to disentangle departures from Eqs. (4.16) and (4.17) from errors in accounting for the pressure-strain and pressure-scalar-gradient processes. So, a common practice (Lumley, 1978) is to adopt the isotropic relations for ε_{ij} and $\varepsilon_{\theta j}$ and to absorb any departure from isotropy in the dissipation processes into the turbulent parts of Φ_{ij} and $\Phi_{\theta j}$ whose approximation within the basic model has been considered above.

4.3.6 *Diffusive transport,* $\mathcal{D}_{ij}$ *and* $\mathcal{D}_{\theta j}$

The usual approach for representing diffusive transport in second-moment closures employing the basic pressure-strain model is the *generalized gradient diffusion hypothesis*, GGDH (Daly and Harlow, 1970), which may be written as:

$$\overline{\varphi u_k} = -c_\varphi \frac{k}{\varepsilon} \overline{u_k u_l} \frac{\partial \Phi}{\partial x_l} \tag{4.18}$$

where φ and Φ denote any fluctuating and mean values of a transported property. Thus, if φ denotes the instantaneous product of fluctuating velocities, $u_i u_j$:

$$\overline{u_i u_j u_k} = -c_s \frac{k}{\varepsilon} \overline{u_k u_l} \frac{\partial \overline{u_i u_j}}{\partial x_l} \tag{4.19}$$

with $c_s \approx 0.2$. Or, for the transport of scalar flux, $\overline{\theta u_j}$:

$$\overline{\theta u_j u_k} = -c_\theta \frac{k}{\varepsilon} \overline{u_k u_l} \frac{\partial \overline{\theta u_j}}{\partial x_l}. \tag{4.20}$$

One evident weakness of these forms is that while the indices j and k on the left side of the equation can be interchanged without altering the resultant product, such a rearrangement on the right intrinsically alters the form. No ambiguity arises because, in the $\overline{u_i u_j}$ and $\overline{\theta u_j}$ transport equations, a $\partial/\partial x_k$ operation is applied to the triple moments; nevertheless, the difference in character between the exact and the modelled forms of the correlations would appear to be a significant shortcoming.

In fact, as will be discussed more fully in §4.6, forms similar to (4.19) and (4.20) can be obtained by making sweeping closure simplifications to the transport equations for the triple moments (Hanjalić and Launder, 1972b; Launder, 1976). The form emerging from that simplification is a model for $\overline{u_i u_j u_k}$ consisting of three terms, each of the same form as the right side of (4.19) but with a permutation of the indices i, j and k:

$$\overline{u_i u_j u_k} = -c_s \frac{k}{\varepsilon} \left(\overline{u_i u_l} \frac{\partial \overline{u_j u_k}}{\partial x_l} + \overline{u_j u_l} \frac{\partial \overline{u_i u_k}}{\partial x_l} + \overline{u_k u_l} \frac{\partial \overline{u_i u_j}}{\partial x_l} \right) \tag{4.21}$$

https://doi.org/10.1017/9781108875400.006 Published online by Cambridge University Press

(with the coefficient c_s now being smaller to compensate for the additional terms, typically 0.10). Likewise, that for $\overline{\theta u_j u_k}$ also consists of three terms in which u_k, u_i, θ successively occupy the position of u_k in (4.20):

$$\overline{\theta u_i u_j} = -c_\theta \frac{k}{\varepsilon}\left(\overline{u_j u_l}\frac{\partial \overline{\theta u_i}}{\partial x_l} + \overline{u_i u_l}\frac{\partial \overline{\theta u_j}}{\partial x_l} + \overline{\theta u_l}\frac{\partial \overline{u_i u_j}}{\partial x_l}\right) \tag{4.22}$$

where $c_\theta \approx 0.11$.

The last term in Eq. (4.22), which has the character of an additional source term in the equation for $\overline{\theta u_j}$, is usually omitted. The remaining simpler expression, which contains heat-flux gradients only, is still frame invariant. Dol *et al.* (1999) showed that in a side-heated vertical channel, this reduced invariant form Eq. (4.22) reproduced the non-zero (wall-normal and streamwise) heat-flux diffusion components reasonably well, substantially better than the GGDH model, Eq. (4.20).

Mellor (1973) suggested still simpler forms that respected interchangeability of subscripts:

$$-\overline{u_k u_i u_j} \propto \nu_t\left[\frac{\partial \overline{u_i u_j}}{\partial x_k} + \frac{\partial \overline{u_k u_i}}{\partial x_j} + \frac{\partial \overline{u_j u_k}}{\partial x_i}\right], \tag{4.23}$$

$$-\overline{\theta u_j u_k} \propto \nu_t\left[\frac{\partial \overline{\theta u_j}}{\partial x_k} + \frac{\partial \overline{u_k \theta}}{\partial x_j}\right] \tag{4.24}$$

where ν_t denotes the turbulent eddy viscosity. These somewhat more elaborate and, superficially, more correct models do not, in practice, seem to bring better agreement when used in numerical solvers. This could be due, at least partly, to the fact that those workers who have adopted (4.19) and (4.20) for the triple moments have generally not included any model for the pressure diffusion terms:

$$-\frac{\partial}{\partial x_k}\left(\frac{\overline{p u_j}}{\rho}\delta_{ik} + \frac{\overline{p u_i}}{\rho}\delta_{jk}\right) \quad \text{and} \quad -\frac{\partial}{\partial x_k}\left(\frac{\overline{p\theta}}{\rho}\delta_{jk}\right) \tag{4.25}$$

which appear in the $\overline{u_i u_j}$ and $\overline{\theta u_j}$ transport equations. In these pressure terms the indices i or j are *not* interchangeable with k. Thus, perhaps Eqs. (4.19) and (4.20) should really be regarded as models for the *complete* turbulent diffusion of $\overline{u_i u_j}$ and $\overline{\theta u_j}$.

More rigorous and comprehensive algebraic models of triple moments have been put forward by Lumley (1978); André *et al.* (1979); Reynolds (1984); Dekeyser and Launder (1985); Nagano and Tagawa (1991) and Magnaudet (1992). A discussion and a comparative analysis of various advanced models in a channel flow can be found in Hanjalić (1994). Some of these proposals are discussed in §4.6.

https://doi.org/10.1017/9781108875400.006 Published online by Cambridge University Press

4.3.7 Determining the turbulence energy dissipation rate, ε, with the basic model

So far nothing has been said about how ε, the viscous dissipation rate of turbulence energy, is to be computed. This question will be addressed more comprehensively in Chapter 5; here just a very brief account is provided of the rationale for determining that quantity so that the Basic Model may be seen in its entirety and some computations resulting from its use presented.

First, it is noted that the practice of prescribing the length scale as an algebraic function of position in a shear flow (as was done in a number of the early second-moment closures, e.g. Donaldson *et al.*, 1972) is not seen as a useful approach at this level of closure as it both greatly limits the range of flows that can be computed and, at best, continually requires detailed empirical information from the user. Determining ε from a transport equation is thus the only route considered though, in Chapter 5, alternative strategies will also be presented. (In Chapter 7, however, brief mention is made of transported eddy-viscosity models while, more extensively, prescribed-length-scale schemes are also considered for the viscosity-affected region very close to a wall.)

Although starting from the exact equation for ε and the conceptual ideas of Davidov (1959, 1961), the closed equation for ε (in the form first proposed by Hanjalić, 1970) is, to a large extent, empirical. Its form is shaped by the modelled form of the turbulent kinetic energy equation and dimensional consistency in which the empirical coefficients are chosen to accord with key experimental data. First, recall that the k transport equation (3.2) (with the GGDH model substituted for the complete diffusion term) may be written as:

$$\frac{Dk}{Dt} = \frac{\partial}{\partial x_k}\left(c_s \frac{\overline{u_k u_l} k}{\varepsilon}\frac{\partial k}{\partial x_l}\right) + \mathcal{P}_k - \varepsilon \tag{4.26}$$

with the second and third terms on the right of Eq. (4.26) being source and sink terms. Clearly, a transport equation for ε must also contain such source and sink terms and these need to be linked to the production and dissipation rates of k in order to avoid the risk that k grows without limit following an increased shearing rate or, even less realistic, k becomes negative some time after the shear is removed. By direct analogy with Eq. (4.26), therefore, the tentative form of ε transport equation may be written as:

$$\frac{D\varepsilon}{Dt} = \frac{\partial}{\partial x_k}\left(c_\varepsilon \frac{\overline{u_k u_l} k}{\varepsilon}\frac{\partial \varepsilon}{\partial x_l}\right) + c_{\varepsilon 1}\frac{\mathcal{P}_k \varepsilon}{k} - c_{\varepsilon 2}\frac{\varepsilon^2}{k} \tag{4.27}$$

where the coefficients (which are here assumed to be constants) remain to be determined. The coefficient $c_{\varepsilon 2}$ can be obtained unambiguously by considering the

https://doi.org/10.1017/9781108875400.006 Published online by Cambridge University Press

decay (in time or in space) of grid-generated turbulence. For this case the k- and ε-equations above reduce to:

$$\frac{dk}{dt} = -\varepsilon; \quad \frac{d\varepsilon}{dt} = -c_{\varepsilon 2}\frac{\varepsilon^2}{k}. \tag{4.28}$$

If a power-law decay for k is assumed ($k \propto t^{-n}$), it is readily deduced from inserting this form into the foregoing equations that $c_{\varepsilon 2} = (n+1)/n$. Experimental data on grid turbulence decay suggest values for the decay exponent in the range 1.1–1.25, leading to values of $c_{\varepsilon 2}$ in the range 1.8–1.9. The value of the coefficient of the source term, $c_{\varepsilon 1}$, is habitually fixed from computer optimization by requiring that the rate of spread of a strong free shear flow (i.e. a flow where the shear generation term is large, such as the plane mixing layer) is correctly predicted. That leads to a value of $c_{\varepsilon 1}$ of approximately 1.4.

Finally, since we would want the ε-equation to be applicable both in free shear flows and in near-wall flows, an interconnection between the coefficients is determined from considering flow in an equilibrium near-wall flow where k production and dissipation rates are in balance. In this case, with convective transport assumed negligible, with the mean velocity following the standard logarithmic variation with distance from the wall and the turbulent shear stress being replaced by the wall shear stress, the dissipation equation can be converted to the following relation among the three empirical coefficients:

$$c_\varepsilon = -(c_{\varepsilon 2} - c_{\varepsilon 1})\frac{U_\tau^6}{\kappa^2 k^2 \overline{u_2^2}} \tag{4.29}$$

where U_τ denotes the friction velocity and κ is the von Karman constant. On inserting the values of the stress ratios indicated in Table 4.1 the value of c_ε is obtained as approximately 0.15, which is of similar magnitude to values indicated above for stress diffusion.

This is the form of the ε-equation used in the inhomogeneous flow examples shown in §4.3.8. Over the years since its first appearance there have been numerous refinements proposed and alternative strategies for obtaining ε. As indicated above, these matters form the subject of Chapter 5.

4.3.8 Illustrative applications of the Basic model

There have been numerous successful computations with the model described in the foregoing sections. There follow five quite different applications illustrating strengths and weaknesses of the form presented. In all these cases the most crucial element in the modelling is the pressure-strain term, including the wall-correction terms, Eqs. (4.12) and (4.14). In all examples the wall boundary conditions were provided from the standard wall functions (see Chapter 8).

https://doi.org/10.1017/9781108875400.006 Published online by Cambridge University Press

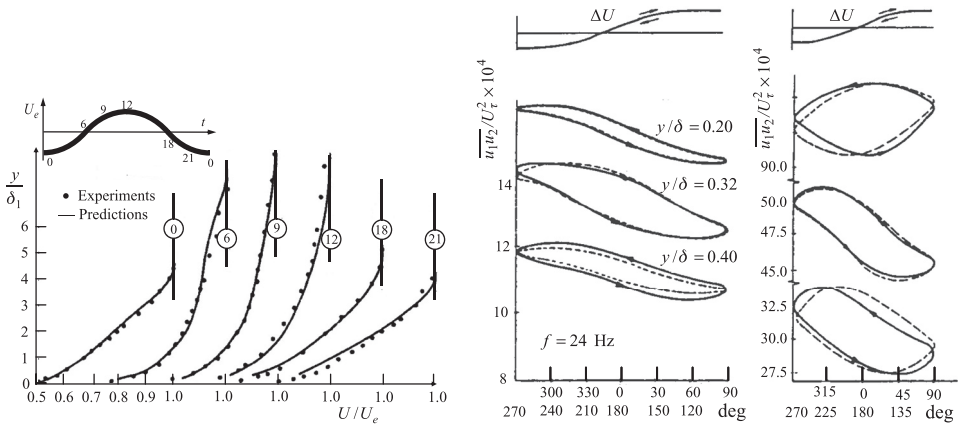

Fig. 4.5 Computations of a pulsating boundary layer with the Basic SMC (full lines). Left: phase-averaged velocity profiles at different time instants (phase angles); symbols are experimental values (from Cousteix *et al.*, 1979). Right: hysteresis of turbulent stresses at different boundary-layer depths; dashed lines are experimental values (Acharya and Reynolds, 1975). From Hanjalić and Stošić (1985).

As a first application of the closure, we consider two-dimensional boundary layers subjected to imposed sinusoidal oscillations of free-stream velocity or pressure gradient. First, comparison is made with the measurements of Cousteix *et al.* (1979) for a free-stream velocity amplitude of 37%. Figure 4.5, left, shows profiles for a sequence of phase angles. Agreement with the measured mean velocity profiles is good (though, admittedly, similar quality predictions were reported by Cousteix *et al.* with two variants of a simpler eddy-viscosity model). The variations of individual components of the turbulent stress over a cycle provide a more searching test of the model's ability to capture the stress dynamics since changes in the velocity gradient will be felt differently by each stress component causing phase differences. Figure 4.5, right, indicates that the Basic Model also satisfactorily resolves the different responses of the shear stress and streamwise normal stress, observed in the measurements of Acharya and Reynolds (1975) of small-amplitude, pulsating channel flow at 24 Hz. To illustrate better the different phase shifts of the stress components at different distances from the wall, the results are shown in the form of hysteresis loops by folding back the curves for the second half of the cycle.

The second example, Fig. 4.6, from Jones and Manners (1989) shows predictions of the flow through an annular diffuser typical of that found in a gas turbine. The flow is unseparated but the successive imposition of the inlet bend, the straight diffusing section and the outlet bend provides a searching test case that the linear eddy-viscosity model fails to mimic at a useful level. Indeed, because the mean velocity with this model gives the peak velocity near the diffuser exit towards

https://doi.org/10.1017/9781108875400.006 Published online by Cambridge University Press

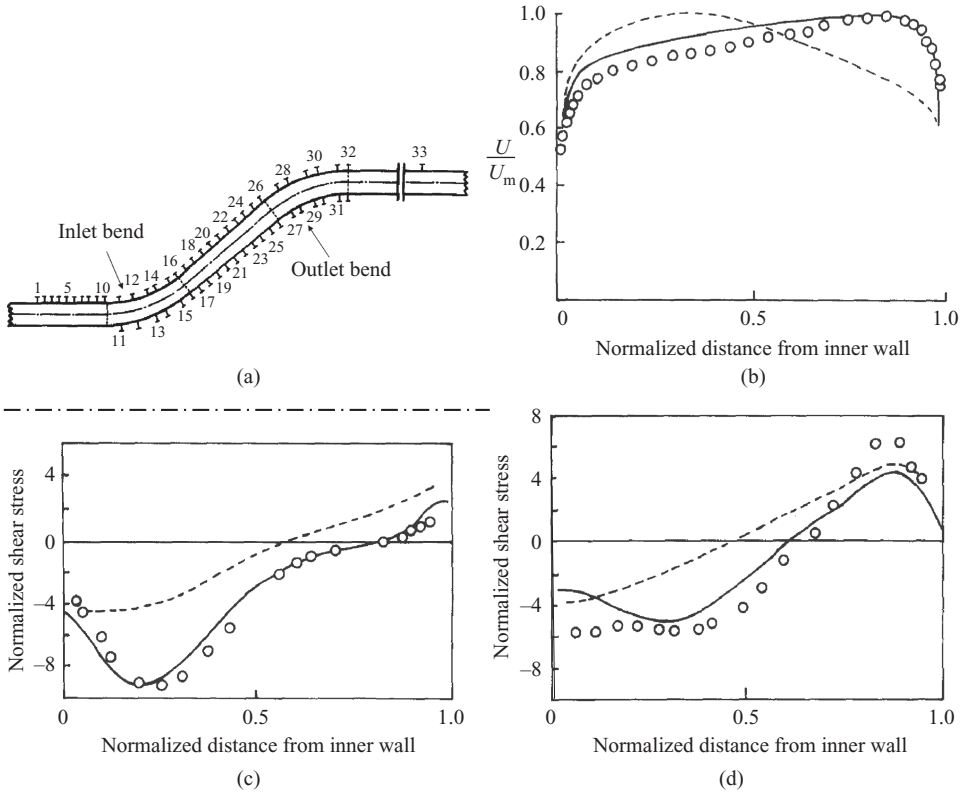

Fig. 4.6 Flow development through a faired diffuser: (a) annular flow configuration; (b) mean velocity at the exit from the diffuser; (c) and (d) shear stress profiles at the end of the inlet bend and at the end of a straight diffusing section respectively. Symbols: experimental data, Stephens and Fry (1973); – – – computed using the $k - \varepsilon$ linear eddy-viscosity model; —— computed with the Basic Model (second-moment closure). From Jones and Manners (1989).

the inner wall, contrary to the experiment, the results are arguably worse than if one simply assumed a uniform velocity distribution at the exit from the diffuser (to compute the flow in the combustor). The basic second-moment closure, by comparison, captures the experiments of Stevens and Fry (1973) in all important respects.

The next illustrations show some examples of swirling flow. A distinction is made between strong swirl in a short cylindrical container (such as a combustion chamber) and that in a long pipe. In both types of configuration, linear eddy-viscosity models usually perform poorly because, just as in flows with system rotation (§4.5.2), the equations for the scalar variables used to determine the eddy viscosity (in particular, the turbulence energy, k) are also 'blind' to swirl, apart from indirect effects due to the swirl altering the mean-flow velocity field. Moreover, swirl causes substantial changes in the stress anisotropy in both configurations,

https://doi.org/10.1017/9781108875400.006 Published online by Cambridge University Press

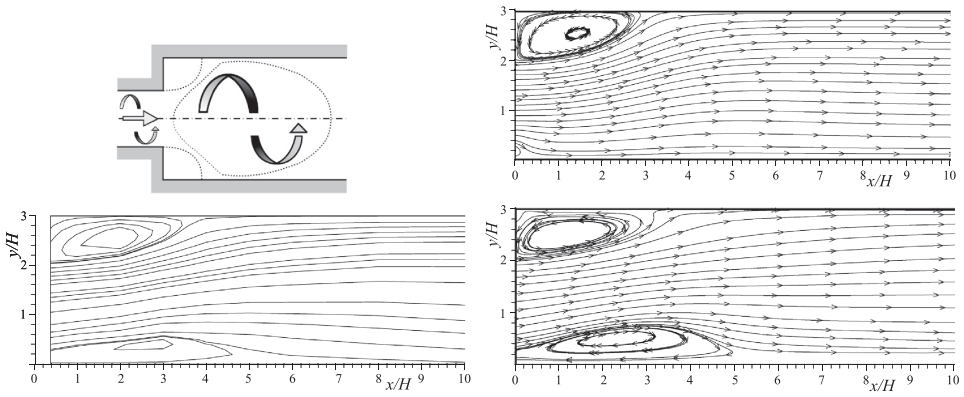

Fig. 4.7 Streamlines in the vertical cross-section of a combustor-type swirling flow. Left: sketch of the configuration (top), experiments by Nejad *et al.* (1989) (bottom). Right, computations: k–ε EVM (top); Basic SMC (bottom). Expansion ratio 1.5; swirl intensity S_w = 0.4, Re = 125.000 (based on entry pipe diameter and axial bulk velocity). From Jakirlić (2004).

which cannot be captured with a linear eddy viscosity. This is illustrated in Figs. 4.7 and 4.8, which compare computations using the Basic SMC and the linear k–ε eddy viscosity model (EVM) with experiments in the two types of swirling flows noted above. Figure 4.7 (from Jakirlić, 2004) compares the streamline patterns in the vertical cross-section of a simple combustor-type configuration (in fact a swirling flow passing through a sudden pipe expansion). This is a well-defined case suitable for model validation since the inflow swirl for the computations can be generated by computing an upstream portion of the flow and checked with the experimental data at the expansion, or just before it. The experiments, for a swirl intensity, $S_w \equiv \int_0^R UWr^2\,dr/R\int_0^R U^2 r\,dr$, of 0.4 clearly show a recirculation bubble in the central flow region of the entry zone, which is well reproduced by the Basic SMC and yet totally absent in the k–ε EVM computations. Similar evidence has been reported by other authors showing the superiority of second-moment closure over an eddy-viscosity treatment for different configurations and swirl origin (e.g. Hogg and Leschziner, 1989).

Swirl in long pipes, even of weak intensity, is still more difficult to capture with an EVM. Jakirlić (1997) (see also Jakirlić *et al.*, 2002) reported computations of swirling flow in long pipes with an imposed free vortex ($W \propto 1/r$) at the pipe entry for two swirl intensities, $S_w = 1.0$ and 0.1 corresponding, respectively, to the experiments of Kitoh (1991) and Steenberger (1995). While the strong swirl poses a challenge, especially for high-Re models (because the initial free vortex persists over a large pipe length and the strong circumferential stabilizing effect penetrates the core region which may lead eventually to a collapse to laminar flow), the weak swirl seems to be reasonably well handled by the Basic Model. The computed

https://doi.org/10.1017/9781108875400.006 Published online by Cambridge University Press

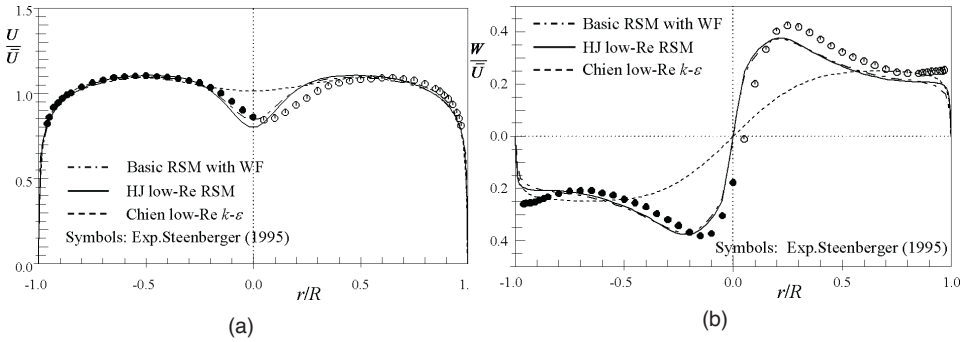

Fig. 4.8 Profiles of axial and tangential velocity in weakly swirling flow in a long pipe at $x/D = 7.7$, Re $= 50,000$, $S_w = 0.1$, computed with the Basic Model using the standard wall functions, compared with the wall-integrated second-moment closure of Hanjalić and Jakirlić (1993) (HJ) (see Chapter 6), and the Chien (1982) low-Re k–ε model (see Chapter 7). Symbols: experiments of Steenberger (1995). From Jakirlić (1997).

stress profiles (not shown here, see Jakirlić *et al.*, 2002) are in very close agreement with Steenberger's experiments for the annular region $0.3 < r/R < 1.0$ over a large fraction of the pipe length, though in the developing region (up to $x/D \approx 35$, still dominated by the entry free vortex) the results in the core for $r/R < 0.3$ deviate notably from the experiments. However, the axial and tangential velocities do not seem to be much affected by these discrepancies, as illustrated in Fig. 4.8, where the basic SMC gives good agreement with experiments even in the early stage of flow development (at $x/D = 7.7$). It is interesting to note in Fig. 4.8 that integration up to the wall using a low-Re SMC (denoted HJ, Hanjalić and Jakirlić, 1993; Hanjalić *et al.*, 1995), considered in detail in Chapter 6, returned results for weak swirl, $S_w = 0.1$ very similar to the basic high-Re model, in contrast to the case of strong swirl, $S_w = 1.0$, where the HJ model showed distinct improvements (Jakirlić, 1997). Suspecting that the simple models for the pressure strain terms used in the Basic SMC may have caused the failure to capture the stresses in the core, both flows were subsequently computed with the more advanced high-Re second-moment closure (SMC) of Speziale, Sarkar and Gatski (SSG) (considered in §4.4.4). The results were, however, nearly identical to those obtained with the Basic Model shown in Fig. 4.8. All three SMCs reproduce the main flow features much better than the low-Re k–ε eddy-viscosity model of Chien (1982).

As a fourth, quite different example of 'wall correction' applied within the Basic Model, the free-surface plane jet examined by McGuirk and Papadimitriou (1988) is considered. The inset sketch in Fig. 4.9 shows the configuration: a plane jet of pure water is injected smoothly over a reservoir of denser saline water. In this case buoyant effects are important and these results anticipate the treatment of

https://doi.org/10.1017/9781108875400.006 Published online by Cambridge University Press

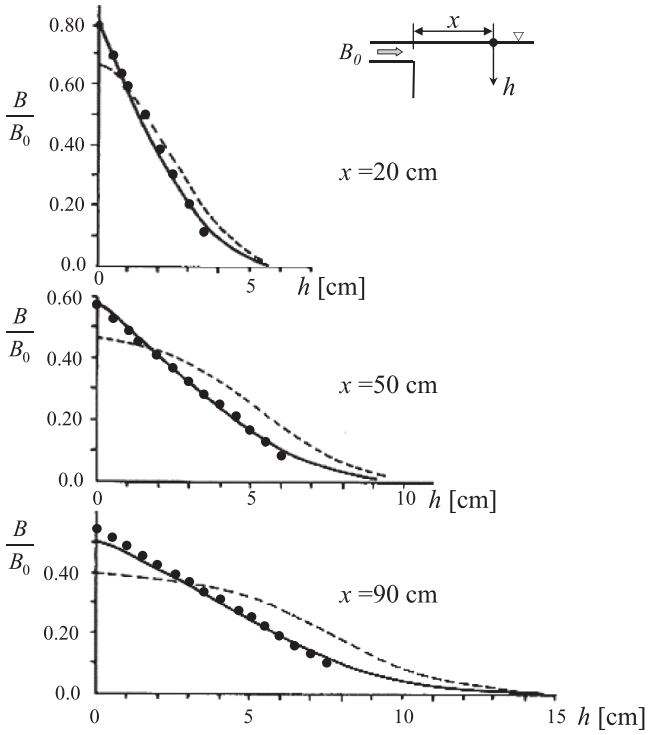

Fig. 4.9 Development of salinity profiles in a stably stratified free-surface jet. From McGuirk and Papadimitriou (1988). Symbols: experimental data, Chu and Baddour (1984). Computations: – – – Basic Model, free-flow version; – Basic Model, including wall reflection at the free surface, i.e. Eqs. (4.12) and (4.14).

stratification presented in §4.5.3. The free surface in this case was treated in two ways: as a symmetry plane precisely as in computing a free jet; and, again, as a free jet *except that*, in the stress-transport equations, the wall-proximity correction was applied to the free surface and this exerted a redistributive effect on the stresses precisely as for a rigid wall. Figure 4.9 compares the resultant computed vertical salinity profiles for these two versions at three stations with the experimental data. Very clearly, retention of the wall-redistributive effect has had a major and beneficial effect in bringing the computed behaviour into very close accord with the experimental data. Indeed, McGuirk and Papadimitriou indicate that the wall corrections in *both* the stress and heat-flux equations are important.

Further applications of a reduced form of the Basic Model are presented in Chapter 7, in which algebraic approximations of the stress-transport terms are explored. In many cases very satisfactory results are achieved even with such a simplified version. To conclude the presentation on the complete Basic Model, however, attention is turned to a class of flows where an element of the model presented so far is evidently not successful. Indeed, a weakness of the form of the wall-proximity

correction used in the above examples becomes apparent if, instead of the flow being parallel to the wall or free surface, it is directed towards the bounding surface, as in an impinging jet. In that case, because normal straining provides a dominant mechanism in stress production, it may readily be verified that, far from dampening the velocity fluctuations perpendicular to the wall, the above form of wall correction leads, quite erroneously, to an augmentation of wall-normal fluctuations! An alternative formulation was thus proposed by Craft and Launder (1992). This retained the form of wall correction for the 'slow' part, $\Phi^w_{ij_1}$, given above but, in place of Eq. (4.14), the following approximation was adopted for $\Phi^w_{ij_2}$:

$$\Phi^w_{ij_2} = \left[\begin{array}{c} -0.08\dfrac{\partial U_l}{\partial x_m}\,\overline{u_l u_m}\,(\delta_{ij} - 3n_i n_j) + 0.4k\dfrac{\partial U_l}{\partial x_m} n_l n_m \left(n_i n_j - \dfrac{1}{3}\delta_{ij}\right) \\ -0.1k\, a_{lm}\left(\dfrac{\partial U_k}{\partial x_m} n_l n_k \delta_{ij} - \dfrac{3}{2}\dfrac{\partial U_i}{\partial x_m} n_l n_j - \dfrac{3}{2}\dfrac{\partial U_j}{\partial x_m} n_l n_i\right) \end{array}\right] \left(\frac{l}{2.5x_n}\right) \tag{4.30}$$

where a_{lm} denotes the dimensionless stress anisotropy, Eq. (3.2). This equation is purely empirical, being tuned simply to give approximately the correct response both in an equilibrium near-wall shear flow, Fig. 4.4, and for the normal straining encountered in stagnation flow conditions. Figure 4.10 shows its application in conjunction with the Basic Model to compute an axisymmetric impinging jet discharged two diameters above the plate. This flow has long posed a challenge for turbulence modelling because of normal-strain turbulence generation very close to the symmetry axis, strong streamline curvature due to deflection of the flow, and the singularity associated with zero shear stress at the stagnation point (features uncommon to most wall-attached flows). The figure of the rms velocity fluctuations normal to the wall at the stagnation point confirms that, for this impinging flow, Eq. (4.30) (solid line) achieves much better agreement with experiments than the earlier (and more widely used) proposal of Gibson and Launder (1978), Eq. (4.14), shown by the broken line.

It would, however, seriously misrepresent the situation to leave the impression that modelling of near-wall influences with this Basic Model was in a satisfactory state. Equation (4.30) and similar approaches may be adequate if one is dealing with a single plane or mildly curved surface. In most engineering applications, however, one needs to predict flows within an enclosure or around bodies with several distinct faces. In these cases the approach indicated by Eq. (4.30) is, at best, a scheme that requires *ad hoc*, case-specific interpretation, while in others it is simply unworkable. In flow through a square duct, for example, there are four vector directions normal to a wall and, correspondingly, four wall-normal distances. Analogous (and, indeed, more vexing) problems arise in handling flow through tube banks, within internal combustion engines or in turbomachinery flows. It is

https://doi.org/10.1017/9781108875400.006 Published online by Cambridge University Press

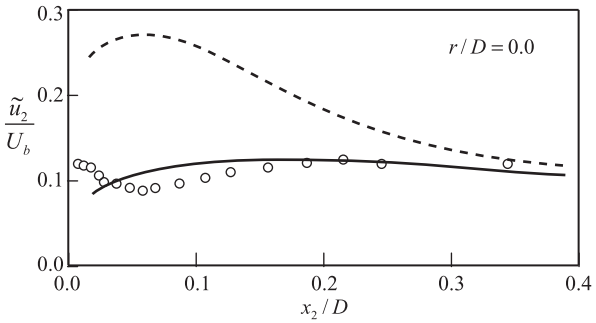

Fig. 4.10 Component rms velocity fluctuation normal to a wall on the axis of an axisymmetric impinging jet. From Craft and Launder (1992). Symbols: experiment (Cooper *et al.*, 1993). Lines: computations with alternative wall-reflection terms, Eq. (4.30) (full line) and Eq. (4.14) (dotted line).

this geometrical complexity that has spurred efforts to eliminate from the closure the very parameters on which traditional 'wall-proximity' corrections depend, namely wall distance and unit vectors. The inadequacies of predictions with the Basic Model will be seen in some of the examples considered in §4.4.5. What has come in its place? First, as will be discussed in detail in sections that follow, the use of non-linear models for Φ_{ij_1} and Φ_{ij_2} has meant that there is a much reduced need for wall-proximity corrections. Second, there is the recognition that, within the immediate vicinity of the wall, where viscous effects are large, turbulence is varying so rapidly in the direction normal to the wall that some explicit correction for inhomogeneity should arguably be made to the pressure-strain process (Bradshaw *et al.*, 1987). This effect, which is mainly of significance in the viscosity-affected near-wall region, will be considered further in Chapter 6.

4.4 Pressure-strain models from tensor expansion

4.4.1 Principles of tensorial expansion

In the absence of more exact yet practically feasible approaches to formulating general models of the pressure-containing products, an alternative route has been widely adopted based on representing the variable in question as some initially unknown function of the plausible quantities (e.g. Pope, 2000). The function is then expanded in a series containing all possible combinations of the available quantities (termed *integrity bases*), each of which is allocated a numerical coefficient whose value is determined by requiring that the approximation should satisfy at least some of the mathematical and physical constraints listed in §4.1. The Cayley–Hamilton theorem[7] is then invoked to identify the highest order terms and to truncate the

[7] For any second-order tensor b_{ij} one can write its characteristic equation, $b^3_{ij} - Ib^2_{ij} + IIb^1_{ij} - IIIb^0_{ij} = 0$, where $b^0_{ij} \equiv \delta_{ij}$, $b^1_{ij} \equiv b_{ij}$, $b^2_{ij} \equiv b_{ik}b_{kj}$, $b^3_{ij} \equiv b_{ik}b_{kn}b_{nj}$, and $I = b_{ii}$, $II = (b_{ii}b_{jj} - b^2_{ii})/2$, $III = (b_{ii}b_{jj}b_{kk} - 3b_{ii}b^2_{jj} + 2b^3_{ii})/6$ are the first, second and third invariants of b_{ij}. Multiplying the

https://doi.org/10.1017/9781108875400.006 Published online by Cambridge University Press

tensor expression to a practically manageable form. This approach has been used in modelling not only Φ_{ij}, but also other unknown terms in the second-moment equations such as ε_{ij} and $\overline{u_i u_j u_k}$. Moreover, the same approach has been applied to modelling $\overline{u_i u_j}$ itself in the context of non-linear eddy-viscosity/diffusivity or algebraic stress/flux models (see Chapter 7). Applied to the pressure-strain term, the tensor function can be written in terms of the available, traceless, symmetric second-rank tensors as[8]

$$\Phi_{ij} = \mathcal{F}_{ij}\,(a_{mn},\ S_{mn},\ W_{mn},\ \delta_{mn},\ \mathcal{T}) \quad \text{or} \quad \Phi_{ij} = \mathcal{F}_{ij}\,(a_{mn},\ \mathcal{P}_{mn},\ D_{mn},\ \delta_{mn},\ \mathcal{T}) \tag{4.31}$$

where a_{mn} is the stress anisotropy tensor, S_{ij} and W_{ij} are the mean rate of strain and rate of rotation, respectively, $\mathcal{P}_{mn}$ and D_{mn} are the stress-production tensor and its complement (see §4.4.3, Eq. (4.47)) and $\mathcal{T}$ is the characteristic time scale.

Usually, an expansion is sought in a non-dimensional series (Pope, 2000)

$$\Phi_{ij}/\varepsilon = \sum_{n=1}^{m} \alpha_n \mathbb{T}_{ij}^{(n)} \tag{4.32}$$

where α_n are the coefficients to be determined, and $\mathbb{T}_{ij}^{(n)}$ are the *integrity bases* – second-order deviatoric (i.e. traceless) tensors (because Φ_{ij} is redistributive) consisting of various combinations of the available quantities as indicated in Eq. (4.31). The expansion can be applied to the complete Φ_{ij} or, as usually practised, separately to each of its constituent parts. The latter approach is followed here. As a word of caution, however, the strategy of expanding a tensor function, while rigorously satisfying the chosen physical and mathematical constraints, may not necessarily recover the essential physics driving the process. Thus, it must still be regarded as an approximation.

4.4.2 Non-linear models of the 'slow' terms, Φ_{ij_1} and $\Phi_{\theta_{j_1}}$

The return to isotropy of anisotropic turbulence is by a non-linear process, as may be seen from the underlying equation, (4.3). Thus, Rotta's (linear) model can serve only as a first approximation (though reasonably valid over a limited range

characteristic equation by b_{ij}^n gives $b_{ij}^{3+n} - Ib_{ij}^{2+n} + IIb_{ij}^{1+n} - IIIb_{ij}^n = 0$. On the other hand, any tensor ϕ_{ij} which is a function of b_{ij}, i.e. $\phi_{ij} = f(b_{ij})$, can be expanded in a series $\phi_{ij} = \alpha_1 b_{ij}^0 + \alpha_2 b_{ij}^1 + \alpha_3 b_{ij}^2 + \alpha_4 b_{ij}^3 + \ldots + \alpha_{n+1} b_{ij}^n$. The Cayley–Hamilton theorem stipulates that in n dimensions, b_{ij}^n is a linear combination of lower powers of n. This means that one can express any b_{ij}^n in terms of b_{ij}^0, b_{ij}^1 *and* b_{ij}^2 and the functions of invariants of b_{ij}, i.e. $\phi_{ij} = \beta_1\delta_{ij} + \beta_2 b_{ij} + \beta_3 b_{ij}^2$, where $\beta_1,\ \beta_2,\ \beta_3 = f(I, II, III)$. For example, for $n = 1$, $b_{ij}^4 - Ib_{ij}^3 + IIb_{ij}^2 - IIIb_{ij} = 0$ (where $b_{ij}^4 = b_{ik}b_{km}b_{mn}b_{nj}$), or $b_{ij}^4 - I(Ib_{ij}^2 - IIb_{ij} + IIIb_{ij}^0) + IIb_{ij}^2 - IIIb_{ij} = 0$, or $b_{ij}^4 = \beta_1\delta_{ij} + \beta_2 b_{ij} + \beta_3 b_{ij}^2$ where $\beta_1 = I \times III$, $\beta_2 = III - I \times II$ and $\beta_3 = I \times I - II$. For a traceless tensor, such as the stress anisotropy, $I = b_{ii} = 0$, and the principal second and third invariants become $II = -b_{ii}^2/2 = -b_{ik}b_{ki}/2$ and $III = b_{ii}^3/3 = b_{ik}b_{kn}b_{ni}/3$.

[8] To account for viscosity and make the expansion applicable within the near-wall viscosity-affected layer, the characteristic turbulence Reynolds number should be added to the independent variable set, as discussed in Chapter 6.

https://doi.org/10.1017/9781108875400.006 Published online by Cambridge University Press

of anisotropies). More general approximations have adopted a non-linear expansion of Φ_{ij_1} in terms of $\mathbb{T}_{ij}^{(n)}$ comprising combinations of the stress anisotropy tensor, a_{ij}. The Cayley–Hamilton theorem leads to the conclusion that all terms higher than quadratic in a_{ij} can be expressed in terms of the lower order terms, so that only two independent tensor constituents can be defined, $\mathbb{T}_{ij}^{(1)} = a_{ij}$ and $\mathbb{T}_{ij}^{(2)} = a_{ik}a_{kj} - \frac{1}{3}a_{kl}a_{lk}\delta_{ij}$, so that the complete non-linear model (Lumley, 1978; Speziale *et al.*, 1991) is

$$\Phi_{ij_1} = -c_1\varepsilon a_{ij} + c_1'\varepsilon(a_{ik}a_{kj} - \tfrac{1}{3}A_2\delta_{ij}) \tag{4.33}$$

where A_2 is the second invariant of the stress anisotropy tensor and the coefficients may be functions of the second and/or third invariant, A_2, A_3 (defined in §3.7.2, Eqs. (3.26) and (3.27)). Despite being complete in the tensor-expansion sense and reproducing better the return to isotropy in homogeneous flow than the linear model, Eq. (4.33) fails in inhomogeneous near-wall flows if the coefficients are kept constant. The matter will be discussed further in Chapter 6 when considering the modifications of the model to account for viscosity and wall-proximity effects.

Versions in which the coefficient of the linear part is also made a function of one or other (or usually both) of the invariants have been proposed (Lumley, 1978; Reynolds, 1984; Fu *et al.*, 1987b), which are conveniently expressed as:

$$\Phi_{ij_1} = -c_1\varepsilon(1+c_1''A_2)a_{ij} + c_1'\varepsilon\left(a_{ik}a_{kj} - \tfrac{1}{3}A_2\delta_{ij}\right). \tag{4.34}$$

The second term in Eq. (4.34) produces an interesting asymmetry of response. Suppose all the a_{ij} are zero except $a_{11} = \delta$ and $a_{22} = -\delta$ (so $A_2 = 2\delta^2$). If c_1' is positive, Φ_{111} takes a larger negative value than the (positive) value of Φ_{22_1}. Consequently $\overline{u_1^2}$ will tend to revert more rapidly to isotropy from above than will $\overline{u_2^2}$ from below, which in turn means that a_{33} will depart from its initial zero value.

The coefficients c_1 and c_1' may be chosen so that the resultant expression for Φ_{ij_1} exactly satisfies the two-component limit.[9] If, as before, we take $\overline{u_1^2} = k(1+\delta)$, $\overline{u_3^2} = k(1-\delta)$, the requirement that a_{22} should vanish irrespective of the size of δ leads to $c_1' = 3/2$ and $c_1'' = -3/4$. A problem that the use of these values introduces is that for moderate levels of anisotropy (A_2 in the range 0.2–0.5, say) experiments and computer simulations on the return to isotropy of highly anisotropic stress fields indicate a *faster* proportionate rate of return than when the stress field is only weakly anisotropic. The negative value of c_1'' on its own produces the reverse of the desired effect. One can, in principle, offset the consequences of a negative c_1'' by causing c_1 to increase rapidly with A_2. No firm proposals of this type have so far

[9] Clearly, Rotta's original form does not satisfy this limit since if one component of Reynolds normal stress vanishes, its value of a_{ij} is -2/3, so Φ_{ij_1} for this component equals $+(2/3)\,c_1\varepsilon$ rather than zero.

https://doi.org/10.1017/9781108875400.006 Published online by Cambridge University Press

been advanced, however. A simpler way of making Φ_{ij_1} vanish in two-component turbulence is to arrange that c_1 should contain the factor A^n, where A is the flatness parameter, introduced in §3.7.2, Eq. (3.28). Lumley and co-workers prefer this route and take the coefficients c_1' and c_1'' as zero. Craft and Launder (2002b), while adopting this approach, retain a non-zero value of c_1':

$$c_1 = 3.1A^{1/2}A_2, \quad c_1' = 1.2, \quad c_1'' = 0.$$

Shifting attention to the corresponding term in the scalar flux equation, $\Phi_{\theta j_1}$, it was soon recognized, when computations of heat transport under various boundary conditions began to be made, that more elaborate forms than Monin's original suggestion were needed (Lumley, 1978; Launder and Samaraweera, 1979) beginning with:

$$\Phi_{\theta j_1} = -c_{1\theta}\frac{\varepsilon}{k}(\overline{\theta u_j} + c_{1\theta}' a_{ij}\overline{\theta u_i}). \tag{4.35}$$

Moreover, as noted, several workers (e.g. Launder, 1976; Jones and Musonge, 1988) have suggested the partial or complete replacement of the dynamic time scale k/ε by the scalar time scale $\overline{\theta^2}/\varepsilon_{\theta\theta}$ (though Pope, 1983 argues against such a choice as it is incompatible with the linearity of the exact scalar-transport equation). A further significant and controversial addition to the modelling was proposed by Jones and Musonge (1988), namely that the fluctuating pressure field also acted to modify the generation of scalar flux arising from the mean temperature gradient. This suggestion has been adopted by several other workers, including Dakos and Gibson (1985); Gibson *et al.* (1987) and Craft (1991). The last of these proposed the following version with coefficients calibrated against a broad range of homogeneous flows:

$$\Phi_{\theta j_1} = -c_{1\theta}r^{1/2}\frac{\varepsilon}{k}\left[\overline{\theta u_j}(1+c_{1\theta}''') + c_{1\theta}' a_{jk}\overline{\theta u_k} + c_{1\theta}'' a_{jk}a_{ki}\overline{\theta u_i}\right] - c_{1\theta}^* r k a_{ij}\frac{\partial\Theta}{\partial x_i} \tag{4.36}$$

where

$$c_{1\theta} = -1.7\left[1 + 1.2(A_2A)^{1/2}\right],\ c_{1\theta}' = -0.8,\ c_{1\theta}'' = 1.1,\ c_{1\theta}''' = 0.6,\ c_{1\theta}^* = -0.2A^{1/2}$$

and r denotes the time-scale ratio, $(\varepsilon_{\theta\theta}/\overline{\theta^2})(k/\varepsilon)$. Examples of computations with this form are shown in §4.4.5.

In an attempt to shed further light on modelling this 'slow' term, Dol *et al.* (1999) examined the DNS data of Versteegh and Nieuwstadt (1998) and Boudjemadi *et al.* (1997) for natural convection in a side-heated, infinite vertical plane channel (where the heat flux entering at the hot wall balances that leaving at the opposite cold wall). At the inevitably low Rayleigh numbers of the DNS ($\leq 5 \times 10^6$), where molecular effects permeate much of the flow, it was felt to be preferable to develop

https://doi.org/10.1017/9781108875400.006 Published online by Cambridge University Press

a model[10] in terms of the complete temperature–pressure gradient correlation (i.e. $\Pi_{\theta j}$ rather than $\Phi_{\theta j}$) for which a cubic form was adopted:

$$\Pi_{\theta j_1} = -\frac{\varepsilon}{k}(c_{1\theta}\overline{\theta u_j} + c'_{1\theta}a_{jk}\overline{\theta u_k} + c''_{1\theta}a_{jk}a_{ki}\overline{\theta u_i}). \tag{4.37}$$

Initially, only the two first terms were retained as that enabled Eq. (4.37) to be used to determine the values of $c_{1\theta}$ and $c'_{1\theta}$ across the flow using the DNS data to provide the values of the heat fluxes (both parallel and normal to the wall, i.e. j = 1 and 2) and the corresponding values of $\Pi_{\theta j_1}$. The solution showed that $c_{1\theta}$ was positive and $c'_{1\theta}$ negative, and that their ratio remained reasonably constant with a quotient $c'_{1\theta}/c_{1\theta} \approx -1.4$, broadly in accord with the values generally adopted for these two coefficients (in $\Phi_{\theta j}$) in the literature. In order to evaluate $c''_{1\theta}$, an additional equation would be needed by considering, for example, the third flux component in a three-dimensional flow. Instead, in line with the above result, the ratio $c'_{1\theta}/c_{1\theta}$ was assigned a constant value, thus enabling $c''_{1\theta}$ to be obtained. Away from the wall-dominated region, the model coefficients determined in this way from the DNS database were reasonably constant, $c_{1\theta} \approx 5$, $c'_{1\theta} \approx -7$ and $c''_{1\theta} \approx 13$, while the near-wall behaviour was matched by multiplying all coefficients by an exponential function of the stress invariant A (see Dol *et al.*, 1999). Overall, however, a better, more stable fitting to the data was achieved with $c_{1\theta 0} = 4.9$, $c'_{1\theta 0} = -2c_{1\theta 0}$, $c''_{1\theta 0} = 12.9$, where the inclusion of the zero subscript denotes values in the core of the channel. This choice, Fig. 4.11, reproduced the variation of $\Pi_{\theta j_1}$ for both flux components apart from an unimportant deviation in the central channel region.

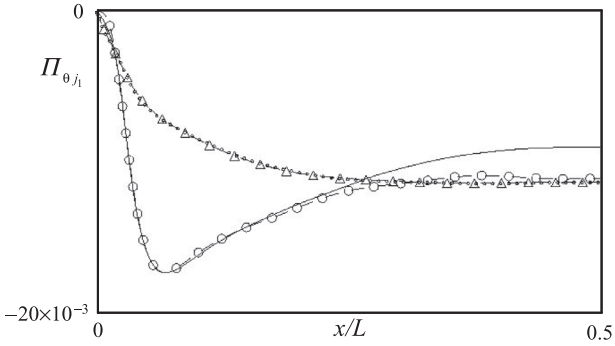

Fig. 4.11 The 'slow' part of the pressure-gradient–temperature correlation in fully-developed natural convection in a vertical channel computed from Eq. (4.37) with values for coefficients given in the text (lines) using the DNS data of Versteegh and Nieuwstadt (1998) for $\overline{\theta u_j}$ and a_{ij} (Model 2, from Dol *et al.*, 1999). Symbols: DNS, ○: $j = 1$, Δ: $j = 2$.

[10] Note that $\Pi_{\theta j}$ goes to zero at a wall, whereas $\Phi_{\theta j}$ is finite and must balance turbulent pressure diffusion.

https://doi.org/10.1017/9781108875400.006 Published online by Cambridge University Press

4.4.3 The general linear model of Φ_{ij_2} and $\Phi_{\theta j_2}$: the quasi-Isotropic (QI) model

We return now to Eqs. (4.3) and (4.5) and consider more formal routes to approximating the rapid terms Φ_{ij_2} and $\Phi_{\theta j_2}$. First, it is assumed that the mean velocity gradient can be considered uniform over the region where the two-point correlations in that equation are significantly different from zero (an assumption sometimes referred to as *local homogeneity*).[11] The mean velocity gradient can then be taken out of the integral and the term Φ_{ij_2} written as:

$$\Phi_{ij_2} = \frac{\partial U_l}{\partial x_m}(b_{lj}^{mi} + b_{li}^{mj}) \tag{4.38}$$

where[12]

$$\begin{aligned} b_{lj}^{mi} + b_{li}^{mj} &= -\frac{1}{4\pi}\int_V \overline{\left(\frac{\partial u_m}{\partial x_l}\right)'\left(\frac{\partial u_i}{\partial x_j} + \frac{\partial u_j}{\partial x_i}\right)}\frac{dV}{r} \\ &= +\frac{1}{4\pi}\int_V \left(\frac{\partial^2 \overline{u'_m u_i}}{\partial r_l \partial r_j} + \frac{\partial^2 \overline{u'_m u_j}}{\partial r_l \partial r_i}\right)\frac{dV}{r}. \end{aligned} \tag{4.39}$$

For isotropic turbulence the two-point correlation functions appearing in Eq. (4.39) are functions only of the radius of separation of the two points and, thus, the integrals can be obtained analytically, as was shown first by Naot *et al.* (1973). This leads to what they termed the '*quasi-isotropic*' model. In shear flows or for turbulence subjected to force fields, the two-point correlations will not be spherically symmetric, however, so the quasi-isotropic assumption is an approximation that may be far from the truth, especially in extreme states such as near a wall. For these more general situations, no purely analytical route has yet been proposed. However, by adopting the tensorial expansion approach one can first obtain

[11] This means that in modelling the exact expression for Φ_{ij_2} in Eq. (4.3), it is assumed that $\partial U'_l/\partial x'_m$ (i.e. the mean velocity gradient evaluated at a distance r from the point where Φ_{ij} is to be determined) can be replaced by the corresponding velocity gradient at the point itself. Launder and Tselepidakis (1994) and later workers have proposed refining this approximation by including the second derivative of velocity. As this effect is only of importance in the viscous near-wall region, it is considered further in Chapter 6.

[12] If a two-point velocity correlation, $R_{im}(r) \equiv \overline{u_i(\mathbf{x})u_m(\mathbf{x}+\mathbf{r})} \equiv \overline{u_i u'_m}$ (where $\mathbf{r} = \mathbf{x}'$- x is the separation vector, and $r = |\mathbf{r}|$), is differentiated first with respect to x_j and then with respect to x_l (with u_i being independent of x'_l and u'_m independent of x_j), then

$$\frac{\partial}{\partial x_j}(\overline{u_i u'_m}) = \overline{\frac{\partial u_i}{\partial x_j}u'_m} \equiv \frac{\partial R_{mi}}{\partial x_j} = -\frac{\partial R_{mi}}{\partial r_j}$$

and

$$\frac{\partial}{\partial x'_l}\left(\overline{\frac{\partial u_i}{\partial x_j}u'_m}\right) = -\frac{\partial}{\partial x'_l}\left(\frac{\partial R_{mi}}{\partial r_j}\right) = -\frac{\partial^2 R_{mi}}{\partial r_l \partial r_j} = \overline{\left(\frac{\partial u_m}{\partial x_l}\right)'\frac{\partial u_i}{\partial x_j}}.$$

https://doi.org/10.1017/9781108875400.006 Published online by Cambridge University Press

the quasi-isotropic result of Naot *et al.* (1973) and then, by introducing further constraints, satisfy higher order terms in the expansion, which become significant for states far removed from isotropic turbulence, as will be shown below.

We focus on modelling b_{lj}^{mi}, a fourth-rank tensor comprising Reynolds-stress elements, which we shall insist, as a minimum, should satisfy the following constraints:

- symmetry in indices m and i, as well as in l and j, so that

$$b_{lj}^{mi} = b_{lj}^{im} = b_{jl}^{im} \tag{4.40}$$

- continuity (as follows from (4.3))

$$b_{li}^{mi} = 0 \tag{4.41}$$

- normalization (direct integration of the Poisson equation for the contraction formed by setting $j = l$ and applying Green's theorem)

$$b_{jj}^{mi} = 2\overline{u_m u_i}. \tag{4.42}$$

Note that the postulated model, like $p_{(2)}$, Eq. (4.2), depends linearly on the mean velocity gradient. The form of b_{1j}^{mi} is unknown at the outset so one begins by writing the most general form

$$b_{lj}^{mi} = \mathcal{F}_{ij}\left(\overline{u_i u_j},\ \overline{u_i u_l},\ \overline{u_i u_m},\ \ldots,\ \delta_{ij},\ \delta_{im},\ \ldots\right) = \sum \alpha_n \mathbb{T}_{ij}^{(n)} \tag{4.43}$$

where now $\mathbb{T}_{ij}^{(n)}$ is a second-rank tensor consisting of any combination of Reynolds stress components and Kronecker unit tensors.

With attention restricted to terms *linear* in the Reynolds stress, a general expansion will contain nine terms each with its unknown coefficient. However, by insisting that the expansion should respect the desired symmetry properties, Eq. (4.40), only five independent coefficients remain so that the expansion can be written as

$$\begin{aligned} b_{lj}^{mi} = {} & \alpha\overline{u_m u_i}\delta_{lj} + \beta(\overline{u_i u_j}\delta_{ml} + \overline{u_i u_l}\delta_{mj} + \overline{u_m u_j}\delta_{il} + \overline{u_m u_l}\delta_{ij}) \\ & + \gamma\overline{u_l u_j}\delta_{mi} + \left[\eta\delta_{ml}\delta_{\iota j} + \zeta\left(\delta_{ml}\delta_{ij} + \delta_{mj}\delta_{il}\right)\right]k. \end{aligned} \tag{4.44}$$

The continuity and normalization constraints (4.41) and (4.42) each furnishes two relations that the coefficients α, β, etc. must satisfy; for example, the latter requires that

$$(3\alpha + 4\beta) = 2 \quad \text{and} \quad (2\alpha + 3\eta + 2\zeta) = 0. \tag{4.45}$$

So, four of the five unknown coefficients can be determined in terms of the fifth. Then, with the form of b_{lj}^{mi} determined (save for the single unknown) the expression for Φ_{ij_2} can be computed from Eq. (4.38). After some algebra the result can be

https://doi.org/10.1017/9781108875400.006 Published online by Cambridge University Press

expressed in terms of the stress production tensor, $\mathcal{P}_{ij}$, and its complement, D_{ij}, and mean rate of strain, $\mathcal{S}_{ij}$:

$$\Phi_{ij_2} = -c_2\left(\mathcal{P}_{ij} - \tfrac{1}{3}\mathcal{P}_{kk}\delta_{ij}\right) - c_3\left(D_{ij} - \tfrac{1}{3}D_{kk}\delta_{ij}\right) - c_4 k S_{ij} \tag{4.46}$$

where

$$D_{ij} \equiv -\left(\overline{u_i u_k}\frac{\partial U_k}{\partial x_j} + \overline{u_j u_k}\frac{\partial U_k}{\partial x_i}\right), \quad S_{ij} \equiv \frac{1}{2}\left[\frac{\partial U_i}{\partial x_j} + \frac{\partial U_j}{\partial x_i}\right] \tag{4.47}$$

and the coefficients c_2, c_3 and c_4 are all related to a single parameter γ. This result is identical to the quasi-isotropic model obtained earlier from direct analysis by Naot *et al.* (1973). By adopting $\gamma = 2/5$ (based on the arguments discussed below) the coefficients take the following values:

$$c_2 = \frac{\gamma+8}{11} = 0.764, \quad c_3 = \frac{8\gamma - 2}{11} = 0.109, \quad c_4 = \frac{60\gamma - 4}{55} = 0.364. \tag{4.48}$$

Equation (4.46) has been invented and rediscovered many times in the past 50 years. An analysis by the authors was perhaps the earliest derivation (Hanjalić and Launder, 1972b). However, we found that that version did not reproduce satisfactorily the measurements in the nearly homogeneous shear flow of Champagne *et al.* (1970) (due, it was subsequently discovered, to an inappropriately large value adopted for the Rotta constant, $c_1 = 2.8$). Consequently, as noted in §4.4.4, certain non-linear terms like $\overline{u_l u_m}\,\overline{u_i u_j}/k$ were added to b_{lj}^{mi}. Some years later, with a smaller value of the Rotta constant ($c_1 = 1.5$) the linear model, Eqs. (4.44) to (4.46), *did* mimic the near-equilibrium shear-flow data satisfactorily (Launder *et al.*, 1975).[13] A few years later, however, the model was found to be quite unsatisfactory in predicting swirling jets (Launder and Morse, 1979), while, to predict boundary layer flows, the wall-proximity correction needed to be nearly as strong as it was with the Basic Model considered in §4.3.4 (Launder *et al.*, 1975).

The same approximation strategy can be applied to modelling the pressure-scalar-gradient correlation $\Phi_{\theta j_2}$, except that one then deals with a vector, i.e.

$$\Phi_{\theta j_2} = 2b_{kj}^{l}\frac{\partial U_k}{\partial x_l} \tag{4.49}$$

[13] Lumley (1975a; 1978) and Reynolds (1984) followed similar tensor-expansion routes, but different strategies were adopted in fixing the final constant, γ. Naot *et al.* (1973) and Launder *et al.* (1975) chose γ to optimize the relative stress levels in an equilibrium simple shear (γ = 2/5); Reynolds (1984) took $\gamma = \frac{10}{7}$ in order that the resultant expression should be formally independent of the mean vorticity, while Lumley (1978) took $\gamma = -\frac{2}{3}$. These widely different values for γ have little effect on the first of the three groups in Eq. (4.46) (which is the major term in components where $\mathcal{P}_{ij}$ is large) but give large variations in the coefficients of the other two. This has major effects on stress components which play only a passive role in simple shear (but which can exert substantial importance in other types of flow).

https://doi.org/10.1017/9781108875400.006 Published online by Cambridge University Press

where

$$b_{ki}^{l} = -\frac{1}{4\pi}\int_V \overline{\frac{\partial u_l'}{\partial x_k}\frac{\partial \theta}{\partial x_i}}\frac{dV}{r} = -\frac{1}{4\pi}\int_V \frac{\partial^2 \overline{\theta u_l'}}{\partial r_k \partial r_i}\frac{dV}{r}.$$

The term to be approximated is now a third-rank tensor, which is *linear* in the scalar. Just like b_{lj}^{mi}, it should satisfy the continuity and normalization constraints, $b_{ki}^{k} = 0, b_{kk}^{l} = \overline{\theta u_l}$, respectively. Thus, on observing symmetry in i and k, b_{ki}^{l} can be expressed as a linear combination of scalar flux components:

$$b_{ki}^{l} = \alpha_1^{\theta}\overline{\theta u_l}\delta_{ik} + \alpha_2^{\theta}(\overline{\theta u_k}\delta_{li} + \overline{\theta u_i}\delta_{lk}), \tag{4.50}$$

i.e. the equivalent of Eq. (4.44) for Φ_{ij}, which in this case leads to a model with no free coefficient (Launder, 1973, 1975b; Lumley, 1975a):

$$\Phi_{\theta i_2} = +0.8\,\overline{\theta u_k}\frac{\partial U_i}{\partial x_k} - 0.2\,\overline{\theta u_k}\frac{\partial U_k}{\partial x_i}. \tag{4.51}$$

In a simple shear flow where the temperature gradient is in the same direction as the velocity gradient, the above form does not predict the correct ratio of heat fluxes down the mean temperature gradient and in the stream direction. The fact that it has nevertheless been successfully used in computing thermal boundary-layer flows simply underlines that turbulent heat fluxes in the streamwise direction are usually not important (being far outweighed by mean convection). The problems with Eq. (4.51) can be largely overcome by extending the 'quasi-isotropic' analysis to include non-linear products of Reynolds stresses as discussed in §4.4.5.

4.4.4 'Quasi-linear' models of Φ_{ij_2}

Both Reynolds and Lumley recognized that the values of γ selected for use in their versions of the QI model of Φ_{ij_2} led to unacceptable normal-stress ratios. To compensate, they introduced non-linear terms to b_{lj}^{mi} as originally proposed by Hanjalić and Launder (1972b). This latter model (denoted hereafter as HL) can be written as:

$$b_{lj}^{mi} = (b_{lj}^{mi})_{lin} + \vartheta\left[(\overline{u_m u_j}\;\overline{u_i u_l} + \overline{u_m u_l}\;\overline{u_i u_j}) - (\overline{u_m u_i}\;\overline{u_l u_j})\right]/k \tag{4.52}$$

where $(b_{lj}^{mi})_{lin}$ is simply the linear version given by Eq. (4.44).

By inserting Eq. (4.52) into (4.38) and with some rearrangement of the non-linear term, the model of Φ_{ij_2} can be expressed in the same form as (4.46), but containing an additional, non-linear term,

$$\Phi_{ij_2} = -c_2\left(\mathcal{P}_{ij} - \frac{1}{3}\mathcal{P}_{kk}\delta_{ij}\right) - c_3\left(D_{ij} - \frac{1}{3}D_{kk}\delta_{ij}\right) - c_4 k S_{ij} - c_5 a_{ij}\mathcal{P}_{kk}. \tag{4.53}$$

This simple model (termed 'quasi-linear' because it contains only one term of the complete quadratic expansion) has the additional coefficient, c_5 not present in the

https://doi.org/10.1017/9781108875400.006 Published online by Cambridge University Press

linear model, Eq. (4.46).[14] By imposing the requisite tensor-symmetry conditions together with the continuity and, partially, the normalization constraints, the coefficients in (4.53) can be expressed in terms of ϑ only. A value of about 0.45 for ϑ gives the best fit to the homogeneous shear flow data of Champagne *et al.* (1970), resulting in the values indicated below:[15]

$$c_2 = \frac{8-2\vartheta}{11} = 0.645, \quad c_3 = \frac{6\vartheta-2}{11} = 0.0636,$$
$$c_4 = \frac{6\vartheta-2}{55} = 0.0254, \quad c_5 = -\vartheta = -0.45.$$

A very similar approach has been independently developed by Speziale *et al.* (1991). Their SSG model, although derived by a different, more rigorous path, can be presented in the same form as the HL model, Eq. (4.53), except that the coefficients take different values – some being expressed as functions of the stress-anisotropy invariants. Instead of expanding b_{li}^{mi} in terms of Reynolds-stress components as in (4.43) and (4.44), Speziale *et al.* (1991) favoured expanding the complete Φ_{ij_2} as a function of the Reynolds-stress anisotropy, a_{ij}, the mean rate-of-strain tensor S_{ij}, and mean rate-of-rotation tensor W_{ij}. The proposed tensor expansion included up to quadratic combinations of a_{ij}; but, after applying several constraints (strictly valid for homogeneous flows), all but one of the quadratic terms were eliminated, leading to:

$$\begin{aligned}\Phi_{ij_2} &= c_2^* k(a_{ik}S_{jk} + a_{jk}S_{ik} - \tfrac{2}{3}a_{kl}S_{kl}\delta_{ij}) + c_3^* k(a_{ik}W_{jk} + a_{jk}W_{ik}) \\ &\quad + c_4^* k S_{ij} - c_5^* a_{ij}\mathcal{P}_{kk} \qquad (4.54)\\ c_2^* &= 0.625, \quad c_3^* = 0.2, \quad c_4^* = 0.8 - 0.65A_2^{1/2}, \quad c_5^* = 0.45.\end{aligned}$$

The above model of Φ_{ij_2} was combined with the quadratic model of the slow term

$$\Phi_{ij_1} = -c_1\varepsilon\left\{a_{ij} + c_1'\left(a_{ik}a_{kj} - \tfrac{1}{3}A_2\delta_{ij}\right)\right\} \qquad (4.55)$$

where $c_1 = 1.7$ and $c_1' = 1.05/1.7 = 0.617$.

If expressed in terms of production tensors,[16] the complete SSG model for Φ_{ij} becomes:

[14] The last term in Eq. (4.53) can be also written as $c_5 a_{ij}\varepsilon(\mathcal{P}_k/\varepsilon)$ in which form it can be regarded as a modification of Φ_{ij_1} to account for departures from local energy equilibrium, i.e. when $\mathcal{P}_k$ is much different from ε.

[15] Though, as noted by Hanjalić and Launder (1972b), Eq. (4.52) cannot satisfy exactly the normalization constraint (4.42) if $c_5(c_5 = -\vartheta)$ is to be non-zero.

[16] The transformation of (4.53) to (4.54) and vice versa can easily be obtained by recalling that

$$\frac{\partial U_i}{\partial x_j} \equiv S_{ij} + W_{ij}, \quad S_{ij} \equiv \frac{1}{2}\left(\frac{\partial U_i}{\partial x_j} + \frac{\partial U_j}{\partial x_i}\right),$$
$$W_{ij} = -W_{ji} \equiv \frac{1}{2}\left(\frac{\partial U_i}{\partial x_j} - \frac{\partial U_j}{\partial x_i}\right), \quad a_{ij} \equiv \left(\frac{\overline{u_i u_j}}{k} - \frac{2}{3}\delta_{ij}\right)$$

https://doi.org/10.1017/9781108875400.006 Published online by Cambridge University Press

$$\Phi_{ij} = -c_1\varepsilon\left\{a_{ij} + c_1'\left(a_{ik}a_{kj} - \tfrac{1}{3}A_2\delta_{ij}\right)\right\} - c_2\left(\mathcal{P}_{ij} - \frac{1}{3}\mathcal{P}_{kk}\delta_{ij}\right) - c_3\left(D_{ij} - \frac{1}{3}D_{kk}\delta_{ij}\right) - c_4 k S_{ij} - c_5 a_{ij}\mathcal{P}_{kk}. \tag{4.56}$$

The coefficients in the 'rapid' part of Eq. (4.56) can be re-calculated using the transformation relations

$$c_2^* = c_2 + c_3, \quad c_3^* = c_2 - c_3, \quad c_4^* = \tfrac{4}{3}(c_2 + c_3) - c_4, \quad c_5^* = c_5$$
$$c_2 = \tfrac{1}{2}(c_2^* + c_3^*), \quad c_3 = \tfrac{1}{2}(c_2^* - c_3^*), \quad c_4 = \tfrac{4}{3}c_2^* - c_4^*, \quad c_5 = c_5^*$$

to give

$$c_2 = 0.4125, \quad c_3 = 0.2125, \quad c_4 = 0.033 + 0.65A_2^{1/2}, \quad c_5 = 0.45.$$

We note that there is a significant difference in the assigned coefficients in the models considered so far. Some light can be thrown on the validity of the modelling approach by making an *a posteriori* evaluation for selected simple flows for which direct numerical simulations (DNS) are available. Indeed, each (exact) term and its model can be checked separately if the corresponding data are available. Hadžić (1999) evaluated coefficients in the SSG and HL models for fully developed channel flow (for $\mathrm{Re}_\tau = 180$ and 390), expressed in the form given by Eq. (4.56), using DNS data for all non-zero components of Φ_{ij}. It is noted first that the complete SSG model contains six modelling coefficients. If DNS or experimental data are available for all six components of the Φ_{ij} tensor in a general flow, one can form a set of five independent equations (the sixth being redundant due to the redistributive form of the tensor) and thus evaluate all coefficients. However, in plane channel flow, only four components of Φ_{ij} are non-zero and thus only three independent equations are available. To overcome this problem, first the earlier assigned values of the coefficients in the model of Φ_{ij_1} (i.e. c_1 and c_1') are adopted: the justification for doing so is that these coefficients have been tuned in shear-free flows prior to tuning the rapid term. Furthermore, the value already assigned to the coefficient c_5 associated with the non-linear term is retained. All coefficients that were evaluated showed significant variations across

and expanding

$$\mathcal{P}_{ij} = -k\left[a_{ik}(S_{jk} + W_{jk}) + a_{jk}(S_{ik} + W_{ik}) + \frac{4}{3}S_{ij}\right]$$
$$D_{ij} = -k\left[a_{ik}(S_{jk} - W_{jk}) + a_{jk}(S_{ik} - W_{ik}) + \frac{4}{3}S_{ij}\right]$$
$$k(a_{ik}S_{jk} + a_{jk}S_{ik}) = -\frac{1}{2}\left(\mathcal{P}_{ij} + D_{ij}\right) - \frac{4}{3}kS_{ij}$$
$$k(a_{ik}W_{ik} + a_{jk}W_{ik}) = -\frac{1}{2}(\mathcal{P}_{ij} - D_{ij}), \quad ka_{lm}S_{lm} = -\mathcal{P}_{kk}/2.$$

https://doi.org/10.1017/9781108875400.006 Published online by Cambridge University Press

the flow. Suspecting that for such low Reynolds numbers viscous effects had substantial influence, the exercise was repeated for $\mathrm{Re}_\tau = 2000$ using more recent DNS results of Hoyas and Jimenez (2006). Figure 4.12 still shows notable variations of all three coefficients, c_2, c_3 and c_4, across the channel cross-section which contrasts with the constant values assumed in the models. (For comparison, the values of the coefficients in the SSG and HL models are also indicated by horizontal lines at the sides of the diagram. While the SSG model of c_4 provides a non-constant value, its variation follows neither the trend nor the magnitude of the DNS-based distribution.)

A word of caution is warranted for several reasons. First, the outcome of the exercise depends on the adopted model of Φ_{ij_1} and the values of the coefficients c_1, c_1' and c_5. It is possible that a similar scrutiny of a quite different flow might lead to different conclusions. Nevertheless, Fig. 4.12 illustrates qualitatively that, irrespective of the model complexity, it should not be expected that constant values of the coefficients would achieve close agreement of each modelled term with the actual distribution in real flows. However, if the model is regarded as a 'package', the overall agreement of the Reynolds stresses and the mean flow may still be in reasonable agreement with actual values.

We close this section by summarizing in Table 4.2 the values adopted for the coefficients in the models of Φ_{ij} considered so far (linear and quadratic for Φ_{ij_1} and linear and quasi-linear models for Φ_{ij_2}) when expressed in the terms of the rate of strain and rate of rotation tensors, Eq. (4.54).

As seen in Table 4.2, when using the form (4.54) the values of the coefficients for the models shown do not differ very much. However, the subtle differences that *do* exist, especially when expressed as functions of turbulence invariants, can

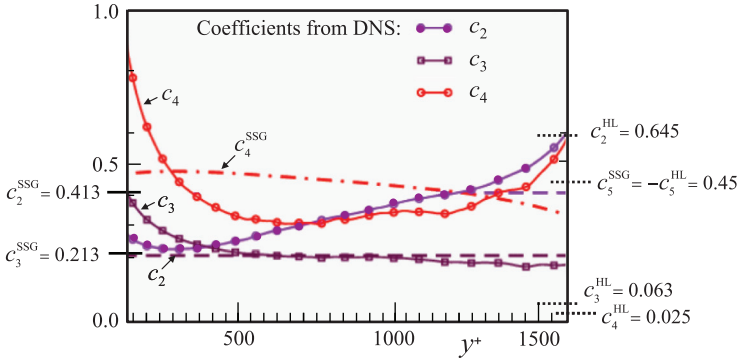

Fig. 4.12 Coefficients c_2, c_3 and c_4 in Eq. (4.56) evaluated from DNS of Hoyas and Jimenez (2006) for a plane channel flow for $\mathrm{Re}_\tau = 2000$. The values suggested by Speziale *et al.* (1991) and Hanjalić and Launder (1972b) are indicated for comparison.

https://doi.org/10.1017/9781108875400.006 Published online by Cambridge University Press

Table 4.2 *Comparison of coefficients in the general expressions for some popular models*

	Φ_{ij_1}		Φ_{ij_2}			
	Linear	Quadratic	Linear			Quasi-linear
	c_1	c_1'	c_2^*	c_3^*	c_4^*	c_5^*
HL	2.8	0	0.71	0.582	0.8	−0.45
GL IP	1.8	0	0.6	0.6	0.8	0
LRR QI	1.5	0	0.873	0.655	0.8	0
SSG	1.7	−1.05	0.625	0.2	$0.8 - 0.65A_2^{1/2}$	0.45

GL: Gibson and Launder (1978); HL: Hanjalić and Launder (1972b); LRR: Launder, Reece and Rodi (1975); SSG, Speziale, Sarkar and Gatski (1991).

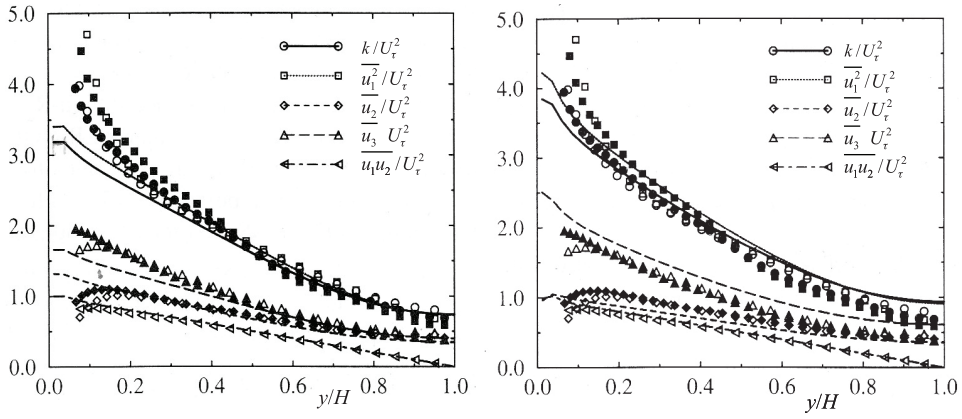

Fig. 4.13 Reynolds stresses in a plane channel. Symbols: DNS (Kim *et al.*, 1987) at $\mathrm{Re}_\tau = 395$ (open symbols), and 595 (filled symbols). Lines: computations for $\mathrm{Re}_\tau \approx 2000$. Left, SSG model; right, Basic Model with wall correction, Eqs. (4.7), (4.9), (4.12) and (4.14). From Hadžić (1999).

bring about visible improvements. This is illustrated by the SSG model which – in contrast to the other linear and quasi-linear models discussed above – reproduces reasonably well the near-wall stress anisotropy in wall-attached flows without any wall-correction term, Fig. 4.13, left. The agreement with the DNS data is, however, somewhat inferior to that achieved with the Basic Model *with* the wall corrections (4.12) and (4.14) or (4.30) shown on the right. Nevertheless, it has been considered by many as satisfactory for industrial applications (though not as good as the non-linear TCL model – which likewise employs no wall-reflection term – discussed in §4.4.5).

https://doi.org/10.1017/9781108875400.006 Published online by Cambridge University Press

4.4.5 Non-linear models of the rapid terms Φ_{ij_2} and $\Phi_{\theta j_2}$: the TCL approach

In contrast to the linear and quasi-linear models of Φ_{ij_2} considered in §4.4.3 and §4.4.4, the complete form of the general expression (4.32) closed by the Cayley–Hamilton theorem contains terms up to *fourth* order in a_{ij} (Johansson and Hällback, 1994; Ristorcelli *et al.*, 1995). However, cubic models have also been developed that meet most of the constraints (e.g. Fu and Wang, 1997). In the following section we consider the joint approach of Fu *et al.* (1987b) and Craft and Launder (1996), which, in addition to the general constraints of symmetry, continuity and normalization (introduced in §4.4.3 and §4.4.4), satisfies the *two-component limit*, and is thus commonly referred to as the *TCL model*.

The TCL Methodology Applied to Modelling Φ_{ij}

Following the general statement of principles in his 1978 paper, in the mid-1980s Lumley and co-workers set out the essential strategy for constructing a model of mean-strain effects on the pressure-containing correlations that fully satisfied the two-component limit (Shih and Lumley, 1985; Shih and Lumley *et al.*, 1985). As with the earlier quasi-isotropic model, the starting point is a representation of the process for homogeneous flows, Eq. (4.38):

$$\Phi_{ij_2} = \left(b_{kj}^{li} + b_{ki}^{lj}\right) \frac{\partial U_k}{\partial x_l}$$

where b_{kj}^{li} is defined by Eq. (4.39) above.

However, in addition to the constraints that this tensor must satisfy for the QI model, i.e. Eqs. (4.40)–(4.42), the additional and vital condition to be applied is that if one of the normal stresses should fall to zero, so too must Φ_{ij_2} in order to avert the risk of negative normal stresses from appearing (which, in the real world, would be physically impossible). The constraint is simply that:

$$\Phi_{\alpha\alpha_2} = 0 \quad \text{if} \quad \overline{u_\alpha^2} = 0. \tag{4.57}$$

It is not possible to choose the free coefficient in the QI model so that the above constraint is met. Accordingly, higher order terms were added (e.g. Shih and Lumley 1985). Here the version of that strategy developed by Fu *et al.* (1987b) is presented as it has been applied extensively and successfully to a wide range of free and wall-bounded turbulent flows. The most general cubic expansion for b_{kj}^{li} was chosen, which can be written as:

$$\begin{aligned}\frac{b_{kj}^{li}}{k} = {} & \lambda_1\delta_{li}\delta_{kj} + \lambda_2(\delta_{lj}\delta_{ki} + \delta_{lk}\delta_{ij}) \\ & + \lambda_3 a_{li}\delta_{kj} + \lambda_4 a_{kj}\delta_{li} + \lambda_5(a_{lj}\delta_{ki} + a_{lk}\delta_{ij} + a_{ij}\delta_{lk} + a_{ki}\delta_{lj}) \\ & + \lambda_6 a_{li}a_{kj} + \lambda_7(a_{lj}a_{ki} + a_{lk}a_{ij}) + \lambda_8 a_{lm}a_{mi}\delta_{kj} + \lambda_9 a_{km}a_{mj}\delta_{li}\end{aligned}$$

https://doi.org/10.1017/9781108875400.006 Published online by Cambridge University Press

$$
\begin{aligned}
&+\lambda_{10}\left(a_{lm}a_{mj}\delta_{ki}+a_{lm}a_{mk}\delta_{ij}+a_{im}a_{mj}\delta_{lk}+a_{km}a_{mi}\delta_{lj}\right)\\
&+a_{mn}a_{nm}\left(\lambda_{11}\delta_{li}\delta_{kj}+\lambda_{12}[\delta_{lj}\delta_{ki}+\delta_{lk}\delta_{ij}]\right)\\
&+\lambda_{13}a_{li}a_{km}a_{mj}+\lambda_{14}a_{kj}a_{lm}a_{mi}\\
&+\lambda_{15}\left(a_{lj}a_{km}a_{mi}+a_{lk}a_{im}a_{mj}+a_{ij}a_{lm}a_{mk}+a_{ki}a_{ml}a_{mj}\right)\\
&+\lambda_{16}a_{mn}a_{np}a_{pm}\delta_{li}\delta_{kj}+\lambda_{17}a_{mn}a_{np}a_{pm}(\delta_{lj}\delta_{ki}+\delta_{lk}\delta_{ij})\\
&+a_{mn}a_{nm}\left(\lambda_{18}a_{li}\delta_{kj}+\lambda_{19}a_{kj}\delta_{li}+\lambda_{20}[a_{lj}\delta_{ki}+a_{lk}\delta_{ij}+a_{ij}\delta_{lk}+a_{ki}\delta_{lj}]\right).
\end{aligned}
\tag{4.58}
$$

The coefficients in the above equation are to be regarded as *constants* which, following the analysis of Fu (1988), can be determined as follows. First, applying the continuity constraint ($b^{li}_{ki}=0$) and making use of the Cayley–Hamilton theorem (see Footnote 7 on page 84) yields six equations:

$$
\begin{aligned}
&\lambda_1+\lambda_2=0,\quad \lambda_3+\lambda_4+\lambda_5=0,\quad \lambda_6+\lambda_7+\lambda_8+\lambda_9+\lambda_{10}=0,\\
&\lambda_{10}+\lambda_{11}+\lambda_{12}=0,\quad \lambda_{13}+\lambda_{14}+4\lambda_{15}+2\lambda_{18}+2\lambda_{19}+10\lambda_{20}=0,\\
&\lambda_{16}+4\lambda_{17}+\tfrac{1}{3}(\lambda_{13}+\lambda_{14}+2\lambda_{15})=0.
\end{aligned}
$$

Similarly, the normalization constraint provides a further six interrelations:

$$
\begin{aligned}
&3\lambda_1+2\lambda_2=4/3,\quad 3\lambda_3+4\lambda_5=2,\quad 2\lambda_7+3\lambda_8+4\lambda_{10}=0,\\
&\lambda_9+3\lambda_{11}+2\lambda_{12}=0,\quad \lambda_{13}+2\lambda_{15}+3\lambda_{18}+4\lambda_{20}=0,\\
&4\lambda_{15}+9\lambda_{16}+6\lambda_{17}=0.
\end{aligned}
$$

The two-component-limit constraint is handled most conveniently in principal axes so that $\overline{u_iu_j}=0$ if $i\neq j$. Let us take $\overline{u_2^2}$ as the vanishing normal stress. Then the other two components can be written as $\overline{u_1^2}=(1+\delta)k$ and $\overline{u_3^2}=(1-\delta)k$, where δ can take any value in the range $-1\leq\delta\leq+1$. The two-component limit requires that

$$
b^{l2}_{k2}\frac{\partial U_k}{\partial x_l}=0\quad\text{if}\quad \overline{u_2^2}=0. \tag{4.59}
$$

Substitution of the above values for the normal stresses into this equation, with b^{li}_{kj} given by Eq. (4.58), leads to the following four relations among the model coefficients:

$$
\begin{aligned}
&\lambda_1+\lambda_2-\tfrac{2}{3}(\lambda_3+\lambda_4)-\tfrac{7}{3}\lambda_5+\tfrac{4}{9}\lambda_6+\tfrac{10}{9}\lambda_7+\tfrac{4}{9}(\lambda_8+\lambda_9)+\tfrac{11}{9}\lambda_{10}+\tfrac{2}{3}(\lambda_{11}+\lambda_{12})\\
&\quad-\tfrac{8}{27}(\lambda_{13}+\lambda_{14})-\tfrac{34}{27}\lambda_{15}-\tfrac{2}{9}(\lambda_{16}+\lambda_{17})-\tfrac{4}{9}(\lambda_{18}+\lambda_{19})-\tfrac{14}{9}\lambda_{20}=0\\
&3\lambda_5-2\lambda_7+2\lambda_{10}+2\lambda_{20}=0,\quad 2\lambda_{20}=0\\
&3\lambda_{10}-6(\lambda_{11}+\lambda_{12})-2\lambda_{15}-6(\lambda_{16}+\lambda_{17})+4(\lambda_{18}+\lambda_{19})+6\lambda_{20}=0.
\end{aligned}
$$

The sixteen constraints above can be used to express the λ in terms of four unknowns (see Craft and Launder, 2002b) though it turns out that two of those unknowns have no effect on the resultant form of Φ_{ij_2}. In consequence, the equation for mean-strain effects on Φ_{ij} can be written as:

https://doi.org/10.1017/9781108875400.006 Published online by Cambridge University Press

$$
\begin{aligned}
\Phi_{ij_2} = & -0.6\left(\mathcal{P}_{ij} - \tfrac{1}{3}\delta_{ij}\mathcal{P}_{kk}\right) + 0.3a_{ij}\mathcal{P}_{kk} \\
& - 0.2\left[\frac{\overline{u_k u_j}\;\overline{u_l u_i}}{k}\left(\frac{\partial U_k}{\partial x_l} + \frac{\partial U_l}{\partial x_k}\right) - \frac{\overline{u_l u_k}}{k}\left[\overline{u_i u_k}\frac{\partial U_j}{\partial x_l} + \overline{u_j u_k}\frac{\partial U_i}{\partial x_l}\right]\right] \\
& - c_2\left[A_2(\mathcal{P}_{ij} - D_{ij}) + 3a_{mi}a_{nj}(\mathcal{P}_{mn} - D_{mn})\right] \\
& + c_2'\left\{\left(\frac{7}{15} - \frac{A_2}{4}\right)\left(\mathcal{P}_{ij} - \tfrac{1}{3}\delta_{ij}\mathcal{P}_{kk}\right) + 0.1\left[a_{ij} - \tfrac{1}{2}\left(a_{ik}a_{kj} - \tfrac{1}{3}\delta_{ij}A_2\right)\right]\right. \\
& - 0.05a_{ij}a_{lk}\mathcal{P}_{kl} + 0.1\left[\left(\frac{\overline{u_i u_m}}{k}\mathcal{P}_{mj} + \frac{\overline{u_j u_m}}{k}\mathcal{P}_{mi}\right) - \tfrac{2}{3}\delta_{ij}\frac{\overline{u_l u_m}}{k}\mathcal{P}_{ml}\right] \\
& + 0.1\left[\frac{\overline{u_l u_i}\;\overline{u_k u_j}}{k^2} - \tfrac{1}{3}\delta_{ij}\frac{\overline{u_l u_m}\;\overline{u_k u_m}}{k^2}\right]\left[6D_{lk} + 13k\left(\frac{\partial U_l}{\partial x_k} + \frac{\partial U_k}{\partial x_l}\right)\right] \\
& \left. + 0.2\frac{\overline{u_l u_i}\;\overline{u_k u_j}}{k^2}\left(D_{ik} - \mathcal{P}_{ik}\right)\right\}. \qquad (4.60)
\end{aligned}
$$

There are several striking things to note in this equation. First, the leading term is simply the IP element of the Basic Model with the same coefficient as is often used empirically in computations with that model and which (naturally) agrees with the exact result for isotropic turbulence (Crow, 1968). The second term also appears in the quasi-linear model, Eq. (4.53). As noted in §4.4.4, this term can be written as $+0.6\ \varepsilon a_{ij}(\mathcal{P}_{kk}/\varepsilon)$ and recognized as a correction to Φ_{ij_1}, essentially reducing the return-to-isotropy coefficient as the turbulence energy generation rate becomes larger relative to the dissipation rate. The two empirical coefficients, c_2 and c_2', multiply terms of very unequal length. In the first applications of the model to homogeneous and free flows the quantity c_2' was set to zero (with $c_2 = 0.6$), a choice that considerably simplified the task of implementing the model into a large-scale computer code (Fu *et al.*, 1987a). However, Fu (1988) concluded that slightly better results were obtained for the range of free flows he was considering by choosing c_2' equal to 0.6 with $c_2 = 0.55$. The issue of which was the better choice only became resoundingly clear some years later when it was found that, by choosing the combination with both c_2 and c_2' non-zero, that choice also enabled the fully turbulent region in flow near walls (or adjacent to free surfaces) to be computed without any modification to the coefficients outside the viscosity-affected sublayer (Li, 1992; Launder and Li, 1994; Kidger, 1999; Craft *et al.*, 2004b). This discovery greatly improved fidelity in computing complex three-dimensional near-wall flows. Moreover, the absence of empirical wall-correction terms is some compensation for the elaborate algebraic form of the model. Indeed, the major wall correction that had to be added to the IP model in §4.3.4 in order that it should model reasonably closely the stress field near walls is, to a large extent, an indication that the *IP scheme does not cope well with high levels of stress anisotropy rather than of wall proximity*. While it may be noted from Eq. (4.3) that a wall effect *should* nevertheless be expected, provided one does not enter the viscosity-affected sublayer, the direct influence of wall proximity with this more complete TCL model, at least

Table 4.3 *Coefficients in the expression (4.61) for the TCL model (Craft and Launder, 1996)*

Φ_{ij_1}		Φ_{ij_2}						
Linear	Quadratic	Linear			Quasi-linear	Quadratic		Cubic
c_1	c_1'	c_2^*	c_3^*	c_4^*	c_5^*	c_6^*	c_7^*	c_8^*
$A^{1/2} + 3.1$ $(A_2 A)^{1/2}$	1.1	0.6	0.866	0.8	0.3	0.2	0.2	1.2

in flows directed reasonably parallel to a wall, seems to be small enough to be neglected. Indeed, the model is more successful in mimicking the near-wall normal stress variation than the SSG model, though at the expense of greater algebraic complexity.

The TCL model may alternatively be formulated in terms of the rate of strain and rate of rotation tensors, S_{ij} and W_{ij} (for details of this transformation, see footnote 16). In that case the TCL model Eq. (4.60) can be rearranged as:

$$\begin{aligned}\Phi_{ij_2} = {} & c_2^* k \left(a_{ik}S_{jk} + a_{jk}S_{ik} - \tfrac{2}{3}a_{kl}S_{kl}\delta_{ij}\right) + c_3^* k(a_{ik}W_{jk} + a_{jk}W_{ik}) \\ & + c_4^* k S_{ij} - c_5^* a_{ij}\mathcal{P}_{kk} + c_6^* k \left(a_{ik}a_{kl}S_{jl} + a_{jk}a_{kl}S_{il} - 2a_{kj}a_{li}S_{kl} - 3a_{ij}a_{kl}S_{kl}\right) \\ & + c_7^* k(a_{ik}a_{kl}W_{jl} + a_{jk}a_{kl}W_{il}) \\ & + c_8^* k \left[a_{mn}^2(a_{ik}W_{jk} + a_{jk}W_{ik}) + 3a_{mi}a_{nj}(a_{mk}W_{nk} + a_{nk}W_{mk})/2\right] \end{aligned} \tag{4.61}$$

with coefficients c_2^* to c_8^* summarized in Table 4.3

Sample computed results are compared below with experiments in Fig. 4.14–Fig. 4.17 and Tables 4.4 and 4.5. The results shown were all obtained with the same mathematical form of model in which the coefficients had been tuned by reference to simple homogeneous flows. The model for the 'slow' pressure strain term used in these computations was:

$$\Phi_{ij_1} = -c_1\left[a_{ij} + c_1'(a_{ik}a_{jk} - \tfrac{1}{3}A_2\delta_{ij})\right] - A^{1/2}\varepsilon a_{ij} \tag{4.62}$$

with the values for c_1 and c_1' indicated in Table 4.3; as a reminder, $A \equiv 1 - \frac{9}{8}[A_2 - A_3]$.

A further element that affects the results is the path adopted for finding ε. The results presented below have all been obtained by solving the transport equation for that quantity presented in Chapter 5, the source-term models being given in Eq. (5.1) and in the text that follows, while diffusion is handled by the GGDH, Eq. (5.11).

A comparison from the thesis of Fu (1988) of the performance of the TCL and Basic Models in mimicking homogeneous flows is provided in Figs. 4.14 and 4.15. Figure 4.14a shows the configuration for the plane-strain experiment of Tucker

https://doi.org/10.1017/9781108875400.006 Published online by Cambridge University Press

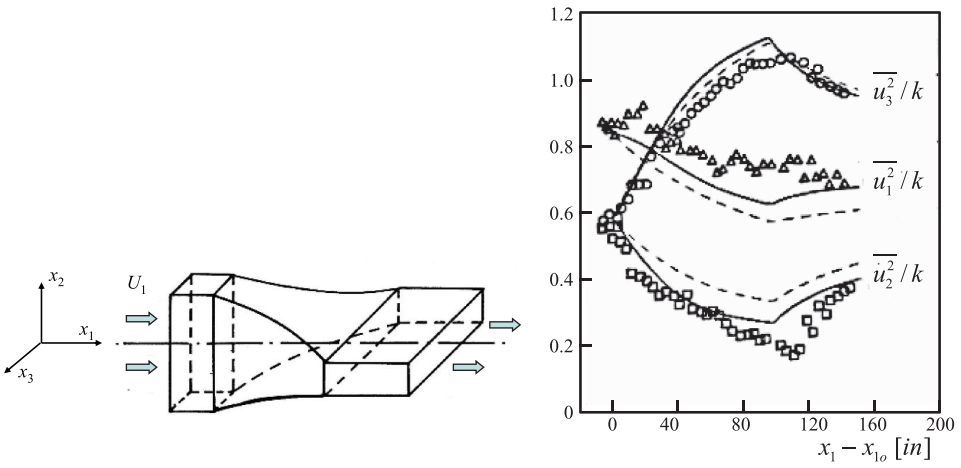

Fig. 4.14 Development of normal stresses in plane-strain distortion: (a) flow configuration; (b) development of Reynolds stresses. Symbols, experiments (Tucker and Reynolds, 1968); – – – Basic Model; —— TCL model. From Fu (1988).

and Reynolds (1968): grid-generated turbulence is passed through a duct whose dimensions in the cross-sectional plane undergo change in such a way that the cross-sectional area does not alter. This is then followed by a section of uniform cross-sectional dimensions. In the computations the flow was idealized by ignoring boundary-layer growth on the duct walls so the streamwise velocity was constant while in the cross-sectional plane the strain rates ($dU_2/dx_2 = -dU_3/dx_3$) were obtained from the changing cross-sectional shape. In that way a very rapid one-dimensional computation could be made though, particularly at the abrupt changeover to the uniform cross-section, the actual straining on the centre-line would not have altered quite as rapidly as idealized. In fact, for this flow the absence of shear strains and shear stresses means that only the first two terms on the right side of Eq. (4.60) are non-zero and the first, as noted, is just the IP model used in the Basic Model. Thus, the difference between the two sets of computations is mainly due to the modelling of the slow term in Φ_{ij}. In view of the idealizations of the flow, both forms perform reasonably well though clearly the TCL results are in closer accord with the experiments.

The homogeneous shear flow shown in Fig. 4.15 also gives a good guide to how a model will behave in two-dimensional *inhomogeneous* flows in simple shear. Two cases are shown, one where the strain rate is such that the flow is close to local equilibrium ($\mathcal{P}_k \approx \varepsilon$) while, in Fig. 4.15b, the turbulence energy production is some 50% greater than the dissipation rate. For the local-equilibrium case both models capture quite successfully the development of the shear stress downstream. However, the Basic Model fails to reproduce the differences between the normal stresses acting perpendicular to the flow direction. Of course, in two-dimensional

https://doi.org/10.1017/9781108875400.006 Published online by Cambridge University Press

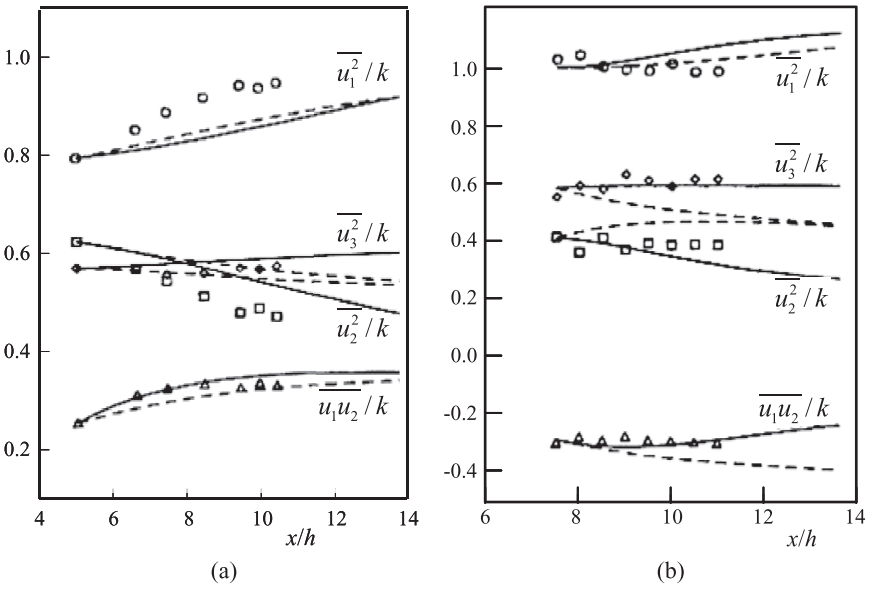

Fig. 4.15 Reynolds stress developments in homogeneous shear flows (U_1 varies linearly with x_2) (note $x \equiv x_1$: (a) $\mathcal{P}_k/\varepsilon \approx 1.0$; (b) $\mathcal{P}_k/\varepsilon = 1.55$. Symbols, experiments: (a) Champagne *et al.* (1970), (b) Harris *et al.* (1977). Lines, computations, as Fig. 4.14. From Fu (1988).

thin shear flows that weakness is not of importance. At the higher strain rate, shown in Fig. 4.15b, the errors in modelling those normal stresses are more pronounced but in practical terms the most serious weakness with the Basic Model is that the magnitude of the shear stress continues to increase with distance downstream, whereas experiments indicate that under more intense straining the shear stress diminishes. The TCL model is clearly superior both in this respect and in mimicking the measured normal-stress variation.

Turning to inhomogeneous free flows, Table 4.4 summarizes the asymptotic rates of spread of the axisymmetric and plane two-dimensional jets. Here it should be noted that the numbers appearing in the table differ from those reported in many of the originally published papers. First, the experimental value of spreading rate for the round jet (for many years regarded as 0.086, following the review by Rodi (1975)) was chosen as 0.095 (the mean of the values obtained from LDA/flying-hot-wire data of Hussein *et al.* (1994) and flying-hot-wire data by Panchapakesan and Lumley (1993)). Moreover, El Baz *et al.* (1993) showed from an exhaustive numerical study that the conventional parabolic (boundary-layer) approximation applied to free jets in stagnant surroundings led to excessive spreading rates for the round jet by more than 10% and by around 4% for the plane case (due mainly to the neglect of source terms arising from streamwise gradients, particularly of ε). The values shown in the table are those obtained from a fully developed elliptic solution

https://doi.org/10.1017/9781108875400.006 Published online by Cambridge University Press

Table 4.4 *Spreading rates of round and plane jets with Basic and TCL models compared with experiment (from a review by Launder, 1989)*

	$dy^{1/2}/dx$		
Flow	Basic Model	Experimental value	TCL model
Plane jet	0.100	0.110	0.110
Round jet	0.105	0.095	0.101
Plane wake*	0.078	0.098	0.100

*Rate of spread for wake $[U_\infty/\Delta U]dy_{1/2}/dx$.

assuming self-preserving profiles at entry and exit. Unlike the Basic Model, the TCL scheme gives a lower rate of spread for the round jet than the plane. While the spreading rate for the round jet is still too high by some 6%, this is a similar percentage excess obtained with the TCL model for the axisymmetric plume considered in §4.5.3, Table 4.6. The plane asymptotic wake, whose dimensionless rate of spread ($[U_\infty/\Delta U]dy_{1/2}/dx$) is computed too low with the Basic Model, is also predicted satisfactorily with the TCL scheme. The major contributor to this last improvement is the more elaborate form of dissipation rate equation used with this model though the TCL pressure-strain model also makes a significant contribution. Further predictions of non-equilibrium wakes using the TCL model may be found in Chapter 5.

Turning to near-wall flows, the case of fully developed channel flow is normally adopted as the initial check point (or basis for calibration, if a wall correction is applied) and for such flows, as noted above, the TCL model (with no wall correction) does reasonably well. The main challenge, however, is in predicting the much more complex three-dimensional flows near walls that one continually encounters in practical applications. A case in point is the three-dimensional wall jet where an initially round jet is discharged parallel to and in contact with a plane surface, Fig. 4.16a. In this case, due to the proximity of the surface, fluctuations normal to the wall are damped and, arising from the resultant large stress anisotropy in the cross-sectional plane, a streamwise vorticity source is created that induces a secondary flow in that plane, Fig. 4.16b. In consequence, there is a rapid lateral divergence of the jet and a slower growth normal to the wall than in the free jet (Newman *et al.*, 1972; Craft and Launder, 2002a).

Table 4.5 shows that the standard k–ε eddy viscosity model leads to a *lower* spreading rate of the wall jet in the lateral than the normal directions while, if one adopts the Basic Model (second-moment closure), a much too strongly

https://doi.org/10.1017/9781108875400.006 Published online by Cambridge University Press

Table 4.5 *Spreading rates of three-dimensional wall jet from Craft and Launder (2002a); $y_{1/2}, z_{1/2}$ denote half-widths in wall-normal and lateral directions*

Source	$dy_{1/2}/dx$	$dz_{1/2}/dx$	$dz_{1/2}/dx/dy_{1/2}/dx$
Experiment (Abrahamsson *et al.*, 1997)	0.065	0.32	4.94
Linear eddy viscosity	0.079	0.069	0.88
Basic model	0.053	0.814	15.3
TCL model	0.060	0.51	8.54
TCL model at 70 diameters	0.055	0.308	5.6

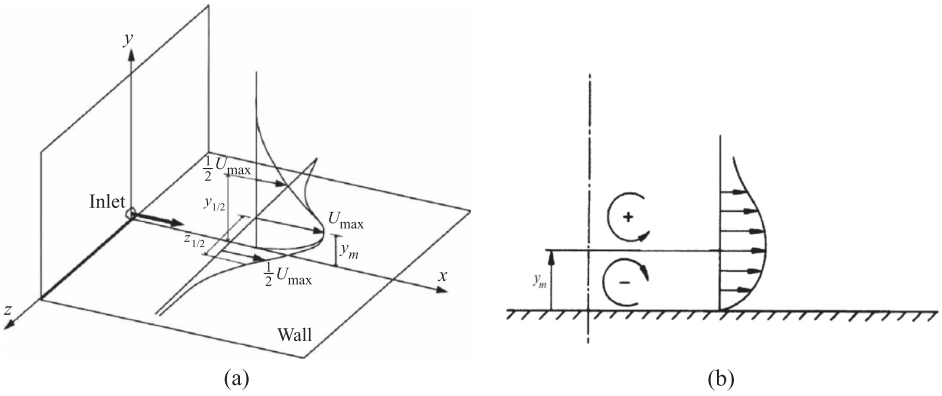

Fig. 4.16 Three-dimensional wall jet: (a) flow configuration, (b) induced secondary flow in a cross-sectional plane. From Craft and Launder (2002c).

anisotropic growth is produced. This latter behaviour arises directly from applying the same wall correction to this three-dimensional jet as had been calibrated by reference to two-dimensional channel flow. The TCL scheme gives results much closer to experiment though that too displays higher lateral spreading rates than the data. The cause of this discrepancy lies in the fact that with the TCL model this flow takes far longer to reach full development than the downstream range covered in the experiment. If, instead of the fully developed results, those obtained from a marching solution were compared then, at the same distance downstream as in the experiment, the lateral growth rate is close to that reported from experiment.

A similar improvement results for the case of the three-dimensional free-surface jet (Kidger, 1999; Craft *et al,*, 2000). In contrast to the case of the *two*-dimensional surface jet, where the Basic Model, including 'wall-reflection' from the free surface, showed good behaviour (Fig. 4.9), when this model is applied to the three-dimensional case, just as for the three-dimensional wall jet, a too large lateral rate of spread is recorded. As is shown in Craft and Launder (2002b, p. 114), significantly closer agreement with experiment is achieved with the TCL scheme.

https://doi.org/10.1017/9781108875400.006 Published online by Cambridge University Press

A further sensitive test is provided by the case of fully-developed flow through straight ducts of non-axisymmetric cross-section. As was discovered by Prandtl and his students in the 1930s, weak secondary motions are then created which significantly modify the friction and heat transfer around the duct periphery. The underlying cause of these motions is the anisotropy of the turbulent stress field in the plane of the duct cross-section (i.e. the same source as in the three-dimensional wall jet considered above). A linear eddy-viscosity scheme provides a purely diffusive model for the turbulent stresses and consequently no secondary flows are computed with such schemes. Because of the stress anisotropy predicted by second-moment closures they are in principle capable of mimicking the flow pattern. A particularly challenging test is provided by the experiment of Hinze (1973) of flow through a 5:1 rectangular duct in which symmetric roughened strips were included on the lower wall, a feature which greatly augmented the secondary flow. Figure 4.17 a compares the measured axial velocity contours over the cross section with those predicted using the Basic and TCL models (Launder and Li, 1994). While the former scheme predicts distortions of the axial velocity of the correct overall type, equally clearly, the TCL computations mimic far more closely the

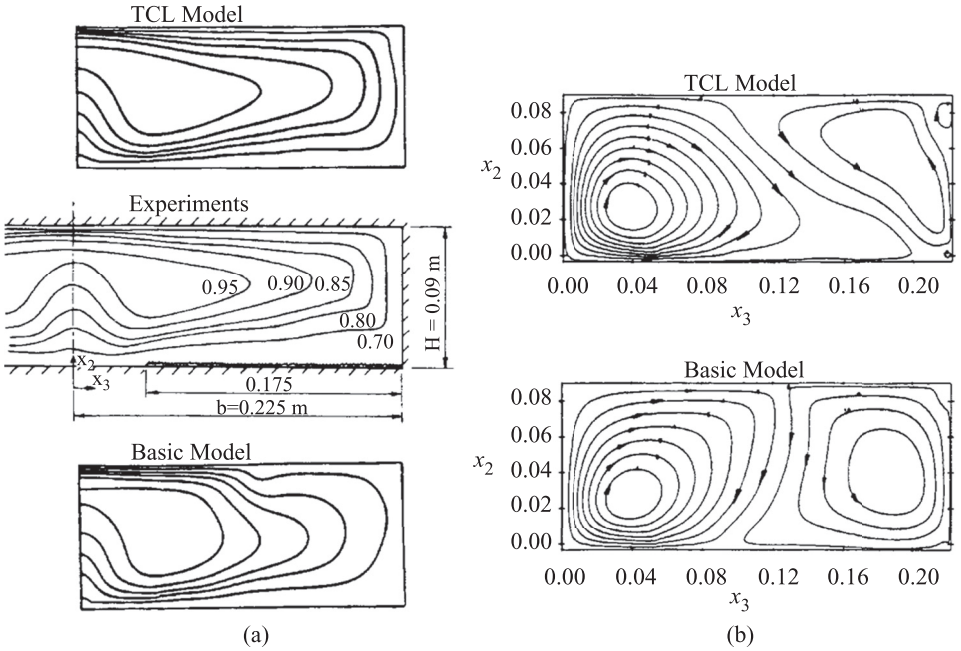

Fig. 4.17 Flow through a rectangular-sectioned duct with a partially roughened lower wall. (a) Contours of mean velocity; computations of Launder and Li (1994); experiments of Hinze (1973). (b) Predicted secondary flows. From Launder and Li (1994).

https://doi.org/10.1017/9781108875400.006 Published online by Cambridge University Press

reported shape of the velocity contours. Although the secondary flow was not reported by Hinze, the computed patterns for the two models are substantially different, Fig. 4.17b, and it is this which is responsible for the differences in the primary flow distribution.

The TCL strategy for modelling $\Phi_{\theta i}$

The starting point here is Eq. (4.49) used earlier to obtain the QI model of this process. The object is to provide a model of the third-rank tensor b^l_{ki} that is compatible not just with the continuity and normalization constraints that were applied to obtain the QI form (Eqs. (4.41) and (4.42)) but with the two-component limit too. Adopting the same approach to modelling this tensor as for b^{li}_{kj} above, the third-rank tensor b^l_{ki} is represented as a sum of products of scalar fluxes and Reynolds stresses. Noting, however, that the integral in Eq. (4.49) is linear in the fluctuating scalar, θ, requires that the expansion for b^l_{ki}, whilst containing nonlinear terms in the Reynolds stresses, should be linear in the scalar flux. Including all possible terms which respect the required symmetry in i and k, such an expansion up to cubic order can be written as:

$$\begin{aligned} b^l_{ki} = {} & \alpha_1\overline{\theta u_l}\delta_{ik} + \alpha_2(\overline{\theta u_k}\delta_{li} + \overline{\theta u_i}\delta_{lk}) + \alpha_3\overline{\theta u_l}a_{ik} \\ & + \alpha_4(\overline{\theta u_k}a_{li} + \overline{\theta u_i}a_{lk}) + \alpha_5\overline{\theta u_m}a_{ml}\delta_{ik} + \alpha_6\overline{\theta u_m}(a_{mk}\delta_{li} + a_{mi}\delta_{lk}) \\ & + \alpha_7\overline{\theta u_m}a_{mi}a_{ik} + \alpha_8\overline{\theta u_m}(a_{mk}a_{il} + a_{mi}a_{kl}) + \alpha_9\overline{\theta u_l}a_{mi}a_{mk} \\ & + \alpha_{10}a_{ml}(\overline{\theta u_k}a_{im} + \overline{\theta u_i}a_{km}) + a_{mn}a_{mn}\left[\alpha_{11}\overline{\theta u_l}\delta_{ik} + \alpha_{12}(\overline{\theta u_i}\delta_{lk} + \overline{\theta u_k}\delta_{li})\right] \\ & + \overline{\theta u_n}a_{mn}\left[\alpha_{13}a_{ml}\delta_{ik} + \alpha_{14}\left(a_{mk}\delta_{li} + a_{mi}\delta_{lk}\right)\right]. \end{aligned} \tag{4.63}$$

Constraints analogous to those adopted in modelling Φ_{ij_2} can now be applied to determine as many of the model coefficients as possible. The continuity and normalization conditions require:

$$\text{continuity } b^k_{ki} = 0, \quad \text{normalization } b^l_{kk} = \overline{\theta u_l}.$$

Applying these conditions gives the following eight relations among the α coefficients:

- from continuity

$$\alpha_1 + 4\alpha_2 = 0, \quad \alpha_7 + \alpha_8 + \alpha_9 + \alpha_{10} + \alpha_{13} + \alpha_{14} = 0$$
$$\alpha_{10} + \alpha_{11} + 4\alpha_{12} = 0, \quad \alpha_3 + \alpha_4 + \alpha_5 + 4\alpha_6 = 0$$

- from normalization

$$3\alpha_1 + 2\alpha_2 = 1, \quad 2\alpha_8 + 2\alpha_{10} + 3\alpha_{13} + 2\alpha_{14} = 0$$
$$2\alpha_4 + 3\alpha_5 + 2\alpha_6 = 0, \quad \alpha_9 + 3\alpha_{11} + 2\alpha_{12} = 0.$$

https://doi.org/10.1017/9781108875400.006 Published online by Cambridge University Press

We recall that if only linear terms are retained (i.e. only α_1 and α_2 non-zero) one finds $\alpha_1 = 0.4$ and $\alpha_2 = -0.1$, which leads to the quasi-isotropic model, Eq. (4.51).

Different approaches have been used in applying the TCL constraint. Shih and Lumley (1985) ensured compliance with the Schwarz inequality:

$$(\overline{\theta u_\alpha})^2 \leq \overline{\theta^2} \cdot \overline{u_\alpha^2} \tag{4.64}$$

(where the subscript α denotes any component direction rather than summation). They did this by requiring that the rate of change of $\left[(\overline{\theta u_\alpha})^2 - \overline{\theta^2} \cdot \overline{u_\alpha^2}\right]$ should be zero when equality held and thus that:

$$2\overline{\theta u_\alpha}\frac{D\overline{\theta u_\alpha}}{Dt} = \overline{u_\alpha^2}\frac{D\overline{\theta^2}}{Dt} + \overline{\theta^2}\frac{D\overline{u_\alpha^2}}{Dt} \quad \text{when} \quad (\overline{\theta u_\alpha})^2 = \overline{\theta^2} \cdot \overline{u_\alpha^2}.$$

This constraint, however, links the models of Φ_{ij_2} and $\Phi_{\theta j_2}$, and the outcome is that not only are all the α coefficients determined but also that both free coefficients in the TCL model of Φ_{ij_2} are required to be zero. However, the presence of the terms with coefficients c_2 and c_2' is vital to securing satisfactory agreement in the wide variety of simple and complex shear flows presented above. For this reason Craft (1991) (see also Craft and Launder (2002b), adopted a different strategy, requiring that the net mean-strain contribution to the $\overline{u_i\theta}$ transport equation, $\Phi_{\theta i_2} + \mathcal{P}_{\theta i_2}$, should be zero in the two-component limit. This condition translates to:

$$\frac{\partial U_k}{\partial x_l} b_{k2}^l = \frac{1}{2}\overline{\theta u_l}\frac{\partial U_2}{\partial x_l} \quad \text{when } u_2 = 0.$$

By considering the situation again in principal axes of the stresses, this condition leads to the following inter-linkages among the α coefficients:

$$\begin{aligned}
&\alpha_1 - \tfrac{2}{3}\alpha_2 + \tfrac{1}{3}\alpha_3 - \tfrac{2}{9}\alpha_7 + \tfrac{4}{9}\alpha_9 + \tfrac{2}{3}\alpha_{11} + \tfrac{1}{9}\alpha_{13} = \tfrac{1}{2}, \quad && \alpha_5 - \tfrac{2}{3}\alpha_7 + \tfrac{2}{3}\alpha_{13} = 0\\
&\alpha_2 - \tfrac{2}{3}\alpha_4 + \tfrac{1}{3}\alpha_6 - \tfrac{2}{9}\alpha_8 + \tfrac{4}{9}\alpha_{10} + \tfrac{2}{3}\alpha_{12} + \tfrac{1}{9}\alpha_{14} = 0, \quad && 2\alpha_{11} + \alpha_{13} = 0\\
&\alpha_6 - \tfrac{2}{3}\alpha_8 + \tfrac{2}{3}\alpha_{14} = 0, && 2\alpha_{12} + \alpha_{14} = 0.
\end{aligned}$$

Solving these equations for the α coefficients together with the further equations arising from continuity and normalization constraints above (Craft and Launder, 2002b) enables the pressure–scalar gradient correlation to be written as:

$$\begin{aligned}
\Phi_{\theta i_2} = {} & 0.8\overline{\theta u_k}\frac{\partial U_i}{\partial x_k} - 0.2\overline{\theta u_k}\frac{\partial U_k}{\partial x_i} + \tfrac{1}{3}\frac{\varepsilon}{k}\overline{\theta u_i}\frac{\mathcal{P}_k}{\varepsilon} - 0.4\overline{\theta u_k}a_{il}\left(\frac{\partial U_k}{\partial x_l} + \frac{\partial U_l}{\partial x_k}\right)\\
& + 0.1\overline{\theta u_k}a_{ik}a_{ml}\left(\frac{\partial U_m}{\partial x_l} + \frac{\partial U_l}{\partial x_m}\right) - 0.1\overline{\theta u_k}\left(a_{im}\mathcal{P}_{mk} + 2a_{mk}\mathcal{P}_{im}\right)/k\\
& + 0.15a_{ml}\left(\frac{\partial U_k}{\partial x_l} + \frac{\partial U_l}{\partial x_k}\right)\left(a_{mk}\overline{\theta u_i} - a_{mi}\overline{\theta u_k}\right)
\end{aligned}$$

https://doi.org/10.1017/9781108875400.006 Published online by Cambridge University Press

$$- 0.05a_{ml}\left[7a_{mk}\left(\overline{\theta u_i}\frac{\partial U_k}{\partial x_l} + \overline{\theta u_k}\frac{\partial U_i}{\partial x_l}\right) - \overline{\theta u_k}\left(a_{ml}\frac{\partial U_i}{\partial x_k} + a_{mk}\frac{\partial U_i}{\partial x_l}\right)\right]. \tag{4.65}$$

In this case *all* the unknown coefficients are determined by the constraints applied. Again the leading two terms are the QI model and, as with the TCL pressure-strain model, the third term may be seen as a correction to the 'slow', turbulence-driven process. The Shih and Lumley (1985) model, which, as noted above, was truncated to terms quadratic in the stress field, shows close similarity with the first four terms in the above equation, albeit with different numerical coefficients:

$$\begin{aligned}\Phi_{\theta j_2} = {} & 0.8\overline{\theta u_k}\frac{\partial U_j}{\partial x_k} - 0.2\overline{\theta u_k}\frac{\partial U_k}{\partial x_j} + 0.3\frac{\varepsilon}{k}\overline{\theta u_j}\frac{\mathcal{P}_k}{\varepsilon} \\ & + 0.1\overline{\theta u_k}a_{jl}\frac{\partial U_l}{\partial x_k} - 0.3\overline{\theta u_k}a_{jl}\frac{\partial U_k}{\partial x_l} + 0.2\overline{\theta u_k}a_{kl}\frac{\partial U_j}{\partial x_l}.\end{aligned} \tag{4.66}$$

For a simple, homogeneous shear flow close to local equilibrium where the temperature and velocity gradients are in the same direction (y), Craft (1991) reports that Eq. (4.65), used in conjunction with Eq. (4.36) to approximate $\Phi_{\theta i_1}$, returns a turbulent Prandtl number, σ_θ, of approximately 0.7 and a ratio of streamwise to cross-stream heat flux ($-\overline{\theta u}/\overline{\theta v}$) of approximately 1.1. This is very close to the values that are returned by both experimental data and, indeed, most other second-moment closures. (This is because this case is regarded as an essential reference data-set to satisfy as it resembles the situations found in many simple shear flows.) Figure 4.18, however, shows the corresponding experimental data (Tavoularis and Corrsin, 1981) for the case where the production to dissipation ratio of k has been increased to approximately 1.8. As seen, the Basic Model now leads to a *reduction* in turbulent Prandtl number to around 0.5 (compared with the measured *increase* to values slightly greater than unity). Moreover, for that model, the ratio of streamwise to cross-stream heat flux reaches an asymptotic level of only about 1.6 compared with a value of approximately 2.2 reported in the experiments. For both quantities, however, the TCL scheme predicts a streamwise development closely in accord with the experiments. Of the two other closures appearing in Fig. 4.18, the model of (Gibson *et al.*, 1987) is a composite representation of both the 'rapid' and 'slow' parts of $\Phi_{\theta j}$:

$$\Phi_{\theta j} = -\left(\frac{3}{1 + 1.5A_2^{1/2}}\right)\frac{\varepsilon}{k}\overline{\theta u_j} + 0.12a_{ij}k\frac{\partial\Theta}{\partial x_i} + 1.09\overline{\theta u_k}\frac{\partial U_j}{\partial x_k} + 0.51\overline{\theta u_k}\frac{\partial U_k}{\partial x_j}. \tag{4.67}$$

This form gives reasonable agreement with the high-strain-rate case shown in Fig. 4.18 but, for the case of a local equilibrium shear flow (not shown), Craft

https://doi.org/10.1017/9781108875400.006 Published online by Cambridge University Press

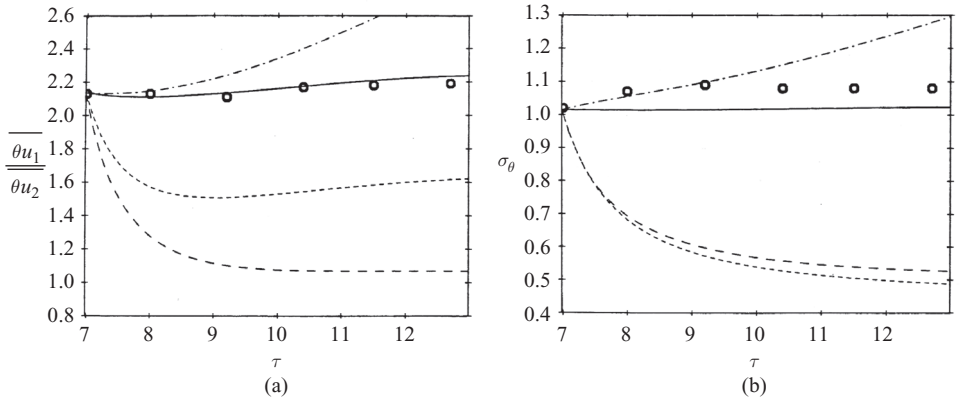

Fig. 4.18 Scalar transport in highly strained homogeneous shear flow: (a) ratio of streamwise to cross-stream heat flux; (b) turbulent Prandtl number. From Craft (1991). Symbols, experiments (Tavoularis and Corrsin, 1981). Predictions: —— TCL model; - - - - - - Basic Model; – – – Shih and Lumley (1985); – · – · – Gibson *et al.* (1987).

(1991) reports that the value of $-\overline{\theta u}/\overline{\theta v}$ is nearly 50% too low (though this in itself is not a disastrous weakness since, as already noted, in the flow direction turbulent diffusion is far outweighed by convective transport). The Shih–Lumley model does poorly for this flow though this is entirely associated with their very complex model of $\Phi_{\theta j_1}$ (not presented here). Craft (1991) showed that if, instead, the version used in his own work was adopted for $\Phi_{\theta j_1}$, Eq. (4.36), the Shih–Lumley model of $\Phi_{\theta j_2}$, Eq. (4.66), gave very nearly the same development as the TCL model. This is an encouraging result for the two models adopt quite different strategies in satisfying realizability. As a final inference from this high-strain-rate homogeneous shear flow, the increase in the turbulent Prandtl number as the strain-rate parameter is increased is, arguably, the principal reason that, in a boundary layer, the near-wall turbulent Prandtl number is higher than in a free shear flow.

We turn finally to a further experiment of the homogeneous shear flow for $\mathcal{P}_k/\varepsilon \approx 1.8$ (Tavoularis and Corrsin, 1985) where, in this case, the linear temperature gradient is imposed at right angles to the mean shear (thus, aligned with the flow's vorticity). In this case the experimental data return a correlation coefficient for the lateral heat flux of approximately 0.45. As Fig. 4.19 indicates, all the closure models return higher values than this and, indeed, that of Gibson *et al.* (1987) produces levels in excess of 0.9! The TCL model is the closest to the data, on average about 12% too high. Rogers *et al.* (1989) have produced DNS simulations of nominally the same homogeneous shear flows but with the time-scale ratio r some 50% different and, inevitably, much lower turbulent Reynolds numbers.

https://doi.org/10.1017/9781108875400.006 Published online by Cambridge University Press

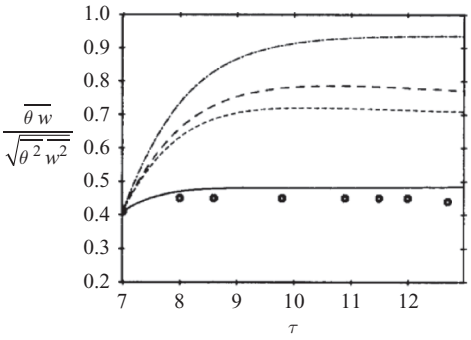

Fig. 4.19 Heat-flux correlation coefficient in a homogeneous shear flow at high strain rates where the mean temperature gradient is orthogonal (z) to the shear (y). Symbols, experiment (Tavoularis and Corrsin, 1985); —— TCL model; - - - - - - Basic Model;– – – Shih and Lumley; · – · – · – Gibson *et al.* (1987).

Computations reported by Craft (1991) for those cases are generally consistent with the above comparisons.

Application of the TCL scheme to further, more complex inhomogeneous cases may be found in §4.5 and §4.6 where the effects of a gravitational force field also become important.

4.4.6 Final remarks on non-linear models of Φ_{ij_2}

As remarked at the start of §4.4.5, a number of other non-linear models of Φ_{ij_2} have been proposed in the literature. Several groups argue that the tensor expansion should, in principle, include up to fourth-order terms in a_{ij} as required by the Cayley–Hamilton theorem for a 'complete' model, see for example Shih and Lumley (1985), Johansson and Hällback (1994) and Ristorcelli *et al.* (1995). These models were all required to satisfy realizability constraints (i.e. requiring that solutions for the stress components should under no circumstances leave the realizable domain within the stress-invariant map, Fig. 3.12), a property that neither the linear IP and QI models nor the quasi-linear models guarantee. Other constraints have also been proposed (e.g. Pope, 2000, p. 426). In contrast to the TCL model, most models have been tested in only a limited range of flows making it difficult to judge fully their merits or their potential width of applicability.

It is noted finally that some authors (Speziale, 1991; Pope, 2000) dispute the whole concept of non-linear models of Φ_{ij_2}, arguing that this process should be linear in a_{ij} because b_{lj}^{mi} is linear in the stress spectrum. However, the *shapes* of the two-point velocity correlations in the exact integrals that appear in the definition of b_{lj}^{mi} (cf. Eq. (4.39)) will themselves be deformed by the strain field and the inclusion of non-linear elements which, in any event, contribute little when turbulence is

https://doi.org/10.1017/9781108875400.006 Published online by Cambridge University Press

close to isotropy, would seem to be a justified way of accounting for such effects. The incontestable fact is that the approach leads to models that mimic the response of real turbulence to an imposed strain field far better than any currently available strictly linear model.

4.5 Turbulence affected by force fields

4.5.1 Introduction

In this section the role played by force fields on the turbulence structure is the focus of attention. Their direct effect appears transparently through the generation terms in the second-moment equations. Nearly always, however, there will be important corresponding effects in the processes that need modelling, most importantly in the pressure-containing terms in the second-moment equations. In some flows, effects of force fields on the turbulent length scale (or energy dissipation rate) are important while, in cases where there is a strong damping of the second moments by the force field, careful attention also needs to be paid to the diffusive processes which may then assume a greater significance. In those cases buoyant influences on the *triple* moments need to be considered.

The direct effects of body forces on the exact second-moment equations have been presented in Chapter 2 (Eqs. (2.18) and (2.19) for the stress transport and Eqs. (2.22) and (2.23) for the scalar flux), while the exact forms of the buoyant contributions to the non-dispersive pressure correlations are included in Eqs. (4.3) and (4.5). In the sections which follow, the modelling and consequences of different types of force field are examined.

4.5.2 System rotation: Coriolis effects

When fluid is contained in a rotating, closed container, or, indeed, when it is passed through a region with rotating rigid surfaces, as in flow through a rotor stage of a gas turbine, it is usually convenient to examine the flow in a coordinate system that rotates with the rotating surfaces, thereby bringing the rigid boundaries apparently to rest. However, in adopting such a non-inertial reference frame, one acquires additional terms in the momentum equations (see, for example Aris, 1962; Greenspan, 1962) which may be thought of as a force-field contribution to the transport process. In this case the instantaneous force field $\hat{F}_i$ is equal to $-2\Omega_k \hat{U}_j \epsilon_{ijk}$, where ϵ_{ijk} is the third-rank alternating unit tensor, which takes the values +1 when the subscripts i, j and k are all different and in cyclic order (i.e. 1,2,3 or 2,3,1 or 3,1,2), -1 for all different values in anti-cyclic sequencing, and zero if the values of two or more subscripts are the same. As noted in Eq. (2.19), the corresponding contribution from the fluctuating part of this term (commonly called the Coriolis term) to the Reynolds-stress generation rate is:

https://doi.org/10.1017/9781108875400.006 Published online by Cambridge University Press

$$\mathcal{F}_{ij} \equiv \mathcal{R}_{ij} = -2\Omega_k \left[\overline{u_j u_m} \epsilon_{ikm} + \overline{u_i u_m} \epsilon_{jkm} \right]. \tag{4.68}$$

Thus, within the framework of second-moment closure in which each stress component is obtained by solving its transport equation, the Coriolis production term is obtained without any need for modelling.

Stress generation due to system rotation

Before considering effects of the fluctuating Coriolis force on other processes, it is instructive to examine briefly the nature of the term and its action in the turbulent stress production tensor. As an example, the case of fully developed flow through a plane channel which is itself rotating in what is known as orthogonal-mode rotation, Fig. 4.20, is considered.

As implied above, the flow is examined in a coordinate system that rotates with the duct so that the flow appears steady. The rotation vector Ω_k is here equal to $(0, 0, \Omega)$. Thus, while in (4.68) there is an implied summation on both k and m, the only significant value for k is 3 since only $\Omega_3 = \Omega$ is non-zero. The Coriolis and strain production terms in the component stress transport equation associated with rotation and shear are thus:

$$\begin{array}{lll} \overline{u_1^2} & \mathcal{R}_{11} = +4\,\Omega \overline{u_1 u_2} & \mathcal{P}_{11} = -2\overline{u_1 u_2}\,\dfrac{\partial U_1}{\partial x_2} \\ \overline{u_2^2} & \mathcal{R}_{22} = -4\,\Omega \overline{u_1 u_2} & \mathcal{P}_{22} = 0 \\ \overline{u_1 u_2} & \mathcal{R}_{12} = -2\,\Omega(\overline{u_1^2} - \overline{u_2^2}) & \mathcal{P}_{12} = -\overline{u_2^2}\,\dfrac{\partial U_1}{\partial x_2} \end{array} \tag{4.69}$$

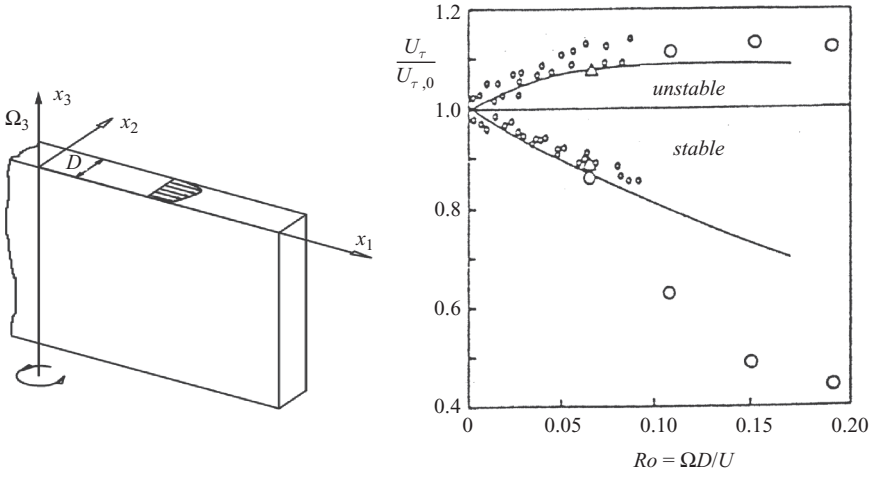

Fig. 4.20 Plane channel rotating about the spanwise axis, x_3. Left, configuration and notation; right, friction velocities on the pressure (unstable) and suction (stable) surface for different rotation rates, normalized with the friction velocity with no rotation for the same flow rate conditions. Symbols, experiment Johnston *et al.* (1972); lines, computations, Basic Model. From Launder *et al.* (1987).

https://doi.org/10.1017/9781108875400.006 Published online by Cambridge University Press

Now, referring to Fig. 4.20, close to the near face of the rotating duct the mean velocity gradient is positive, so, for the case of no rotation, $\overline{u_1 u_2}$ is negative, i.e. of the same sign as $\mathcal{P}_{12}$. The contribution $\mathcal{R}_{12}$ is also negative since the streamwise normal stress, $\overline{u_1^2}$, is greater than $\overline{u_2^2}$. Thus, as Ω is progressively increased (i.e. as the Coriolis contribution to the generation is steadily raised), the (negative) generation rate of $\overline{u_1 u_2}$ increases. In the far wall in Fig. 4.20, the mean velocity gradient is negative and so $\mathcal{P}_{12}$ is positive. $\mathcal{R}_{12}$ is still negative, however, since near that wall $\overline{u_1^2}$ is greater than $\overline{u_2^2}$. Thus, as rotation increases, the rotational contribution leads to a reduction in the rate of generation of shear stress and thus in the shear stress itself. With rotation in the direction shown, the near wall is known as the *pressure surface* (since the static pressure of the fluid will be highest at that surface) and, correspondingly, the far wall is known as the *suction surface*. Because the overall production of turbulence near the pressure surface is enhanced, this region is sometimes referred to as the *unstable side*, whereas the region with a reduced production near the suction surface is known as the *stable side* of the channel. Clearly then, our consideration of the generation terms suggests that as rotation increases, the wall shear stress should be raised on the pressure surface but reduced on the suction surface.

Figure 4.20 on the right (ignoring for the moment the solid lines to be discussed shortly) shows experimental data of the variation of the friction velocity (i.e. the square root of the wall shear stress) on each wall versus the rotation parameter $\mathrm{Ro} \equiv \Omega D/\overline{U}$ (sometimes termed the inverse Rossby number), where $\overline{U}$ denotes the channel mean velocity. The behaviour shown certainly confirms the inferences drawn in the previous paragraph. There is, however, a notable asymmetry in the behaviour on the two surfaces: on the suction surface the friction decreases steadily as Ro increases, while on the pressure surface the friction velocity levels off for $\mathrm{Ro} > 0.07$. The reason for this differing behaviour can be inferred by considering the effect of the Coriolis generation terms for the normal stresses lying in the $x_1 - x_2$ plane. Near the pressure surface, since $\overline{u_1 u_2}$ is negative there, the Coriolis term is also negative for $\mathcal{R}_{11}$ but positive for $\mathcal{R}_{22}$. Thus, as Ro is progressively raised, near that surface $\overline{u_1^2}$ is reduced while $\overline{u_2^2}$ is increased. That, as seen in Eq. (4.69), progressively weakens the increase of the Coriolis term in $\mathcal{R}_{12}$, which causes the friction factor to level out.

As a final remark on the Coriolis generation terms, we note that because the rotation source term in $\mathcal{R}_{11}$ is precisely the same magnitude as and of opposite sign from that of $\mathcal{R}_{22}$ (and there is no contribution in $\mathcal{R}_{33}$ since that is the direction in which the rotation vector points), the Coriolis generation term in the turbulence energy equation is zero. Thus, there is no effect of rotation captured by eddy-viscosity models since neither in the basic stress–strain formula nor in the

transport equations for dynamic turbulence properties (such as k and ε) does any explicit effect of rotation appear. Eddy-viscosity models applied to such rotating flows thus require empirical corrective terms to be added. Usually this has been done by adding an additional source term to the modelled transport equation for ε.

Coriolis effects on the pressure-strain correlation

Before closure is complete and second-moment computations made, the corresponding pressure-strain term, denoted Φ_{ij_3}, needs modelling in terms of known or calculable quantities. One possibility – indeed, the simplest plausible assumption – is that the pressure fluctuations redistribute the generation due to rotation in just the same way that they do with the isotropization of production (IP) scheme introduced in Section 4.3. However, if one intends to follow that route, care must be taken as to what strictly should be interpreted as the Coriolis *production* term. The need for caution arises from the fact that the substantial derivative, $D\overline{u_i u_j}/Dt$, is not, as it stands, materially invariant. However, a frame-invariant convective derivative may be readily formed in several ways. Two that suffice for present purposes are either to add the mean-strain production tensor, $\mathcal{P}_{ij}$, to the substantial derivative and (to maintain equality) to add the same quantity to the right side of Eq. (2.21) (Eringen, 1962)

$$\left(\frac{D\overline{u_i u_j}}{Dt} + \mathcal{P}_{ij}\right) = 2\mathcal{P}_{ij} + \mathcal{R}_{ij} + \cdots \tag{4.70}$$

or to transfer half of the Coriolis contribution, $\mathcal{R}_{ij}$, to the convection term (Thomas and Takhar, 1988)

$$\left(\frac{D\overline{u_i u_j}}{Dt} - \tfrac{1}{2}\mathcal{R}_{ij}\right) = \mathcal{P}_{ij} + \tfrac{1}{2}\mathcal{R}_{ij} + \cdots \tag{4.71}$$

Either version leads to the conclusion that the true Coriolis generation is only half as large relative to mean-strain generation as it would appear to be from Eq. (4.68).[17] Thus, in employing the IP model (with necessarily the same coefficient used for the mean-strain and effective Coriolis generation[18]) one is supposing that:

$$\Phi_{ij_2} + \Phi_{ij_3} = -c_2\left(\mathcal{P}_{ij} + \tfrac{1}{2}\mathcal{R}_{ij} - \mathcal{P}_{kk}\delta_{ij}/3\right). \tag{4.72}$$

As remarked in §4.3.2, the coefficient c_2 is normally assigned the value 0.6, which satisfies the exact expression derived by Crow (1968) for isotropic turbulence. Note

[17] In fact, as Bertoglio *et al.* (1980) and Cousteix and Aupoix (1981) have pointed out, the approximation for the mean-strain and Coriolis parts of the pressure-strain correlation can also be obtained together, merely by replacing $\partial U_\ell/\partial x_m$ by $(\partial U_\ell/\partial x_m + \Omega_p \epsilon_{\ell pm})$. With the IP approximation for Φ_{ij_2}, that also leads to Eq. (4.72).

[18] Otherwise, in computing a flow like a swirling axisymmetric jet, which can be computed in either a stationary, axisymmetric frame or one that rotates at any speed about the axis, the computed behaviour would differ according to the rate at which one chose to rotate the axis.

that, because $\mathcal{R}_{kk}$ is zero, the form given automatically satisfies the requirement that the trace of Φ_{ij_3} should be zero. This form of the Basic Model, with the standard wall-reflection terms included, was used by Launder *et al.* (1987) to compute the velocity distributions shown in Fig. 4.21 and the variation of friction velocity on the two walls of the rotating continuous lines in Fig. 4.20. The computations assumed fully developed flow and used logarithmic 'wall functions' (see Chapter 8) to avoid having to enter the viscosity-affected near-wall sublayer. Figure 4.21 indicates that the asymmetry in the mean velocity distribution in the channel induced by the rotation is reasonably well captured by this simple model. Up to moderate rotation rates the computed friction velocities also accord well with the experimental data, including the asymmetric behaviour on the two surfaces, Fig. 4.21, right. At higher rotation rates, however, the computations fail to produce sufficient damping of the wall stress on the suction surface due, it is thought, to the fact that the flow close to that surface 'laminarizes' and the logarithmic wall law ceases to be appropriate. The treatment of such far-from-equilibrium nearâĂŘwall flows is the subject of Chapter 6. Indeed, further computations of the flow through a duct rotating in orthogonal mode are included there with early forms of the TCL model (Fig. 6.16) where computations extend all the way to the wall and only weak 'wall-proximity' terms are included. More recent computations by Manceau (2005) for a range of rotation numbers up to 1.5 using an elliptic second-moment closure ('elliptic blending model', EBM) are discussed in §6.5.3, Fig. 6.33.

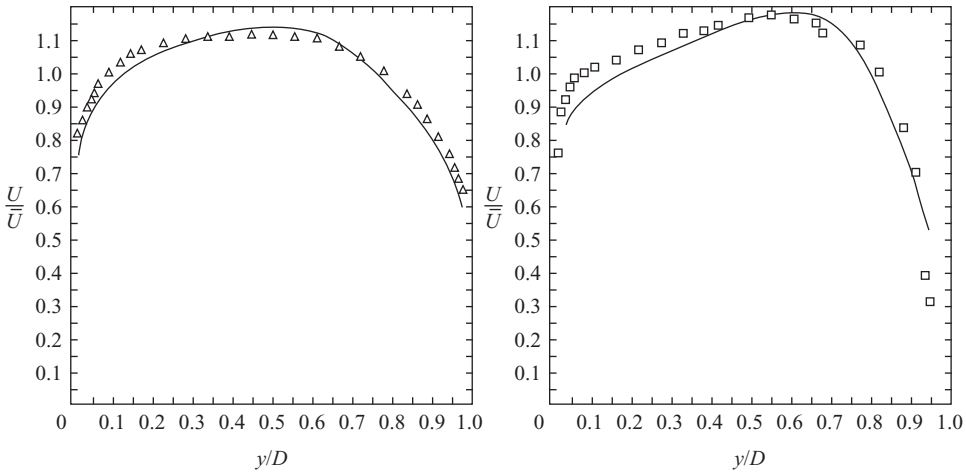

Fig. 4.21 Mean velocity profile in a rotating plane channel. Left, Ro = 0.068, Re = 35 000; right, Ro = 0.21, Re = 11 500. Symbols, experiment (Johnston *et al.*, 1972); line, computations, Basic Model. From Launder *et al.* (1987).

https://doi.org/10.1017/9781108875400.006 Published online by Cambridge University Press

4.5.3 Buoyant effects

Stress production due to buoyancy

For the case where the force field is that of buoyancy, the kinematic fluctuating force in the instantaneous velocity equation is given by:

$$f_i \equiv \rho' g_i / \rho. \tag{4.73}$$

Thus, with density fluctuations expressed in terms of temperature fluctuations, the force-field term in Eqs. (2.18) and (2.19) for the turbulent stress transport becomes:

$$\mathcal{F}_{ij} \equiv \mathcal{G}_{ij} \equiv \left(\overline{\rho' u_j} g_i + \overline{\rho' u_j} g_i\right) / \rho = -\beta \left(\overline{\theta u_j} g_i + \overline{\theta u_i} g_j\right) \tag{4.74}$$

where β denotes the expansion coefficient defined by

$$\beta \equiv -\frac{1}{\rho} \frac{\partial \rho}{\partial \Theta}\bigg|_P \tag{4.75}$$

where the P subscript simply indicates that the derivative with respect to temperature is at constant pressure. It is noted that for an ideal gas β is the reciprocal of the local mean (absolute) temperature.

The corresponding gravitational source in the scalar-flux equation, Eqs. (2.22) with (2.23), becomes:

$$\mathcal{G}_{i\theta} \equiv \overline{f_i \theta} = -\beta g_i \overline{\theta^2}. \tag{4.76}$$

Note that, just as the mean momentum equation is coupled to the mean temperature equation through the buoyant source, the Reynolds stress equation is likewise coupled with that for the turbulent heat flux. A complete second-moment closure thus entails solving an equation for $\overline{\theta^2}$ too which, from Eq. (4.76), appears as unknown in Eq. (2.22). The $\overline{\theta^2}$ equation contains no buoyant term, however, and remains in the form presented earlier, Eq. (3.20).

Before considering the modelling of buoyancy effects on the unknown terms in the foregoing equations, it is instructive to note the couplings among the different contributors to the equation set and the way their interaction changes depending upon the orientation of the flow. Figure 4.22 compares this intercoupling for a two-dimensional thin shear flow orientated horizontally and vertically. For both situations x_1 is the mean flow direction and x_2 the direction in which the mean velocity and density varies. The lines indicate coupling between the respective second moments, the arrows indicating that the second moment at the upstream end of any line contributes to generating the component at the downstream end.

It is clear that there is a great difference in the way stratification impacts the different second moments in the two cases. In a non-buoyant flow in simple shear, the normal stress $\overline{u_2^2}$ directed along the gradient of mean velocity and density has a great effect on the turbulent transport of momentum and matter. In a horizontal

https://doi.org/10.1017/9781108875400.006 Published online by Cambridge University Press

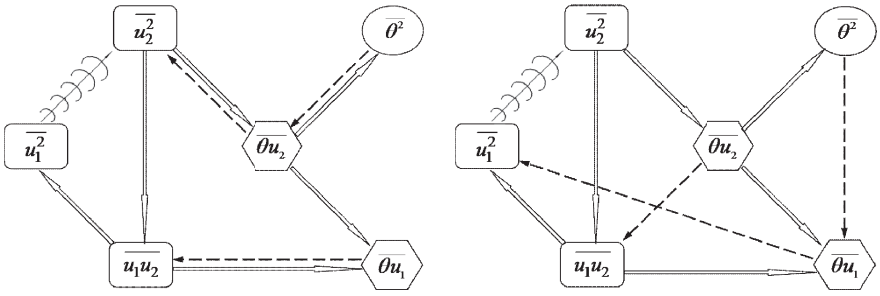

Fig. 4.22 Contrasting buoyant couplings among the second moments in horizontal (left) and vertical (right) two-dimensional thin shear flows. Broken arrows indicate buoyant coupling; full arrows denote coupling through mean velocity/scalar gradient; pressure-strain coupling is indicated symbolically by 'waves'.

stratified flow this normal-stress component is directly affected by buoyancy but in a vertical flow it is not since x_2 is then horizontal. Principally for that reason, horizontally directed shear flows require more careful attention to modelling buoyant effects than do vertical ones. Accordingly, the main attention in the remainder of this section is on the case of horizontally directed flows.

IP modelling of non-dispersive roles of pressure fluctuations

Let us turn first to modelling the pressure correlations. The IP strategy introduced in §4.3.2 would imply (Launder, 1975a):

$$\Phi_{ij_3} = -c_3 \left(\mathcal{G}_{ij} - \mathcal{G}_{kk}\delta_{ij}/3\right) \tag{4.77}$$

where now there is no strict need (as there was with a Coriolis force) to make the proportionality coefficient the same as for Φ_{ij_2}. Nevertheless, the value of c_3 has in practice usually been taken equal to or close to that of c_2 with values in the range 0.5–0.6.

In fact, another more analytical route may be followed that also leads to Eq. (4.77).

We note from Eq. (4.3) that:

$$\begin{aligned}\Phi_{ij_3} &\equiv -\frac{1}{4\pi}\overline{\int \left(\frac{\partial f_k}{\partial x_k}\right)' \left(\frac{\partial u_i}{\partial x_j} + \frac{\partial u_j}{\partial x_i}\right) \frac{dVol}{|r|}} \\ &= +\frac{g_k}{4\pi}\overline{\int \beta' \left(\frac{\partial \theta}{\partial x_k}\right)' \left(\frac{\partial u_i}{\partial x_j} + \frac{\partial u_j}{\partial x_i}\right) \frac{dVol}{|r|}}.\end{aligned} \tag{4.78}$$

As a first step to extracting a model, it is assumed that the mean temperature varies slowly over the two-point volumetric integral, thus β' is replaced by β and moved

https://doi.org/10.1017/9781108875400.006 Published online by Cambridge University Press

through the integral. Now, the integral

$$\frac{1}{4\pi}\int \overline{\left(\frac{\partial\theta}{\partial x_k}\right)'\left(\frac{\partial u_i}{\partial x_j}\right)}\frac{dVol}{|r|} \equiv a^i_{kj} \tag{4.79}$$

is of the same form as that considered in Eq. (4.49) for approximating $\Phi_{\theta i_2}$, though of only half its magnitude. Thus, with the assumption that the term can be expressed in terms of a sum of scalar fluxes and assuming the turbulence to be homogeneous, so that the form is symmetric in k and j,

$$a^i_{kj} = \lambda_1\overline{\theta u_i}\delta_{kj}+\lambda_2(\overline{\theta u_k}\delta_{ij} + \overline{\theta u_j}\delta_{ik}). \tag{4.80}$$

Contracting on i and j, the integrand in (4.79) clearly vanishes by continuity:

$$a^j_{kj} = 0 = (\lambda_1+4\lambda_2)\overline{\theta u_k}$$

while, for the limiting case of an isotropic turbulence field, with k equal to j, the integral is readily found from Green's theorem

$$a^i_{kk} = \overline{\theta u_i} = (3\lambda_1+2\lambda_2)\overline{\theta u_i}.$$

This pair of constraints implies $\lambda_1 = 0.4$, $\lambda_2 = -0.1$. Thus, from Eq. (4.80):

$$\Phi_{ij_3} = \beta\left[0.3(g_j\overline{\theta u_i} + g_i\overline{\theta u_j}) - 0.2g_k\overline{\theta u_k}\delta_{ij}\right] \tag{4.81}$$

or

$$\Phi_{ij_3} = -0.3\left(\mathcal{G}_{ij} - \mathcal{G}_{kk}\delta_{ij}/3\right). \tag{4.82}$$

Evidently, the above analysis produces a result (sometimes referred to as the quasi-isotropic result, QI) of the same form as the IP model, Eq. (4.77), but with a coefficient only about one-half the (empirical) value usually employed by the latter.

Proceeding analogously for the corresponding pressure-temperature gradient product in the heat-flux equation, Eq. (2.22), the IP model would lead to:

$$\Phi_{\theta i_3} = -c_{3\theta}\mathcal{G}_{\theta i} = +c_{3\theta}\beta g_i\overline{\theta^2}. \tag{4.83}$$

The coefficient $c_{3\theta}$ is normally assigned the same value as $c_{2\theta}$ of about 0.5 (Launder, 1975a). However, following the quasi-isotropic route, as was done above forΦ_{ij_3}, leads to the same form as Eq. (4.83) but with a coefficient equal to 1/3 (Launder, 1975b; Lumley, 1975a). Nevertheless, most computations have adopted the assumption that $c_{3\theta}$, like c_3, is approximately equal to 0.5. As an illustration, Fig. 4.23 shows the application of such a model to the case of the nominally homogeneous, stably stratified, free shear flows measured by Webster (1964). The strength of the stratification is expressed in terms of the Richardson number. The flux Richardson number, R_f, is the ratio of the rate of removal of turbulence energy by working against gravity to that supplied by mean-strain action; the gradient

https://doi.org/10.1017/9781108875400.006 Published online by Cambridge University Press

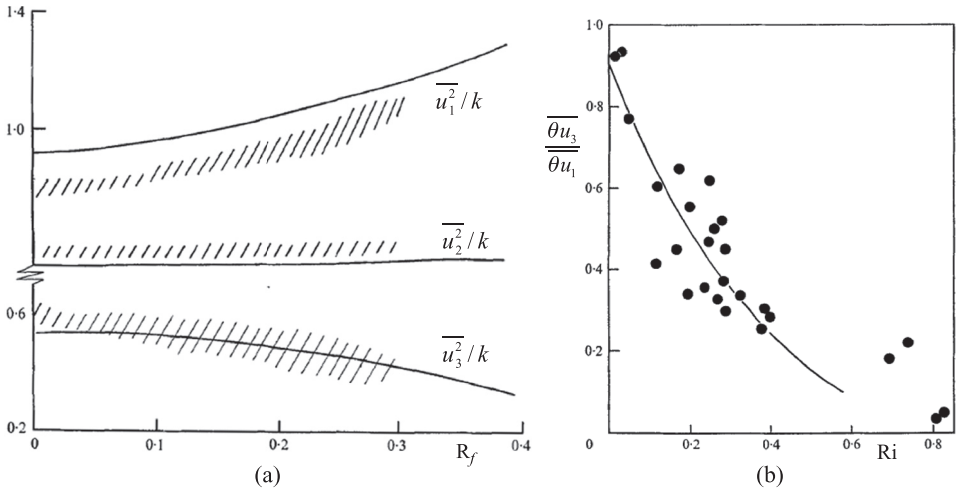

Fig. 4.23 Normal stresses and heat fluxes in stable stratification. (a) Relative normal stress levels as a function of flux Richardson number. (b) Variation of vertical to streamwise heat flux with gradient Richardson number. Symbols/shading, experiments (Webster, 1964); lines, computations. From Launder (1975a). Note: x_1 denotes the main flow direction (horizontal); x_3 vertical.

Richardson number, Ri, is the product of R_f and σ_Θ. In the computations it was assumed that the dissipation rate of turbulence energy balanced production by shear and stratification (the latter, of course, being negative under stable stratification). The left figure shows that, as the stable stratification gets stronger, the proportion of fluctuating energy in the vertical direction decreases while that in the stream direction increases, a feature that is well captured by the model. So far as the heat fluxes are concerned, vertical transport is very severely reduced relative to the streamwise heat flux with increasing stable stratification. This feature too is reasonably well mimicked by the IP model.

For forced-convection flows near walls, as was noted in §4.3.4, in using the IP model it is essential to include some wall-reflection strategy in order that the normal stress perpendicular to the wall is damped sufficiently. However, this correction has usually not been applied to Φ_{ij_3}. This is because, at a practical level, better overall agreement was achieved by omitting such buoyant wall corrections than including them. In turn this may suggest that Eq. (4.82) is a better model of Φ_{ij_3} than Eq. (4.9) is of Φ_{ij_2}. The IP model has been applied by Gibson and Launder (1978) to examine various near-ground features of the atmospheric boundary layer assuming local-equilibrium conditions. Figure 4.24, left, compares the predicted variation of the rms vertical velocity fluctuations under unstable conditions with the experimental data of Wyngaard *et al.* (1971) where x_3 is the height above the ground and L is the Obukhov length defined as $L \equiv -U_\tau^3/\kappa\beta g\overline{\theta u_3}$, κ being

https://doi.org/10.1017/9781108875400.006 Published online by Cambridge University Press

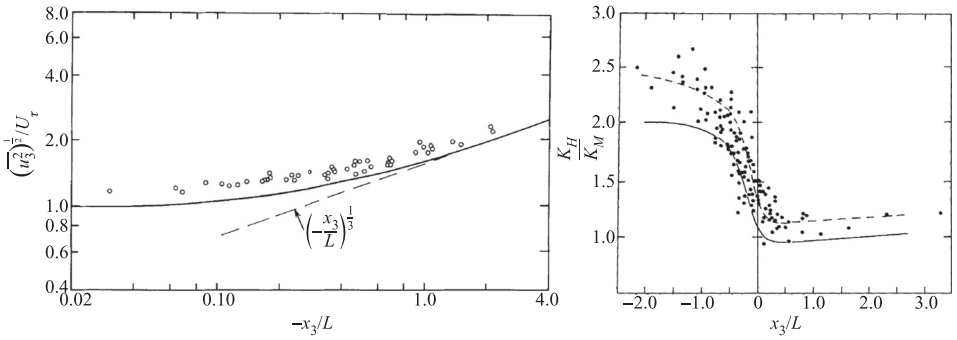

Fig. 4.24 Left: measured and predicted rms vertical velocity fluctuations under unstable conditions (atmospheric boundary layer data of Wyngaard *et al.* (1971). Right: measured and predicted dependence on stability of the ratio of the exchange coefficients (atmospheric boundary layer data of Businger *et al.* (1971). From Gibson and Launder (1978) using the Basic Model.

the von Karman constant and U_τ the friction velocity. The corresponding ratio of the diffusivities for heat and momentum (the inverse of the turbulent Prandtl number, σ_Θ) from the data of Businger *et al.* (1971) appears in Fig. 4.24, right. For both cases the agreement of the model with the experimental data is broadly satisfactory given the doubt as to how close the data were to the presumed local-equilibrium state. In fact, in Fig. 4.24, right, the broken line shows predicted values that have been increased by 20% to bring the data for neutral buoyancy into accord with the non-buoyant flow data. The implied dependence of turbulent Prandtl number on stability is quite different from that found for the homogeneous *free* shear flow where the turbulent Prandtl number increases monotonically with Richardson number (Webster, 1964). It has been suggested that the different qualitative behaviour in the wall boundary layer is linked to the fact that, in increasingly stable conditions, the turbulent length scale normal to the ground is reduced, thereby reducing wall-reflection effects (Gibson and Launder, 1978).

McGuirk and Papadimitriou (1988) have applied the IP model to examine the development of several of the free-surface, stably stratified jets measured by Chu and Baddour (1984). Figure 4.9, shown earlier in relation to 'wall-reflection' from the free surface, gives the computed normalized density profiles reproduced from their work for a case without a hydraulic jump for an initial Froude number, Fr, of 12 (Fr $\equiv U_{in}/\sqrt{gH}$, where U_{in} is the inlet velocity and H the height of the inlet slot).

TCL approach to modelling Φ_{ij_3} and $\Phi_{\theta j_3}$

Just as with Φ_{ij_2} and $\Phi_{\theta j_2}$, TCL constraints have been applied to the buoyant parts of the non-dispersive pressure correlations in order to obtain a more comprehensive model. These analyses have been presented in Craft (1991), Craft *et al.* (1996a) and

https://doi.org/10.1017/9781108875400.006 Published online by Cambridge University Press

Craft and Launder (2002a). As noted in connection with Eq. (4.79), to obtain the TCL form for Φ_{ij_3} it suffices to note that the two-point integrand appearing in that equation is the same as appeared in the corresponding model for $\Phi_{\theta j_2}$. Thus the resultant form for the integral in that analysis may be taken over to obtain (after considerable algebra) Φ_{ij_3}, just as was done above for the 'quasi-isotropic' analysis that led to Eq. (4.82). The resultant form can be written as:

$$\begin{aligned}\Phi_{ij_3} = &-\left(\frac{3}{10}+\frac{3A_2}{80}\right)\left(\mathcal{G}_{ij}-\tfrac{1}{3}\delta_{ij}\mathcal{G}_{kk}\right)+\frac{1}{6}a_{ij}\mathcal{G}_{kk}\\ &+\frac{2}{15}\overline{\theta u_m}\left[\beta_i a_{mj}+\beta_j a_{mi}\right]-\frac{1}{3}\beta_k\left[a_{ik}\overline{\theta u_j}+a_{jk}\overline{\theta u_i}\right]\\ &+\frac{1}{10}\delta_{ij}\beta_k a_{mk}\overline{\theta u_m}+\frac{1}{4}\beta_k a_{ij}a_{mk}\overline{\theta u_m}\\ &+\frac{\beta_k}{8}\left\{\overline{\theta u_m}\left[a_{ki}a_{mj}+a_{kj}a_{mi}\right]-a_{mk}\left[a_{mj}\overline{\theta u_i}+a_{mi}\overline{\theta u_j}\right]\right\}\\ &-\frac{3}{40}\left\{a_{mk}\overline{\theta u_k}(\beta_i a_{mj}+\beta_j a_{mi})-\frac{2}{3}\delta_{ij}\beta_k a_{mk}a_{mn}\overline{\theta u_n}\right\}. \end{aligned} \tag{4.84}$$

In the above, the vector β_i denotes for brevity the group βg_i. It is clear that for isotropic turbulence the quasi-isotropic result is recovered since the anisotropic stress tensor, a_{ij}, is then zero in all components.

The corresponding TCL approximation for $\Phi_{\theta i_3}$ is much simpler and its derivation is thus summarized below. To begin, let us rewrite this as:

$$\Phi_{\theta i_3} = \beta_k b_{ki} \tag{4.85}$$

where

$$b_{ki} \equiv \frac{1}{4\pi}\int \overline{\frac{\partial\theta'}{\partial x'_k}\frac{\partial\theta}{\partial x_i}}\frac{dVol}{r} = -\frac{1}{4\pi}\int \frac{\partial^2\overline{\theta'\theta}}{\partial r_k \partial r_i}\frac{dVol}{r}. \tag{4.86}$$

To devise an approximation for b_{ki} consistent with that obtained for the other two-point correlations, it is supposed that:

$$b_{ki} = \overline{\theta^2}(\alpha_1\delta_{ki}+\alpha_2 a_{ki}+\alpha_3 a_{mn}a_{mn}\delta_{ki}+\alpha_4 a_{km}a_{im}) \tag{4.87}$$

where the α coefficients are constants to be determined below. This is the most general form for a model at the same level as earlier TCL contributions. Now, on contracting Eq. (4.86) for $i = k$ one can carry out the integral for a radially symmetric two-point correlation to conclude that $b_{kk} = \overline{\theta^2}$ and hence:

$$\alpha_1 = 1/3, \quad 3\alpha_3 + \alpha_4 = 0.$$

Then, on imposing the TCL requirement that if, say, $\overline{u_2^2}$ should fall to zero,

$$\mathcal{G}_{\theta 2} + \Phi_{\theta 2_3} = 0,$$

https://doi.org/10.1017/9781108875400.006 Published online by Cambridge University Press

Table 4.6 *Rate of growth of half-widths of jets and plumes in stagnant surroundings from Craft et al. (1996a)*

Flow	IP model	Experiment	TCL model
Plane plume	0.078	0.120	0.118
Axisymmetric plume	0.088	0.112	0.122
Plane jet	0.100	0.110	0.110
Axisymmetric jet	0.105	0.095	0.101

one concludes that $\alpha_2 = -1,\ \alpha_3 = \alpha_4 = 0$ and thus, finally, that:

$$\Phi_{\theta i_3}. = \tfrac{1}{3}\beta_i\overline{\theta^2} - \beta_k\overline{\theta^2}a_{ik}. \tag{4.88}$$

It is noted that the TCL result differs from the QI model only by the appearance of the second term on the right of Eq. (4.88).

Applications of the TCL models above have been discussed in Craft and Launder (2002a) for a range of buoyantly modified shear flows. For the supposedly homogeneous, stably stratified shear layer in local equilibrium, the performance is of similar overall quality to the IP model and is not included here. The predicted and measured behaviour for the inhomogeneous, buoyantly driven, self-preserving plane and axisymmetric plumes are compared with the corresponding dynamically driven jets in Table 4.6. Agreement across the flows is far superior with the TCL version than with the IP model. While some of the improvement shown in Table 4.6 is attributable to the modified form of dissipation rate equation used with the TCL version (cf. Eq. (5.10) and with adopting $c_{\varepsilon 1} = 1.0$), a large proportion arises from the more comprehensive modelling of pressure interactions. Even though the TCL model predicts growth rates for both axisymmetric flows to be somewhat too large, the fact that a similar percentage error arises for each suggests that the cause of this fairly modest discrepancy may be attributable to some other feature of axisymmetric flows in stagnant surroundings, such as intermittency, which is disregarded in steady-state RANS closures. Intermittency is also present, of course, in plane free shear flows but it is more important in axisymmetric flows where a much larger proportion of the shear flow's cross-section is 'contaminated' by its effects.

A further test case computed with both the TCL and the Basic Model is the negatively buoyant wall jet illustrated in Fig. 4.25a: a downward directed jet of warm water is injected parallel to the wall into a slowly upward moving cool stream, causing the wall jet to break away from the wall, reversing its direction. The goal is to measure the depth of penetration of the wall jet and its subsequent mixing. This has proved to be a sensitive test case for the turbulent field, with regard to both how the sublayer is handled and the turbulence model for the fully turbulent

https://doi.org/10.1017/9781108875400.006 Published online by Cambridge University Press

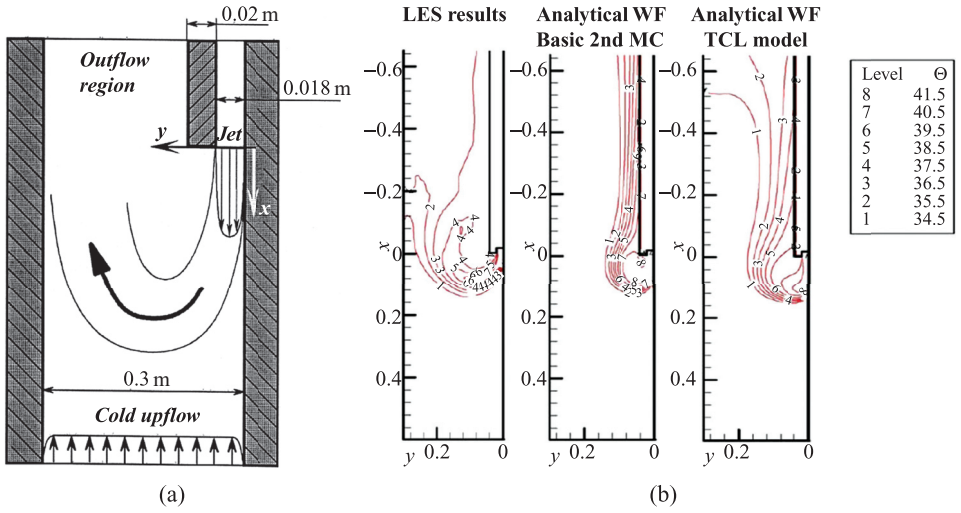

Fig. 4.25 Temperature contours for the negatively buoyant wall jet, comparison of different models: (a) flow configuration, (b) RANS computations, Craft *et al.* (2004b); LES data from Addad *et al.* (2004).

flow beyond. Figure 4.25b compares RANS predictions adopting the TCL and Basic Model approaches (Craft *et al.*, 2004b). In both cases the more successful of the sublayer treatments is used (the 'AWF scheme') for which details are given in Chapter 8. Comparison is drawn with the LES of this flow by Addad *et al.* (2004) (which is in close agreement with the far less detailed experimental data of Jackson *et al.*, 2002). While neither scheme captures fully the level of mixing exhibited by the LES results, the TCL model clearly achieves the better performance. Other buoyancy-affected test cases examining the performance of the TCL scheme are reported in Craft and Launder (2002a) and Launder (2005).

A further challenging test case, the horizontal salinity-stratified mixing layer region, is presented in §4.6 in which the modelling of the triple moments is considered. The reason for postponing discussion until then is that, in this strongly stably stratified flow, accounting for second-moment diffusion processes turns out to be just as vital as the choice of second-moment pressure-containing correlations.

Double scalar fields

Finally, attention is turned briefly to the case where simultaneous salinity and thermal gradients combine in the presence of a gravitational field to exert important effects in modifying the diffusive transport. Such double-diffusive systems arise not only in the external environment as in the oceans, salty lakes, solar ponds and diurnal heating in the near-ground-level atmosphere (examples of the last of these

https://doi.org/10.1017/9781108875400.006 Published online by Cambridge University Press

are examined in Chapter 9) but also in engineering problems such as metal solidification, crystal growth and heavy-gas storage. The density fluctuations can then be expressed as:

$$\rho' = -\beta\theta + \gamma s \tag{4.89}$$

where $\beta \equiv -1/\rho(\partial\rho/\partial\Theta)|_{P,S}$ and $\gamma \equiv 1/\rho(\partial\rho/\partial S)|_{P,\Theta}$ are the volume expansion coefficients caused by unit temperature and concentration changes, respectively (defined with opposite signs because the density will generally increase with a decrease in temperature but with an increase in concentration). A feature of double-diffusive systems that poses a severe challenge to turbulence modelling is the frequently encountered opposing action of the two scalar fields on turbulence. In most situations, the species concentration *increases* in the direction of the gravitational or centrifugal force, i.e. a *stable* salinity stratification, which damps the turbulence. Thus, if the fluid is heated from below or cooled from above (e.g. night cooling of a lake or ocean surface due to radiation to space), the temperature gradient creates an unstable stratification that generates turbulence. This in turn will cause vertical mixing within a region, known as the mixed layer, in which all flow properties take very nearly uniform values. Thus, the transport of heat and species is not driven by (nor can it be related to) the temperature or concentration gradients. Moreover, the opposing effects of the two scalar fields on turbulence are not independent of one another; on the contrary, there is a strong coupling and interaction between them. Consequently, the most appropriate closure within RANS for such problems is at second-moment level, which implies modelling and solving the transport equation (2.22) for both heat and salinity flux. It is noted, however, that the two equations are interconnected through the correlation of the fluctuations in the two scalars, $\overline{\theta s}$, associated with the gravity vector, which appears in both equations (term $\mathcal{F}_{\theta i}$), i.e.

$$\frac{D\overline{\theta u_i}}{Dt} = \cdots\left(-\beta g_i\overline{\theta^2} + \gamma g_i\overline{\theta s}\right) + \cdots, \quad \frac{D\overline{s u_i}}{Dt} = \cdots\left(-\beta g_i\overline{\theta s} + \gamma g_i\overline{s^2}\right) + \cdots \tag{4.90}$$

Thus, closure of Eq. (4.90) requires providing $\overline{\theta^2}$, $\overline{s^2}$ and $\overline{\theta s}$ from separate transport equations, which in turn contain scalar fluxes, e.g.

$$\frac{D\overline{\theta s}}{Dt} = -\overline{s u_j}\frac{\partial\Theta}{\partial x_j} - \overline{\theta u_j}\frac{\partial S}{\partial x_j} - \varepsilon_{\theta s} + \mathcal{D}_{\theta s}. \tag{4.91}$$

Hence, a complete second-moment closure to a double-diffusive system involves a large number of equations to be solved. In practice, however, one-dimensional diffusion problems are the most challenging so far as physical modelling is concerned and for such systems the scale of the numerical task is reasonable. Armitage (2001) (see also Armitage *et al.*, 1998) has considered this problem using both

https://doi.org/10.1017/9781108875400.006 Published online by Cambridge University Press

the Basic and TCL models and throughout making the GGDH approximation for second-moment diffusion. In her computations the dissipative term in Eq. (4.91) was, following Hanjalić and Musemic (1997), approximated as

$$\varepsilon_{\theta s} = \frac{\varepsilon \overline{\theta s}}{k} \tag{4.92}$$

which implicitly assumes equality of the scalar and mechanical time scales.

Figure 4.26 shows the profiles of temperature at two time instants across the mixed layer for an initially linear vertical decrease in salinity with uniform initial temperature, subjected at time zero to strong bottom heating. Both Basic and TCL models certainly capture a mixed-layer type of temperature profile and, for the TCL model, agreement with the measurements of Bergman *et al.* (1985) is close. Hanjalić and Musemić (1997) have applied a simplified algebraic truncation to examine a wider range of test flows, including cases where the unstable thermal stratification is less strong (which pose a greater challenge than the strong stratification considered above). A sample of those results appears in Chapter 7.

An alternative approach to modelling unstably stratified turbulent flows is provided by the unsteady Reynolds-averaging strategy, URANS. It has been argued that in flows with strong internal forcing, where the large-scale convective structures dominate the flow and the 'stochastic' turbulence can be treated as almost a passive scalar, major flow parameters can be reproduced by way of such an approach using a relatively simple turbulence model. Indeed, Kenjereš and Hanjalić (2002) found that the important prerequisite is to apply a well-tuned RANS

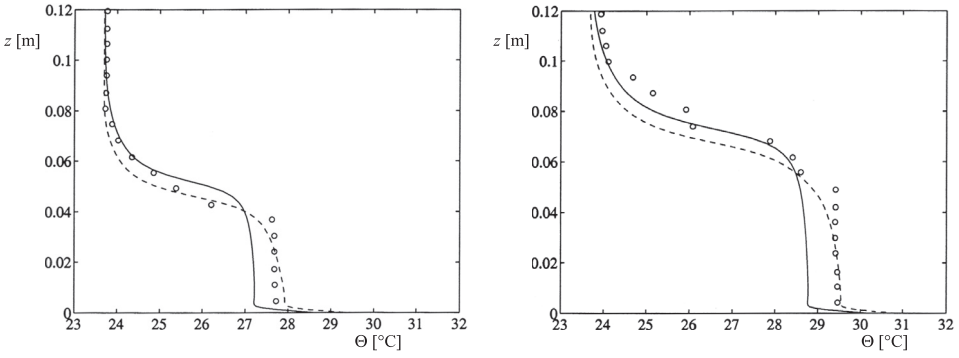

Fig. 4.26 Profiles of temperature at two time instants across the mixed layer for an initially linear vertical decrease in salinity and uniform initial temperature subject to strong bottom heating at $t = 0$: (a) $t = 30$ min; (b) $t = 60$ min. Experiments, ○, Bergman *et al.* (1985); computations, ——— Basic model, – – – – – TCL model. From Armitage (2001).

https://doi.org/10.1017/9781108875400.006 Published online by Cambridge University Press

model for the near-wall region, and this can be done (at least for the flows over horizontal heated walls) with a model simpler than full second-moment closure, since the large-scale convective transport is resolved in time and space. An account of that approach and a selection of the results obtained is also provided in Chapter 9.

4.5.4 Electromagnetic force fields

If a moving electrically conductive fluid is subjected to a magnetic field having a flux density **B**, the velocity and magnetic fields will interact. As a result, in the general case both fields will be modified. The relative movement of the two fields will generate an electromagnetic force (emf) which drives an electric current with density in space equal to $\sigma \mathbf{U} \times \mathbf{B}$, where σ is the electric conductivity of the fluid and **U** is the velocity vector.[19] This induced current generates a second, *induced* magnetic field which adds to and modifies the original magnetic field. Moreover, the combined (imposed and induced) magnetic field interacts with the induced current density, generating a Lorentz force (per unit volume) $\mathbf{F}^L = \mathbf{J} \times \mathbf{B}$ which modifies the velocity field. Here **J** denotes the total electric current density, which, from Ohm's law for moving media, can be written as $\mathbf{J} = \sigma(\mathbf{E} + \mathbf{U} \times \mathbf{B})$, where **E** is the electric field. The term in brackets is the effective electric field 'felt' by the fluid in a reference frame moving with the fluid. The Lorentz force per unit volume can now be defined as $\mathbf{F}^L = \sigma(\mathbf{E} + \mathbf{U} \times \mathbf{B}) \times \mathbf{B}$ or, as is often more convenient, in terms of the electric potential, Φ, as $\mathbf{F}^L = \sigma(-\nabla\Phi + \mathbf{U} \times \mathbf{B}) \times \mathbf{B}$ (for more details, see Moreau, 1990; Davidson, 2004).

It is immediately evident that the second term, involving a double vector product with **B** appearing twice, is aligned with the fluid velocity vector **U**, but acting in the opposite direction. This means that the second term (which is often dominant in magnetohydrodynamic (MHD) problems) acts to diminish the velocity in the direction of the Lorentz force. This feature has been widely utilized in applying a magnetic field to control flow and heat transfer by suppressing the fluid motion and turbulence in the desired direction.

Switching to the more convenient index notation for turbulent flows described in Cartesian coordinates and using the identity $\epsilon_{ijk}\epsilon_{lmk} \equiv \delta_{il}\delta_{jm} - \delta_{im}\delta_{jl}$, the instantaneous Lorentz force can be written as

$$\hat{F}_i^L = \sigma(-\epsilon_{ijk}\hat{E}_j\hat{B}_k + \hat{U}_k\hat{B}_i\hat{B}_k - \hat{U}_i\hat{B}_k\hat{B}_k) \tag{4.93}$$

where, in general, all variables may fluctuate in time and space.

The Reynolds decomposition and averaging of Eq. (4.93) for RANS applications will result in a large number of terms (originating from triple products) involving the velocity and magnetic-field fluctuations. However, cases in which

[19] As appropriate for general vector fields and customary in the theory of electromagnetism, the direct (vector) notation will be used briefly in introducing the subject.

https://doi.org/10.1017/9781108875400.006 Published online by Cambridge University Press

both fields fluctuate and exert influence on each other are encountered only in very large-scale systems of interest within geophysics and astrophysics, such as planets, stars and galaxies. For such situations, the momentum equations (with the Lorentz force accounting for the magnetic effects on the velocity field) need to be solved simultaneously with the magnetic induction equation for the magnetic flux, B_k, which contains the fluid velocity and its gradients (see e.g. Kenjereš *et al.*, 2006b; Kenjereš and Hanjalić, 2007). In industrial applications of MHD, such as electromagnetic control of flow and heat transfer in metallurgy and materials technologies (e.g. crystal growth, magnetic-brake stabilization of continuous metal casting), as well as in MHD generators, pumps or propulsion units, the far greater effect is that of the Lorentz force on the fluid flow, whereas the feedback into the magnetic field can usually be neglected. The parameter which identifies whether this is justified or not is the magnetic Reynolds number $\mathrm{Re}_M \equiv \mu_0 \sigma U L$, where μ_0 is the magnetic permeability of the free space and $1/(\mu_0\sigma)$ is known as the magnetic diffusivity. In industrial MHD, where liquid metals are the fluid media, flow velocities and dimensions are relatively small (compared with those in geophysics and astrophysics); hence, even for highly conductive fluids, Re_M is of order unity or less. This permits the neglect not only of any fluctuations in the magnetic field, but also of the feedback of the velocity into the magnetic field.

The Lorentz force in the averaged momentum equation will then have the same form as Eq. (4.93) but involving only the averaged velocity and magnetic flux, U_i and B_j. The contribution of the magnetic field to turbulence appearing through the Lorentz-force fluctuation is

$$f_i^L = \sigma(\epsilon_{ijk} e_j B_k + u_k B_i B_k - u_i B_k^2) \tag{4.94}$$

where, just as for the mean field, the electric-field fluctuation can be expressed in terms of the gradient of the fluctuating electric potential, $e_j \equiv -\partial\phi/\partial x_j$.

Even when confining attention to one-way coupling (i.e. considering only the Lorentz force effects and not the velocity feedback into the magnetic field, as appropriate for low magnetic Reynolds number), accounting for the magnetic field in closing the stress-transport equation, Eq. (2.17), requires several processes to be modelled, as discussed below.

Magnetic contribution to the stress generation

Using the expression for the Lorentz force fluctuations, Eq. (4.94), the body-force production term in the transport equation for the turbulent stress tensor, Eq. (2.18), $\mathcal{M}_{ij} = \left(\overline{f_i^L u_j} + \overline{f_j^L u_i}\right) \Big/ \rho$ can be written as:

$$\mathcal{F}_{ij} \equiv \mathcal{M}_{ij} = \frac{\sigma}{\rho} \underbrace{\left(\epsilon_{imn} B_n \overline{e_m u_j} + \epsilon_{jmn} B_n \overline{e_m u_i}\right)}_{\mathcal{M}_{ij_1}} + \underbrace{B_i B_n \overline{u_j u_n} + B_j B_n \overline{u_i u_n} - 2 B_n B_n \overline{u_i u_j}}_{\mathcal{M}_{ij_2}} . \tag{4.95}$$

https://doi.org/10.1017/9781108875400.006 Published online by Cambridge University Press

Table 4.7 *Contribution of magnetic production to the components of the stress tensor in a plane channel flow of an electrically conducting fluid, subjected to a uniform transverse magnetic flux*

	$\overline{u_1^2}$	$\overline{u_2^2}$	$\overline{u_3^2}$	$\overline{u_1 u_2}$
$\mathcal{M}_{ij_1}$	$-2B_2\overline{u_1 e_3}$	0	$+2B_2\overline{u_3 e_1}$	$-B_2\overline{u_2 e_3}$
$\mathcal{M}_{ij_2}$	$-B_2^2\overline{u_1^2}$	0	$-B_2^2\overline{u_3^2}$	$-B_2^2\overline{u_1 u_2}$

The importance of magnetic stress production compared with other terms can be assessed by transforming the stress-transport equation (2.18) to non-dimensional form using the characteristic length, velocity and magnetic flux scales, $\mathcal{L}, \mathcal{U}$ and $\mathcal{B}$, respectively. Just as the non-dimensional viscous diffusion term will contain (1/Re), permitting its order of magnitude to be evaluated, so the non-dimensional magnetic production term $\mathcal{M}_{ij}$ will appear multiplied by the so-called Stuart number (also known as the *interaction parameter*), $N \equiv \sigma \mathcal{B}^2 \mathcal{L} \big/ (\rho_0 U)$, which represents the ratio of the Lorentz and inertial forces. Its physical meaning becomes clearer by noting that $N \equiv \mathrm{Ha}^2/\mathrm{Re}$, where $\mathrm{Ha} \equiv \mathcal{B}\mathcal{L}\sqrt{\left(\sigma \big/ \rho_0 \nu\right)}$ is the Hartmann number (the ratio of the Lorentz and viscous forces) and Re is the flow Reynolds number. Thus, the importance of the magnetic stress production $\mathcal{M}_{ij}$ will depend on the value of the Stuart number or, more precisely, on the ratio of the magnetic field intensity defined by the Hartman number, and the inertial forces represented by the Reynolds number.

Returning now to the contents of $\mathcal{M}_{ij}$, it is noted that the terms in brackets form two groups. Clearly, the second term, $\mathcal{M}_{ij_2}$, requires no modelling and, for a given (imposed) magnetic flux B_i, it can be retained in its exact form using the available stress components. However, the term $\mathcal{M}_{ij_1}$ involving correlations between fluctuations in the electric field and velocity, $\overline{e_i u_j}$, requires approximation. But, before considering possible modelling options, let us examine the effects of both terms, $\mathcal{M}_{ij_1}$ and $\mathcal{M}_{ij_2}$, for the case of a plane-channel flow in the x_1 direction, subjected to a uniform transverse (wall-normal) magnetic field $B_i = (0, B_2, 0)$. The contributions of $\mathcal{M}_{ij_1}$ and $\mathcal{M}_{ij_2}$ to the stress production, as follows from Eq. (4.95), are summarized in Table 4.7. These show that the Lorentz force has no effect on the stress component aligned with the magnetic flux. In contrast, the other two normal stress components *are* affected, as is also the shear stress. It is interesting to note that $\mathcal{M}_{ij_2}$ appears with a negative sign for all components, whereas $\mathcal{M}_{ij_1}$ takes opposite signs in the equations for $\overline{u_1^2}$ and $\overline{u_3^2}$, the implications of which will be discussed below.

https://doi.org/10.1017/9781108875400.006 Published online by Cambridge University Press

Further insight into the nature of the contribution of the exact term $\mathcal{M}_{ij_2}$ can be gained by identifying the stress component aligned with the uniform magnetic flux vector (here denoted as $\overline{u_B^2}$), and rearranging the terms (Naot *et al.*, 1990):

$$\mathcal{M}_{ij_2} = \frac{\sigma}{\rho}\Bigg[\underbrace{-\frac{2}{3}B_k^2\left(2k-\overline{u_B^2}\right)\delta_{ij}}_{\mathcal{M}'_{ij_2}}\underbrace{-2B_k^2\left(\overline{u_iu_j}-\frac{2}{3}k\delta_{ij}\right)}_{\mathcal{M}''_{ij_2}} \underbrace{+\left(B_jB_k\overline{u_iu_k}+B_iB_k\overline{u_ju_k}-\frac{2}{3}B_k^2\overline{u_B^2}\delta_{ij}\right)\Bigg]}_{\mathcal{M}'''_{ij_2}}. \tag{4.96}$$

Since $\overline{u_B^2}$ is unaffected by the Lorentz force, the first term, $\mathcal{M}'_{ij_2}$, represents the decay of turbulent kinetic energy (in fact the decay of the two normal-stress components other than $\overline{u_B^2}$), forcing turbulence towards the one-component limit (see §3.7.2). The other two terms are redistributive and have zero trace. Through the first of these, $\mathcal{M}''_{ij_2}$, the magnetic field acts to make the stress field more isotropic, whereas the second term, $\mathcal{M}'''_{ij_2}$, redistributes the stress components with respect to the direction of the magnetic flux vector.

Turning now to $\mathcal{M}_{ij_1}$, the challenge is in providing a model for the velocity–electric-field correlation $\overline{u_ie_j} = -\overline{u_i\partial\varphi/\partial x_j}$. A closure consistent with the second-moment approach would require the modelling and solution of a transport equation for $\overline{u_ie_j}$. This equation can easily be derived following the same steps as in deriving Eq. (2.18) for the stress tensor (i.e. by multiplying Eq. (2.17) for the u_i velocity fluctuation by e_j and averaging, and then adding the same equations with the indices i and j interchanged). Unfortunately, very little is known about the behaviour of $\overline{u_ie_j}$ and of the terms appearing in its transport equation. Naot *et al.* (1990) argued that for the lowest order interactions (very low Re_M) as a first approximation the term $\mathcal{M}_{ij_1}$ involving $\overline{u_ie_j}$ correlations can be neglected. Kenjeres *et al.* (2004) estimated the order of magnitude of different terms in the $\overline{u_ie_j}$ equation for a low Re_M and, after severe pruning, proposed the following first approximation:

$$-\overline{u_ie_j} = \overline{u_i\frac{\partial\varphi}{\partial x_j}} = c_M\epsilon_{jkl}B_l\overline{u_iu_k} \tag{4.97}$$

where c_M is an empirical coefficient. The approximation on the right-hand side of Eq. (4.97) has the same form as the terms in $\mathcal{M}_{ij_2}$, and can be regarded as a correction to this term if the induced electric field fluctuation is appreciable. Indeed, this would imply that the electric field in the fluctuating Lorentz force, $\mathbf{f}^L = \sigma(\mathbf{e}+\mathbf{u}\times\mathbf{B})\times\mathbf{B}$, is assumed to originate from the current induced by the velocity and magnetic field interactions, $\mathbf{e}\propto\mathbf{u}\times\mathbf{B}$, i.e. $e_j\propto\epsilon_{jkl}u_kB_l$.

https://doi.org/10.1017/9781108875400.006 Published online by Cambridge University Press

Kenjeres *et al.* (2004) arrived at $c_M = 0.6$ from an *a priori* evaluation of the total magnetic contribution, $\mathcal{M}_{ij}$, to the budget of the normal stress components using the DNS database of Noguchi *et al.* (1998) for a plane channel subjected to two different magnetic fields.[20]

Magnetic effects in the pressure-strain correlation Φ_{ij_3}

Inserting the fluctuating Lorentz force, Eq. (4.94), into the Φ_{ij_3} term in Eq. (4.3) provides some indication of the effects of the magnetic field on the total pressure-strain correlation. However, just as in the case of other body forces and, indeed, the mean rate of strain contribution, a formal integration of the two-point integral has not proved to be a practical route forward. Closure proposals have thus adopted tensorial expansions of greater or (more usually) lesser rigour, analogous to the approximations made for other force fields (though no TCL analysis for the present case seems to have been reported). It is noted, nevertheless, that the first proposal for Φ_{ij_3} originated from an exact spectral analysis analogous to that of Crow (1968) for Φ_{ij_2}. Schumann (1976) reported the numerical simulation of initially three-dimensional, isotropic turbulence that evolves to a two-dimensional state when subjected to a uniform magnetic field. He thus arrived at an IP model for the magnetic correction to the pressure-strain term. Although the derivation was performed in spectral space for homogeneous anisotropic turbulence, Schumann argued that the expression should be valid over all wave numbers (and thus applicable also to one-point closures like RANS) and that the form (and, indeed, the coefficient, 0.6) was the same as for other (shear and buoyancy induced) contributions to the pressure-strain process.

Aiming at more general, inhomogeneous flow configurations, Naot *et al.* (1990) followed the route applied earlier for the mean-strain contribution, Φ_{ij_2}, and arrived at a magnetic-field analogue of the hydrodynamic quasi-isotropic (QI) model (Naot *et al.*, 1973) discussed in §4.4.4.

Kenjeres *et al.* (2004) focused on wall-bounded flows and, just as in the Basic Model for the pressure-strain term, adopted the simple IP model

$$\Phi^L_{ij_3} = -c^L_3 \left(\mathcal{M}_{ij} - \mathcal{M}_{kk}\delta_{ij}/3\right) \tag{4.98}$$

complemented by a wall-correction analogue of the Gibson and Launder (1978) expression (4.14)

$$\Phi^{L,w}_{ij_3} = c^L_{3w}\left[\Phi^L_{km_3} n_k n_m \delta_{ij} - \tfrac{3}{2}\left(\Phi^L_{ik_3} n_k n_j + \Phi^L_{jk_3} n_k n_i\right)\right] \frac{k^{3/2}}{\varepsilon x_n}. \tag{4.99}$$

[20] A plane channel flow at $\mathrm{Re}_\tau = 150$ subjected to a transverse and a longitudinal magnetic flux (both uniform), characterized, respectively, by $\mathrm{Ha} = 6$ and $\mathrm{Ha} = 20$.

https://doi.org/10.1017/9781108875400.006 Published online by Cambridge University Press

The model coefficients, allowed to be variable, were evaluated with reference to the above-mentioned DNS data of Noguchi *et al.* (1998). For that purpose an algebraic version of the second-moment closure (obtained by setting all transport terms to zero, see Chapter 7) was used to compute the turbulent stress components which were compared with the DNS results. In order to reduce uncertainty, the magnetic source terms $\mathcal{M}_{ij}$, together with the model (4.97) with $c_M = 0.6$, were adopted from the DNS data. In this way, only the pressure-strain term was exposed to testing. Initially, c_3^L was set to 0.6 as suggested by Schumann and the tuning was focused on c_{3w}^L. Subsequent fine tuning resulted in the recommendation $c_3^L = 0.6A^{1/2}$ and $c_{3w}^L = 1.2$ (where A is the Lumley flatness parameter).

Of course, the model coefficients evaluated with reference to one simple flow such as that of a fully developed plane-channel flow may not hold in more complex situations. However, the two quite different orientations of the magnetic field do provide some basis for model verification since their effects are quite different. A longitudinal (streamwise) magnetic flux in a thin shear flow influences only the velocity fluctuations, i.e. the turbulent stress components, but has no direct effect on the mean flow since the magnetic flux is aligned with the mean flow velocity resulting in a zero mean Lorentz force. In contrast, a transverse magnetic field generates a mean Lorentz force aligned with the mean velocity, which *does* directly affect the mean flow.

A further possible shortcoming in the above determination of the model coefficients is that the available DNS data are for a rather low Reynolds number, $Re_\tau = U_\tau D/2\nu = 150$, which corresponds to a bulk-flow Reynolds number of about 4600. Nevertheless, the subsequent computations for a range of Re up to 10^5 showed satisfactory agreement with the available experiments, providing reasonable confidence in the model (Kenjeres *et al.*, 2004). It is noted, however, that because MHD industrial applications are usually found in wall-confined flows, and the magnetic field generally dampens the turbulence, low-Reynolds-number effects become important. Thus, all computations of MHD flows discussed here have been performed with a low-Reynolds-number second-moment closure accounting for viscous and wall-blocking effects as considered in detail in Chapter 6. Illustrations of MHD computations with a second-moment closure will thus be deferred to that chapter, where comparison with both LES data and experiments are made.

4.6 Modelling the triple moments

Simple models of the triple moments have already been reported in §4.3 in order to complete the closure of the stress-transport equations by way of the Basic Model for pressure interactions. In most of the cases examined with such simple models, the importance of the diffusive terms on the mean flow field was small. In the

https://doi.org/10.1017/9781108875400.006 Published online by Cambridge University Press

present section more elaborate treatments are discussed even though they have not always led to marked improvements in overall predictions of the mean field.

It is an interesting if unexpected historical feature of modelling the second moments that most of the early papers also proposed the solution of transport equations for at least some of the triple moments, for example Chou (1945); Davidov (1961) and Kolovandin and Vatutin (1972). This level of complexity was at least partly because of the influence of a paper by Millionshtchikov (1941), suggesting that the quadruple moments (which appear in the third-moment equations) could be satisfactorily approximated in terms of products of the second moments, an idea which naturally appeared to make third-moment closure the most reliable truncation level. That approximation will be re-examined in the course of this section. It may be remarked here, however, that while elaborate models were proposed, none was actually used: the advocates were armchair explorers! The first use of triple-moment transport equations in numerical computations appears to have been by André *et al.*, (1976 1978) in modelling various aspects of the atmospheric boundary layer. The relatively simple closure approximations made did not ensure realizability but this group also devised a strategy known as the 'clipping approximation' (André *et al.*, 1979) which greatly assisted convergence. Essentially, at every point, as iterations proceeded, the second-moment fields were tested to see whether they satisfied the Schwarz inequality, i.e. $\left|\overline{\alpha\beta}\right| \leq \sqrt{\overline{\alpha^2}.\overline{\beta^2}}$. Where they did not, the values were overwritten by the limiting value imposed by the inequality.

In presenting schemes for modelling the triple moments we shall largely be reporting results from models that stop short of solving closed transport equations for those quantities. Nevertheless, it will be helpful to start by presenting the exact transport equations for those triple products. These are easily formed by noting that

$$\frac{D\alpha\beta\gamma}{Dt} \equiv \alpha\beta\frac{D\gamma}{Dt} + \gamma\alpha\frac{D\beta}{Dt} + \beta\gamma\frac{D\alpha}{Dt} \tag{4.100}$$

where α, β, and γ denote instantaneous values of turbulent velocity, temperature or concentration levels. The exact transport equation for the triple velocity products (to which attention is limited here) is formed by following the path indicated above:

$$\frac{D\overline{u_i u_j u_k}}{Dt} = \overline{u_j u_k \frac{Du_i}{Dt}} + \overline{u_i u_k \frac{Du_j}{Dt}} + \overline{u_i u_j \frac{Du_k}{Dt}}. \tag{4.101}$$

After manipulation of the terms, this can be written as

$$\begin{aligned}\frac{D\overline{u_i u_j u_k}}{Dt} = &+ \left[\overline{u_j u_k}\frac{\partial \overline{u_i u_l}}{\partial x_l} + \overline{u_i u_k}\frac{\partial \overline{u_j u_l}}{\partial x_l} + \overline{u_i u_j}\frac{\partial \overline{u_k u_l}}{\partial x_l}\right] \\ &- \left[\overline{u_j u_k u_l}\frac{\partial U_i}{\partial x_l} + \overline{u_i u_k u_l}\frac{\partial U_j}{\partial x_l} + \overline{u_i u_j u_l}\frac{\partial U_k}{\partial x_l}\right]\end{aligned}$$

https://doi.org/10.1017/9781108875400.006 Published online by Cambridge University Press

$$+\frac{1}{\rho}\left[\overline{u_j u_k f_i}+\overline{u_i u_k f_j}+\overline{u_i u_j f_k}\right]+\overline{\frac{p}{\rho}\left[\frac{\partial u_j u_k}{\partial x_i}+\frac{\partial u_i u_k}{\partial x_j}+\frac{\partial u_i u_j}{\partial x_k}\right]}$$
$$-\nu\left[\overline{\frac{\partial u_i}{\partial x_l}\frac{\partial u_j u_k}{\partial x_l}}+\overline{\frac{\partial u_j}{\partial x_l}\frac{\partial u_i u_k}{\partial x_l}}+\overline{\frac{\partial u_k}{\partial x_l}\frac{\partial u_i u_j}{\partial x_l}}\right]$$
$$-\frac{\partial}{\partial x_l}\left[\overline{u_i u_j u_k u_l}+\overline{\frac{p u_j u_k}{\rho}}\delta_{il}+\overline{\frac{p u_i u_k}{\rho}}\delta_{jl}+\overline{\frac{p u_i u_j}{\rho}}\delta_{kl}-\nu\frac{\partial\overline{u_i u_j u_k}}{\partial x_l}\right] \tag{4.102}$$

or, symbolically

$$\frac{D\overline{u_i u_j u_k}}{Dt}=\mathcal{P}^{(1)}_{ijk}+\mathcal{P}^{(2)}_{ijk}+\mathcal{F}_{ijk}+\Phi_{ijk}-\varepsilon_{ijk}+\mathcal{D}_{ijk}. \tag{4.103}$$

Notice that, in contrast to the stress transport equation, here production arises both from the mean strain $\left(\mathcal{P}^{(2)}_{ijk}\right)$ and directly from the stress field alone $\left(\mathcal{P}^{(1)}_{ijk}\right)$. There is also a contribution from any active force field ($\mathcal{F}_{ijk}$). None of these processes requires modelling if closure is at third-moment level. Then there are the processes that *do*: the non-diffusive pressure interactions, Φ_{ijk}, the dissipative term, ε_{ijk}, and the diffusive transport, $\mathcal{D}_{ijk}$. A common (though not universal) approach in this and in other triple-moment equations has been to regard the convective transport term on the left of the equation as negligible and seek rudimentary approximations for the terms on the right of the equation (invoking the principle of receding influence, §4.1). The following summarizes the principal approximations proposed.

(i) For $\Phi_{\iota jk}$ the same strategy is adopted as in the Basic Model for $\Phi_{\iota j}$, namely a linear return to isotropy (i.e. homogeneity) and a reduction of the production terms:

$$\Phi_{ijk}=-c_1^{uuu}\frac{\varepsilon}{k}\overline{u_i u_j u_k}-c_2^{uuu}\left[\mathcal{P}^{(1)}_{ijk}+\mathcal{P}^{(2)}_{ijk}+\mathcal{F}_{ijk}\right]. \tag{4.104}$$

The first term on the right contains, explicitly, the target quantity for approximation and, if convective transport is discarded, that will move to the left side of Eq. (4.103). Dekeyser and Launder (1985) suggest $c_1^{uuu}\approx 1\big/0.075$ in order that for the simplest flows the diffusion term should be of the correct magnitude while, for the reduction-of-production terms, in common with the practice in the second-moment equations, a value of 0.5 was suggested.

(ii) For ε_{ijk} two simple practices have been adopted. André *et al.* (1978) assumed local isotropy leading to

$$\varepsilon_{ijk}=0. \tag{4.105}$$

Dekeyser and Launder (1985) approximated the dissipative term via the GGDH approximation in terms of gradients in the stress dissipation tensor

https://doi.org/10.1017/9781108875400.006 Published online by Cambridge University Press

and then assumed local isotropy, $\varepsilon_{ij} = \frac{2}{3}\delta_{ij}\varepsilon$, to obtain finally:

$$\varepsilon_{ijk} = c_\varepsilon^{uuu}\frac{k}{\varepsilon}\frac{\partial\varepsilon}{\partial x_l}\left[\overline{u_k u_l}\delta_{ij} + \overline{u_j u_l}\delta_{ki} + \overline{u_i u_l}\delta_{jk}\right]. \tag{4.106}$$

(iii) The remaining term to be approximated, the diffusion term, $\mathcal{D}_{ijk,}$ has in the past usually been represented by the Millionshtchikov (1941) hypothesis, strictly valid for a Gaussian distribution of the quadruple products which meant that they could be represented as a sum of the quadratic products. Thus, in terms of general variables:

$$\overline{\alpha\beta\gamma\delta} = \overline{\alpha\beta}\cdot\overline{\gamma\delta} + \overline{\alpha\gamma}\cdot\overline{\beta\delta} + \overline{\alpha\delta}\cdot\overline{\beta\gamma} \tag{4.107}$$

or, particularized to the case of the velocity products:

$$\overline{u_i u_j u_k u_l} = \overline{u_i u_j}\cdot\overline{u_k u_l} + \overline{u_i u_k}\cdot\overline{u_j u_l} + \overline{u_i u_l}\cdot\overline{u_j u_k}. \tag{4.108}$$

The pressure-containing terms that also appear in $\mathcal{D}_{ijk}$ (see Eq. (4.102)) have been uniformly neglected. An argument against using Eq. (4.108) for the diffusion of third moments is that the Gaussian distribution of the turbulent fluctuations on which that approximation rests will be least accurate in regions where quadruple products are most influential, i.e. where the turbulence is strongly inhomogeneous.

Kawamura *et al.* (1995) have made an interesting modification to the Millionshtchikov hypothesis, arguing that, to model $\overline{u_i u_j u_k u_l}$, departures from Eq. (4.108) should be accounted for by a gradient-transport model. Thus, they proposed:

$$\begin{aligned}
-\frac{\partial\overline{u_i u_j u_k u_l}}{\partial x_l} &\equiv -\frac{\partial}{\partial x_l}\left[\overline{u_i u_j u_k u_l} - (\overline{u_i u_j}\cdot\overline{u_k u_l} + \overline{u_i u_k}\cdot\overline{u_j u_l} + \overline{u_i u_l}\cdot\overline{u_k u_j})\right] \\
&\quad - \frac{\partial}{\partial x_l}\left[\overline{u_i u}_j\cdot\overline{u_k u_l} + \overline{u_i u_k}\cdot\overline{u_j u_l} + \overline{u_i u_l}\cdot\overline{u_k u_j}\right] \\
&= c^{uuu}\frac{\partial}{\partial x_l}\left[\overline{u_l u_m}\frac{k}{\varepsilon}\frac{\partial}{\partial x_m}\overline{u_i u_j u_k}\right] \\
&\quad - \frac{\partial}{\partial x_l}\left[\overline{u_i u}_j\cdot\overline{u_k u_l} + \overline{u_i u_k}\cdot\overline{u_j u_l} + \overline{u_i u_l}\cdot\overline{u_k u_j}\right].
\end{aligned} \tag{4.109}$$

In comparing the alternative practices actually used in computations, it is convenient to identify them simply by way of the equation numbers of the relevant formulae. Hanjalić and Launder (1972b) discarded convective transport and neglected $\mathcal{P}_{ijk}^{(2)}$ on the grounds that diffusive transport in the stress-transport equation would only be important where mean velocity gradients were weak (so mean-strain contributions were discarded). Their algebraic model of stress diffusion (introduced in §4.3.6, Eq. (4.21)) resulted from adopting Eqs. (4.104), (4.105) and (4.108):

$$\overline{u_i u_j u_k} = -c_s\frac{k}{\varepsilon}\left[\overline{u_i u_l}\frac{\partial\overline{u_j u_k}}{\partial x_l} + \overline{u_j u_l}\frac{\partial\overline{u_i u_k}}{\partial x_l} + \overline{u_k u_l}\frac{\partial\overline{u_i u_j}}{\partial x_l}\right]. \tag{4.110}$$

https://doi.org/10.1017/9781108875400.006 Published online by Cambridge University Press

Cormack *et al.* (1978) concluded that, of the models they considered, that version achieved the best agreement with experimental test data. André *et al.* (1978) who, as noted, solved the third-moment transport equations in computing the atmospheric boundary layer, likewise retained Eqs. (4.104) (but with mean strain *and* buoyant contributions neglected), (4.105) and (4.108). However, as remarked above, as an override limiter, their software checked whether at any point the values returned for the triple moments violated the Schwartz inequality for the third moments and, where they did, substituted the limiting values instead.

Dekeyser and Launder (1985) compared three versions with experimental data of a plane jet bounded on one side by stagnant surroundings and on the other by a moving stream (Dekeyser, 1982). The models considered were the Hanjalić–Launder model noted above, a variant in which Eq. (4.106) was adopted for ε_{ijk} rather than (4.105), and a further variant in which, in addition to the preceding model for ε_{ijk}, $\mathcal{P}^{(2)}_{ijk}$ was also retained, both in its direct role in production and in Eq. (4.104). For the active components (those for which stress diffusion is driven in the cross-stream direction) Fig. 4.27 shows that all schemes mimic the general shape of the measured profiles reasonably well, with the last of the above schemes achieving, overall, the closest agreement. However, the levels recorded by all three models were only 50% (or less) of the measured values on the side of the jet that entrains stagnant fluid.

The above adaptation of the Millionshtchikov (1941) hypothesis by Kawamura *et al.* (1995) was also adopted by Kidger (1999) for the case of a two-dimensional

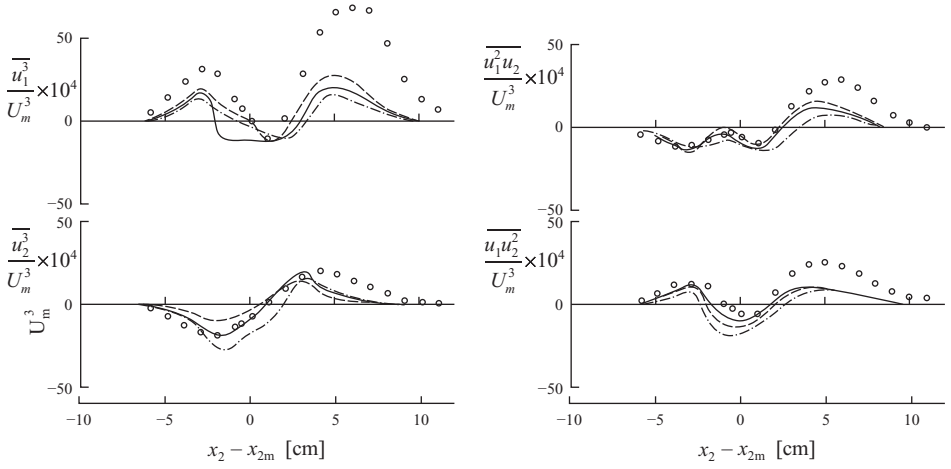

Fig. 4.27 Comparison of measured (Dekeyser, 1982) and modelled triple velocity moments. Symbols, experiments; –·– · – Hanjalić and Launder (1972b); – – – HL plus Eq. (1.7); ———— HL plus Eq. (1.7) and inclusion of $\mathcal{P}^{(2)}_{ijk}$. From Dekeyser and Launder (1985).

https://doi.org/10.1017/9781108875400.006 Published online by Cambridge University Press

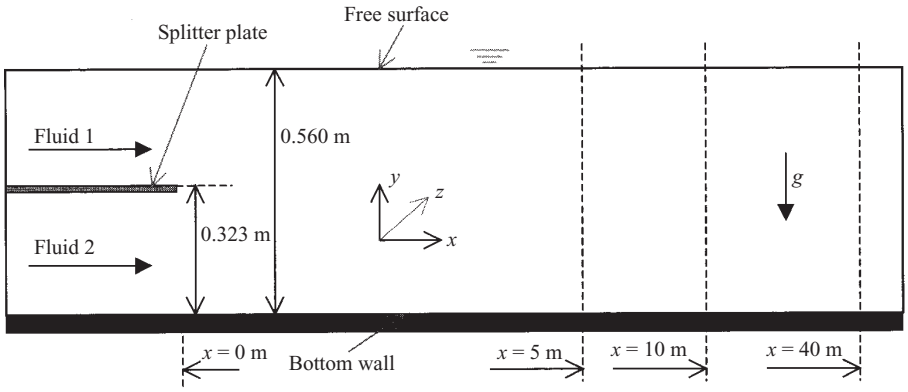

Fig. 4.28 Geometry of the stably stratified mixing layer of Uittenbogaard (1988).

horizontal, stably stratified mixing layer between fresh and salt water (see also Craft *et al.*, 1997a). For this problem, as explained below, a refined treatment of all the triple moments directly affecting the turbulent density fluctuations was vital to obtain reasonable accord between experiment and computation. Thus, in addition to the triple *velocity* moments (which were approximated using the GGDH), transport equations were solved for the scalar-containing triple products $\overline{\theta u_l u_j}$, $\overline{\theta^2 u_l}$ and $\overline{\theta^3}$ – six equations in all for this two-dimensional flow – as these had a great effect on the flow (the last of these arises as the term appears as an unknown in the gravitational generation term of the $\overline{\theta^2 u_i}$ equation). Further details of the modelling applied are given in Kidger (1999) and Craft and Launder (2002b, p. 418). The flow configuration examined is shown schematically in Fig. 4.28 with the faster moving stream of fresh water flowing above a denser stream of saline water. The *initial* computations of this flow were made with the Basic and TCL second-moment closures discussed in earlier sections using the GGDH model for second-moment diffusion in *all* equations. For that case the vertical normalized concentration profiles measured at a station 40 m downstream from the end of the splitter plate are shown in Fig. 4.29a. A superficial inspection of the computations suggests that the two second-moment closures are a good deal closer to the experimental data of Uittenbogaard (1988) than the computations based on a k–ε eddy-viscosity model. However, the second-moment computations also exhibited a serious and quite unexpected anomaly: the maximum density at 40 m downstream was greater than that at entry while, correspondingly, the minimum density was less than the entering value. That is, salt in solution was being removed from regions where its concentration was lowest and transferred by turbulence to the stream where it was already highest! This result, which was clearly not physically credible, turned out to be due to the quite unrealistic predicted vertical salinity flux profile, Fig. 4.30. The second-moment equations, closed with the TCL model

https://doi.org/10.1017/9781108875400.006 Published online by Cambridge University Press

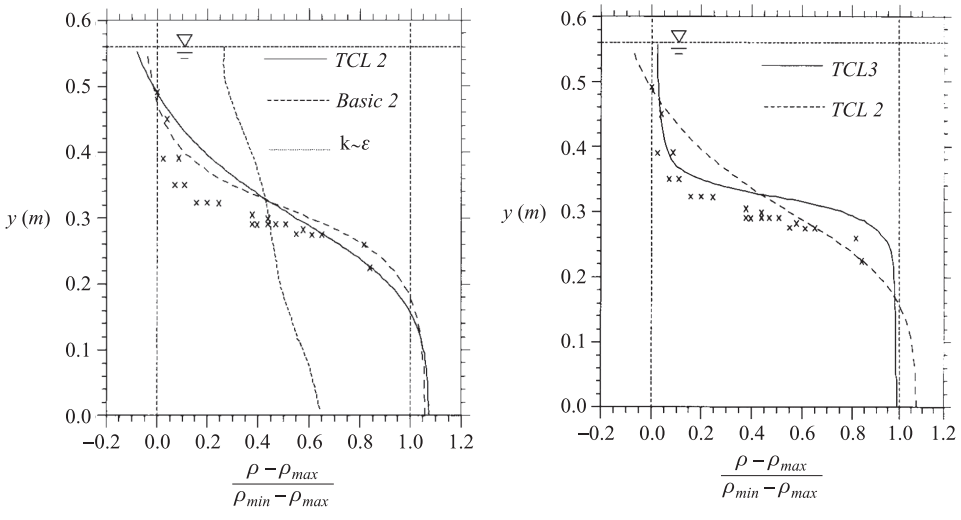

Fig. 4.29 Normalized mean density profile in the stably stratified mixing layer 40 m downstream of the origin. (a) Predictions using TCL and Basic second-moment closure and the k–ε model. (b) Predictions using the TCL second-moment (TCL 2) and partial triple-moment (TCL 3) closures. Symbols, experiments (Uittenbogaard, 1988). From Kidger (1999).

plus the simple GGDH model for the diffusion of the salinity flux, led to the predicted vertical salinity flux shown by the broken line in Fig. 4.30. When, instead of that simple diffusion model, the transport equations for the non-zero values of the salinity-containing third moments noted above were solved, a quite different density flux profile was returned (solid line), which was much closer to the measurements. The resultant vertical variation of normalized salinity profiles shown in Fig. 4.29b is not only in closer agreement with the experimental data in the mixing-layer region, it also removes the unphysical under-and over-shoots at the extreme boundaries. (Corresponding improvements also resulted from applying the same triple-moment equations to the Basic Model but in that case, although much reduced, the over- and under-shoots were not entirely eliminated.)

We note, finally, three other proposals for the triple moments that cannot be expressed directly as simplified closures of the third-moment equations. Based on kinematic arguments, Lumley (1978) developed the following expression for the triple correlation said to be strictly valid in weakly inhomogeneous flows:

$$\overline{u_i u_j u_k} = -\frac{1}{3C_L}\frac{k}{\varepsilon}\left[G_{ijk} + \frac{C_L}{4C_L+5}9G_i\delta_{jk} + G_j\delta_{ik} + G_k\delta_{ij}\right] \qquad (4.111)$$

https://doi.org/10.1017/9781108875400.006 Published online by Cambridge University Press

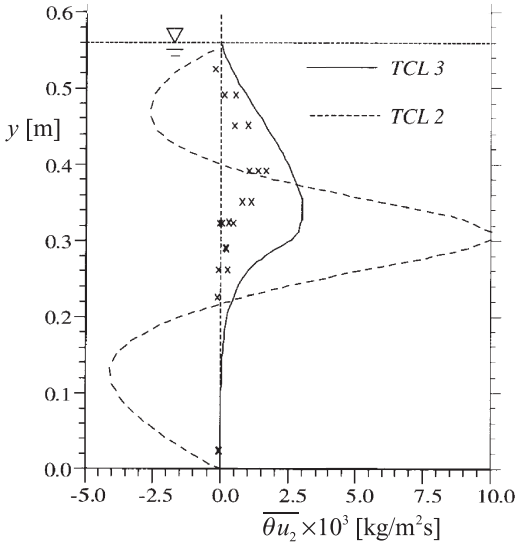

Fig. 4.30 Vertical salinity flux at $x = 10\,\mathrm{m}$ in a stably stratified mixing layer. Symbols, experiments (Uittenbogaard, 1988); – – – TCL closure adopting GGDH approximation for triple moments; ——— TCL closure solving transport equations for third moments containing θ. From Kidger (1999).

where

$$G_{ijk} = \left(\overline{u_i u_l} \frac{\partial \overline{u_j u_k}}{\partial x_l} + \overline{u_j u_l} \frac{\partial \overline{u_k u_i}}{\partial x_l} + \overline{u_k u_l} \frac{\partial \overline{u_i u_j}}{\partial x_l} \right)$$

and $G_i \equiv G_{ikk}$.

The similarities of the leading term with the HL model are evident. Lumley (1978) originally proposed C_L as a function of Re_t, A_2 and A_3 though Schwarz and Bradshaw (1994) chose a fixed value of 3.4 for the coefficient in their tests of various models against their own data of two- and three-dimensional boundary layers. With this choice, in some components it gave marginally better agreement than the Mellor and Herring (1973) and HL schemes though, overall, all three schemes were satisfactory.

Magnaudet (1992) argued that the foregoing proposals did not respect the two-component limit (particularly in situations close to a free surface) and proposed instead the following:

$$\begin{aligned} \overline{u_i u_j u_k} = -\frac{k}{\varepsilon} \Bigg[& c_{s1} \left(\overline{u_i u_l} \frac{\partial \overline{u_j u_k}}{\partial x_l} + \overline{u_j u_l} \frac{\partial \overline{u_k u_i}}{\partial x_l} + \overline{u_k u_l} \frac{\partial \overline{u_i u_j}}{\partial x_l} \right) \\ & + c_{s2} \left(\overline{u_i u_j} \frac{\partial \overline{u_k u_l}}{\partial x_l} + \overline{u_j u_k} \frac{\partial \overline{u_i u_l}}{\partial x_l} + \overline{u_k u_i} \frac{\partial \overline{u_j u_l}}{\partial x_l} \right) \\ & + \frac{1}{k} (\overline{u_i u_j} \cdot \overline{u_k u_l} + \overline{u_i u_k} \cdot \overline{u_j u_l} + \overline{u_j u_k} \cdot \overline{u_i u_l}) \\ & \times \left(c_{s3} \frac{\partial k}{\partial x_l} + c_{s4} \frac{k}{\varepsilon} \frac{\partial \varepsilon}{\partial x_l} \right) \Bigg] \end{aligned} \tag{4.112}$$

https://doi.org/10.1017/9781108875400.006 Published online by Cambridge University Press

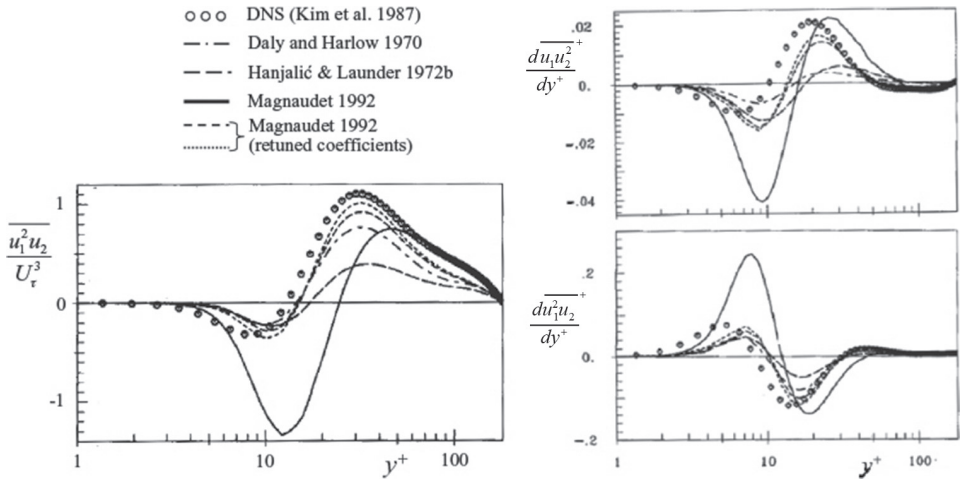

Fig. 4.31 Illustration of predictions of triple velocity moment (left) and some of the gradients (right) with different models for a plane-channel flow at Re = 5600. From Hanjalić (1994).

where all four coefficients have non-zero values. Hanjalić (1994) re-tuned the coefficients in this model for flow in a plane channel and obtained satisfactory agreement with DNS data at Re = 5.600 with the following values: $c_{s1} = 0.125$, $c_{s2} = 0$, $c_{s3} = 0.03$, $c_{s4} = 0.09$, Fig. 4.31.

Finally, mention is made of the proposal of Nagano and Tagawa (1991) based on structural characteristics of shear-generated turbulence in which the level of $\overline{u_i u_j u_k}$ is determined from the skewness factors of the velocity fluctuations. Tested in several types of two-dimensional flow, the method showed good agreement with measurements. However, a disadvantage is that this approach requires solving modelled transport equations for each non-zero component of the skewness factor, $\overline{u_\alpha^3}$.

https://doi.org/10.1017/9781108875400.006 Published online by Cambridge University Press

5

Modelling the scale-determining equations

It remains to provide a route for determining the dissipation rate of turbulence energy, ε, which has appeared in all the modelled forms of second- and third-moment equations presented in Chapter 4. A path is also required for calculating the dissipation rate of $\overline{\theta^2}$ that will be denoted $\varepsilon_{\theta\theta}$. Since, however, contraction of the Reynolds-stress tensor leads to (twice) the turbulent kinetic energy k (a scalar quantity that has been used, along with ε, to provide a turbulent time scale $k/\varepsilon \equiv \mathcal{T}$), the scale-determining variable, clearly, does not have to be ε itself. The subject of the equation could, in principle, just as well be $\mathcal{T}$ and then ε could then be obtained from $\varepsilon = k/\mathcal{T}$. Or, equally, if one focused on the representative turbulent energy-containing length scale, l, ε could then be obtained as $k^{3/2}/l$. Such alternative scales will be examined in §5.2. Indeed, in some circumstances one may decide that it is desirable to employ more than one scale, possibly to characterize different parts of the turbulence energy spectrum. Such possibilities form the subject of §5.3. Finally, in §5.4, schemes for determining the appropriate scales for heat or mass transport are briefly examined. First, however, attention is given to the question of determining the energy dissipation rate directly from its own closed transport equation. At second-moment-closure level, this approach has been adopted by the great majority of modellers.

5.1 The energy dissipation rate, ε

In Chapter 3, the exact transport equation for ε was derived, Eq. (3.15), and the physical significance and order-of-magnitude of the various terms appearing as sources or sinks in the equation were discussed. Unfortunately, the conclusion reached was that the equation was dominated by two terms: a vortex-stretching process, caused predominantly by the turbulent motion itself, intensifying local fine-scale velocity gradients and thus the level of ε, and a viscous dissipation process that provided the primary sink in the equation. Both processes occur in the

https://doi.org/10.1017/9781108875400.007 Published online by Cambridge University Press

very finest scales of turbulence present in the flow and are inaccessible to measurement and, equally, to modelling via analysis. Moreover, as the turbulent Reynolds number of the flow increases, these source and sink terms dwarf other terms in the equation. However, the difference in magnitude between them remains small. Thus, the central task in closing the equation is that of approximating that relatively small difference! (The task of developing a model for ε in the immediate vicinity of a wall, where the other processes in the equation are not all 'dwarfed' by those primary terms, poses just as challenging a task; however, that issue is deferred until Chapter 6.) To proceed, one is driven to discard formal analysis in favour of the more basic weapons: dimensional analysis, intuition and experimental data! It was a limited form of such an approach that was applied in §4.3.7 to complete closure with the Basic Model. To paraphrase what was said there: there must be at least one source and one sink in the modelled transport equation for ε that are appropriately coupled with the dynamic turbulence field in order to avoid the possibility of either runaway growth of turbulence energy or, at the other extreme, of negative turbulence energies being computed. In view of the foregoing, the ε transport equation is written as:

$$\frac{D\varepsilon}{Dt} = \mathcal{S}_{\varepsilon 1} + \mathcal{F}_{\varepsilon} - \mathcal{S}_{\varepsilon 2} + \mathcal{D}_{\varepsilon} \tag{5.1}$$

where $\mathcal{S}_{\varepsilon 1}$ contains mean velocity gradients the overall effect of which is normally positive, $\mathcal{F}_{\varepsilon}$ denotes force-field contributions (which may be positive or negative), while $\mathcal{S}_{\varepsilon 2}$ comprises purely turbulence quantities and, by virtue of the minus sign that precedes it, is conveniently regarded as a sink. Finally, $\mathcal{D}_{\varepsilon}$ denotes diffusional transport of ε.

5.1.1 *Effects of mean velocity gradients*

In §4.3.7, the source affected by mean strain was provided by a term proportional to the turbulent kinetic energy generation rate, $\mathcal{P}_k$. This process is not the only way of introducing mean-flow-deformation effects, however. Intuitively, it might seem that the process of transferring energy across the spectrum from the large scales to successively finer scales of turbulence (until viscous effects become sufficiently large for energy dissipation to ensue) could be achieved with a model more in tune with the actual processes taking place in the flow. In other words, by a model based on a different type of mean-flow deformation than that which creates the turbulent kinetic energy. Thus, initially, one may suppose that the positive source in the ε-equation, $\mathcal{S}_{\varepsilon 1}$, comprises ε itself divided by a time scale, which then multiplies a series of terms – all dimensionless invariants – comprising products of velocity gradients and, possibly, Reynolds stresses. It is convenient to express this series of sources in terms of products of the three dimensionless second-rank tensors:

https://doi.org/10.1017/9781108875400.007 Published online by Cambridge University Press

$$a_{ij}; \qquad \tilde{S}_{ij} \equiv \frac{k}{\varepsilon} S_{ij}; \qquad \tilde{W}_{ij} \equiv \frac{k}{\varepsilon} W_{ij}. \tag{5.2}$$

The general form of generation term containing mean-field-deformation terms for an incompressible flow containing up to cubic products of the above tensors may then be written as:

$$\mathcal{S}_{\varepsilon 1} = \frac{\varepsilon^2}{k}[\alpha_1 a_{mn}\tilde{S}_{nm} + \alpha_2 \tilde{S}_{mn}\tilde{S}_{nm} + \alpha_3 \tilde{W}_{mn}\tilde{W}_{nm} + \alpha_4 a_{mk}a_{nk}\tilde{S}_{nm} + \alpha_5 a_{mn}\tilde{S}_{mk}\tilde{S}_{nk} + \alpha_6 a_{mn}\tilde{W}_{mk}\tilde{W}_{nk} + \alpha_7 \tilde{S}_{mn}\tilde{S}_{mk}\tilde{S}_{nk} + \alpha_8 \tilde{S}_{mn}\tilde{W}_{mk}\tilde{W}_{nk}]. \tag{5.3}$$

Note that terms containing the mean vorticity[1] only appear in the equation where quadratic products arise (linear or cubic terms in vorticity in Eq. (5.3) would give rise to products which are zero).[2] One may note from Eq. (5.3) that, in an incompressible flow, the first term provides the conventional source proportional to $\mathcal{P}_k$ (where $\alpha_1 \equiv -c_{\varepsilon 1}$, the symbol used in §4.3.7, to which we shall henceforth revert) when the mean field is incompressible. The second, with coefficient α_2, would be of the same form as the first if an eddy-viscosity assumption were made to link the stress and strain fields. Second-moment closure thus provides an opportunity to introduce a distinction between the two not available at the level of linear eddy-viscosity modelling.

No strategies appear to have been devised for determining the unknown α-coefficients other than that of comparison with experimental data and, even so, workers who have ventured along this route have included only one of the terms in addition to the leading term with coefficient α_1 (i.e. $-c_{\varepsilon 1}$). Perhaps the earliest proposal of this type was made by Pope (1978). He specifically addressed the failure of models at that time to predict the development of the round jet in stagnant surroundings with the same values of the coefficients that satisfactorily reproduced the growth of plane jets and other simple shear flows where turbulence energy production and dissipation rates were of comparable overall magnitude. (This weakness had first been identified by Rodi and Spalding, 1970.) Specifically, with the coefficients chosen to suit the plane jet and other strong shear flows, the predicted growth of the round jet was some 35% greater than the experimental value then accepted. To remedy this problem, Pope recommended the inclusion of the term with coefficient α_8. He recognized that in a round jet the mean-flow vortex lines are stretched as the jet spreads downstream while, in the plane jet, no such vortex-line stretching occurs. In a non-swirling round jet the selected term is equal to:

[1] Strictly, it is the mean rate of rotation, $W_{ij} \equiv \frac{1}{2}(\partial U_i/\partial x_j - \partial U_j/\partial x_i)$, that appears in Eq. (5.3), which is related to mean vorticity through the identity $W_{ij} \equiv -\frac{1}{2}\epsilon_{ijk}\Omega_k$ (note also $\Omega_i = -\epsilon_{ijk}W_{jk}$).

[2] Since up to cubic products of the second-rank tensors appearing in Eq. (5.2) may figure in Eq. (5.3), coefficients $\alpha_1 - \alpha_3$ may depend on invariants such as $A_2^{1/2}$ or $S \equiv \left(\tilde{S}_{mn}\tilde{S}_{nm}\right)^{1/2}$, etc., while $\alpha_4 - \alpha_8$ are constants.

https://doi.org/10.1017/9781108875400.007 Published online by Cambridge University Press

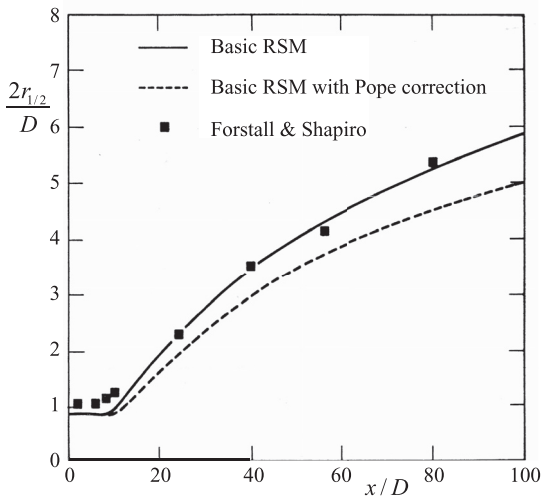

Fig. 5.1 The rate of spread of a round jet in a moving stream Symbols: Experiment, Forstall and Shapiro (1950); – – – – – Basic Model with Pope correction included; ——— Basic Model without correction. From Huang (1986).

$$\frac{1}{4}\left[\frac{k}{\varepsilon}\right]^3\left[\frac{\partial U}{\partial r}-\frac{\partial V}{\partial x}\right]^2\frac{V}{r};$$

but, in a plane flow, the term is zero. So, in the round jet this extra mode of vortex stretching would hasten the spectral transfer of energy, thus reducing the turbulence energy and the spreading rate. By choosing $\alpha_8 = 0.79$ the correct rate of spread was achieved for both the round and plane jets.

The above conclusions were, admittedly, arrived at using a two-equation eddy-viscosity model[3]; but it was subsequently found (Launder and Morse, 1979) that the excessive spreading rate was even more severe when one switched to the versions of second-moment closure then available (specifically, for Φ_{ij2}, the Basic Model and the Quasi-Isotropic model). Huang (1986), working with the Basic Model, re-optimized the coefficient α_8 to 1.13, which led to a half-radius spreading rate of 0.086, the accepted value at the time.[4] He found, however, that, while the fully developed spreading rate was thus corrected, if calculations began with a uniform velocity profile at the jet exit, the length of the potential core was substantially longer than measured. Moreover, when the same model was applied to the round jet in a co-flowing stream, Fig. 5.1 , the rate of spread with the correction term included was substantially too slow, while the standard Basic Model faithfully

[3] Until the late 1970s, modellers did not include the axisymmetric jet in the package of basic test flows for second-moment closures because of mathematical problems of handling stress diffusion at the axis.

[4] As reported more fully in §4.4.5, the experimental spreading rate for the round jet has more recently been convincingly established as 0.095 ± 0.002, while the neglect within parabolic solvers of streamwise gradients of source terms in the turbulence-model equations leads to an over-prediction of spreading rate which is more severe for the round than the plane jet.

https://doi.org/10.1017/9781108875400.007 Published online by Cambridge University Press

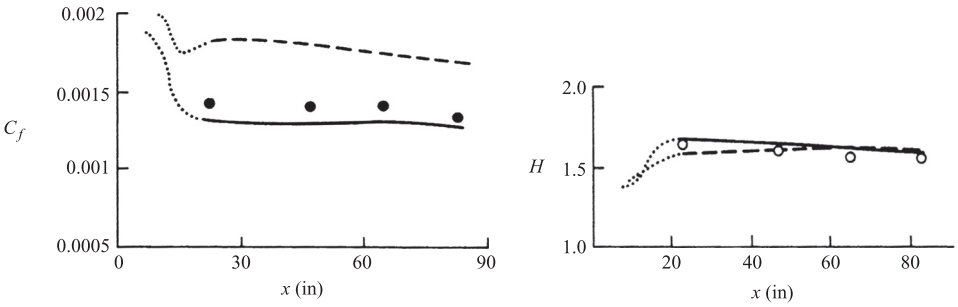

Fig. 5.2 Development of a turbulent boundary layer in an equilibrium adverse pressure gradient. Left: skin-friction coefficient; right: boundary-layer shape factor. Symbols: Experiment, Case C, Bradshaw (1967); Predictions: – – – – Basic Model with standard ε-equation; —— Basic Model, including supplementary vorticity source in ε-equation. From Hanjalić and Launder (1980).

captured the measured growth of the jet. Rubel (1985) has also reported that, when the Pope correction was applied to the *radial* jet in stagnant surroundings, the spreading rate was reduced to less than half the measured value. Thus, the proposed modification lacked generality even for flows similar to that for which it had been calibrated. As presented in Chapter 4, newer models of Φ_{ij} used (as discussed below) with modifications to the source and sink coefficients in the Basic-Model form of the ε-equation come much closer to accounting for the round/plane jet anomaly. Thus, a coefficient α_8 in the range 0.1–0.2 may well prove sufficient to bring complete agreement for the round jet in stagnant surrounding without damaging repercussions in other flows.

A further modification to the ε-equation was proposed by Hanjalić and Launder (1980), who effectively took just α_3 (and α_1) non-zero. In fact, in a *straight* thin shear flow, the term with coefficient α_3 takes the same form as the turbulence energy production rate if the turbulent stress is approximated by a turbulent viscosity and k-production via normal stresses is neglected. Thus, one may choose the α-coefficients so that, in combination, they may augment the role of the normal stresses relative to the shear stresses (the underlying idea being that normal straining might be more effective in reducing an eddy's size than shear straining). With $c_{\varepsilon 1} = -\alpha_1 = 4.44$ and $\alpha_3 = 1.08$ the authors obtained much improved predictions of the round jet and a far better accord with experimental data in boundary layers developing in a positive (adverse) pressure gradient. Figure 5.2, for example, compares predictions obtained with the Basic Model with the measured development of one of the equilibrium boundary layers reported by Bradshaw (1967); evidently a much improved computation of the skin friction coefficient results with the use of this extra term. Subsequently, however, Leschziner and Rodi (1981) found that giving such a major role to $\tilde{W}_{mn}\tilde{W}_{nm}$ led to serious undesirable effects

https://doi.org/10.1017/9781108875400.007 Published online by Cambridge University Press

in flows with recirculation and the use of the scheme has largely been discontinued. Thus, the remarks made of Pope's (1978) modification may also be applied to this scheme. Namely, that on its own while the modification brought some significant improvements to closures available in the 1980s, continued testing revealed situations where seriously worse agreement resulted. Again, with a much smaller value for α_3 (and with α_1 taking a value much closer to its standard value), it is possible that some contribution from the term may be helpful.

Other related approaches have simply retained $\mathcal{P}_k$ as the basic source of ε generation but have then made the coefficient $c_{\varepsilon 1}$ a function of the second-invariants of the dimensionless strain and rate of rotation introduced above: $\mathrm{S} \equiv \sqrt{\tilde{S}_{ij}\tilde{S}_{ij}}$, $W \equiv \sqrt{\tilde{W}_{ij}\tilde{W}_{ij}}$ (e.g. Speziale and Gatski, 1997). However, none of the functions tested appeared to be suitable over a wide range of flows. By introducing sweeping simplifications within the framework of the Renormalization Group Theory (RNG), Yakhot and Orszag (1986) arrived at the same basic form of the equation for ε, Eq. (4.27), but with somewhat modified coefficients.[5] Subsequently, Yakhot *et al.* (1992) introduced an additional source term based on a scale expansion for the production of ε in terms of their variant of the non-dimensional strain-rate, $\mathrm{S}^* \equiv \sqrt{2\tilde{S}_{ij}\tilde{S}_{ij}} (\equiv \sqrt{2}\mathrm{S})$ (chosen so that $\mathrm{S}^* = (k/\varepsilon)\, dU/dy \equiv S$ in a simple shear), which can be lumped together with the original production term with the joint coefficient

$$c_{\varepsilon 1}^{RNG} = c_{\varepsilon 1} - \frac{\mathrm{S}^*\left(1 - \mathrm{S}^*/\mathrm{S}_0^*\right)}{1 + \beta \mathrm{S}^{*3}}. \tag{5.4}$$

This extra term is designed to make the equation more sensitive to strain rate. The reference strain rate S_0^* is that typical of a homogeneous equilibrium shear flow, a value of about 4.5 being suggested, while 0.012 is the value proposed for the coefficient β (Yakhot *et al.*, 1992). The results of including the correction have been inconsistent, particularly poor agreement resulting for flows such as that through a tube-bank and in other cases where normal straining plays a major role. A partial explanation for the behaviour can be traced to the insensitivity of the term to the sign of the (normal) strain rate $S_{\alpha\alpha}$; the term produces the same effect for the same strain intensity irrespective of whether the flow is subjected to acceleration or deceleration, to compression or expansion. For example, it has been applied in conjunction with the Basic Model to flows in an axisymmetric contraction and expansion at similar strain rates ($\mathrm{S}^* = 62.2$ and 86.6, respectively) and the resulting behaviour compared with the DNS results of Lee and Reynolds (1985). While the standard model gives indifferent results for both cases, the RNG term led to

[5] The RNG ε-equation was developed for use within an eddy-viscosity modelling framework, i.e. with the turbulent diffusion term expressed in terms of eddy diffusivity, $\partial(\nu_t/\sigma_\varepsilon \partial\varepsilon/\partial x_j)/\partial x_j$, as in Eq. (7.29) rather than as in Eq. (5.11).

https://doi.org/10.1017/9781108875400.007 Published online by Cambridge University Press

improved agreement in the expansion, but produced even worse predictions of flow in the contraction (Hanjalić, 1996; see also Hanjalić and Jakirlić, 2002).

As a result of the succession of unfulfilled 'improvements' to the source terms of the ε-equation outlined above, the turbulence energy production, $\mathcal{P}_k$, is usually the only term containing mean velocity gradients retained in $\mathcal{S}_{\varepsilon 1}$, prefixed by a constant coefficient (or, at least, one not directly dependent on the mean-flow deformation). Consequently, modellers have tended to look at other processes in the equation as their target for improving the overall performance of the equation, a subject taken up in §5.1.3.

5.1.2 Force field effects on the energy-dissipation rate

The exact transport equation for ε, Eq. (3.15), contains the following term arising from force-field effects

$$\mathcal{F}_\varepsilon = \sum\nolimits_n 2\nu\overline{\left(\partial f_i^n/\partial x_m\right)\left(\partial u_i/\partial x_m\right)}.$$

However, if a sizing of the term analogous to that made for the other terms in Eq. (3.15) had been made, one would have concluded that the contribution made by the force field (like that of the mean-strain terms) was negligible by comparison with the vortex-stretching and dissipation terms in the equation. Nevertheless, if we take the view that, really, one is trying to model the rate at which kinetic energy is transferred across the spectrum by the successive breaking down of the large eddies into smaller and smaller scales, it seems reasonable that any significant fluctuating force field should make a contribution to that process. Indeed, in Rayleigh–Bénard convection there is no turbulence generation by shear since the mean flow is stationary. Thus, in unstably stratified turbulence, the consequent intensification of the turbulence would seem likely to promote eddy breakdown. It is presumably for that reason that it has been common to model the force-field contribution to the production of ε as directly analogous to that of the turbulence energy generation rate by mean shear. Thus, it has usually been assumed that:

$$\mathcal{F}_\varepsilon^n = c_{\varepsilon 3}^n \mathcal{F}_k^n \frac{\varepsilon}{k} \tag{5.5}$$

which is used often with the same value of coefficient as that for the mean-strain generation term, $c_{\varepsilon 1}$, though, as noted below, there have also been many variations on this practice.[6]

[6] Although adopting the same coefficient for shear and buoyant generation of ε is the usual practice, it should be recognized that production of turbulence energy by mean shear is in most circumstances positive, whereas buoyant production, in common with most other force fields, can be positive or negative. This fact lends some support to those who have used different coefficients for the buoyant source depending upon whether stratification is stable or unstable.

https://doi.org/10.1017/9781108875400.007 Published online by Cambridge University Press

Table 5.1 *Overview of the exact force-field effects in the k-equation and their modelled counterparts in the ε-equation*

	Coriolis effects	Gravitational buoyancy effects	Electromagnetic effects
f_i/ρ	$-2\Omega_n u_m \epsilon_{imn}$	$\rho' g_i/\rho = -\beta g_i \theta$	$\frac{\sigma}{\rho}\left(\epsilon_{imn} e_m B_n + u_n B_i B_n - u_i B_n^2\right)$
$\mathcal{F}_k = \frac{1}{\rho}\overline{f_i u_i}$	0	$-\beta g_i \overline{\theta u_i}$	$\frac{\sigma}{\rho}\left(\epsilon_{imn}\overline{e_m u_i} B_n + \overline{u_i u_n} B_i B_n - 2k B_n^2\right)$
$\mathcal{F}_\varepsilon = c_{\varepsilon 3}\mathcal{F}_k \mathcal{T}$	0	$-c_{\varepsilon 3}^g \beta g_i \overline{\theta u_i}\,\varepsilon/k$	$c_{\varepsilon 3}^L \frac{\sigma}{\rho}\left(\epsilon_{imn}\overline{e_m u_i} B_n + \overline{u_i u_n} B_i B_n - 2k B_n^2\right)\frac{\varepsilon}{k}$

We can now set out the implied models of the force-field source terms in the ε-equation. First, it is noted that if we follow this approximation route for $\mathcal{F}_\varepsilon^{\mathcal{R}}$, the additional dissipation source associated with coordinate rotation, we conclude from Eq. (5.5) that, just as in the equation for the kinetic energy, the fluctuating Coriolis force exerts no effect on the dissipation rate. That assumption has indeed been made in most second-moment studies of rotating flows.

For thermally induced buoyancy, replacing f_i from Eq. (4.73), and contracting the term $\mathcal{G}_{ij}$ in Eq. (4.74) and dividing by 2, the force field source in the ε-equation becomes

$$\mathcal{F}_\varepsilon^g \equiv \mathcal{G}_\varepsilon = c_{\varepsilon 3}\mathcal{G}_k \frac{\varepsilon}{k} = -c_{\varepsilon 3}^g \beta g_i \frac{\overline{\theta u_i}}{k}\varepsilon \tag{5.6}$$

where $\beta \equiv -\left(\partial\rho/\partial\Theta\right)|_P/\rho$.

For magnetic-field effects, one can follow the same route as above. First, halving the contraction of Eq. (4.95) gives the magnetic-field source in the kinetic energy equation

$$\mathcal{F}_k^L = \frac{\sigma}{\rho}\left(\epsilon_{ijk}\overline{e_j u_i} B_k + \overline{u_i u_k} B_i B_k - 2k B_k^2\right) \tag{5.7}$$

from which the modelled contribution to the dissipation rate equation may be inferred to be

$$\mathcal{F}_\varepsilon^L = c_{\varepsilon 3}^L \frac{\sigma}{\rho}\left(\epsilon_{ijk}\overline{e_j u_i} B_k + \overline{u_i u_k} B_i B_k - 2k B_k^2\right)\frac{\varepsilon}{k}. \tag{5.8}$$

A summary of the different forms adopted in the dissipation equation for different types of force field is provided in Table 5.1.

Thermally created buoyancy is the force field that has been the most extensively examined. A range of values for the coefficient $c_{\varepsilon 3}^g$ may be found in the literature. Depending on the type of turbulence model considered, values range from zero in the work of André *et al.* (1978) and the simplified version of the Basic Model used by Gibson and Launder (1976) to 0.8 by Hanjalić and Vasić (1993). The coefficient in the mixed-layer study of Zeman and Lumley (1976) varies according to the

https://doi.org/10.1017/9781108875400.007 Published online by Cambridge University Press

stress anisotropy from a very small value in the unstable limit (where virtually all the fluctuations are vertical) to unity in isotropic turbulence. In more recent work (Craft *et al.*, 1996a, 2004b; Kenjeres *et al.*, 2004), there has been a trend to make the coefficient $c_{\varepsilon 3}^{g}$ equal to $c_{\varepsilon 1}$ (a choice that was made within the TCL closure framework used for the buoyant shear flows shown in Figs 4.23 and 4.24 and the plumes summarized in Table 4.6).

Nevertheless, it is acknowledged that the way buoyant sources are handled in the ε-equation has not yet reached a settled state. For while $c_{\varepsilon 3}^{g}$ is now commonly taken equal to $c_{\varepsilon 1}$, the latter varies widely depending on whether other contributing mean-strain or mean-vorticity terms are retained in Eq. (5.3) (which may cause the value assigned to $c_{\varepsilon 1}$ to be either much greater or much less than the value used with the Basic Model of around 1.44) or, indeed, on the form of the sink term in the ε-equation, considered below. These, however, are not factors that should affect the way buoyant effects are handled! Moreover, Lumley (1978) indicated two further terms that he suggested should contribute as buoyant sources of ε, one of which appears never to have been tried while the other was tested just in the Zeman–Lumley study of the mixed layer noted above.

Finally, we note that for magnetic effects, simply setting $c_{\varepsilon 3}^{L}$ equal to $c_{\varepsilon 1}$did not appear appropriate as the anisotropizing effect of the magnetic field close to a wall (i.e. the selective damping of the component in the direction of the Lorentz force) requires near-wall modifications. After examining several constant values, Kenjeres *et al.* (2004) found that choosing a coefficient dependent on the stress-anisotropy invariant, $c_{\varepsilon 3}^{L} = 6.5\ \min(A_2, 0.25)$, provided satisfactory predictions for a range of flows for different orientations of the magnetic field.

5.1.3 Modelling the sink processes in the ε-equation

Attention is now turned to the sink of ε, $\mathcal{S}_{\varepsilon 2}$. In §4.3.7, that was taken as directly proportional to ε^2/k. While that form is still retained in several more recent closures, there is scope for making the sink depend in more subtle ways on the character of the anisotropic stress tensor a_{ij}. While that term has already appeared in the source term, Eq. (5.3), only products of the stress anisotropy with mean-flow deformation terms were retained. But, clearly, it is consistent with the level of approximation of Eq. (5.3) to retain in $\mathcal{S}_{\varepsilon 2}$ double and triple scalar products of a_{ij} alone: in other words, of A_2 and A_3. The first proposal of this kind was made by Lumley and Khajeh-Nouri (1973). In fact, they omitted $\mathcal{S}_{\varepsilon 1}$ entirely and took $\mathcal{S}_{\varepsilon 2}$ as:

$$\mathcal{S}_{\varepsilon 2} = \frac{\varepsilon^2}{k}[1.865 - 3.74A_2]. \tag{5.9}$$

Thus, the stress anisotropy invariant was being used in place of invariants containing mean velocity gradients as a source of ε. The underlying idea was that

https://doi.org/10.1017/9781108875400.007 Published online by Cambridge University Press

it was predominantly the anisotropy of the turbulent fluctuations that promoted the breakdown of large eddies into successively finer ones. Arguably, these are better correlated in terms of the stress anisotropy than mean-field deformation parameters. The model was calibrated to give good agreement with experiment for homogeneous shear and plane strain. However, when subsequently its potential for use with inhomogeneous-flow solvers was explored (Zeman and Lumley, 1976; Morse, 1980), the need to include mean-strain effects in addition to a dependence of $\mathcal{S}_{\varepsilon 2}$ on A_2 became inescapable. Indeed, Morse found that within a parabolic or 'marching' solver with only $\mathcal{S}_{\varepsilon 2}$ as a source (approximated in a form similar to Eq. (5.9)), for a developing jet in stagnant surroundings the spreading rate exhibited continual large-amplitude oscillations due to a too weak coupling between the dissipation rate and the turbulence energy. This general problem has been removed by re-introducing deformation invariants among which the generation rate of turbulence energy remains the most popular.

Continuing research by the group at Manchester confirmed the essence of Morse's study, namely that one could not avoid using mean-strain invariants but that the overall performance of the ε-equation could certainly be improved by using the stress invariants too. Over the years, the form of ε-equation sink used by that group has evolved to:

$$\mathcal{S}_{\varepsilon 2} = \frac{1.92}{(1 + 0.7 A_2^{1/2} A)} \frac{\varepsilon^2}{k} \tag{5.10}$$

with, as noted in the previous section, the source term, $\mathcal{S}_{\varepsilon 1}$, taking the very simple form adopted with the Basic Model, i.e. $\mathcal{S}_{\varepsilon 1} = c_{\varepsilon 1} \varepsilon \mathcal{P}_k / k$, except that the coefficient $c_{\varepsilon 1}$is reduced to 1.0.

The use of stress anisotropy parameters in $\mathcal{S}_{\varepsilon 2}$ as indicated in Eq. (5.10) has been found to widen considerably the range of free shear flows that may be correctly predicted. As was reported in Chapter 4, the use of the TCL model for Φ_{ij_2} together with the above form for the source and sink terms in the ε-equation achieved much closer accord with experiments for the round and plane jets in stagnant surroundings and the asymptotic wake than did the Basic-Model form of the stress and dissipation equations (Table 4.4). For the non-equilibrium wakes examined experimentally by Wygnanski *et al.* (1986) equally favourable agreement has been reported. In these experiments, by the use of different wake generators – in one case an airfoil and in the other a strip held at right-angles to the flow – while the wake momentum-thickness Reynolds numbers were the same, quite different initial levels of turbulence energy and spreading rates were generated for the two wakes, differences which persisted far beyond the range of the measurements. This feature was quite successfully captured with the form of $\mathcal{S}_{\varepsilon 1}$ and $\mathcal{S}_{\varepsilon 2}$ noted above, Fig. 5.3, whereas the Basic Model with the form of ε-equation presented in §4.3.7 gave virtually identical behaviour for the two wakes beyond about 50 momentum

https://doi.org/10.1017/9781108875400.007 Published online by Cambridge University Press

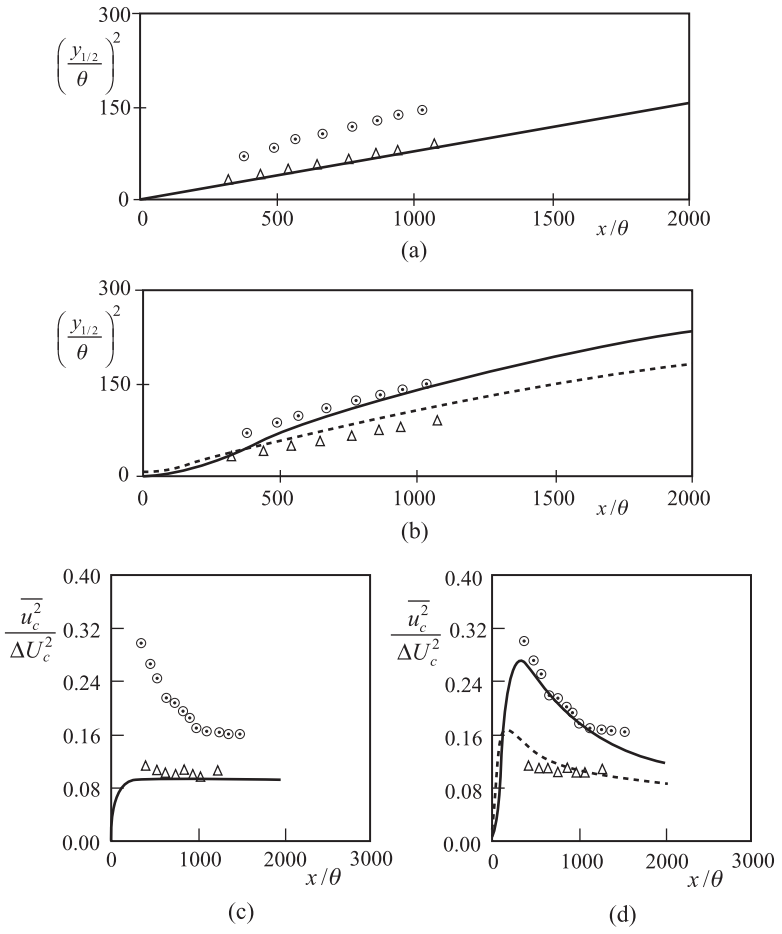

Fig. 5.3 Development of half-width and centre-line streamwise normal stress for plane wakes with same Reynolds numbers created by different wake generators. Symbols: Experiments: ⊙ Airfoil; △ Solid strip; Lines: computations: (a) and (c): Basic model with ε computed from Eq. (4.27) with constant coefficients; (b) and (d) TCL model with ε sink from Eq. (5.10) and $c_{\varepsilon 1} = 1.0$. From El Baz *et al.* (1989), see also Launder (1989).

thicknesses (θ) downstream. In this case, it was the stress-invariant dependence of $\mathcal{S}_{\varepsilon 2}$ shown in Eq. (5.10) (rather than the TCL modelling for the stress field) that was mainly responsible for the striking improvement.

5.1.4 Diffusion of ε

Finally, there is the diffusion of ε to consider. Here the great majority of schemes have adopted the generalized gradient-diffusion hypothesis employed with the Basic Model:

https://doi.org/10.1017/9781108875400.007 Published online by Cambridge University Press

$$\mathcal{D}_\varepsilon = \frac{\partial}{\partial x_k}\left[c_\varepsilon \frac{k\overline{u_k u_j}}{\varepsilon}\frac{\partial \varepsilon}{\partial x_j}\right] \tag{5.11}$$

with the diffusion constant, c_ε, being assigned a constant value of around 0.15. However, there is a well-known weakness in the ε-equation for separated flows near walls and even in boundary layers developing in an adverse pressure gradient close to separation. There the near-wall levels of ε are found to be too low, leading to excessive predicted heat transfer rates to or from the wall, or to computed boundary layers that do not separate when experimental data show clearly that they ought to! This problem, which may be linked to weaknesses in the diffusion model, does not arise if the scale-determining variable is, instead, chosen as ω, a quantity proportional to ε/k, that has been extensively and successfully applied by Wilcox (1993, 2000) to the prediction of many aerodynamic flows where the reliable prediction of separation is vital. The difference between the ε and ω equations can be linked to differences in the effective diffusion processes in the two equations. Further examination of closures using the ω equation is provided in §5.2. If, however, one remains with the dissipation equation, the usual practice has been to introduce a near-wall *source term* specifically to raise the dissipation rate in situations where the turbulent length scale $k^{3/2}/\varepsilon$ is appreciably above the local equilibrium level, i.e. c_l times the wall-normal distance. Thus, the so-called *Yap correction* (Yap, 1987) adds the term:

$$\mathcal{S}_\varepsilon^{YAP} = \text{Max}\left[0.83\frac{\varepsilon^2}{k}\left(\frac{l}{c_l x_n} - 1\right)\left(\frac{l}{c_l x_n}\right)^2, 0\right] \tag{5.12}$$

where $l \equiv k^{3/2}/\varepsilon$, c_l= 2.44 and x_n denotes normal distance from the wall (rather than a tensor distance). Evidently, if l is greater than the equilibrium value, $c_l x_n$, the term acts to increase ε and thus to decrease the length scale. This form has been successfully adopted when treating nearly plane surfaces but the use of the normal distance limits its utility on highly curved or irregular surfaces. Jakirlić and Hanjalić (1995) proposed replacing explicit reference to wall distance by the gradient of length-scale normal to the wall:

$$\mathcal{S}_\varepsilon^{H} = \text{Max}\left\{A\frac{\varepsilon\tilde{\varepsilon}}{k}\left[\left(\frac{1}{c_l}\frac{\partial l}{\partial x_n}\right)^2 - 1\right]\left(\frac{1}{c_l}\frac{\partial l}{\partial x_n}\right)^2, 0\right\}. \tag{5.13}$$

Equation (5.13) was proposed in the context of a second-moment closure that allows integration up to the wall (to be considered in detail in Chapter 6) and thus involves the stress flatness invariant A and the so-called quasi-homogeneous dissipation rate $\tilde{\varepsilon}$ (defined by Eq. (6.12)). As reported in Chapter 7, however, it can also be used with an eddy-viscosity model if $A\varepsilon\tilde{\varepsilon}/k$ is replaced by $0.83\tilde{\varepsilon}^2/k$ to match the Yap correction, Eq. (5.12).

https://doi.org/10.1017/9781108875400.007 Published online by Cambridge University Press

Iacovides and Raisee (1997) proposed a similar expression in terms of length-scale gradients that directly reflects the Yap formulation,

$$\mathcal{S}_{\varepsilon}^{IR} = \max\left[0.83\frac{\varepsilon^2}{k}\left(F-1\right)F^2, 0\right] \tag{5.14}$$

where $F \equiv \left[\left(\partial l/\partial x_j\right)\left(\partial l/\partial x_j\right)\right]^{1/2}/c_l$.

Again, both forms, (5.13) and (5.14), evidently raise the dissipation rate when the gradient of the length scale exceeds that occurring in equilibrium near-wall turbulence, c_l. A somewhat more elaborate form has been used within the viscosity-affected sublayer (Craft, 2002). Suga (2004a, 2004b) has employed Eq. (5.14) to limit the near-wall length scale, together with the TCL model, in computing a number of separated flows. As an example, Fig. 5.4 compares the measurements of mean velocity, turbulent shear stress and the square root of the normal stresses downstream from a backward-facing step with the very detailed particle-tracking velocimetry data of Kasagi and Matsunaga (1995). The flow Reynolds number is 5500 based on step height and centre-line velocity upstream of the step. Suga added an elaborate model for pressure diffusion (noted in Chapter 4) but in this flow the effects of the model of that process were minimal. For both versions, the accord between experiment and the computed behaviour is remarkably close.

Hanjalić and Jakirlić (1998) also examined the prediction of flow downstream of a back-step providing predictions over a twenty-fold range of Reynolds number and for expansion ratios from 1.2 to 2.0. Their computations were based on the Basic Model for closing the stress transport equations (both in the form presented in Chapter 4 and in a version integrated to the wall to be presented in Chapter 6). For the dissipation-rate equation the extra source given by Eq. (5.13) was adopted throughout to provide the near-wall damping of length scale in separated regions. That enabled the subtle changes linked to expansion ratio and Reynolds number in both the length and shape of the separated flow zone behind the step to be captured accurately, Fig. 5.5.

5.2 Other scale-determining equations

Over the years a number of other scale-determining variables have been proposed in place of ε. One of the motives has been to derive and solve directly a transport equation for a characteristic turbulence length or time scale, l or $\mathcal{T}$ (for which, intuitively, the user is better able to sense a physically plausible variation than for ε), or even for the effective turbulent diffusivity. Other motives for seeking an alternative variable have been to adopt a quantity whose boundary conditions (e.g. at a solid wall or at a free-surface) can be prescribed with less ambiguity; or to

https://doi.org/10.1017/9781108875400.007 Published online by Cambridge University Press

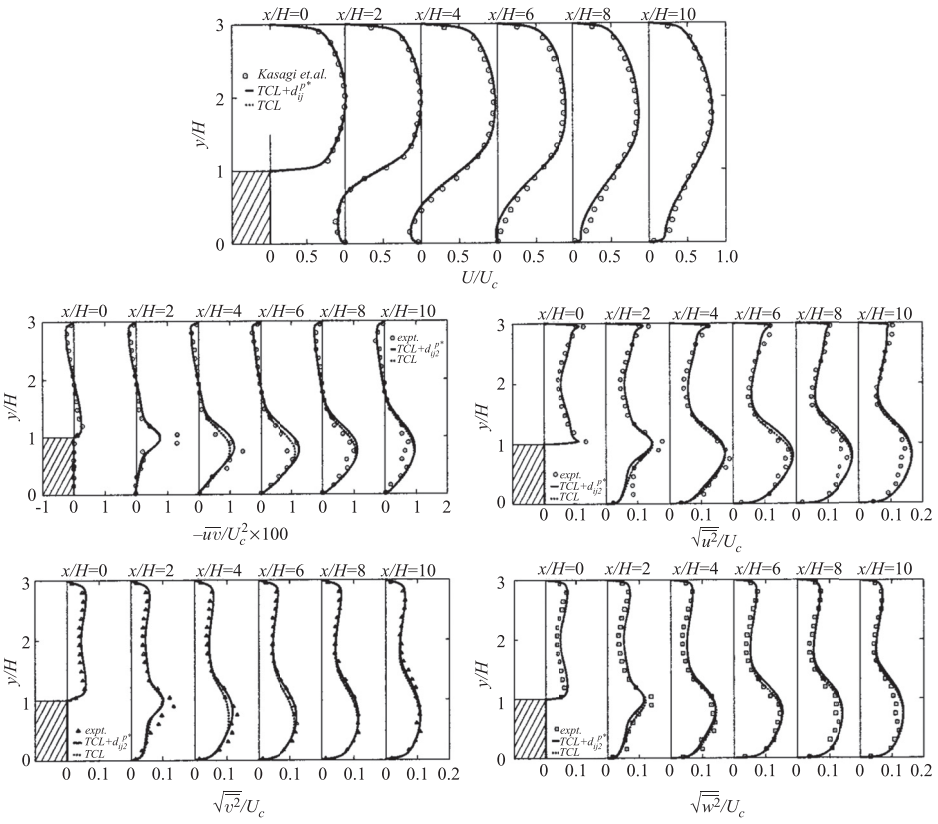

Fig. 5.4 Flow over a backward-facing step for an expansion ratio of 1.5. Symbols: Experiment (Kasagi and Matsunaga, 1995); lines computations with and without the inclusion of modelled pressure diffusion. From Suga (2004b).

provide an equation that is less prone to numerical instabilities than the ε equation, i.e. one that is numerically more robust.

To provide an overview of the range of alternative choices that have been explored, it is helpful to write the generic scale-determining variable as $k^m \varepsilon^n$, denoted by Ψ. The transport equation for Ψ (for high Re numbers, thus neglecting viscous and near-wall effects, and in the absence of body forces) is then supposed to be described by:

$$\frac{D\Psi}{Dt} = (c_{\psi 1}\mathcal{P}_k/\varepsilon - c_{\psi 2})\frac{\varepsilon\Psi}{k} + \frac{\partial}{\partial x_j}\left(\frac{\nu_t}{\sigma_\Psi}\frac{\partial \Psi}{\partial x_j}\right) + \mathcal{S}_\Psi \qquad (5.15)$$

where $\mathcal{S}_\Psi$ denotes additional sources that might be required to achieve satisfactory agreement for the common generic flows. Most of the entries in Table 5.2 have been made in the context of eddy-viscosity turbulence models while, at the other extreme, Davidov's (1961) third-moment closure provides transport equations for

https://doi.org/10.1017/9781108875400.007 Published online by Cambridge University Press

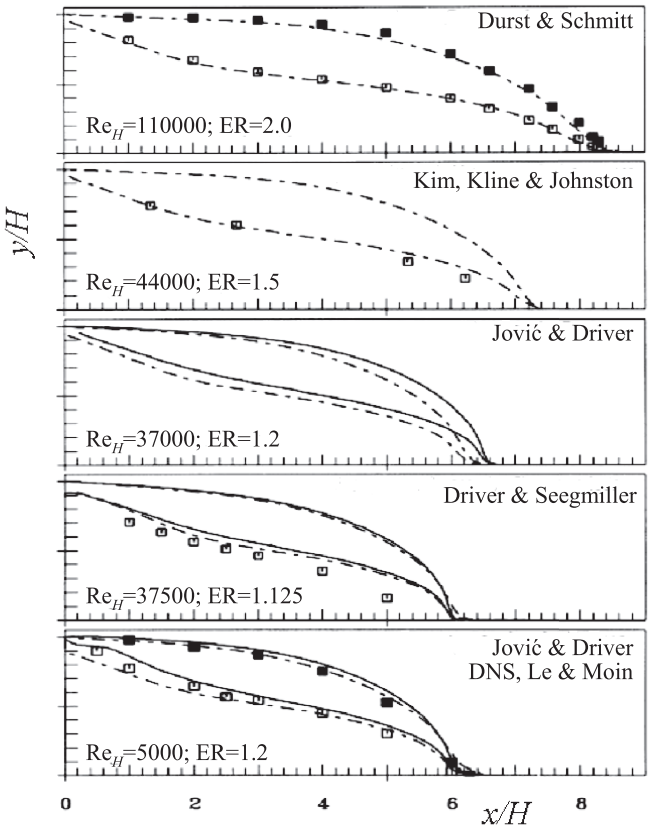

Fig. 5.5 Loci of dividing streamlines between recirculating and non-recirculating flow and of zero streamwise velocity in plane backward-facing step flow. Dependence on Reynolds number and expansion ratio. Symbols: Experiments or DNS data; —— Computations using model integrated to wall; — – — – Computations using wall functions (Ch. 8). Both computational strategies adopt Eq. (5.13). From Hanjalić and Jakirlić (1998).

$\overline{u_i u_j u_k}$ (i.e. the diffusion rate of $\overline{u_i u_j}$) and for both ε and *its* diffusion rate. The earliest proposal for a scale transport equation was made by Kolmogorov (1942) though his proposal for the quantity ω (which may be interpreted as ε/k) lacked any source term from the mean velocity field and was never used for sheared flows. The same variable, ω, has, however, repeatedly served as the subject of the second scale equation, an extensive historical account being provided by Wilcox (2000). The most widely applied version of the ω-equation was due to Wilcox (1988b). As remarked above, when applied to two-dimensional boundary layers developing in adverse pressure gradients, that version has proved to be significantly more reliable than the ε-equation (at least when none of the length-scale-damping practices discussed above was used with the latter equation). Moreover, it requires

https://doi.org/10.1017/9781108875400.007 Published online by Cambridge University Press

Table 5.2 *Alternative choices of scale-determining variable*

Model	Ψ	Dimension	ν_t/c_μ	m	n	$c_{\Psi 1}$	$c_{\Psi 2}$
$k-\varepsilon$	ε	$[m^2s^{-3}]$	k^2/ε	0	1	1.44	1.92
$k-\omega$	$\omega=\varepsilon/k$	$[s^{-1}]$	k/ω	-1	1	0.44	0.92
$k-\mathcal{T}$	$\mathcal{T}=1/\omega=k/\varepsilon$	[s]	$k\mathcal{T}$	1	-1	-0.44	-0.92
$k-l$	$l=k^{3/2}/\varepsilon$	[m]	$k^{1/2}l$	3/2	-1	0.06	-0.42
$k-kl$	$kl=k^{5/2}/\varepsilon$	$[m^3s^{-2}]$	$(kl)/k^{1/2}$	5/2	-1	1.06	0.58
$k-\tilde{\nu}_t$	$\tilde{\nu}_t=k^2/\varepsilon$	$[m^2s^{-1}]$	$\tilde{\nu}_t$	2	-1	0.56	0.08

little modification if one chooses or needs to carry the numerical solution all the way to the wall (Chapter 6). The seemingly inconvenient wall boundary condition $\omega_w=\infty$ can be easily dealt with by assigning a very large value to ω, or applying a hyperbolic variation, $\omega\propto 1/y^2$, at the first grid point. In consequence, the equation has been widely adopted in boundary-layer applications in aeronautics where the reliable prediction of separation is essential. However, as reported in Wilcox (2000) (his Table 4.5, p. 140), that original version of the equation was distinctly unsuccessful in reproducing the behaviour of self-preserving free shear flows. A major re-optimization of the coefficients was thus undertaken which, it is claimed, retains the performance of the original for boundary-layer flows but achieves much improved behaviour for free shear flows. This revised form of ω-equation may be written as:

$$\frac{D\omega}{Dt}=\alpha\frac{\omega}{k}\mathcal{P}_k-\beta\omega^2+\frac{\partial}{\partial x_j}\left[\left(\nu\delta_{ij}+\frac{c_\omega\overline{u_iu_j}}{\omega}\right)\frac{\partial\omega}{\partial x_i}\right] \tag{5.16}$$

where $\alpha=0.52$; $\beta=0.072[1+70\chi_\omega]/[1+80\chi_\omega]$ and

$$\chi_\omega\equiv\left|\frac{W_{ij}W_{jk}S_{ki}}{(0.09\omega)^3}\right|.$$

In fact, while the GGDH approximation has been inserted above for the diffusion of ω, Wilcox's (2000) prescription for this term was the usual simple eddy diffusivity model, i.e. where $c_\omega\overline{u_iu_j}/\omega$ is replaced by $0.5k/\omega$. Indeed, the proposed form for (5.16) has arisen from calibration within a two-equation linear eddy-viscosity formulation; but Wilcox also recommends the same form for use within his second-moment closure, Wilcox (2000). Notice that the product of vorticity and strain rate appearing in χ_ω is the same grouping as was used as a supplementary source term by Pope (1978) to remove the plane jet/round jet anomaly. Wilcox (2000) specifically calibrated Eq. (5.16) to ensure that the plane jet, the round jet and the radial jet *all* displayed a growth rate close to that of available experimental data. Whether or not the indicated form is also satisfactory for the case of the round jet in a moving stream (e.g. Forstall and Shapiro, 1950) apparently remains to be determined. Nevertheless, Wilcox's textbook reports a substantial range of near-wall flows, of

https://doi.org/10.1017/9781108875400.007 Published online by Cambridge University Press

both boundary layers and recirculating flows, that gives a good overall impression of the capabilities and shortcomings of the equation when used with his closure of the stress-transport equation.

Before leaving discussion of the ω equation, it has been reported (e.g. Menter, 1994) that the equation is undesirably sensitive to the free-stream boundary condition. A non-zero value of k must be prescribed and the flow behaviour can be highly sensitive to that value, even at levels where free-stream turbulence in practice has negligible effect. To escape that problem, Menter (1994) has proposed a composite form which uses the ω equation close to a solid wall, but which transforms into the ε equation away from walls by using a set of empirical blending functions.

Of the other transport equations for the second variable, the earliest to be applied to a range of free shear flows was the kl-equation proposed by Rodi and Spalding (1970), based on the earlier derivation by Rotta (1951, 1968). However, when that same approach was applied to simple near-wall boundary layers, it was found that a substantial correction term had to be introduced to make the equation compatible with the semi-logarithmic mean velocity distribution close to the wall, Ng and Spalding (1972). Consequently, the form has been subsequently little used.[7]

How may one determine the 'best' scalar variable? Indeed, is there really a *best* version or is it essentially a question of 'horses for courses'? Evidently, a transport equation for any chosen variable (i.e. for particular values of m and n) can be derived from any other. For homogeneous flows (zero diffusion) these equations are all equivalent since the source and sink terms are algebraic in form. However, for inhomogeneous flows, the equations will differ in the diffusion term, and it is *this* that predominantly leads to a range of performances from models adopting different choices of Ψ.

If the ε equation is used as the basis for comparison, equations for other variables (in combination with the k-equation) can be derived in the form (5.15) with the coefficients of the source terms taking the values

$$c_{\Psi i} = m + n c_{\varepsilon i} \tag{5.17}$$

where i may take the values 1 or 2 (for mean-strain production and viscous destruction). The resultant values of these coefficients for different choices for the physical quantity Ψ is given in Table 5.2.[8]

[7] More recently, Menter and Egorov (2010) have revived Rotta's (1951) original kl model and included the second derivative of the mean velocity (rather than the third derivative originally proposed by Rotta). For presentational purposes the second-velocity derivative was re-expressed in terms of the von Karman length scale, which was employed as an additional turbulence scale (hence, the label applied to the approach: 'scale-adaptive-simulations'. This topic is considered further in §10.6.)

[8] The transformation of the scale equation from one variable to another is straightforward. First Ψ is differentiated by parts:

$$\frac{D\Psi}{Dt} \equiv \frac{D\left(k^m \varepsilon^n\right)}{Dt} = \varepsilon^n m k^{m-1} \frac{Dk}{Dt} + k^m n \varepsilon^{n-1} \frac{D\varepsilon}{Dt} = m \frac{\Psi}{k} \frac{Dk}{Dt} + n \frac{\Psi}{\varepsilon} \frac{D\varepsilon}{Dt}.$$

https://doi.org/10.1017/9781108875400.007 Published online by Cambridge University Press

5.3 Multi-scale approaches

Since the inclusion of a scale equation greatly widened the applicability of models that had formerly had the length scale prescribed algebraically, perhaps the addition of a second scale equation could extend a model's range of performance still further. Moreover, the cost implications are negligible since, for a 3D flow, one is already solving 11 differential equations even in an isothermal flow. So, why not add a further scale equation to make it a round dozen? This was the line of thought that appears to have led Schiestel (1974) (see also Gosse and Schiestel, 1974) to suggest a closure in which a transported-scale equation was solved for the fine-scale motion in addition to one for the large-scale, energy-containing motions. The former variable (essentially the inverse square of the Taylor microscale) was used in modelling the dissipative terms while a macro-length-scale equation (similar to that used by Rotta, 1951) was solved to determine the effective diffusivity and in forming a time scale associated with the 'slow' part of the pressure-strain term (if stress-transport equations were solved). The cited references show applications to a number of simple thin shear flows.

Subsequently, Schiestel, in collaboration with the present authors, formulated a different multi-scale approach based on an informal partitioning of the energy

Replacing the material derivatives Dk/Dt and $D\varepsilon/Dt$ by the right-hand sides of their respective equations leads to

$$\frac{D\Psi}{Dt} = m\frac{\Psi}{k}\left(\mathcal{P}_k - \varepsilon + \mathcal{D}_k\right) + n\frac{\Psi}{\varepsilon}\left(c_{\varepsilon 1}\frac{\mathcal{P}_k\varepsilon}{k} - c_{\varepsilon 2}\frac{\varepsilon^2}{k} + \mathcal{D}_\varepsilon\right)$$

$$\text{or } \frac{D\Psi}{Dt} = \left[\underbrace{(m + nc_{\varepsilon 1})}_{c_{\Psi 1}}\mathcal{P}_k - \underbrace{(m + nc_{\varepsilon 2})}_{c_{\Psi 2}}\varepsilon\right]\frac{\Psi}{k} + m\frac{\Psi}{k}\mathcal{D}_k + n\frac{\Psi}{\varepsilon}\mathcal{D}_\varepsilon$$

$$\text{where } \mathcal{D}_\phi \equiv \frac{\partial}{\partial x_j}\left(\frac{\nu_t}{\sigma_\phi}\frac{\partial\phi}{\partial x_j}\right)$$

.

This confirms Eq. (5.17) for the source-term coefficients. If, however, the turbulent diffusion of Ψ is to be expressed simply in terms of its gradient as indicated by Eq. (5.15), the exact transformation from the k and ϵ equations gives

$$\frac{D\Psi}{Dt} = \underbrace{c_{\Psi 1}\frac{\mathcal{P}_k\Psi}{k}}_{\mathcal{P}_\Psi} - \underbrace{c_{\Psi 2}\frac{\Psi^{(1+1/n)}}{k^{(1+m/n)}}}_{\Upsilon_\Psi} + \underbrace{\frac{\partial}{\partial x_j}\left(\frac{1}{\sigma_\varepsilon}\frac{\partial\Psi}{\partial x_j}\right)}_{(\mathcal{D}_\Psi\sigma_\Psi/\sigma_\varepsilon)} + \mathcal{S}_\Psi$$

where

$$\mathcal{S}_\Psi = \left(1 - \frac{\sigma_k}{\sigma_\varepsilon}\right)m\frac{\Psi}{k}\mathcal{D}_k + \frac{\nu_t\Psi}{\sigma_\varepsilon}\left[\frac{1-n}{n}\left(\frac{1}{\Psi}\frac{\partial\Psi}{\partial x_j}\right)^2 - 2\frac{m}{n}\left(\frac{1}{\Psi}\frac{\partial\Psi}{\partial x_j}\right)\left(\frac{1}{k}\frac{\partial k}{\partial x_j}\right) + \frac{m\,(m+n)}{n}\left(\frac{1}{k}\frac{\partial k}{\partial x_j}\right)^2\right].$$

For convenience, irrespective of the definition of Ψ, one would like to omit the extra term $\mathcal{S}_\Psi$, but for some choices of m and n this leads to seriously inaccurate results even in simple generic flows. Thus, for example, both the equations for l ($m = 3/2$; $n = -1$) and kl ($m = 5/2$; $n = -1$) require an extra term to return broadly correct velocity profiles even for such simple cases as plane-channel or flat-plate boundary-layer flows.

https://doi.org/10.1017/9781108875400.007 Published online by Cambridge University Press

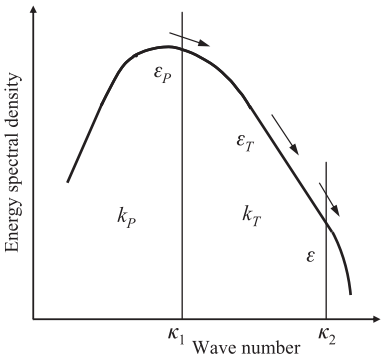

Fig. 5.6 The spectral division adopted in the split-spectrum concept.

spectrum, as illustrated in Fig. 5.6, Hanjalić *et al.* (1980). As with the original strategy in Schiestel (1974), the goal was to address situations where the turbulence was far from spectral equilibrium. For this purpose, the energy spectrum is divided into a production region and a transfer region (see the discussion on this subject in Chapter 3). Within the production region, turbulence energy is captured from the mean flow but, while there is no direct dissipation of energy, there is a spectral flow of energy from the region, due to the continual breaking down of the eddy size (corresponding to an increase in wave number). Within the transfer region there is, thus, an energy inflow from the production region, ε_P, but the generation by the mean strain is assumed negligible. The energy outflow from this region, ε_T, is supposed to be equal to that directly dissipated, i.e. ε. The task, in the present context, is thus to provide appropriate transport equations for ε_P and ε_T.

The system of differential equations for the partial energies and the energy transfer rate are written as:

$$\frac{Dk_P}{Dt} = \mathcal{P}_k - \varepsilon_P + \mathcal{D}_{k_P} \tag{5.18}$$

$$\frac{Dk_T}{Dt} = \varepsilon_P - \varepsilon_T + \mathcal{D}_{k_T} \tag{5.19}$$

$$\frac{D\varepsilon_P}{Dt} = c_{P1}\mathcal{P}_k\frac{\varepsilon_P}{k_P} + c'_{P1}k_P\frac{\partial U_l}{\partial x_m}\frac{\partial U_i}{\partial x_j}\epsilon_{lmk}\epsilon_{ijk} - c_{P2}\frac{\varepsilon_P^2}{k_P} + \mathcal{D}_{\varepsilon_P} \tag{5.20}$$

$$\frac{D\varepsilon_T}{Dt} = c_{T1}\frac{\varepsilon_P\varepsilon_T}{k_T} - c_{T2}\frac{\varepsilon_T^2}{k_T} + \mathcal{D}_{\varepsilon_T}. \tag{5.21}$$

In the above, the diffusion terms were uniformly represented by the GGDH in the form:

$$\mathcal{D}_\phi = 0.22\frac{\partial}{\partial x_k}\left(\overline{u_k u_l}\frac{k_P}{\varepsilon_P}\frac{\partial\phi}{\partial x_l}\right). \tag{5.22}$$

https://doi.org/10.1017/9781108875400.007 Published online by Cambridge University Press

Notice that, in the ε_P equation, as in the single-scale approach of Hanjalić and Launder (1980) considered in §5.1, a supplementary source of mean-strain energy transfer is included. The coefficient of the sink term in that equation, c_{P2}, may be found from grid-turbulence decay. It is assumed that during the decay the spectrum reaches an equilibrium shape, i.e. that k_P/k_T does not change. Thus, with $k_P \propto k \propto t^{-n}$, it is readily inferred that $c_{P2} = 1 + 1/n$. A value of 1.25 for n is assumed giving an asymptotic value for c_{P2} of 1.8.

A choice that needs to be made prior to assigning values to the remaining model coefficients is the proportion of the total turbulent kinetic energy contained in the production and transfer regimes under equilibrium grid-turbulence decay. (Essentially, this is equivalent to choosing where the boundary between the production and transfer zones should be drawn.) Hanjalić *et al.* (1980) chose k_P equal to k_T in that grid-turbulence-decay limit. This is the smallest value of k_P/k_T found since, in situations where there is a direct production of energy, this will have the effect of increasing k_P relative to k_T.

It is also noted that, with a split-spectrum approach, the value of k_P/k_T and the ratio of the two energy transfer rates are both available as further dimensionless parameters of which the coefficients could be made dependent. This flexibility was introduced into the coefficients c_{P2} and c_{T1}. The complete set of coefficients chosen for the energy-transfer equations is:

$$c_{P1} = 2.2;\ \ c'_{P1} = -0.11;\ \ c_{P2} = 1.8 - 0.3\frac{k_P - k_T}{k_P + k_T};\ \ c_{T1} = 1.08\frac{\varepsilon_P}{\varepsilon_T};\ \ c_{T2} = 1.15$$

The above set of equations was solved for a number of test cases in conjunction with essentially the stress-transport equations from the Basic Model presented in Chapter 4. With the multi-scale scheme, however, ε_P/k_P was used as the inverse time scale both in the slow part of the pressure-strain term, Φ_{ij1} (Eq. (4.7)), and in the diffusion model (Eq. (4.19)), while ε_T was adopted in the stress dissipation rate (Eq. (4.17)).

The application of the scheme to the evolution of grid turbulence through a sharp area contraction brings out clearly the potential of the method in accounting for rapidly developing flows. The test case for which results are shown in Fig. 5.7 is the one-dimensional flow of grid turbulence through a 4:1 area contraction followed by its subsequent decay in the absence of further straining, Uberoi (1957). To remove any contribution of possible closure weaknesses in the stress-transport equations, simply the four basic equations for k_P, k_T, ε_P and ε_T were solved with the mean velocity field and the turbulent stresses appearing in the production term of the k_P and ε_P equations being directly supplied from the experimental data. Figure 5.7a indicates that in the initial decay phase at uniform velocity ε_T is larger than ε_P but that, in the flow-contraction region, because of the action of mean-strain generation

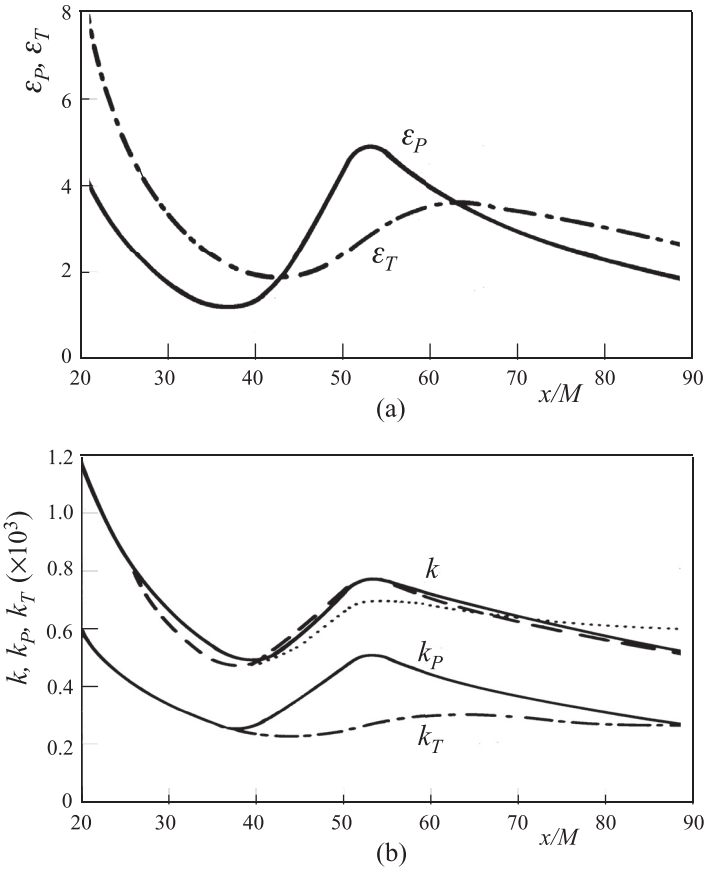

Fig. 5.7 Two-scale model of turbulence energy development in 4:1 contraction (from Hanjalić *et al.*, 1980). (a) Energy transfer rates, (b) turbulence energy levels.– – – – Experiment, Uberoi (1957); —— Two-scale model; ····· Single-scale model.

in its source term, ε_P rapidly increases to nearly twice that of ε_T. Finally, as the flow continues downstream at uniform velocity, ε_T decays less rapidly than ε_P as the turbulent field gradually reverts towards equilibrium decay. The effects of the changing relative values of ε_P and ε_T on the turbulent kinetic energy are shown in Fig. 5.7b. Recall that the model coefficients were chosen so that in equilibrium grid-turbulence decay the same energy levels would be found in the production and transfer parts of the spectrum. On the application of the streamwise straining due to the flow contraction k_P rises sharply, while k_T undergoes a later and much weaker increase. When the two component parts of the energy are added together, one finds an evolution of k closely in accord with the experiments. By contrast, the corresponding computations with a single-scale system exhibit a too slow rise of k in the strained region and thereafter a too slow decrease.

https://doi.org/10.1017/9781108875400.007 Published online by Cambridge University Press

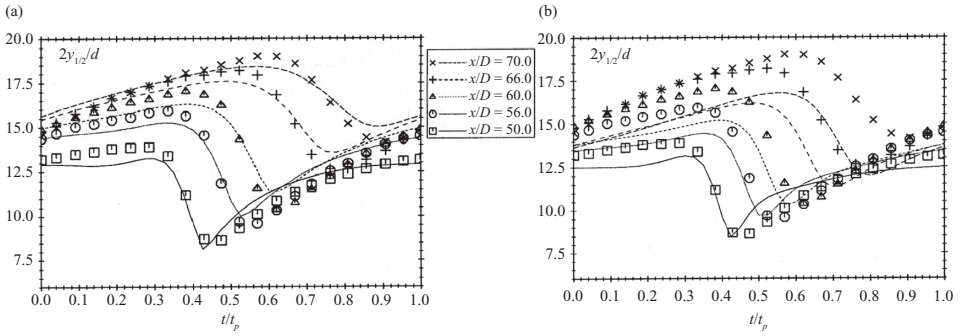

Fig. 5.8 Computations of pulsed round jet from Bremhorst *et al.* (2003). Symbols: Experiments, Bremhorst and Gehrke (2000); Lines: Computations. (a) Two-scale model; (b) TCL model.

The model has also been applied to the pulsed jet studied experimentally by Bremhorst and Gehrke (2000). In Bremhorst *et al.* (2003), those data were compared with predictions obtained with the split-spectrum approach and with the TCL model. This pair of schemes was chosen as each model predicted with tolerably small error both the steady round and plane jets in stagnant surroundings (i.e. they essentially resolved the round/plane jet anomaly). Figure 5.8 compares the jet spreading rate at many points through the cycle for five stations downstream, the experimental data being shown as symbols. Evidently, the multi-scale scheme is far more successful than the TCL scheme in capturing the observed behaviour of the pulsed jet. Further comparisons of this test flow were later made by Kim *et al.* (2008), essentially confirming the conclusions of the earlier computations.

Other applications of the model to steady flows, both to free shear flows and to boundary layers in adverse pressure gradients, are reported by Hanjalić *et al.* (1980). The model's performance, while better than earlier single-scale stress-transport models, showed hardly any difference from the results of the single-scale scheme developed in parallel by Hanjalić and Launder (1980), which, as noted above, also included the supplementary source with coefficient c'_{P1}. The reason that the single and multi-scale model gave nearly the same results became clear on examining the distribution of turbulent kinetic energy between the production and transfer regions: in shear flows some 90% of the energy resides in the production region – so that, in steady shear flows, the multi-scale model effectively acts as a single-scale scheme! This behaviour is not an inevitable consequence of the approach. However, to keep a larger proportion of the energy in the transfer region under steady shear requires shifting the boundary between the production and transfer regions to lower wave number and consequently abandoning the idea that mean strain exerts no effect on turbulence in the transfer region.

Over the years following the original development of the multi-scale model, Schiestel's group (Schiestel, 1987; Gleize *et al.*, 1996; Chaouat and Schiestel, 2005, 2007; Schiestel and Dejoan, 2005) have made further contributions to developing multi-scale models. Their focus has especially been that of placing the energy-transfer equations on a more precise analytical base both for RANS closures as discussed here and within the context of LES (and also models that adopt a blending of the two approaches, as considered in Chapter 10). Schiestel's (2008) textbook provides an overview. The general case developed by Schiestel has included multiple spectral slices though in practice, in actually applying the scheme, just two slices have been used, as in the originally conceived model. A further elaboration has been a proposal to solve separate stress-transport equations for the large-scale and fine-scale parts, Schiestel (1987). While the scheme led to interesting predictions for one-dimensional flows, it is doubtful whether in complex three-dimensional flows it would be seen as worthwhile to solve transport equations for two second-rank tensor quantities.

Following Schiestel (1987) and Clark and Zemach (1995), Cadiou *et al.* (2004) have also developed a multi-scale model based on the integration of a presumed spectral distribution of energy in conjunction with second-moment closure. In contrast to Schiestel's (1987) strategy of spectrally splitting the stress tensor, the turbulent stress tensor was considered in its integral form in which the sink terms were represented by the stress dissipation rate (modelled analogously to the single-scale model, Eq. (4.17). The spectral transfer ε_P was used in combination with the kinetic energy, k, to define the time scale employed for modelling the pressure-strain and turbulent diffusion for the stresses. The two-scale variables, ε_P and ε_T, are obtained from separate equations analogous to Eqs. (5.20) and (5.21). In fact, while the ε_T equation closely resembled Eq. (5.21) (but with a production term, $c'_{T1}\mathcal{P}_k\varepsilon_T/k$, included), Cadiou *et al.* also explored an alternative equation for $kl \equiv k^{5/2}/\varepsilon_P$, from which ε_P could be obtained.[9] For homogeneous flows the kl and ε_P equations are convertible one from another, though a difference may appear depending on the treatment of the sink term, i.e. whether and in which form $\varepsilon_T$is used. For more discussion, see Stawiarski and Hanjalić (2005). An eddy-viscosity variant of the model was also considered, which solves a transport equation for the total kinetic energy, k, instead of $\overline{u_i u_j}$, in combination with the two-scale equations.

The $k - kl - \varepsilon_T$ model was applied to the 4:1 contraction considered above and returned very nearly the same results as the original four-equation split spectrum

[9] Starting from the wave-number weighted integral of the energy spectrum $I^{(m)} = \int_0^{+\infty} \kappa^m E(\kappa) d\kappa$, different scale integral equations can be obtained for various values of the parameter m. It is readily seen that for $m = 1$, the integral equals the kinetic energy, k, for $m = 2$, it gives ε_T, whereas for $m = -1$, it provides the product of kinetic energy and the length scale, kl. Replacing l by $k^{3/2}/\varepsilon_P$ and using the k-equation leads to the transport equation for ε_P that can be written in a form that closely resembles Eq. (5.20) (though without the second term on the right-hand side).

https://doi.org/10.1017/9781108875400.007 Published online by Cambridge University Press

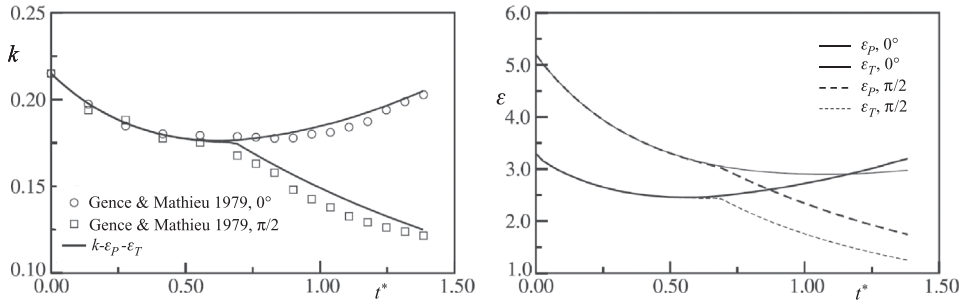

Fig. 5.9 (a) Turbulent kinetic energy and (b) scale variables, ε_P and ε_T, in a plane-strain distortion. Symbols: Experiments: Gence and Mathieu (1979); Lines: computations with the $k - \varepsilon_P - \varepsilon_T$ model (from Cadiou *et al.*, 2004).

model of Hanjalić *et al.* (1980) that appeared in Fig. 5.7. The second example, shown in Fig. 5.9, is the plane-strain experiment of Gence and Mathieu (1979). Here grid-generated turbulence is passed through a constant area duct in which the initially elliptic cross-section changes gradually to circular and then reverts back to the original elliptic cross-section. The wind tunnel was constructed so that at the circular cross-section the downstream portion of the duct could be rotated on its axis relative to the upstream portion so there was the possibility of the flow being strained in a different sense than in the first half. Two cases were considered, corresponding to a duct rotation of zero and 90 degrees. The predicted kinetic energy evolution shown on the left shows very close agreement with experiments for both cases, while the two-scale variables shown on the right illustrate the scale dynamics.

To offer an overall assessment, despite the clear conceptual merit of including a multi-scale approaches to account for large departures from spectral equilibrium, it has only been in rapidly deformed and periodic flows that the power of the approach has shown unequivocal advantages over single-scale schemes. Moreover, it seems likely that the forms currently used are still some way from optimal.

5.4 Determining $\varepsilon_{\theta\theta}$, the dissipation rate of $\overline{\theta^2}$

In principle, one would expect to use some broadly similar route to those discussed in §5.1 and §5.2 when the process of interest is heat or mass transfer through a fluid in turbulent motion – that is, a scale equation for $\varepsilon_{\theta\theta}$ or some equivalent. However, if we exclude force-field effects, thermal turbulence owes its existence to dynamic turbulence created by deformations of the mean velocity field; so there would seem to be an argument for using the dynamic field to provide the time or length scales for the thermal turbulence, too. In fact, different views are found in the literature as to whether one may satisfactorily approximate thermal turbulence scales by way of

https://doi.org/10.1017/9781108875400.007 Published online by Cambridge University Press

the dynamic scales. The present brief account thus attempts to provide an overview of strategies applied.

The early attempts to model the decay of temperature fluctuations via transport equations considered homogeneous, nearly isotropic turbulence decay, e.g. Lumley and Newman (1977). The feature of the scalar turbulence especially considered was the fact that $r \equiv k\varepsilon_{\theta\theta}/(\overline{\theta^2}\varepsilon)$, the dynamic-to-scalar time-scale ratio[10] (which could be made to take very different values at the start by altering the spacing of heated wires in the turbulence-generating grid array, Warhaft and Lumley, 1978), subsequently evolved only very slowly downstream.[11] Newman *et al.* (1981) and Elghobashi and Launder (1983) and many later workers thus adopted a transport equation for $\varepsilon_{\theta\theta}$ of the form:

$$\frac{D\varepsilon_{\theta\theta}}{Dt} = -c_{\varepsilon_{\theta 2}}\frac{\varepsilon_{\theta\theta}}{\overline{\theta^2}}\overline{\theta u_j}\frac{\partial \Theta}{\partial x_j} - c_{\varepsilon_{\theta 3}}\frac{\varepsilon_{\theta\theta}^2}{\overline{\theta^2}} - c_{\varepsilon_{\theta 4}}\frac{\varepsilon\,\varepsilon_{\theta\theta}}{k} + \frac{\partial}{\partial x_j}\left(c_{\varepsilon_\theta}\overline{u_j u_k}\,\mathcal{T}\frac{\partial \varepsilon_{\theta\theta}}{\partial x_k}\right). \quad (5.23)$$

Newman *et al.* (1981) showed that provided $c_{\varepsilon_{\theta 3}}$ was greater than unity, in the absence of mean temperature gradients the equation did lead to the time-scale ratio approaching an asymptotic equilibrium; but, because experiments showed that that approach was only very slow, the coefficient should only be slightly greater than unity. The values adopted in Elghobashi and Launder (1983) for the above coefficients are:

$$c_{\varepsilon_{\theta 2}} = 2.0; \quad c_{\varepsilon_{\theta 3}} = 1.1; \quad c_{\varepsilon_{\theta 4}} = 0.8; \quad c_{\varepsilon_\theta} = 0.35$$

where the time-scale $\mathcal{T}$ was taken as the purely thermal scale, i.e. $\mathcal{T} = \mathcal{T}_\theta \equiv \overline{\theta^2}/\varepsilon_{\theta\theta}$. The same time scale was also used in the slow part of the pressure-temperature-gradient correlation which had the effect (compared with using a mixed thermal-dynamic time scale) of halving the recommended decay coefficient, $c_{\theta 1}$ (cf. the discussion in connection with Eq. (4.8)), to a little over 2.0 (i.e. of bringing it closer to the corresponding return-to-isotropy coefficient in the stress-transport equation).

Jones and Musonge (1988) considered the more general case where mean velocity gradients were also present. Their equation is similar in form to that given above though because they included shear flows in the range of test cases, a term containing the turbulence energy generation rate was included. Moreover, in the term containing mean temperature gradients, the dynamic time scale was preferred to the thermal time scale:

[10] The reciprocal of the above time-scale ratio is also frequently used, $R \equiv (\overline{\theta^2}/\varepsilon_{\theta\theta})/(k/\varepsilon)$.

[11] Other examples of non-universal time-scale ratios where shear and/or buoyancy play substantial roles are cited by Newman *et al.* (1981).

https://doi.org/10.1017/9781108875400.007 Published online by Cambridge University Press

$$\frac{D\varepsilon_{\theta\theta}}{Dt} = c_{\varepsilon_{\theta 1}}\frac{\varepsilon_{\theta\theta}}{k}\mathcal{P}_k - c'_{\varepsilon_{\theta 2}}\frac{\varepsilon}{k}\overline{\theta u_j}\frac{\partial\Theta}{\partial x_j} - c_{\varepsilon_{\theta 3}}\frac{\varepsilon_{\theta\theta}^2}{\overline{\theta^2}} - c_{\varepsilon_{\theta 4}}\frac{\varepsilon\,\varepsilon_{\theta\theta}}{k} + \frac{\partial}{\partial x_j}\left(c_{\varepsilon_\theta}\frac{k}{\varepsilon}\overline{u_j u_k}\frac{\partial\varepsilon_{\theta\theta}}{\partial x_k}\right) \tag{5.24}$$

with: $c_{\varepsilon_{\theta 1}} = 1.4$; $c'_{\varepsilon_{\theta 2}} = 1.6$; $c_{\varepsilon_{\theta 3}} = 1.0$; $c_{\varepsilon_{\theta 4}} = 0.9$ $c_{\varepsilon_\theta} = 0.22$.

They applied the above equation within a second-moment closure to a range of homogeneous and inhomogeneous simply sheared flows with impressive results. A similarly wide range of free flows was successfully examined by Craft (1991) also using a version of Eq. (5.24) in conjunction with the TCL closure (see Craft and Launder, 1989, 1991) in which:

$$c_{\varepsilon_{\theta 1}} = 2.6/r; \quad c'_{\varepsilon_{\theta 2}} = 1.6/r; \quad c_{\varepsilon_{\theta 3}} = 1.0f; \quad c_{\varepsilon_{\theta 4}} = 0.92f;$$
$$c_{\varepsilon_\theta} = 0.18 \text{ where } f = \left(1 + {}^1\!/_2\, A_2^{1/2} A\right)^{-1}.$$

Moreover, in the first term on the right of Eq. (5.24), instead of strictly the production of k, Craft (1991) found that the eddy-viscosity form of $\mathcal{P}_k$, i.e. $\nu_t(\partial U_i/\partial x_j)^2$ gave overall better results.

While the above studies had examined exclusively free flows, several groups in Japan (notably those of the late Professors Nagano and Kasagi) have addressed problems of heat transfer through wall-bounded shear flows for a variety of thermal boundary conditions and Prandtl numbers in which a transport equation for $\varepsilon_{\theta\theta}$ has been solved. The focus has been almost exclusively on flows for which DNS data are available to assist the calibration of the various terms requiring modelling, with especial focus being given to the low-Reynolds-number sublayer. This work has been summarized in some detail by Nagano (2002) in a chapter of the book edited by Launder and Sandham (2002). For that reason no attempt is made to repeat that coverage here. It is worth noting, however, that some of the source-term coefficients are assigned substantially smaller values than in the free shear flow models discussed above; for example, the high-Reynolds-number asymptotes proposed by Nagano (2002) are:

$$c_{\varepsilon_{\theta 1}} = 0.77; \quad c_{\varepsilon_{\theta 2}} = 1.8; \quad c_{\varepsilon_{\theta 3}} = 1.0; \quad c_{\varepsilon_{\theta 4}} = 0.9.$$

Despite the considerable research efforts summarized above, a large proportion of the CFD community still prefers to prescribe the thermal to dynamic time-scale ratio rather than solve a transport equation for $\varepsilon_{\theta\theta}$. While acknowledging that such simplified approaches cannot deal with extreme situations such as the grid-turbulence decay with different initial levels of r, it is felt that, for the majority of flows, a simpler algebraic approach offers a satisfactory and less costly route. The use of a constant time-scale ratio (Spalding, 1971) is now recognized to have only limited use but later contributions have linked values of r to stress or heat-flux

invariants. For example, Craft *et al.* (1996a) recommended:

$$r = 1.5\,(1 + A_{2\theta})\,; \quad A_{2\theta} \equiv \left(\overline{\theta u_i}\right)^2 / k\overline{\theta^2} \tag{5.25}$$

a version currently widely used for free shear flows, including flows substantially modified by buoyancy. Indeed, that approach is now generally preferred by the Manchester group to the transport-equation strategy of Craft and Launder (1989) noted above.

https://doi.org/10.1017/9781108875400.007 Published online by Cambridge University Press

6

Modelling in the immediate wall vicinity and at low Re_t

6.1 The nature of viscous and wall effects: options for modelling

The turbulence models considered in earlier chapters were based on the assumption that the turbulent Reynolds numbers were high enough everywhere to permit the neglect of viscous effects. Thus, they are not applicable to flows with a low bulk Reynolds number (where the effects of viscosity may permeate the whole flow) or to the viscosity-affected regions adjacent to solid walls (commonly referred to as the *viscous sublayer* and *buffer* regions but which we shall normally collectively refer to as the *viscous region*), which always exist on a smooth wall irrespective of how high the bulk Reynolds number may be. In other words, while at high Reynolds number, viscous effects on the energy-containing turbulent motions are indeed negligible throughout most of the flow, the condition of no-slip at solid interfaces always ensures that, in the immediate vicinity of a wall, viscous contributions will be influential, perhaps dominant. Figure 6.1 shows the typical 'layered' composition for a near-wall turbulent flow (though with an expanded scale for the near-wall region) as found in a constant-pressure boundary layer, channel or pipe flow. Although the thickness of this viscosity-affected zone is usually two or more orders of magnitude less than the overall width of the flow (and decreases as the Reynolds number increases), its effects extend over the whole flow field since, typically, half of the velocity change from the wall to the free stream occurs in this region.

Because viscosity dampens velocity fluctuations equally in all directions, one may argue that viscosity has a 'scalar' effect. However, turbulence in the proximity of a solid wall or a phase interface is also subjected to non-viscous damping arising from the impermeability of the wall and the consequent reflection of pressure fluctuations. This 'wall-blocking' effect, which is also felt outside the viscous layer well into the fully turbulent wall region, directly dampens the velocity fluctuations in the wall-normal direction and thus it has a 'vector' character. A good illustration

https://doi.org/10.1017/9781108875400.008 Published online by Cambridge University Press

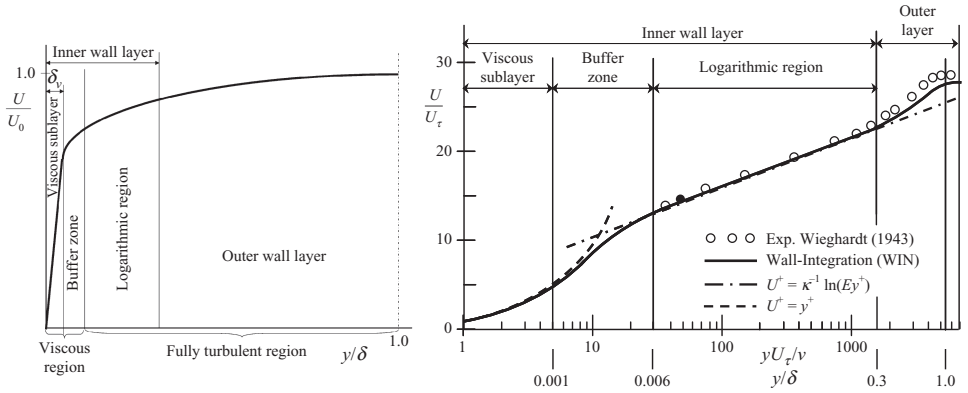

Fig. 6.1 Velocity distribution and the characteristic flow regions in a constant-pressure boundary layer. Left: a linear plot normalized with the free stream velocity U_0 and boundary-layer thickness δ. Right: the same profile in a semi-log plot $U^+ = U/U_\tau = f(yU_\tau/\nu)$, with experimental data of Wieghardt (1943), $\mathrm{Re}_\theta = 15,570$, and a computation with a WIN model.

of this effect is the reduction of the surface-normal velocity fluctuations that has been observed in flow regions close to a phase interface, where there are no viscous effects, for example the DNS of Perot and Moin (1995).

Non-viscous wall effects have already been recognized in Chapter 4 where the influence of the wall was accounted for by adding (for the simple linear models) 'wall-echo' corrections to the pressure-strain term, associated with the surface integral in the Poisson equation for pressure, Eq. (4.3), or by imposing empirical constraints (such as via the stress invariant A which vanishes in the two-component limit at a wall). The direct effect of the wall on turbulence becomes ever stronger, however, when approaching even closer to a rigid surface through the viscosity-affected layer. Thus, if the governing equations are to be integrated up to the wall (hereafter, the *Wall-INtegration* or 'WIN' strategy), in addition to including viscous effects, a number of other modifications to the turbulence models need to be introduced to account properly for the impact on the turbulence that a solid wall imposes.

Yet, provided that flow conditions are not too extreme, a popular approach that avoids the complications of the viscous region and the need for modifying the high-Re form of the turbulence models is commonly adopted. It draws on the fact that the important mean and turbulent flow quantities are nearly functions just of the normal distance from the wall (provided that all variables are non-dimensionalized by the wall shear stress, the density and the fluid viscosity). Thus, in making calculations of flow over rigid surfaces, all the dependent variables appearing in the closure scheme are matched to the 'universal' values at some point beyond the viscous region. In this way the viscosity-affected region is 'bridged' and, instead

https://doi.org/10.1017/9781108875400.008 Published online by Cambridge University Press

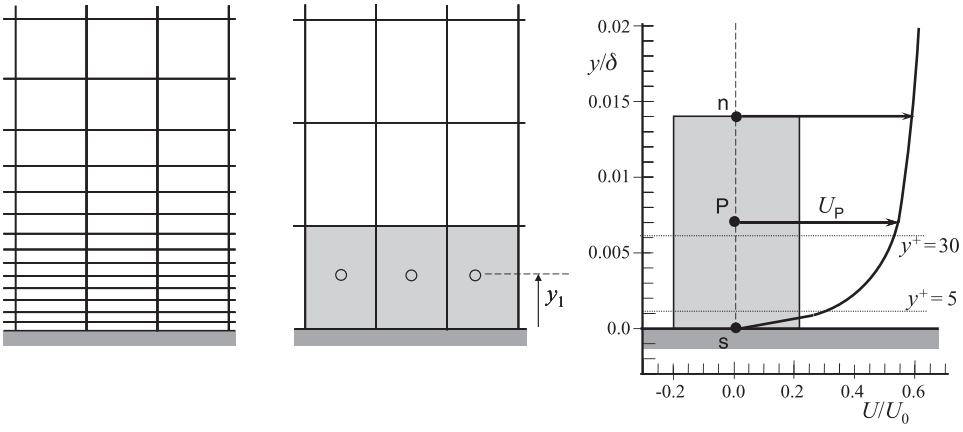

Fig. 6.2 Illustrations, from left, of computational grids for integration up to the wall (Wall Integration, WIN) and for wall functions (WF), with a typical velocity distribution and wall-nearest grid node P used in the WF approach.

of exact boundary conditions at the wall, these are replaced by conditions at the first grid node (lying outside the viscosity-affected layer) using a set of algebraic relations or *wall functions* (WF). These wall functions may be obtained either by prior integration of much simplified forms of the governing equations (momentum, energy, turbulence quantities) or by using experimental or DNS information about the variation of mean velocity, temperature or other scalars (plus the required turbulence variables) in terms of the non-dimensional wall distance and wall shear stress. This approach has long been regarded as an appealing, economical alternative to integration up to the wall, because – in principle – it makes it possible to use unmodified high-Re models and a much coarser computational grid than is needed to solve the flow and turbulence equations all the way to the wall. The two options are illustrated in Fig. 6.2.

The near-wall region is insufficiently universal, however, for the above approach to be satisfactory in all circumstances. Transpiration through the wall, steep streamwise pressure gradients, buoyancy, swirl (as, for example, near a spinning disc) and steep temperature gradients (due to large imposed wall heat fluxes or frictional heating) are some of the influences that may cause this region to differ from its so-called universal behaviour that is presumed to apply in the chosen wall function. Many other situations are even more critical, for example, separated and re-attaching flows.

The surest way to account for such influences is to extend the calculations up to the wall itself; but as implied above in the left illustration of Fig. 6.2, such computations require many more grid points clustered in the vicinity of the solid walls, frequently requiring an order-of-magnitude increase in computation time.

https://doi.org/10.1017/9781108875400.008 Published online by Cambridge University Press

At the practical level there is thus always an issue of whether it is better to save computational cost and turnaround time (or, equally, to use the computational time saved by covering the main part of the flow with a finer grid). In fact, the newer wall functions, considered in Chapter 8, can cope reasonably well with many of the complex flow features that lie beyond the scope of the original wall-function approaches. For flow situations that cannot be thus modelled, however, the WIN treatment to be presented in this chapter is advocated.

6.2 The structure of the near-wall sublayer

6.2.1 Wall-limiting behaviour of the Reynolds-stress and stress-dissipation components

For flows parallel and very close to an impermeable wall the rates of change of fluid velocity in the streamwise and spanwise directions (here denoted as x_1 and x_3, respectively) are small compared with the steep variation normal to the wall. The fluctuating velocity can then conveniently be expanded in a Taylor series in terms of the wall-normal coordinate x_2, i.e.[1]

$$u_i(x_2, t) = a_i + b_i x_2 + c_i x_2^2 + d_i x_2^3 + \cdots \tag{6.1}$$

where coefficients a_i, b_i and c_i are random functions of time and x_1 and x_3 (but not of x_2) with zero mean values. For flows in the continuum regime there is no relative velocity between a rigid, impermeable surface and the fluid in contact with it. This constraint applies not simply to the mean velocity in a turbulent flow but to the fluctuating turbulent velocities too, so that $a_i = 0$ in all fluctuating velocity components. Consequently, the Reynolds stresses all go to zero at the wall and thus the shear stress transmitted between the fluid and the wall must be exerted by viscous action alone, just as in a laminar flow. The turbulent velocity components do not all increase in a similar way as one moves away from the wall, however. Now, the continuity equation for the velocity fluctuations in an incompressible flow is divergence free, i.e.

$$\frac{\partial u_1}{\partial x_1} + \frac{\partial u_2}{\partial x_2} + \frac{\partial u_3}{\partial x_3} = 0. \tag{6.2}$$

This equation applies everywhere, including the fluid–wall interface, $x_2 = 0$. There, however, $\partial u_1/\partial x_1 = \partial u_3/\partial x_3 = 0$ since at the wall u_1 and u_3 are zero for all x_1 and x_3. It then follows from Eq. (6.2) that

[1] In parallel with the general index notation, $u_i = f(t, x_i)$, velocity fluctuations and coordinates will also sometimes be denoted in common Cartesian coordinates $u_i \equiv (u, v, w) = f(t, x, y, z)$, where y is the direction normal to the wall.

https://doi.org/10.1017/9781108875400.008 Published online by Cambridge University Press

$$\left.\frac{\partial u_2}{\partial x_2}\right|_{x_2=0} = 0. \tag{6.3}$$

Thus, from the above expansion, while u_1 and u_3 increase linearly with wall distance for small x_2, the component normal to the wall, u_2, can only increase as x_2^2. As a result, the turbulent stress components take the following wall asymptotes (i.e. for $x_2 \to 0$)

$$\begin{aligned}
\overline{u_1^2}(x_2) &= \overline{b_1^2}x_2^2 + \overline{2b_1c_1}x_2^3 + \left(2\overline{b_1d_1} + \overline{c_1^2}\right)x_2^4 + \cdots \\
\overline{u_2^2}(x_2) &= \overline{c_2^2}x_2^4 + \cdots \\
\overline{u_3^2}(x_2) &= \overline{b_3^2}x_2^2 + 2\overline{b_3c_3}x_2^3 + \left(2\overline{b_3d_3} + \overline{c_3^2}\right)x_2^4 + \cdots \\
\overline{u_1u_2}(x_2) &= \overline{b_1c_2}x_2^3 + (\overline{b_1d_2} + \overline{c_1c_2})x_2^4.
\end{aligned} \tag{6.4}$$

(The last of these equations presumes that u_1 *and* u_2 are correlated at the wall, i.e. that $\overline{b_1c_2}$ is non-zero or, equivalently, that $\lim_{x_2\to 0}(\overline{u_1u_2})^2 \big/ \overline{u_1^2}\,\overline{u_2^2} \neq 0$, as is well confirmed by DNS data.)

Note also that

$$\begin{aligned}
k &= \frac{1}{2}\Bigg[\underbrace{\left(\overline{b_1^2} + \overline{b_3^2}\right)}_{A}x_2^2 + \underbrace{2(\overline{b_1c_1} + \overline{b_3c_3})}_{B}x_2^3 \\
&\qquad + \underbrace{\left(\overline{c_1^2} + \overline{c_2^2} + \overline{c_3^2} + 2(\overline{b_1d_1} + \overline{b_3d_3})\right)}_{C}x_2^4 + \cdots\Bigg] \\
&= \frac{1}{2}(Ax_2^2 + Bx_2^3 + Cx_2^4 + \cdots).
\end{aligned} \tag{6.5}$$

Thus, in summary, for small x_2:

$$\overline{u_1^2} \sim \overline{u_3^2} \sim k \propto x_2^2, \quad \overline{u_2^2} \propto x_2^4, \quad \overline{u_1u_2} \propto x_2^3 \ . \tag{6.6}$$

These inferences are directly confirmed by Fig. 6.3, which shows the near-wall variation of the four stress components for the DNS of fully developed flow through a plane channel at two Reynolds numbers,[2] plotted in logarithmic coordinates and non-dimensionalized by the friction velocity and the kinematic viscosity. The lines superimposed on the DNS results have slopes 2, 3 and 4 and, as seen, these accord very well with the stress variations given in Eq. (6.6).

The fact that $\overline{u_1u_2}$ increases as the cube of the distance from the wall implies that initially, for small x_2, this turbulent shear stress will be negligible compared with

[2] Note the different definitions of the channel Reynolds number used: $\mathrm{Re}_\tau = hU_\tau/\nu$ and $\mathrm{Re}_m = 2hU_m/\nu$, where h is the channel half-width, U_τ is the wall friction velocity and U_m the channel mean (bulk) velocity.

https://doi.org/10.1017/9781108875400.008 Published online by Cambridge University Press

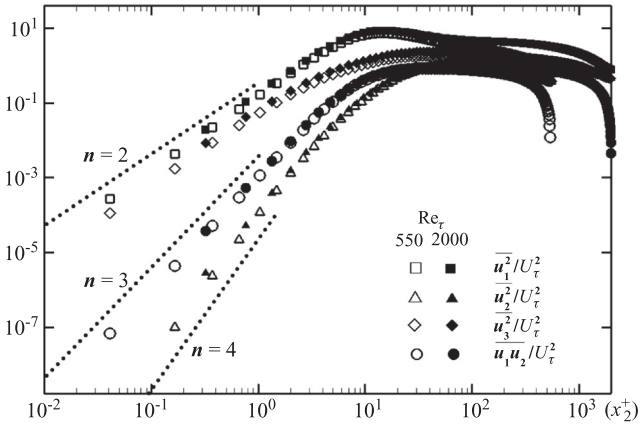

Fig. 6.3 Variation of turbulent stress components in a channel flow for $\mathrm{Re}_\tau = 550$ and 2,000, showing the slopes of the wall asymptotes. From DNS data of Hoyas and Jimenez (2006).

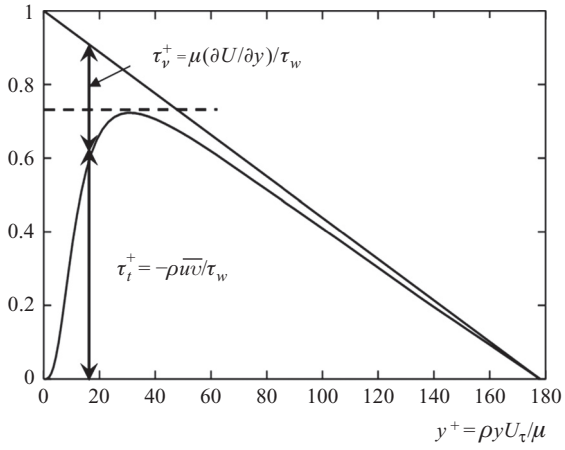

Fig. 6.4 A sketch of the turbulent, viscous and total shear stress across a fully developed channel or pipe flow

viscous shear stress. As one proceeds further from the wall, however, one enters a region where there is a rapid changeover to a regime where the turbulent stress becomes the dominant contributor to momentum transfer (Fig. 6.4). Since the total (viscous plus turbulent) shear stress is very nearly constant over what is a very thin layer (compared with the shear flow as a whole), there will inevitably be a rapid reduction in the slope of the mean velocity as one moves from a region where viscous action ($\nu\ \partial U_1/\partial x_2$) is the predominant mechanism for momentum transfer to one where most of the momentum transport is by turbulence ($-\overline{u_1 u_2}$). This rapid changeover is clearly evident from the mean velocity profiles in Fig. 6.1.

https://doi.org/10.1017/9781108875400.008 Published online by Cambridge University Press

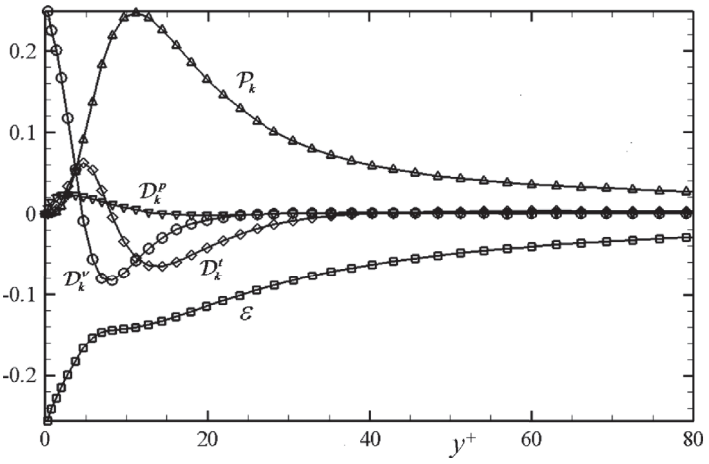

Fig. 6.5 Near-wall budget of kinetic energy in a plane channel flow for higher Reynolds number, $\mathrm{Re}_\tau = 2{,}000$, normalized with the inner-wall scales (in terms of U_τ and ν). From DNS data of Hoyas and Jimenez (2006).

It has already been shown in §1.4 that, in a simple shear flow, the maximum generation rate of turbulent kinetic energy occurs right in this changeover region. To re-cap, this occurs where

$$\frac{d}{dx_2}\left[\overline{u_1u_2}\frac{dU_1}{dx_2}\right]=0$$

or, on expanding the differential, where:

$$\overline{u_1u_2}\frac{d^2U_1}{dx_2^2}+\frac{dU_1}{dx_2}\frac{d\,\overline{u_1u_2}}{dx_2}=0. \tag{6.7}$$

On the assumption that the total shear stress ($\nu dU_1/dx_2 - \overline{u_1u_2}$) is changing much less rapidly than its constituent parts, we can replace the turbulent shear-stress derivative in Eq. (6.7) by the (negative of the) corresponding derivative of viscous stress. With this substitution and after cancelling the common factor d^2U_1/dx_2^2, it emerges that the maximum turbulence energy generation rate occurs where $-\overline{u_1u_2} = \nu dU_1/dx_2$, i.e. where the turbulent and viscous stresses are equal. That is why, in simple shear flows along a wall, the peak in turbulence energy production and thus of the turbulence energy itself generally occurs within the viscosity-affected sublayer, as seen in Fig. 6.5 derived from the DNS of plane channel flow by Hoyas and Jimenez (2006).

Next, let us examine the behaviour of the viscous dissipation rate $\varepsilon = \nu\overline{(\partial u_i/\partial x_j)^2}$ very close to the wall. Steep u_1 and u_3 velocity gradients occur only in the x_2

https://doi.org/10.1017/9781108875400.008 Published online by Cambridge University Press

direction while, from continuity, $\partial u_2/\partial x_2 = 0$ at the wall. The turbulent dissipation rate is thus obtained as:

$$\varepsilon = \nu \left\{ \begin{array}{l} \underbrace{(\overline{b_1^2} + \overline{b_3^2})}_{A} + \underbrace{4(\overline{b_1 c_1} + \overline{b_3 c_3})}_{2B} x_2 \\ \quad + \left[4\left(\overline{c_1^2} + \overline{c_2^2} + \overline{c_2^2}\right) + \left(\overline{b_1 d_1} + \overline{b_3 d_3}\right) \right] x_2^2 + \mathcal{O}\left(x_2^3\right) + \cdots \end{array} \right\}. \tag{6.8}$$

Now, at the wall itself ($x_2 = 0$), the dissipation rate is expressible as:

$$\varepsilon_w \equiv \nu \left[\overline{\left(\frac{\partial u_1}{\partial x_2}\right)^2} + \overline{\left(\frac{\partial u_3}{\partial x_2}\right)^2} \right]\Bigg|_w. \tag{6.9}$$

Moreover, since for small x_2, $k = \frac{1}{2} A x_2^2 +$ higher order terms, the wall value of the dissipation rate may alternatively be written as (Jones and Launder, 1972a):

$$\varepsilon_w = \lim_{x_2 \to 0} \frac{2\nu k}{x_2^2} = \nu \frac{\partial^2 k}{\partial x_2^2}. \tag{6.10}$$

The first of the equalities on the right-hand side of Eq. (6.10) has often been used in numerical computations as a boundary condition for ε, while the second is just the diffusive rate of turbulence-energy transport to the wall. That is, turbulence energy is diffused towards the wall by viscous action at precisely the rate at which it is being destroyed by viscous dissipation. In Fig. 6.5 these processes are shown by ε and $\mathcal{D}_k^{\nu}$.

An alternative expression (Jones and Launder, 1972a) has sometimes been used to define the wall boundary conditions for ε, namely

$$\varepsilon_w = 2\nu \left(\frac{\partial k^{1/2}}{\partial x_2}\right)^2 \Bigg|_w. \tag{6.11}$$

It is interesting to note that unlike Eq. (6.10), which complies only with the first term of the exact expansion, Eq. (6.11) agrees up to the second (linear) term.[3] This prompted Jones and Launder (1972a) to introduce a new variable, the 'quasi-homogeneous' dissipation rate (called by them the 'isotropic' dissipation rate)

$$\tilde{\varepsilon} \equiv \varepsilon - 2\nu \left(\frac{\partial k^{1/2}}{\partial x_l}\right)^2 \propto x_2^2 + \cdots \tag{6.12}$$

which conveniently goes to zero at a solid wall, Fig. 6.6. An alternative transport equation was then proposed for $\tilde{\varepsilon}$, with $\tilde{\varepsilon}_w = 0$ as the wall boundary condition. The

[3] Note that $\varepsilon = \nu\left[A + 2Bx_2 + \mathcal{O}(x_2^2)\right]$ and $2\nu(\partial k^{1/2}/\partial x_2)^2 = \nu\left[A + 2Bx_2 + \mathcal{O}(x_2^2)\right]$, whereas $2\nu k^2/x_2^2 = \nu\left[A + Bx_2 + \mathcal{O}(x_2^2)\right]$. In numerical computations, however, the latter (applied at the first node adjacent to the wall, deep within the viscous sublayer) has been reported as the more stable wall boundary condition.

https://doi.org/10.1017/9781108875400.008 Published online by Cambridge University Press

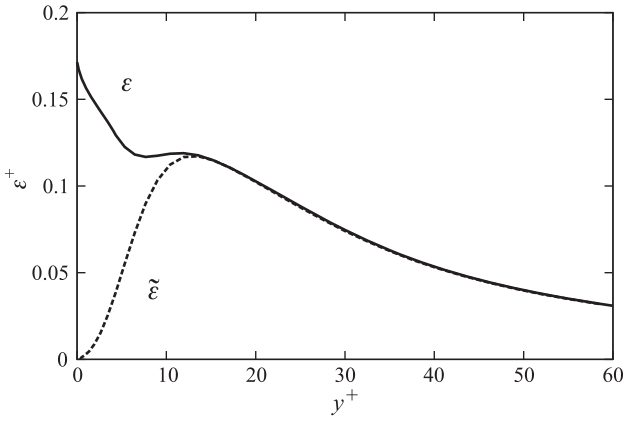

Fig. 6.6 The true and 'quasi-homogeneous' dissipation rate in a plane channel for Re = 5,600, $\mathrm{Re}_\tau = 180$. From DNS data of Kim *et al.* (1987).

variation of ε and $\tilde{\varepsilon}$ in a plane channel flow obtained from DNS data shows that their difference disappears at the edge of the viscous region even though for the chosen case the Reynolds number is particularly low (Re = 5,600, i.e. $\mathrm{Re}_\tau = 180$).

(An analogous 'quasi-homogeneous' version of the scalar dissipation rate is sometimes applied in the near-wall modelling of the thermal field, see for example Nagano (2002). Then, in terms of $\varepsilon_\theta (\varepsilon_\theta \equiv \varepsilon_{\theta\theta}/2)$ a quantity $\tilde{\varepsilon}_\theta$ is introduced where $\tilde{\varepsilon}_\theta \equiv \varepsilon_\theta - \alpha(\partial^2\overline{\theta^2}/\partial x_2^2)$, which, like the corresponding quasi-homogeneous dynamic dissipation rate, $\tilde{\varepsilon}$, vanishes at the wall.[4])

It is noted in passing that the standard linear eddy-viscosity stress−strain relationship assumes that:

$$\overline{u_i u_j} = -\nu_t \left(\frac{\partial U_i}{\partial x_j} + \frac{\partial U_j}{\partial x_i} \right) + \frac{2}{3}\delta_{ij} k.$$

Thus, it follows that for a two-dimensional flow within the viscous sublayer, where $\partial U_i/\partial x_j$ reduces to $\partial U_1/\partial x_2 = \text{const}$,

$$\nu_t = -\overline{u_1 u_2} \Big/ \frac{\partial U_1}{\partial x_2} \propto x_2^3 \tag{6.13}$$

as confirmed also by the DNS data, Fig. 6.7, where the non-dimensional distribution of $\nu_t^+ \equiv \nu_t/\nu$ is shown for plane channel flows over a range of Re. Note that the usual turbulent Reynolds number is closely related to the above-defined eddy viscosity ratio, i.e. $\mathrm{Re}_t \equiv k^2/(\nu\varepsilon) = \nu_t/(\nu c_\mu) \approx 11\nu_t/\nu$.

[4] Nagano also considers situations where the turbulent temperature fluctuations at the wall do not vanish but he appropriately re-defines $\tilde{\varepsilon}_\theta$ so that that quantity still vanishes at the wall.

https://doi.org/10.1017/9781108875400.008 Published online by Cambridge University Press

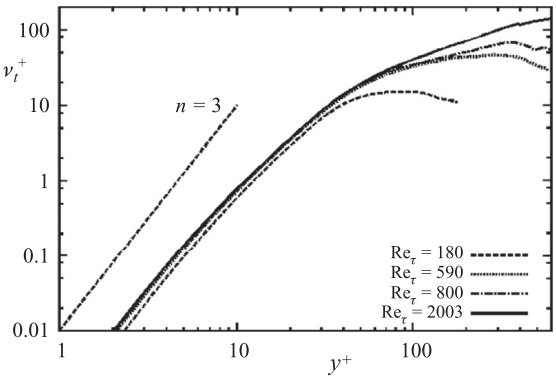

Fig. 6.7 Normalized eddy viscosity ($\nu^+ = \nu_t/\nu$) in a fully developed plane channel flow for different Reynolds numbers. Evaluated from DNS data of Moser *et al.* (1999) and Hoyas and Jimenez (2006).

Regarding the component dissipation rates at the wall, from the expansions for u_1 *and* u_3 above it is readily deduced that:

$$\frac{\varepsilon_{11}}{\overline{u_1^2}} = \frac{\varepsilon_{33}}{\overline{u_3^2}} = \frac{\varepsilon_w}{k}. \tag{6.14}$$

This result may be recognized as consistent with the formulation:

$$\varepsilon_{ij} = \varepsilon \frac{\overline{u_i u_j}}{k} \tag{6.15}$$

which essentially implies the equality of the deviatoric stress and dissipation rate tensors, i.e.

$$a_{ij} = e_{ij}$$

where, as a reminder,

$$a_{ij} \equiv \frac{\overline{u_i u_j}}{k} - \frac{2}{3}\delta_{ij}, \qquad e_{ij} \equiv \frac{\varepsilon_{ij}}{\varepsilon} - \frac{2}{3}\delta_{ij}$$

presented in Chapter 3, (Eqs. (3.23) and (3.29)). This form has been proposed either as a possible modelling for ε_{ij} in terms of ε and the Reynolds stress, e.g. Daly and Daly and Harlow (1970), or (more usually) as the asymptotic limit at the wall (among others by Hanjalić and Launder, 1976).

To deduce the corresponding forms for the 22 and 12 components of $\overline{u_i u_j}$ and ε_{ij} (Fig. 6.8) we recall that

$$u_2 = c_2 x_2^2 + \text{higher order terms}$$

https://doi.org/10.1017/9781108875400.008 Published online by Cambridge University Press

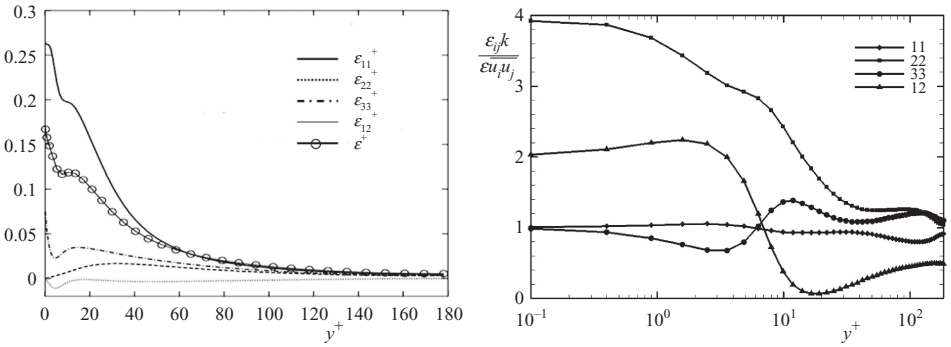

Fig. 6.8 Components of the stress dissipation-rate tensor ε_{ij} in a fully developed plane channel flow for $\mathrm{Re}_\tau = 180$. Left: actual variation of the dissipation components. Right: variation of the normalized dissipation-rate/stress ratios $(\varepsilon_{ij}/\overline{u_i u_j})/(\varepsilon/k)$. Data from DNS of Moser *et al.* (1999).

and, thus, that the wall asymptote of ε_{22} is $2\nu\overline{(\partial u_2/\partial x_2)^2} = 8\overline{c_2^2}x_2^2$. Consequently:

$$\frac{\varepsilon_{22}}{\overline{u_2^2}} = 8\frac{\nu}{x_2^2} = 4\frac{\varepsilon_w}{k}. \tag{6.16}$$

The corresponding result for ε_{12} is readily shown to be:

$$\frac{\varepsilon_{12}}{\overline{u_1 u_2}} = 2\frac{\varepsilon_w}{k}. \tag{6.17}$$

Thus, the last two results (Launder and Reynolds, 1983) show that Eq. (6.15) does *not* correctly capture the limiting ratios of dissipation rates in all components of the dissipation tensor. Models that *do* return the desired limiting levels in all components are presented in §6.3.4. One final item to notice from Fig. 6.8 is that the normalized dissipation for the shear-stress component ε_{12} does in fact fall to very nearly its isotropic value (i.e. zero) by $y^+ = 20$; but thereafter it increases again. At such a low bulk Reynolds number, however, one should not take that result as a general indicator that local isotropy will not apply for flows at much higher Reynolds number.

6.2.2 The variability of the sublayer thickness

In this subsection, to avoid the appearance of double subscripts and to align with conventional terminology (employed in the figures), the distance normal to the wall is denoted by y with the streamwise direction and mean velocity being x and U.

As indicated at the start of this chapter, it is often assumed that the thickness of the viscous sublayer y_v (which we may take as the distance from the wall at which the turbulent shear stress falls to some fixed small fraction of the wall shear stress, 5%, say) is a universal constant when it is cast dimensionlessly in 'wall

https://doi.org/10.1017/9781108875400.008 Published online by Cambridge University Press

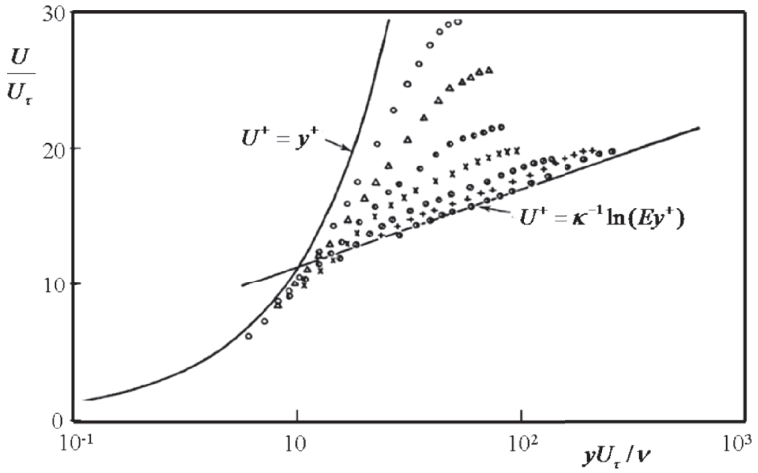

Fig. 6.9 Velocity profiles in 'universal' coordinates for pipe flow at low bulk Reynolds number. $\overline{U}D/\nu \equiv \mathrm{Re}_D$:○, 1,740 (laminar); △, 2,440; ◐, 2,615; ×, 2,975; ⊘, 4,430, +, 7,260; ◐, 9,200. From Patel and Head (1969).

coordinates': $y_\nu U_\tau/\nu$ or, for brevity, y_ν^+. In fact, the dimensionless thickness of the sublayer is *highly sensitive* to the variation of shear stress across this thin region, which in turn depends directly on the imposed streamwise pressure gradient or body force *and* the bulk Reynolds number.

With $\tau^+ = \tau/\tau_w$ (where τ is the *total* shear stress), it is found that noticeable changes in the size of y_ν^+ occur when, within the viscous region:

$$\left|\frac{d\tau^+}{dy^+}\right| > 3 \times 10^{-3}. \tag{6.18}$$

In fully developed pipe or channel flow (where $d\tau^+/dy^+ = \nu/(hU_\tau) \equiv 1/\mathrm{Re}_\tau$ is uniform across the duct of half-width or radius, h) this amounts to a bulk Reynolds number of about 8×10^3, Fig. 6.9, (Page *et al.*, 1952; Patel and Head, 1969). As the Reynolds number is reduced below this value (and the negative dimensionless shear-stress gradient normal to the wall, $d\tau/dy^+$, becomes larger) there is a progressive increase in y_ν^+ which continues until eventually the Reynolds number is so low that the flow collapses to laminar flow. It is important to recognize, however, that prior to collapse to laminar flow, the motion is genuinely turbulent although, as noted, the dimensionless sublayer thickness is greater than is found in pipe flow at much higher Reynolds numbers.

The phenomenon of increasing sublayer thickness is by no means limited to duct flows. In accelerated boundary layers there is a strong decrease in shear stress across the inner region of the layer and, again, the dimensionless thickness increases noticeably when the parameter $K \equiv (\nu/U_\infty^2)dU_\infty/dx$ is greater than about 1.5×10^{-6} (Launder, 1964a,1964b; Jones and Launder, 1972b; Spalart,

https://doi.org/10.1017/9781108875400.008 Published online by Cambridge University Press

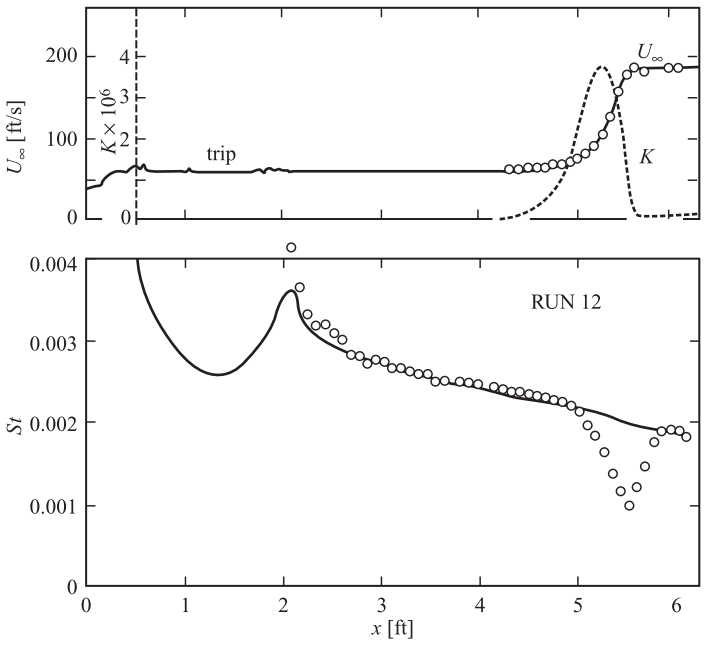

Fig. 6.10 Variation of the Stanton number along a flat heated plate with a suddenly applied flow acceleration. Upper, free-stream velocity variation and K; lower, variation in Stanton number: ○ ○ ○, experiment; —— predictions with the simple integral method used by Moretti and Kays. From Moretti and Kays (1965).

1986). Such boundary layers are sometimes referred to as *laminarescent* (Kline *et al.*, 1967). Moretti and Kays (1965) showed that the thickening viscous layer in strong accelerations may lead to a reduction in the Stanton number by more than 50%, Fig. 6.10. While, unsurprisingly, their simple integral method shown in the figure was blind to the changes in turbulence structure causing the decrease in St, even today many current models also fail to predict the phenomenon. Complete collapse of the boundary layer to laminar (termed *laminarization or relaminarization*) eventually ensues if K is maintained at levels in excess of 3×10^{-6} (Launder, 1964a; Spalart, 1986).

Corresponding effects have been reported by McEligot and co-workers for gas flows in ducts where the flow acceleration has been caused by intense heating applied at the duct wall (e.g. Perkins and McEligot, 1975). Here again an equivalent K value of the order of 10^{-6} produces significant thickening of the near-wall sublayer. Finally, for the case of negative shear-stress gradients, it is noted that closely analogous behaviour has been found in vertical upflow through heated pipes and on vertical plates due to the action of buoyancy (e.g. Carr *et al.*, 1973). In this case the shear-stress gradient arises from the reduction in fluid density as the wall is approached. For a plane wall:

https://doi.org/10.1017/9781108875400.008 Published online by Cambridge University Press

$$\partial\tau/\partial y \approx (\rho - \rho_\infty)g \tag{6.19}$$

a quantity that is negative since (it is presumed) the density decreases as the temperature rises so that $\rho < \rho_\infty$. A review of the related experimental data up to the late 1980s has been provided by Jackson *et al.* (1989). These authors note that the serious effects of decreasing heat transfer coefficients of liquids operating near the critical point were initially attributed to a form of film boiling ('pseudo-boiling', Ackerman, 1970); only subsequently was it recognized that the associated strong peaks in wall temperature were due to buoyancy increasing the effective sublayer thickness.

When the shear stress rises with distance from the wall the effects are reversed: that is, the sublayer thickness (normalized by friction velocity and viscosity) reduces and skin friction and heat transfer coefficients are increased relative to what would be expected with a strictly 'universal' sublayer thickness. Thus, for the case of a mixed-convection *downflow* in a heated pipe, the sign of the buoyancy contribution is reversed (since gravitational acceleration now acts in the direction of motion of the flow) and heat transfer coefficients are increased[5] (e.g. Cotton and Jackson, 1987; Jackson *et al.*, 1989). That is one of the reasons why, in heat exchangers, the heated tube fluid is generally directed vertically downwards. The shear stress also rises with distance from the wall in an adverse pressure gradient where the boundary layer is heading towards separation and on a porous surface through which there is blowing (e.g. Simpson *et al.*, 1967; Baker and Launder, 1974). The measurement of wall friction in such circumstances is fraught with uncertainties yet at least for the blown boundary layer it is established that a marked reduction in the dimensionless sublayer thickness occurs.

Later sections (and chapters) will address, inter alia, the question of how the thickening and thinning behaviour of the sublayer can be modelled. Finally, it is noted that the above discussion has limited attention to flows *parallel to* a plane wall. The *impingement* of the flow on the wall or surface curvature brings further complications, some of which have been noted in Chapter 2.

6.2.3 Inviscid wall blocking, its nature and implications

As indicated above (§6.1), the influences of viscosity and non-viscous blocking due to wall proximity upon the turbulent motion are very different in nature. Yet, in the past, these effects have frequently been modelled jointly because both manifest themselves in a damping of turbulence transport of momentum or heat normal to the wall. However, as is well known, if Re_t is small enough, viscosity affects all turbulent interactions, leading, in the presence of shear, to a departure from isotropy

[5] Collected experimental data for the Nusselt number in mixed convection for both upflow and downflow in vertical tubes are included in Fig. 7.24.

https://doi.org/10.1017/9781108875400.008 Published online by Cambridge University Press

in even the smallest-scale motions (rendering invalid the principle of local isotropy). In contrast, a solid wall or a phase interface flattens the turbulent structure and imposes a selective damping, primarily of the normal-to-the-wall fluctuations, causing the turbulence to approach a two-component state. Indeed, the wall reflects the pressure pulsations, affecting the stress redistribution process over a region that extends well into the fully turbulent flow. In contrast, the influence of viscosity upon the turbulent stresses in high-Re flows remains restricted to the viscous region, and even there it does not seem to be very strong. Simple eddy-viscosity models, designed for integration up to the wall, employ a variety of damping functions in terms of turbulence Reynolds number and wall distance to account for the presence of the wall without distinguishing the true source of these effects. Such a practice obscures the separate effects of viscosity and wall blocking and often results in poor predictions in flow regions where these effects take different relative magnitudes than in the simple wall flows used for calibration. A more consistent approach requires each of the effects to be modelled separately, with coefficients and functions tuned on the basis of experimental data obtained in flows where each effect can be isolated. An illustrative example is the transition from the initial to the final period of decay of isotropic turbulence. Calibrating that decay enables the sink-term coefficient in the dissipation equation to be determined purely as a function of Re_t. Likewise, in a turbulent flow close to a *free* surface, where there are no viscous effects (since there is no shear), the 'impermeability' of the interface surface dampens the stress component normal to the interface surface (and indirectly affects other stress components) in much the same way as in flows close to a solid wall (e.g. McGuirk and Papadimitriou, 1988; Perot and Moin, 1995). Another important example is provided in Table 4.1, §4.3.4, where it was shown that the stress anisotropy in the fully turbulent region of a wall boundary layer (i.e. outside the viscosity-affected region) is larger than in a homogeneous shear flow subjected to a similar shear rate.

By discarding convective and diffusive contributions, the shear-stress transport equation for the fully turbulent near-wall region (using the simple IP and linear return-to-isotropy models, Eqs. (4.9) and (4.7), respectively, with near-wall corrections (4.12) and (4.14)) reduces to an eddy-viscosity form:

$$-\overline{u_1 u_2} = \underbrace{0.263\frac{\overline{u_2^2}}{k}}_{c_\mu f_\mu}\frac{k^2}{\varepsilon}\frac{\partial U_1}{\partial x_2}. \tag{6.20}$$

In the conventional eddy-viscosity terminology the quantity $0.263\overline{u_2^2}/k$ would be termed $c_\mu f_\mu$, where c_μ is habitually taken as 0.09 and f_μ is seen as a function of a turbulence Reynolds number introduced to enable the eddy-viscosity formula to apply all the way to the wall. Figure 6.11 compares the measured variation of

https://doi.org/10.1017/9781108875400.008 Published online by Cambridge University Press

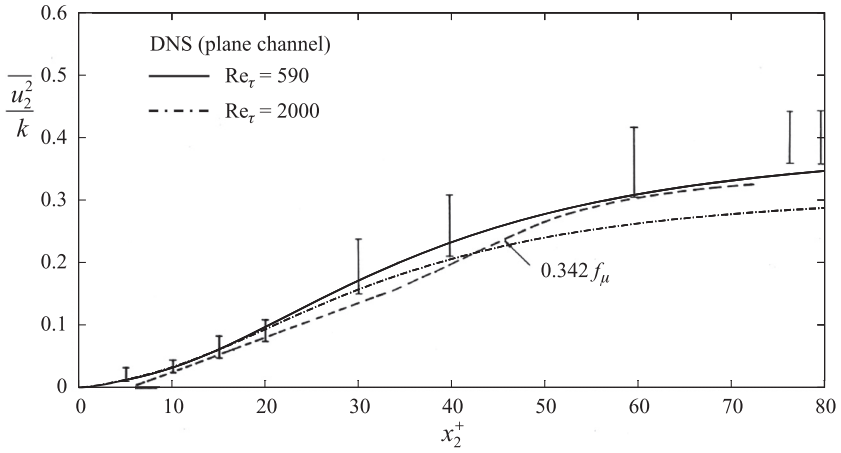

Fig. 6.11 Variation of $\overline{u_2^2}/k$ (vertical bars denoting the range of uncertainty of the data) and $0.342\,f_\mu$ (- - - -) across the inner region of turbulent wall flows estimated from experimental data then available (Patel *et al.*, 1985; Launder, 1986). DNS data of $\overline{u_2^2}/k$: ——— $\mathrm{Re}_\tau = 590$ (Moser *et al.*, 1999); – – – $\mathrm{Re}_\tau = 2{,}000$ (Hoyas and Jimenez, 2006).

$\overline{u_2^2}/k$ across the near-wall region for early high-Reynolds-number near-wall flows (compiled by Patel *et al.*, 1985) and more recent DNS data of the same quantity with $0.342\,f_\mu$ (the numerical coefficient is just 0.09/0.263). The variation of f_μ was estimated by Launder (1986), again from the then available experimental data, from Eq. (6.20) following its rearrangement as:

$$f_\mu = -\overline{u_1 u_2} \Big/ \left[c_\mu (k^2/\varepsilon) \partial U_1/\partial x_2 \right].$$

Evidently, this latter quantity varies in much the same way as the normalized variation of $\overline{u_2^2}$, suggesting that most of what is conventionally regarded as *viscous* damping is, rather, the preferential damping of the fluctuations normal to the wall principally by non-viscous effects! Equation (6.20) subsequently inspired Durbin (1991) to propose an eddy-viscosity model in which a separate transport equation was solved for a scalar 'surrogate' of $\overline{u_2^2}$ (designated 'v^2'), in conjunction with an *elliptic relaxation* parameter 'f', that has become known as the v^2–f *model* (see §7.4.4). Later, Hanjalić *et al.* (2004a) and Laurence *et al.* (2004) independently proposed versions of this model in which a transport equation is solved for the ratio $\zeta = \overline{u_2^2}/k$, which offers a number of computational advantages.

Of course, solving transport equations for all stress components, as is done with a full second-moment closure, would naturally provide the wall-normal stress component. In such models, viscous effects are still present but their influence is weaker and confined to a thinner region next to the wall than with linear eddy-viscosity schemes. Models of this kind are considered in the sections that follow. Before that,

https://doi.org/10.1017/9781108875400.008 Published online by Cambridge University Press

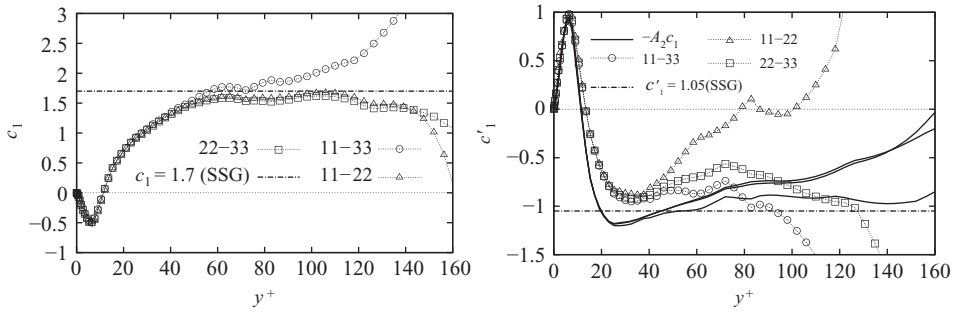

Fig. 6.12 Evaluation of c_1 and c'_1 from DNS results of Φ_{ij_1} in a plane channel flow for $\mathrm{Re}_m = 5{,}600$ (Kim *et al.*, 1987). From Hanjalić and Jakirlić (2002).

however, it is instructive to examine the behaviour of the terms and coefficients using the available DNS data for some simple generic wall flows.

Consider first the quadratic model of the slow pressure-strain term, Eq. (4.33)

$$\Phi_{ij_1} = -c_1 \varepsilon a_{ij} + c'_1 \varepsilon (a_{ik}a_{kj} - \tfrac{1}{3}A_2\delta_{ij}) \tag{6.21}$$

in a fully developed channel flow. From the DNS results for the components of Φ_{ij_1} and a_{ij}, one can evaluate the two coefficients, c_1 and c'_1, in Eq. (6.21). In such a flow, four components of Φ_{ij} are non-zero, but to evaluate the two coefficients only two components are needed.[6] Thus, using different combinations of two from the four available components provides another test of the validity of the model: if all combinations were to collapse into single curves for c_1 and c'_1, this would provide support for the form of the model of Φ_{ij_1} given by Eq. (6.21).

Figure 6.12 shows that this is indeed the case, at least for the near-wall region, i.e. for $y^+ < 50$. (Further from the wall the curves obtained from different pairs of data, denoted 11–22, 11–33, 22–33, start to diverge.) However, even close to the wall where the different pairings produce essentially the same results, the coefficients are far from constant: they exhibit a very strong variation across the flow and even change sign. In fact, the data for $y^+ < 50$ suggest that the two coefficients can be related to one another by $c'_1 = -A_2 c_1$, shown by the solid lines in the right-hand graph of Fig. 6.12. It should be noted that this large variation of both coefficients is partly due to the (so far unaccounted for) viscous effects because the flow considered is at a rather low Reynolds number, $\mathrm{Re}_m = 5{,}600$ (corresponding to $\mathrm{Re}_\tau = 180$).[7]

[6] For example, if for the case $i = j$ the normal stresses are successively given the values 1 and 2, Eq. (6.21) gives $-\Phi_{11_1}/\varepsilon = c_1 a_{11} + c'_1(a_{11}^2 + a_{12}^2 - \frac{1}{3}A_2)$ and $-\Phi_{22_1}/\varepsilon = c_1 a_{22} + c'_1(a_{12}^2 + a_{22}^2 - \frac{1}{3}A_2)$. From these, c_1 and c'_1 can be evaluated across the flow by feeding the DNS profiles of Φ_{ij_1} and Φ_{ij_2} and the components of a_{ij}.

[7] Unfortunately, this is apparently the only set of DNS data for which results are available for both the slow and rapid parts of the pressure-strain term, Φ_{ij}.

https://doi.org/10.1017/9781108875400.008 Published online by Cambridge University Press

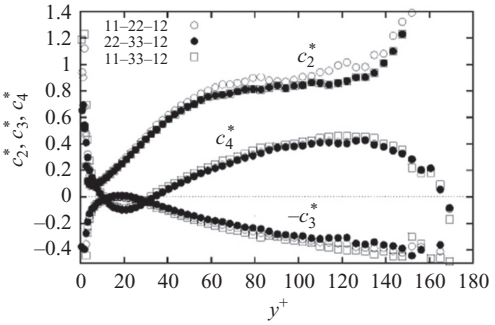

Fig. 6.13 Coefficients of the linear model of Φ_{ij_2}, Eq. (6.22), evaluated from DNS data for a channel flow at $\mathrm{Re}_m = 5,600$ (Kim *et al.*, 1987). From Jakirlić (2004).

A similar analysis can be applied to the models of the rapid term, Φ_{ij_2}. For example, in the general linear model, Eq. (4.46), expressed in terms of S_{ij} and W_{ij},

$$\Phi_{ij_2} = c_2^* k(a_{ik}S_{jk} + a_{jk}S_{ik} - \tfrac{2}{3}a_{kl}S_{kl}\delta_{ij}) + c_3^* k(a_{ik}W_{kj} + a_{jk}W_{ki}) + c_4^* k S_{ij} \quad (6.22)$$

all three coefficients c_2^*, c_3^* and c_4^* can be evaluated directly using any combination of the DNS data for three components of Φ_{ij_2}[8].The outcome is illustrated in Fig. 6.13. The remarkable collapsing of solutions when using different components supports the form (6.22) for modelling Φ_{ij_2}, but the strong variation of all three model coefficients across the channel cross-section indicates the need to express the coefficients as functions of suitable turbulence parameters, especially when approaching the wall.

Following the same approach, one can also evaluate the coefficients in quasi-linear models, Eq. (4.54) (i.e. Eq. (6.22) with the addition of the term quadratic in stress, $-c_5^* a_{ij}\mathcal{P}_{kk}$). However, such models contain four coefficients while only three equations are at our disposal (see footnote 6, above). An analysis of the coefficients for the two quasi-linear models, the HL (Hanjalić and Launder, 1972b) and the SSG (Speziale et al., 1991) models, can be found in Jakirlić (2004), who adopted the values for the coefficient c_4^* as proposed by the model proponents (a constant value, $c_4^* = 0.8$, for the HL model and the functional form, $c_4^* = 8.0 - 0.625AA_2^{1/2}$ for the SSG model (see Table 4.2)) and evaluated the remaining three coefficients, c_2^*, c_3^* and c_5^*.

The coefficients evaluated from different combinations of Φ_{ij_2} components again follow almost identical profiles, with similar shapes for the HL and SSG models, as seen in Fig. 6.14. The coefficients c_2^* and c_3^* of the linear terms show reasonably constant values over a large portion of the cross-section y^+ between 35 and 140.

[8] Three different combinations of indices using two diagonal components (recall that $\Phi_{11_2} + \Phi_{22_2} + \Phi_{33_2} = 0$) and the only non-zero off-diagonal component Φ_{12_2} lead to a three-equation system, from which the three model coefficients can be obtained.

https://doi.org/10.1017/9781108875400.008 Published online by Cambridge University Press

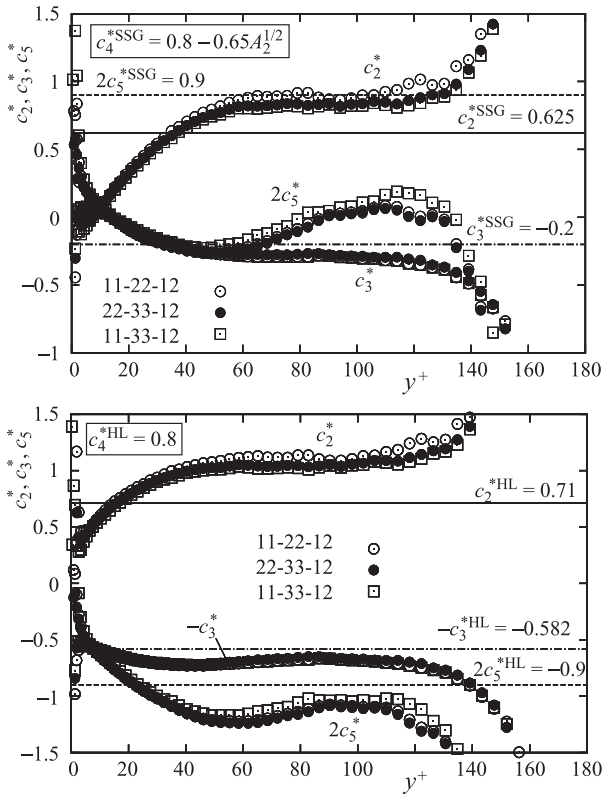

Fig. 6.14 Variation of coefficients c_2^*, c_3^* and c_5^* with the adopted c_4^* (in box) in Eq. (4.54) evaluated from DNS results for a channel flow at $\mathrm{Re}_\tau = 180$ for the SSG model (top) and HL model (bottom). From Jakirlić (2004).

These values correspond reasonably closely with those proposed by the originators of the models, Table 4.2, but clearly all coefficients need modifying as the wall is approached. It is noted that in the region away from the wall the DNS data suggest that the coefficient $2c_5^*$ of the quadratic term takes a negative value of -1.25, which is in reasonable agreement with the value -0.9 proposed earlier in the HL model, but in contrast to the positive value, $+0.9$, proposed in the SSG model.

6.3 Wall integration (WIN) schemes

Integration of the turbulent transport equations to the wall is, in principle, a more generally applicable strategy than adopting 'wall functions' (the subject of Chapter 8). As will be inferred from the preceding section, the approach requires substantial modifications to the high-Re turbulence models in order to account for effects arising from low turbulent Reynolds number and non-viscous pressure reflection by the rigid wall. This in turn requires a much finer grid resolution in

https://doi.org/10.1017/9781108875400.008 Published online by Cambridge University Press

and around the viscosity-affected sublayer, and, consequently, greatly increases demands on computational resources, with often formidable constraints on the numerical solver to ensure convergent solutions. WIN schemes (known also as 'low Reynolds number models' or 'near-wall models') are available as eddy-viscosity (linear and non-linear) as well as stress-transport models. While developed primarily for treating the near-wall viscous region under non-equilibrium conditions, some models have also been reasonably successful in predicting transition from laminar to turbulent flow in certain circumstances. As would be expected, models that can distinguish between non-viscous blocking and viscous wall effects are generally the more successful in predicting laminar-to-turbulent and reverse transition (such as bypass or separation-induced transition, or the revival of inactive background turbulence and its subsequent laminarization, as may arise in periodic flows).

6.3.1 Overview of the task

Numerous proposals for modifying second-moment closures (SMCs) to account for low-Reynolds-number and wall-proximity effects can be found in the literature. These modifications are based on a reference high-Re SMC which serves as the asymptotic model to which the low-Re version should reduce for sufficiently high Reynolds numbers and at a sufficient distance from any wall. Hanjalić and Launder (1976), Launder and Shima (1989), Hanjalić and Jakirlić (1993), Iacovides and Toumpanakis (1993), Shima (1993) and Hanjalić *et al.* (1995) all developed their modifications from the basic SMC with linear pressure-strain models (see Chapter 4), in which the coefficients are defined as functions of turbulent Reynolds number and invariant turbulence parameters. Earlier models also used the distance from the nearest solid wall. Most recent models are based on DNS data and a term-by-term modelling that ensures model realizability, compliance with the near-wall two-component limit for the second moments, as well as with the limit of vanishing turbulence Reynolds number. Launder and Li (1994), Craft and Launder (1996) and Craft (1998) used the cubic pressure-strain model, presented in Chapter 4, in which the coefficients were determined by imposing, in addition to the kinematic criteria discussed earlier, the two-component limit. Including this constraint in the original model formulation for free flows reduces the need to introduce further dependence on the available turbulence parameters to handle wall-proximity effects. However, the complete elimination of 'damping functions' was not possible: some of the coefficients had to be formulated as functions of the turbulent Reynolds number to account for viscosity, even though their influence is limited to the viscous layer (e.g. Launder and Li, 1994).

Finally, as noted in §6.2.3, Durbin (1991, 1993) used elliptic relaxation to account for the non-viscous blockage effect of a solid wall, while a switch of time

https://doi.org/10.1017/9781108875400.008 Published online by Cambridge University Press

and length scales from the high-Re energy-containing scales to Kolmogorov scales when the latter become dominant, accounted for viscous effects.[9] The elliptic relaxation approach seems to be somewhat less demanding on near-wall grid refinement, but at present it has not been used to predict transitional phenomena, though some modifications for this purpose have been proposed (Lien *et al.*, 1998).

In principle, all proposals for extending the validity of the base model entail the following:

- inclusion of viscous diffusion in all equations;
- provision of a non-isotropic model for ε_{ij};
- addition of further terms in the ε-equation (or other scale-determining equation where used);
- replacement of some constant coefficients by functions of turbulent Reynolds number, $\mathrm{Re}_t = k^2/\nu\varepsilon$, and turbulent-stress invariants or other available turbulence parameters.

In constructing a consistent model that satisfies the conditions in the near-wall region, one seeks to satisfy the limiting behaviour of *each* component of the turbulent stress, as indicated in Eq. (6.6).

6.3.2 Stress budget at an impermeable wall

To gain some impression of the relative magnitude of the terms in the stress-transport equation as one approaches very close to the wall, we turn to Eq. (6.1) and add a similar polynomial expansion for the fluctuating pressure:

$$u_i(x_2,\, t) = a_i + b_i x_2 + c_i x_2^2 + d_i x_2^3 + \cdots \tag{6.23}$$

$$p(x_2,\, t) = a_p + b_p x_2 + c_p x_2^2 + d_p x_2^3 + \cdots \tag{6.24}$$

Recall that x_2 is the direction perpendicular to the wall and that all coefficients are functions of time (with a zero mean) and, in general, of $x_1$and x_3. Moreover, for incompressible flow assumed here, $a_i = 0$ and $b_2 = 0$; however $a_p \neq 0$ since there will be pressure fluctuations at the wall surface. To facilitate the presentation, the stress-transport equation (2.18) is written in the symbolic form (see Eq. (2.21)):

$$\mathcal{C}_{ij} = \mathcal{P}_{ij} + \Phi_{ij} + \mathcal{D}^p_{ij} + \mathcal{D}^t_{ij} + \mathcal{D}^\nu_{ij} - \varepsilon_{ij}. \tag{6.25}$$

Deep within the viscous region convective transport, $\mathcal{C}_{ij}$, is often negligible as are also the stress-production terms. The diffusion of stress by turbulent velocity fluctuations $\mathcal{D}^t_{ij}$ may also be shown from Eq. (6.23) to be smaller than the remaining terms in Eq. (6.25), the largest contributors being proportional to x_2^3 for

[9] In fact, this scale switching does, implicitly, introduce the influence of turbulent Reynolds number.

https://doi.org/10.1017/9781108875400.008 Published online by Cambridge University Press

$i = j = 1$ or 3. Using Eqs. (6.23) and (6.24) to estimate the wall-limiting values of the remaining terms in Eq. (6.25) produces the estimates given in Table 6.1. For terms containing the derivative of fluctuating pressure, at the wall the momentum equation for the fluctuating motion reduces to $(\partial p/\partial x_i)/\rho = \nu \partial^2 u_i/\partial x_k^2$ from which it follows that $\partial a_p/\partial x_1 = 2\nu c_1$, etc. In addition to the two columns for the terms containing the fluctuating pressure, the second column provides the values for their sum, Π_{ij}, to assist later discussion.

It is noted that for i or j equal to 1 or 3 (in any combination) the stress-dissipation rate ε_{ij} at the wall is finite and balanced by viscous diffusion, $\mathcal{D}^{\nu}_{ij}$, whereas, for all other stress components, both terms go to zero at the wall.[10] It is also interesting to note that the velocity–pressure-gradient correlation Π_{ij} goes to zero at the wall for all components, whereas the usual splitting into pressure-strain and pressure diffusion, $\left(\Pi_{ij} \equiv \mathcal{D}^{p}_{ij} + \Phi_{ij}\right)$, results in finite (mutually balanced) values of both terms for the shear-stress components $\overline{u_1 u_2}$ and $\overline{u_2 u_3}$.

The specific steps to modify a second-moment closure model for low-Re and wall-proximity effects will be considered shortly. The modifications to be introduced depend on the chosen high Reynolds number model, to which the near-wall model reduces in regions sufficiently far from a rigid wall or free surface. In §6.3.4 we consider the steps required for the modification of models adopting the linear IP and QI models of the pressure-strain term as outlined in §4.3 with the wall-echo model of §4.4.5. This is followed by a brief account of the relatively small corresponding adaptations with TCL models.

6.3.3 Scalar flux budget at a wall

A similar analysis can be performed for the scalar-flux equation by adding to Eqs. (6.23) and (6.24) the polynomial expansion of the fluctuating temperature in the wall-normal direction

$$\theta(x_2, t) = a_\theta + b_\theta x_2 + c_\theta x_2^2 + d_\theta x_2^3 + \cdots \tag{6.26}$$

For a wall at a constant temperature, there are no temperature fluctuations and $a_\theta = 0$, but for other thermal wall conditions (in particular, the case of an imposed heat flux) this is not the case.

Recalling the exact scalar-flux equation (Eq. (2.22)) for a steady flow (neglecting convection and body forces other than buoyancy)

$$0 = \mathcal{P}^{\Theta}_{\theta i} + \mathcal{P}^{U}_{\theta i} + \mathcal{G}_{\theta i} + \Phi_{\theta i} + \mathcal{D}^{\alpha}_{\theta i} + \mathcal{D}^{\nu}_{\theta i} + \mathcal{D}^{t}_{\theta i} + \mathcal{D}^{p}_{\theta i} - \varepsilon_{\theta i} \tag{6.27}$$

and implementing Eqs. (6.23), (6.24) and (6.26), one can arrive at the wall budget for an impermeable wall. However, unlike the stress budget, the situation is not

[10] Although obtained by way of a quite different path, this result for ε_{ij} is not in conflict with the linkage between dissipation rates and stresses obtained in §6.2.1.

https://doi.org/10.1017/9781108875400.008 Published online by Cambridge University Press

Table 6.1 *Wall-limiting behaviour of the leading terms in the Reynolds stress budget*

ij	Φ_{ij}	$\Pi_{ij} \equiv \left(\mathcal{D}^p_{ij} + \Phi_{ij}\right)$	$\mathcal{D}^p_{ij}$	$\mathcal{D}^\nu_{ij}$	$-\varepsilon_{ij}$
11	$2\overline{a_p \partial b_1/\partial x_1} x_2$	$-4\nu\overline{b_1 c_1} x_2$	$-\left(2\overline{a_p \partial b_1/\partial x_1} + 4\nu\overline{b_1 c_1}\right) x_2$	$2\nu\overline{b_1 b_1} + 12\nu\overline{b_1 c_1} x_2$	$-2\nu\overline{b_1 b_1} - 8\nu\overline{b_1 c_1} x_2$
22	$4\overline{a_p c_2} x_2$	$-4\nu\overline{c_2 c_2} x_2^2$	$-\left(4\overline{a_p c_2} x_2 + 4\nu\overline{c_2 c_2} x_2^2\right)$	$12\nu\overline{c_2 c_2} x_2^2$	$-8\nu\overline{c_2 c_2} x_2^2$
33	$2\overline{a_p \partial b_3/\partial x_3} x_2$	$-4\nu\overline{b_3 c_3} x_2$	$-\left(2\overline{a_p \partial b_3/\partial x_3} + 4\nu\overline{b_3 c_3}\right) x_2$	$2\nu\overline{b_3 b_3} + 12\nu\overline{b_3 c_3} x_2$	$-2\nu\overline{b_3 b_3} - 8\nu\overline{b_3 c_3} x_2$
12	$\overline{a_p b_1}$	$-2\nu\overline{b_1 c_2} x_2$	$-\left(\overline{a_p b_1} + 2\nu\overline{b_1 c_2} x_2\right)$	$6\nu\overline{b_1 c_2} x_2$	$-4\nu\overline{b_1 c_2} x_2$
23	$\overline{a_p b_3}$	$-2\nu\overline{b_3 c_2} x_2$	$-\left(\overline{a_p b_3} + 2\nu\overline{b_3 c_2} x_2\right)$	$6\nu\overline{b_3 c_2} x_2$	$-4\nu\overline{b_3 c_2} x_2$
13	$\overline{a_p \left(\partial b_1/\partial x_3 + \partial b_3/\partial x_1\right)} x_2$	$-2\nu\left(\overline{b_1 c_3} + \overline{b_3 c_1}\right) x_2$	$-\overline{a_p \left(\partial b_1/\partial x_3 + \partial b_3/\partial x_1\right)} x_2$ $-2\nu\left(\overline{b_1 c_3} + \overline{b_3 c_1}\right) x_2$	$2\nu\overline{b_1 b_3}$ $+6\nu\left(\overline{b_1 c_3} + \overline{b_3 c_1}\right) x_2$	$-2\nu\overline{b_1 b_3}$ $-4\nu\left(\overline{b_1 c_3} + \overline{b_3 c_1}\right) x_2$

unique because the budget will depend on the thermal conditions at the wall (whether in the form of a prescribed constant or variable temperature, or of an imposed flux, including a perfectly insulated wall). Moreover, if buoyancy effects are significant, requiring the inclusion of $\mathcal{G}_{\theta i}$, the wall budget will also depend on the orientation of the wall with respect to the gravitational vector. A further parameter that influences the wall scalar flux budget is the molecular Prandtl number which expresses the ratio of the molecular diffusion of $\overline{\theta u_i}$ by viscosity and thermal diffusivity ($\mathcal{D}^{\nu}_{\theta i}$ and $\mathcal{D}^{\alpha}_{\theta i}$, respectively), see §2.3.2. The reader can find such an analysis for different non-buoyant flows in Nagano (2002) and in Dol (1998) and Dol *et al.* (1999) for natural convection in a side-heated vertical plane channel.[11]

Two extreme situations where the wall boundary condition on $\overline{\theta^2}$ may be important are flows at very high Prandtl number, where because of the very low *molecular* thermal conductivity turbulent heat transport is still important deep within the viscous layer, and cases such as arise in nuclear-reactor heat exchangers where temperature fluctuations at the wall may cause long-term fatigue damage to the metal surface of the heat exchanger.

6.3.4 Accounting for near-wall effects in second-moment closures

Stress production and redistribution

We begin by noting the obvious: stress production due to the rate of strain, $\mathcal{P}_{ij}$, is treated in its exact form and thus needs no modification. Concerning the pressure-containing correlations, although the Poisson equation, Eq. (4.2), governing the fluctuating pressure, p, contains no viscosity (since $\partial \big/ \partial x_i \; (\nu \partial^2 u_i \big/ \partial x_j^2) = 0$), there are clearly strong viscous influences on the other terms, which in turn affect the pressure fluctuations. Even so, the importance of this effect is not certain because the pressure fluctuations are found from integration over space. As a result, a significant contribution to p arises from interactions outside the viscosity-affected region. Partly for this reason and partly because there were no indications of significant viscous effects on $\overline{u_2^2} \big/ k$, the early models (Hanjalić and Launder, 1976, and

[11] In contrast to the viscous stress diffusion in Eq. (2.18), the molecular diffusion of $\overline{\theta u_i}$ cannot be considered in its exact form except when the molecular Prandtl number, $\mathrm{Pr} \equiv \nu/\alpha$, is unity. For more general cases when the molecular effects are significant, the molecular diffusion of $\overline{\theta u_i}$ needs to be modelled. Dol *et al.* (1999) used

$$\mathcal{D}^{\alpha+\nu}_{\theta i} = \frac{\partial}{\partial x_k}\left[\alpha \overline{u_i \frac{\partial \theta}{\partial x_k}} + \nu\theta \overline{\frac{\partial u_i}{\partial x_k}}\right] = \frac{1}{2}(\nu+\alpha)\frac{\partial^2 \overline{\theta u_i}}{\partial x_k^2} + \frac{1}{2}(\nu-\alpha)\left(\theta \overline{\frac{\partial^2 u_i}{\partial x_k^2}} + \overline{u_i \frac{\partial^2 \theta}{\partial x_k^2}}\right).$$

Due to the large difference between the typical scales of the fluctuations and their second derivatives, the correlations in the last terms are small and can be neglected (a position supported by the DNS of Versteegh and Nieuwstadt (1998), at least for the side-heated infinite vertical channel).

https://doi.org/10.1017/9781108875400.008 Published online by Cambridge University Press

subsequent publications) found no justification for including viscous modifications to Φ_{ij}. However, the evidence from more recent direct numerical simulations has suggested substantial influences of both viscous and non-viscous wall effects on Φ_{ij} (though it is difficult to distinguish one from the other). This is implied in Fig. 6.12 by the strong variations of coefficients in the quadratic model for the slow pressure-strain term, Φ_{ij_1}. Similar remarks can be made for the rapid term, Φ_{ij_2}, concerning the near-wall variation of the coefficients shown in Figs. 6.13 and 6.14 for the linear and quasi-linear models, respectively.

In addition to the high-Re wall corrections introduced in §4.3.4, there have been several proposals to account for near-wall effects on Φ_{ij} that extend up to the wall. Basically, such modifications entail expressing coefficients of the models of Φ_{ij} in terms of the turbulent Reynolds number and turbulence invariants (the latter aiming to represent non-viscous wall blocking). Some specific models are discussed below. First, however, some general ideas and constraints are considered.

Let us examine the behaviour of the exact terms in the $\overline{u_i u_j}$ equation, particularly of terms involving the fluctuating pressure, in the limit as the wall is approached. As seen in Table 6.1, at the wall, $\Phi_{ij} = 0$ for all $i = j$, but $\Phi_{12} \neq 0$ and is balanced by the pressure diffusion. By way of contrast, expansion of Eqs. (6.23) and (6.24) implies $a_{ij} \neq 0$ for all $i = j$, but $a_{12} = 0$. As has already been noted in Chapter 4, Rotta's linear model of Φ_{ij_1} with c_1 a constant, Eq. (4.7) (or Eq. (4.33), with $c_1' = 0$), cannot satisfy the wall-limiting behaviour of the exact pressure-strain term. Experience suggests that it will be too demanding to devise a selective function c_1 that will distinguish the diagonal from the off-diagonal components of Φ_{ij}. As mentioned earlier, Launder and Tselepidakis (1993) ensure that c_1 satisfies the wall limit by multiplying it not only by A, but also by a function of Re_t, $c_1 = 6.3AF(1-f)$, where $F = \min(0.6, A_2^{1/2})$ and $f = \max[1 - \mathrm{Re}_t/140, 0]$. Used in conjunction with an early form of TCL model for Φ_{ij_2}, and with modifications of the ε-equation, as discussed later, they reproduce satisfactorily the near-wall DNS stress profiles of Kim *et al.* (1987) for $\mathrm{Re} = 5,600$ and $\mathrm{Re} = 13,750$.

As seen in Table 6.1, the sum of pressure-strain and pressure diffusion, $\Pi_{ij} \equiv \mathcal{D}_{ij}^p + \Phi_{ij}$, goes to zero (though not at the same rate) for all i and j. This is why some researchers have proposed modelling Π_{ij} instead of Φ_{ij}, or at least (since boundary conditions and model constraints more appropriate to the former have been applied and no explicit modelling of $\mathcal{D}_{ij}^p$ has been proposed) interpreting the model as simulating Π_{ij} rather than Φ_{ij}. Lumley and Newman (1977) modelled $\Pi_{ij} - \varepsilon_{ij}$ jointly, whereas Launder and Shima (1989) (subsequently with reoptimized functions by Shima, 1993) proposed a model of $\Phi_{ij} - \varepsilon_{ij}$ which employs the standard high-Re Basic Model of Φ_{ij} with the Gibson and Launder (1978) wall correction, Φ_{ij}^w, but with all coefficients dependent on the stress invariants, A_2 and A_3.

https://doi.org/10.1017/9781108875400.008 Published online by Cambridge University Press

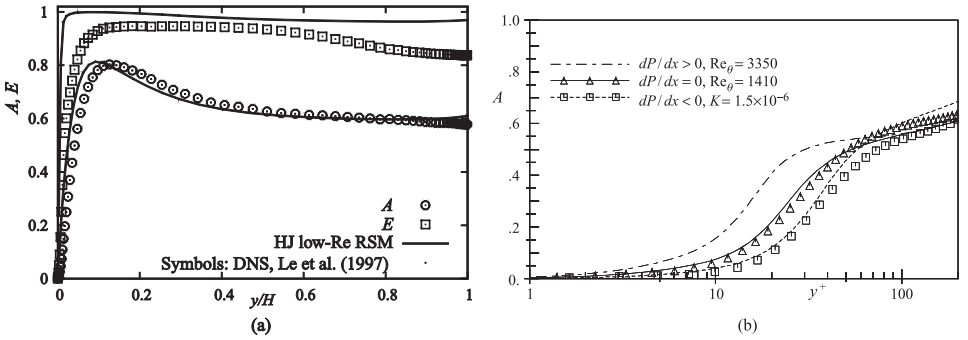

Fig. 6.15 Lumley's two-component ('flatness') parameter for turbulent stress (A) and its dissipation-rate equivalent (E) in the recirculation region behind a backward-facing step (a); stress flatness parameter in boundary layers in zero, favourable and adverse pressure gradients (b). Symbols, from DNS data; lines, computations with the HJ model.

Hanjalić and Jakirlić (1993) and subsequently Hanjalić *et al.* (1994, 1995) also used the high-Re Basic Model as their starting point but, recognizing that close to a wall the turbulence spectrum is largely populated by smaller-scale eddies, they included the anisotropy invariants of the dissipation-rate tensor, ε_{ij}, to modify the coefficients of the model. Thus, in addition to Re_t, invariants of both the turbulent-stress and dissipation-rate anisotropies, A_2, A_3, E_2, and E_3, appear as parameters in the coefficients. This enables separate account to be taken of wall effects on the anisotropy of the stress-bearing and dissipative scales, respectively. The DNS data reveal the stress and dissipation invariants to be strikingly different in their distribution (Hanjalić *et al.*, 1997, 1999). As shown in Fig. 3.14(b), as one proceeds away from the wall, the dissipation-rate flatness parameter E approaches its isotropic value of unity faster than the stress flatness parameter A, a behaviour that also occurs in the flow behind a backward-facing step, Fig. 6.15a. The sensitivity of the stress invariants to the variation of the total shear stress normal to the wall (arising from the streamwise pressure gradient) is evident in Fig. 6.15b where the flatness parameter A is plotted for boundary layers in zero, favourable and adverse pressure gradients. Based on the above arguments, the following modifications (hereafter referred to as the HJ model) were introduced which made it possible to reproduce the wall-limiting behaviour of all stress components (and thus, indirectly, the two-component limit):

$$c_1 = 2.5AF^{1/4}f + A^{1/2}E^2$$

where $F = \min(0.6, A_2)$, $f = \min[(\mathrm{Re}_t/150)^{3/2}, 1]$

$$c_2 = 0.8A^{1/2}, \quad c_1^w = \max(1 - 1.75AF^{1/4}f), \quad c_2^w = \min(A, 0.3).$$

https://doi.org/10.1017/9781108875400.008 Published online by Cambridge University Press

Let us now turn to the corresponding developments with models using the two-component-limit (TCL) approach to modelling near-wall turbulence. Because these versions are designed so that Φ_{22} vanishes when $\overline{u_2^2}/k$ goes to zero, it would be expected that only a modest amount of viscous damping would need to be added to enable the TCL model presented in Chapter 4 to be extended directly to the wall. That is not entirely the case, however. Making a model *consistent with* the two-component limit is not the same thing as *enforcing compliance* with it. However, in working with TCL models, the wall corrections relating to the pressure-strain correlation are indeed less strong and are effective over a smaller range of Re_t than those used with the Basic or QI Models.

First, we note a feature of the rapid part of Φ_{ij} that was brought to light from an examination of DNS data by Bradshaw *et al.* (1987) at the first of the CTR-Stanford Summer Schools on turbulence (but which has not, apparently, been published elsewhere). In developing models for mean-strain effects on Φ_{ij_2} it has been assumed that the mean velocity gradient that appears under the integral in Eq. (4.3) could be assumed to be uniform for distances over which the two-point velocity correlation appearing in the equation was significant. Bradshaw *et al.* (1987) showed that while this approximation was indeed satisfactory over most of the flow, it did not apply across the buffer layer where the mean velocity gradient changes so rapidly with distance from the wall. Launder and Tselepidakis (1994) and a number of later workers thus adopted an effective velocity gradient to be used in Φ_{ij} of the form:

$$\left.\frac{\partial U_l}{\partial x_m}\right|_{eff} = \frac{\partial U_l}{\partial x_m} + c_I l^2 \frac{\partial f^*(A)}{\partial x_k}\frac{\partial^2 U_l}{\partial x_k \partial x_m} \tag{6.28}$$

where, in the later paper by Launder and Li (1994), $f^*(A)$ was taken as $A^{0.3}(1 + 2.5A^3)$, $l = k^{3/2}/\varepsilon$ and $c_I = 0.07$. The only other modification applied to Φ_{ij_2} was to limit the value of the coefficient c_2 in Eq. (4.60) to $c_2 = \min(0.55,\ A)$ with c_2' remaining unaltered at 0.6.

Modifications to the 'slow' part of Φ_{ij} are of a similar form to those shown above for the Basic Model (though the wall-reflection coefficients do not appear). Thus, Launder and Tselepidakis (1994) suggest that the coefficients in Eq. (4.34) should become:

$$c_1 = 6.3A(\min[0.6,\ A_2])^{1/2}(1 - f), \quad c_1' = 0.07, \quad f \equiv \max\left[\left(1 - R_t/140\right), 0\right]$$

a version retained by Launder and Li (1994). The scheme has been applied to a number of simple shear flows, including plane channel flow, with a similar level of agreement to that achieved by the HJ model above. Figure 6.16, from Launder and Tselepidakis (1994),[12] shows the distribution of turbulence intensities and

[12] This version preceded the final form of the model and did not contain the term with coefficient c_2' in Φ_{ij_2}; in compensation a weak wall-reflection term was employed.

https://doi.org/10.1017/9781108875400.008 Published online by Cambridge University Press

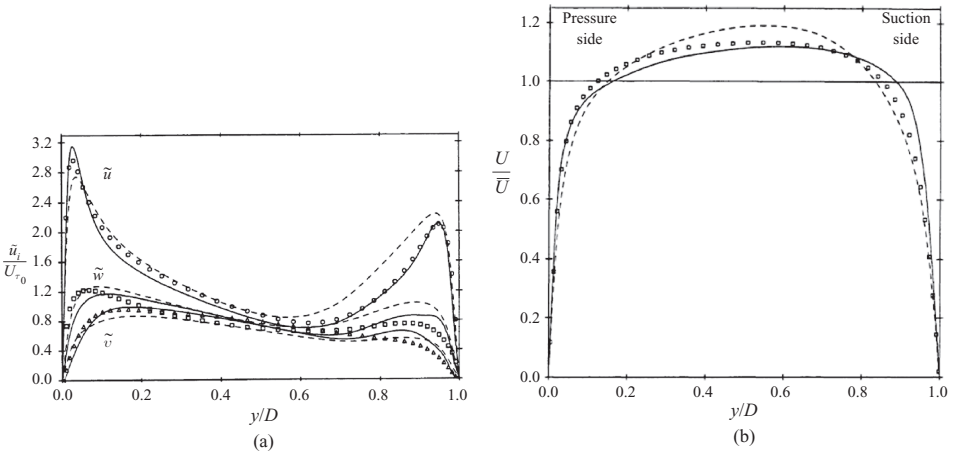

Fig. 6.16 Flow in a plane channel in orthogonal mode rotation, Ro = 0.05, Re = 6,200; (a) rms normal stresses; (b) mean velocity profile. Symbols, DNS data (Kristoffersen and Andersson, 1993); solid lines, TCL computations; broken lines computations by Kristoffersen and Andersson (1993) using the Launder and Shima (1989) model. From Launder and Tselepidakis (1994). ($\tilde{u}_i$ is the rms fluctuating velocity in direction x_i; U_{τ_0} is the friction velocity for zero rotation at the same Re.)

mean velocity for fully developed flow in a channel in orthogonal mode rotation. Comparison is with the DNS data of Kristoffersen and Andersson (1993) and the computations of Kristoffersen *et al.* (1990) from using the earlier second-moment closure of Launder and Shima (1989) (which had been created when TCL ideas were still being formulated and, as noted above, is thus based around adaptations to the Basic Model). The data are at a sufficiently low bulk Reynolds number ($\approx 6{,}000$) that, with the effects of rotation (Ro = 0.05), the wall-adjacent region does not match the 'universal' state used as near-wall boundary conditions in the application of the Basic Model (for higher Re and lower Ro) discussed in §4.5.2. Recall that the Coriolis force arising from the rotation acts to augment velocity fluctuations normal to the wall on the pressure side of the channel and to suppress them on the suction side. There are equal and opposite effects on the streamwise velocity fluctuations (so there is no net Coriolis force in the turbulence energy equation) but these are outweighed by Coriolis effects on the shear stress which acts to increase streamwise fluctuations on the pressure side. While both closure models reproduce correctly the asymmetry that is induced in the flow, the TCL computations are in especially close accord with the DNS data.

Craft (1998) has provided a more elaborate version of near-wall corrections to the TCL model which he has applied over a somewhat wider range of flows, including cases with impingement, separation and reattachment for subsonic and

https://doi.org/10.1017/9781108875400.008 Published online by Cambridge University Press

transonic flows. Many of these are included in Craft (2002), which appears in Launder and Sandham (2002). In view of the algebraic complexity of the form proposed, the interested reader is referred for further details to that publication.

Turbulent diffusion

In principle, one would expect significant effects of viscosity and wall blocking on triple velocity and scalar moments close to a wall which would need to be accounted for, especially if the simple gradient-diffusion models presented in §4.3.5 are used. The simplest approach is to make the 'diffusion' coefficients c_s and c_θ in Eqs. (4.21) and (4.22) functions of the turbulent Reynolds number and stress-anisotropy invariants. However, the DNS of channel flow at $\mathrm{Re}_\tau = 180$ and 2,000 indicate that the turbulent diffusion becomes a minor part of the stress budget (reaching a maximum for y^+ between 15 and 50, as indicated in Fig. 6.5) (Kim *et al.*, 1987; Mansour *et al.*, 1988; Hoyas and Jimenez, 2006). With the exception of flows near a reattachment point, the triple moments and $\mathcal{D}^t_{ij}$ diminish rapidly as the wall is approached (recall, $\mathcal{D}^t_{ij} \propto x_2^{n+1}$, where $n \geq 2$ is the exponent of the relevant stress component, i.e. $\overline{u_i u_j} \propto x_2^n$; see Hanjalić, 1994). The same can also be said for $\mathcal{D}^t_{\theta j}$, except that in flows dominated by buoyancy the gradient-diffusion hypothesis is generally less satisfactory (see §4.6, Fig. 4.28). In view of the above, the usual approach is to retain broadly the same model for $\mathcal{D}^t_{\theta j}$ adopted in high-Re regions, with possibly some empirical adjustments or the imposition of a lower bound on the time scale, k/ε.

The DNS results for the plane channel (Kim *et al.*, 1987) showed that the stress diffusion by pressure fluctuations, $\mathcal{D}^p_{ij}$, reaches a maximum close to the wall within or close to the edge of the viscous layer, but even here it is negligible compared with other budget contributors. This finding provided justification for neglecting the term (or modelling it jointly with the velocity transport), as discussed in §4.3.6.[13] However, because of the non-zero pressure fluctuations at a rigid surface, for $\overline{u_2^2}$ and $\overline{u_1 u_2}$ it is $\mathcal{D}^p_{ij}$ that closes the budget of the $\overline{u_i u_j}$ equation at the wall. The budget could be closed by an appropriate model of $\Pi_{ij} \equiv \Phi_{ij} + \mathcal{D}^p_{ij}$ that approaches the wall linearly (see Table 6.1). However, the $\overline{u_2^2}$ equation would still remain unbalanced. Because most current models use quadratic or higher order damping of Φ_{ij}, some workers introduce a separate model of pressure diffusion in a form that uses unit vectors normal to the wall, which thus contribute only to the $\overline{u_2^2}$ and $\overline{u_1 u_2}$ components, i.e. to components containing velocity fluctuations normal to the wall (Launder *et al.*, 1987; Lai and So, 1990; see also Demuren, 1996). Nevertheless,

[13] This practice may not be justified in flows governed by buoyancy, such as in Rayleigh–Bénard convection where the DNS results (Wörner and Grötzbach, 1997) indicate that the pressure transport exceeds (and even has the opposite sign from) the velocity diffusion.

wall-normal vectors are best avoided unless the influence of the terms of which they form a part is essentially confined to the viscous region.

Stress-dissipation rate

Most stress-transport models treat the dissipation tensor ε_{ij} as isotropic even at relatively low bulk Reynolds numbers; so the most frequent form of the model – at least for high-Re flows – is $\varepsilon_{ij} = 2/3\varepsilon\delta_{ij}$. Equipartition of dissipation among the normal stress components and neglect of the viscous terms in the shear-stress equation at sufficiently high Re_t has been seen as justified, since, even when the dissipation is not entirely isotropic, its anisotropy will still be weaker than the stress anisotropy. Even where this condition is not in fact satisfied, any anisotropy can still be absorbed in the model of Φ_{ij}, as argued by Lumley (1978). Anisotropic forms of ε_{ij} have generally been adopted only for the region very close to a wall, the degree of anisotropy usually being linked to the local stress anisotropy a_{ij} and the turbulent Reynolds number. A form, introduced by Hanjalić and Launder (1976), and frequently used for modelling low-Re_t turbulence is

$$\varepsilon_{ij} = {}^2\!/_3\varepsilon\delta_{ij}(1 - f_s) + \varepsilon\frac{\overline{u_i u_j}}{k} f_s \tag{6.29}$$

where f_s is a function of Re_t. As $f_s \to 1$, Eq. (6.29) expresses the proportionality of the large-scale (stress) and small-scale (dissipation) anisotropies, i.e. $e_{ij} = f_s a_{ij}$, where $e_{ij} \equiv \varepsilon_{ij}/\varepsilon - 2/3\delta_{ij}$ was introduced in Chapter 3 (Eq. (3.29)). The empirical function $f_s(\mathrm{Re}_t)$ should ensure a transition from one mode to another over the appropriate range of Re_t. Hanjalić and Launder (1976) chose f_s to decay rapidly with distance from the wall so that an isotropic ε_{ij} was returned in the outer part of the wall region even at relatively low bulk Reynolds numbers. However, DNS data subsequently revealed a different trend: in plane channel flow for both $\mathrm{Re}_m = 5{,}600$ (Mansour *et al.*, 1988) and 14,000 (Kim *et al.*, 1987): over most of the wall region (up to $y^+ = 60$) the dissipation tensor exhibited a high degree of anisotropy very much in accord with $\varepsilon_{ij} = \varepsilon\overline{u_i u_j}/k$, although ε_{12} appeared small everywhere except very close to the wall ($y^+ < 10$). These findings seem to substantiate arguments presented earlier that the dissipation anisotropy in near-wall flows is predominantly caused by the strong wall influence, which permeates well beyond the viscosity-affected region. Partly for that reason, but also to gain more flexibility, several groups have introduced the second and third stress invariants, A_2 and A_3, as well as the 'flatness' parameter A, Eq. (3.28) (Gilbert and Kleiser, 1991; Launder and Tselepidakis, 1993). Hanjalić and Jakirlić (1993) argued that neither Re_t nor A was well suited for modelling the type of variation of ε_{ij} exhibited by the DNS data. A comparison of the variations of Re_t for $\mathrm{Re}_m = 5{,}600$ and 14,000 (corresponding to Re_τ of 180 and 390, respectively) shows that the

https://doi.org/10.1017/9781108875400.008 Published online by Cambridge University Press

turbulent Reynolds numbers coincide reasonably well up to $y^+ = 10$ but thereafter depart; thus the data indicate that Re_t cannot be used to generate a universal f_s up to $y^+ = 60$. On the other hand, the same data show that the stress-anisotropy invariants and the flatness parameter A remain almost uninfluenced by the bulk Reynolds number (see Fig. 3.14b), especially when plotted against y^+ (as shown in Fig. 2 from Hanjalić and Jakirlić, 1993). In contrast, the stress dissipation rate, ε_{ij}, becomes isotropic progressively closer to the wall as Re_m increases. In fact, for the highest Re_m, ε_{ij} already becomes isotropic by the edge of the viscous region, as indicated by the dissipation-rate flatness E nearly reaching unity, Fig. 3.14b. For low Re_m ($\mathrm{Re}_\tau = 180$) the function $f_s = 1 - \sqrt{A}$ (Gilbert and Kleiser, 1991) produced a variation of ε_{ij} close to that of DNS data apart from the near-wall limits. However, that function produces the same degree of anisotropy in ε_{ij} at very high bulk Re_m, contrary to real flows, where ε_{ij} is essentially isotropic. The function $f_s = \exp(-20A^2)$, proposed by Launder and Tselepidakis (1993), satisfies the high Reynolds number limit, but not the low Re_m case ($\mathrm{Re}_\tau = 180$), since the function already decays sharply by $y^+ = 30$. For these reasons, Hanjalić and Jakirlić (1993) proposed that f_s should be modelled in terms of the flatness parameter of the small-scale motion, $E \equiv 1 - 9(E_2 - E_3)/8$, where, it is recalled, $E_2 \equiv e_{ij}e_{ji}$ and $E_3 \equiv e_{ij}e_{jk}e_{ki}$ are, respectively,[14] the second and third invariants of the stress-dissipation-rate tensor e_{ij}.

An expression of the form $f_s = 1 - E^4$ satisfies the condition of local isotropy of the small-scale motion at high Reynolds numbers, where $E = 1$ and ε_{ij} becomes isotropic irrespective of a_{ij}. It also satisfies the two-component limit where $E = 0$ and $e_{\alpha\alpha} = a_{\alpha\alpha}$ for the remaining normal stress components (11 and 33). A test, using the DNS data for ε and $\overline{u_i u_j}$, reproduced ε_{ij} in close agreement with DNS data for all three normal components of the dissipation, although it failed to bring much improvement to ε_{12} (Fig. 6.17). Equally as good results were achieved by including both the stress- and dissipation-rate anisotropy invariants: $f_s = 1 - A^{1/2}E^2$. While not fully satisfying the small-scale isotropy limits noted above, this form still proved to be satisfactorily accurate and computationally, more robust. The dissipation anisotropy can then be expressed as:

$$e_{ij} = a_{ij}\left(1 - A^{1/2}E^2\right). \tag{6.30}$$

A formally more rigorous non-linear relationship between e_{ij} and a_{ij} was proposed by Hallbäck *et al.* (1990) based on the tensorial expansion of ε_{ij} in terms of the stress-anisotropy tensor a_{ij} up to quadratic terms and the second stress invariant.

[14] Strictly, since e_{ij} is expressible in terms of a_{ij} and the stress invariants, there is no necessity to introduce the dissipation invariants, i.e. the same result could have been expressed in terms of stress invariants and Reynolds number. However, it helps algebraic transparency to do so and underlines clearly the different response of the energy-containing and dissipation ranges to changes in Reynolds number and wall proximity.

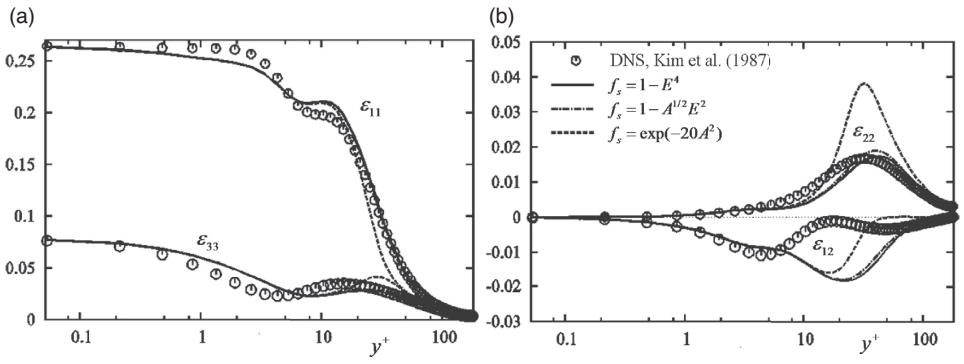

Fig. 6.17 Components of ε_{ij} from Eq. (6.29) for different proposals for f_s (using $\overline{u_i u_j}$ and ε from DNS data of Kim *et al.* (1987) as a function of y^+. From Hanjalić and Jakirlić (1993). The variations of A and E across the channel for different Re are shown in Fig. 3.14.

After imposing symmetry conditions, zero trace, and the Cayley–Hamilton theorem on the a_{ij} tensor, and truncating at third-order terms, the expression reduces to

$$e_{ij} = a_{ij}\left[1 + \alpha\left(\frac{1}{2}A_2 - \frac{2}{3}\right) - \alpha\left(a_{ik}a_{jk} - \frac{1}{3}A_2\delta_{ij}\right)\right]. \tag{6.31}$$

In fact, Eq. (6.31) can be recast in an alternative form to display better the near-wall and far-from-the-wall contributions, which allows a more direct comparison with the simpler linear model, Eq. (6.29),

$$\varepsilon_{ij} = \varepsilon\left[\frac{2}{3}\delta_{ij}\,(1 - f_s) + \frac{\overline{u_i u_j}}{k}\,f_s\right] - \alpha\varepsilon\left(a_{ik}a_{jk} - \frac{1}{3}A_2\delta_{ij}\right) \tag{6.32}$$

where $f_s = 1 + \alpha(A_2/2 - 2/3)$. The first term is obviously the usual linear approximation introduced earlier, Eq. (6.29), whereas the second introduces non-linear effects. With $\alpha = 3/4$, the model satisfactorily reproduced several sets of DNS results for *homogeneous* turbulence (in contrast to the rather poor performance of Eq. (6.29)), but had little success in reproducing the DNS results for plane channel flows (i.e. the wall-limiting values of the ε_{ij} components), see, for example Jakirlić (2004).

As indicated above, Eq. (6.29), while attractively simple, is not an exact limiting form. As shown from the polynomial expansions for the velocity components, it is correct if neither i nor j takes the value 2 (x_2 being the direction normal to the wall), as shown by Eq. (6.14), i.e. $\varepsilon_{11} = \varepsilon_w \overline{u_1^2}/k$ and $\varepsilon_{33} = \varepsilon_w \overline{u_3^2}/k$. However, if either i or j (or both) is 2, the wall asymptotes become $\varepsilon_{12} = 2\varepsilon_w \overline{u_1 u_2}/k$ and $\varepsilon_{22} = 4\varepsilon_w \overline{u_2^2}/k$.

A convenient invariant way of satisfying the above wall-limiting behaviour is to recast Eq. (6.29) in the form

https://doi.org/10.1017/9781108875400.008 Published online by Cambridge University Press

$$\varepsilon_{ij} = \frac{2}{3}\varepsilon\delta_{ij}(1 - f_s) + \varepsilon^*_{ij} f_s \tag{6.33}$$

and formulate ε^*_{ij} in terms of the unit vector normal to the wall n_k so that it *does* satisfy the limiting wall ratios of dissipation rates (Launder and Reynolds, 1983).

Kebede *et al.* (1985) proposed an expression that ensures that the sum of the diagonal components contract to 2ε

$$\varepsilon^*_{ij} = \frac{\varepsilon}{k}\frac{\overline{u_i u_j} + \overline{u_i u_k} n_k n_j + \overline{u_j u_k} n_k n_i + \overline{u_k u_l} n_k n_l \delta_{ij}}{1 + (5/2)\overline{u_p u_q} n_p n_q / k}. \tag{6.34}$$

Hanjalić and Jakirlić (1993) observed that the above wall corrections of ε apply their effect too far beyond the intended near-wall region and devised a modified form of the correction (to be used in conjunction with $f_s = 1 - A^{1/2}E^2$ in (6.33))

$$\varepsilon^*_{ij} = \frac{\varepsilon}{k}\frac{\overline{u_i u_j} + \left(\overline{u_i u_k} n_k n_j + \overline{u_j u_k} n_k n_i + \overline{u_k u_l} n_k n_l n_i n_j\right) f_d}{1 + (3/2)\overline{u_p u_q} n_p n_q f_d / k} \tag{6.35}$$

which differs from the original expression by the introduction of a damping function $f_d = (1 + 0.1\mathrm{Re}_t)^{-1}$ and the replacement of the Kronecker delta by products of the unit wall-normal vector, n_p. This modification was employed to produce the results shown in Fig. 6.17.

'Homogeneous' stress dissipation rate

A different approach to satisfying the wall behaviour of ε_{ij} without resorting to unit vectors is to derive the model from the transport equation for the two-point velocity correlation (Jovanović *et al.*, 1995). Here attention is given just to the viscous terms of the resultant equations, i.e.

$$\frac{D\overline{u_i^A u_j^B}}{Dt} = \cdots + \nu\left[\overline{u_i^A \frac{\partial^2 u_j^B}{\partial x_k^B \partial x_k^B}} + \overline{u_i^B \frac{\partial^2 u_j^A}{\partial x_k^A \partial x_k^A}}\right] \equiv \cdots + V_{ij}^{AB}. \tag{6.36}$$

Introducing a local coordinate system with origin midway between A and B and defining $\xi_k \equiv x_k^B - x_k^A$ and $x_k^{AB} \equiv \frac{1}{2}(x_k^A + x_k^B)$, the viscous term V_{ij}^{AB} can be written for the general case of non-isotropic, inhomogeneous turbulence as

$$V_{ij}^{AB} = \frac{1}{2}\nu\frac{\partial^2 \overline{u_i^A u_j^B}}{\partial x_k^{AB} \partial x_k^{AB}} + 2\nu\frac{\partial^2 \overline{u_i^A u_j^B}}{\partial \xi_l \partial \xi_l}. \tag{6.37}$$

In homogeneous turbulence all derivatives with respect to x_k^{AB} vanish and, for $A \to B$, $V_{ij}^{AB} \to V_{ij}$, the latter representing the stress-dissipation rate in a homogeneous flow, denoted ε^h_{ij}, i.e.

$$V_{ij}^{AB} \to V_{ij} = 2\nu\left[\frac{\partial^2 \overline{u_i^A u_j^B}}{\partial \xi_l \partial \xi_l}\right]_{\xi=0} = -\varepsilon^h_{ij}. \tag{6.38}$$

https://doi.org/10.1017/9781108875400.008 Published online by Cambridge University Press

In *inhomogeneous* turbulence, however, for $A \to B$:

$$V_{ij}^{AB} \to V_{ij} = \frac{1}{2}\nu\frac{\partial^2\overline{u_i u_j}}{\partial x_k \partial x_k} - \varepsilon_{ij}^h = \frac{1}{2}\mathcal{D}_{ij}^{\nu} - \varepsilon_{ij}^h. \tag{6.39}$$

From a comparison with conventional single-point splitting of the total viscous term $V_{ij} = \mathcal{D}_{ij}^{\nu} - \varepsilon_{ij}$ (see Chapter 2) it follows that

$$\varepsilon_{ij} = \varepsilon_{ij}^h + \tfrac{1}{2}\mathcal{D}_{ij}^{\nu}. \tag{6.40}$$

The above equation shows that the stress-dissipation rate tensor ε_{ij} contains a contribution due to *turbulence inhomogeneity*, which appears in the form of the stress diffusion by viscosity, and thus cannot be accounted for exactly by any algebraic interpolation of the type (6.29). However, *that* equation nevertheless seems appropriate for the homogeneous part of the dissipation rate tensor, i.e.

$$\varepsilon_{ij}^h = \frac{2}{3}\varepsilon^h \delta_{ij}\,(1 - f_s) + \varepsilon^h \frac{\overline{u_i u_j}}{k} f_s \tag{6.41}$$

where $\varepsilon^h = \varepsilon - \frac{1}{2}\mathcal{D}_k^{\nu}$ is the homogeneous part of the kinetic energy dissipation rate, which can be obtained from ε, or from the solution of an equation for ε^h instead of for ε (Jakirlić and Hanjalić, 2002). We return to this approach in the treatment of low-Re modifications to ε in the next section.

The components of the full dissipation rate tensor can now be obtained from Eq. (6.40), where $\mathcal{D}_{ij}^{\nu}$ is the viscous diffusion of the corresponding stress component, computed from the solution of the stress transport equation, which can be reformulated in terms of ε_{ij}^h:

$$\frac{D\overline{u_i u_j}}{Dt} = \cdots + \frac{1}{2}\frac{\partial}{\partial x_k}\left(\nu\frac{\partial\overline{u_i u_j}}{\partial x_k}\right) - \varepsilon_{ij}^h \cdots \tag{6.42}$$

where the dots stand for all the other terms in the modelled stress-transport equation which remain unchanged. An advantage of using this approach is immediately apparent: all components of ε_{ij} except ε_{22} now *exactly* satisfy the wall limits of $(\varepsilon_{\alpha\beta}/\varepsilon)(k/\overline{u_\alpha u_\beta})$ (i.e. 1 for $\alpha = \beta = 1$ or 3 and $\alpha = 1,\ \beta = 3$; 2 for $\alpha = 1$ or 3 (or $\beta = 1$ or 3) and $\beta = 2$ (or $\alpha = 2$). The only slight discrepancy appears for the wall-normal component, $\alpha = \beta = 2$, for which the model gives $(\varepsilon_{22}/\varepsilon)(k/\overline{u_2^2}) = 3.5$ instead of the exact limit of 4. Thus, the correction given by Eq. (6.34) or (6.35), which has been used in many low-Re second-moment closures, is not necessary: the wall limits are satisfied directly by considering only the homogeneous portion of the dissipation rate, i.e. using Eqs. (6.40) and (6.41). This is illustrated by an *a priori* evaluation of components of ε_{ij} using the DNS data for $\overline{u_i u_j}$ and ε for several generic flows, including flows in a plane channel, in a rotating pipe and behind a backward-facing step: all show acceptable results (see Figs 3–5 in Jakirlić and Hanjalić, 2002). To illustrate the fidelity with which the

https://doi.org/10.1017/9781108875400.008 Published online by Cambridge University Press

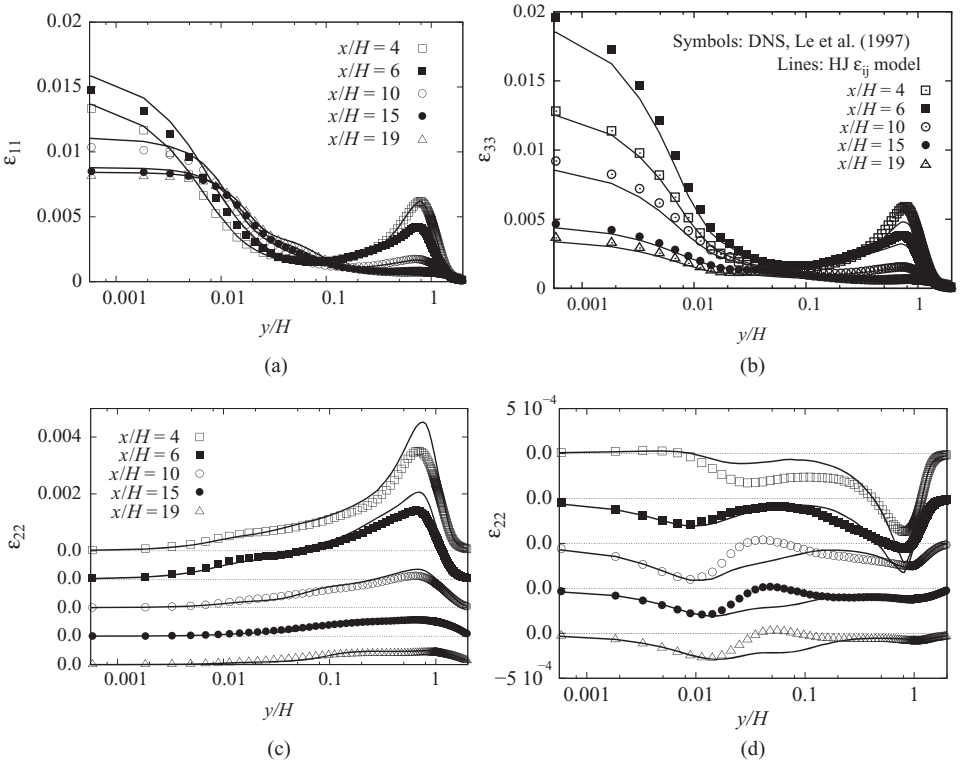

Fig. 6.18 Components of ε_{ij} at five locations ($x/H = 4$, recirculation zone; $x/H = 6$, around reattachment; $x/H = 10$, 15 and 19, recovery region; H is the step height) in the flow behind a backward-facing step at $\mathrm{Re}_H = 5{,}100$. Symbols, DNS, Le *et al.* (1997); lines, Eqs. (6.40) and (4.41). From Jakirlić and Hanjalić (2002).

DNS data are reproduced, Fig. 6.18. shows their results for perhaps the most challenging of the cases, the back-step flow at three locations: within the recirculation zone, around reattachment and in the downstream recovery zone.

Jakirlić (2004) noted that the expression for ε_{ij} proposed by Hallbäck *et al.* (1990) (noted above) based on a non-linear relation between e_{ij} and a_{ij}, Eqs. (6.31) and (6.32), can also accord with the wall limits and provides very satisfactory near-wall behaviour in inhomogeneous flows if the expressions are applied to the *homogeneous* dissipation rate with the addition of the inhomogeneous term (i.e. half the molecular stress diffusion as in Eq. (6.40)):

$$\varepsilon_{ij} = \varepsilon^h \left[\frac{2}{3}\delta_{ij}\,(1 - f_s) + \frac{\overline{u_i u_j}}{k} f_s \right] - \alpha \varepsilon^h \left(a_{ik}a_{kj} - \frac{1}{3}A_2\delta_{ij} \right) + \frac{1}{2}\mathcal{D}^v_{ij}. \quad (6.43)$$

The reconstruction of the ε_{ij} components using Eq. (6.43) for flow in an axially rotating pipe and in the recirculating zone behind a backward-facing step reproduced the DNS data very well (Jakirlić, 2004).

https://doi.org/10.1017/9781108875400.008 Published online by Cambridge University Press

6.3.5 Low Reynolds number and near-wall effects on the dissipation rate equation

In the earlier discussion of the exact equation for ε in high-Re flows remote from walls, §3.4, it was concluded that two source terms, $\mathcal{P}_{\varepsilon 4}$ and Υ_ε, both of order $\varepsilon^{3/2}/\nu^{1/2}$ (or, equivalently, $(\varepsilon/\mathcal{T})\mathrm{Re}_t^{1/2}$) dominate the ε-equation and that their difference balanced the convection and turbulent diffusion of ε. Consequently, all other terms were formally omitted. As the wall is approached, however, the range of eddy scales reduces and (partly because of the decreasing Re_t and partly because of the strong inviscid wall blocking) the assumption of local isotropy of the dissipative motion ceases to be valid. Naturally, the viscous diffusion $\mathcal{D}_\varepsilon^\nu$ now needs to be retained (and *can* be without approximation). Moreover, some of the mean-strain terms that appear directly in the exact ε-equation, $\mathcal{P}_{\varepsilon 1}$, $\mathcal{P}_{\varepsilon 2}$ and $\mathcal{P}_{\varepsilon 3}$ (which were discarded in Chapter 5) also need to be considered. A comparative estimate of the order of magnitude of all production terms can be made in terms of the characteristic velocity scale for which $k^{1/2}$ has usually been adopted, and the two length scales: the energy-containing scale, $l = k^{3/2}/\varepsilon$, and the Taylor scale, λ (after Tennekes and Lumley, 1972)[15]

$$u_i \sim U_i \sim k^{1/2}, \quad x_i \sim l, \quad S_{ij} \sim \frac{\partial U_i}{\partial x_j} \sim \frac{k^{1/2}}{l}, \quad s_{ij} \sim \frac{\partial u_i}{\partial x_j} \sim \frac{k^{1/2}}{\lambda}. \tag{6.44}$$

Recall also that the dissipation rate can be expressed as both $\varepsilon = 15\nu\overline{u_1^2}/\lambda^2$ and $\varepsilon = c_l k^{3/2}/l$, which results in a relationship between l and λ (and between Re_λ and Re_t, Eq. (3.13)). Thus, the formerly neglected terms now scale as follows:

$$\begin{aligned}
\frac{\mathcal{P}_{\varepsilon 1} + \mathcal{P}_{\varepsilon 2}}{\nu} &\sim \overline{s_{il}s_{kl}}S_{ik} = \mathcal{O}\left(\frac{k}{\lambda^2}\frac{k^{1/2}}{l}\right) = \mathcal{O}\left(\frac{k^{3/2}}{\lambda^3}\frac{\lambda}{l}\right) = \mathcal{O}\left(\frac{k^{3/2}}{\lambda^3}\mathrm{Re}_t^{-1/2}\right) \\
\frac{\mathcal{P}_{\varepsilon 3}}{\nu} &\sim \overline{u_k s_{il}}\frac{\partial S_{il}}{\partial x_k} = \mathcal{O}\left(k^{1/2}\frac{k^{1/2}}{\lambda}\frac{k^{1/2}}{l^2}\right) = \mathcal{O}\left(\frac{k^{3/2}}{\lambda^3}\frac{\lambda^2}{l^2}\right) = \mathcal{O}\left(\frac{k^{3/2}}{\lambda^3}\mathrm{Re}_t^{-1}\right) \\
\frac{\mathcal{P}_{\varepsilon 4}}{\nu} &\sim \overline{s_{ik}s_{il}s_{kl}} = \mathcal{O}\left(\frac{k^{3/2}}{\lambda^3}\right).
\end{aligned} \tag{6.45}$$

On noting that $\mathrm{Re}_\lambda \propto \mathrm{Re}_t^{1/2}$, one can replace λ in the estimate of $\mathcal{P}_{\varepsilon 4}$ in the last row of Eq. (6.45) to obtain $\mathcal{P}_{\varepsilon 4} \sim (\varepsilon/\mathcal{T})\mathrm{Re}_t^{1/2}$ as found in Chapter 3. By way of contrast, the production terms in the first two rows of (6.45) decrease in magnitude as Re_t is raised, justifying their omission in modelling the ε-equation for high-Re

[15] The use of the Taylor micro-scale, λ, in combination with the energy-containing velocity scale $k^{1/2}$ is less justifiable for high-Re flows because the two scales correspond to different wave number ranges of the energy spectrum. Here, however, this practice is seen as providing an order of magnitude estimate of terms and the effect of Re_t.

https://doi.org/10.1017/9781108875400.008 Published online by Cambridge University Press

flows (Chapter 5). However, their inclusion is necessary at low Re and, arguably, also in high-Reynolds-number flows in regions of strong wall influence.

In the exact ε transport equation the mean velocity gradient appears through the term:

$$\mathcal{P}_{\varepsilon 1} + \mathcal{P}_{\varepsilon 2} \equiv -2\nu \left(\overline{\frac{\partial u_i \partial u_j}{\partial x_k \partial x_k}} + \overline{\frac{\partial u_k \partial u_k}{\partial x_i \partial x_j}} \right) \frac{\partial U_i}{\partial x_j}. \tag{6.46}$$

Having regard for the fact that, in a thin shear flow, the mean velocity is significant only in directions parallel to the wall (so index i denotes 1 or 3), the second term is evidently small compared with the first since, within the sublayer, rates of change of the instantaneous turbulence field are much larger in direction x_2 than in x_1 or x_3. The first term can, in fact, be expressed in terms of Eq. (6.34) or (6.35). If direction x_1 is aligned with the near-wall mean velocity, both lead to the result (Launder, 1996):

$$\mathcal{P}_{\varepsilon 1} \equiv -2\nu \left(\overline{\frac{\partial u_i \partial u_j}{\partial x_k \partial x_k}} \right) \frac{\partial U_i}{\partial x_j} = -\frac{4\varepsilon \overline{u_i u_j}}{2k + 5\overline{u_2^2}} \frac{\partial U_1}{\partial x_2} = \left(\frac{4}{2 + 5\overline{u_2^2}/k} \right) \frac{\varepsilon \mathcal{P}_k}{k}. \tag{6.47}$$

Equation (6.47) suggests therefore that at the wall the value of $c_{\varepsilon 1}$ should be 2.0 rather than the lower values (typically from 1.0 to 1.44) used at high Reynolds numbers.[16] The changeover from the high Reynolds number limit to Eq. (6.47) should consistently adopt the function f_s, as in Eq. (6.29). Most of the earlier work (e.g. Hanjalić and Launder, 1976) has adopted a value for $c_{\varepsilon 1}$ that is independent of Reynolds number.

Alternatively, since the first term in brackets in Eq. (6.46) is in fact ε_{ij}, one can simply write $\mathcal{P}_{\varepsilon 1} = -\varepsilon_{ij} \partial U_i \big/ \partial x_j$. The second term, while (as argued above) negligible very close to a wall may conveniently be lumped with ε_{ij} since the two contain certain terms in common (the contribution of the second term notionally being recognized by adopting a coefficient somewhat different from unity). If, for example, ε_{ij} can be modelled satisfactorily by Eq. (6.33) with (6.34) or (6.35), or by using Eq. (6.41) in combination with the homogeneous dissipation rate, this would in principle provide the low Reynolds number source of ε. However, at high Reynolds numbers and away from the influence of the wall, ε_{ij} becomes virtually isotropic irrespective of the stress anisotropy, and $\mathcal{P}_{\varepsilon 1}$ then makes a negligible contribution to the total production of ε. However, from Chapter 5, in these circumstances the ε-equation is dominated by the *difference* between the same terms as at high Re, namely $\mathcal{P}_{\varepsilon 4} - \Upsilon_\varepsilon$. The common practice is to model the difference between these two terms as $(c_{\varepsilon 1}\mathcal{P}_k - c_{\varepsilon 2}\varepsilon)(\varepsilon/k)$, though not associating individual terms

[16] For the alternative scenario of flow on the axis of a plane impinging flow, where $\partial U_1/\partial x_1 = -\partial U_2/\partial x_2$ are the only non-zero strain elements, the corresponding expression for $\mathcal{P}_{\varepsilon 1}$ *does* reduce to $c_{\varepsilon 1} = 1.0$.

https://doi.org/10.1017/9781108875400.008 Published online by Cambridge University Press

with either of the terms in the exact equation. Thus, collectively, the modelling of these source terms can be written as:

$$\mathcal{P}_{\varepsilon 1} + \mathcal{P}_{\varepsilon 2} + \mathcal{P}_{\varepsilon 4} - \Upsilon_\varepsilon = -\varepsilon_{ij}\frac{\partial U_i}{\partial x_j} - c_{\varepsilon 1}\overline{u_i u_j}\frac{\partial U_i}{\partial x_j}\frac{\varepsilon}{k} - c_{\varepsilon 2}\frac{\varepsilon^2}{k}. \tag{6.48}$$

There is, as implied in the foregoing, incomplete agreement in the turbulence community as to what exact terms are being approximated by the term with coefficient $c_{\varepsilon 1}$. Those concerned with flows remote from walls favour the idea (presented in Chapter 5) that it is associated with $(\mathcal{P}_{\varepsilon 4} - \Upsilon_\varepsilon)$ since the terms $(\mathcal{P}_{\varepsilon 1} + \mathcal{P}_{\varepsilon 2})$ are then absent or truly negligible. However, Jakirlić and Hanjalić (2002), who examined exclusively internal flows, linked the term with $(\mathcal{P}_{\varepsilon 1} + \mathcal{P}_{\varepsilon 2})$ and cited the DNS results for a plane channel flow which display good support across the viscous region, Fig. 6.19a. It would seem that both points of view have merit. In free shear flows and in the outer regions of flows developing along a wall, the contribution of mean-flow deformation to the spectral transfer of energy seems entirely credible. As one approaches the wall, however, the character of the turbulent fluctuations changes progressively and the range of wave numbers shrinks so there is less and less of a spectral gap between energy generation and dissipation. In these circumstances, the mean-strain contribution to $(\mathcal{P}_{\varepsilon 4} - \Upsilon_\varepsilon)$ will arguably diminish while there could well be a progressive increase in near-wall effects from $(\mathcal{P}_{\varepsilon 1} + \mathcal{P}_{\varepsilon 2})$. It is, moreover, interesting that the coefficient $c_{\varepsilon 1}$ should be constant. Indeed, Jakirlić and Hanjalić (2002), in common with earlier proposals by Launder (1989) (and all subsequent TCL computations, e.g. Craft and Launder (1996)) and Speziale and Gatski (1997), adopted the value $c_{\varepsilon 1} = 1.0$. However, it is noted that if, instead of ε, an equation is solved for the homogeneous dissipation, ε^h (i.e. Eq. (6.54) and with ε^h used consistently in all the modelled terms), the difference between taking $c_{\varepsilon 1} = 1.0$ and the 'old' value, $c_{\varepsilon 1} = 1.44$, is fairly small, Fig. 6.19b.

To complete the contribution of mean shear to the dissipation equation it remains to approximate the source term $\mathcal{P}_{\varepsilon 3}$ in the exact ε-equation which contains $\partial^2 U_i/\partial x_j \partial x_k$. This has commonly been modelled as:

$$2c'_{\varepsilon 1}\nu\overline{u_k u_l}\frac{k}{\varepsilon}\frac{\partial^2 U_i}{\partial x_j \partial x_l}\frac{\partial^2 U_i}{\partial x_j \partial x_k} \tag{6.49}$$

which may be regarded as the result of applying the generalized gradient-diffusion hypothesis (§4.3.6) to close the exact term. In this case the transportable fluctuating quantity, φ, is $\partial u_i/\partial x_j$. The value 1.0 adopted for $c'_{\varepsilon 1}$ by Hanjalić and Launder (1976) is, however, considerably larger than what has more recently been chosen (e.g. Launder and Tselepidakis, 1993, take $c'_{\varepsilon 1} = 0.43$); so, arguably, that choice was compensating for other omissions. The term is important only across the outer part of the viscous region (commonly termed the 'buffer layer').

https://doi.org/10.1017/9781108875400.008 Published online by Cambridge University Press

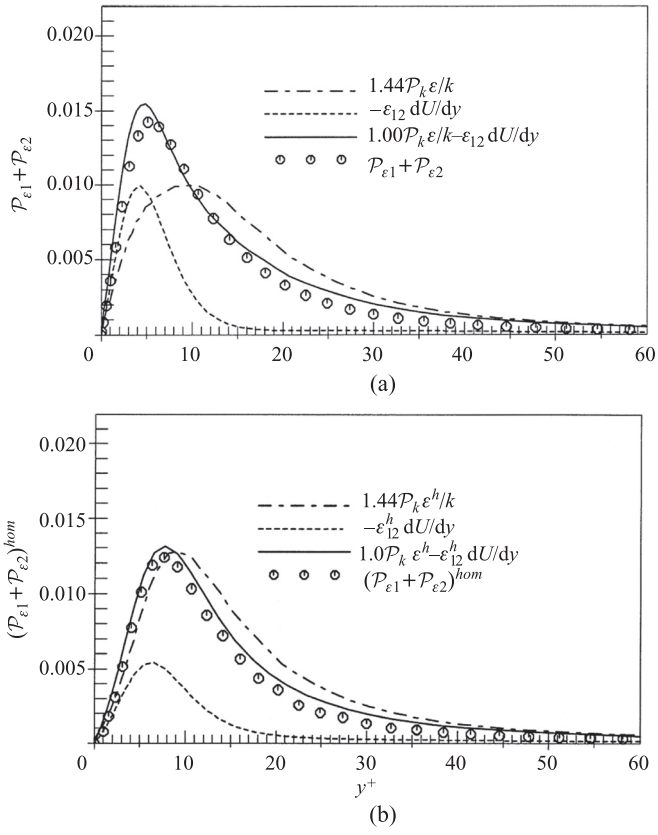

Fig. 6.19 Comparisons of the contributions of $\mathcal{P}_{\varepsilon 1}$ and $\mathcal{P}_{\varepsilon 2}$ in the ε- and ε^h-equations obtained by evaluating exact and modelled terms from the DNS of plane channel flow, $\mathrm{Re_m} = 5{,}600$. Symbols, DNS data (Kim *et al.*, 1987). From Jakirlić and Hanjalić (2002).

A more elaborate model of this process has been proposed by Jakirlić and Hanjalić (2002). Starting from the vorticity transport theory of Bernard (1990), with some assumptions about the turbulence scales, they obtained:

$$\mathcal{P}_{\varepsilon 3} = -2\nu\left(\frac{\partial\overline{u_k u_j}}{\partial x_l}\frac{\partial^2 U_j}{\partial x_k \partial x_l} + c_{\varepsilon 3}\frac{k}{\varepsilon}\frac{\partial\overline{u_k u_l}}{\partial x_j}\frac{\partial U_i}{\partial x_k}\frac{\partial^2 U_j}{\partial x_j \partial x_l}\right) \tag{6.50}$$

where $c_{\varepsilon 3} = 0.2$. Equation (6.50) can be regarded as a rational generalization of the simpler model, Eq. (6.49). This scheme avoids using the square of the second velocity derivative (a form which obviously lacks any sensitivity to the sign of the curvature of the mean velocity profile). When implemented in the HJ near-wall closure, together with the ε^h-equation, it proved to be robust and reproduced well the flows in a plane channel, constant-pressure boundary layer, behind a backward-facing step and in an axially rotating pipe, with stress fields and their budget in good agreement with the available DNS results. Figure 6.20 shows some results for

https://doi.org/10.1017/9781108875400.008 Published online by Cambridge University Press

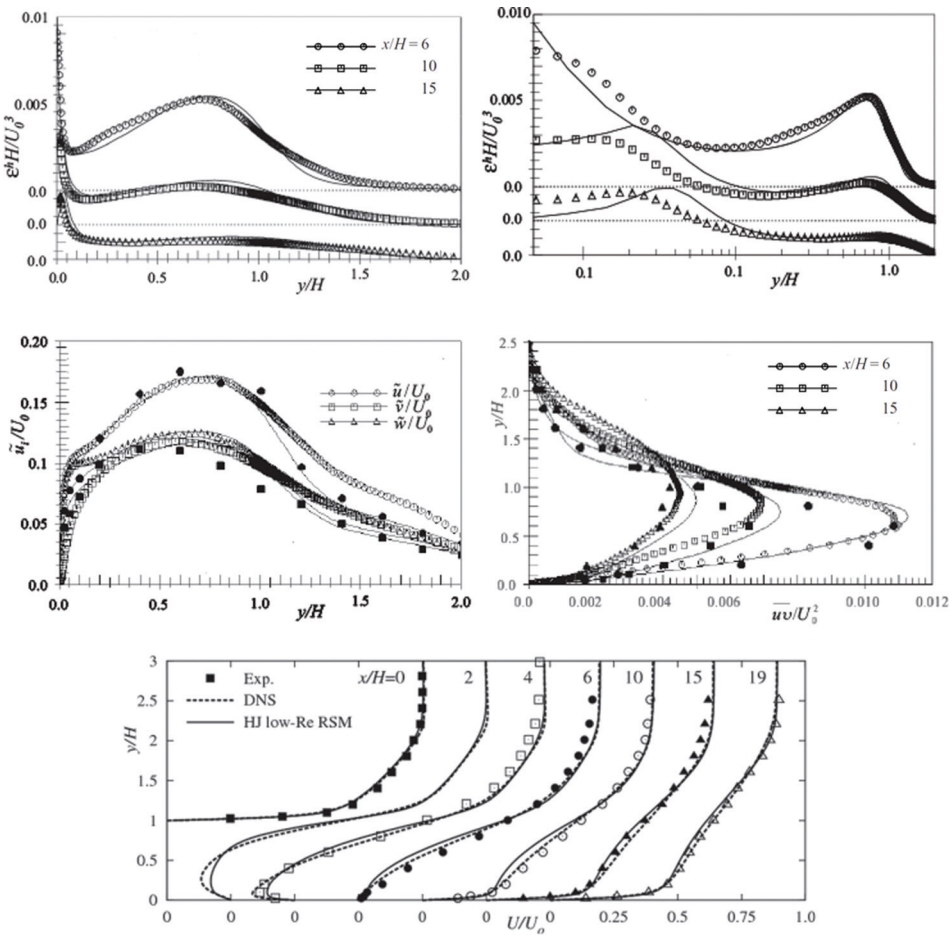

Fig. 6.20 Comparison of computations (lines, HJ RSM model with the ε^h-equation) with DNS and measurements of low-Re flow over a backward-facing step, $\mathrm{Re}_H = 5{,}100$; ER $= 1.2$. Top: homogeneous dissipation rates near the wall (for linear and logarithmic distance scales); Middle: rms normal-stress and shear-stress components. Bottom: mean velocity profiles at selected locations; Open symbols: DNS (Le *et al.*, 1997). Filled symbols: experiments (Jović and Driver, 1994). From Jakirlić and Hanjalić (2002).[17]

the back-step flow, illustrating the model performance in a low Reynolds number separating turbulent flow.

Turning now to the sink term, for high Reynolds number, nearly isotropic turbulence the coefficient $c_{\varepsilon 2}$ was determined by reference to grid turbulence decay,

[17] For this particular test case Craft (1998) found that while the TCL model also gave very satisfactory agreement with measurements, so too did the linear $k-\varepsilon$ eddy-viscosity model (even though in most backward-facing step cases eddy-viscosity schemes seriously under-predict the length of the recirculating zone). It seems that the combination of low Reynolds number and large expansion ratio led, rather fortuitously, to good agreement with the eddy-viscosity model.

https://doi.org/10.1017/9781108875400.008 Published online by Cambridge University Press

and it is natural, therefore, that one should turn to low Reynolds number grid turbulence to decide whether modifications are needed. The most complete experimental turbulence decay data are those of Batchelor and Townsend (1948) whose results were re-confirmed in a later, similarly comprehensive, examination by Bennett and Corrsin (1978). These data sets suggest that below a value of Re_t of about 10 the decay exponent n in the relation $k \propto t^{-n}$ increases from the high Reynolds number limit of about 1.2 to an asymptotic value of 2.5. Consequently, the coefficient $c_{\varepsilon 2} = (n+1)/n$ should reach asymptotically the value 1.4 in the final period of decay. If we assume the changeover to be describable in terms of the local value of Re_t, $c_{\varepsilon 2}$ must be multiplied by some function, f_ε, to give the desired limiting values of the decay exponent. Hanjalić and Launder (1976) took

$$f_\varepsilon = 1.0 - 0.22\exp[-(\mathrm{Re}_t/6)^2]. \tag{6.51}$$

The ability of a model to reproduce the changeover from the initial to the final state of decay of grid turbulence may not seem very important for practical applications. Nevertheless, in transitional flows at low Re_t and, especially, in flows undergoing laminarization, the appropriate accounting for Reynolds number effects is important. There is no reason to suppose much similarity between the low-Re sublayer near a wall and the viscous decay of weak grid turbulence. However, the exponential term in Eq. (6.51) falls to zero so rapidly that f_ε is essentially unity over the whole of the region near the wall where turbulent stresses are important.

There is, in fact, a more important modification to this sink term needed in wall turbulence since, as noted in §6.2.1, ε is non-zero at the wall, while k varies as x_2^2. Even with the introduction of f_ε, therefore, the sink term $c_{\varepsilon 2} f_\varepsilon \varepsilon^2/k$ tends to infinity as x_2 goes to zero. A way to avoid this singularity is to replace ε^2 in the sink term by $\varepsilon\tilde{\varepsilon}$, where $\tilde{\varepsilon}$ was defined by Eq. (6.12).[18] As noted in §6.2.1, $\tilde{\varepsilon}$ varies as x_2^2 near the wall and thus the term $c_{\varepsilon 2} f_\varepsilon \varepsilon\tilde{\varepsilon}/k$ tends to a constant value as the wall is approached. Thus, the model of the sink term can be summarized as:

$$\mathcal{P}_{\varepsilon 4} - \Upsilon_\varepsilon \equiv -2\nu\overline{\frac{\partial u_i}{\partial x_k}\frac{\partial u_i}{\partial x_l}\frac{\partial u_k}{\partial x_l}} - 2\overline{\left(\nu\frac{\partial^2 u_i}{\partial x_k \partial x_k}\right)^2} = -c_{\varepsilon 2} f_\varepsilon \frac{\varepsilon\tilde{\varepsilon}}{k}. \tag{6.52}$$

Virtually all proposals for extending the ε-equation to the wall adopt this form. A notable exception is the ε-equation of Durbin (1991, 1993) in the context of his elliptic relaxation models, where the singularity at a wall was avoided by imposing the Kolmogorov time scale as the lower scale bound. The sink term $c_{\varepsilon 2}\varepsilon^2/k$ is written as $c_{\varepsilon 2}\varepsilon/\mathcal{T}$, with $\mathcal{T} = k/\varepsilon$ prevailing throughout the flow except when it becomes smaller than the Kolmogorov time scale $\vartheta = (\nu/\varepsilon)^{1/2}$, which is finite at a solid wall. (A more detailed overview of Durbin's model is provided in §6.4.)

[18] Models that adopt $\tilde{\varepsilon}$ as dependent variable use $\tilde{\varepsilon}^2$ in the sink term.

https://doi.org/10.1017/9781108875400.008 Published online by Cambridge University Press

Finally, there remains the matter of viscous effects on the turbulent diffusion $\mathcal{D}_\varepsilon^t$ to be accounted for. In most models the high Reynolds number form, $c_\varepsilon \overline{u_k u_l} k/\varepsilon$, is retained as the appropriate diffusion coefficient in the low Reynolds number region, while Prud'homme and Elghobashi (1986) multiply the coefficient c_ε by a viscous damping function, f_μ. All proposals have included the exact viscous transport $\nu \partial\varepsilon/\partial x_k$ as an addition to the high Reynolds number diffusion model. There is also the question of pressure diffusion $\mathcal{D}_\varepsilon^p$ to be considered. In high-Re turbulence no explicit accounting of this process was attempted. An order of magnitude estimate of the term in the exact ε-equation suggests, however, that as the wall is approached the process becomes significant. This suggests that a separate approximation ought to be incorporated. A possible model for the additional term that is significant only in the viscous region has been proposed:

$$\mathcal{D}_\varepsilon^p \equiv -2\frac{\partial}{\partial x_k}\left(\frac{\nu}{\rho}\overline{\frac{\partial p}{\partial x_i}\frac{\partial u_k}{\partial x_i}}\right) = 2c_{\varepsilon 4}\frac{\partial}{\partial x_k}\left(\frac{\nu\tilde{\varepsilon}}{k}\frac{\partial k}{\partial x_k}\right). \tag{6.53}$$

Launder and Tselepidakis (1993) have suggested a value of $c_{\varepsilon 4}$ of 0.92.

Equation for the 'homogeneous' dissipation rate

As discussed in §6.3.3, a way to satisfy the wall-limiting behaviour of ε_{ij} without having to employ wall-normal unit vectors as in Eq. (6.34) or (6.35) is to use the 'homogeneous' stress-dissipation rate defined by Eq. (6.40). This makes it possible to use the algebraic Eq. (6.41) directly without any correction. However, one needs to provide the homogeneous energy-dissipation rate ε^h, which can be computed by contracting indices in Eq. (6.40), i.e. $\varepsilon^h = \varepsilon - 0.5\mathcal{D}_k^v$ and obtaining ε from the solution of its transport equation. However, a preferable (and computationally more convenient) route is to solve a transport equation for ε^h, which can easily be derived from the ε-equation as

$$\frac{D\varepsilon^h}{Dt} = \frac{D\varepsilon}{Dt} - \frac{1}{2}\frac{\partial}{\partial x_k}\left(\nu\frac{\partial \varepsilon^h}{\partial x_k}\right). \tag{6.54}$$

For further details, see Jakirlić and Hanjalić (2002).

6.4 Illustration of the performance of two near-wall models

The near-wall modifications of different terms in the second-moment closure discussed in the previous section have been implemented in various combinations in certain of the high-Re models considered in Chapter 4, thus creating model variants that appear in the literature under the common label: *low-Re second-moment closures*. Models vary in complexity, some focusing solely on handling the near-wall layers to allow integration up to the wall (in which case they might more

https://doi.org/10.1017/9781108875400.008 Published online by Cambridge University Press

appropriately be labelled wall integration (WIN) models). Others are claimed to be more complete and more general in the sense that they can also successfully predict certain phenomena linked explicitly with low Reynolds number effects, such as laminar-to-turbulent and reverse transitions.[19] We show below some examples of the performance of two models presented in the previous section: the HJ and TCL models (the latter as detailed in Batten *et al.*, 1999) representing linear and non-linear models.[20]

6.4.1 Applications of the HJ model

Wall boundary layers in strong pressure gradients

One of the important tests of any turbulence model is its ability to reproduce how turbulence responds to an imposed strong and enduring pressure gradient. In incompressible flows, the pressure gradient affects the turbulence field only indirectly through the changes it brings to the mean strain. Nevertheless, marked effects can be observed in all the turbulence properties, as clearly seen in the changes to the stress anisotropy, which in turn feed into the mean velocity field. Because of these indirect effects, the modification of the mean strain by a prolonged pressure gradient is usually felt by the turbulence field as a cumulative effect which becomes apparent further downstream. By solving transport equations for each of the non-zero stresses one is better able to capture the dynamics of the stress field than with a model directly relating the stress tensor to the deformation tensor.

Adverse and favourable pressure gradients exert important effects on the flow development both in turbomachinery and in external aerodynamics. Strong adverse pressure gradients may cause the flow to separate from the wall, while a strong favourable pressure gradient may lead to boundary-layer laminarization. Figure 6.21 illustrates both cases with computations using the HJ model for boundary-layer flows subjected to a range of pressure gradients: for adverse pressure gradients, $dP/dx > 0$ (Fig. 6.21a), compared with experimental data of Nagano *et al.* (1993), and for sink flows, $dP/dx < 0$ (Fig. 6.21b) for several values of the acceleration parameter K (see §6.2.2), compared with DNS data of Spalart (1986). Most turbulence models can reproduce effects of flow deceleration in the initial region where the pressure gradient is moderate. However, further downstream this becomes more challenging not only because the effective pressure gradient becomes stronger, but also because of the increasing importance of transport on the turbulent stress field. As seen in Fig. 6.21a, for a region below $y^+ = 100$, the

[19] In flows of practical relevance the main interest is in the laminar-to-turbulent transition in a near-wall layer, but in more general terms, a 'low Reynolds number' model should also handle transition away from a solid wall such as the change from the initial (inertial) to the final (viscous) regime in the decay of isotropic grid turbulence, or transition in free shear layers, in separation bubbles, near wakes and other free flows.

[20] Where 'linear' and 'non-linear' refer to the forms of Φ_{ij_2} adopted in the high-Re versions of the models.

https://doi.org/10.1017/9781108875400.008 Published online by Cambridge University Press

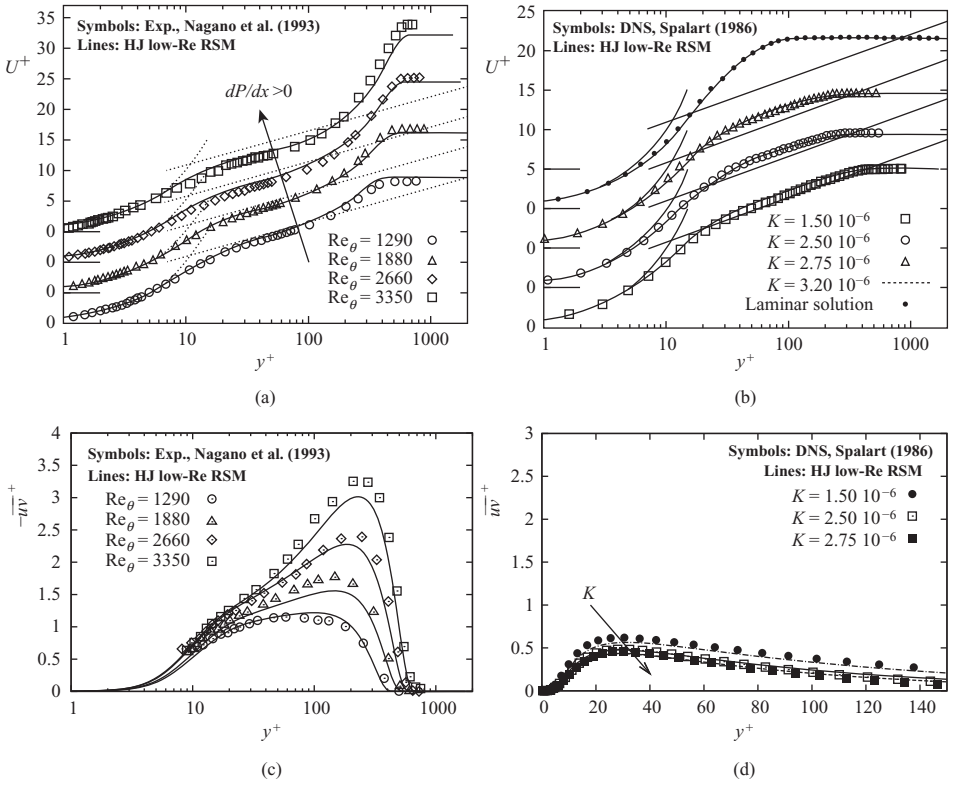

Fig. 6.21 Velocity and turbulent shear stress in a wall boundary layer subjected to an increasing adverse pressure gradient (a) and (c) from Hanjalić *et al.* (1997, 1999); (b) and (d) in a sink flow at different acceleration parameters), Jakirlić (2004).

mean velocity retains the standard log-law slope but with a shift below the standard log-law line, while turbulent fluctuations also show a departure from inner scaling (in terms of friction velocity and viscosity) that extends into the viscous sublayer. A major feature is the marked increase in the peak value of shear stress ($\overline{uv}^+ \equiv \overline{uv}/U_\tau^2$) and a shift of its location away from the wall as the pressure gradient increases (for further details see Hanjalić *et al.*, 1999). All these features are well reproduced by the model, primarily because the dynamics of the stress field are well captured but also, partly, due to the greater sensitivity of the model to irrotational strain, enhanced by the inclusion of the vorticity term in the dissipation equation, as discussed in §5.1.1 (the term in Eq. (5.3) associated with α_3, proposed by Hanjalić and Launder, 1980).[21]

[21] It is noted that this corrective term has been found to worsen agreement in many recirculating flows and is thus not recommended for general use. As seen also in Chapter 5, however, for attached boundary layers (as here) it brings significant improvement.

https://doi.org/10.1017/9781108875400.008 Published online by Cambridge University Press

Figure 6.21b illustrates the performance of the model for strong negative pressure gradients where the acceleration causes departures from the velocity log-law in the opposite sense than in adverse pressure gradients. In a sink flow the acceleration parameter K is uniform and all the flow properties develop to a self-preserving state. A particular target is to predict flow laminarization at the appropriate value of K (see §6.2.2). Computations for four values of K, ranging from moderate, 1.5×10^{-6}, to very strong, 3.2×10^{-6}, show that for the three values below the critical value (of about 3.0×10^{-6}) turbulent flow survives though the dimensionless thickness of the viscous region increases progressively with K. This behaviour accords with that found experimentally by Launder (1964a) and Jones and Launder (1972b) in addition to the DNS by Spalart (1986) with which comparisons are drawn in the figure. For $K = 3.2 \times 10^{-6}$, however, the computations generated a flow field that eventually decayed to laminar.

Transition in a laminar separation bubble on a flat plate

Predicting forward transition is commonly regarded as one of the greatest challenges in fluid mechanics. The actual mechanism of *natural* transition (instability and growth of perturbations in a laminar flow, amplification of instabilities, formation of Tollmien–Schlichting waves and their breakdown into turbulence) is beyond the reach of the RANS modelling strategy. However, transition in situations where most of the development stages of the foregoing sequence of processes are *bypassed* by some externally imposed disturbances can be captured reasonably well by statistical RANS models. Such cases of *bypass transition* may be provoked by diffusion of turbulence into a boundary layer from the free stream or from some other turbulence source, or by the 'revival' of decaying weak turbulence at transitional Reynolds numbers in laminar-like flows[22] when subjected to rapid straining or unstable body force effects. It is equally possible that a boundary layer separates while still laminar, forming a bubble and generating turbulence in the detached shear layer and, at reattachment, some of this 'turbulence-contaminated' fluid penetrates back upstream in the bubble and the incoming laminar flow. This kind of *separation-induced transition* is often associated with adverse pressure gradients and commonly occurs at the leading edge of an airfoil or gas turbine blade if the blade or airfoil is misaligned with the approaching flow.

As an illustration of such separation-induced transition, Fig. 6.22 shows the prediction of transition in a laminar boundary layer on a flat plate, where a separation bubble was created by an adverse pressure gradient induced by imposing suction along the opposite wall. This case provides a convenient test for RANS models because the incoming flow is fully laminar and there are no uncertainties associated

[22] A flow in which turbulence is so weak that mean flow parameters exhibit laminar features.

https://doi.org/10.1017/9781108875400.008 Published online by Cambridge University Press

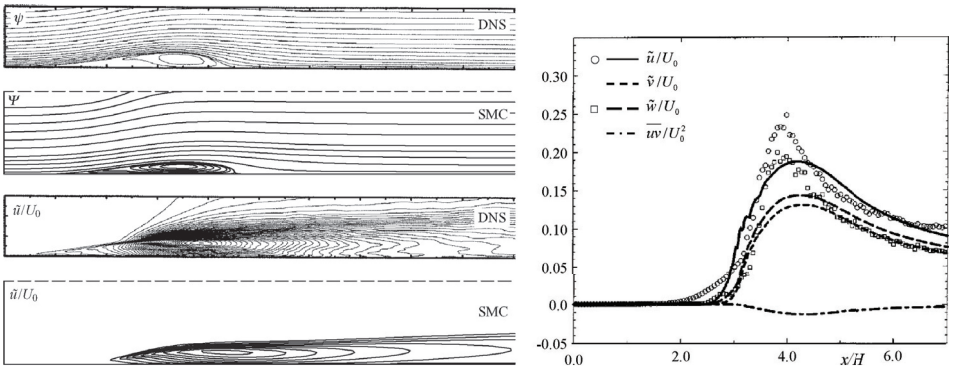

Fig. 6.22 Transition to turbulent flow in a laminar separation bubble. Left: streamlines and rms streamwise velocity fluctuations. Right: evolution of the maximum rms fluctuating velocity components (symbols, DNS of Spalart and Strelets (1997); lines, computations with the HJ SMC). From Hadžić and Hanjalić (1999).

with the inflow state of turbulence at entry.[23] Figure 6.22, left, shows that the HJ model reproduced the streamline pattern and the turbulence intensity contours in good agreement with the DNS results of Spalart and Strelets (1997). The transition to turbulence occurs suddenly, shortly after separation (within the first half of the bubble), as signalled by the sharp increase in the maximum values of the Reynolds-stress components along the flow. The model predicts a flow development in reasonable agreement with the available DNS data though the computed peaks are less pronounced and fall somewhat below the DNS results. In the recovery region downstream of the bubble, the predicted values of stresses are in good agreement with DNS data.

Oscillating boundary layer at transitional Reynolds numbers

Achieving the proper response to an imposed periodic succession of accelerations and decelerations of the flow, such as encountered in oscillating (and other periodic) flows, is another challenging test for a turbulence model. Oscillating flows are encountered in various engineering applications such as in reciprocating engines and their components, in aeronautics, and fluidic, pneumatic or cryogenic devices. They also occur in living organisms. In comparison with a monotonic acceleration or deceleration, oscillating flows may exhibit particular features, such as flow reversal and hysteresis in the response of the turbulent stress components

[23] In making these computations a very small level of isotropic turbulence, $k^{1/2}/U_0 = 10^{-4}$, was introduced into the incoming flow; but this does not need to be a permanent feature: once the bubble is created and a source of turbulence established, this source feeds turbulence continuously upstream into the incoming flow irrespective of the turbulence level of the entering fluid. However, one needs to begin computations with some turbulence field either in the boundary layer or in the whole flow domain. Its level is immaterial provided it is initially large enough to provoke transition in the reattaching flow.

https://doi.org/10.1017/9781108875400.008 Published online by Cambridge University Press

and other turbulence properties to the mean velocity and external flow conditions. Of particular interest are oscillating flows at transitional Reynolds numbers (which includes conditions encountered in blood flow in the arteries of large mammals), where the favourable pressure gradient imposed during the acceleration phase may cause flow laminarization, followed by a sudden 'revival' of weak decaying turbulence following the onset of the deceleration phase, all within a single cycle. The phase angle at which this transition occurs and, indeed, the transition itself are very sensitive to the Reynolds number, Re_{δ_S}, based on peak free-stream velocity and Stokes thickness $\delta_S \equiv \sqrt{2\nu/\omega}$ (where ω is the angular frequency of the flow oscillations). In oscillating flows in pipes or channels, the transition criteria depend on both the conventional Reynolds number and that based on the Stokes thickness (Hanjalić *et al.*, 1995) or, equivalently, on the ratio of the pipe radius R and the Stokes thickness, $\lambda \equiv R/\delta_S$ expressed in the form of the Valensi number $\mathrm{Va} = R^2\omega/\nu = 2\lambda^2$ (or, as is more usual in biofluid mechanics, the Womersley number $\mathrm{W}_o \equiv R\sqrt{\omega/\nu} = \sqrt{\mathrm{Va}}$). As noted by Hino *et al.* (1983), three different turbulent regimes can be identified: a weakly turbulent ('turbulescent') regime, a conditionally turbulent ('bursting') regime and a fully turbulent regime, depending on the mean flow Reynolds and Valensi numbers (for further details see Hanjalić *et al.*, 1995). Although the unsteady dynamics and the true physical processes in the turbulescent and bursting regimes are beyond the reach of RANS modelling, the change to the fully turbulent regime (with a clear indication of the phase location of the onset of the bursting regime) can be captured by a low Reynolds number second-moment closure. This is illustrated in Fig. 6.23 for an oscillating boundary layer. Figures 6.23a and 6.23b show the peak wall-friction factor and the phase lead of the maximum wall stress with respect to the maximum free-stream velocity, while Fig. 6.23c shows the variation of the maximum wall shear stress over the phase angle for a range of Reynolds numbers based on the Stokes thickness. The comparison with the experimental data (for high Re) and the DNS results (for lower Re) shows excellent agreement for all cases considered. These range from the turbulescent regime ($\mathrm{Re}_{\delta_S} = 560$, 600) where the profiles are close to the laminar solution, through the bursting regime with a clear indication of the sudden transition to turbulence (the broken diagonal line in the figure) to the fully turbulent regime (where the flow is turbulent throughout the cycle) at the highest Re_{δ_S} of 3,400.

Rotating and swirling flows

The employment of a full SMC with low Reynolds number modifications that allow integration up to the wall (the WIN approach) may be essential in flows subjected to rotation and swirl. While, in cases of relatively low circumferential velocity, the Basic Model with conventional wall functions (applied to the resultant

https://doi.org/10.1017/9781108875400.008 Published online by Cambridge University Press

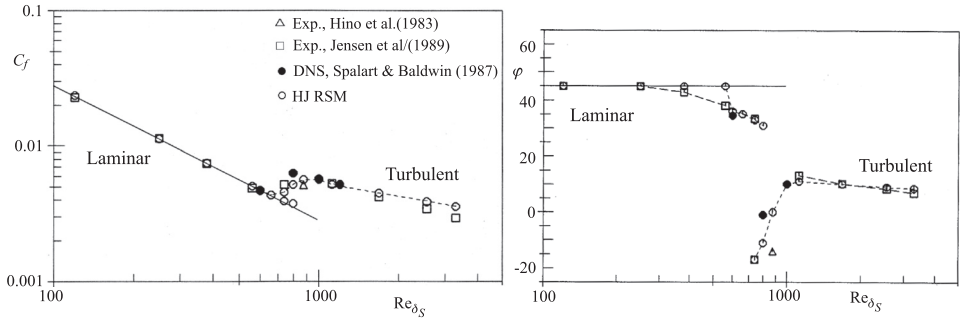

(a) (b)

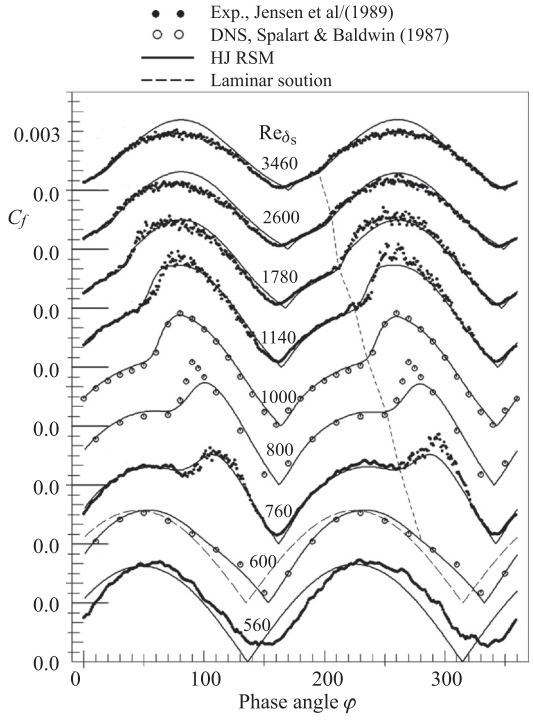

(c)

Fig. 6.23 Oscillating boundary layer over a range of Re_{δ_s} numbers (based on the Stokes thickness $\delta_S = \sqrt{2\nu/\omega}$) and maximum free-stream velocity: (a) friction factor, (b) phase lead of the maximum wall shear stress versus maximum free-stream velocity, (c) variation of wall shear stress through a cycle. From Hanjalić *et al.* (1995).

wall-parallel velocity, $\sqrt{U^2 + W^2}$, in the near-wall cell) may suffice (see §4.3.8), for more intense rotation rates or swirl, both the axial and tangential velocity components, U and W, and their vector sum depart from the common semi-logarithmic law, thus invalidating the use of conventional wall functions. The problem can sometimes be overcome by using more advanced wall functions, as discussed in

https://doi.org/10.1017/9781108875400.008 Published online by Cambridge University Press

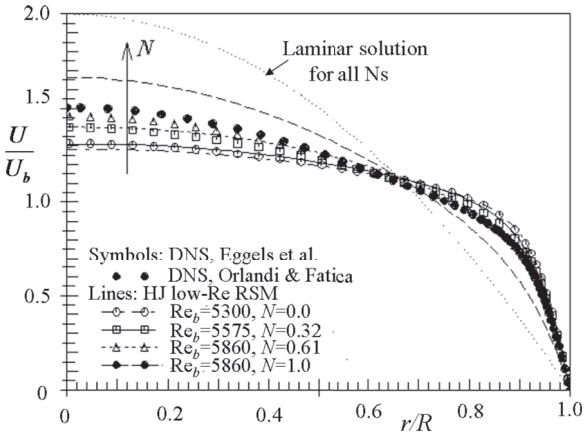

Fig. 6.24 Axial velocity profiles in flow in an axially rotating pipe at different rotation rates, $N \equiv W_{wall}/U_b$ (with the laminar solution for all N). From Jakirlić (2004).

Chapter 8. However, many rotating and swirling flows, especially at high rotation rates, are prone to laminarization, which may require the application of a WIN scheme to account for low Reynolds number effects and the partial or complete collapse of turbulence. A number of examples of such flows can be found in Jakirlić *et al.* (2000) and Jakirlić (2004), including flows in axially rotating pipes, fully developed channel flows rotating in orthogonal mode at high rotation speeds, rotating Couette flows, swirling flows in long straight pipes, in cyclone separators and in a *spin-down* operation of a 'rapid-compression machine'.[24] In the last two examples, in contrast to any eddy-viscosity model, the WIN SMC approach reproduced the vortex breakdown and the complex shape of the axial velocity with sharp peaks and changes of sign, all in accord with the DNS database.

An illustration of the tendency for the flow to laminarize as the rotation rate increases is shown in Fig. 6.24 for the case of flow in an axially rotating pipe. The axial velocity profiles computed with the HJ model clearly show a trend towards laminarization as the spin velocity increases relative to the bulk velocity. Admittedly, the progressive increase of viscous effects as the relative spin rate is increased is too strong compared with the DNS results of Orlandi and Fatica (1997), predicting complete laminarization at N slightly above 1.0, compared with $N \sim 3.0 - 3.5$ suggested by the experiments of Nishibori *et al.* (1987). These presumably non-linear effects could be attributed to an inadequacy of the Basic Model

[24] This name refers to a valveless cylinder – piston assembly used for studying effects of swirl and compression pertinent to idealized IC engines. First, the cylinder (or its head) is set in rotation to generate a swirling fluid motion. After stopping the cylinder rotation abruptly, the fluid inside is subjected to a rapid compression by a piston stroke. Spin-down studies focus on the subsequent evolution of the compressed turbulence in a decaying swirl.

https://doi.org/10.1017/9781108875400.008 Published online by Cambridge University Press

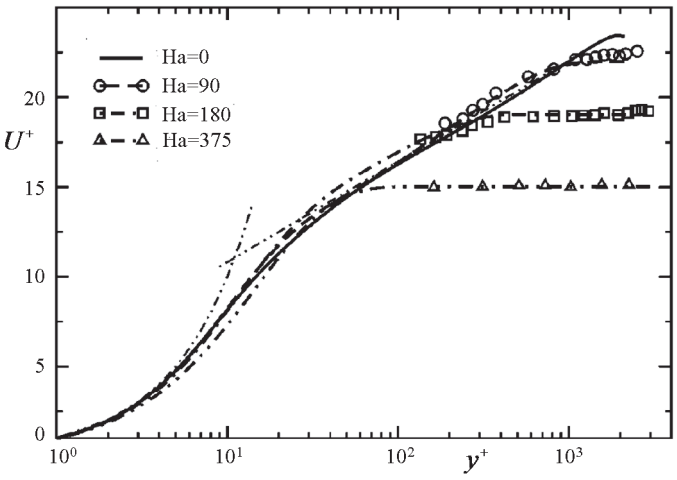

Fig. 6.25 Modification of the mean velocity profile in a channel flow at $\mathrm{Re} = 9 \times 10^4$ due to a transverse magnetic field of different strengths (shown in the usual semi-logarithmic plot). Symbols, experiments by Brouillette and Lykoudis (1967); lines, computations with the HJ SMC+MHD effects. From Kenjereš *et al.* (2004).

of the pressure strain and the HJ viscous modifications. Nevertheless, the example demonstrates clearly the need to apply a WIN scheme.

Effects of a magnetic field

The effects of introducing an electromagnetic field into a general high Reynolds number, second-moment closure were presented in §4.5.4. However, as noted in that section, most industrial applications deal with flows confined by solid walls where an (electro-) magnetic field is used to control the flow, heat or mass transfer, or to generate specific effects (to generate an electric current or a propulsive force or to pump a conducting fluid) such as in MHD devices. Thus, integration up to the wall and accounting for viscous and wall proximity effects is essential to obtain reliable solutions. It is noted, however, that no specific modifications to the model are needed beyond those for a 'neutral' flow; it thus suffices to apply a WIN model which performs well for the same or similar configurations where magnetic field effects are absent.

Figures 6.25 and 6.26 illustrate an application of the HJ model in which the magnetic effects in the $\overline{u_i u_j}$ equation presented in §4.5.4 (Eqs. (4.95)–(4.99)) and in the ε-equation introduced in §5.1.2 (Eq. (5.8)) have been incorporated. The flow is that through a plane channel at moderate Reynolds number ($10^4 \leq \mathrm{Re} \leq 10^5$) with imposed transverse and longitudinal magnetic fields. First, Fig. 6.25 shows for $\mathrm{Re} = 9 \times 10^4$ a very strong 'braking' effect of the transverse magnetic field. (It

https://doi.org/10.1017/9781108875400.008 Published online by Cambridge University Press

is recalled that here the Lorentz force acts in the direction opposite from that of the bulk flow.) For a range of relatively high Hartmann numbers (Ha = 60 to 375), the computations achieve very good agreement with the experiments of Brouillette and Lykoudis (1967). The braking effect, being directly proportional to the magnitude of the velocity, has an increasing influence in the central portion of the channel, while the effects in the near-wall viscous region are much smaller.

The effect of magnetic damping on the velocity fluctuations is illustrated in Fig. 6.26a, where the computations with the same model are also shown for a neutral (i.e. non-magnetic) flow (full lines), compared with the DNS data of Moser *et al.* (1999). As seen, the transverse magnetic field (dashed lines) exerts a much stronger effect than the longitudinal one (chain lines), and dampens all components. It is again recalled that the fluctuating Lorentz force acts only in the streamwise direction, thus suppressing directly only the streamwise velocity fluctuations, $\tilde{u}_1$. Nevertheless, this strong reduction in $\tilde{u}_1^+ \equiv \tilde{u}_1/U_\tau$ reduces the transfer of energy to the other normal-stress components (compared with the neutral case) through the redistribution process, Φ_{ij}, so that both $\tilde{u}_2^+$ and $\tilde{u}_3^+$ are also reduced. As expected, the maximum damping appears around the peak of $\tilde{u}_1^+$ where the fluctuating Lorentz force is a maximum, while in the region very close to the wall the effect is weak. A further increase in Ha would lead to flow laminarization and a velocity distribution typical of a laminar Hartmann magnetic plane channel flow.

In contrast, when a uniform longitudinal magnetic field is applied, the mean Lorentz force is zero and thus has no direct effect on the mean flow. However, the flow is affected indirectly by the fluctuating Lorentz force acting in all coordinate directions. Figure 6.26a indicates that the effect is relatively weak for the case considered (Ha = 50), and even shows an increase in $\tilde{u}_1^+$ compared with neutral flow as one moves away from the wall.

The above conclusion, however, can be misleading as the friction velocity U_τ also changes with the strength of the magnetic field. This is illustrated in Fig. 6.26b, which shows the effects of the transverse and longitudinal magnetic fields on the skin-friction coefficient $C_f \equiv 2\tau_w \big/ \rho U_b^2 = 2(U_\tau/U_b)^2$. For the longitudinal magnetic field, C_f starts to decrease gradually for Ha > 30, but drops suddenly to the laminar value for a neutral flow at Ha ≈ 40, indicating that the velocity fluctuations have been totally suppressed causing the flow to laminarize, with no further influence of the magnetic field. In contrast, for the transverse magnetic field, C_f increases steadily, reflecting the deformation of the mean velocity profile, which becomes fuller as the magnetic strength increases (a consequence of braking the fluid flow in the central region and increasing the velocity gradient at the wall). For Ha > 60, the results approach the so-called *Hartmann line*, characterizing a (laminar) Hartmann flow dominated by the magnetic field. While no experimental data are available to confirm the above findings, it is noted that a very similar

https://doi.org/10.1017/9781108875400.008 Published online by Cambridge University Press

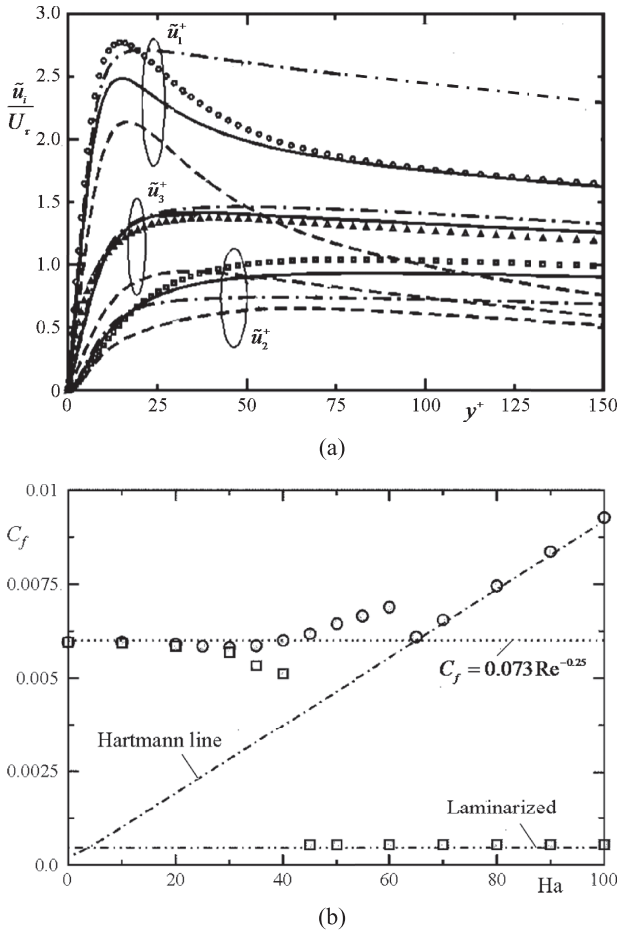

Fig. 6.26 Effect of longitudinal ($\mathbf{B} = [B_1, 0, 0]$) and transverse ($\mathbf{B} = [0, B_2, 0]$) magnetic field on the flow in a plane channel at $\mathrm{Re} = 2.2 \times 10^4$, computed with the HJ SMC + MHD model. (a) rms turbulent velocity fluctuations; symbols, DNS for non-magnetic flow (Moser *et al.*, 1999); lines, computations: full lines $-\mathrm{Ha} = 0$; chain lines – longitudinal magnetic field $\mathrm{Ha} = 50$; dashed lines – transverse magnetic field $\mathrm{Ha} = 50$. (b) Friction factor; symbols, computations, ○ transverse magnetic field, □ longitudinal magnetic field. From Kenjereš *et al.* (2004), Kenjereš and Hanjalić (2007).

distribution of the friction factor has been published by Gardner and Lykoudis (1971) for a pipe flow subjected to a transverse magnetic field.

The above examples, while originally aimed at validating models of magnetic effects in the context of a second-moment closure, also illustrate the potential for using a magnetic field of different orientations to control the velocity or scalar fields for different purposes. An example of such an application to control heat transfer in natural convection (though using an eddy-viscosity/diffusivity formulation derived

https://doi.org/10.1017/9781108875400.008 Published online by Cambridge University Press

from the above second-moment closure applied in the 'unsteady RANS' mode (see Chapter 9) can be found in Kenjereš and Hanjalić (2004).

6.4.2 Applications of the TCL and TCL-compliant models

Representative applications of low-Re models that apply the two-component limit will now briefly be presented. As a reminder, the TCL constraint is applied so that, as the wall is approached, the stress field will, in principle,[25] automatically comply with the requirement $\Phi_{22} \rightarrow 0$ as $\overline{u_2^2}/k \rightarrow 0$, without having to employ wall-damping functions (to modify the pressure-strain and pressure-scalar-gradient models for wall proximity) containing wall-normal distances. The avoidance of such wall-proximity functions is especially helpful when the surface is irregular or in situations where, while the surface may be plane, the flow is strongly three-dimensional. In these cases, as was shown in Chapter 4, the TCL model is clearly superior to the Basic Model.

Historically, the development of the TCL model proceeded in stages that included two major phases of extending computations through the viscous region up to the wall itself. Thus, the computations of the rotating channel flow shown earlier in Fig. 6.16 had been made with the coefficient c_2' in the expression for Φ_{ij_2}, Eq. (4.60), set to zero and thus still needed to retain a wall-proximity term (although of much smaller magnitude than with the Basic Model).

Flow in rotating disc cavities

Effectively, that same model was subsequently successfully applied by Malecki (1994) at ONERA-CERT to three-dimensional separating flows over an airfoil and by Elena (1994) (see also Elena and Schiestel, 1996) to flows in disc cavities. A sample of the latter computations of a rotor-stator cavity is presented in Fig. 6.27. Figure 6.27a provides profiles of radial and tangential velocity at 80% of the disc radius, b (where s is the inter-disc spacing). It shows the characteristic Ekman and Bödewadt layers which are generated adjacent to the spinning and stationary discs respectively while, over the central 70% of the inter-disc gap, the circumferential velocity is uniform. It is clear that the TCL-compliant RSM provides closer agreement with the experimental data of Itoh *et al.* (1990) than the other models examined. The associated Reynolds stress profiles near the stationary disc[26] appear in Fig. 6.27b. The TCL-compliant model returns stress profiles close to those measured, which is consistent with the superior agreement of the

[25] As noted in §4.4.5 and §6.3.4 (immediately following Fig. 6.15), '*compliance with*' does not mean '*enforcement of*'. Reynolds number damping was thus also used to ensure $\overline{u_2^2}/k$ *did* go to zero at the wall.

[26] Near the rotating disc all except the TCL-compliant model exhibited laminar flow which is why the Ekman layer predicted by the three other models is too thin.

https://doi.org/10.1017/9781108875400.008 Published online by Cambridge University Press

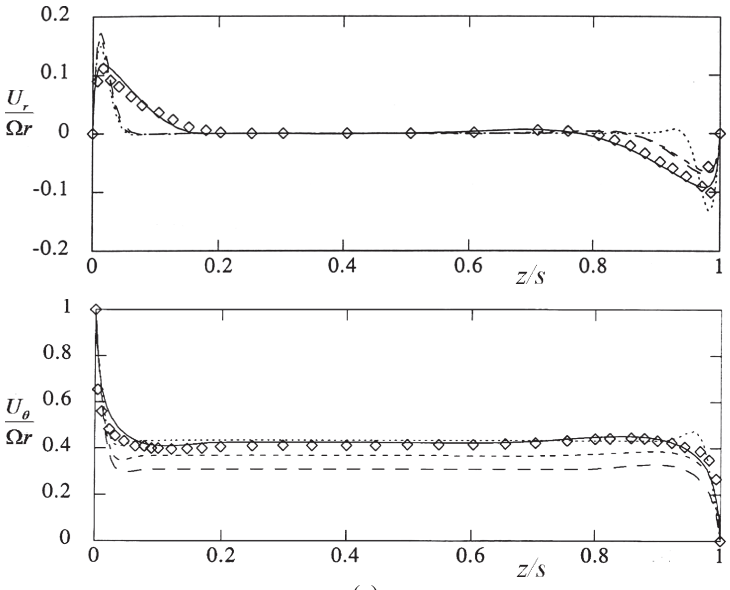

(a)

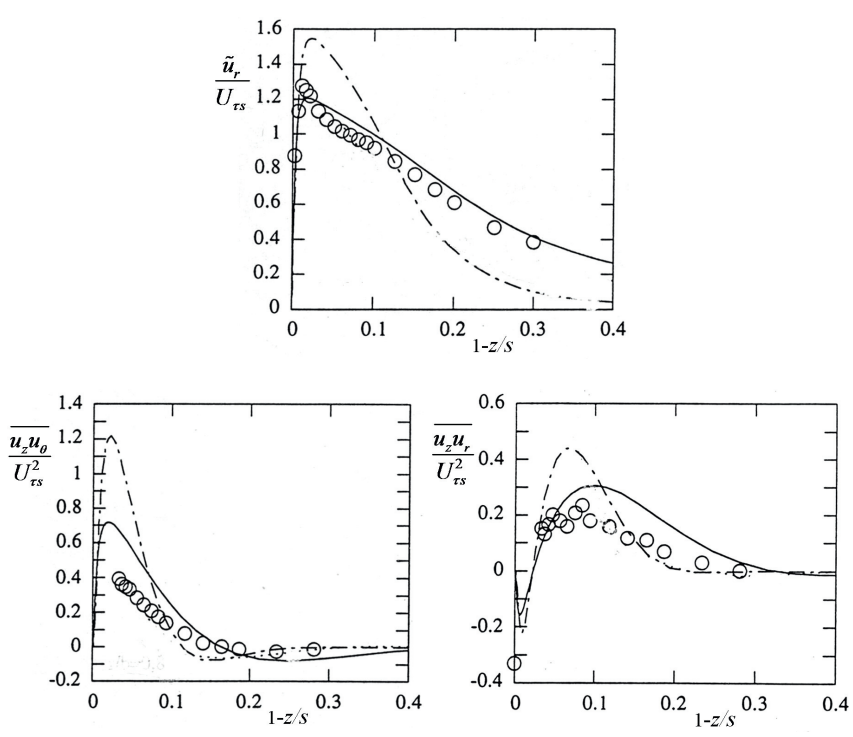

(b)

Fig. 6.27 Flow in a rotor-stator cavity. (a) Radial and tangential profiles of mean velocity at $r/b = 0.8$: symbols, experiment (Itoh *et al.*, 1990); ····· $k-\varepsilon$ EVM; - - - - - ASM; – – – Basic RSM; ——— TCL-compliant RSM. (b) Three components of Reynolds stress tensor near a stationary disc normalized by stator friction velocity $U_{\tau S}$ at $r/b = 0.8$: – – – – – Basic RSM; ——— TCL-compliant RSM. From Elena (1994).

https://doi.org/10.1017/9781108875400.008 Published online by Cambridge University Press

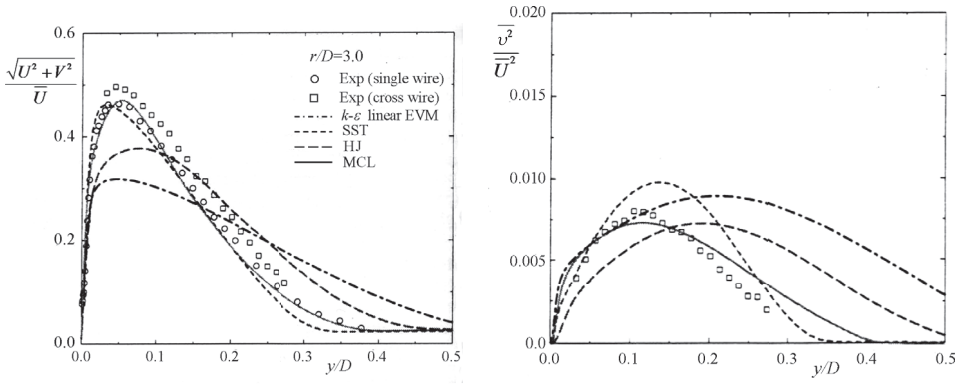

Fig. 6.28 Flow development beneath a circular jet impinging normally on a plane wall (in plane $y = 0$). Fully developed pipe flow at jet discharge two diameters above the plate. Profiles at three pipe diameters from the impingement point. Left: mean velocity profiles. Right: Reynolds stress normal to the wall. Symbols, HWA data by Cooper *et al.* (1993). From Batten *et al.* (1999). MCL indicates the TCL model with minor recalibration of low-Re functions.

mean-velocity predictions. While only three components of the stress tensor are included here, similar agreement was achieved with the remaining three.

Impinging round jet

The more complete TCL model (Craft, 1991, 1998) with the additional elements to Φ_{ij_2} associated with a non-zero coefficient c_2' (i.e. Eq. (4.60)) is fully documented in Batten *et al.* (1999) (including minor refinements to the original empirical sublayer functions). It is from this version that the following examples are drawn. The first example, in Fig. 6.28, compares predictions obtained from several models with experimental data of the axisymmetric impinging jet at a distance of 3 diameters from the jet centre where the flow has become a radial wall jet. The TCL scheme (labelled MCL to indicate the 'modification' to the sublayer functions from the original by Craft, 1998) is in acceptably close agreement with the experimental data with a markedly lower spreading rate than the other models tested.

Axisymmetric transonic bump

The second example is the axisymmetric transonic bump flow of Bachalo and Johnson (1986) that has been used extensively for model benchmarking. The flow geometry consists of a cylinder with streamlined leading edge whose axis is aligned with the flow. Some way from the leading edge there is an axisymmetric 'blister' on the cylinder surface which causes the transonic entering flow to become supersonic. A shockwave forms just downstream of the maximum blister height that

https://doi.org/10.1017/9781108875400.008 Published online by Cambridge University Press

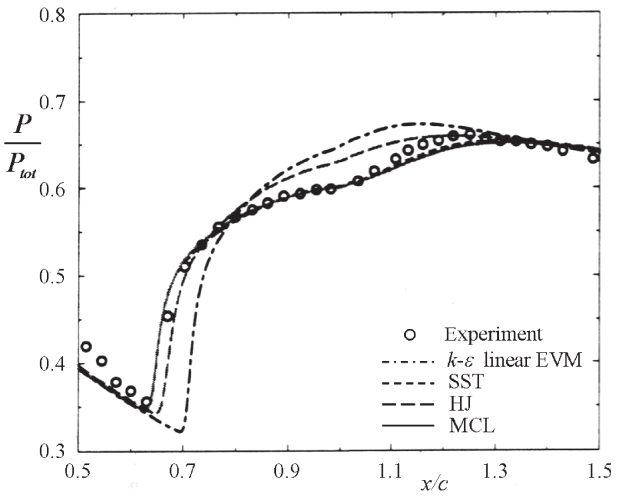

Fig. 6.29 Surface static pressure variation for transonic flow over an axisymmetric bump on a cylinder. From Batten *et al.* (1999).

reduces the flow to subsonic speed and, thereafter, a limited region of flow separation. The variation of surface static pressure along the pipe is shown in Fig. 6.29, starting at the maximum height of the blister ($x/c = 0.5$, where c is the chord length of the blister) and extending to 0.5 c downstream of the blister. The modified TCL scheme predicts the shock location fractionally too early but reproduces the reduced rate of pressure recovery over the range $0.8 < x/c < 1.1$ (caused by the recirculating flow) better than the HJ model.

The final example is the Mach 2, flat-plate boundary layer that encounters a fin-plate junction (Barberis and Molton, 1995), a complex three-dimensional flow that was the subject of a joint European-US CFD workshop on high-speed flows. The experimentally observed streak-line directions on the plate surface shown in the lower half of each diagram in Fig. 6.30 bring out clearly that multiple horseshoe vortices are created upstream of the fin. The TCL scheme, seen on the left, while predicting the separation point a little late, does reproduce the second major recirculating zone. In contrast, as seen from the right-hand figure, eddy-viscosity models such as the SST of Menter (1994) lead to just a single horseshoe vortex. Batten *et al.* (1999) showed that the surface pressure field is also captured most successfully by the TCL scheme.

6.5 Elliptic relaxation concept

Recognizing that the major effect of a solid wall on the pressure fluctuations immediately adjacent to the wall (and the *only* effect in the vicinity of a liquid free surface) originates from the non-local inviscid wall blocking due to impermeability,

https://doi.org/10.1017/9781108875400.008 Published online by Cambridge University Press

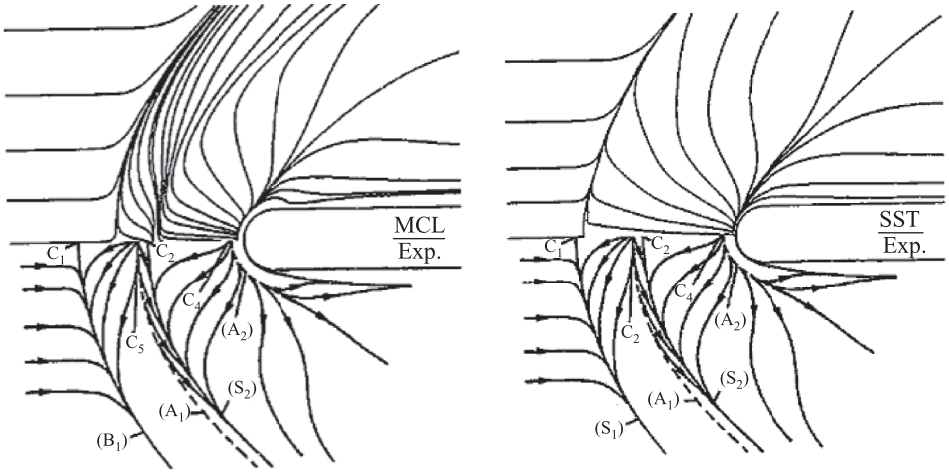

Fig. 6.30 Surface streak-line patterns for flow past a fin-plate junction at Ma = 2. Lower half of each figure: experiment (Barberis and Molton, 1995). Upper half: CFD computations. Left, MCL model; right, SST Model (Menter, 1994). From Batten *et al.* (1999).

Durbin (1993) proposed an *elliptic relaxation* (ER) of the pressure-strain term Φ_{ij}. It is seen from Eq. (4.3) that integration of the Poisson equation for p (multiplied by the instantaneous strain rate) leads to volume integrals consisting of two-point correlations of various quantities evaluated at points $\mathbf{x}$ and $\mathbf{x}'$, which we denote temporarily by $\Psi_{ij}(\mathbf{x}, \mathbf{x}')$. Thus, the part of the pressure-strain term unaffected by boundaries can be written as:

$$\Phi_{ij}(\mathbf{x}) = \overline{\frac{p}{\rho}\left(\frac{\partial u_i}{\partial x_j} + \frac{\partial u_j}{\partial x_i}\right)} = \frac{1}{4\pi}\int_V \Psi_{ij}(\mathbf{x}, \mathbf{x}')\frac{dV(\mathbf{x}')}{|\mathbf{x}' - \mathbf{x}|}. \tag{6.55}$$

Assuming that the two-point correlation $\Psi_{ij}(\mathbf{x}, \mathbf{x}')$ can be expressed in terms of its one-point limit and a simple isotropic exponential function (which corresponds closely to measurements in homogeneous flows), i.e.

$$\Psi_{ij}(\mathbf{x},\ \mathbf{x}') = \Psi_{ij}(\mathbf{x}',\ \mathbf{x}')e^{-\frac{|\mathbf{x}'-\mathbf{x}|}{L}} \tag{6.56}$$

one can write

$$\Phi_{ij}(\mathbf{x}) = \frac{1}{4\pi}\int_V \Psi_{ij}(\mathbf{x}', \mathbf{x}')e^{-\frac{|\mathbf{x}'-\mathbf{x}|}{L}}\frac{dV(\mathbf{x}')}{|\mathbf{x}' - \mathbf{x}|}. \tag{6.57}$$

Here L is the turbulence length scale, $e^{-|\mathbf{x}'-\mathbf{x}|/L}/4\pi(|\mathbf{x}' - \mathbf{x}|)$ is the 'free-space' Green function associated with the *elliptic* operator $-\nabla^2 + 1/L^2$. Thus, Eq. (6.57) can be inverted to

$$\Phi_{ij}(\mathbf{x}) - L^2\nabla^2\Phi_{ij}(\mathbf{x}) = -L^2\Psi_{ij}(\mathbf{x},\ \mathbf{x}). \tag{6.58}$$

https://doi.org/10.1017/9781108875400.008 Published online by Cambridge University Press

In homogeneous turbulent flows the term involving the Laplacian ∇^2 vanishes and the source term on the right can be replaced by a homogeneous expression for the pressure-strain term Φ_{ij}^h for which any quasi-homogeneous model can be used. Thus, Eq. (6.58) can be written as:

$$\Phi_{ij}(\mathbf{x}) - L^2\nabla^2\Phi_{ij}(\mathbf{x}) = \Phi_{ij}^h. \tag{6.59}$$

Equation (6.59) has an elliptic character implying that the Laplacian will account for the conditions on the solid or free surface bounding the flow domain. The characteristic turbulent length scale, L, when sufficiently far from a wall or free surface, can conveniently be taken as $k^{3/2}/\varepsilon$. With the appropriate boundary conditions, Eq. (6.59) preserves the non-local character of the pressure-strain term and exerts its damping due to wall blocking via differential, elliptic equations rather than as an algebraic expression in terms of local quantities and wall distance as, for example, in Shir (1973) and Gibson and Launder (1978) (Eqs. (4.12), (4.14)) or by the use of stress invariants to signal wall proximity.

6.5.1 Durbin's elliptic relaxation second-moment closure

Instead of applying the elliptic relaxation concept directly to the pressure redistribution, Φ_{ij}, as outlined above, Durbin (1993) applied it to a group of terms in the $\overline{u_i u_j}$ equation, denoted Π_{ij}^* (for notation, see Eq. (2.18) and §4.2)

$$\frac{D\overline{u_i u_j}}{Dt} = \mathcal{P}_{ij} + \underbrace{\Pi_{ij} - \varepsilon_{ij} + \frac{\overline{u_i u_j}}{k}\varepsilon}_{\Pi_{ij}^*} - \frac{\overline{u_i u_j}}{k}\varepsilon + \mathcal{D}_{ij}^{\nu} + \mathcal{D}_{ij}^{t}. \tag{6.60}$$

Furthermore, the 'redistributive tensor' Π_{ij}^*, is expressed in terms of an elliptic relaxation function f_{ij}

$$\Pi_{ij}^* = k\, f_{ij} \tag{6.61}$$

so that Eq. (6.59) may be recast in terms of f_{ij}

$$L^2\nabla^2 f_{ij} - f_{ij} = -f_{ij}^h \tag{6.62}$$

where

$$f_{ij}^h = \frac{1}{k}\left[\Phi_{ij}^h - \left(\varepsilon_{ij} - \frac{\overline{u_i u_j}}{k}\varepsilon\right)\right]. \tag{6.63}$$

It is necessary now to provide Φ_{ij}^h, for which one can use any 'homogeneous' model of pressure redistribution (that is, a form unaffected by wall proximity); for example, Rotta's model of the 'slow' term and the IP model for the 'rapid' part (i.e. the combination that has been termed the Basic Model),

$$\Phi_{ij}^h = -c_1\varepsilon\, a_{ij} - c_2(\mathcal{P}_{ij} - \tfrac{2}{3}\mathcal{P}_k\delta_{ij}). \tag{6.64}$$

https://doi.org/10.1017/9781108875400.008 Published online by Cambridge University Press

By assuming isotropic stress dissipation, $\varepsilon_{ij} = 2/3\varepsilon\delta_{ij}$, which should be valid in high-Re homogeneous situations, f_{ij}^h can be expressed as[27]

$$f_{ij}^h = \frac{1}{k}\left[\Phi_{ij}^h + a_{ij}\varepsilon\right] \tag{6.65}$$

in which the second term can be absorbed into the 'slow-term' model in Φ_{ij}^h.

Boundary conditions for f_{ij}

The boundary conditions for f_{ij} are derived from the wall-limiting balance of all terms in the velocity and pressure fluctuations in a Taylor series in the wall-normal direction, Eqs. (6.23) and (6.24), and retaining only the leading terms, see Table 6.1. Examination shows that at the wall Π_{ij}^* is balanced by the viscous diffusion and dissipation rate, giving the following exact wall boundary conditions for the components of f_{ij}:

$$f_{11}^w = f_{33}^w = -f_{22}^w = \frac{20\nu^2\overline{u_2^2}}{\varepsilon x_2^4}, \quad f_{12}^w = f_{23}^w = -\frac{8\nu^2\overline{u_1u_2}}{\varepsilon x_2^4}, \quad f_{13}^w = 0 \tag{6.66}$$

where all variables on the right-hand side of Eq. (6.66) are evaluated at the wall-adjacent grid point. However, for f_{12}^w and f_{23}^w, in place of the above, an empirical boundary condition is recommended, $f_{12}^w = f_{23}^w = -20\nu^2\overline{u_1u_2}/\varepsilon x_2^4$, to compensate for the fact that $\overline{u_1u_2}\varepsilon/k$ does not reproduce exactly the correct behaviour of ε_{ij} in the wall vicinity.[28]

6.5.2 Some shortcomings in and possible improvements to ER-SMC

The primary merit of the elliptic relaxation concept is the correct suppression of the stress redistribution close to a solid wall, imposed by the wall boundary conditions for f_{ij}. That ensures that the pressure-scrambling term is balanced by the difference between the viscous diffusion and dissipation. This in turn ensures the correct asymptotic behaviour of different components of $\overline{u_iu_j}$ and the two-component limit of turbulence within the viscous sublayer where the wall-normal stress component $\overline{u_nu_n}$ becomes negligible due to the effect of wall blocking.

However, Durbin's original model also has some drawbacks. Two of the shortcomings and some proposals for their improvement are considered here. The derivation of the elliptic relaxation equation was based on the assumption that the

[27] Note that, for convenience, Φ_{ij}^h is used instead of Π_{ij}^h to indicate that we can use any of the existing (or other) pressure-strain models; the difference $\mathcal{D}_{ij}^p = \Pi_{ij} - \Phi_{ij}$ is negligible in 'homogeneous' regions away from a solid wall. What matters is that the exact wall limits of Π_{ij}^* (Eq. (6.60), for individual terms see §6.3.2 and Table 6.1) are ensured by the boundary conditions for f_{ij}.

[28] In different applications somewhat different values of the empirical coefficient have been adopted instead of 20.

https://doi.org/10.1017/9781108875400.008 Published online by Cambridge University Press

exponential correlation function in Eq. (6.56) is isotropic and symmetric, which is not adequate in highly inhomogeneous and anisotropic turbulence in the vicinity of a wall (Wizman *et al.*, 1996; Manceau and Hanjalić, 2000; Manceau *et al.*, 2001). This inadequacy is reflected in an amplification of the elliptic relaxation function, f_{ij}, by about 50% over part of the logarithmic wall region which is sufficiently far from the wall for the wall boundary conditions not to be influential. This results in the log-region velocity distribution departing (slightly) from the expected slope. This problem can be removed by adopting an asymmetric correlation function containing the length scale gradient. The simplest, though not entirely satisfactory, proposal is that of Wizman *et al.* (1996), which results in a modified elliptic relaxation equation

$$\nabla^2(L^2 f_{ij}) - f_{ij} = -f_{ij}^h \tag{6.67}$$

instead of Eq. (6.62).

Other, more complex, forms of elliptic relaxation equation can be derived by making different assumptions about the two-point correlation function. Generally these reproduce the logarithmic velocity distribution in a plane channel better (Manceau and Hanjalić, 2000). However, in most cases these modifications lead to some deterioration of the numerical robustness of the equation set because of the need to include L within the elliptic operator.

Another serious drawback of the original ER model is the need to solve six additional elliptic differential equations for components of f_{ij}, which, despite their simple form, make a significant extra demand on computer resources. Moreover, the boundary conditions for f_{22}^w and f_{12}^w, both proportional to a ratio of quantities that vary with x_2^4, are not convenient, especially in thin, high-Re boundary layers where a proper near-wall resolution requires strong mesh clustering: a small imbalance between the numerator and denominator can lead to numerical instability. In the next subsection an alternative approach is presented where this problem is to a large extent avoided.

6.5.3 Elliptic blending second-moment closure (EBM)

In order to reduce the number of auxiliary differential equations needed to account for the elliptic-relaxation effect, Manceau and Hanjalić (2002) proposed an *elliptic blending* model, EBM. Besides reducing the computational task, the approach simplified the boundary conditions, thus making the closure more robust and more attractive for use in complex flows. The basic elliptic-relaxation concept was retained, however. First it is noted that the six elliptic relaxation equations are somewhat redundant: the function f_{ij} is geometrical in nature, its role being to constrain the pressure-scrambling terms to comply with the true near-wall behaviour by satisfying the wall boundary conditions, using a single length scale, L. It was

https://doi.org/10.1017/9781108875400.008 Published online by Cambridge University Press

thus conjectured that these goals could be achieved with a single elliptic equation. This basic idea is not entirely new. Indeed, Durbin (1991) introduced a scalar elliptic relaxation function f used in his $(k-\varepsilon)\,v^2-f$ model (of which more is said in Chapter 7). Manceau and Hanjalić (2002) intended extending the idea to second-moment closure by introducing a scalar function $f \equiv \Phi_{kl}M_{kl}$ from which the pressure-strain term could be reconstructed as $\Phi_{ij} = f\,N_{ij}$, where N_{ij} is another well-chosen tensor. While this approach seemed plausible, they reported that no choice of a linear tensorial expression for M_{kl} and N_{kl} could rigorously ensure the exact reconstruction of Φ_{ij}. Instead, a model was proposed that was based on a blending of the near-wall and far-from-the-wall forms of the redistribution tensor:[29]

$$\Phi_{ij} = (1-\alpha^2)\Phi_{ij}^{w} + \alpha^2\Phi_{ij}^{h} \tag{6.68}$$

where α vanishes at the wall and tends to unity very far from it. The ellipticity of the model is then enforced by solving an elliptic differential equation for the blending function α:

$$L^2\nabla^2\alpha - \alpha = -1. \tag{6.69}$$

For Φ_{ij}^{h}, Manceau and Hanjalić (2002) adopted the SSG model, but omitted the quadratic part in the slow term (Eq. (4.33)), while for Φ_{ij}^{w} the following expression was proposed:

$$\Phi_{ij}^{w} = -5\frac{\varepsilon}{k}\left[\overline{u_iu_k}n_jn_k + \overline{u_ju_k}n_in_k - \frac{1}{2}\overline{u_ku_l}n_kn_l(n_in_j + \delta_{ij})\right] \tag{6.70}$$

where the wall-normal unit vector is computed from

$$\mathbf{n} = \frac{\nabla\alpha}{|\nabla\alpha|}. \tag{6.71}$$

Likewise, the components of the stress-dissipation rate are expressed as

$$\varepsilon_{ij} = (1-\alpha^2)\frac{\overline{u_iu_j}}{k}\varepsilon + \frac{2}{3}\alpha^2\varepsilon\delta_{ij}. \tag{6.72}$$

The model is closed by the equation for the dissipation rate, recast as

$$\frac{D\varepsilon}{Dt} = \frac{c'_{\varepsilon1}\mathcal{P}_k - c_{\varepsilon2}\varepsilon}{\mathcal{T}} + \frac{\partial}{\partial x_k}\left(c'_{\mu}\overline{u_ku_l}\mathcal{T}\frac{\partial\varepsilon}{\partial x_l}\right) + \nu\frac{\partial^2\varepsilon}{\partial x_k\partial x_k} \tag{6.73}$$

where $\mathcal{T}$ is the time scale for which the conventional definition k/ε is adopted away from the wall. However, in order to avoid a singularity at the wall, where $\mathcal{T}$

[29] Originally, Manceau and Hanjalić (2002) proposed a blending in the form $\Phi_{ij} = (1-k\alpha)\Phi_{ij}^{w} + k\alpha\Phi_{ij}^{h}$ and $\varepsilon_{ij} = (1-k\alpha)\varepsilon_{ij}^{w} + 2k\alpha\varepsilon\delta_{ij}/3$. Later, however, Manceau (2005) found that the simpler forms Eqs. (6.68) and (6.72) satisfied the imposed constraints equally well and were more robust and performed better in more complex flows.

https://doi.org/10.1017/9781108875400.008 Published online by Cambridge University Press

(like L) becomes zero, they argued that the turbulence scale at the wall must have some finite, non-zero value to reflect the non-zero velocity correlations. Thus, following Durbin, they imposed the Kolmogorov time and length scales, $\vartheta \equiv (\nu/\varepsilon)^{1/2}$ and $\eta \equiv (\nu^3/\varepsilon)^{1/4}$, respectively, as the lower bounds so that the effective scales are defined as

$$\mathcal{T} = \max\left[\frac{k}{\varepsilon},\ c_\tau\vartheta\right], \quad L = c_L \max\left[\frac{k^{3/2}}{\varepsilon},\ c_\eta\eta\right] \tag{6.74}$$

where $c_\tau = 6,\ c_L = 0.161$ and $c_\eta = 70$.

The coefficients in the source terms of ε are also modified by adopting $c_{\varepsilon 2} = 1.83$ (instead of the conventional 1.92), while $c'_{\varepsilon 1} = c_{\varepsilon 1}(1 + 0.03\sqrt{k/(\overline{u_i u_j} n_i n_j)})$, where $c_{\varepsilon 1} = 1.44$. The functional form of the coefficient $c'_{\varepsilon 1}$ avoids the need to include second derivatives of velocity as employed in the conventional low-Re modifications of the ε-equation (the term defined by Eq. (6.49), for example).

Note that the turbulent diffusion in the stress-transport equation is modelled in the same way as in the ε-equation, i.e. using the time scale $\mathcal{T}$ from Eq. (6.74) with $c'_s = 0.21$,

$$\mathcal{D}^t_{ij} = \frac{\partial}{\partial x_k}\left(c'_s \overline{u_k u_l}\mathcal{T}\frac{\partial \overline{u_i u_j}}{\partial x_l}\right). \tag{6.75}$$

Durbin's ER model involves no damping functions and the only effect of viscosity (apart from viscous diffusion, which is included in both the stress and dissipation rate equations) comes from the Kolmogorov scales, which become effective only in the viscous sublayer very close to a wall.[30] Thus, for flows with low bulk Reynolds numbers and especially for computing laminar-to-turbulent transition it is necessary to introduce separate remedies to account for viscous effects (e.g. Lien *et al.*, 1998). These, inevitably, amount to damping functions in terms of the turbulence Reynolds number as in conventional low-Re models.[31]

The same approach can be applied to a scalar field, i.e. the transport equation for the turbulent scalar flux

$$\frac{D\overline{\theta u_i}}{Dt} = \mathcal{P}^\Theta_{\theta i} + \mathcal{P}^U_{\theta i} + \Phi_{\theta i} - \varepsilon_{\theta i} + \mathcal{D}^\nu_{\theta i} + \mathcal{D}^t_{\theta i} \tag{6.76}$$

$$\Phi_{\theta i} = \left(1 - \alpha^2\right)\Phi^w_{\theta i} + \alpha^2 \Phi^h_{\theta i}. \tag{6.77}$$

[30] The intersection of the two scales, k/ε and ϑ (and, likewise *of* $k^{3/2}/\varepsilon$ and η), in wall-attached flows occurs too close to the wall, typically at $y^+ \approx 1$. In order to make the scale switch effective at least over the viscous sublayer, the Kolmogorov scales need to be multiplied by a coefficient much larger than unity to match DNS data. This effectively shifts the intersection of the two types of scale and enlarges the region over which the Kolmogorov scales are active.

[31] For example, applying the model to homogeneous turbulence with no production (e.g. grid turbulence decay) and assuming that at some point in the final period the Kolmogorov time scale will exceed k/ε, the ε-equation will reduce to $U(d\varepsilon/dx) = -c_{\varepsilon 2}\sqrt{\mathrm{Re}_t}(\varepsilon^2/k)$, which effectively implies that $c_{\varepsilon 2}$ is a function of Re_t. However, its monotonic increase with $\mathrm{Re}_t^{1/2}$ does not correspond to the decay law $k \propto x^{-2.5}$, which is known to prevail in the final decay period.

https://doi.org/10.1017/9781108875400.008 Published online by Cambridge University Press

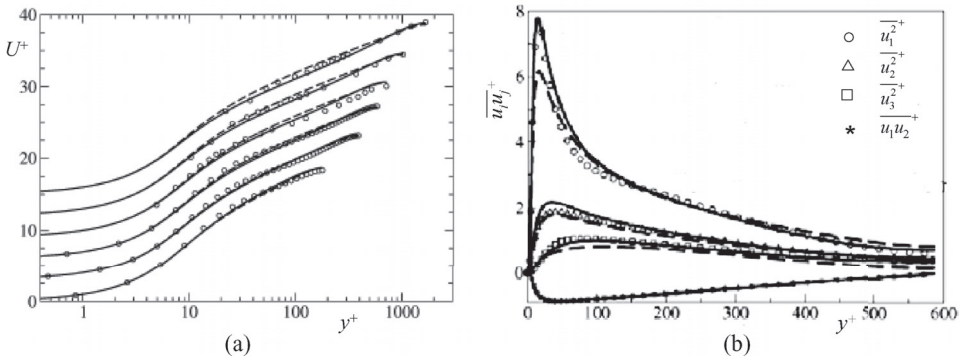

Fig. 6.31 (a) Mean velocity profiles in a plane channel for a range of Reynolds number ($180 \leq \mathrm{Re}_\tau \leq 1{,}800$); (b) turbulent stress components for $\mathrm{Re}_\tau = 590$. Symbols, DNS (for $\mathrm{Re}_\tau = 180,\ 395,\ 590$, Moser *et al.* (1999) and experiments ($\mathrm{Re}_\tau = 708$; 1,011; 1,655, Wei and Willmarth, 1989), $\circ\ \overline{u_1^2}$; $\Delta\ \overline{u_3^2}$; $\square\ \overline{u_2^2}$; broken lines, original EBM model; full lines, modified EBM model. From Manceau (2005).

Figures 6.31 and 6.32 illustrate the performance of the EBM model. First, velocity profiles in a plane channel for a range of Re are presented in Fig. 6.31a, and the components of the turbulent stress tensor are shown in Fig. 6.31b for a single value of Re obtained with both the original Manceau and Hanjalić (2002) form and the modified Manceau (2005) model, showing in both cases very close agreement with the available DNS and experimental data.

The results for a plane channel rotating about a spanwise axis (in orthogonal mode) are shown in Fig. 6.32 for a range of rotation numbers, $\mathrm{Ro} \equiv 2h\Omega/U_b$. It is noted that this flow was computed by simply including the Coriolis (rotational) production tensor $R_{ij} = -2\Omega_k(\overline{u_j u_m}\epsilon_{ikm} + \overline{u_i u_m}\epsilon_{jkm})$ into the stress transport equation (see Eq. (2.19)), where Ω_k ($\Omega_k \equiv \Omega$) is the system rotation vector. In addition, the rotation tensor W_{ij} is replaced by the 'intrinsic' vorticity by adding the system rotation vector, i.e. $W_{ij} = 0.5(\partial U_i/\partial x_j - \partial U_j/\partial x_i) + \epsilon_{mji}\Omega_m$ (see §4.5.2). No other modifications of the model to account for system rotation appeared to be necessary as the adopted SSG model of the pressure strain Φ_{ij} is formulated in terms of frame-indifferent variables a_{ij}, S_{ij} and W_{ij}. Moreover, since, in this case, $\mathcal{R}_{ij}$ was negligible in the budget of all stress components ($\mathcal{R}_{ij}/\Phi_{ij} = \mathcal{O}(y^{-1})$ for all i, j), no modification for rotation was needed in the EBM model (though this may not generally be an appropriate simplification).

Figure 6.32 shows mean velocity, shear stress and the friction velocities on both walls for $\mathrm{Re} = 7{,}000$, all in very good agreement with the LES data even for the highest rotation rate ($\mathrm{Ro} = 1.5$), which shows clear signs of laminarization on the suction side.

https://doi.org/10.1017/9781108875400.008 Published online by Cambridge University Press

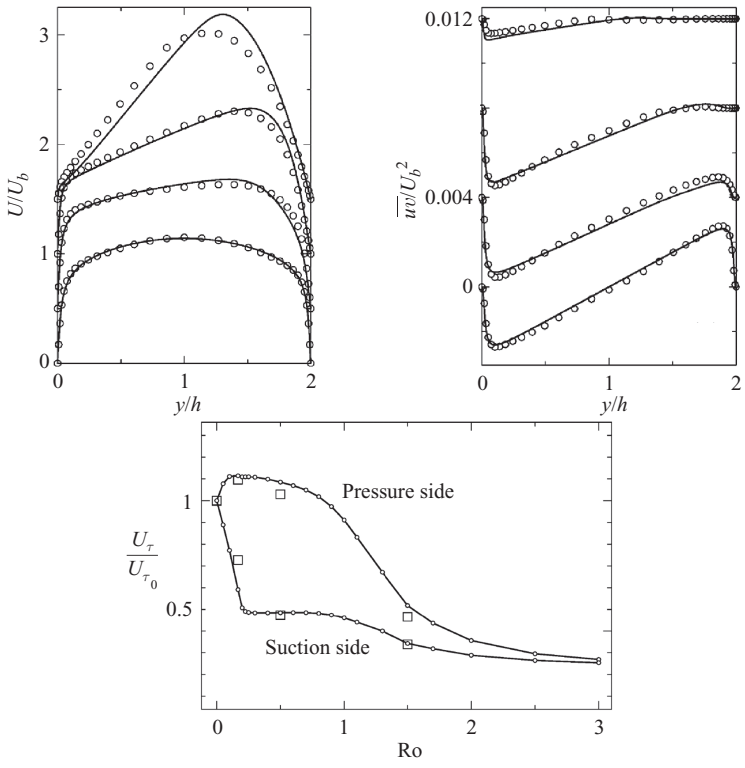

Fig. 6.32 Mean velocity, turbulent shear stress and wall friction velocities in a plane channel rotating around a spanwise axis for a range of rotational number (Ro = 0, 0.16, 0.5 and 1.5) for Re = 7,000. Symbols, LES (Lamballais *et al.*, 1998); lines, EBM computations. From Manceau (2005).

Successful applications of EBM have also been reported for flow and heat transfer in multiple impinging jets (Thielen *et al.*, 2005), compressor cascades and blade tip-leakage flows (Borello *et al.*, 2005). Figure 6.33 illustrates the phenomenon of symmetry breaking in a specific configuration of nine impinging jets in a staggered (diagonally symmetric) arrangement (a quarter of the set is shown in Fig. 6.33) caused by a weak vortex being trapped on one or the other side, off the diagonal. The complex three-dimensional flow (involving mutual interactions of the neighbouring jets, their impingement on the wall, the formation of wall jets and their collision which in turn creates fountain-like upward movements and the radial escape of the fluid) leads to a highly anisotropic stress field that can be reproduced only by a full second-moment closure. While the asymmetry of the near-wall flow pattern has also been captured by some eddy-viscosity models, the EBM SMC reproduced the experimental velocity and stress fields more accurately (Thielen *et al.*, 2003, 2005), which in turn resulted in much better predictions of wall heat transfer.

https://doi.org/10.1017/9781108875400.008 Published online by Cambridge University Press

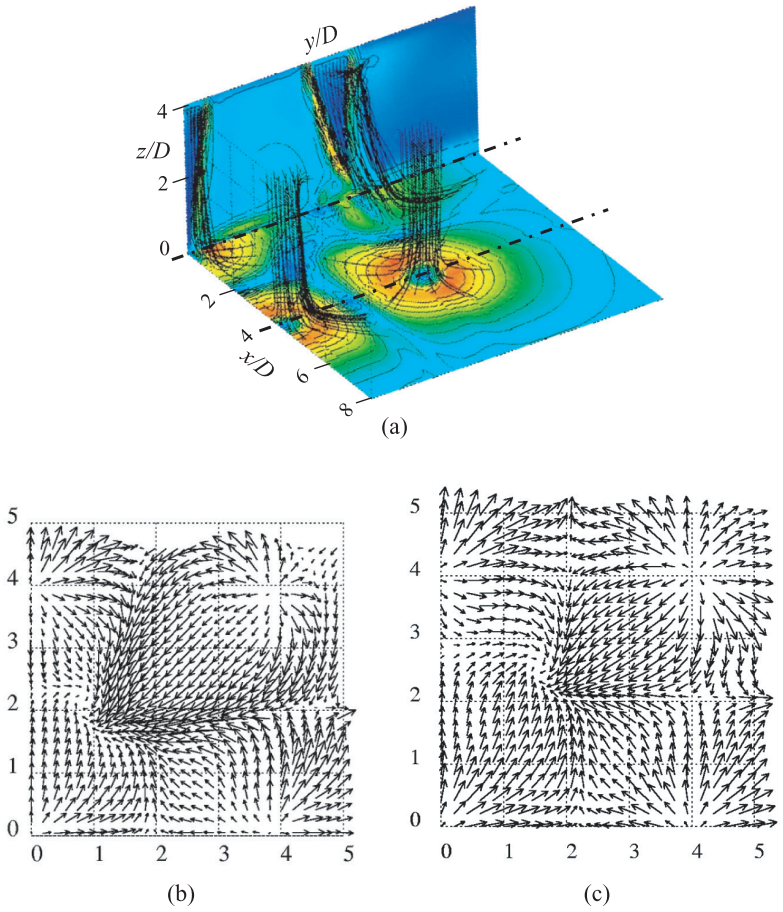

Fig. 6.33 Inherent asymmetry of the flow pattern caused by a weak embedded vortex shifted to the upper side of the diagonal symmetry line in one of the quadrants of multiple-impinging jets. Velocity vectors plotted in a wall-parallel plane at a distance $z/D = 0.54$. (a) Sketch of the configuration (one quadrant). (b) PIV measurements. (c) Computations with the elliptic blending SMC. From Thielen (2005).

In fact, proper resolution of the stress anisotropy proved crucial in predicting heat transfer, as illustrated in Fig. 6.34, which shows the Nusselt number distribution along the two lines through the jet centres, at $x/D = 0$ and 4.0 (denoted by chain lines in the configuration sketch, Fig. 6.33a). Two popular eddy-viscosity models, the k–ε model (with rudimentary log-law wall functions) and Durbin's elliptic relaxation $v^2 - f$ model (both considered in Chapter 7), returned seriously inaccurate Nusselt number distributions, an understandable result in view of the strong three-dimensionality of the flow and its complex structure. In contrast, the EBM SMC reproduced the experimental Nusselt number very well even though

https://doi.org/10.1017/9781108875400.008 Published online by Cambridge University Press

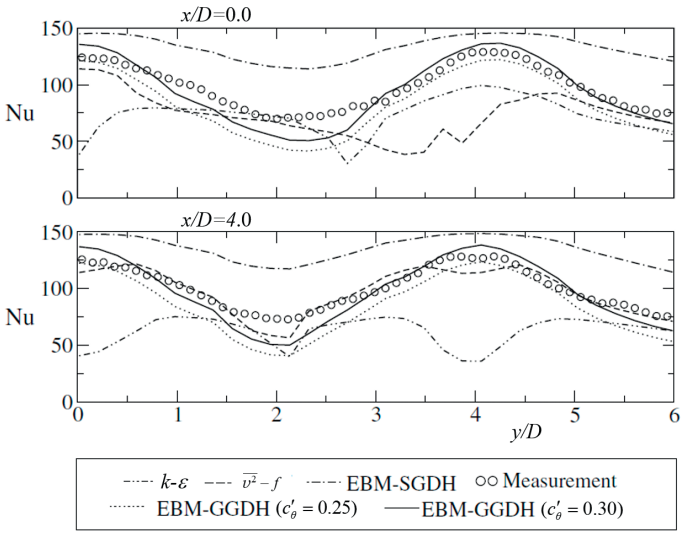

Fig. 6.34 Nusselt number distribution along the target wall at the two cross-sections indicated in the sketch (Fig. 6.33a) at $x/D = 0$ and 4.0. Symbols, experiments (Geers, 2004). From Thielen *et al.* (2005).

the heat flux was computed using the relatively simple GGDH model, Eq. (4.18), $\overline{\theta u_i} = -(c_\theta k \overline{u_i u_j}/\varepsilon)\partial\Theta/\partial x_j$. As discussed in more detail in §7.3.2, the GGDH model can be obtained by truncating the complete second-moment closure for the scalar flux by omitting the transport terms (convection and diffusion). Its use in conjunction with a full second-moment closure for the stress field is strictly an inconsistent mixture of closure levels. However, in the case of a passive scalar with $\mathrm{Pr} = \mathcal{O}(1)$, its dynamics are governed to a large extent by the momentum transport. Nevertheless, use of the GGDH expression requires that *all* components of the stress tensor should be available. In a flow as complex as that considered here, a differential second-moment closure is the only reliable route to obtaining them.

https://doi.org/10.1017/9781108875400.008 Published online by Cambridge University Press

7

Simplified schemes

7.1 Rationale and organization

Models for the turbulent stresses and scalar fluxes have been in widespread use since the 1960s, incorporated within CFD codes of a wide range of types and capabilities. Over this period the vast majority of computations have been made using turbulence models simpler than second-moment closure. Quite clearly, such simpler models *must* deliver satisfactory predictions of some of the flows of interest – for otherwise they would have been discarded. This chapter is devoted to such reduced models. The position adopted is that, *of course*, such simplification makes sense, *provided it is made with an appreciation of what has been lost in the process*.

This truism applies as much to the numerical solver as to the physical model of turbulence employed; for one would surely never use a three-dimensional, elliptic, compressible-flow solver if ones interests were simply in computing a range of axisymmetric, unseparating boundary layers in liquids. But, if we proceed in the reverse direction, while it is not usually possible to apply a simple numerical solver to flows well beyond the solver's capability, it is all too easy to assume that a turbulence model that functioned very satisfactorily in computing simple shear flows will perform equally as well in computing complex strains or in the presence of strong external force fields. That is why it is seen as important that simple (or *simpler*) turbulence models should be arrived at by a rational simplification of the full second-moment closure (having regard for the particular features of the flow to be computed) rather than by adopting some constitutive equation as an article of faith.

The remainder of the chapter has been organized in three parts. The most extensive, §7.3, considers algebraic truncations of the second-moment equations. In favourable circumstances these approaches may lead to just as satisfactory predictions as the complete second-moment closures considered in Chapters 4 and 6, though there are certainly pitfalls for the unwary. The further steps required to reduce such algebraic models to a linear eddy-viscosity form are examined in §7.4.

https://doi.org/10.1017/9781108875400.009 Published online by Cambridge University Press

A major area where such approaches can be beneficially applied is the near-wall sublayer. There gradients of mean and turbulence variables normal to the wall are usually so much steeper than in other directions that one does indeed have what amounts to a flow in simple shear – albeit, as discussed in Chapter 6, with many other complexities arising from wall proximity. First, however, in §7.2, we examine a different route to simplifying stress-transport closure whose useful range of application is limited to two-dimensional shear flows but which can handle more complex phenomena than an eddy-viscosity treatment permits.

7.2 Reduced transport-equation models

When the flows of interest can be treated as *two-dimensional thin shear flows*, the analysis of the flow is simplified; for not only does the number of independent variables decrease but so also does the number of *dependent* variables (since the mean velocity in the third direction no longer appears[1]). That is true whether the flows in question are laminar or turbulent. The present section examines what further simplifications are possible if the flow is turbulent. The idea springs from the fact that in the mean momentum equation only the shear-stress component $\overline{uv}$ exerts a significant effect on the development of the mean flow.[2] (Here and throughout this section the usual boundary-layer notation is adopted with x denoting the primary flow direction and y the principal direction of dependent-variable variation, with the corresponding notation for mean and turbulent velocity components, U, u, V, v.) The stress-transport equations are inter-coupled, of course, and so, even if the normal stresses are not significant in the mean momentum equations, they indirectly affect the development of the mean flow through their influence on other stress components. Yet, the relative magnitude of the normal stresses changes rather little from flow to flow: the streamwise component is always the largest (since that is the only component receiving significant energy input directly from the mean flow), while the other two components are smaller, depending for their sustenance on 'hand-outs' from $\overline{u^2}$. If, then, the normal stresses are approximated as being directly proportional to the turbulent kinetic energy, the number of stress elements found via transport equations is reduced from four to two. Moreover, since the k-equation contains no contribution from the pressure-strain term, the couplings among the equations are simpler.

[1] With the exception of an axisymmetric swirling flow.

[2] The earliest model of this type is that due to Bradshaw (Bradshaw *et al.*, 1967). Rather than solving an equation for the shear stress, however, the turbulent kinetic energy was used as a cipher for it. The shear stress was then recovered from the solution of the k-equation by assuming a direct proportionality between shear stress and turbulence energy, a relationship that applies reasonably well provided one limits attention to external boundary layers and excludes the viscosity-affected sublayer from the computations. The scheme proved particularly successful in predicting the highly non-equilibrium (albeit two-dimensional) boundary layers included in the landmark 1968 Stanford Conference on the prediction of two-dimensional turbulent boundary layers (Kline *et al.*, 1969).

https://doi.org/10.1017/9781108875400.009 Published online by Cambridge University Press

The foregoing is the rationale that led Hanjalić and Launder (1972b) to develop the $k-\overline{uv}-\varepsilon$ model from their form of second-moment closure presented in §4.4.4 by taking $\overline{u^2} = 0.93k$, $\overline{v^2} = 0.50k$, $\overline{w^2} = 0.57k$. The equation set solved was:

$$\begin{aligned}
\frac{D\overline{uv}}{Dt} &= -2.8\left(\frac{\varepsilon}{k}\overline{uv} + 0.07k\frac{\partial U}{\partial y}\right) + c_s\frac{\partial}{\partial y}\left[\frac{k^2}{\varepsilon}\frac{\partial \overline{uv}}{\partial y}\right] \\
\frac{Dk}{Dt} &= \mathcal{P}_k - \varepsilon + 0.8c_s\frac{\partial}{\partial y}\left[\frac{k^2}{\varepsilon}\frac{\partial k}{\partial y}\right] \\
\frac{D\varepsilon}{Dt} &= c_{\varepsilon 1}\frac{\mathcal{P}_k\varepsilon}{k} - c_{\varepsilon 2}\frac{\varepsilon^2}{k} + 0.5c_\varepsilon\frac{\partial}{\partial y}\left[\frac{k^2}{\varepsilon}\frac{\partial \varepsilon}{\partial y}\right].
\end{aligned} \tag{7.1}$$

In the first line of Eq. (7.1) the value 2.8 refers to the value chosen for Rotta's return-to-isotropy coefficient,[3] c_1, and the value 0.07 is the coefficient that results from combining the mean strain production term with the model of the rapid part of the pressure-strain process. The diffusion coefficients c_s and c_ε are those relating to the models of diffusion in the full stress-transport model (i.e. Eqs. (4.19) and (5.11)) which were assigned the values 0.08 and 0.13, respectively. Certain elements of the stress-diffusion term which were negligible in thin shear flows were discarded to leave the particularly simple form in Eq. (7.1).

The primary rationale for the development of this model was because it had long been suspected (and contemporaneously emerging experimental data had confirmed, Tailland and Mathieu, 1967; Hanjalić and Launder, 1972a) that in strongly asymmetric shear flows the shear stress would not vanish where the velocity gradient fell to zero, due principally to the effects of shear-stress diffusion. This difference had proved to be of significant practical importance in choosing the design of rib-roughened fuel pins for use in the UK's advanced gas-cooled nuclear reactors (AGRs). The 'pins', in the form of circular sectioned, ribbed tubes (that would contain the uranium-based fuel in operation), were tested to determine the optimum form of rib roughening by inserting them at the centre of a long test pipe (thus forming an annulus). While the Nusselt number for the ribbed tube could be determined easily (by heating it electrically and measuring the power supply and the wall temperature), to determine the wall shear stress on the ribbed tube one needed to be able to remove the contribution of the smooth containing pipe to the measured pressure drop along the annulus. Initially this was done by measuring the radius of maximum velocity within the annulus (assuming that this was also where the shear stress vanished). The results from these calculations seemed hard to believe, however, and led to the commissioning of research leading to the above model.

[3] The value 2.8 is now seen as spuriously high. See the discussion in Chapter 4, §4.4.3.

https://doi.org/10.1017/9781108875400.009 Published online by Cambridge University Press

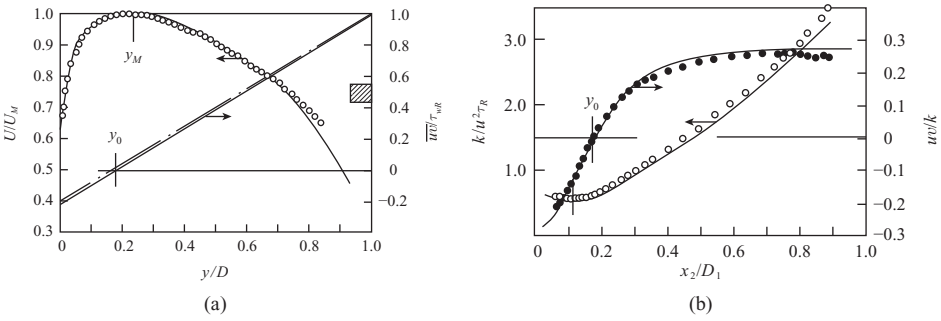

Fig. 7.1 Fully developed flow through a plane channel with ribs on one wall. Symbols and chain line, experimental data (Hanjalić and Launder, 1972a); full lines, computations (Hanjalić and Launder, 1972b).

The model was applied with reasonable success to the computation of the two-dimensional boundary layer in zero pressure gradient, the plane two-dimensional wall jet and to two plane free shear flows as well as to the flow in annuli where, as indicated above, the radii of zero shear stress and maximum velocity did not coincide. The most striking application to a strongly asymmetric flow, however, was that through a plane channel with one of the walls roughened, results from which appear in Fig. 7.1. Figure 7.1a shows that the model correctly captures the displacement (relative to the peak mean velocity) of the position of zero shear stress towards the smooth wall while it is noted, Fig. 7.1b, that the position of minimum turbulence energy lies still closer to the smooth wall. Close accord with the experimental data is achieved by the computations.

Some years later the same authors first addressed the problem of extending second-moment closure to be applicable within the near-wall sublayer (Hanjalić and Launder, 1976). Again, after formulating proposals for a complete stress-transport model, simplifications were sought to reduce the model to the same three-equation format proposed for flows at high turbulent Reynolds numbers. However, a major step in the earlier simplification had to be replaced: one could no longer presume that the normal stress perpendicular to the wall, $\overline{v^2}$, was proportional to the turbulence energy since $\overline{v^2}/k$ fell to zero as one approached the wall (see Fig. 6.11). However, experimental data then available (Eckelmann, 1970) had indicated that the correlation coefficient $\overline{uv}/[\overline{u^2}\cdot\overline{v^2}]^{1/2}$ took a nearly constant value of about ± 0.47 not just in the fully turbulent region but over a large proportion of the viscosity-affected sublayer too. Moreover, the lateral normal stress, $\overline{w^2}$, also retained a value close to the average over most of the flow. Thus the following two constraints were adopted to achieve the desired truncation:

$$\overline{uv}/[\overline{u^2}\cdot\overline{v^2}]^{1/2} = \pm 0.47, \quad (\overline{u^2}+\overline{v^2}) = 4k/3. \tag{7.2}$$

https://doi.org/10.1017/9781108875400.009 Published online by Cambridge University Press

These approximations were then inserted to simplify the complete closure which had adopted the QI model for Φ_{ij_2} with $\gamma = 0.4$ (see Eq. (4.46)) and the linear model for Φ_{ij_1} with Rotta's constant now reduced to 1.5 as in the LRR proposals for high Re_t. The resultant three-equation model (which contained further low-Reynolds-number amendments to both the shear stress and ε-equations) can be written as:[4]

$$\begin{aligned}
\frac{D\overline{uv}}{Dt} &= -(c_1 + f_{s1})\frac{\varepsilon}{k}\overline{uv} - f_{s2}\left[1.4\left(\frac{\overline{uv}}{k}\right)^2 + 0.03\right]k\frac{\partial U}{\partial y} \\
&\quad + \frac{\partial}{\partial y}\left[\left(\nu + 8.0c_s\frac{\overline{uv}^2}{\varepsilon}\right)\frac{\partial \overline{uv}}{\partial y}\right] \\
\frac{Dk}{Dt} &= \mathcal{P}_k - \varepsilon + \frac{\partial}{\partial y}\left[\left(\nu + 5.0c_s\frac{\overline{uv}^2}{\varepsilon}\right)\frac{\partial k}{\partial y}\right] \\
\frac{D\varepsilon}{Dt} &= c_{\varepsilon 1}\frac{\varepsilon}{k}\mathcal{P}_k - c_{\varepsilon 2}f_\varepsilon\frac{\varepsilon\tilde{\varepsilon}}{k} + 4.0c_{\varepsilon 3}\nu\frac{\overline{uv}^2}{\varepsilon}\left(\frac{\partial^2 U}{\partial y^2}\right)^2 \\
&\quad + \frac{\partial}{\partial y}\left[\left(\nu + 4.0c_\varepsilon\frac{\overline{uv}^2}{\varepsilon}\right)\frac{\partial \varepsilon}{\partial y}\right].
\end{aligned} \tag{7.3}$$

The coefficients and functions in Eq. (7.3) were assigned the following values and forms:

c_1	c_2	c_s	$c_{\varepsilon 1}$	$c_{\varepsilon 2}$	$c_{\varepsilon 3}$	c_ε
1.5	0.40	0.11	$c_{\varepsilon 2} - 3.5c_\varepsilon$	1.8	2.0	0.15

f_{s1}	f_{s2}	f_ε
$(1.0 + 0.1\mathrm{Re}_t)^{-1}$	$\exp[-2/(1 + \mathrm{Re}_t/30)]$	$1 - 0.22[\exp -(\mathrm{Re}_t/6)^2]$

All the c coefficients were taken over from the high-Re LRR model, except $c_{\varepsilon 3}$, which multiplies a term that is significant only in the viscous region and was absent from the LRR scheme. That and the Reynolds number functions were chosen by reference to the sublayer shear-stress and k distributions in channel flows at high Reynolds number.

Figure 7.2 shows that, for fully developed flow through a plane channel, the scheme captures the progressive thickening of the viscous layer as the bulk Reynolds number is reduced below 10^4 almost as well as the complete second-moment closures considered in Chapter 6. It also performs satisfactorily when applied to

[4] In principle, solving a transport equation for only one component of a stress tensor is mathematically inconsistent, but at the time of its appearance this model dealt only with two-dimensional flows with only one non-zero shear stress component.

https://doi.org/10.1017/9781108875400.009 Published online by Cambridge University Press

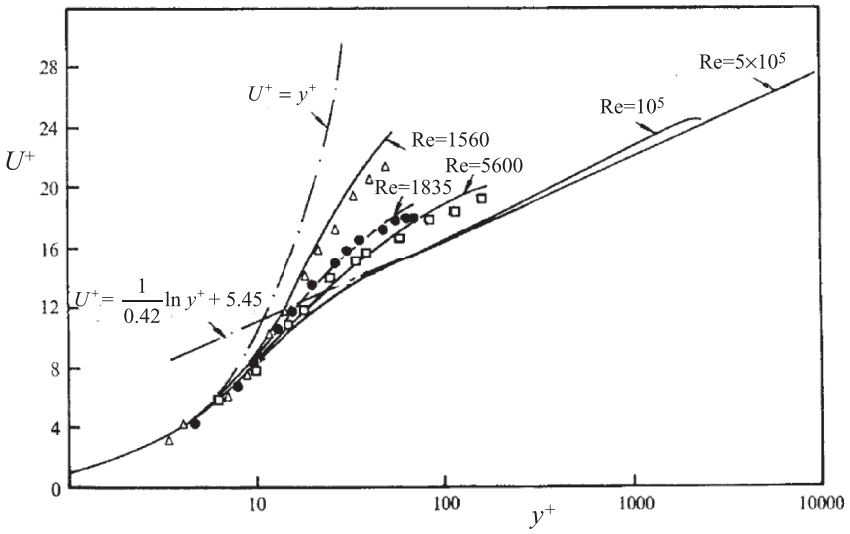

Fig. 7.2 Application to low Reynolds number flow in a plane channel. Experiments: Δ, • Patel and Head (1969); □ Eckelmann (1970); —— computations. From Hanjalić and Launder (1976).

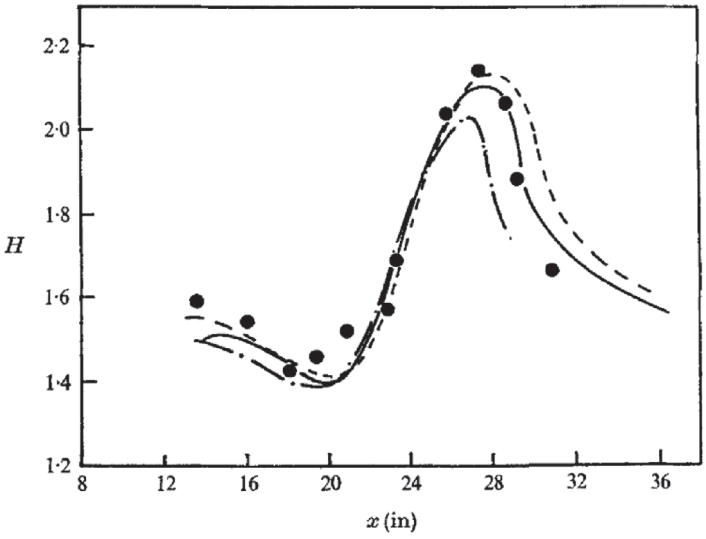

Fig. 7.3 Variation of the shape factor for a strongly accelerated low Reynolds number boundary layer. Symbols, experiment (Launder, 1964b). Lines, computations with different initial conditions. From Hanjalić and Launder (1976).

highly non-equilibrium flows. Figure 7.3 shows the variation of the shape factor, H (the boundary-layer displacement thickness divided by the momentum thickness), for a boundary layer developing initially in zero pressure gradient which is

https://doi.org/10.1017/9781108875400.009 Published online by Cambridge University Press

subjected to severe acceleration between 14 and 21 inches (0.35–0.53 m) from the leading edge before relaxing again in zero pressure gradient. The abrupt increase in shape factor displayed by the data signals the progressive reversion of the boundary layer towards laminar flow. (For a self-similar *laminar* boundary layer in zero pressure gradient $H \approx 2.6$ compared with values of between 1.6 and 1.2 for a turbulent boundary layer, depending on Reynolds number.) Following the end of the acceleration, the measured shape factor continues to increase close to the value for a laminar flow before reverting back towards a value associated with the growth of the Reynolds stresses and the re-establishment of a fully turbulent flow. The computations were somewhat sensitive to initial conditions for the turbulent field. Since neither the complete stress tensor nor the dissipation rate had been measured, three sets of calculations were made to cover a range of alternative, plausible initial conditions. In view of this uncertainty the overall agreement in computing this complex flow appears satisfactory.

The applications to which the above approaches have been put are all two-dimensional thin shear flows where streamline curvature is not significant. Whether the strategy could be extended (based on more recent closure concepts) to resolve accurately two-dimensional *recirculating* flows is not a question that has been seriously examined. For such situations, the usual path to simplification has been one of those considered in the sections which follow.

7.3 Algebraic truncations of the second-moment equations

7.3.1 Simplification of the Basic Model from differential to algebraic form

A considerable simplification of the second-moment closure can, in principle, be achieved by eliminating the transport terms in the individual stress-transport equations. That step reduces the set of differential equations to a system of coupled algebraic equations. The simplest approach is just to set to zero the transport (i.e. the convection and diffusion) terms and keep the form of the equations that is strictly applicable only in local equilibrium. However, perhaps a better approximation can be made for those terms – one that retains wider applicability – by expressing the transport in terms of that for the turbulent kinetic energy. The most common approach is to apply the so-called *weak non-equilibrium hypothesis* (Rodi, 1972, 1976) in which the time and space evolution of the stress anisotropy tensor is set to zero, i.e. one assumes that the stress anisotropy remains unchanged as the flow evolves. In symbolic form this hypothesis can be written as:[5]

$$\left(\frac{D}{Dt} - \mathcal{D}\right) a_{ij} = 0. \tag{7.4}$$

[5] Other transport approximations have also been made to arrive at an algebraic set of equations, for example Mellor and Yamada (1974), Launder (1982).

https://doi.org/10.1017/9781108875400.009 Published online by Cambridge University Press

This hypothesis implies that the evolution of each component of the stress tensor follows that of its trace, i.e. (twice) the turbulent kinetic energy. Inserting $a_{ij} \equiv \overline{u_i u_j}/k - 2/3\delta_{ij}$ and expanding leads to

$$\frac{D\overline{u_i u_j}}{Dt} - \mathcal{D}_{ij} = \frac{\overline{u_i u_j}}{k}\left(\frac{Dk}{Dt} - \mathcal{D}_k\right). \tag{7.5}$$

Replacing each side of Eq. (7.5) by the corresponding source terms on the right-hand side of the transport equations for the Reynolds stress and turbulence energy leads to:

$$\mathcal{P}_{ij} + \mathcal{G}_{ij} + \Phi_{ij} - \varepsilon_{ij} = \frac{\overline{u_i u_j}}{k}(\mathcal{P}_k + \mathcal{G}_k - \varepsilon). \tag{7.6}$$

Equation (7.6), it is underlined, is an *algebraic* equation for $\overline{u_i u_j}$ in which Φ_{ij} denotes the complete pressure-strain correlation comprising the separate parts discussed in Chapter 4, i.e. $\Phi_{ij} \equiv \Phi_{ij_1} + \Phi_{ij_2} + \Phi_{ij_3}$ where here we take the force-field part, Φ_{ij_3}, to be associated with buoyancy. Applications in this section have exclusively employed the Basic Model for the separate parts of Φ_{ij} and assumed local isotropy for the stress dissipation rate, Eq. (4.17). (An alternative strategy, presented in the following section, is based on the SSG model of Speziale *et al.*, 1991.) Insertion of the indicated models leads to the following implicit expression from which $\overline{u_i u_j}$ can be computed:

$$a_{ij} = \frac{(1-c_2)(\mathcal{P}_{ij} - \frac{2}{3}\mathcal{P}_k\delta_{ij}) + (1-c_3)(\mathcal{G}_{ij} - \frac{2}{3}\mathcal{G}_k\delta_{ij})}{c_1\varepsilon + (\mathcal{P}_k + \mathcal{G}_k - \varepsilon)} \tag{7.7}$$

or, equivalently

$$\overline{u_i u_j} = \frac{2}{3}\delta_{ij}k + \frac{k}{\varepsilon}\left[\alpha_1\left(\mathcal{P}_{ij} - \frac{2}{3}\mathcal{P}_k\delta_{ij}\right) + \alpha_2\left(\mathcal{G}_{ij} - \frac{2}{3}\mathcal{G}_k\delta_{ij}\right)\right] \tag{7.8}$$

where α_1 and α_2 are functions of $\mathcal{P}_k/\varepsilon$, $\mathcal{G}_k/\varepsilon$ and of c_1, c_2 and c_3.

This type of simplification is sometimes referred to as an *algebraic stress model* (ASM) but, while retaining the same acronym, we shall designate it an *algebraic second-moment* closure since the same approach is readily applied to scalar transport too. It is noted that the relatively compact appearance of Eq. (7.8) is due to the particularly simple modelled form of Φ_{ij_1} adopted by Rotta's linear return-to-isotropy model, which makes it possible to express $\overline{u_i u_j}$ in what is superficially an explicit form (though this is not in fact the case as stress components appear in the right-hand side of Eq. (7.8) in the production terms). The form given is strictly applicable only to flows uninfluenced by a solid boundary. For wall boundary layers the appropriate wall-reflection terms must be included (Rodi and Scheuerer, 1983). Moreover, for low Reynolds number regions (see Chapter 6), the model of ε_{ij} also contains $\overline{u_i u_j}$, and this process should then be treated jointly with Φ_{ij_1}.

https://doi.org/10.1017/9781108875400.009 Published online by Cambridge University Press

Following an analogous route, one can derive an algebraic model for the scalar flux. By applying the weak non-equilibrium hypothesis to the scalar flux (Gibson and Launder, 1976), which implies that the anisotropy of the scalar flux vector $\overline{\theta u_i}/(\overline{\theta^2}k)^{1/2}$ remains approximately constant in space and time, i.e.

$$\left(\frac{D}{Dt} - \mathcal{D}\right)\left[\frac{\overline{\theta u_i}}{\left(\overline{\theta^2}k\right)^{1/2}}\right] = 0, \tag{7.9}$$

the sum of the transport terms of $\overline{\theta u_i}$ can be expressed as a function of the transport of the turbulent kinetic energy and the scalar variance:

$$\begin{aligned}\frac{D\overline{\theta u_i}}{Dt} - \mathcal{D}_{\theta i} &= \frac{\overline{\theta u_i}}{(\overline{\theta^2}k)^{1/2}}\left[\frac{D}{Dt}\left((\overline{\theta^2}k)^{1/2}\right) - \mathcal{D}(\overline{\theta^2}k)^{1/2}\right] \\ &= \frac{1}{2}\overline{\theta u_i}\left[\frac{1}{\overline{\theta^2}}\left(\underbrace{\frac{D\overline{\theta^2}}{Dt} - \mathcal{D}_{\theta\theta}}_{\mathcal{P}_{\theta\theta}-\varepsilon_{\theta\theta}}\right) + \frac{1}{k}\underbrace{\left(\frac{Dk}{Dt} - \mathcal{D}_k\right)}_{\mathcal{P}_k+\mathcal{G}_k-\varepsilon}\right].\end{aligned}$$

Replacing the total transport of $\overline{\theta u_i}$, $\overline{\theta^2}$ and k by their source terms in the corresponding transport equations leads to:

$$\mathcal{P}_{\theta i} + \mathcal{G}_{\theta i} + \Phi_{\theta i} - \varepsilon_{\theta i} = \frac{\overline{\theta u_i}}{2}\left[\frac{1}{k}(\mathcal{P}_k + \mathcal{G}_k - \varepsilon) + \frac{1}{\overline{\theta^2}}(\mathcal{P}_{\theta\theta} - \varepsilon_{\theta\theta})\right]. \tag{7.10}$$

Again, on inserting the Basic Model approximations for the separate contributions to $\Phi_{\theta i}$ and noting that $\varepsilon_{\theta i}$ is zero in locally isotropic turbulence, the following implicit algebraic expression is obtained for the turbulent scalar-flux vector:

$$\overline{\theta u_i} = \frac{\overline{u_i u_k}\dfrac{\partial\Theta}{\partial x_k} + (1-c_{2\theta})\overline{\theta u_k}\dfrac{\partial U_i}{\partial x_k} + (1-c_{\theta 3})g_i\beta\overline{\theta^2}}{-c_{1\theta}\dfrac{\varepsilon}{k} + \dfrac{1}{2\overline{\theta^2}}\left(2\overline{\theta u_k}\dfrac{\partial\Theta}{\partial x_k} + \varepsilon_{\theta\theta}\right) + \dfrac{1}{2k}\left(\overline{u_i u_k}\dfrac{\partial U_i}{\partial x_k} + g_i\beta\overline{\theta u_i} + \varepsilon\right)}. \tag{7.11}$$

Equations (7.8) and (7.11) have been applied quite extensively, particularly in two-dimensional thin shear flows where a marching scheme can be adopted for solving explicitly what is strictly a highly non-linear set of equations (see, e.g. Hossain and Rodi, 1982; Rodi and Scheuerer, 1983). In such an approach the 'new' values of $\overline{u_i u_j}$ and $\overline{\theta u_i}$ at a downstream station (i.e. the quantities appearing on the left-hand sides of those equations) are obtained using, on the right-hand sides of (7.8) and (7.11), the values of the stresses and fluxes and the mean velocity and temperature gradients from the already calculated upstream values. The new downstream stresses and fluxes are then used in computing the mean velocity and temperature

https://doi.org/10.1017/9781108875400.009 Published online by Cambridge University Press

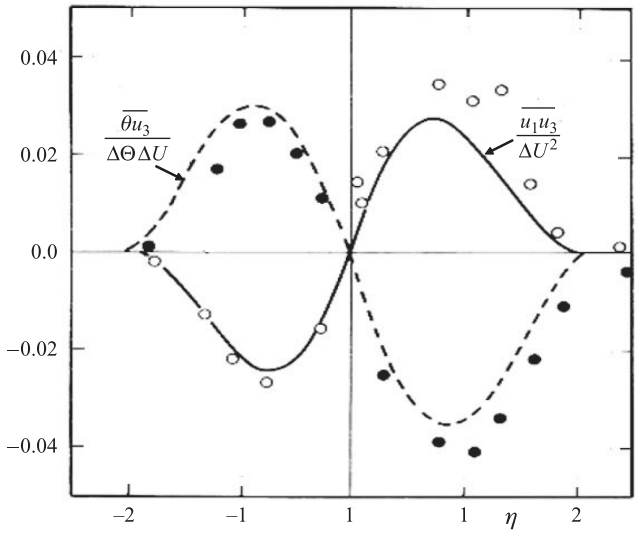

Fig. 7.4 Profiles of turbulent shear stress and heat flux across a slightly buoyant turbulent thermal plane wake. Symbols, experiments (Kovasznay and Ali, 1974); lines, ASM computations (Gibson and Launder, 1976). NB: the flow direction is horizontal (x_1) and the mean velocity and temperature gradients are vertical (x_3). The abscissa, η, denotes vertical displacement from the geometric symmetry plane normalized by the wake half-width.

fields at the downstream station by solving the streamwise momentum and thermal energy (or mean concentration) equations.[6]

An early application of this approach reported by Gibson and Launder (1976) compares predictions of the spread of the wake of a horizontal, heated flat plate (Kovasznay and Ali, 1974). Although apparently not intended, the Richardson number of the wake was sufficiently high to cause weak buoyant effects which are thought to be responsible for the different magnitudes of the shear stress and heat flux on the two sides of the wake centre-line, Fig. 7.4. These are captured reasonably well by the computations.

A further interesting application is taken from the work of Rodi and Scheuerer (1983) on mimicking the effects of streamline curvature on the development of shear flows. They examined three different shear flows subjected to streamline curvature, one of which was the mixing layer turned through 90° by the presence of a nearby wall. Figure 7.5 compares the development of the boundary-layer thickness arising from an array of different models. The experiments of Castro and Bradshaw (1976), shown by open circles, clearly bring out a distinct levelling off of

[6] An explicit expression in $\overline{\theta u_j}$ has also been developed by Abe and Suga (2001), for the case of non-buoyant flows from a local-equilibrium analysis of the scalar flux transport equation. This is examined further in §7.3.3.

https://doi.org/10.1017/9781108875400.009 Published online by Cambridge University Press

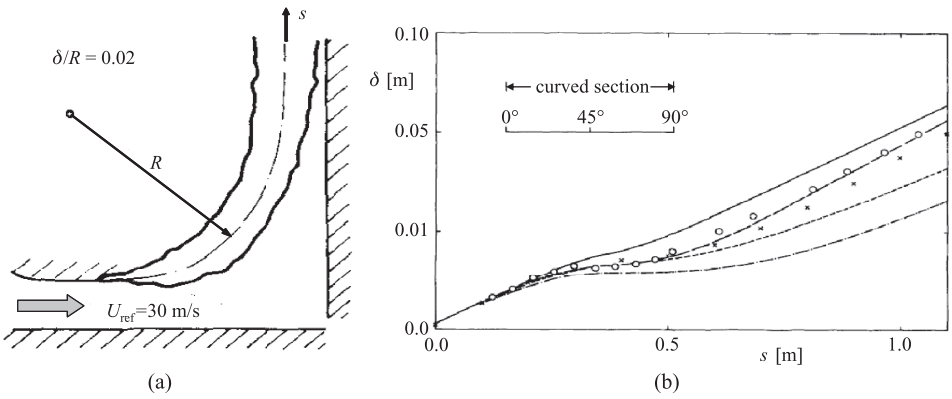

Fig. 7.5 Development of a mixing layer turned through 90° and subsequent downstream development. From Rodi and Scheuerer (1983). (a) Flow configuration; (b) development of mixing-layer thickness with distance: ○○○ experiment (Castro and Bradshaw, 1976); × × × stress-transport computations (Gibson and Rodi, 1981); —- —- —- ASM; —— linear eddy viscosity; – – – and · – · – · empirically tuned eddy-viscosity models.

the thickness of the mixing layer where the shear layer experiences the steepest turning and, further downstream, a rapid restoration to a nearly linear growth rate. This behaviour is well captured by the earlier DSM computations of this flow by Gibson and Rodi (1981) using the Basic Model. The Rodi–Scheuerer computations show, however, that the ASM scheme (long broken line) does just as well in mimicking the development of this flow, substantially better than the standard linear eddy-viscosity model (solid line) and two other EVM schemes tuned empirically to reproduce non-equilibrium effects in certain other cases involving streamline curvature. However, both of the latter schemes exhibit, in the present case, a too slow recovery. (One of these empirically modified eddy-viscosity schemes is noted in §7.4.3, immediately following Eq. (7.38)).

ASM approaches have also been applied by Rodi and Scheuerer (1983) and others to curved *boundary layers* where, in that case, Φ_{ij}^{w}, the wall-reflection part of the pressure-strain correlation, must be included (if a linear model for Φ_{ij_2} is adopted). Although this adds considerable complexity to the algebraic form, if used within a two-dimensional marching code, the additional terms can, as noted above, mainly be computed at the upstream station in determining the downstream stresses so there is little penalty in computing time. The approach has also been applied by Naot and Rodi (1982a) to the computation of fully developed flows in straight ducts and conduits of non-axisymmetric cross-section.[7] Transport effects in such

[7] However, the need to introduce influential wall-effect terms in a situation where all four duct walls may affect the flow simultaneously involves an undesirable level of *ad hoc* interpretation. This weakness provided a motivation for developing the more complete models of Φ_{ij} considered in §4.4.5.

https://doi.org/10.1017/9781108875400.009 Published online by Cambridge University Press

flows are small and, as would be expected, the predicted behaviour with an ASM is little different from that obtained with the corresponding complete stress-transport closure. Secondary flows (and thus transport effects) created in three-dimensional flow around bends in a duct will ordinarily be much larger than the weak motions in a straight duct generated by the anisotropic stress field. For flow through U-bends of both round and square cross-section, Iacovides and Launder (1985) and Choi *et al.* (1989), respectively, obtained much improved predictions from using the ASM truncation than with earlier attempts using a linear EVM.

However, it should be emphasized that ASM closures have, in general, met with less success in the prediction of *free* shear flows. Transport effects are far more important in these flows (especially in axisymmetric – as opposed to plane – flows) than in those developing along a wall so they pose a more significant challenge for the ASM concept. Moreover, while the property of axisymmetry enables the flow to be examined mathematically with only two space coordinates, so far as the turbulence is concerned, the large eddies are being stretched in a more complex way (see the discussion on the Pope correction in §5.1.1). Thus, if one were to resolve the flow using a purely Cartesian (rather than a cylindrical polar) mesh, the strain field would be unambiguously three-dimensional. As an illustration, Fu *et al.* (1988) computed the round jet in stagnant surroundings with both differential and algebraic versions of the Basic Model. They found that while the DSM scheme gave (as reported in Chapter 4) significantly too great a spreading rate, the ASM scheme was substantially worse because of the excessive levels of predicted turbulent shear stress with a peak value 40% greater than with the DSM, Fig. 7.6, left. Seeking the source of the anomaly, the transport contribution of the complete DSM was compared with the approximation made for it with the ASM closure, Fig. 7.6, right. If the ASM approximation were perfect, the normalized values shown in the figure would return for each component the value unity. In fact, the estimate is quite satisfactory for the normal stresses, but for the shear-stress component the approximation fails very badly (being of the wrong sign over much of the flow), a fault that Fu *et al.* (1988) concluded was due principally to the diffusional transport simplification.

To handle flows more complex than thin shear flows it is not possible to escape the uncomfortable fact that ASM models such as that presented above for the stress and scalar-flux components are *implicit* in $\overline{u_i u_j}$ and $\overline{\theta u_j}$. Moreover, the coefficients α_1 and α_2 have expressions in their denominators which may become very small or even zero. These features may lead to singularities and numerical instabilities sufficiently severe to prevent convergence in elliptic flows or, at least, to slow down convergence to such an extent that it is faster to solve the complete second-moment transport equations. In order to overcome such numerical problems, several *explicit* ASMs have been proposed, a route examined in §7.3.3.

https://doi.org/10.1017/9781108875400.009 Published online by Cambridge University Press

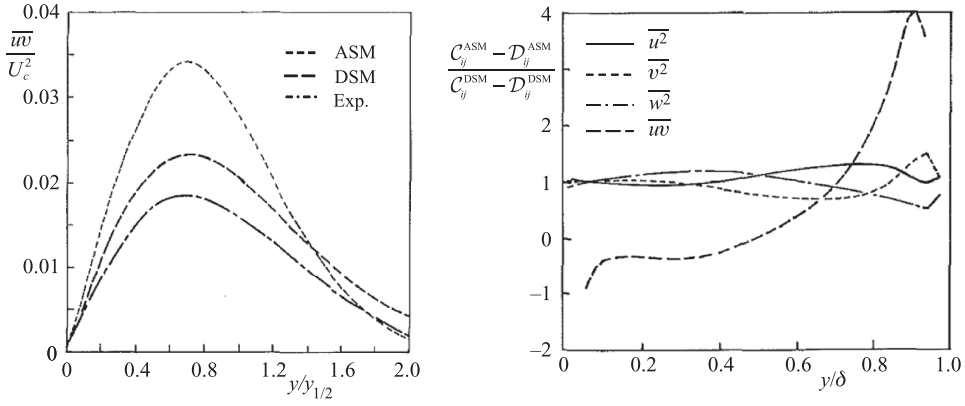

Fig. 7.6 Comparison of ASM and DSM predictions for a round jet. Left: shear-stress profiles; right: comparison of ASM approximations of transport with that of a stress-transport (DSM) model (a value of 1.0 indicates perfect correspondence). From Fu *et al.* (1988).

7.3.2 *Further simplifications of ASM closures: implications for buoyant flows*

In fact, the numerical instabilities that arise when the values of the denominators in Eqs. (7.7) and (7.11) become extremely small can to a large extent be avoided by introducing further simplifications, primarily by imposing the equilibrium conditions, $\mathcal{P}_k + \mathcal{G}_k = \varepsilon$ and $\mathcal{P}_{\theta\theta} = \varepsilon_{\theta\theta}$, which imply the complete neglect of the transport terms (convection and diffusion). In this case the ASM model for the stresses still takes the form of Eq. (7.8) but the quantities α_1 and α_2 are functions only of the coefficients figuring in the adopted models for Φ_{ij} and $\Phi_{\theta j}$.

Likewise the algebraic scalar flux can be written as:

$$\overline{\theta u_i} = -\frac{1}{c_{1\theta}}\frac{k}{\varepsilon}\left[\overline{u_i u_j}\frac{\partial \Theta}{\partial x_j} + (1 - c_{2\theta})\overline{\theta u_j}\frac{\partial U_i}{\partial x_j} + (1 - c_{3\theta})\beta g_i \overline{\theta^2}\right]. \tag{7.12}$$

It is noted that the neglect of the two last terms in Eq. (7.12) leads to the widely adopted eddy-diffusivity model for a scalar field with tensorial diffusion coefficients, known also as the *generalized gradient diffusion hypothesis* (GGDH; Daly and Harlow, 1970),

$$\overline{\theta u_i} = -c_\theta \frac{k\overline{u_i u_j}}{\varepsilon}\frac{\partial \Theta}{\partial x_j}. \tag{7.13}$$

This form has already been introduced in Chapter 4 as a popular basis for approximating the diffusion of the second moments and ε. Its use as a model for the second moments themselves, however, is a much more sensitive modelling choice.

While the complete neglect of the transport terms is obviously a cruder approximation than the weak equilibrium hypothesis, Eqs. (7.5) and (7.9), neither is correct

https://doi.org/10.1017/9781108875400.009 Published online by Cambridge University Press

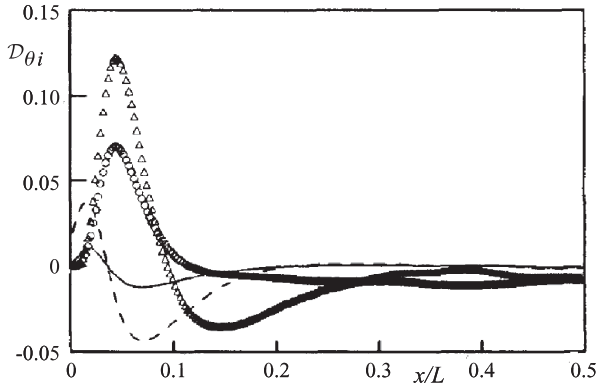

Fig. 7.7 Assessment of the weak-equilibrium hypothesis for turbulent diffusion of the heat flux $\overline{\theta u_i}$ in an infinite vertical side-heated channel: Symbols, ∘ horizontal component ($i = 1$), Δ vertical component ($i = 2$), from DNS of Versteegh and Nieuwstadt (1998). Lines, Eq. (7.14), —— $i = 1$, – – $i = 2$. From Dol *et al.* (1997).

even for relatively simple flows, as Fig. 7.6 makes clear. The situation is possibly exacerbated when buoyancy is involved, as may be illustrated by evaluating the constituent parts of the ASM approximation from the available DNS data. For example, for an infinite (fully developed) side-heated vertical plane channel, where the flow is driven solely by buoyancy, convection is zero and the weak equilibrium hypothesis relates only to the diffusive transport, i.e.

$$\mathcal{D}_{\theta i} = \frac{1}{2}\overline{\theta u_i}\left(\frac{1}{\overline{\theta^2}}\mathcal{D}_{\theta\theta} + \frac{1}{k}\mathcal{D}_k\right). \tag{7.14}$$

As seen in Fig. 7.7, the turbulent diffusion $\mathcal{D}_{\theta i}$, evaluated from Eq. (7.14) using the DNS results for $\mathcal{D}_{\theta\theta}$ and $\mathcal{D}_k$, follows, to a limited extent, the DNS trend but the agreement with the DNS data is far from complete. Whether or not that is important, however, depends on how significant diffusion is relative, say, to generation. Thus, in some flows, whether one adopts the weak-equilibrium hypothesis or totally neglects transport does not make a large difference – both suppositions are inaccurate but unimportant. What is more important in ASM approaches is that even the *reduced* algebraic flux relation includes *all production* mechanisms: those due to mean scalar gradient, mean rate of strain *and* buoyancy.

Naturally, the inclusion of the terms involving gravity can be important in flows driven or affected by scalar buoyancy. This is demonstrated by the two canonical cases of natural convection on a heated wall, which differ only in the wall orientation, i.e. the orientation of the imposed bulk temperature gradient, which we may take as $(\Theta_w - \Theta_b)/\delta$, with respect to the gravitational vector, **g**, where suffixes w and b indicate the temperatures of the wall and bulk fluid, respectively, and δ

https://doi.org/10.1017/9781108875400.009 Published online by Cambridge University Press

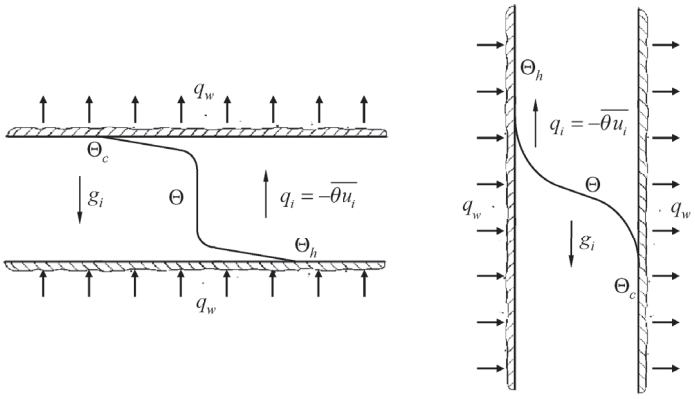

Fig. 7.8 Sketch of Rayleigh–Bénard convection, $\nabla\Theta||\mathbf{g}$ (left), and of a vertical side-heated infinite channel, $\nabla\Theta\perp\mathbf{g}$ (right).

denotes the fluid layer thickness. For fluid above a horizontal heated surface (or beneath a horizontal cooled surface), known as the *penetrative convective mixed layer*, the bulk temperature gradient is aligned (though with an opposite orientation) with the gravitational vector. In the case of a vertical heated wall, however, the temperature-gradient and gravitational vectors are perpendicular. Analogous situations are also encountered in an infinite plane channel with one wall heated and the other cooled where the duct axis may be either horizontal or vertical. When orientated horizontally with the bottom wall heated, Fig. 7.8, left, there is no *mean* flow and the resultant turbulent motion is known as Rayleigh–Bénard convection, whereas in a vertical orientation, Fig. 7.8 right, it is simply referred to as side-heated vertical channel flow. In both configurations, over the long-term average, dependent variables change only in the direction normal to the plates. These may be regarded as generic cases for wall-bounded natural convection. It is important that any model which aims to reproduce flows where the wall orientation relative to gravity is changing over the domain can reproduce both cases.

As discussed in general terms in Chapter 4 with reference to Fig. 4.22, the difference in relative orientation of the temperature-gradient and gravitational vectors leads to striking differences in both the turbulence and bulk flow properties in the two cases. The Rayleigh–Bénard case cannot be modelled accurately with simple eddy-diffusivity models. Due to the horizontal homogeneity of the boundary conditions, the mean temperature becomes almost uniform owing to the large buoyancy-induced vertical mixing (except within the thin conductive sublayers adjacent to the walls). Moreover, as noted above, the mean velocity is zero; thus, the only non-zero source in the equation for the turbulent heat flux, whether it be the complete or reduced ASM form, Eq. (7.11) or (7.12), is the third term (in

https://doi.org/10.1017/9781108875400.009 Published online by Cambridge University Press

the numerator, so far as (7.11) is concerned) representing the buoyant production. Clearly, the GGDH formula, Eq. (7.13), cannot provide sensible results for this case since it links heat fluxes purely to temperature gradients.

In the case of a convective boundary layer along a heated vertical wall or an infinite side-heated channel, the problem is somewhat different, but still challenging. Here the wall-normal (*horizontal*) heat-flux component, which is the primary interest for heat transfer, can be reproduced reasonably well from a simple or generalized gradient-diffusion approximation; but the buoyant source in the k- and (if one adopts the usual modelling strategy) ε-equations is associated with the *vertical* flux component (i.e. aligned with the gravitational vector). It is true that modelling the vertical heat flux in terms of the (negligible) vertical mean-temperature gradient effectively eliminates the effect of buoyancy on the turbulence field. This is not as serious as it may at first appear, however, for in this configuration most of the turbulence energy is created by mean shear (that arises from the buoyancy-driven shearing of the *mean* velocity field).

Overall, but especially for vertically stratified flows (of which Rayleigh–Bénard convection is an important limiting case), an essential prerequisite for reproducing the turbulent heat flux correctly is to determine the scalar variance, $\overline{\theta^2}$, by solving its modelled transport equation rather than by applying a local-equilibrium algebraic truncation.[8] While, in Chapter 4, complete second-moment closures (and even a partial third-moment closure) were applied to this type of flow, here the use of an algebraic flux model, even in the reduced form, Eq. (7.12), has been found to be adequate in modelling the observed flow phenomena provided that the above strategy for obtaining $\overline{\theta^2}$ is followed.

To illustrate this last point, Fig. 7.9 shows the wall-normal heat flux in an infinite plane channel with one wall heated and the other cooled for the two generic cases (i.e. horizontal and vertical orientations) introduced above. The symbols denote the DNS results. Kenjereš *et al.* (2005) found that neither of the gradient models (SGDH and GGDH) nor even the reduced algebraic expression containing all the production terms, Eq. (7.12), reproduced the turbulent heat flux accurately in *both* flows. They then proposed an equation derived by truncating a closed form of the transport equation for $\overline{\theta u_i}$, using the non-linear part of Eq. (4.35) and including the controversial proposal of Jones and Musonge (1988) to remove a proportion, $c^*_{1\theta}$,

[8] The scalar variance has sometimes been evaluated from the truncation of its transport equation (3.16) by assuming local equilibrium, $\mathcal{P}_{\theta\theta} = \varepsilon_{\theta\theta}$, and a constant scalar-to-dynamic time-scale ratio, $\overline{\theta^2}\varepsilon / k\varepsilon_{\theta\theta}$, resulting in $\overline{\theta^2} \propto -(\overline{\theta u_j} k/\varepsilon)(\partial\Theta/\partial x_j)$. Obviously, in flows driven solely by buoyancy, this approximation would make the algebraic flux models (7.11) and (7.12) grossly in error as both would result in zero levels of flux when the mean scalar is uniform, as in the examples discussed above. In practice, appreciable levels of $\overline{\theta^2}$ may be present, driven by diffusion or convection from nearby regions; but to capture *that* a transport equation must be solved for the mean-square temperature variance.

https://doi.org/10.1017/9781108875400.009 Published online by Cambridge University Press

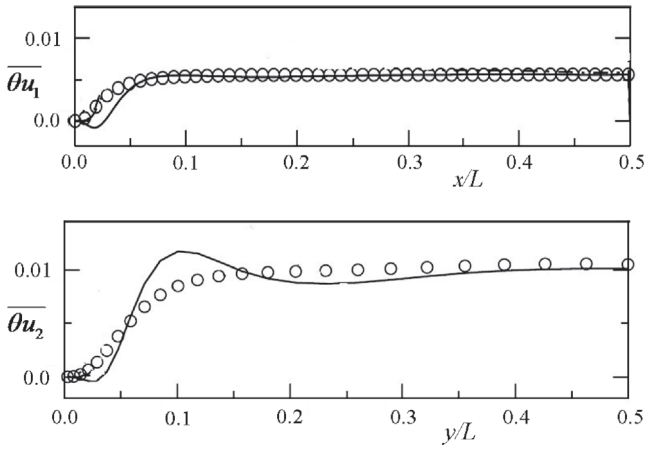

Fig. 7.9 Wall-normal turbulent heat flux in a side-heated infinite vertical plane channel for $\mathrm{Ra} = 5 \times 10^6$ (upper) and in Rayleigh–Bénard convection for $\mathrm{Ra} = 6.3 \times 10^5$ (lower), computed from Eq. (7.15) using the DNS data for all variables appearing in the expressions. Symbols, DNS by Versteegh and Nieuwstadt (1998) (upper) and Wörner (1994) (lower). Lines, Eq. (7.15). From Kenjereš *et al.* (2005).

of the production of heat flux by mean temperature gradients.[9] The model takes the form

$$\overline{\theta u_i} = -\frac{1}{c_{1\theta}}\frac{k}{\varepsilon}\left[(1-c^*_{1\theta})\overline{u_i u_j}\frac{\partial \Theta}{\partial x_j} + (1-c_{2\theta})\overline{\theta u_j}\frac{\partial U_i}{\partial x_j} + (1-c_{3\theta})\beta g_i \overline{\theta^2}\right] + c'_{1\theta} a_{ij}\overline{\theta u_j} \tag{7.15}$$

with $c^*_{1\theta} = c_{2\theta} = c_{3\theta} = 0.4$, $c'_{1\theta} = 1.5$. Figure 7.9 shows the application of Eq. (7.15) to the two generic cases sketched in Fig. 7.8. The lines have been calculated by feeding the DNS results for all variables on the right-hand sides of Eq. (7.15), showing reasonably satisfactory agreement with the DNS data.

The algebraic flux model (7.15) has also been applied successfully, in conjunction with the elliptic-relaxation EVM, to a range of buoyancy-driven enclosed flows (Kenjereš *et al.*, 2005). Further illustration is provided in Fig. 7.10, left, which shows the evolution with time of the mean temperature profile in a stagnant, stratified layer from the initially linear distribution (from 22°C at the bottom to 37°C at the top), as heating from the bottom progresses.[10] Apart from the sharp temperature fall from the hot wall within the thin conductive layer, the temperature over the mixed layer is almost uniform, though there is also a slight overshooting at the

[9] The proposal is controversial because pressure fluctuations (the only mechanism for causing such an effect) do not appear in the part of the heat-flux equation that contains mean temperature gradients, i.e. $\overline{u_i D\theta}/Dt$. Nevertheless, as remarked in Chapter 4, Jones and Musonge (1988) make a reasonable case for including the modification.

[10] In common with the usual practice for flows in the atmosphere, the vertical coordinate is taken as z.

https://doi.org/10.1017/9781108875400.009 Published online by Cambridge University Press

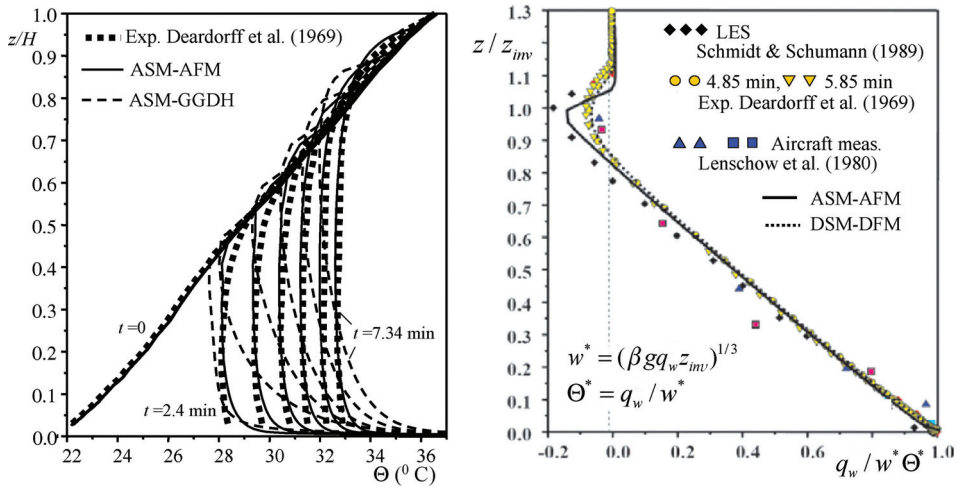

Fig. 7.10 Penetrative convection into an initially thermally stable layer heated from below. Left: the mean temperature field at $t = 0$, 2.40, 3.38, 4.38, 5.36, 6.39 and 7.34 minutes after the onset of bottom heating. Right: vertical heat flux. From Kenjereš and Hanjalić (2002, 2009).

upper edge of the mixed layer, indicating efforts to penetrate the upper, stably stratified fluid. Early computations by Zeman and Lumley (1976) of this type of mixing using an elaborate second-moment closure have successfully captured the main features. However, the predictions obtained by the reduced algebraic stress and flux models, Eqs. (7.8) and (7.12), reproduce the experimental results of Deardorff *et al.* (1969) equally as well.[11] In contrast, the inadequacy of the gradient-transport model for the heat flux (i.e. the GGDH model) is brought out by the dotted lines in the figure: the mean temperature profiles display a non-uniform distribution with substantial gradients across the whole layer, an inevitable consequence imposed by this model since it relies on temperature gradients to produce the vertical heat flux which removes heat supplied from the bottom.

Figure 7.10, right, shows the vertical component of the heat flux, normalized by the characteristic velocity and temperature scales, $w^* \equiv (\beta g q_w z_{inv})^{1/3}$ and $\Theta^* \equiv q_w/w^*$, where $q_w = q_w''/(\rho c_p)$ denotes the kinematic heat flux and z_{inv} the height of the mixed layer.[12] When plotted against the vertical coordinate normalized with z_{inv}, all predictions collapse onto a single curve showing remarkable congruence with several laboratory and aircraft field measurements as well as with the available LES results. It is noted that the heat flux is positive over the bulk of the mixed layer,

[11] Similar quality predictions were also obtained with a reduced differential stress/flux model in which the differential transport equations were solved for the vertical heat flux $\overline{\theta w}$, the temperature variance $\overline{\theta^2}$ and the vertical normal stress $\overline{w^2}$ (or, alternatively, for the kinetic energy k) (Kenjereš, 1999).

[12] The use of z as the vertical coordinate in horizontal stratified flows is so well established in the literature that it seemed preferable to conform with this tradition.

https://doi.org/10.1017/9781108875400.009 Published online by Cambridge University Press

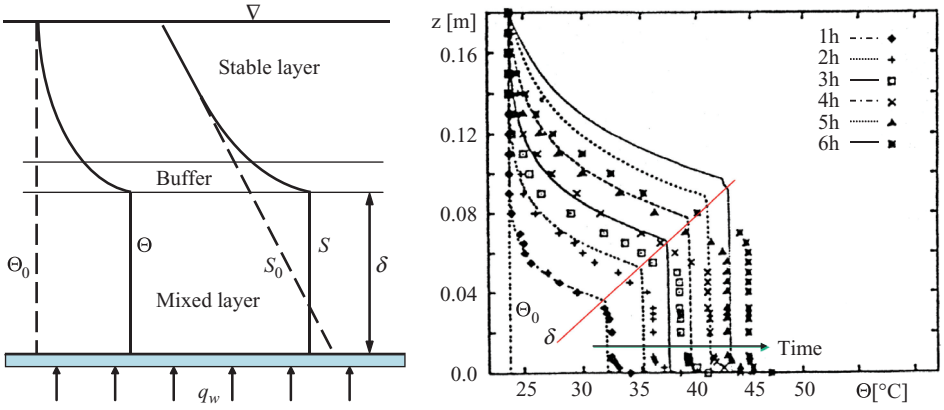

Fig. 7.11 Development of a mixed layer in a double-diffusive system. Left: sketch of the configuration illustrating the initial salt-stratified layer with a uniform temperature (broken lines) and the typical temperature and concentration profiles after heating from below (full lines). Right: temperature profiles at different times (hours) after the onset of heating. Symbols, experiments (Bergman *et al.*, 1985); lines, predictions with an AFM model. From Hanjalić and Musemić (1997).

reducing in intensity with height as the fluid gradually absorbs the heat supplied from below. Close to the top of the upper layer, an inversion is created where the heat flux changes sign since here somewhat cooler fluid penetrating the upper stable layer is heated by the warmer fluid around and above it. It is interesting that in this inversion layer the AFM shows better agreement with the LES results of Schmidt and Schumann (1989), whereas the reduced differential flux model agrees better with the laboratory experiments of Deardorff *et al.* (1969).

Similar, if still more challenging, problems are encountered in double-diffusive systems with buoyant effects arising from both thermal and concentration fluxes. Figure 7.11 examines the development of such a mixed layer in a double-scalar field, a situation already introduced in §4.5.3 where Fig. 4.26 showed some results of a full second-moment-closure application. It is recalled that the mixed layer is formed when an initial isothermal layer, stably stratified by a salt concentration which increases with the layer depth, is subjected to heating from below, Fig. 7.11, left. Here the same situation has been computed with a version of the algebraic flux model showing reasonable agreement with measurements for a succession of time instants, Fig. 7.11, right.[13]

[13] In fact, the results in Fig. 7.11 have been obtained with a still simpler model using the GGDH expression, but with a variable turbulent Prandtl–Schmidt number (determined analytically from the AFM truncation as in Gibson and Launder, 1976) and expressed in terms of buoyancy parameters $g\beta(k/\varepsilon)^2(\partial\Theta/\partial z)$ and $g\gamma(k/\varepsilon)^2(\partial S/\partial z)$, where β and γ are the temperature and concentration expansibilities, defined by Eq. (4.89). The fact that the model reproduces uniform temperature and concentration despite using the GGDH (which, as argued above, would produce zero scalar flux) can be explained by the variable turbulent Prandtl–Schmidt

https://doi.org/10.1017/9781108875400.009 Published online by Cambridge University Press

The reduced algebraic flux model, Eq. (7.12), in conjunction with either the differential or algebraic model for the stresses, has been successfully applied to Rayleigh–Bénard convection, as well as to a range of buoyancy-driven flows in various enclosures (Kenjereš and Hanjalić, 1996; Kenjereš, 1999; Hanjalić, 2002). The same model used in an unsteady mode (URANS) was also found to reproduce a winter diurnal cycle in a mountain valley capped by an inversion layer, subjected to daily ground heating and night cooling (Kenjereš and Hanjalić, 2009); for further details see Chapter 9.

7.3.3 Explicit algebraic second-moment closures (EASMs)

Perhaps recognizing the inconvenience of employing the implicit ASM approaches discussed above in other than 'marching' flows, Pope (1975) proposed transforming the system of implicit algebraic equations for the Reynolds stresses into explicit form although the algebraic complexity of the task meant that attention was limited to two-dimensional flows. Subsequently, however, Gatski and Speziale (1993) (GS), with the help of *Mathematica*™ (Wolfram, 1988), developed a general transformation for any linear model of Φ_{ij}. A full account of the approach is provided by Gatski and Rumsey (2002) (in Launder and Sandham, 2002). The resultant equation, including terms up to quadratic in strain-and-rotation-rate products, can be written as:

$$a_{ij} = -\lambda_1 \tilde{S}_{ij} - \lambda_2(\tilde{S}_{ik}\tilde{W}_{kj} + \tilde{S}_{jk}\tilde{W}_{ki}) + \lambda_3(\tilde{S}_{ik}\tilde{S}_{kj} - \delta_{ij}S^2/3) \tag{7.16}$$

where, as a reminder, the dimensionless strain and rotation parameters introduced in Chapter 5 are defined as follows:

$$\tilde{S}_{ij} \equiv \frac{1}{2}\frac{k}{\varepsilon}\left(\frac{\partial U_i}{\partial x_j} + \frac{\partial U_j}{\partial x_i}\right), \quad \tilde{W}_{ij} \equiv \frac{1}{2}\frac{k}{\varepsilon}\left(\frac{\partial U_i}{\partial x_j} - \frac{\partial U_j}{\partial x_i}\right), \quad S \equiv \sqrt{\tilde{S}_{mn}\tilde{S}_{mn}}.$$

The λ coefficients take the following form:

$$\lambda_1 = n\left[(4/3) - c_2\right], \quad \lambda_2 = (1/2)n^2\left[2 - c_4\right]\left[(4/3) - c_2\right],$$
$$\lambda_3 = n^2\left[2 - c_3\right]\left[(4/3) - c_2\right]$$

where $n = (c_1/2 + \mathcal{P}_k/\varepsilon - 1)^{-1}$ and $c_1, \ldots, c_4$ are coefficients in the GS presentation of linear pressure-strain models. For the Basic Model these take the values $c_1 = 3.6$, $c_2 = 0.8$, $c_3 = 1.2$, $c_4 = 1.2$; for the SSG model the values are

$$c_1 = [3.4 + 1.8\mathcal{P}_k/\varepsilon],\ c_2 = 0.8\ - 0.65A_2^{1/2},\ c_3 = 1.25,\ c_4 = 0.4.$$

numbers which contain the scalar gradients in both the numerator and denominator making the model sensitive to very small gradients.

https://doi.org/10.1017/9781108875400.009 Published online by Cambridge University Press

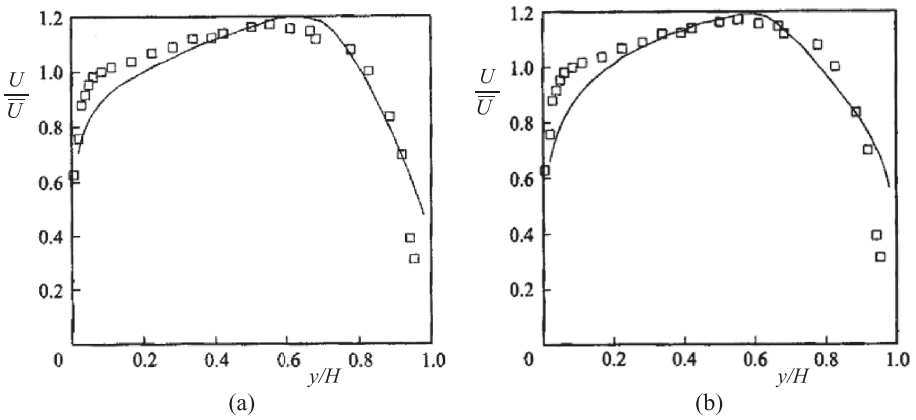

Fig. 7.12 Mean velocity profiles for channel flow rotating in orthogonal mode, Ro = 0.21. Symbols, experiment (Johnston *et al.*, 1972); lines, computations: (a) DSM of Speziale *et al.* (1991); (b) EASM based on the closure model of Speziale *et al.* (1991). From Gatski and Speziale (1993). $\overline{U}$ denotes the bulk velocity.

For a more complete presentation the reader is referred to Gatski and Speziale (1993). The performance of their EASM scheme was compared with results obtained with the original, complete SSG DSM for a number of rotating flows. As an example, Fig. 7.12 compares results for these two options for the case of fully developed flow through a plane channel rotating in orthogonal mode from which it is seen that there are only small differences between the two sets of calculations. Of course, diffusional transport is not a highly important ingredient in fully developed channel flow (while convective transport is zero) so the result here should not be seen as being inconsistent with the less satisfactory comparison between ASM and the parent DSM found by Fu *et al.* (1988).

Further analysis in transforming the ASM equations to explicit form has been contributed *inter alia* by Taulbee (1992), Girimaji (1996) and Wallin and Johansson (2000). The last of these adopted the quasi-isotropic model (Eq. (4.46)) for Φ_{ij_2}, following the suggestion of Taulbee (1992) that the free coefficient in that formulation, denoted c_2, should be assigned the value 5/9 (rather than the originally proposed value of 0.4), a choice that considerably simplified the algebra. Later, Johansson's group (Grundestam *et al.*, 2005) proposed a more elaborate formulation based on a non-linear form of Φ_{ij_2} together with the $k-\omega$ turbulence energy and scale equations which they also applied to channel flow in orthogonal-mode rotation for values of the rotation parameter (inverse Rossby number), Ro, up to 0.77. At these extremely high rotation rates the DNS data of the turbulent shear stress with which they compared their computations apparently showed no change

https://doi.org/10.1017/9781108875400.009 Published online by Cambridge University Press

of sign as the suction surface was approached. The EASM scheme captured this complex behaviour fairly well.

7.3.4 Empirical non-linear eddy-viscosity models (NLEVMs)

Both before and after the work of Gatski and Speziale (1993) discussed in §7.3.3 above, several groups of workers proposed *ad hoc* explicit quadratic non-linear models for the connection between the stress and the mean strain and rotation tensors. These had been developed with the goal of removing specific weaknesses of linear eddy-viscosity models. These schemes can be expressed as follows:

$$a_{ij} = -2\frac{\nu_t}{k}S_{ij} + c_a\frac{\nu_t}{\varepsilon}\left[S_{ik}S_{kj} - S_{kl}S_{kl}\delta_{ij}/3\right] + c_b\frac{\nu_t}{\varepsilon}\left[W_{ik}S_{kj} - W_{jk}S_{ki}\right] + c_c\frac{\nu_t}{\varepsilon}\left[W_{ik}W_{jk} - W_{lk}W_{lk}\delta_{ij}/3\right] \tag{7.17}$$

where $\nu_t \equiv c_\mu k^2/\varepsilon$.

Proposals of this type were made, *inter alia*, by Nisizimi and Yoshizawa (1987), Speziale (1987b), Myong and Kasagi (1990), Rubinstein and Barton (1990) and Shih *et al.* (1995). Yet, from a comparison of the different proposals, Suga (1995) concluded that there was scarcely any point of concurrence in the proposed values of the empirical coefficients among the various schemes, other than that of the linear term c_μ. That fact suggested that the proposals would have added little breadth of applicability since they were calibrated to cope just with simple plane shear flows and the particular class of 'difficult' flows for which the non-linear terms were tuned to resolve. The above conclusion led Suga (see also Craft *et al.*, 1996b, 1997b) to focus on developing cubic non-linear EVMs. The coefficients were still based on calibration against test flows where a linear eddy-viscosity model failed to return satisfactory predictions. By formulating the model at cubic level, however, an appreciably larger number of empirical coefficients became available to allow tuning against a substantially wider range of flows.

On converting to the dimensionless strain and rotation rates used earlier, the constitutive relation adopted can be written as:

$$\begin{aligned} a_{ij}/c_\mu f_\mu = &-2\tilde{S}_{ij} + c_a(\tilde{S}_{ik}\tilde{S}_{jk} - S^2\delta_{ij}/3) + c_b(\tilde{W}_{ik}\tilde{S}_{jk} + \tilde{W}_{jk}\tilde{S}_{ik}) \\ &+ c_c(\tilde{W}_{ik}\tilde{W}_{jk} - \tilde{W}_{kl}\tilde{W}_{kl}\delta_{ij}/3) + c_d(\tilde{S}_{ki}\tilde{W}_{lj} + \tilde{S}_{kj}\tilde{W}_{li})\tilde{S}_{kl} \\ &+ c_g\tilde{S}_{ij}\tilde{W}_{kl}\tilde{W}_{kl} + c_e(\tilde{W}_{il}\tilde{W}_{lm}\tilde{S}_{mj} + \tilde{S}_{il}\tilde{W}_{lm}\tilde{W}_{mj} \\ &- 2\tilde{S}_{lm}\tilde{W}_{mn}\tilde{W}_{nl}\delta_{ij}/3) + c_f\tilde{S}_{ij}\tilde{S}_{kl}\tilde{S}_{kl} \end{aligned} \tag{7.18}$$

where here the dimensionless strain and rotation parameters employ the 'quasi-homogeneous dissipation rate', $\tilde{\varepsilon} \equiv \varepsilon - 2\nu(\partial k^{1/2}/\partial x_j)^2$, introduced in Chapter 6,

https://doi.org/10.1017/9781108875400.009 Published online by Cambridge University Press

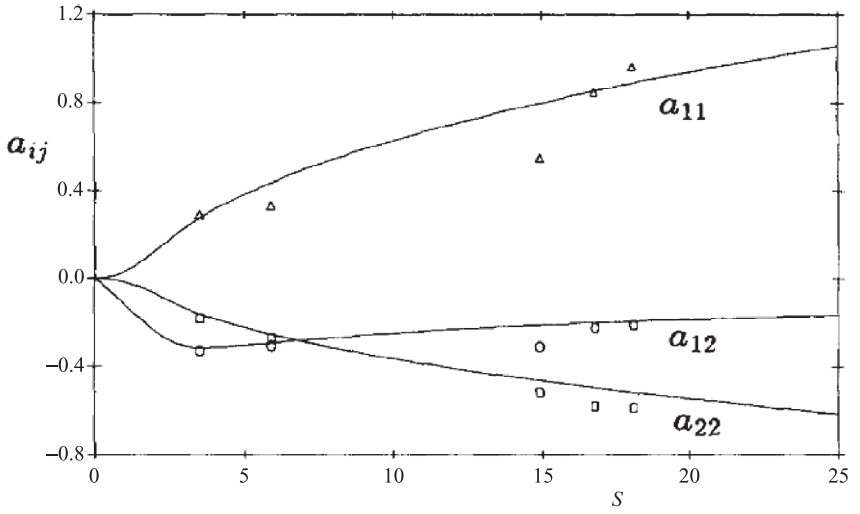

Fig. 7.13 Stress anisotropies for homogeneous turbulence subjected to different dimensionless shear rates. Symbols, $S = 3.5$, Champagne *et al.* (1970); $S = 6.0$, Tavoularis and Corrsin (1981); $S \geq 15$, DNS, Lee et al. (1990). Lines model the calibration from Eq. (7.19). From Craft *et al.* (1996b).

which goes to zero at the wall. The coefficient c_μ was tuned by reference to the various data of simply strained homogeneous shear flows, Fig. 7.13.[14] The adopted form of this coefficient was:[15]

$$c_\mu = \frac{0.3}{1 + 0.59[\max(S,\, W)]^{1.5}} \left(1 - \exp\left[\frac{-0.36}{\exp(-1.26\max[S,\, W])}\right]\right) \qquad (7.19)$$

where as a reminder, W is the scalar rotation rate parameter, $W \equiv \sqrt{\tilde{W}_{ij}\tilde{W}_{ij}}$.

The near-wall damping function f_μ was proposed as:

$$f_\mu = 1 - \exp\left[-(\mathrm{Re}_t/90)^{1/2} - (\mathrm{Re}_t/400)^2\right] \qquad (7.20)$$

though it is unlikely that viscous effects are in fact active in modifying turbulence for values of Re_t as high as Eq. (7.20) implies.[16] The recommended values for the other coefficients are listed in Table 7.1.

Figure 7.13 shows the variation of the anisotropic stress tensor as a function of the dimensionless strain rate from the experiments of Champagne *et al.* (1970)

[14] With $c_f = -c_g$, see Table 7.1, the linear term is the only one that contributes to the shear stress in simple shear.

[15] The use of *both* turbulent Reynolds number and a dimensionless strain rate in reducing the turbulent viscosity as the wall is approached is a strategy also adopted within a linear eddy-viscosity scheme by Cotton and Ismael (1998).

[16] In a subsequent study, Craft et al. (1997b), Reynolds number effects were active only within the buffer layer while additional near-wall damping was applied through the variation of A_2, which was obtained from its own transport equation, Eq. (7.21).

https://doi.org/10.1017/9781108875400.009 Published online by Cambridge University Press

Table 7.1 *Coefficients in the NLEVM of Suga (1995) and Craft et al. (1996b)*

c_a	c_b	c_c	c_d	c_e	c_f	c_g
-1.6	1.6	4.16	$-640c_\mu^2$	0	$-320c_\mu^2$	$320c_\mu^2$

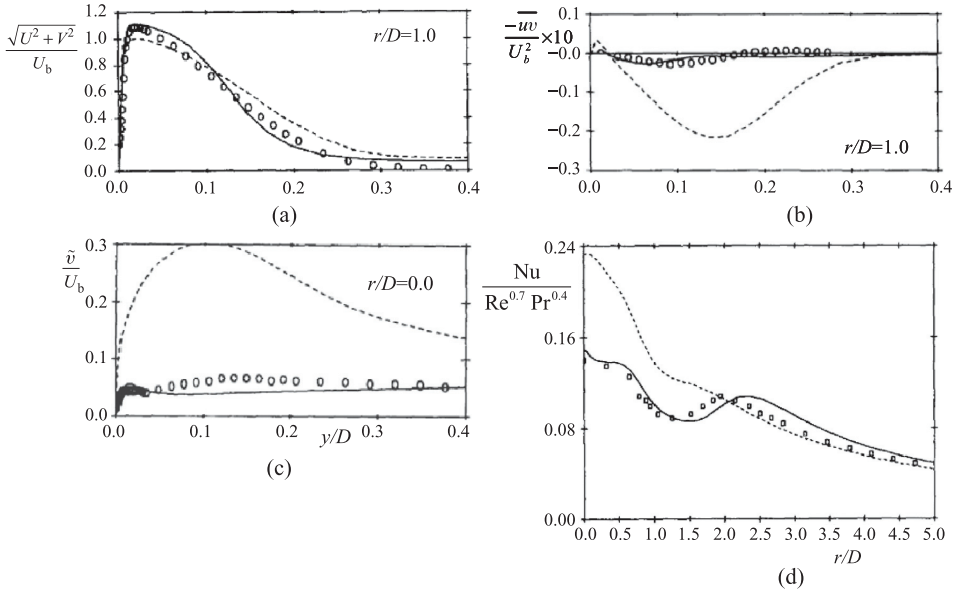

Fig. 7.14 Axisymmetric impinging jet for Re = 22,000, $H/D = 2$; r radial distance from stagnation point, D jet diameter, H jet discharge height above plate: (a) mean velocity; (b) shear stress; (c) rms turbulent velocity normal to plate; (d) Nusselt number distribution along plate. Symbols, experiments: ○○○ Cooper *et al.* (1993); □□□ Baughn and Shimizu (1989), Baughn *et al.* (1992); computations: - - - linear EVM; —— NLEVM. From Craft (1996b).

and Tavoularis and Corrsin (1981) and from DNS simulations (Lee *et al.*, 1990). Agreement of the three component anisotropies with these data is satisfactorily close though, as noted above, the functional dependence of c_μ was explicitly tuned to achieve the best results possible. The (negative of the) value of the ordinate for a_{12} is proportional to c_μ. The decrease in the value of this quantity at high strain rates is an important feature that should be built into any model aspiring to reasonable generality.

The scheme was applied by its originators to a range of flows in which significant straining other than simple shear was present, including curved channel flow and swirling flow through a straight pipe. Figure 7.14 shows results for the turbulence field in an impinging round jet close to the stagnation point and the resultant effect

https://doi.org/10.1017/9781108875400.009 Published online by Cambridge University Press

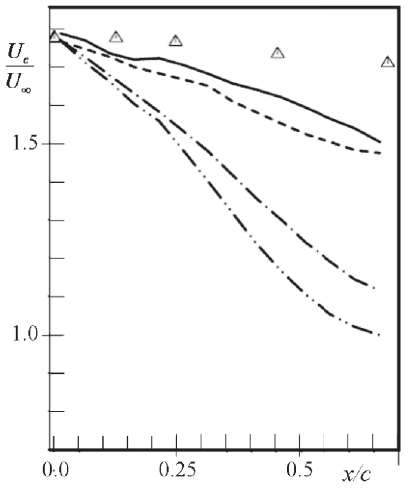

Fig. 7.15 Decay of axial velocity at the centre of a wingtip vortex downstream from the wing trailing edge. Symbols, experiments (Chow *et al.*, 1997); computations, – ·· – linear $k-\varepsilon$ EVM, · – · – · cubic NLEVM, - - - - Basic Model DSM, ——— TCL DSM. From Craft *et al.* (2006b). The too rapid decay of the axial velocity signals a too rapid mixing out of the vortex. The coordinate origin is the trailing edge of the wing and c denotes the wing chord.

on the mean velocity and heat transfer coefficient. The very great improvement relative to that of a linear eddy-viscosity model is plain; in turn this led to the markedly greater accuracy in the computed distribution of Nusselt number along the plate shown in Fig. 7.14d.

Some years later, however (Craft *et al.*, 2006b), it was found that the wingtip vortex downstream from an aircraft diffused much too rapidly with this scheme, the results being only slightly better than those obtained using a linear EVM, whereas the TCL stress-transport closure reproduced a good deal more accurately the slow decay of the vortex, Fig. 7.15. (The decay of the swirl velocity means that the static pressure at the centre of the vortex rises with distance downstream and thus the streamwise velocity at the centre of the vortex – which is what is shown in Fig. 7.15 – decreases downstream. The too rapid decay predicted, especially with the linear and non-linear EVMs, signals the fact that too much mixing with the outer non-swirling fluid is occurring.) In this case, as part of the calibration process, the model had been tuned to capture correctly the damping when angular momentum increased with radius. It had not been similarly tested when the angular momentum decreased with radius for evidently, in the form applied, excessive mixing is then provoked. This failure underlines the fact that empirically based models run the risk of generating spurious answers if one strays far beyond the range of flows used in calibrating the coefficients of the model.

https://doi.org/10.1017/9781108875400.009 Published online by Cambridge University Press

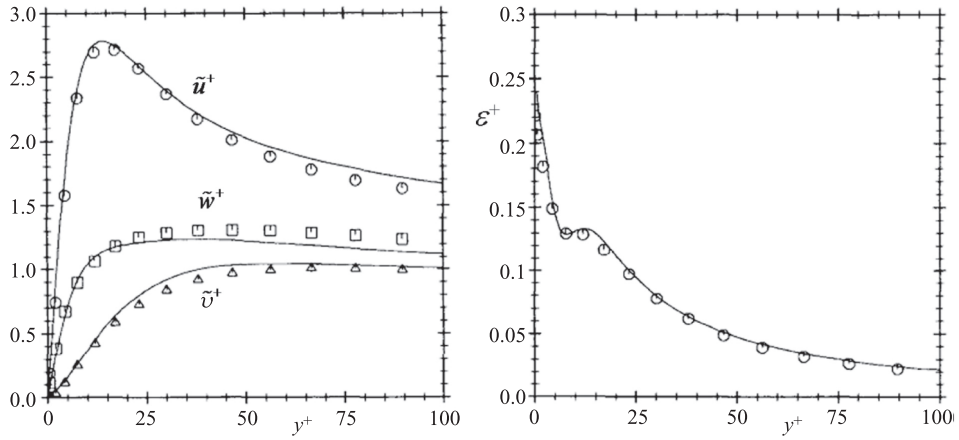

Fig. 7.16 Near-wall normalized profiles of rms turbulence intensities and dissipation rate. Symbols, DNS (Kim, 1989); lines, computed behaviour with a $k-\varepsilon-A_2$ NLEVM. From Craft *et al.* (1997b).

A further weakness emerged when extending the model to handle simple shear flows within the viscosity-affected sublayer. For, while the profiles of shear stress and turbulence energy were well predicted, there was too little difference in the levels of the normal stresses. It was felt that this weakness was linked with the fact that while the model was designed to be *consistent with* the two-component limit it did not *enforce* it. To address that shortcoming, Craft *et al.* (1997b) solved an additional transport equation for the second invariant of the Reynolds stress, A_2 (as well as those for k and $\tilde{\varepsilon}$). The exact transport equation for this quantity can be organized in the form:

$$\frac{DA_2}{Dt} = 2\frac{a_{ij}}{k}[\mathcal{D}_{ij} + \mathcal{P}_{ij} + \Phi_{ij} - \varepsilon_{ij}] - 2\frac{A_2}{k}[\mathcal{D}_k + \mathcal{P}_k - \varepsilon]. \tag{7.21}$$

In order to complete closure, approximations for the diffusion, pressure-strain and dissipation processes in (7.21) were made, drawn from second-moment-closure experience, while the coefficients appearing in Table 7.1 became functions of turbulent Reynolds number and the stress invariants. The reader is referred to the original publication or to the later and slightly modified version of Suga *et al.* (2001) for further details. Figure 7.16 provides an impression of the performance of this three-equation scheme for low Reynolds number flow in a plane channel. Figure 7.16a indicates that the variation of the normal stresses across the near-wall region agrees closely with the DNS of Kim (1989), while Fig. 7.16b shows close accord with the corresponding dissipation rate profile, including the sharp increase in ε very close to the wall.

https://doi.org/10.1017/9781108875400.009 Published online by Cambridge University Press

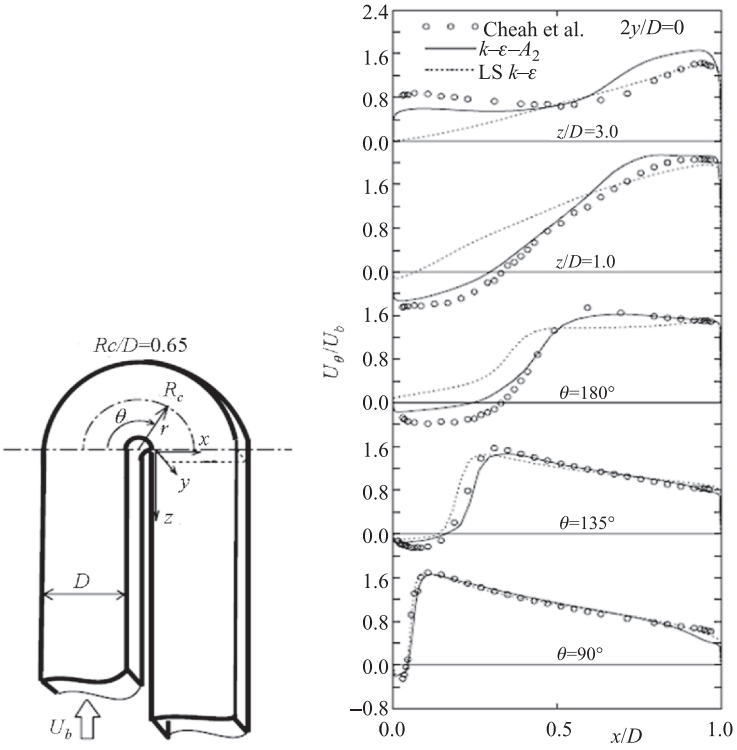

Fig. 7.17 Velocity profiles on the symmetry plane of a sharp, square-sectioned U-bend. Left: flow configuration. Right: mean velocity profiles at selected stations around and downstream from the bend. Symbols, experiments (Cheah *et al.*, 1996); · · · · · · · · · Launder–Sharma, linear EVM; ——$k-\varepsilon-A_2$ NLEVM. From Suga *et al.* (2001).

An extensive testing of this model was subsequently made at the Toyota Research Laboratories for more complex three-dimensional flows relevant to situations found inside IC engines and to external automobile aerodynamics (Suga *et al.*, 2001). As an example, Fig. 7.17 examines the flow around a very tight square-sectioned U-bend comparing computations with the NLEVM and linear EVM schemes against experiment. The figures start 90° around the bend where already the flow on the inside of the bend has separated. At this position both models are in good agreement with the experimental data. Further, around the bend the separated flow region becomes thicker and only the NLEVM tracks the experimental data at all closely. An interesting difference between the results of the two models is that the NLEVM recovers from the separation much more rapidly downstream of the bend than the linear EVM even though at one diameter downstream a large separation is still predicted with the former. This behaviour is fully in accord with the experimental data.[17]

[17] In a separate paper, Suga (2001) reports that for this flow the NLEVM model even gives superior predictions to the TCL SMC presented in Chapter 4. Taking account of all the test cases examined, however, the TCL scheme returned the better overall agreement with data.

https://doi.org/10.1017/9781108875400.009 Published online by Cambridge University Press

The Toyota group has also made proposals for corresponding algebraic models for the turbulent heat or species fluxes, $\overline{\theta u_i}$ (Suga and Abe, 2000). Here it is first noted that the generalized gradient diffusion hypothesis (GGDH) of Daly and Harlow (1970), Eq. (7.13), has been widely used to approximate the heat fluxes in forced-convection situations in both near-wall and free flows. One of its virtues (compared with simple gradient diffusion) is that, in a shear flow, it produces a heat flux in the streamwise direction (where the mean temperature gradient is negligible) as large as or larger than that down the temperature gradient in the cross-stream direction. However, this streamwise heat flux is in fact still much smaller than what actually occurs. The anomaly is usually of little importance as the streamwise flux is negligible compared with the mean-flow convective transport of heat. However, Suga and Abe (2000) and Abe and Suga (2001) concluded from an extensive study of near-wall heat transfer that there were distinct benefits in developing a more general form than Eq. (7.13), not only to model the streamwise flux but also to approximate the important cross-stream flux for varying states of turbulence over a wide range of Prandtl number. Their recommended form (Abe and Suga, 2001) is:[18]

$$\overline{\theta u_i} = -\frac{c_\theta k^2}{\varepsilon}\left[c_{\sigma 1}\frac{\overline{u_i u_j}}{k} + c_{\sigma 2}\frac{\overline{u_i u_k}\cdot\overline{u_j u_k}}{k^2}\right]\frac{\partial \Theta}{\partial x_j} \tag{7.22}$$

where $c_\theta = 0.4(1-\exp[-(20A)^2])^{-0.25}$, $c_{\sigma 1} = 0.15 f_b - f_{\mathrm{Pr}}$, $c_{\sigma 2} = 1 - f_b - f_{\mathrm{Pr}}$ and

$$f_{\mathrm{Pr}} = 1/[1+(\mathrm{Pr}/0.085)^{1.5}], \qquad f_b = (1-f_{\mathrm{Pr}})^2 \exp[-\mathrm{S}^* - (A/0.6)^2]$$

where S* is the dimensionless strain rate $S\sqrt{2}$ and A is the stress flatness parameter, $1-(9/8)[A_2 - A_3]$.

An example of their dimensionless temperature and heat-flux profiles for fully developed plane channel flow is shown in Fig. 7.18. The walls were maintained at different temperatures; thus, if the molecular transport contribution were zero, the level of $\overline{\theta v}^+$ would be equal to unity across the channel. The level of agreement with the DNS/LES results is indeed impressive at all Prandtl numbers though it should be emphasized that the model has been calibrated purely for two-dimensional heat transport. It does not necessarily follow that agreement would be as satisfactory for three-dimensional transport processes.

[18] The form quoted in Suga and Abe (2000) also contains additional terms containing the mean vorticity tensor, W_{ij}. However, Suga (personal communication) advises that these added terms had little effect.

https://doi.org/10.1017/9781108875400.009 Published online by Cambridge University Press

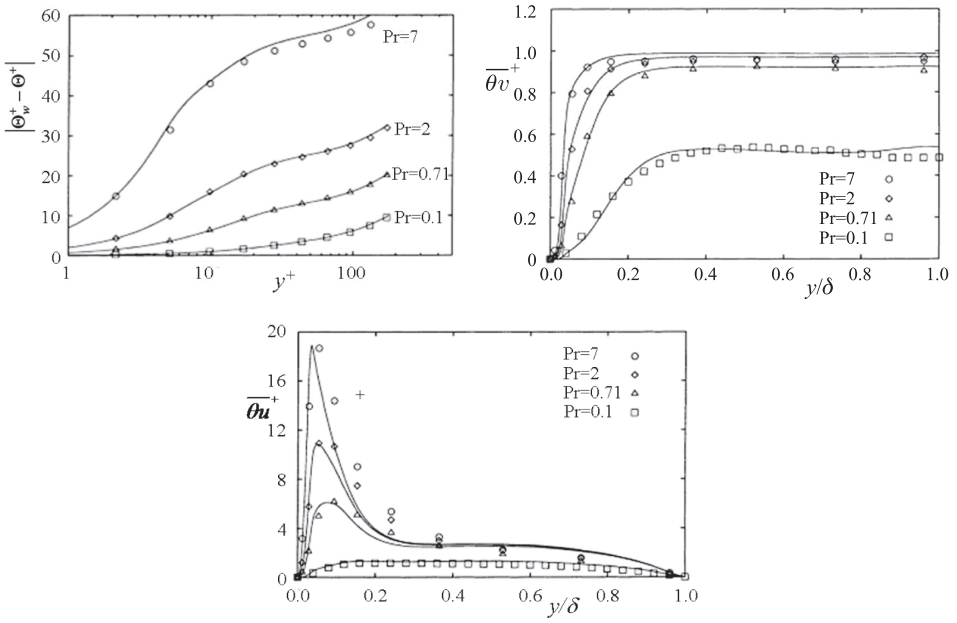

Fig. 7.18 Normalized turbulent thermal field for fully developed flow in a plane channel with different temperatures applied to the two walls. Symbols, DNS/LES, Pr = 7.0, 2.0, 0.71 (Abe and Suga, 1998); Pr = 0.1 (Rogers *et al.*, 1989).

7.4 Linear eddy-viscosity models

7.4.1 Origins and scope

A turbulent flow in local equilibrium that is undergoing simple shearing – so that the production rate of turbulence energy just balances the local dissipation rate – satisfies the constraint:

$$\mathcal{P}_k = -\overline{uv}\frac{\partial U}{\partial y} = \varepsilon. \tag{7.23}$$

(Here and elsewhere in this section we revert to conventional Cartesian coordinates with y denoting the coordinate normal to the wall, or in the direction of shearing for a free flow.) First we define a quantity c_μ such that:

$$c_\mu k^2 \equiv \overline{uv}^2. \tag{7.24}$$

Let us now multiply the left side of (7.23) by the left side of (7.24) and do likewise with the right sides of these two equations to maintain the equality. Then, on dividing each side by ε and $\overline{uv}$, it emerges that:

$$-\overline{uv} = c_\mu \frac{k^2}{\varepsilon}\frac{\partial U}{\partial y}. \tag{7.25}$$

https://doi.org/10.1017/9781108875400.009 Published online by Cambridge University Press

In this form, the quantity $c_\mu k^2/\varepsilon$ is seen to play the role of a turbulent kinematic viscosity. The quantity c_μ is a contrived quantity introduced for convenience but Townsend (1956) observed that in various two-dimensional thin shear flows it was fairly constant, while, as noted in §7.2, Bradshaw *et al.* (1967) developed a very successful early computational scheme for two-dimensional boundary layers which included the supposition that $\overline{uv}/k$ was indeed constant.

An alternative and arguably somewhat deeper insight into why turbulent shear flows will exhibit a viscosity-like transport behaviour in local equilibrium and simple shear is provided by the Basic Model. For then, as discussed in §6.2.3, the shear-stress equation reduces to:

$$-\overline{uv} = \underbrace{\frac{(1-c_2)}{c_1}\frac{\overline{v^2}}{k}}_{c_\mu} \cdot \frac{k^2}{\varepsilon}\frac{\partial U}{\partial y}. \tag{7.26}$$

In the above c_1 and c_2 are, respectively, the coefficients in Rotta's linear return-to-isotropy model of Φ_{ij_1} and the isotropization-of-production (IP) model for Φ_{ij_2}, whose values are recommended as 1.8 and 0.6. The quantity $\overline{v^2}/k$ is by no means constant close to a wall, diminishing continuously as the wall is approached; but this variation can usually be disregarded in the fully turbulent region while the practice of mimicking the damping within the viscosity-affected sublayer by making c_μ a function of the local turbulent Reynolds number is long established despite its obvious physical shortcoming.[19]

In fact, paradoxically, the immediate near-wall region of a turbulent shear flow turns out to be the area where resort to linear eddy-viscosity models has often been made, even when a higher order closure model has been adopted further from the wall. For, while this is physically the most complex region encountered in terms of the interactions expressed in the second-moment equations, there are also simplifying features. Indeed, the flow there – away from the immediate vicinity of stagnation or separation points – really *is* in a state of (intense) simple shear. Consequently, the upstream history is usually of negligible importance even though, in regions of the shear flow further from the wall, its influence may be vital. (It is *that* fact of turbulence life that leads in many attached flows to a nearly universal variation of the near-wall velocity and temperature when scaled suitably in terms of wall variables.) Moreover, because of the complex form of DSM or ASM closures in the viscosity-affected sublayer, the numerical solution of the strongly coupled equation set is not straightforward. Indeed, charting a route between divergence

[19] As discussed in Chapter 6, the damping of $\overline{v^2}$ relative to k as the wall is approached is largely an inviscid wall blocking such as also occurs adjacent to the interface in free-surface flows or other moving interfaces where viscous effects are normally negligible (e.g. Perot and Moin, 1995).

https://doi.org/10.1017/9781108875400.009 Published online by Cambridge University Press

of the iterative solution and generating spurious converged results rendered worthless by numerical diffusion or inadequately resolved source terms is not a task for those needing rapid answers or with little accumulated experience! In these circumstances, a relatively economical and prudent approach that is often adopted is to use a linear eddy-viscosity model to cover just the near-wall region where viscous/wall-blocking effects are substantial, whether at two-equation level (where most of the present examination is directed) or simpler schemes (one-equation k-models or algebraic schemes, such as the mixing-length hypothesis).

Regarding the sections which follow, attention is given in §7.4.2 to models which determine the turbulent viscosity by solving (in addition to the turbulence energy equation) an equation for either the turbulence energy dissipation rate ε (or its associated 'quasi-homogeneous' part $\tilde{\varepsilon}$) or the quantity ω (which may be taken as the reciprocal of the turbulent time scale, k/ε). An important issue addressed is what represents the best way of damping the turbulent viscosity as one approaches the wall so that one mimics the y^3 variation of shear stress that simple analysis and DNS data have shown to apply. Simple eddy-viscosity models are nearly blind to the effects of body forces or streamline curvature on turbulence structure. Thus, in §7.4.3, simple *ad hoc* devices for restoring an appropriate sensitivity to these external influences are briefly noted. In §7.4.4, the elliptic relaxation scheme, introduced in Chapter 6 to handle near-wall influences in stress-transport models, reappears as a useful component of eddy-viscosity models. Finally, in §7.4.5, we consider situations where zero- and one-equation models can perform as well as models requiring an order of magnitude more computing power.

7.4.2 Popular two-equation EVMs

In the presentation above, two scalar properties of turbulence have emerged which are evidently transported by the flow: the turbulent kinetic energy, k, for which an exact transport equation was first published by Reynolds (1895) in his direction-changing 'Reynolds averaging' paper, and its dissipation rate, ε. Or, since a transport equation for k is nearly always adopted, some quantity comprising powers of k and ε would, in principle, suffice just as well as the second variable. In fact, the first proposal for a two-equation eddy-viscosity model was made by Kolmogorov (1942) in a paper based simply on physical insight, intuition and dimensional analysis. His choice of second variable was the rate of energy dissipation scaled with respect to the turbulence energy itself, ε/k, which is nowadays commonly given the symbol ω. Kolmogorov's insight into the nature of turbulence led him to conclude that fine-scale dissipative interactions should be unaffected by processes modifying the large scales of turbulence such as mean shear. Thus his transport equation for ω contained a sink term but no source. Kolmogorov's logic had led him to overlook

https://doi.org/10.1017/9781108875400.009 Published online by Cambridge University Press

the realities of the supply chain, however. The finest scales of turbulence responsible for energy destruction had themselves been created (as Richardson, 1926, had much earlier remarked) by the successive breakdown of large eddies into finer and finer scale structures – and this breakdown was certainly affected by large-scale interactions.

In fact, many years later, Saffman (1970) proposed a transport equation for ω^2 which, since $D\omega^2/Dt = 2\omega D\omega/Dt$ and conversion between the two is straightforward, we may regard as embracing the essence of a $k-\omega$ model. Saffman's version of the ω^2 equation did, however, contain a source term proportional to the mean velocity gradient squared and he applied the equation set (for k and ω^2 with the turbulent viscosity ν_t proportional to k/ω) to several self-preserving shear flows. Over the ensuing 30 years there have been numerous contributions to refining the model, initially, like Saffman, adopting ω^2 as the dependent variable but, more recently, following Wilcox, in terms of a transport equation for ω itself. A more comprehensive account of the evolution of the $k-\omega$ linear EVM may be found in the textbook by Wilcox (2000).

The other widely applied eddy-viscosity closure is the so-called $k-\varepsilon$ model which was originally developed in the late 1960s in D. B. Spalding's group at Imperial College, London. The initial development work was stimulated by the ε-equation proposed by Davidov (1961) (as an element of a much more elaborate closure) and Spalding's encouragement for his group to explore several alternative two-equation EVMs. The first work on the high-Re form of the ε-equation was undertaken by Hanjalić (1970). Following the rigorous derivation of the ε-equation by Davidov (1959, 1961) and some of his conceptual proposals for its closure, Hanjalic formulated a high-Re $k-\varepsilon$ model and demonstrated its satisfactory performance in a number of wall-bounded and free parabolic flows, especially in symmetric configurations. However, the main focus of his doctoral research lay in predicting flows where the surfaces of maximum velocity and zero shear stress were not coincident, see §7.2. Consequently, his effort shifted to stress-transport modelling (Hanjalić and Launder, 1972b) while the considerable further development of the $k-\varepsilon$ model required to enable integration of the dependent variables across the viscosity-affected sublayer (with the goal of predicting partial or complete boundary-layer laminarization, discussed in Chapter 6) was taken up by Jones (1971) (see also Jones and Launder, 1972a). Minor adjustments of the model were subsequently made to make the scheme consistent with an overall optimization of the model for free shear flows (Launder *et al.*, 1973; Launder and Sharma, 1974). In the 1980s, several alternative forms were proposed by other groups, most of which were included in the first comparative testing of two-equation models for wall boundary layers by Patel *et al.* (1985), whose findings are reported below.

Table 7.2 *Coefficients in turbulence models, from Patel et al. (1985)*

Model	Code	D	$\tilde{\varepsilon}_w$ (WBC)	c_μ	$c_{\alpha 1}$	$c_{\alpha 2}$	σ_k	σ_α
Launder–Sharma	LS	$2\nu\left(\frac{\partial k^{1/2}}{\partial y}\right)^2$	0	0.09	1.44	1.92	1.0	1.3
Chien	CH	$2\nu k/y^2$	0	0.09	1.35	1.8	1.0	1.3
Lam–Bremhorst	LB1	0	$\partial\varepsilon/\partial y = 0$	0.09	1.44	1.92	1.0	1.3
Wilcox–Rubesin	WR	0	see note in text	0.09	1.11	0.15	2.0	2.0

Subscript α denotes ε or ω, as appropriate. WBC indicates 'wall boundary condition'.

Other choices for the second dependent variable have also been made but these have been neither as successful nor as extensively tested as those named above. That is not to say that the above versions do not have their weaknesses. Besides the inherent limitations associated with adopting the constitutive equation for a linear eddy-viscosity model, both $k-\omega$ and $k-\varepsilon$ schemes have their own particular weak points as will be pointed out in this section. Fortunately, the weaknesses of the models are, on the whole, rather different and arise in different types or regions of flows. So, depending on the flow to be predicted one can choose which model is the more likely to yield predictions closer to reality. One quite successful scheme is a composite blend of the two models that transforms from one model to the other depending on the proximity to a wall (Menter, 1994; Menter *et al.*, 2003). Before considering that, however, the mathematical forms, the major successes and the principal shortcomings of the individual $k-\varepsilon$ and $k-\omega$ models, will be presented.

In their early comparative assessment of two-equation EVMs, Patel *et al.* (1985) concluded that from the ten models tested, '*it appears that the models of* Launder and Sharma (1974) *and, to some extent*, Chien (1982), Lam and Bremhorst (1981) *which are based on the* $k-\varepsilon$ *model, and that of* Wilcox and Rubesin (1980) [based on the $k-\omega^2$ model] *yield comparable results and perform considerably better than the others*'. As remarked above, the Launder–Sharma model was just a minor (though modestly beneficial) recalibration of the original model of Jones and Launder (1972a). The equations below together with Tables 7.2 and 7.3 set out the forms of these four models (the forms for all ten are given by Patel *et al.*, 1985):

$$\frac{Dk}{Dt} = \nu_t\left(\frac{\partial U}{\partial y}\right)^2 - \varepsilon + \frac{\partial}{\partial y}\left(\left[\nu + \frac{\nu_t}{\sigma_k}\right]\frac{\partial k}{\partial y}\right) \tag{7.27}$$

https://doi.org/10.1017/9781108875400.009 Published online by Cambridge University Press

Table 7.3 *Low Reynolds number functions, from Patel et al. (1985)*

Code	f_1	f_2	f_μ	E
LS	1.0	$1 - 0.3\exp(-\mathrm{Re}_t^2)$	$\exp\left[\dfrac{-3.4}{(1+\mathrm{Re}_t/50)^2}\right]$	$2\nu\nu_t\left(\dfrac{\partial^2 U}{\partial y}\right)^2$
CH	1.0	$1 - 0.22\exp[-(\mathrm{Re}_t^2/6)]$	$1 - \exp(-0.115y^+)$	$2\nu(\tilde{\varepsilon}/y^2)\exp[-0.5y^+]$
LB1	$1 + (7.05/f_\mu)^3$	$1 - \exp(-\mathrm{Re}_t^2)$	$[1 - \exp(-0.0165\mathrm{Re}_y)]^2 \times (1 + 20.5/\mathrm{Re}_t)$	0
WR	$1 - 0.992\exp(-\mathrm{Re}_t/2)$	1.0	$1 - 0.992\exp(-\mathrm{Re}_t)$	$-\dfrac{2}{\sigma_\omega}\left(\dfrac{\partial \ell}{\partial y}\right)^2\omega^3$

$k-\varepsilon$ model

$$\begin{aligned} \nu_t &= c_\mu f_\mu \frac{k^2}{\tilde{\varepsilon}}, \quad \varepsilon = \tilde{\varepsilon} + D \\ \frac{D\tilde{\varepsilon}}{Dt} &= c_{\varepsilon 1} f_1 \frac{\tilde{\varepsilon}}{k} \nu_t \left(\frac{\partial U}{\partial y}\right)^2 - c_{\varepsilon 2} f_2 \frac{\tilde{\varepsilon}^2}{k} + E + \frac{\partial}{\partial y}\left(\left[\nu + \frac{\nu_t}{\sigma_\varepsilon}\right]\frac{\partial \tilde{\varepsilon}}{\partial y}\right) \\ \mathrm{Re}_t &\equiv k^2/\nu\tilde{\varepsilon}, \quad \mathrm{Re}_y \equiv k^{1/2} y/\nu, \quad y^+ \equiv y U_\tau/\nu \end{aligned} \tag{7.28}$$

$k-\omega^2$ model

$$\begin{aligned} \nu_t &= f_\mu k/\omega, \quad \varepsilon = c_\mu k/\omega, \quad \ell = k^{1/2}/\omega \\ \frac{D\omega^2}{Dt} &= c_{\omega 1} f_1 \omega \left(\frac{\partial U}{\partial y}\right)^2 - c_{\omega 2}\omega^3 + E + \frac{\partial}{\partial y}\left(\left[\nu + \frac{\nu_t}{\sigma_\omega}\right]\frac{\partial \omega^2}{\partial y}\right). \end{aligned} \tag{7.29}$$

An important difference among the various models is the choice of characterizing Reynolds numbers that modify the form of the model in the sublayer. Throughout, the Launder–Sharma model adopts $k^2/\nu\tilde{\varepsilon}$ as the turbulence Reynolds number, while Chien in places takes y^+ as the relevant form, and the Lam–Bremhorst scheme employs Re_y in the f_μ function. The impacts arising from these various choices are by no means negligible if one is considering flows far from equilibrium. For example, cases of laminar-to-turbulent transition in the presence of substantial free-stream turbulence (sometimes referred to as *diffusion-controlled* or *bypass transition*) are modelled more successfully by schemes using exclusively a turbulent Reynolds number based purely on scalar properties of turbulence – see Savill (2002a), who provides an extensive survey of conventional turbulence models applied to this class of flows.[20] On the other hand, because the distance of a node from the wall does not change from iteration to iteration, the use of the normal distance y in the Reynolds number tends to be the more stable practice.

Regarding the wall boundary condition, the use of the quasi-homogeneous dissipation (as in LS and CH) removes any ambiguity but at the expense of using a variable that, as one approaches the wall, first rises to a peak then plunges to zero at the wall itself. In consequence, these models are more costly to use for they will require 20–30 nodes to resolve just the viscosity-affected region with reasonable numerical accuracy. For the ω^2 equation WR propose a wall-adjacent value equal to $20/(c_{\omega 2} y^{+2})$. For the test cases that Patel *et al.* (1985) examined, however, they reported that their results were sensitive to the value of y^+ at the near-wall node. Their calculations reproduced below were made with the application point chosen as $y^+ = 0.2$. They observed that 'smaller values did not lead to satisfactory results'.

[20] He concludes, however, that while two-equation EVMs with damping controlled by Reynolds numbers based on turbulence properties produce satisfactory predictions of transition in some cases, a more comprehensive model based on second-moment closure, possibly together with an equation for intermittency, is needed to achieve reasonable breadth of applicability, especially when external turbulence levels are low (Savill, 2002b).

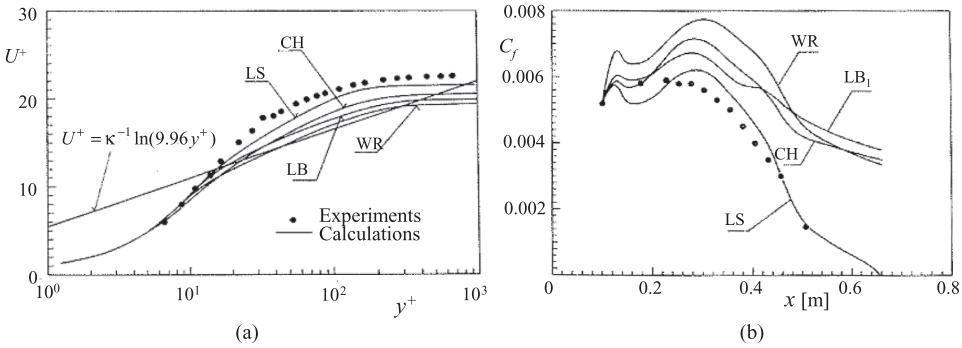

Fig. 7.19 Prediction of turbulent boundary layers in sink flows. Symbols, experiments (a) velocity profile in a near-equilibrium boundary layer, $K \approx 2 \times 10^{-6}$, Simpson and Wallace (1975); (b) skin friction in a laminarizing boundary layer, $K \approx 7 \times 10^{-6}$, Badri Narayanan and Ramjee (1969). Lines, computations. From Patel *et al.* (1985). Note that a turbulent boundary layer undergoes decay towards laminar for $K \approx 3 \times 10^{-6}$.

As Patel *et al.* (1985) also remarked, the conclusions drawn depend on the criteria (or, essentially, the test cases) chosen for judging performance. From the perspective offered by several decades, it may be said that the survey gave rather too much attention to accelerating flows and too little to boundary layers in adverse pressure gradients. Moreover, three-dimensional and recirculating flows lay outside of what could then be included within the scope of a single Ph.D. thesis (Scheuerer, 1983). The four accelerating flows examined produced effects ranging from moderate departures from the 'universal' wall law to complete laminarization. This range is covered in the two examples in Fig. 7.19, the near-equilibrium flow of Simpson and Wallace (1975) and the very severe acceleration of Badri Narayanan and Ramjee (1969). The Jones–Launder model had been developed with strongly accelerating flows in mind so it is less than surprising that the LS scheme emerged well from that comparison. The only adverse-pressure-gradient flow considered was an equilibrium boundary layer where the boundary layer skin-friction coefficient did not fall below 0.0028, i.e. well removed from separation, and where both the LS and WR models did well. It was only over the years that followed that the shortcomings of the above modelled form of the ε-equation in strong adverse pressure gradients became apparent. As has been discussed in Chapter 5 (in connection with complete second-moment closures), arising from deficiencies in modelling the diffusion of ε, the equation then creates too large length scales close to the surface. This problem is even more severe when used within an EVM – a weakness that the ω-equation does not share.

Further Developments of the $k - \varepsilon$ EVM: Scale Limiters

The intervening decades since the first extensive use of the above schemes has seen a continuous development in two-equation eddy-viscosity models both in

https://doi.org/10.1017/9781108875400.009 Published online by Cambridge University Press

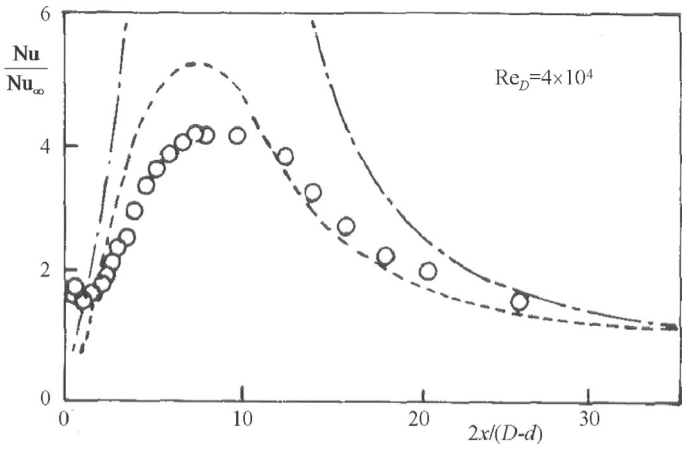

Fig. 7.20 Nusselt numbers downstream of an abrupt 2.5:1 enlargement in pipe diameter; $\mathrm{Re}_D = 4 \times 10^4$. Symbols, experiments, Lee (1984); – —— – —— $k - \varepsilon$ EVM without Yap correction; – - - - - $k - \varepsilon$ EVM including Yap correction. From Yap (1987).

eliminating weaknesses (where possible) and in providing an assessment of performance over a greatly increased range of flows. To a large extent the former activity went hand-in-hand with the latter since the exposure of a model's glaring weakness naturally provided a stimulus for further development. For example, an early signal of the excessive computed levels of near-wall length scales generated by the ε-equation in near-separating and recirculating flows was provided by computations of the thermal field downstream of an abrupt pipe enlargement (Chieng and Launder, 1980) where the computed heat transfer coefficient at the reattachment point was several times the measured value! A correction was thus subsequently devised to drive the length scale back towards the level found in an equilibrium near-wall flow.[21] This took the form of an additional source, $\mathcal{S}_\varepsilon$, in the ε-equation presented in Chapter 5, Eq. (5.12), known as the 'Yap correction' (Yap, 1987). Figure 7.20 shows the application of this correction to an abrupt pipe expansion with a radius ratio of 2.5. Experiments show that the peak Nusselt number, close to the flow's reattachment point, is four times the level found in fully developed pipe flow. Computations with the original LS model, however, return a peak level some 10 times greater than the fully developed value. Evidently, inclusion of the Yap correction brought the computed values (with a peak 5 times that in fully developed pipe flow) a good deal closer to the experimental data.

[21] Here it is important to stress that 'towards' does not mean 'to'. Tests using a one-equation EVM where the length scale was assigned the same variation with distance from the wall as found in fully developed plane channel flow led to Nusselt numbers up to 50% below those measured (Yap, 1987; Launder, 1988).

https://doi.org/10.1017/9781108875400.009 Published online by Cambridge University Press

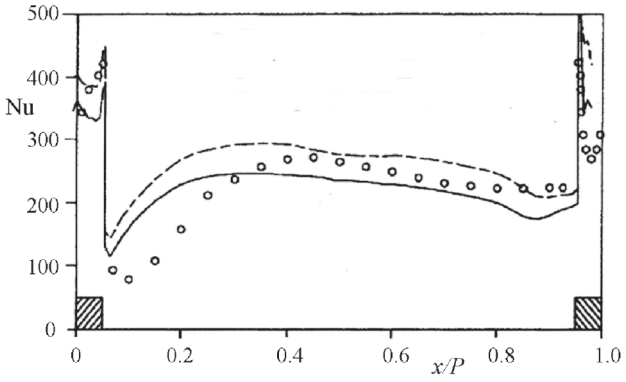

Fig. 7.21 Application of damping functions for length scale control. Nusselt number distribution on the symmetry line for three-dimensional flow through a square duct with square ribs placed symmetrically on two facing walls: experiments, Baughn *et al.* (1991); – – – Eq. (5.12); ——— Eq. (5.14). From Iacovides and Raisee (1999).

An unsatisfactory feature of the original Yap correction is the appearance of the normal distance, y; so, while the term has been found to be effective in controlling the near-wall levels of turbulent kinetic energy (and thus of skin-friction and heat transfer coefficients) over a range of separated flows, in complex geometries its appropriate interpretation involves a high degree of arbitrariness. Iacovides and Raisee (1999), extending a suggestion of Hanjalić (1996), therefore proposed a differential form of the Yap correction that was also introduced in Chapter 5, Eq. (5.14). Figure 7.21 shows the variation of Nusselt number on the centre-plane for repeating flow through a square-sectioned duct on which square ribs have been mounted on two opposite faces. For this case the differential length scale limiter returns results similar to (though somewhat better than) those obtained with the original Yap correction in acceptably close agreement with experiment except immediately downstream of the rib.

Both the extra source terms, together with the alternative version, Eq. (5.13), due to Hanjalić (1996), have enabled the dissipation equation to return reasonably satisfactory agreement with experiment over a range of separated flows such as examined above. Indeed, for the case considered in Fig. 7.21, agreement was as good as for the second-moment-closure computations by the same authors (not shown). Unfortunately, news of these amendments has not spread as far as that of the original model. Thus, in a number of published comparisons, the original Launder– Sharma version without any length scale constraining terms is used for separated flow computations. The above corrections were designed specifically to improve the prediction of turbulent stresses and remove excessive wall heat transfer rates in recirculating flows. However, they also reduce the tendency for the

near-wall length scale to grow undesirably in adverse-pressure-gradient boundary layers, leading to improved predictions of skin friction coefficient.

If one's attention is confined purely to non-recirculating flows, however, an alternative route is to put additional emphasis on irrotational straining in the mean-strain source term in the ε-equation. This approach (Hanjalić and Launder, 1980) has been discussed in §5.1 in connection with second-moment closure (Fig. 5.2). It was, however, also used with the $k-\varepsilon$ EVM and brought significant improvements to equilibrium adverse-pressure-gradient boundary layers (as well as to the rate of spread of the round jet). Rodi and Scheuerer (1986) confirmed the effectiveness of the additional source showing, *inter alia*, excellent agreement with the nearly separating boundary layer of Samuel and Joubert (1974). However, as remarked in Chapter 5, this irrotational-strain modification performs poorly in separated flows – for example, shortening the already too short reattachment length behind a backward-facing step – so it is not suitable as a general purpose corrector.

Finally, as already discussed in §5.1 for general cases, a way to introduce into EVMs some control on the turbulence scale growth in non-equilibrium flows is to make some of the coefficients in the basic ε-equation functions of the available turbulence parameters, such as the moduli of the non-dimensional mean strain and rotation rates, $S \equiv \sqrt{\tilde{S}_{ij}\tilde{S}_{ij}}$ and $W \equiv \sqrt{\tilde{W}_{ij}\tilde{W}_{ij}}$, or of the ratio of the turbulence energy production and dissipation, $\mathcal{P}_k/\varepsilon$. For example, Durbin (1995) proposed that the source-term coefficient in the ε-equation should take the following form: $c_{\varepsilon 1} = 1.4\left(1 + a\sqrt{\mathcal{P}_k/\varepsilon}\right)$, where a is a coefficient, or the later variant $c_{\varepsilon 1} = 1.4\left(1 + 0.045\sqrt{k/\overline{v^2}}\right)$ proposed in the context of the elliptic relaxation EVM (known as the $\overline{v^2} - f$ model, to be considered in §7.4.4).

The $k-\omega$ Model and the SST Variant

Over the years, the $k-\omega^2$ EVM has also been the subject of successive refinements, the first major step being the decision to adopt ω as the scale-determining variable rather than ω^2, Wilcox (1988b). The model could be applied with fewer adaptations to the viscous sublayer than the $k-\varepsilon$ model but, conversely, was less proficient in the outer region of a boundary layer, especially in the absence of free-stream turbulence. In the mid-1990s Menter (1994) proposed adapting the model so that it behaved like the $k-\varepsilon$ model away from the wall (in particular, being able to cope with external stream turbulence without anomalies) while reverting to the well-calibrated original version of the $k-\omega$ model close to a wall. This approach was blended with certain other limiters that caused the model, in a two-dimensional shear, to respond more like a shear-stress-transport equation (leading to the scheme being labelled the *SST model*). This version has been successfully applied to many

https://doi.org/10.1017/9781108875400.009 Published online by Cambridge University Press

two-dimensional boundary layers. Apsley and Leschziner (2000) report results from consolidating and analysing multi-instition computions of a diversity of models attempting to capture separation in the asymmetric diffuser flow of Obi et al. (1993). They concluded for this case the SST scheme, while separating too early, did give the best overall agreement among the several linear eddy-viscoity models tested. Indeed it achieved a level of agreement with experiment comparable with that returned by the basic second-moment closure. Thus, to some extent, the model does live up to its 'SST' label. Leschziner and Lien (2002) found, however, that in the supersonic, three-dimensional recirculating flow created by the intersection of a strut with a wing, the scheme created only a single horseshoe vortex compared with the double vortices produced in both the experiments and the genuine second-moment closures they examined. It appeared from this that, despite the carefully conceived physical ideas that went into its construction, the model lacked the capability of the *real* stress-transport schemes used in computing the same flows. However, subsequently, Menter (2003) proposed a revised version of the model that Levchenya *et al.* (2010) have applied to the wing-strut flow measured by Praisner and Smith (2006a, 2006b), a flow very similar to that examined by Leschziner and Lien (2002) except that the former flow was subsonic. Figure 7.22 brings out clearly the multiple vortex structures created with the modified SST model, which Levchenya *et al.* (2010) show is absent with the original $k-\omega$ model. The consequent variations in Stanton number along the symmetry plane approaching the stagnation point obtained with the different models are shown in Fig. 7.22 (c) and (d). These lend strong support to the predicted vortex structure.

The most comprehensive account of developments with the $k-\omega$ model can be found in the textbook by Wilcox (2000). The version recommended by Wilcox incorporates improvements arising from a decade of testing and refining the original model. The recommended form is:

$$\frac{Dk}{Dt} = -\overline{u_i u_j}\frac{\partial U_i}{\partial x_j} - \beta^* k\omega + \frac{\partial}{\partial x_j}\left[\left(\nu + \frac{\nu_t}{\sigma_k}\right)\frac{\partial k}{\partial x_j}\right]$$
$$\frac{D\omega}{Dt} = -\alpha\frac{\omega}{k}\overline{u_i u_j}\frac{\partial U_i}{\partial x_j} - \beta\omega^2 + \frac{\partial}{\partial x_j}\left[\left(\nu + \frac{\nu_t}{\sigma_\omega}\right)\frac{\partial \omega}{\partial x_j}\right] \qquad (7.30)$$

where

$$\sigma_k = \sigma_\omega = 2, \quad \alpha = 13/25, \quad \beta = \beta_0 f_\beta \quad \beta^* = \beta_0^* f_{\beta^*},$$
$$\beta_0 = 9/125, \quad \beta_0^* = 9/100$$

and

$$f_\beta = \frac{1 + 70\chi_\omega}{1 + 80\chi_\omega}, \qquad f_{\beta^*} = 1.0 \quad (\text{for } \chi_k \le 0)$$

or

$$f_{\beta^*} = \frac{1 + 680\chi_k^2}{1 + 400\chi_k^2} \quad (\text{for } \chi_k > 0);$$

https://doi.org/10.1017/9781108875400.009 Published online by Cambridge University Press

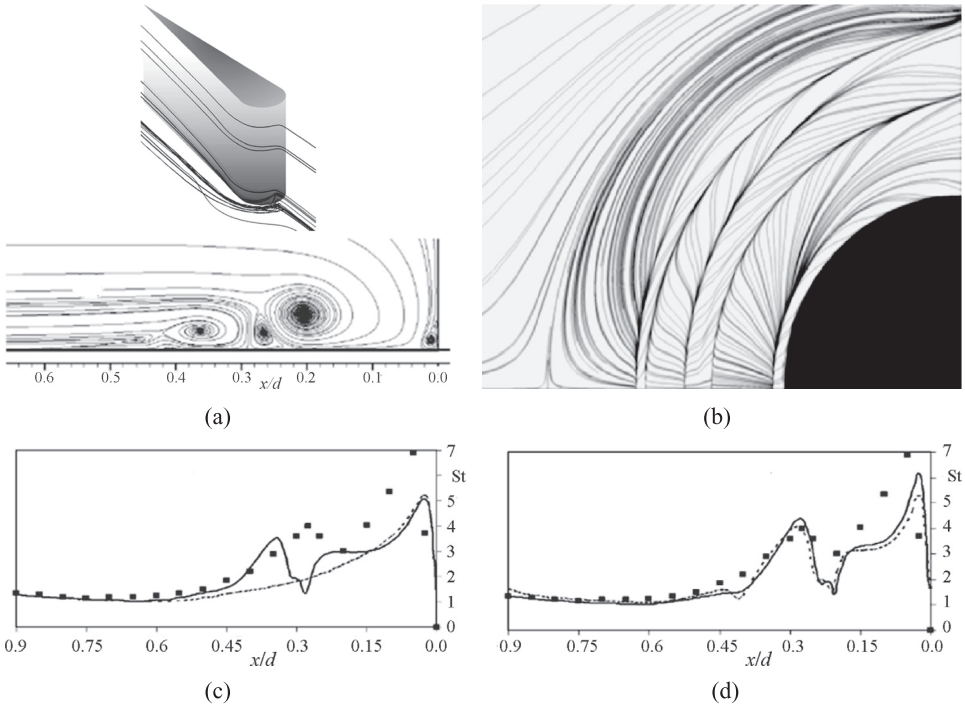

Fig. 7.22 Flow past a symmetric airfoil abutting a smooth wall. (a) Flow configuration and streamline pattern on the symmetry plane upstream of the airfoil. (b) Plan view of surface streaklines on the wall computed with the modified SST model (Menter, 2003). (c) Computed Stanton number on the wall ahead of the wing: symbols, experiments (Praisner and Smith, 2006b); computations – – – Wilcox (1993) model; ——— Menter (1994). (d) As (c) except the lines denote computations with the modified SST model (Menter, 2003) using – – – ANSYS-CFX; —— in-house code. From Levchenya *et al.* (2010).

where

$$\chi_\omega \equiv \left| \frac{W_{ij} W_{jk} S_{ki}}{(\beta_0^* \omega^3)} \right|, \qquad \chi_k \equiv \frac{1}{\omega^3} \frac{\partial k}{\partial x_j} \frac{\partial \omega}{\partial x_j}$$

and W_{ij} and S_{ij} are the conventional mean rotation and strain rate tensors.

The empirical calibration of the coefficients and functions has clearly been done with much care and, for example, impressive results are reported for the three most commonly encountered self-preserving free shear flows, Table 7.4. As Wilcox (2000) acknowledges, the earlier $k-\omega$ model (Wilcox, 1988a) clearly gave too rapid spreading rates for these free-shear flows while the more recent version achieves broadly satisfactory agreement – better on average than the original $k-\varepsilon$ model which is seriously unsuccessful for the round jet. Indeed, the $k-\varepsilon$ model's spreading rate for this flow is similar to that for the Basic Model (second-moment closure) whose performance was discussed in Chapter 4.

https://doi.org/10.1017/9781108875400.009 Published online by Cambridge University Press

Table 7.4 *Spreading rates of commonly occurring self-preserving free shear flows for three eddy-viscosity models, from Wilcox (2000)*

Flow	Experimental spread rate	$k-\omega$ EVM, Wilcox (2000)	$k-\varepsilon$ EVM	$k-\omega$ EVM Wilcox (1988b)
Mixing layer	0.115	0.105	0.098	0.141
Plane jet	0.110	0.101	0.108	0.135
Round jet	0.095	0.088	0.120	0.369

The entries under experimental values are those of the present authors, based on our interpretation of the best available experimental data.

Two cautionary remarks need to be made about the results reported in Table 7.4, however. First, the rate of decay of ε with distance downstream in the round jet is very rapid – so rapid that *streamwise* diffusion plays some role in the spreading. El Baz *et al.* (1993) report that a boundary layer solver that neglects streamwise diffusion overestimates the spreading rate strictly implied by the model by around 7% irrespective of grid density. Second, the relatively successful prediction of the round jet spreading rate by the current $k-\omega$ model is acknowledged to be due in large measure to the parameter χ_ω which, as discussed in Chapter 5, §5.1.1, is proportional to the 'Pope correction'. The parameter provides a dimensionless measure of the stretching of cross-stream vortex lines. It is zero in plane flows but in axisymmetric flows, as the jet spreads, the circumference increases and the consequent stretching of the vortex lines acts (according to the model) to increase the dissipation rate and thus to reduce the turbulent viscosity. While the parameter does enable the spreading rate of the self-preserving round jet to be predicted (while having no effect on the plane jet and mixing layer), as reported in §5.1, Huang (1986) found that, in the form proposed by Pope (1978), it leads to poor predictions of the round jet in a moving stream, a flow where the standard form of the ε-equation proves satisfactory.

It needs to be said, however, that the Wilcox-2000 version of the $k-\omega$ model provides more intricate interconnections than Pope's original proposal. Indeed, Wilcox (2000) reports satisfactory spreading rates for the radial jet (where vortex line stretching also occurs), whereas Rubel (1985) had found that the Pope correction in its original form gave a spreading rate for the radial jet less than half the reported experimental value! So, it is possible that the most recent form of the Wilcox $k-\omega$ model may also cope with round jets in co-flowing streams of arbitrary magnitude.

One of the main virtues of the original $k-\omega$ model had always been that it predicted, reasonably faithfully, the development of turbulent boundary layers in positive (adverse) pressure gradients (in contrast to the too slow approach towards

https://doi.org/10.1017/9781108875400.009 Published online by Cambridge University Press

separation with the original $k-\varepsilon$ model, discussed above). Wilcox (2000) notes that the various corrective terms embedded in the newer form of his model have been chosen so that they have little if any effect on two-dimensional boundary layers developing on plane surfaces. It may thus be supposed that the newer formulation is equally as successful as its predecessor versions.

Durbin's Realizability Constraints

Intrigued by the serious failure of the common two-equation EVMs to reproduce properly the flow (and especially the heat transfer) in the stagnation region of an impinging flow associated with the excessive production of turbulent kinetic energy, Durbin (1996) proposed to cure the 'stagnation-point anomaly' by imposing the *realizability* constraint $2k \geq \overline{u_\alpha^2} \geq 0$ on the stress–strain equation, i.e. $\overline{u_i u_j} = -2\nu_t S_{ij} + 2/3k\delta_{ij}$. By noting that $S_{ij}$is symmetric, with only diagonal components in principal coordinates (with eigenvalues λ_1, λ_2, λ_3), applying the (more critical) lower bound on the principal stress components leads to

$$\overline{u_\alpha^2} = -2\nu_t\lambda_\alpha^2 + \frac{2}{3}k \geq 0 \quad \text{and} \quad 2\nu_t\lambda_{\max}^2 \leq \frac{2}{3}k. \tag{7.31}$$

Moreover, the λ are related by the continuity equation and the second strain invariant (for an incompressible fluid):

$$\lambda_1 + \lambda_2 + \lambda_3 = 0, \quad \lambda_1^2 + \lambda_2^2 + \lambda_3^2 = S_{ij}S_{ij} = \mathcal{S}^2$$

resulting in the eigenvalues[22]

$$\lambda_1 = -\tfrac{1}{2}\lambda_2 \pm \tfrac{1}{2}\sqrt{2\mathcal{S}^2 - 3\lambda_2^2}, \quad \lambda_3 = -\tfrac{1}{2}\lambda_2 \mp \tfrac{1}{2}\sqrt{2\mathcal{S}^2 - 3\lambda_2^2},$$
$$\lambda_2 = -\tfrac{1}{2}\lambda_1 \pm \tfrac{1}{2}\sqrt{2\mathcal{S}^2 - 3\lambda_1^2}.$$

For all the λ to be real the condition to be satisfied is $2\mathcal{S}^2 - 3\lambda^2 \geq 0$. Thus,

$$|\lambda_{\max}| \leq \sqrt{\tfrac{2}{3}}\mathcal{S}. \tag{7.32}$$

Eliminating $\lambda_{\max}$ leads to the realizability constraint on the eddy viscosity that can be applied to any EVM

$$\nu_t \leq \frac{k}{\sqrt{6}\,\mathcal{S}}. \tag{7.33}$$

[22] Note that $\mathcal{S} \equiv \sqrt{S_{ij}S_{ij}}$ is the modulus of the absolute strain rate, not to be confused with two other non-dimensional strain-rate parameters, $\mathrm{S} \equiv \sqrt{\tilde{S}_{ij}\tilde{S}_{ij}} = \mathcal{S}k/\varepsilon$ or $S \equiv (k/\varepsilon)dU/dy$, introduced earlier.

https://doi.org/10.1017/9781108875400.009 Published online by Cambridge University Press

By noting that $\nu_t = c_\mu\, k\mathcal{T}$, the realizability constraint can be expressed in terms of the upper bound on c_μ or on the time scale $\mathcal{T} = k/\varepsilon$

$$c_\mu \le \frac{1}{\sqrt{6}}\frac{\varepsilon}{k\mathcal{S}} \quad \text{or} \quad \mathcal{T} \le \frac{1}{\sqrt{6}c_\mu\mathcal{S}} \tag{7.34}$$

or in a more convenient form

$$\mathcal{T} = \min\left[\frac{k}{\varepsilon}, \frac{a}{\sqrt{6}c_\mu\mathcal{S}}\right] \tag{7.35}$$

where $a \approx 0.6$, evaluated by fine tuning in some impinging and separating flows.

Note that this constraint limits the kinetic energy production to a *linear* dependence on strain rate:

$$\mathcal{P}_k \le k\mathcal{S}/\sqrt{6}\ . \tag{7.36}$$

Equation (7.35) implemented in the standard $k-\varepsilon$ and $k-\omega$ models was shown to reduce the anomaly in stagnation regions for a range of flows (Medić and Durbin, 2002, among others) and would seem to be a generally desirable feature to incorporate within any eddy-viscosity model. However, it is not a panacea: in an impinging flow turbulent stresses are really not created in the way that an eddy-viscosity model supposes. Thus, rather like the numerous safety features in a modern automobile, the limiter enables one to avoid the more serious consequences of taking an ill-advised route.

7.4.3 Accounting for curvature, rotation and other body forces in EVMs

Most flows that one is interested in computing in an industrial or environmental context will be affected by complex straining or body forces. The subtle responses of the stress field to streamline curvature and other secondary strains (that are mimicked, albeit imperfectly, in full second-moment closures or NLEVMs) are not remotely captured by the simplistic stress–strain connection used by linear EVMs. Moreover, force fields exert different effects on different components of the Reynolds stress. Thus, while the aggregate effect of the force field will appear in the turbulent kinetic energy equation, that will usually not capture the effects that the stress and scalar-flux fields actually experience. Indeed, in the case of Coriolis force, we have seen in §4.5.2 that the effects on the axial and wall-orthogonal normal stresses are equal and opposite, and zero in the third direction. Thus, in orthogonal-mode rotation in a duct, with any linear EVM, precisely the same flow pattern is predicted as for a non-rotating channel!

In these situations, three levels of advice for the intended user of linear EVMs may be offered.

https://doi.org/10.1017/9781108875400.009 Published online by Cambridge University Press

Level 1: take no corrective action. Despite appearances to the contrary, the weaknesses of the model may not in practice produce major errors in the prediction of the flows of interest.
Level 2: make *ad hoc* adjustments to the model that are tailored to match the conditions that apply specifically to the types of flow to be calculated.
Level 3: upgrade the level of closure.

Nothing more will be said here about Level 3 since that class of options is what the rest of the book has been about. In the paragraphs which follow, the other two approaches will be exemplified briefly.

As the first example of the Level 1 approach, the case of flow around a square-sectioned bend is considered. Indeed, the three-dimensional flow around a square-sectioned 90° bend had been chosen as one of the test cases for the 1980–81 Stanford Conference (Kline *et al.*, 1981, 1982). The computations submitted by contributing groups produced a rather puzzling outcome, for two of the simplest schemes, based on algebraic mixing-length models, gave the best results. Certainly, the curvature was sufficiently strong that if the flow had been two-dimensional, it would have been essential to account for curvature effects on the stress field. For this highly non-equilibrium flow, however, the main problem was not the use of turbulence models that were insensitive to the streamline curvature but rather the scheme used next to the wall across the viscosity affected sublayer. In 1981, given the modest available computing resource, only the groups using the simplest models could employ a fine enough grid to resolve this low-Re near-wall region. Those using 'advanced' transport-equation models instead employed *wall functions* (the subject of Chapter 8). At the time, however, only the most rudimentary versions of wall functions were available. Now, the radial pressure gradient induced by the bend creates a strong secondary flow in which the slow moving near-wall fluid is carried to the inside of the bend. Indeed, the peak secondary velocity occurs right in the viscous region. The implied skewing of the mean velocity vector within the viscous region was entirely missed by the wall functions then in use. When, a few years later, the sublayer *was* resolved by blending a two-equation EVM used for the main flow with the mixing-length hypothesis across the near-wall sublayer, excellent agreement with the experimental data resulted, Fig. 7.23. The details of the mixing-length model employed are given in §7.4.7. The same approach was also applied to the more complicated case of an unseparated 180° U-bend and gave results that were less successful but which would probably be acceptable for most engineering applications (though not as good as with an ASM closure) (Choi *et al.*, 1989). However, for the separated flow around the hairpin bend considered in Fig. 7.17, the differences between the $k-\varepsilon$ EVM predictions and the measurements are so great that the computational results with that model are probably not useful.

https://doi.org/10.1017/9781108875400.009 Published online by Cambridge University Press

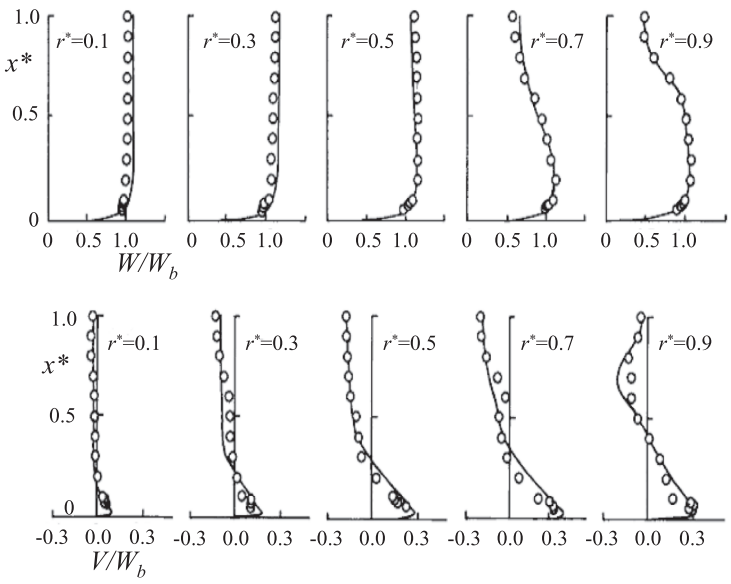

Fig. 7.23 Velocity profiles $0.25D_h$ downstream of a 90° bend: ○ ○ ○ experiments (Taylor *et al.*, 1982); ——— computations using $k-\varepsilon$ EVM with MLH sublayer model. From Iacovides *et al.* (1987). W and W_b are the mean and bulk-mean axial velocities, V is the negative of the radial mean velocity; r^* and x^* are radial and span-wise normalized coordinates.

Thus, it is clear that the accuracy of the computations declines progressively as the ratio of bend radius to duct side length diminishes and the flow becomes separated and increasingly chaotic.

As a second example of where the 'do-nothing' policy is satisfactory, we consider buoyantly modified flow (mixed convection) in vertical tubes, for example Jackson *et al.* (1989), or natural convection in narrow vertical cavities – the double-glazing problem (Ince and Launder, 1989). The gravitational vector directly modifies the vertical velocity fluctuations – but, for a vertically directed flow, *that* is not the direction in which the mean velocity and temperature are varying rapidly. The crucial direction of velocity fluctuation is normal to the wall; and this direction for the flows considered is *horizontal* where buoyancy makes no direct contribution. There are, of course, indirect contributions to the stress budgets (via the pressure fluctuations) but these we may suppose to be not dissimilar in their overall effect from simply including the buoyant term in the production term of the k-equation. Figure 7.24 compares data of the mean Nusselt number for a range of experiments, covering both up-flow and down-flow in vertical tubes, *with* those emerging from a large number of test runs using a low-Re form of the $k-\varepsilon$ EVM (Cotton and Jackson, 1990). It is seen that the experimental behaviour is very well

https://doi.org/10.1017/9781108875400.009 Published online by Cambridge University Press

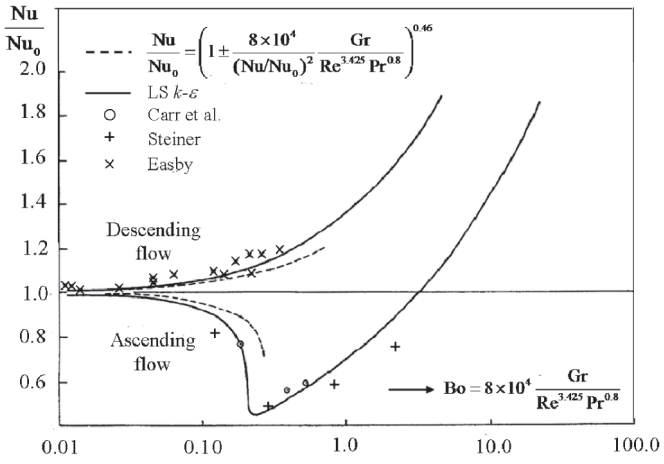

Fig. 7.24 Effect of buoyancy on Nusselt number in flow through vertical heated pipes. Symbols, collected experimental data; – – – earlier theoretical estimate; ——— predictions with LS low-Re $k-\varepsilon$ model. From Cotton and Jackson (1990).

captured by the model, including the serious impairment of the Nusselt number relative to forced convection that occurs in up-flow when the buoyancy parameter, $\mathrm{Bo} \equiv 8 \times 10^4\ \mathrm{Gr}/\mathrm{Re}^{3.425}\ \mathrm{Pr}^{0.8}$, falls between 0.1 and 1.0. In contrast, substantial augmentation of the Nusselt number is found in down-flow and also in up-flow for sufficiently high values of the buoyancy parameter.[23] However, capturing these effects is not at all due to the buoyant terms in the turbulence equations (whose contribution to the k budget is minor). Indeed, the most crucial aspect of the model is the choice of the turbulent Reynolds number functions used to enable the equations to be integrated up to the pipe wall!

Attention is now turned to situations where some explicit modification of the model is essential. At Level 2, if one is keeping the eddy-viscosity stress–strain relation, the routes for modifying the predicted behaviour are to make c_μ a function of some dimensionless parameter relevant to the flow under study and/or to make changes in the relevant transport equations. For example, in *horizontal* stably stratified shear flows, standard EVMs produce excessive mixing because the crucial velocity fluctuations affecting mixing and entrainment are now *vertical* and are thus directly damped by the stable density gradient. To mimic this, one can make c_μ a function of a buoyancy parameter (usually the flux Richardson number) or, more simply, one can include the buoyant source in the k-equation but omit it

[23] The rather cumbersome parameter adopted for the abscissa in Fig. 7.24 was first proposed by Hall and Jackson (1969), who advocated the relation given at the top of Fig. 7.24 and shown by the broken line. Although not included in the figure, other data sets shown in Cotton and Jackson (1990) confirm that the computed behaviour in Fig. 7.24 for the buoyancy parameter greater than three in both upward and downward flow is closely in line with experimental data.

https://doi.org/10.1017/9781108875400.009 Published online by Cambridge University Press

from the ε-equation,[24] a practice which has been extensively adopted (see Chen and Rodi, 1980). Since the buoyant contribution to k generation is negative in stable stratification, this omission leads to higher dissipation rates and thus to lower kinetic energy and turbulent viscosity levels. Either approach is cheap and simple but needs re-tuning as attention shifts from one type of flow to another. Moreover, in really complicated flows, such as modelling flows in a room with discrete air inflow and outflow ports and heat sources (whether from radiators, people or PCs), a single choice of modification is unlikely to suffice.

Eddy-viscosity models have also been modified to account for the Lorentz force acting on an electrically conductive fluid subjected to an electromagnetic field (e.g. Ji and Gardner, 1997; Kenjereš and Hanjalić, 2000b). The straightforward approach is to introduce additional source terms in both the k- and ε-equation listed in Table 5.1. It is recalled that these terms have been derived from the exact definition of the fluctuating Lorentz force, using Eq. (4.97) to model the correlation of the fluctuating electric field and velocity, $\overline{e_i u_j}$. For a uniform transverse magnetic field of constant strength, B_0[25] (which is the most common configuration in the magnetic control of metals), the expressions for both equations each reduce to a single term. The tests showed, however, that this remedy was not sufficient and that a magnetic damping was needed in both terms. Ji and Gardner (1997) multiplied the additional source terms (as well as the eddy viscosity) by an exponential function, $\exp(-c_{2M}N)$, where $N \equiv \sigma B_0^2 L/\rho U$ is the bulk flow Stuart number (a magnetic interaction parameter). The above function was derived from an approximate analysis of the velocity decay under the action of a transverse magnetic field, $U(t) = U_0 \exp(-t/\mathcal{T}_M)$, by taking $\mathcal{T}_M \equiv \rho/\sigma B_0^2$ as the characteristic magnetic braking time. Kenjereš and Hanjalić (2000b) replaced N by the ratio of the dynamic to magnetic time scales, $\mathcal{T}/\mathcal{T}_M$, and thus approximated the extra source terms in the k- and ε-equations as

$$S_k^M = -\frac{\sigma}{\rho} B_0^2 k \exp\left(-c_{1M}\frac{\sigma}{\rho}B_0^2\frac{k}{\varepsilon}\right), \quad S_\varepsilon^M = -\frac{\sigma}{\rho} B_0^2 \varepsilon \exp\left(-c_{1M}\frac{\sigma}{\rho}B_0^2\frac{k}{\varepsilon}\right) \tag{7.37}$$

where $c_{1M} = 0.025$ was determined from the validation of Eqs. (7.37) against the DNS data for a plane channel flow subjected to a uniform transverse magnetic field (Noguchi *et al.*, 1998). An illustration of the performance of the above model is provided in Fig. 7.25 arising from the high-Re flow of mercury in a rectangular channel subjected to a finite length transverse magnetic field. The results were obtained with the low Reynolds number $k-\varepsilon$ model of Launder and Sharma (1974) with the additional source terms from Eqs. (7.37) (in which just one additional

[24] The discussion is centred on modifications to the k–ε model because that seems to have been the model chosen for these adaptations. Equivalent modifications could be made to (and would also be needed for) the $k-\omega$ model.

[25] This symbol is unrelated to the Hall-Jackson symbol of the same form appearing in Fig. 7.24.

https://doi.org/10.1017/9781108875400.009 Published online by Cambridge University Press

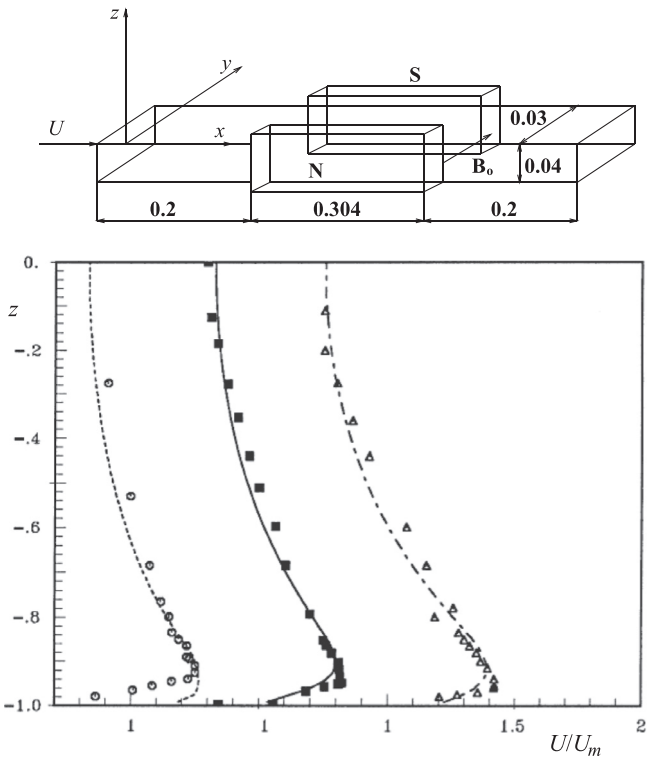

Fig. 7.25 Upper: a sketch of a mercury flow passing through a finite length magnetic field. Lower: velocity profiles at the magnet inlet ($x = 0.2$ m), half-way through ($x = 0.352$ m) and at the magnet outlet ($x = 0.504$ m). Lines: computations with the Launder and Sharma (1974) low-Re $k-\varepsilon$ model with magnetic source terms, Eq. (7.37). Symbols, measurements by Tananaev (from Branover, 1978). $\mathrm{Re} = 2\times10^5$, $\mathrm{Ha} = 700$, $N = 2.45$. From Kenjereš and Hanjalić (2000b).

model constant, c_{1M}, appears and with no magnetic damping of eddy viscosity). This form produced the characteristic M-shaped mean velocity profile (only the lower half of the profiles is shown) in satisfactory agreement with the available experimental data.

It is likely, however, that for more complex and variable magnetic fields, which, as discussed in §4.5.4, are known to exert a strong effect on the turbulent stress anisotropy, such a relatively simple EVM will be too crude to capture the interactions between the velocity and magnetic fields.

A further example of a modification of an EVM for forced convection is that made by Kato and Launder (1993). The problem of interest was the very complex coupling between the natural vibration frequency of a square-sectioned bridge beam pinned at its ends and the natural vortex shedding from the downstream edges of the beam due to the wind normal to the beam. Only a short time period was available for the study and, thus, modelling at a more complex level than a simple eddy

https://doi.org/10.1017/9781108875400.009 Published online by Cambridge University Press

viscosity could not be contemplated. However, it was known that EVMs generated excessive turbulence-energy levels near the front stagnation point due to the erroneous assumed relation between the stress and strain fields in what is close to an irrotational deformation. That would lead, in turn, to the suppression (or, at least, a strong damping) of the Karman vortex street on the downstream side of the bar. This natural vortex shedding was, however, central to the problem under study and had to be maintained. Accordingly, the energy-generation term that appears in both the k- and ε-equations was modified by introducing the vorticity to replace partially the strain rate. Thus, in place of $\mathcal{P}_k = 2c_\mu \varepsilon \mathrm{S}^2$ the form $\mathcal{P}'_k = 2c_\mu \varepsilon \mathrm{SW}$ was adopted, where S and W represent non-dimensional rates of strain and rotation introduced earlier, in §5.1.1.

Thus, in an irrotational deformation (such as occurs near the front stagnation point) the generation rate is zero, while in simple shear the same generation rate is returned as with the conventional EVM generation term. This modification does indeed avoid the very severe damping of the Karman vortex on the downstream side of the beam that would otherwise occur due to the excessive turbulent viscosity generated in the region of the front stagnation point. Although not suitable for general use, this simple device led to close agreement with experiments and has been applied by several other groups seeking to predict similar phenomena.

Several groups have added special-purpose source terms to the ε-equation to account for the effects of streamline curvature. Streamline curvature arises over such a wide variety of flows in such a range of forms, however, that one cannot expect that a source term devised for one class of curvature-modified flow will carry over, without modification, to some other class. The severity of the effect is greatest if the radius of curvature points in the direction of maximum mean velocity gradient. Thus, a substantial correction is needed to mimic the flow induced by a spinning cylinder (where the principal velocity gradients occur in the radial direction), while for a spinning disc (where the radius of curvature is parallel to the disc while the velocity gradient is normal to it) in principle no correction should be needed. An early attempt to provide a curvature correction by Launder *et al.* (1977) made the sink term in the ε-equation a function of the local curvature 'Richardson number':

$$\text{Sink of } \varepsilon = -c_{\varepsilon 2} \frac{\varepsilon^2}{k} \left[1 - c_c \mathrm{Ri}_c\right], \quad \mathrm{Ri}_c \equiv \frac{k^2}{\varepsilon^2} \frac{V_\theta \cos\alpha}{r^2} \frac{\partial (r V_\theta)}{\partial r} \tag{7.38}$$

where V_θ is the swirl velocity and α is the angle between the radius of curvature vector and the mean velocity gradient vector. This proposal led to satisfactory predictions for flow past cones, a spinning cylinder and for boundary layers on curved surfaces. However, as seen from the computations of the curved mixing layer by Rodi and Scheuerer (1983) in Fig. 7.5, this modification (which gave the predicted

https://doi.org/10.1017/9781108875400.009 Published online by Cambridge University Press

behaviour shown by the lowest curve in that figure) led to a much too slow recovery downstream from the effects of curvature in that flow.

From the above it may be concluded that if one needs to account accurately for streamline curvature in a flow significantly different from cases where such *ad hoc* curvature modifications have been successfully calibrated, upgrading the model to a NLEVM is a safer route to follow for modest additional cost.

7.4.4 Elliptic relaxation applied to EVMs

As shown in §7.4.1, application of the basic second-moment closure to an equilibrium near-wall flow leads, for the case of simple shear, to Eq. (7.26) for the shear stress, $\overline{u_1 u_2}$:

$$-\overline{u_1 u_2} = c'_\mu \frac{\overline{u_2^2}}{k} \frac{k^2}{\varepsilon} \frac{\partial U_1}{\partial x_2}.$$

This, in turn, suggests that the eddy viscosity should be defined as

$$\nu_t = c'_\mu \overline{u_2^2} k/\varepsilon \equiv c'_\mu \overline{u_2^2}/\mathcal{T} \tag{7.39}$$

and not as $\nu_t = c_\mu k^2/\varepsilon \equiv c_\mu k/\mathcal{T}$, as would be adopted by a conventional eddy-viscosity model. As remarked in §7.4.1, due to inviscid wall-blocking effects, close to a solid wall or a free surface, the wall-normal stress component, $\overline{u_2^2}$, is much smaller than k, and so c'_μ would need to be larger than c_μ to give the correct level of turbulent viscosity. In the semi-logarithmic region, which usually serves for calibrating some of the model coefficients, $\overline{u_2^2}/k$ is about 0.3–0.4. Indeed, the kinematic eddy viscosity evaluated from $\nu_t = -\overline{u_1 u_2}/(\partial U_1/\partial x_2)$ using the DNS data for a plane channel (or equally the earlier experimental data appearing in Fig. 6.11) shows a very close similarity with that obtained from Eq. (7.39) across the whole wall layer except very close to the wall, deep within the viscous sublayer ($x_2^+ < 5$), Fig. 6.11. Thus, the use of Eq. (7.39) largely removes the need for the damping function, f_μ. However, the problem is that two-equation eddy-viscosity models do not provide the wall-normal turbulent stress component, $\overline{u_2^2}$, which is a vital element of Eq. (7.39). An option would be to solve a modelled transport equation for $\overline{u_2^2}$ from a second-moment closure in addition to k and ε; but such an approach would be mathematically inconsistent and not coordinate-frame invariant since $\overline{u_2^2}$ is just one component of a second-rank stress tensor, $\overline{u_i u_j}$.

The $\overline{v^2} - f$ Model

By noting that in the wall layer of attached, near-equilibrium flows the production of the wall-normal stress component, $\mathcal{P}_{22}$, is nearly zero and that the other terms in the stress-transport Eq. (6.60) involve only $\overline{u_2^2}$, k and ε, Durbin (1991)

https://doi.org/10.1017/9781108875400.009 Published online by Cambridge University Press

proposed a surrogate scalar transport equation for a quantity he termed $\overline{v^2}$ derived from Eqs. (6.60) and (6.61). Thus, in addition to the k- and ε-equations, elements of the elliptic relaxation model, Eqs. (6.62) to (6.65), are introduced but for a single *scalar* function f ($f \equiv f_{22}$). In a turbulent wall boundary layer $\overline{v^2}$ is indeed the wall-normal stress component, $\overline{u_2^2}$; but its role in an elliptic-relaxation EVM is to provide an additional velocity scale that characterizes the turbulent transport as implied by Eq. (7.39). The k-equation takes the standard form, while Eq. (6.73) is applied to obtain ε, except that $\overline{v^2}$ appears in the model for turbulent viscosity in both equations (and, of course, in the momentum equations). The complete model can be summarized by the following equation set (in addition to Eq. (7.39) and including also Durbin's realizability constraint (7.35) implemented in the definitions of the time and length scales, Eq. (6.74)):

$$\frac{Dk}{Dt} = \mathcal{P}_k - \varepsilon + \frac{\partial}{\partial x_k}\left[(\nu + \nu_t)\frac{\partial k}{\partial x_k}\right] \tag{7.40}$$

$$\frac{D\varepsilon}{Dt} = \frac{c_{\varepsilon 1}\mathcal{P}_k - c_{\varepsilon 2}\varepsilon}{\mathcal{T}} + \frac{\partial}{\partial x_k}\left[\left(\nu + \frac{\nu_t}{\sigma_\varepsilon}\right)\frac{\partial \varepsilon}{\partial x_k}\right] \tag{7.41}$$

$$\frac{D\overline{v^2}}{Dt} = kf - \frac{\overline{v^2}}{k}\varepsilon + \frac{\partial}{\partial x_k}\left[(\nu + \nu_t)\frac{\partial \overline{v^2}}{\partial x_k}\right] \tag{7.42}$$

$$f - L^2\frac{\partial^2 f}{\partial x_k^2} = (c_1 - 1)\frac{\left(2/3 - \overline{v^2}/k\right)}{\mathcal{T}} + c_2\frac{\mathcal{P}_k}{k} \tag{7.43}$$

$$\mathcal{T} = \max\left[\min\left(\frac{k}{\varepsilon}, \frac{ak}{\overline{v^2}c_\mu\sqrt{6S_{ij}S_{ij}}}\right), c_\mathcal{T}\left(\frac{\nu}{\varepsilon}\right)^{1/2}\right] \tag{7.44}$$

$$L = c_L \max\left[\min\left(\frac{k^{3/2}}{\varepsilon}, \frac{k^{3/2}}{\overline{v^2}c_\mu\sqrt{6S_{ij}S_{ij}}}\right), c_\eta\left(\frac{\nu^3}{\varepsilon}\right)^{1/4}\right]. \tag{7.45}$$

In the above, a is the symbol that appeared in Eq. (7.35) with the proposed value of 0.6. It is noted that coefficients c_1 and c_2 originate from the linear pressure-strain model (the former coming from Rotta's return-to-isotropy model, Eq. (4.7), and the latter being the coefficient γ in Eq. (4.48)). Originally, Durbin used the values from the LRR (QI) model (1.5 and 0.4, respectively) but subsequently settled for $c_1 = 1.4$ and $c_2 = 0.3$ with $c_{\varepsilon 1} = 1.4[1 + 0.045\sqrt{k/\overline{v^2}}]$. The coefficients in the expressions for the time and length scales, (7.44) and (7.45), take values $c_\mathcal{T} = 6$, $c_L = 0.17$ and $c_\eta = 80$, which are slightly different from those in the second-moment-closure version (§6.5).

The equation set (7.39)–(7.45) is designed to be integrated up to the wall, using the exact boundary conditions for k and $\overline{v^2}$ (both equal to zero) and $\varepsilon_w = 2\nu k/y^2$

https://doi.org/10.1017/9781108875400.009 Published online by Cambridge University Press

at the wall-adjacent node, while the wall value of f, i.e. f_w, is determined from the wall-limiting balance of the terms in the $\overline{v^2}$ equation:

$$\left.\frac{D\overline{v^2}}{Dt}\right|_{y\to 0} = 0 = \underbrace{kf}_{\propto y^2} - \underbrace{\frac{\overline{v^2}}{k}}_{\propto y^2}\varepsilon + \underbrace{\frac{\partial}{\partial y}\left(\nu_{eff}\frac{\partial \overline{v^2}}{\partial y}\right)}_{\propto y^2} \tag{7.46}$$

which results in

$$f_w = \frac{-20\nu^2\overline{v^2}}{\varepsilon y^4}. \tag{7.47}$$

Successful predictions of a range of flows have been reported by Durbin (1991, 1995), Behnia *et al.* (1998) and Medić and Durbin (2002) among others.

However, the wall boundary condition for f, Eq. (7.47), may cause computational instability as the equation is sensitive to the near-wall grid clustering: a small imbalance between the numerator and denominator (both varying as y^4 since, in the wall limit, $\overline{v^2} \propto y^4$). Thus, contrary to most other WIN models, the original $\overline{v^2} - f$ model does not tolerate very small wall-normal dimensions of the wall-adjacent grid cell. The problem can be avoided by solving the $\overline{v^2}$ and f equations, (7.42) and (7.43), simultaneously; but most CFD codes use the more convenient segregated-solver approach. Alternative formulations of the $\overline{v^2}$- and f-equations have been proposed which enable one to set $f_w = 0$ (e.g. Lien *et al.*, 1998), but these perform less satisfactorily than the original model and require some re-tuning of the coefficients. An alternative strategy is to derive an equation for some product of $\overline{v^2}$ and k that has more convenient wall boundary conditions. Such approaches are considered below.

The $\overline{v^2}/k - f$ Models

An improvement in the computational robustness can be achieved by solving a transport equation for the ratio $\zeta = \overline{v^2}/k$ instead of $\overline{v^2}$ as proposed by Hanjalić *et al.* (2004a) and, independently, by Laurence *et al.* (2004). The ζ-equation can be derived directly from the $\overline{v^2}$ and k-equations, but unavoidably an extra 'cross-diffusion' term, X, appears.[26] Hanjalic et al. neglected that term (compensating for its omission by a slight adjustment of some of the coefficients) so that the equation

[26] The extra diffusion term X originating from the direct derivation of the ζ -equation from the k and $\overline{v^2}$ equations

$$X = \frac{2}{k}\left(\nu + \frac{\nu_t}{\sigma_\zeta}\right)\frac{\partial \zeta}{\partial x_k}\frac{\partial k}{\partial x_k}$$

is generally insignificant, though close to a wall it may exert some influence.

https://doi.org/10.1017/9781108875400.009 Published online by Cambridge University Press

Table 7.5 *Summary of coefficients in the $\zeta - f$ model*

c'_μ	$c_{\varepsilon 1}$	c_1	$c_{\varepsilon 2}$	c_5^*	σ_k	σ_ε	σ_ζ	$c_{\mathcal{T}}$	c_L	c_η
0.22	$1.4(1 + 0.012/\zeta)$	1.4	1.9	0.65	1.0	1.3	1.2	6.0	0.36	85

retains the simple source−sink diffusion form.[27] Another novelty is the application of the quasi-linear pressure-strain model in the f-equation, based on the SSG formulation of Speziale *et al.* (1991), which brings additional improvements for non-equilibrium wall flows.

After some simplification, the model equations for ζ and f (thus termed the $\zeta - f$ *model*) are:[28]

$$\frac{D\zeta}{Dt} = f - \frac{\zeta}{k}\mathcal{P}_k + \frac{\partial}{\partial x_k}\left[\left(\nu + \frac{\nu_t}{\sigma_\zeta}\right)\frac{\partial \zeta}{\partial x_k}\right] \tag{7.48}$$

$$f - L^2\frac{\partial^2 f}{\partial x_k^2} = \left(c_1 - 1 + c_5^*\frac{\mathcal{P}_k}{\varepsilon}\right)\frac{(2/3 - \zeta)}{\mathcal{T}} \tag{7.49}$$

where $c_5^* = 0.65$ (compared with the value 0.45 in the SSG model, Eq. (4.54)). Some further minor adjustments to other coefficients were also made, the full set of coefficients being given in Table 7.5.

From the computational point of view, the ζ–f model offers two advantages compared with the original $\overline{v^2} - f$ model:

- Instead of ε appearing in the $\overline{v^2}$-equation, which is difficult to model correctly very close to a wall, the ζ-equation contains the kinetic energy production $\mathcal{P}_k$ (this replacement comes directly from the derivation of the ζ-equation). This is much easier to reproduce accurately if the local turbulent stress and, hence, the mean velocity gradient are captured properly – which is the main goal of all models.
- Because $\zeta \propto y^2$ as $y \to 0$, the wall boundary condition for ζ (deduced from the limiting form of the ζ budget, Eq. (7.48)) reduces to a balance of only two terms,[29] the elliptic-relaxation function, f, and the viscous diffusion $\mathcal{D}_\zeta^\nu$, both with finite values at the wall. In comparison, $\mathcal{P}_k\zeta/k$ is negligible as it varies as y^3 (indeed, as y^4 if an eddy viscosity is used),

[27] While adopting the same variable, Laurence *et al.* (2004) follow somewhat different arguments and keep the form of the $\overline{v^2}/k$ equation (in their article denoted as φ) in the form directly derived from the k and $\overline{v^2}$ equations, thus retaining the cross-diffusion term, X.

[28] The application of the SSG model, Eq. (4.54), results in an additional source term in the f-equation $(c_2^*/3 - c_3^*)\mathcal{P}_k/k \approx 0.008\mathcal{P}_k/k$, which can be neglected.

[29] Provided the extra term X is neglected.

https://doi.org/10.1017/9781108875400.009 Published online by Cambridge University Press

$$\left.\frac{D\zeta}{Dt}\right|_{y\to 0} = 0 = \underbrace{f}_{\propto y^0} - \underbrace{\frac{\zeta}{k}\mathcal{P}_k}_{\propto y^3} + \underbrace{\frac{\partial}{\partial y}\left(\nu_{eff}\frac{\partial \zeta}{\partial y}\right)}_{\propto y^0}. \tag{7.50}$$

Thus, the wall boundary condition for f becomes:

$$f_w = \frac{-2\nu\zeta}{y^2}. \tag{7.51}$$

The fact that both the numerator and the denominator of f_w are proportional to y^2 (instead of y^4 in the original $\overline{v^2} - f$ model, and with $y = 0$ being a singular point in both cases) improves the stability of the computational scheme even in a segregated solver.

It is noted that Eq. (7.51) is identical in form to ε_w, Eq. (6.10) (apart from the opposite sign), and can thus be treated jointly in the computational procedure. Alternatively, by analogy with the Jones-Launder (1972a) model for the 'quasi-homogeneous' dissipation rate $\tilde{\varepsilon}$ (see Eq. (6.12)), one can solve (7.49) for a variable $\tilde{f}$, which conveniently goes to zero at a solid wall or surface interface, i.e. $\tilde{f}_w = 0$. Then one can evaluate f (for use in the ζ-equation) from

$$f = \tilde{f} - \frac{2\nu\zeta}{y^2}. \tag{7.52}$$

Illustrations of the performance of both the $\zeta - f$ model and the original $\overline{v^2} - f$ model are provided in Fig. 7.26, which shows predictions of heat transfer in a round impinging jet issuing from a fully developed pipe flow, and in a pipe expansion. Both models, as expected, show similar performance, though the $\zeta - f$ model reproduces the trough in Nusselt number in the impinging jet, Fig. 7.26a, slightly better. The main advantage, however, is the improved computational stability and faster convergence. More details can be found in Hanjalić *et al.* (2004a) and Tatschl *et al.* (2006).

Subsequently, elliptic-relaxation-based linear EVMs, both in the original $\overline{v^2} - f$ and $\overline{v^2}/k - f$ formulations, were extended to non-linear versions (e.g. Pettersson Reif, 2006) and applied to buoyancy-driven flows (e.g. Kenjereš *et al.*, 2005).

7.4.5 *Hybrid blending of DSM and EVM schemes for numerical stability*

It is common numerical practice, in applying high-level CFD to elliptic and three-dimensional flows, to employ a simple linear EVM during the initial stages of iteration and then to switch over to a physically better founded turbulence model when the residuals have dropped sufficiently. This practice is designed to cope with the fact that higher order models are numerically less stable than a purely diffusive stress–strain linkage, especially during the early stages when the system of equations is very far from converged. Basara and Jakirlić (2003) have, however, proposed an interesting variant on this strategy, in which DSM and EVM

https://doi.org/10.1017/9781108875400.009 Published online by Cambridge University Press

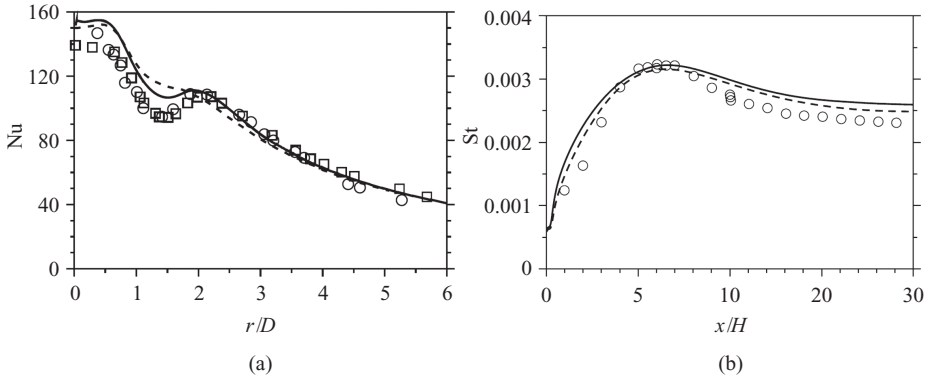

Fig. 7.26 (a) Nusselt number along the wall beneath an impinging jet (Re $=$ 23, 000, $h/D = 2$); symbols, experiments of Baughn and Shimizu (1989) and Baughn *et al.* (1991). (b) Stanton number downstream from a backward-facing step (Re $=$ 28, 000 based on step height and free-stream velocity at step); symbols, experiments (Vogel and Eaton, 1985). Full line $\zeta - f$ model; dotted line $\overline{v^2} - f$ model. From Hanjalić *et al.* (2004a).

approaches are *blended together from the outset* in such a way that the scheme largely retains the stability of eddy-viscosity models but with an enhanced model performance more reminiscent of DSM schemes.

The procedure is as follows. First one solves for all the stress components with the chosen DSM model but uses the output from this step simply to compute the turbulence energy, k, (obtained as half the sum of the normal stresses) and its generation rate, $\mathcal{P}k$. The stresses that are applied in the momentum equations are then found from a linear eddy-viscosity approach that indirectly employs information from the stress transport equations. Thus, in terms of a $k-\varepsilon$ model:

$$\overline{u_i u_j} - \frac{2}{3}\delta_{ij}k = -2\nu_t S_{ij} \quad \text{where } \nu_t = c_\mu k^2/\varepsilon.$$

Unlike a conventional EVM, however, the quantity c_μ is now a variable to be computed at each point in the solution domain from:

$$c_\mu = \mathcal{P}_k/(k^2 S^2/\varepsilon), \quad S \equiv \sqrt{2S_{ij}S_{ij}}.$$

It is readily shown that this choice amounts to minimizing the sum of the mean-square differences between the values of the stresses computed from the eddy-viscosity formula and those obtained from the stress-transport equation. For one then seeks the value of c_μ for which $[\overline{u_i u_j} - 2/3\delta_{ij}k + 2c_\mu k^2 S_{ij}/\varepsilon]^2$ is a minimum. On differentiating this with respect to c_μ and setting the result to zero, the above expression for c_μ is obtained.

On the face of it, it would seem that this strategy entails doing all the work associated with a DSM without benefiting from using the computed stresses (obtained

https://doi.org/10.1017/9781108875400.009 Published online by Cambridge University Press

from their individual transport equations) where they could be most effective – i.e. in the momentum equations. However, Basara and Jakirlić (2003) have reported the application of this approach to a range of flows involving significant streamline curvature that produces poor agreement when used with a conventional linear EVM (including stagnation flow, flow around a U-bend and swirling pipe flow). In all cases the predictions with the hybrid scheme outlined above were only marginally inferior to those obtained with the SSG second-moment closure, both approaches displaying generally satisfactory agreement with the experiments.

7.4.6 One-equation EVMs based on a transport equation for ν_t

The idea of providing the eddy viscosity directly from a transport equation for this term emerged at an early stage in the development of RANS closures (Nee and Kovasznay, 1969). It was perhaps felt that, by determining the quantity that an EVM needed directly from its own transport equation, the scheme would be more generally applicable than, say, a one-equation scheme based on the k transport equation. Several proposals for such one-equation models have subsequently been proposed, whether derived empirically or from the modelled k and ε (or ω) equations using the eddy-viscosity definition $\nu_t = c_\mu k^2/\varepsilon$. A more rigorous route may also be considered starting from $D\nu_t/Dt = -D(\overline{u_i u_j} S_{ij}/2S^2)$, but the resultant equation is complex and has not led to a usable form of model. Currently, the model of Spalart and Allmaras (1992), developed primarily for boundary layers in external aerodynamics, has gained substantial popularity among the aeronautics community. The model is highly empirical, however, with a number of functions lacking a transparent physical basis. Thus, like any other one-equation EVM, it has serious limitations in flows other than those for which it was specifically tuned. It is thus our view that if one seeks to compute other than a limited range of attached boundary layers (for which the model has a very good track record), it is preferable to confine the use of one-equation approaches to cover just the near-wall region. This is what is done in the next section. Alternatively, the use of the model should at least be limited to the attached region of a turbulent flow if one adopts the hybrid RANS-LES strategy, DES, considered in Chapter 10.

7.4.7 Prescribed length-scale schemes for the near-wall sublayer

While, as noted above, algebraic and one-equation eddy-viscosity models *are* still used in a few particular areas to cover the whole shear flow to be computed (see also the textbooks by Cebeci, 1999 and Wilcox, 2000), the role considered here is their employment as models to cover simply the near-wall sublayer. The superficially illogical rationale for adopting a simpler closure right in the region where the turbulence interactions are the most complex arises from two directions of thought.

https://doi.org/10.1017/9781108875400.009 Published online by Cambridge University Press

First, this is a region where convective transport is often negligible, where the flow is essentially in simple shear and where, over the years, a lot has been learned empirically about using such simple models to capture the essentials of the flow. Second, there are considerable computer savings to be gained from such a simplification – at least 60% and probably more if one would otherwise adopt the $k-\varepsilon$ EVM, not to mention savings in user-diagnosis time. There are certainly situations where the approach is not appropriate – transition from laminar to turbulent flow triggered by external turbulence is one – but at this level of modelling no one is claiming universality.

Two levels of modelling are examined. One-equation EVMs, in which a transport equation is provided for the turbulent kinetic energy; while determining the near-wall energy dissipation rate and turbulent viscosity by way of a prescribed length scale:

$$\varepsilon = k^{3/2}/l, \quad \nu_t = c_\mu k^{1/2} l. \tag{7.53}$$

A further level of simplification leads to the mixing-length hypothesis (Taylor, 1915; Prandtl, 1925), a zero-equation model. The form follows directly from manipulating the turbulent kinetic energy equation as follows. Using the above prescribed-length-scale form for the turbulent viscosity, the turbulence energy equation in local equilibrium (i.e. zero transport) is just:

$$c_\mu k^{1/2} l \left[\frac{\partial U_i}{\partial x_j} \left(\frac{\partial U_i}{\partial x_j} + \frac{\partial U_j}{\partial x_i} \right) \right] = \frac{k^{3/2}}{l}. \tag{7.54}$$

If now the turbulent kinetic energy is eliminated from Eq. (7.54) by using the turbulent viscosity formula, it becomes

$$c_\mu l^2 \left[\frac{\partial U_i}{\partial x_j} \left(\frac{\partial U_i}{\partial x_j} + \frac{\partial U_j}{\partial x_i} \right) \right] = \frac{\nu_t^2}{c_\mu^2 l^2}$$

or, finally, on taking the square root of each side and rearranging:

$$\nu_t = l_m^2 \left[\frac{\partial U_i}{\partial x_j} \left(\frac{\partial U_i}{\partial x_j} + \frac{\partial U_j}{\partial x_i} \right) \right]^{1/2} \tag{7.55}$$

where $l_m \equiv c_\mu^{3/4} l$, the mixing length, is to be prescribed. In fact, both G. I. Taylor and L. Prandtl arrived at their results not from a local-equilibrium analysis but by considering the momentum transfer associated with the displacement of a small fluid package in a simple shear flow by a distance proportional to l_m in the direction of the mean velocity gradient. Taylor (1932) later argued that rather than momentum it was more appropriate that vorticity should be considered as the transported fluid property. It is arguably for that reason that Eq. (7.55) is nowadays known as Prandtl's mixing-length hypothesis (MLH). An assumed mixing length increasing linearly with wall distance or a uniform value proportional to the width of a free

shear flow enabled Prandtl and his students to compute a number of simple flows. Their proposals did not extend up to the wall itself, however. For the viscosity-affected sublayer, the van Driest (1956) proposal is the most commonly adopted formula for the near-wall variation of l_m. This arose from the recognition that the linear variation of l_m in the fully turbulent region had to be further damped as one approached the wall and the turbulence Reynolds number decreased (a quantity which, at the algebraic level of modelling adopted by the MLH, was taken proportional to y^+):

$$l_m = \kappa y \left[1 - \exp(-y^+/A^+)\right]. \tag{7.56}$$

Van Driest proposed that the coefficient A^+ should take the constant value, 26. In many (but by no means all) cases the velocity vector over the sublayer region where the MLH is to be employed can be treated as unidirectional and then Eq. (7.55) reduces to the form originally proposed by Prandtl (1925):

$$\nu_t = l_m^2 \left| \frac{\partial U}{\partial y} \right|. \tag{7.57}$$

However, the more general form of the sublayer model, Eq. (7.55), was used to compute the flow around the 90° bend shown in Fig. 7.23, because of the strong skewing of the velocity vector across the sublayer that occurred in that case. As noted in §4.4.3, the use of the MLH across the near-wall sublayer made a low-Re treatment feasible (at a time when a low-Re $k-\varepsilon$ model was simply too costly to use in this three-dimensional elliptic flow) and achieved very satisfactory accord with experiment.

By the late 1960s, several groups had found that the form proposed by van Driest (used within two-dimensional boundary-layer solvers) did not adequately mimic the effects of strong streamwise pressure gradients or wall mass transfer discussed in Chapter 6. Thus, attention was turned to altering A^+ from the constant value of 26 to a functional form that depended on dimensionless acceleration or wall mass-transfer parameters (e.g. Launder and Jones, 1969; Cebeci and Mosinskis, 1971; Kays and Moffat, 1975). The most widely tested form of such proposals, at least from the standpoint of forced convection heat transfer, is probably that in the textbook by Kays *et al.* (2004). They suggest a two-step correction: first the equilibrium value of A^+ is obtained from

$$A^+_{eq} = 25/(\tau_{ref}/\tau_w)^{1/2} \tag{7.58}$$

where τ_{ref} is the shear stress evaluated at $y^+ = 3A^+_{eq}$. Then, because of the lag between the actual value of A^+ and its equilibrium value, the current value of A^+ itself is determined from:

$$dA^+/dx^+ = C(A^+_{eq} - A^+) \tag{7.59}$$

https://doi.org/10.1017/9781108875400.009 Published online by Cambridge University Press

where, the authors remark, '*a value of* $C = 2.5 \times 10^{-4}$ *has frequently been used*'. This proposal does not seem to have been adopted as a sublayer model in conjunction with a more elaborate treatment for the fully turbulent part of the flow but, in view of the extensive empirical calibration, such a combination should be both successful and economical.

The principal reason that mixing-length schemes are not used to resolve the wall sublayer region in most CFD codes is that the MLH does not cope well in separated flows where mean-velocity gradients are low but turbulence levels are high. Then, the one-equation approach has more commonly been adopted in which a transport equation is solved for k. A popular route has been to adopt the proposals of Wolfshtein (1969). In this scheme the length scale variation is prescribed for the two roles indicated in Eq. (7.53), i.e. to determine, from knowledge of the turbulence energy, the energy dissipation rate and the turbulent viscosity. While the length scale appearing in the two parts of Eq. (7.53) is the same in the fully turbulent region, as the turbulent Reynolds number becomes low it is damped at different rates in its two roles:

$$l_\varepsilon = c_l y(1 - \exp[-y^*/A_\varepsilon^*]), \quad l_\nu = c_l y(1 - \exp[-y^*/A_l^*]) \tag{7.60}$$

where $y^* \equiv yk^{1/2}/\nu$, $A_\varepsilon^* = 3.8$, $A_l^* = 62.5$.

The greatly different values for the two exponential damping coefficients above mean that the dissipation length scale reaches its linear, high Reynolds number form much faster than the viscous length scale (which is also having to account for the non-viscous damping of $\overline{v^2}$). This one-equation near-wall strategy has been applied in several studies, including that of Iacovides and Raisee (1999) predicting flow through a rib-roughened channel and that of Yap (1987) for heat transfer downstream of a backward-facing step. Both these explorations led to the conclusion that the above choice of coefficients, calibrated for flat plate conditions, underestimates heat transfer coefficients by typically 30% in separated-flow regions. It would appear that the above damping coefficients depend (just as does the MLH) on the way the shear stress varies across this low-Re sublayer, i.e. that some correction of the same type as (though possibly weaker than) that recommended in Kays *et al.* (2004) for determining A^+ should really be added. While this approach does not appear to have been used with one-equation EVMs, the concept has been successfully imported into one of the newer, even more economical 'wall-function' schemes discussed in Chapter 8.

https://doi.org/10.1017/9781108875400.009 Published online by Cambridge University Press

8

Wall functions

8.1 Early proposals

The term *wall functions* was first applied by Patankar and Spalding (1967) as the collective name for the set of algebraic relations linking the values of the effective wall-normal gradients of dependent variables between the wall and the wall-adjacent node (in a numerical solver) to the shear stress, heat or mass flux at the wall.

The underlying purpose of wall functions, as originally proposed, was to allow computations to escape the need to model the very complex flow dynamics associated with the low-Re region that formed the subject of Chapter 6. It may seem absurd that in the region which, from a physical point of view, contains the most complex viscous and turbulent interactions, one resorts to algebraic rather than differential relations to resolve the flow. We note, however, that in Chapter 7 the ability of very simple eddy-viscosity models of turbulence to handle the sublayer has been demonstrated. Wall functions may be seen simply as an extrapolation of that simplification strategy, i.e. an even cheaper approach to capturing the essentials of the viscosity-affected layer, by exploiting the fact that gradients of dependent variables normal to the wall are dominant and that transport effects are relatively uninfluential. The present chapter first summarizes conventional wall functions and then introduces four more powerful approaches that the authors and their colleagues have developed more recently.

The link between near-wall values of a variable and the associated wall fluxes is often the primary connection one needs to establish. However, even if one is not immediately interested in wall fluxes, they often need to be evaluated to serve as boundary conditions. In the limiting case, when the computational grid is fine enough for the first node to lie within the viscous sublayer, where the velocity, temperature, etc. vary linearly with the wall distance, one can use the exact laminar-flow boundary conditions with the molecular transport properties. In that case, if

https://doi.org/10.1017/9781108875400.010 Published online by Cambridge University Press

the wall values of velocity and temperature are prescribed, the wall fluxes can be computed explicitly from the wall gradients of velocity and temperature evaluated simply from the difference between the values at the wall and the first node. Alternatively, if the wall flux is known, as is often the case in heat transfer, one can use that to evaluate the wall temperature from the temperature at the near-wall node. However, when the grid is too coarse to resolve properly the viscous/molecular sublayer – as is usually the case in industrial computations – an alternative strategy is needed. Either the mean velocity and scalar gradients between the wall and the near-wall node are multiplied by the effective *averaged* value of diffusivity or some other equivalent prescription is provided to determine the wall fluxes. In either case, the appropriate connections are provided by what are known as *wall functions*.

The best known and still widely used wall function for the momentum equation is more commonly known as the *law of the wall*. If it is supposed that, close to a wall, in a slowly developing, two-dimensional turbulent flow, the mean velocity U at a point is a function only of the height y above the wall, the local wall shear stress τ_w and the fluid properties ρ and ν, one can express the velocity in dimensionless form as:

$$\frac{U}{U_\tau} = f\left(\frac{yU_\tau}{\nu}\right) \quad \text{or} \quad U^+ = f(y^+) \tag{8.1}$$

where $U_\tau \equiv \sqrt{\tau_w/\rho}$ is the already introduced friction velocity. This and the viscous length, ν/U_τ, provide what Eq. (8.1) implies are *universal* inner velocity and length scales, respectively. The above form, which developed from a series of experiments in Germany in the 1930s, led Coles (1956), following an exhaustive re-analysis of the then available data, to comment: 'The relationship [(8.1)] is taken for practical purposes as a unique and universal similarity law for every turbulent flow past a smooth surface.'

Deep in the viscous sublayer this relation simply expresses the linear connection between velocity and distance from the wall: $U^+ = y^+$. Of more practical interest is the form that Eq. (8.1) takes in the region close enough to the wall for the equation still to be valid but far enough from it for direct viscous effects to be negligible. Several arguments have been advanced that in these circumstances the velocity should increase as the logarithm of wall distance:

$$U^+ = \frac{1}{\kappa}\ln y^+ + B \quad \text{or} \quad U^+ = \frac{1}{\kappa}\ln Ey^+ \tag{8.2}$$

where $\kappa \approx 0.41$ is the von Karman constant, $E \approx 8.4$ and $B = (1/\kappa)\ln E \approx 5.1$.

Indeed, as Coles (1956) had so emphatically shown, many flows measured in the laboratory (or resolved by DNS), such as two-dimensional boundary layers in weak streamwise pressure gradients and duct flows, do accord closely with this form; some illustrations are provided in Fig. 8.1. However, most of the flows that,

https://doi.org/10.1017/9781108875400.010 Published online by Cambridge University Press

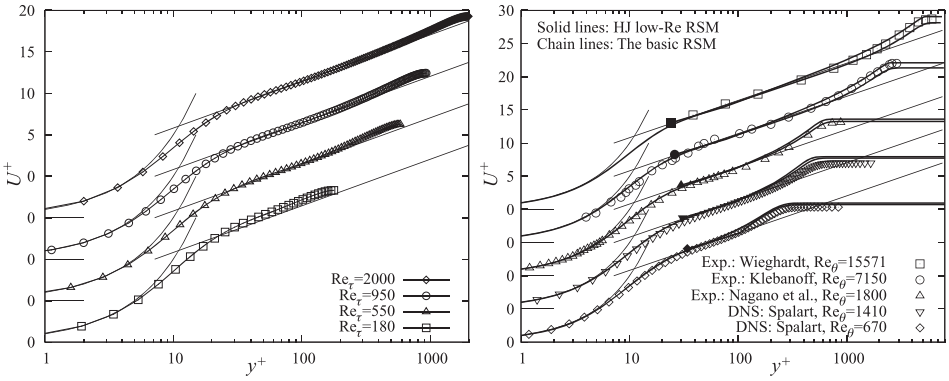

Fig. 8.1 Semi-logarithmic velocity distribution for various Reynolds numbers. Left: DNS of a fully developed plane channel (Hoyas and Jimenez, 2006). Right: experiments and DNS data for constant-pressure boundary layers. Solid lines show the variation of $U^+ = y^+$ and Eq. (8.2).

practically, one wishes to compute are not of such relatively simple form and, for these, Coles' declaration cited above is manifestly incorrect.

The limitations of Eq. (8.2) are shared by the corresponding formula for the temperature variation:

$$\Theta^+ \equiv \frac{\rho c_p \sqrt{\tau_w/\rho}(\Theta - \Theta_w)}{q''_w} = \frac{1}{\tilde{\kappa}} \ln y^+ + \tilde{B} \equiv \frac{1}{\tilde{\kappa}} \ln \tilde{E}\, y^+ \tag{8.3}$$

where $\tilde{\kappa}$ stands for the thermal von Karman constant (usually taken to be 0.38), and the quantity $\tilde{E}$ depends on the molecular Prandtl number of the fluid, Pr. Alternatively, by eliminating y^+ with the help of Eq. (8.2), the following widely used form of equation for Θ^+ is obtained:

$$\Theta^+ = \frac{\kappa}{\tilde{\kappa}} \left[U^+ + \frac{1}{\kappa} \ln \frac{\tilde{E}}{E} \right] \equiv \sigma_\Theta [U^+ + J]. \tag{8.4}$$

In the above equations, q''_w is the heat flux to the wall (i.e. heat transfer rate per unit surface area) from the fluid and σ_Θ is the turbulent Prandtl number for heat transport. The quantity J (often termed the Jayatilleke function) depends on the ratio of the molecular to turbulent Prandtl numbers and can be determined from experimental data (Jayatilleke, 1969) or from analysis, assuming a distribution of turbulent viscosity and Prandtl number over the viscous region. A particularly simple analytical form proposed by Spalding (1967) has been widely used:

$$J = 9.24 \left\{ \left(\frac{\mathrm{Pr}}{\sigma_\Theta} \right)^{3/4} - \left(\frac{\mathrm{Pr}}{\sigma_\Theta} \right)^{1/4} \right\} \tag{8.5}$$

https://doi.org/10.1017/9781108875400.010 Published online by Cambridge University Press

but other somewhat different forms are also found in the literature.[1] The function J provides a measure of the relative 'resistances' of the sublayer to heat and momentum transport. When Pr is less than σ_Θ, J is evidently negative.

Suppose that the heat flux, q''_w, is the quantity one wishes to find from a numerical solution of the flow and thermal energy equations. If the semi-logarithmic velocity and temperature profiles are assumed to apply in the fully turbulent near-wall region, there would be no need to adopt the highly compressed and expensive gridding required to extend the numerical calculations right down to the wall where the molecular-conduction boundary condition applies. One could employ a relatively coarse near-wall mesh with the near-wall node located in the turbulent regime; then, one simply rearranges Eq. (8.4) to obtain the heat transfer rate in terms of the distance of the wall-adjacent node, y_P, and the temperature, Θ_P:

$$q''_w = \frac{\tilde{\kappa}\,\rho c_p \sqrt{\tau_w/\rho}\,[\Theta_\mathrm{P} - \Theta_w]}{\ln\,\tilde{E} y^+_\mathrm{P}}. \tag{8.6}$$

While Eq. (8.6) has been used successfully to compute heat transfer rates in many attached flows, a disastrous weakness of this approach is that if the wall shear stress should fall to zero, so also does the wall heat transfer rate. It is, in fact, commonly the case that heat transfer coefficients are close to a *maximum* at stagnation points; so *then* the equation gives patently absurd results!

An important step towards improving this situation was proposed by Spalding (see Launder and Spalding, 1974). He recognized that while the friction velocity, $\sqrt{\tau_w/\rho}$, provided a satisfactory proxy for the turbulent velocity scale in local equilibrium, in far-from-equilibrium situations (where there was no longer that close connection between turbulent velocities and wall friction) it was necessary to employ a velocity scale directly related to the turbulence itself. The chosen scale was the square root of turbulence energy, $k^{1/2}$. Now, in local equilibrium, $\sqrt{\tau_w/\rho} = c_\mu^{1/4} k^{1/2}$. Moreover, in Eq. (8.2), the wall stress implicitly appears in two roles: as the proxy for k, just noted, and as a measure of mean strain rate; in this latter role the friction velocity needs to be retained. The law of the wall for velocity and temperature is thus reorganized as:[2]

[1] Jayatilleke (1969) proposed originally.

$$J = 9.0\left[\left(\frac{\mathrm{Pr}}{\sigma_\Theta}\right)^{3/4} - 1\right]\left[1 + 0.28\,\exp\left(-0.007\frac{\mathrm{Pr}}{\sigma_\Theta}\right)\right].$$

[2] In the literature, $c_\mu^{1/4}$ is sometimes absorbed into y^* rather than into E, i.e. $y^* = c_\mu^{1/4} k^{1/2} y/\nu \equiv (c_\mu^{1/4} k^{1/2}/U_\tau) y^+$, in which case Eqs. (8.7) and (8.8) would contain E and $\tilde{E}$ instead of E^* and $\tilde{E}^*$.

https://doi.org/10.1017/9781108875400.010 Published online by Cambridge University Press

$$U^* \equiv \frac{Uk^{1/2}}{(\tau_w/\rho)} = \frac{1}{c_\mu^{1/4}\kappa} \ln\left(\frac{E\, c_\mu^{1/4} k^{1/2} y}{\nu}\right) = \frac{1}{\kappa^*} \ln\, E^* y^* \tag{8.7}$$

$$\Theta^* \equiv \frac{(\Theta - \Theta_w)\, \rho c_p k^{1/2}}{q_w''} = \frac{1}{c_\mu^{1/4}\tilde{\kappa}} \ln\left(\frac{\tilde{E} c_\mu^{1/4} k^{1/2} y}{\nu}\right) = \frac{1}{\tilde{\kappa}^*} \ln \tilde{E}^* y^* \tag{8.8}$$

where $\kappa^* \equiv \kappa c_\mu^{1/4}$, $\tilde{\kappa}^* \equiv \tilde{\kappa} c_\mu^{1/4}$, $E^* \equiv E\, c_\mu^{1/4}$, $\tilde{E}^* \equiv \tilde{\kappa} c_\mu^{1/4}$ and $y^* \equiv k^{1/2} y/\nu = (k^{1/2}/U_\tau) y^+$.

If now Eq. (8.8) is rearranged, the following formula for heat flux is obtained from the temperature at the near-wall node, y_P:

$$q_w'' = \frac{\tilde{\kappa}^* \rho c_p k_\mathsf{P}^{1/2} [\Theta_\mathsf{P} - \Theta_w]}{\ln \tilde{E}^* y_\mathsf{P}^*}. \tag{8.9}$$

The change from Eq. (8.6) to (8.9) has a very great effect on computed Nusselt numbers in impinging flows. Now, instead of returning zero values at impingement or reattachment points, since the near-wall levels of k are high, heat transfer coefficients are always large and of the right order of magnitude (even if they might be in error by 50% or so). If the wall heat flux is prescribed as a boundary condition, Eq. (8.9) can equally be used to obtain Θ_w.

In precisely the same way, Eq. (8.7) can be arranged to provide an expression for the wall shear stress in terms of values appearing at y_P:

$$\frac{\tau_w}{\rho} = \frac{\kappa^* U_\mathsf{P} k_\mathsf{P}^{1/2}}{\ln E^* y_\mathsf{P}^*}. \tag{8.10}$$

In computational codes, Eq. (8.10) is usually reformulated as:

$$\tau_w = \mu_w^{\mathit{eff}} \frac{U_\mathsf{P} - U_w}{y_\mathsf{P}} \tag{8.11}$$

where U_w stands for the velocity of the wall if it is moving relative to the coordinate frame. That has the same form as for laminar flows or when equations are integrated up to the wall, except that, instead of the molecular viscosity, one adopts an effective 'wall' turbulent viscosity:

$$\mu_w^{\mathit{eff}} = \frac{\rho \kappa^* k_\mathsf{P}^{1/2} y_\mathsf{P}}{\ln(E^* y_\mathsf{P}^*)}. \tag{8.12}$$

The above treatment naturally raises the question of how the level of turbulence energy used in the above formulae is to be obtained. The recommended approach is to solve a transport equation for k in the usual way (or, for the components of the normal stresses, if a second-moment closure is used), a choice that focuses attention on how the kinematic generation and dissipation terms are to be computed. Boundary-layer solvers (which deal for the most part with flows near local

https://doi.org/10.1017/9781108875400.010 Published online by Cambridge University Press

equilibrium) sometimes adopt simply the values of these quantities evaluated at the near-wall node, P:

$$\mathcal{P}_{k,\,\mathsf{P}} = \frac{\tau_w^2}{\rho^2 \kappa^* k_{\mathsf{P}}^{1/2} y_{\mathsf{P}}} \quad \text{and} \quad \varepsilon_{\mathsf{P}} = \frac{k_{\mathsf{P}}^{3/2}}{c_l y_{\mathsf{P}}} \tag{8.13}$$

where $c_l = \kappa^*/c_\mu = \kappa/c_\mu^{3/4} \approx 2.5$.

However, because production and dissipation rates vary so greatly over the thin viscosity-affected zone next to the wall, it is preferable to determine their average values by direct integration over the near-wall control volume. A commonly adopted approach, simplified from Chieng and Launder (1980), is to assume a distinct switch-over at a dimensionless wall distance, y_{v}^*, from a purely viscous sublayer to a fully turbulent region where the length scale increases as[3] $\kappa^* y/c_\mu$. Now, if it is assumed that over the fully turbulent part of the control volume (i.e. for $y_{\mathrm{v}} \le y \le y_{\mathrm{n}}$) the turbulent shear stress is uniform and equal to (τ_w/ρ), while being zero within the viscous layer, the mean turbulence energy generation rate over the near-wall control volume, $\overline{\mathcal{P}_k}$, is given by:

$$\overline{\mathcal{P}_k} = \frac{1}{y_{\mathrm{n}}} \int_{y_{\mathrm{v}}}^{y_{\mathrm{n}}} \frac{(\tau_w/\rho)^2}{\kappa^* k_{\mathsf{P}}^{1/2} y} dy = \frac{(\tau_w/\rho)^2}{\kappa^* k_{\mathsf{P}}^{1/2} y_{\mathrm{n}}} \ln\left(\frac{y_{\mathrm{n}}}{y_{\mathrm{v}}}\right). \tag{8.14}$$

Unlike the production rate, the dissipation rate is non-zero in the viscous layer. Assuming that across the viscous layer the energy dissipation rate is given by Eq. (6.10) and that the value of k at the edge of the viscous layer may be taken as that at node P, then the dissipation rate within the sublayer is uniform, equal to $2\nu k_{\mathsf{P}}/y_{\mathrm{v}}^2$. Within the turbulent region the dissipation rate is given by:

$$\varepsilon = \frac{k^{3/2}}{\underbrace{\kappa^* c_\mu^{-1}}_{c_l}\, y}. \tag{8.15}$$

Thus, the spatially averaged dissipation rate over the near-wall control volume can be expressed as:

$$\bar{\varepsilon} = \frac{1}{y_{\mathrm{n}}} \left[\int_0^{y_{\mathrm{v}}} \frac{2\nu k_{\mathsf{P}}}{y_{\mathrm{v}}^2} dy + \int_{y_{\mathrm{v}}}^{y_{\mathrm{n}}} \frac{k_{\mathsf{P}}^{3/2}}{c_l y} dy \right] = \frac{1}{y_{\mathrm{n}}} \left[\frac{2\nu k_{\mathsf{P}}}{y_{\mathrm{v}}} + \frac{k_{\mathsf{P}}^{3/2}}{c_l} \ln\left(\frac{y_{\mathrm{n}}}{y_{\mathrm{v}}}\right) \right]. \tag{8.16}$$

The strategy set out above (but with Eq. (8.13) being adopted rather than the more elaborate, and accurate (8.14) and (8.16)) is what is commonly termed 'standard wall functions' (SWF).

[3] This length scale is consistent with a local-equilibrium situation where production and dissipation of turbulence energy are in balance.

https://doi.org/10.1017/9781108875400.010 Published online by Cambridge University Press

It is noted that the above basic rationale has also been extended to provide 'standard' wall functions for flows over *rough* walls by simply replacing the reciprocal of the viscous length $k^{1/2}/\nu$ (or U_τ/ν) by the equivalent (sand-grain) wall roughness h, so that the non-dimensional wall distance of the point P in Eqs. (8.7)–(8.12) is defined as $y^* = y/h$. The resultant expressions are then entirely independent of the fluid viscosity, a state known as 'fully rough'.

8.2 Towards a generalization of the wall-function concept: preliminaries

As outlined above, commonly used wall functions are based on several assumptions that are supposed to be valid throughout the *fully turbulent near-wall layer*.

1. The mean velocity follows a semi-logarithmic distribution, Eq. (8.2), which is universal in form when scaled with the inner velocity and length scales, U_τ and (ν/U_τ). The same applies for mean scalar properties – temperature or species concentration – using the corresponding inner wall scales, Eq. (8.4).
2. The turbulent shear stress is presumed to be equal to the wall shear stress, i.e. $-\rho\overline{uv} \approx \tau_w$.
3. The ratio of the turbulent shear stress and kinetic energy (sometimes termed the 'structure parameter', Bradshaw *et al.*, 1967) is presumed to be constant, i.e. $-\overline{uv}/k = c_\mu^{1/2} \approx 0.3$.
4. The turbulent kinetic energy is in local equilibrium, i.e. the net transport by convection and diffusion is negligible so that $\mathcal{P}_k \approx \varepsilon$.
5. As an indirect corollary of the above assumptions, the turbulent length and time scales increase linearly across this flow region, i.e. $l = k^{3/2}/\varepsilon = c_l y$ and $\mathcal{T} = k/\varepsilon = c_\mathcal{T} y$ (where $c_l = \kappa/c_\mu^{3/4}$ as already defined and $c_\mathcal{T} = \kappa/(c_\mu^{1/2} U_\tau)$).

These assumptions are reasonably well satisfied in simple wall flows such as the constant-pressure boundary layer, plane channel or pipe flow, as has been established from numerous experiments and DNS studies. None of the above assumptions can be relied on, however, in more complex flows.

A question that sometimes arises in computing complex flows (where the wall-adjacent flow structure undergoes very great variations with position along the wall) is what remedial measure should be taken if a limited number of wall-adjacent nodes have y^+ (or y^*) values below that for which the appropriate log-law wall function is applicable. This may occur if the mesh density is increased without due care, especially when using automatic gridding, a practice often employed in industrial computations. In some commercial CFD codes a remedy is provided for such eventualities where the wall functions for the velocity and temperature

https://doi.org/10.1017/9781108875400.010 Published online by Cambridge University Press

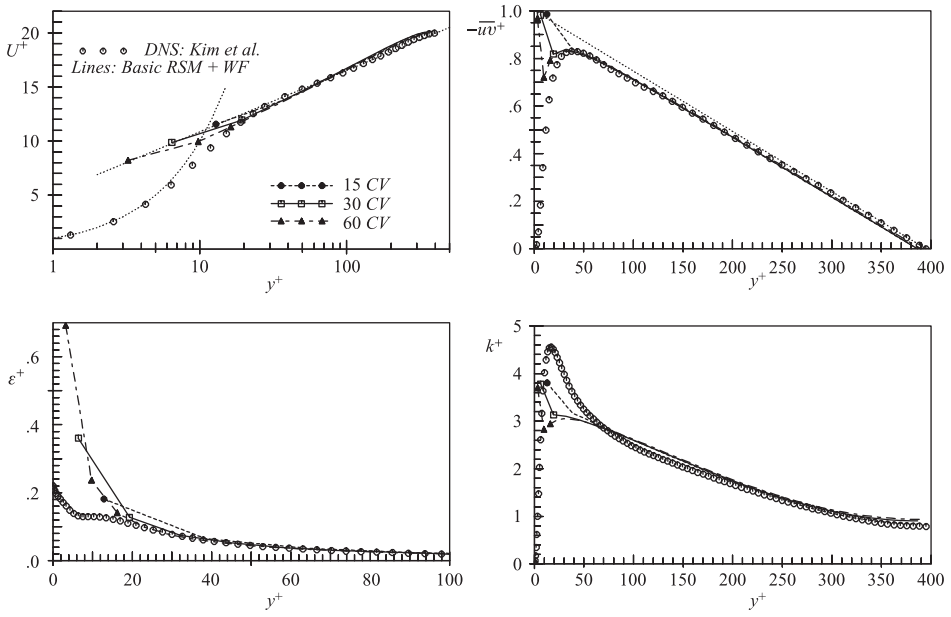

Fig. 8.2 Numerical computations of flow in a plane channel with different uniform grids, using standard wall functions, Re = 13,750. From Jakirlić (1997).

are switched from the logarithmic expressions, Eqs. (8.2) and (8.3), to linear ones, $U^+ = y^+$ and $\Theta^+ = \mathrm{Pr}\, y^+$ whenever $y^+ < 11.6$ (this being approximately the value at which the linear and the logarithmic velocity profiles intersect). This practice is not advised, however, when used with a high-Re closure and a coarse mesh. While it will correctly place the first grid point on the linear (laminar) line (thus, if $y_\mathrm{P}^+ = 5$, the value of U_P^+ would also be set to 5), in computing the next node from the wall, a high-Re model will not have the essential embedded viscous damping effects. The outcome of following such a practice is that the velocity profile would still follow a semi-logarithmic curve, but one lying well below the correct line. In these circumstances, less damage is done if no switch is activated at all: at the first node U^+ will lie incorrectly on the logarithmic line, but apart from that, the profile will generally follow the proper logarithmic distribution and return reasonably correct levels of wall friction. This is illustrated in Fig. 8.2, where computed profiles for fully developed flow in a plane channel at a relatively low Reynolds number are presented using three different uniform grids, with 15, 30 and 60 grid nodes across the channel half-width. In all cases the standard high-Re basic second-moment closure is used with the standard wall functions. Very similar values of wall friction (within 2%) were obtained in all three cases, despite the fact that for the two finer grids the first grid nodes lie deep in the viscous region. In all three cases the results for the mean velocity, shear stress, kinetic energy and its dissipation rate

https://doi.org/10.1017/9781108875400.010 Published online by Cambridge University Press

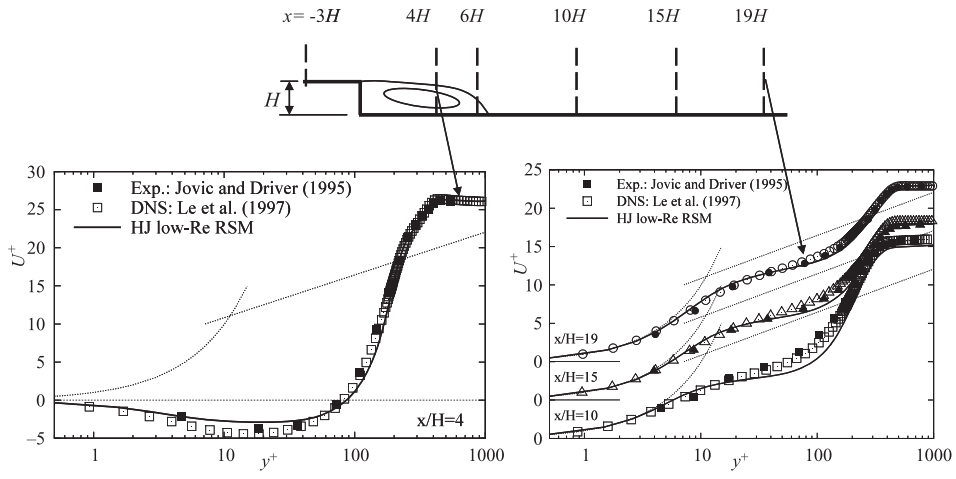

Fig. 8.3 Velocity profiles for flow behind a backward-facing step. Symbols, DNS and experimental data; lines, low-Re SMC computations with the Hanjalić–Jakirlić model. From Hanjalić and Jakirlić (1998).

collapse well with the DNS results in the fully turbulent region for $y^+ > 30$. Much larger errors would be generated by adopting the above noted 'switch' to the linear 'laminar' wall function.

Of course, for more complex flows that depart far from equilibrium, the use of standard wall functions is in any case not appropriate, as illustrated in Fig. 8.3. The figure shows velocity profiles (in wall coordinates) at two positions for the flow development behind a backward-facing step. While it is to be expected that the velocity profile in the separation bubble should not follow the semi-logarithmic distribution, it is seen that long after reattachment in the recovering boundary layer the velocity is still significantly different from the equilibrium distribution. In such flows, especially when laminar-to-turbulent or reverse transition (laminarization) is expected, one should never attempt to compute the flow behaviour using standard wall functions. For flows at high Re or Pe, when tackling a problem requiring a too extensive or complex solution domain for a WIN treatment to be feasible, one should rather employ one of the more advanced wall treatments described in the remainder of this chapter, which do not rely on the equilibrium assumptions listed above. Four such generalized approaches are presented, each of which has certain specific merits and appeal. These are:

- analytical wall functions (AWF) (the Manchester scheme);
- simplified analytical wall functions (SAWF) (the Delft scheme);
- blended wall treatment (BWT);
- numerical wall functions (NWF).

https://doi.org/10.1017/9781108875400.010 Published online by Cambridge University Press

8.3 Analytical wall functions (AWFs)

The greatest problem with the rudimentary (though widely used) standard wall functions presented in §8.1 is that CFD is used to predict *difficult* flows. In such situations the near-wall mean velocity only rarely displays the presumed logarithmic variation with wall distance. Besides the effects of severe pressure gradients, which take the near-wall flow far from its equilibrium state, force fields (most commonly due to gravity, but also from other agencies as considered in Chapter 4) or unusual boundary conditions (like a porous surface) can have a similar effect. So, if wall functions are to be a useful replacement for WIN treatments, a different basis must be adopted for their construction. The schemes proposed in this and the following section take as their starting point the idea that – instead of the profile of mean velocity – the near-wall variation of *turbulent viscosity* should be prescribed. While the normalized turbulent viscosity does not follow a universal pattern, its variation displays much less change from flow to flow than the mean velocity profile, especially if the thickening or thinning of the viscous sublayer noted in the survey of §6.1 is incorporated empirically.

In adopting such an approach it is necessary to prescribe a sufficiently simple distribution of turbulent viscosity to permit the analytical integration of a reduced form of the momentum equation. In the scheme developed by Gerasimov (2003) (see also Craft *et al.*, 2002, 2004b), the turbulent viscosity, Fig. 8.4, is taken as zero out to a distance y_v from the wall and thereafter increases linearly with distance.

Thus, the turbulent viscosity may be prescribed as:

$$\frac{\mu_t}{\mu} = \begin{cases} 0 & \text{for } y^* < y_v^* \\ \kappa^*(y^* - y_v^*) & \text{for } y^* \geq y_v^* \end{cases} \tag{8.17}$$

where $\kappa^* \equiv c_\mu c_l$ and $y^* = \rho k^{1/2} y/\mu$.

To this, in weakly non-isothermal flows, a uniform molecular viscosity is added to provide the effective viscosity in the momentum equation. In flows with intense wall or frictional heating, the variation of molecular properties across the sublayer naturally needs to be accounted for. The reader is referred to Craft *et al.* (2002) for suggestions of how this should be approximated analytically so as still to permit analytical integration. A sketch of the distribution of molecular and turbulent viscosities is provided in Fig. 8.4.[4]

[4] The sketch and all the subsequent discussion presumes that the viscous layer thickness is less than y_P. However, this may occasionally not be the case. Craft *et al.* (2002) include the corresponding analysis for the exceptional situation where node P lies within the viscous layer. Where such situations are encountered in some regions it is important that the transport equations used to resolve the flow beyond the sublayer should include any viscous and wall-proximity terms appropriate to the model in question.

https://doi.org/10.1017/9781108875400.010 Published online by Cambridge University Press

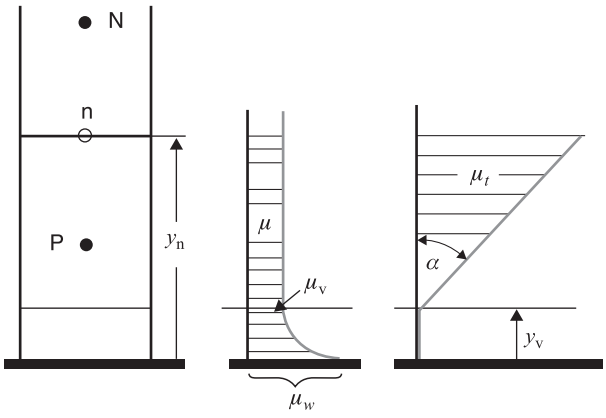

Fig. 8.4 Assumed molecular and eddy-viscosity variation with the AWF scheme.

Having prescribed the viscosity variation, the task is to integrate the momentum equation for the resultant velocity parallel to the wall, making simplifications to enable the integration to be carried out analytically. The partial differential equation in question may be written for the case where body forces in the x direction are absent:[5]

$$\frac{\partial}{\partial y}\left[(\mu+\mu_t)\frac{\partial U}{\partial y}\right] = \rho U\frac{\partial U}{\partial x} + \rho V\frac{\partial U}{\partial y} + \frac{dP}{dx} = C_U. \tag{8.18}$$

The conventional law of the wall presented in §8.1 may be thought of as resulting from neglecting *entirely* the effects of convection and pressure gradient on the right-hand side of Eq. (8.18). In the present case, for an impermeable wall, it is usually assumed that the second convection term involving the mean velocity normal to the wall can be discarded and that the remaining terms can be treated as independent of y, equal to the value prevailing at the near-wall grid node, P. These values are available, being computed during the course of a numerical computation of the flow-field under study. Here the right-hand side is simply denoted as C_U, a quantity assumed to be independent of y.

A justification for this assumption is provided in Fig. 8.5 where the convection and pressure gradient (extracted from prior solutions using a WIN near-wall model[6]) are plotted along the walls for various heights above the wall typical of applications using wall functions ($y^+ = 20$, 40 and 60). Two cases are shown: the flow behind a backward-facing step (including the separation bubble) and in a round impinging jet. All three lines in both (strongly non-equilibrium) flows show

[5] The more general case with a gravitational force acting in the x direction is considered in Craft *et al.*, (2002; 2004b).

[6] Specifically, here the elliptic relaxation $\zeta-f$ model was used (see §7.4.4), but any other WIN model that satisfactorily reproduces the flows in question, or DNS results, could have been used, leading to the same general conclusions.

https://doi.org/10.1017/9781108875400.010 Published online by Cambridge University Press

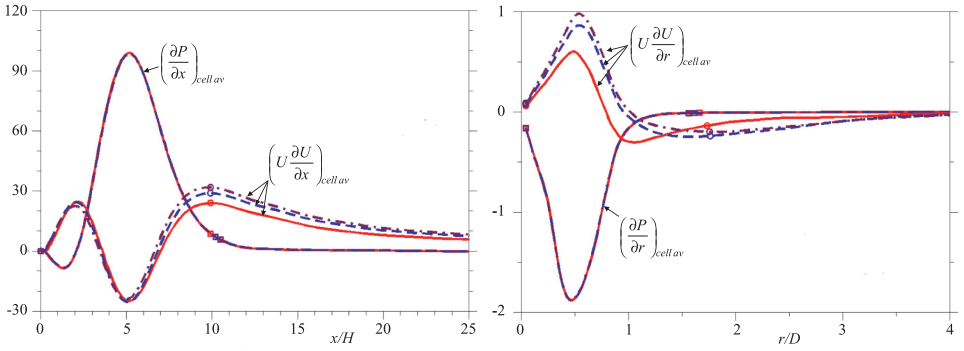

Fig. 8.5 Illustration of the insensitivity of the non-equilibrium effects represented by C_U to the size of the wall-adjacent grid in flows over a backward-facing step flow (left) and in an axisymmetric impinging jet (right). Pressure gradient and convection terms are evaluated at the wall-adjacent grid nodes positioned at —— $y_1^+ = 20$, – – – $y_1^+ = 40$, - · - · $y_1^+ = 60$, indicating that pressure variation is essentially the same for all grid sizes. From Popovac and Hanjalić (2007).

remarkable coincidence, justifying the assumption that C_U is reasonably constant over the wall-adjacent cell for a variety of cell sizes[7].

Equation (8.18) can thus be integrated first across the viscous sublayer, then across the turbulent region out to $y = y_n$. At the interface, $y = y_v$, the mean velocity, U, and its normal gradient are made continuous across the two regions, which enables (after considerable algebra) the resultant velocity profile in the turbulent region and the expression for the wall shear stress to be obtained as:

$$\mu_v U = \frac{C}{\kappa^*}\left[y^* - \left(\frac{1}{\kappa^*} - y_v^*\right)\ln Y\right] + \frac{A}{\kappa^*}\ln Y + B \tag{8.19}$$

$$\tau_w = \frac{\sqrt{k_P}}{\nu_v} A \tag{8.20}$$

where

$$A \equiv \frac{\mu_v U_n - \frac{C}{\kappa^*}\left[y_n^* - y_v^* - \left(\frac{1}{\kappa^*} - y_v^*\right)\ln Y_n + \frac{\kappa^* y_v^{*2}}{2}\right]}{[(\ln Y_n/\kappa^*) + y_v^*]} \tag{8.21}$$

$$Y \equiv [1 + \kappa^*(y^* - y_v^*)]; \quad C \equiv \frac{\nu_v^2}{k_P} C_U; \quad B \equiv y_v^* C\left(\frac{y_v^*}{2} - \frac{1}{\kappa^*}\right) + A y_v^*. \tag{8.22}$$

In applying the above formulae, the quantities in the definition of A with subscript n are evaluated at the boundary of the control volume most distant from the wall,

[7] The inclusion of streamwise pressure gradient to modify the standard wall functions was also proposed by Ng *et al.* (2002), while it was also a common feature of earlier mixing-length schemes. However, as seen in Fig. 8.5, the pressure gradient is in part balanced and compensated by convection with an opposite sign.

https://doi.org/10.1017/9781108875400.010 Published online by Cambridge University Press

Fig. 8.4. If the numerical scheme does not generate explicit values for velocity there, the value may be interpolated from those at node P and the adjacent grid node, N.

The corresponding thermal wall function is obtained by solving a reduced form of the enthalpy equation for the near-wall temperature, again for the case of negligible sources, e.g. from viscous dissipation,

$$\frac{\partial}{\partial y^*}\left[\left(\frac{\mu}{\mathrm{Pr}}+\frac{\mu_t}{\sigma_\Theta}\right)\frac{\partial \Theta}{\partial y^*}\right]=\frac{\mu_\mathrm{v}^2}{\rho_\mathrm{v}^2 k_\mathrm{P}}\left(\rho U\frac{\partial \Theta}{\partial x}+\rho V\frac{\partial \Theta}{\partial y}\right)\approx C_\Theta \tag{8.23}$$

where the second convective term may usually be neglected for an impermeable wall:

$$C_\Theta=\frac{\mu_\mathrm{v}^2}{\rho_\mathrm{v}^2 k_\mathrm{P}}\left(\rho U\frac{\partial \Theta}{\partial x}\right)$$

and the term in parentheses is normally evaluated at node P and treated as independent of y. Integration of this equation with the expression for the turbulent viscosity inserted leads, after requiring continuity of temperature and its gradient at $y = y_\mathrm{v}$, to the following expression for the temperature variation in the turbulent region:

$$\begin{aligned}(\Theta-\Theta_w)=\frac{\mathrm{Pr}}{\mu_\mathrm{v}\tilde{\kappa}^*}&\left[C_\Theta(y^*-y_\mathrm{v}^*)+\left(A_\Theta+C_\Theta\left[y_\mathrm{v}^*-\frac{1}{\tilde{\kappa}^*}\right]\right)\ln Y_\Theta\right]\\&+\frac{\mathrm{Pr}\,y_\mathrm{v}^*}{\mu_\mathrm{v}}\left(C_\Theta y_\mathrm{v}^*/2+A_\Theta\right)\end{aligned} \tag{8.24}$$

where $\tilde{\kappa}^* \equiv \mathrm{Pr}\kappa^*/\sigma_\Theta$; $Y_\Theta \equiv \left[1+\tilde{\kappa}^*(y^*-y_\mathrm{v}^*)\right]$; $A_\Theta \equiv -q_w''\mu_\mathrm{v}/(c_p\rho_\mathrm{v}\sqrt{k_\mathrm{P}})$.

If the wall heat flux is known, the wall temperature is obtained by evaluating Eq. (8.24) at y_n or y_P. Alternatively, if the wall temperature is prescribed and the wall heat flux is to be determined, Eq. (8.24) is rearranged to provide an equation for A_Θ from which q_w'' is obtained. For the more general case where buoyant forces and/or large sublayer variations in viscosity occur, the reader is referred to the appendices of Craft *et al.* (2002) or, in greater detail, Gerasimov (2003). The latter is available in electronic form from the University of Manchester library.

In determining the *turbulence energy* for node P, ideally a finite-volume budget over the near-wall cell should be applied in which diffusion to the wall is set to zero (recall, k varies as y^2 immediately adjacent to the wall). Diffusion and convection through the other faces are handled by the same approximations made for any standard interior cell in the solver being used. For the production and dissipation rates within the control volume the following practices are recommended.

Because the local generation rate of k over the near-wall cell varies in a highly non-linear way, its *mean* value, $\overline{\mathcal{P}_k}$, may be obtained by integrating numerically the local formula for production rate over the cell as in Eq. (8.14):

https://doi.org/10.1017/9781108875400.010 Published online by Cambridge University Press

$$\overline{\mathcal{P}_k} \equiv \frac{1}{y_\mathrm{n}} \int_0^{y_\mathrm{n}} \nu_t \left(\frac{\partial U}{\partial y}\right)^2 dy = \frac{\left(\tau_w/\rho\right)^2}{\kappa c_\mu^{1/4} k_\mathrm{P}^{1/2} y_\mathrm{n}} \ln\left(\frac{y_\mathrm{n}}{y_\mathrm{v}}\right). \tag{8.25}$$

Recall from §8.1 that the contribution to k production by the viscous region is zero.

The dissipation rate over the cell should likewise be found by integration. Across the sublayer it has been noted earlier (Eq. (6.10)) that

$$\varepsilon = 2\nu \left(\partial k^{1/2}/\partial y\right)^2 \approx 2\nu k/y^2$$

and, with a parabolic profile for k across this layer, a uniform value of ε is returned, ε_ν. For the turbulent region, ε is assumed to vary inversely with wall distance:

$$\varepsilon = k^{3/2}/(c_l y).$$

Of course, at the interface between the two regions, the dissipation rates given by these two formulae should be the same. If, however, the thickness of this dissipation sublayer is taken as y_v, the level of dissipation on the 'viscous sublayer' side turns out to be much less than on the turbulent side of the y_v interface, Fig. 8.6.

This anomaly can be removed by allowing the interface for dissipation to lie much closer to the wall than the edge of the conventional viscous sublayer. Indeed, by choosing the dissipation interface so that the two formulae give equal vales of ε at that interface position, y_d, one obtains

$$y_\mathrm{d} k^{1/2}/\nu = 2c_l \approx 5.1. \tag{8.26}$$

Choosing a smaller sublayer thickness for dissipation than for production was, in fact, a practice established in early one-equation models for the low-Re region (e.g. Wolfshtein, 1969) as discussed in Chapter 7, Eq. (7.60). It also makes the distribution of ε using the AWF much closer in appearance to the variation revealed many years later by DNS (e.g. Kim *et al.*, 1987). In practice, the quantity k appearing in Eq. (8.26) is normally taken as that at the cell node P, a choice that will usually overestimate k but which is numerically stable and will have relatively little effect on the solution since it is the square root of turbulence energy that appears in (8.26).

A further refinement of this AWF practice is important if the shear stress changes so rapidly across the sublayer that the flow is either nearly separating or undergoing such rapid acceleration that laminarescence occurs (i.e. where the viscosity-affected layer becomes significantly thicker in terms of y^+ than its 'universal' value). In these extreme conditions, as discussed in §6.2.2, the dimensionless sublayer thickness, y_v^*, does not remain constant at its nominally universal level. In some of the early mixing-length models (e.g. Cebeci and Smith,

https://doi.org/10.1017/9781108875400.010 Published online by Cambridge University Press

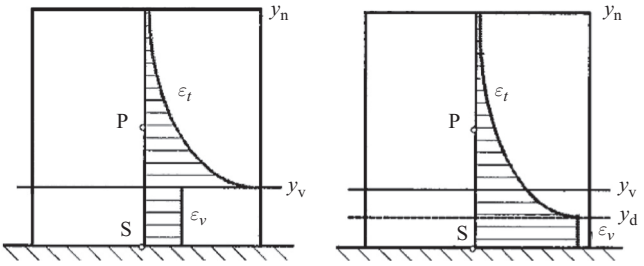

Fig. 8.6 Assumed dissipation rate; left, Chieng and Launder (1980); right, Craft *et al.* (2002).

1974; Kays and Moffat, 1975) the viscous sublayer thickness was made directly dependent on the normalized change in the shear stress across the sublayer (or an approximation to it in terms of the streamwise pressure gradient). The above practice was used only with parabolic (boundary layer) solvers, however. Craft *et al.* (2002) reported that such an approach seemed to be endemically unstable within the present wall-function treatment applied in an elliptic solver. Instead, the desired sensitivity was captured by making the *mean dissipation rate* in the sublayer cell (which is inversely proportional to the length scale) dependent on the ratio of the shear-stress change across the sublayer, λ, where:

$$\lambda \equiv \frac{\mu_w \sqrt{(\partial U_i/\partial x_j)^2_w}}{\mu_v \sqrt{(\partial U_k/\partial x_l)^2_v}}. \tag{8.27}$$

Further details are given in Craft *et al.* (2002).

Some impression of the importance of applying the above correction may be gathered from Fig. 8.7, which shows, for the upward flow of air through a mildly heated vertical pipe, the variation of Nusselt number with distance along the pipe. Due to the decrease in density the near-wall flow is accelerated, which increases the wall shear stress and, likewise, augments the rate of fall-off of shear stress with distance from the pipe wall, which, in turn, causes a drop in Nusselt number. Even in this mild heating case, the inclusion of sublayer thickening (through λ) makes a noticeable contribution to reducing the Nusselt number; for if y_v^* is held constant (the computational line denoted as 'without F(λ)') at its uniform-shear-stress level, the resultant value of Nu is some 20% higher.

If the flow is directed downwards, the reverse effect occurs. Then the buoyant force on the lighter near-wall fluid opposes the downward motion, reducing the friction at the wall and thus causing a rise in shear stress as one moves away from the wall. The sublayer thickness is then reduced, leading to higher heat transfer coefficients.

https://doi.org/10.1017/9781108875400.010 Published online by Cambridge University Press

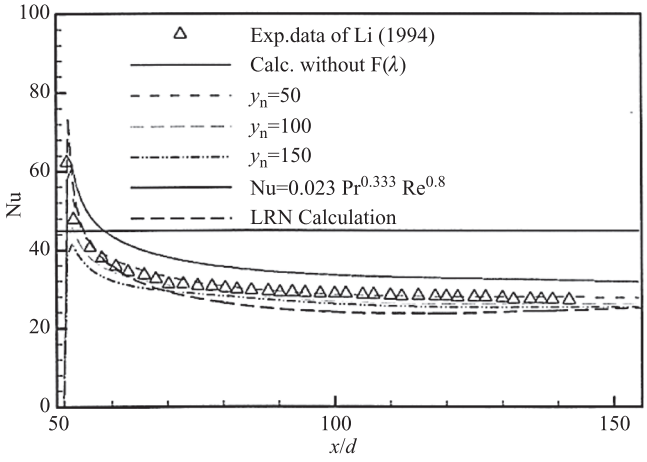

Fig. 8.7 Predicted Nusselt number for mixed convection at Re = 15,000 and Gr = 2.2×10^8 in upward flow in a heated pipe. From Craft *et al.* (2002).

Figure 8.8 shows the outcome of computing two cases of downward flow in an annulus with several turbulence treatments. First, the very significant effect of buoyancy on this flow is evident from the two runs using a WIN (or low Reynolds number, LRN) model integrated up to the wall: in one case the density was set uniform, eliminating any buoyant influence (denoted 'forced convection'). Computations are shown for two values of the buoyancy parameter $\mathrm{Bo} \equiv 8 \times 10^4\ \mathrm{Gr/Re}^{3.425}\mathrm{Pr}^{0.8}$. The inclusion of buoyant terms in the momentum equation led, for the case of the low-Reynolds number model, to Nusselt numbers for the two cases raised by 80% and 150% relative to the uniform-density case. The low-Reynolds-number model (including buoyancy) matches the experimental data particularly closely. However, nearly as close agreement is achieved with the AWF treatment, strikingly better than with the standard wall functions (StWF).

The above examples adopted an eddy-viscosity model (see Chapter 7) in the core region of the flow, a practice that is satisfactory for the simply sheared flows considered. For the more complex flow field created by the opposed wall jet illustrated in Fig. 8.9a, computed by the large-eddy simulation of Addad *et al.* (2004), a jet of hot liquid is discharged vertically downward (with mean velocity U_{jet}) against a slow, upward-moving cold stream (with velocity U_{ch}). In this case, the stress-transport (TCL) closure leads to better modelling of the strongly recirculating flow away from the wall, while the type of wall-function treatment predominantly affects the depth of penetration of the thin, high-velocity wall jet. Figure 8.9b compares, for different RANS treatments, the skin friction coefficient immediately downstream from the wall-jet discharge with the LES results. There is evidently closer agreement with the LES results as one successively refines the wall-function treatments

https://doi.org/10.1017/9781108875400.010 Published online by Cambridge University Press

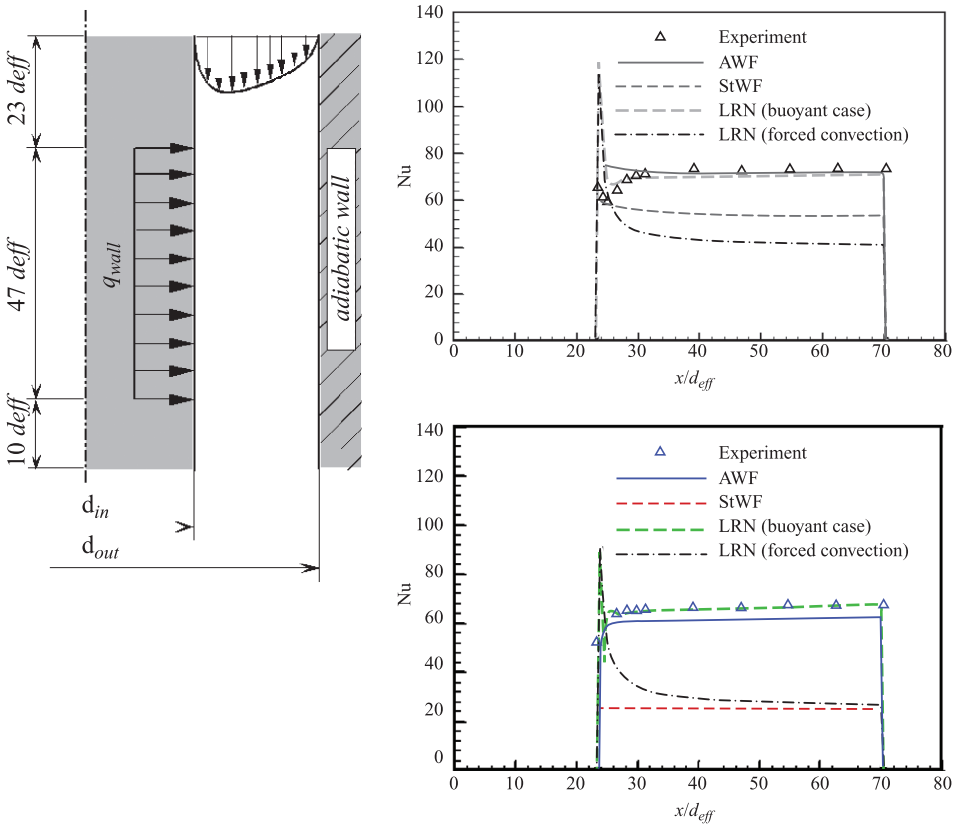

Fig. 8.8 Mixed convection in downward-directed flow through a vertical annulus. Left, flow configuration; right, Nusselt number variation for two values of the buoyancy parameter. Upper, Bo = 0.78, Re = 6,000; lower, Bo = 2.89, Re = 4,000. Symbols, experiments (Jackson *et al.*, 2002). From Gerasimov (2003); see also Craft *et al.* (2006a).

from the standard version to the AWF treatment and from an eddy-viscosity model to the TCL second-moment closure. The corresponding temperature contours in this flow have been examined in Chapter 4, Fig. 4.25, which showed that the TCL model together with the AWF treatment also led to the best agreement with the LES results.

The AWF approach has been extended to swirling flows by Zacharos (2010) (see also Craft *et al.*, 2008) for situations where the velocity vector parallel to the wall undergoes strong skewing across the sublayer (as arises, for example, in flow around a bend or close to a spinning disc). In that case, Fig. 8.10, left, one applies the scheme as described above in the direction of the mean velocity vector at P and also in the direction orthogonal to that velocity vector. For the latter case, the velocity component is zero at both P and the wall (for a stationary wall), but due

https://doi.org/10.1017/9781108875400.010 Published online by Cambridge University Press

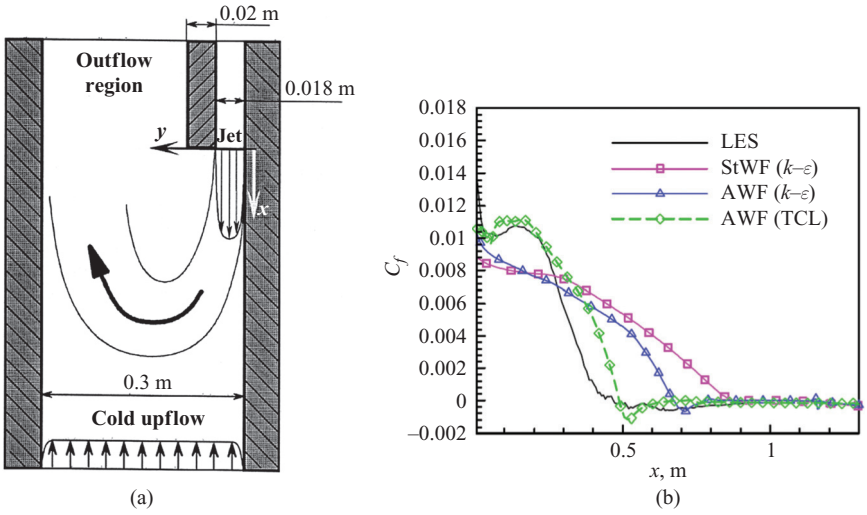

Fig. 8.9 (a) Sketch of a downward-directed wall-jet flow. (b) Predicted distribution of the friction coefficient in the isothermal case at $U_{ch}/U_{jet} = 0.077$. From Craft *et al.* (2004b).

to the pressure gradient in that direction there will be a secondary-flow velocity profile as sketched in the figure. An impression of the very great difference between the flow pattern predicted by this wall-function treatment and the 'standard' log-law approach appears in Fig. 8.10, right. This shows mean velocity contours for a geometrically axisymmetric swirling flow close to the stationary wall within a very thin rotor-stator disc cavity (though the computations are three-dimensional and unsteady – a so-called URANS treatment, which is the subject of Chapter 9). The AWF computation, Fig. 8.10a, brings out clearly the presence of spiral vortices that are known to exist (see, for example, the review by Launder *et al.*, 2010) within what is known as the Bödewadt layer but which are not captured when standard log-law wall functions, Fig. 8.10b, are used.

The AWF approach has been successfully adopted and extended by Professor Suga and his co-workers at the Osaka Prefecture University, Japan. The first extension, in collaboration with the Manchester group, was to the flow over rough walls, Suga *et al.* (2006). In this case the scheme was first calibrated so that it reproduced data for a range of roughened pipes and was then successfully applied to separated flows over sand dunes and a curved backward-facing step.

Next, the application of the AWF concept to the case of heat transfer from a wall to high-Prandtl-number fluids was addressed, Suga (2007). As one considers fluids of lower and lower thermal conductivity (or, in dimensionless terms, progressively higher values of Pr), the action of turbulence within the viscous region (while being insignificant to momentum transport) makes a greater and greater

https://doi.org/10.1017/9781108875400.010 Published online by Cambridge University Press

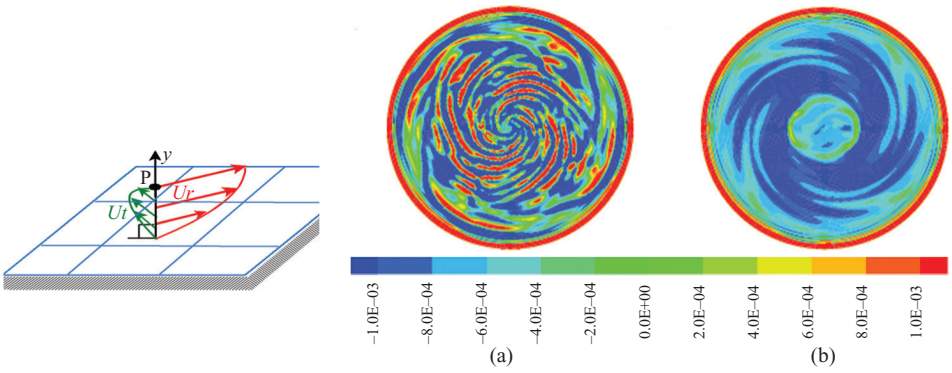

Fig. 8.10 Left: a sketch of velocity profiles for skewed near-wall motion. Right: predicted vortical flow structures close to the stationary disc of a rotor-stator disc cavity using (a) AWF and (b) the standard log-law wall function, (StWF). Figures show contours of velocity normal to the disc, $U/\Omega R$, according to the indicated scale. From Craft *et al.* (2008).

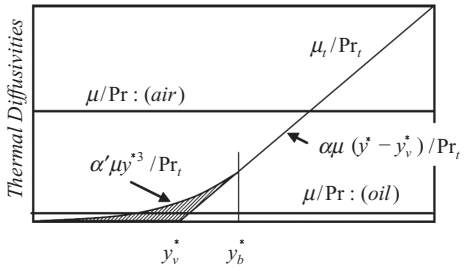

Fig. 8.11 Near-wall thermal diffusivity distribution for high-Pr flows. Reprinted from Suga (2007), Figure 3, with permission from Elsevier.

contribution to the resultant Nusselt number. The assumption of zero turbulent diffusivity for $y^* < y_v^*$ self-evidently cannot capture this phenomenon. Suga (2007) thus added a supplementary turbulent viscosity proportional to y^{*3} (since $\overline{uv} \sim y^3$ deep in the viscous layer, Eq. (6.6)), which was blended smoothly with the original linear increase of turbulent diffusivity further from the wall, at $y^* = y_b^*$ (in Suga's scheme, $y_v^* = 10.7$, $y_b^* = 11.7$), Fig. 8.11. Although integrable, the resultant complex equations are not reproduced here. The scheme was shown to reproduce the Nu-Re variations over a wide range of Pr for duct and channel flows, including rough walls. Subsequently, Suga and Kubo (2010) applied the same approach to compute mass transport at a liquid−air interface.

Suga *et al.* (2013) have also examined in detail the use of the AWF approach in impinging and separated flows. They concluded from examining a range of test flows that the near-wall distribution of turbulent viscosity could not be satisfactorily

https://doi.org/10.1017/9781108875400.010 Published online by Cambridge University Press

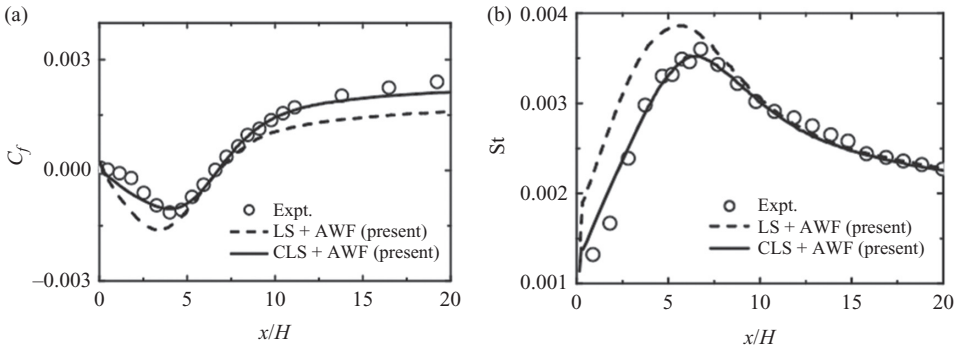

Fig. 8.12 Friction and heat transfer distributions from computations of a back-step flow using the linear LS and the non-linear CLS $k-\varepsilon$ models for ER = 1.25 and $\mathrm{Re}_H = 28{,}000$: (a) friction coefficient; (b) Stanton number. Reprinted from Suga *et al.* (2013), Figure 16, with permission from Elsevier.

modelled as a unique function of y^*. Their recommendation was, effectively, that κ^* rather than being a constant should be a function of the local average mean strain rate across the wall-adjacent control volume. For the cases reported, covering plane and axisymmetric impinging jets as well as abrupt pipe expansions, this adjustment clearly brought improved agreement with the experimental thermal data. An important secondary finding from this study was that the overall agreement with experiment also depended strongly on the level of turbulence modelling used in the main part of the flow. This is illustrated by their computations of flow over a back-step in Fig. 8.12, which shows that the use of the AWF scheme gives much better results when used with the cubic non-linear EVM (Craft *et al.*, 1996b) than with a linear EVM. This result, consistent with that shown in Fig. 8.9, is hardly surprising since, in separated and impinging flows, the turbulence structure is far from that of a local equilibrium, simple shear flow for which linear eddy-viscosity models are best suited. Indeed it underlines the fact that in making CFD computations with wall functions the user needs to consider the best combination of the wall function with the model adopted for the rest of the shear flow.

8.4 A simplified AWF (SAWF)

A simpler version of AWF, organized into a form closer to the standard wall functions[8] (while still accounting for certain non-equilibrium effects), has been developed by Popovac and Hanjalić (2007). The SAWF scheme is based on the same principal ideas used in the above AWF, but starts with a prescribed linear distribution of *effective* viscosity, as shown in Fig. 8.13 (here assuming constant fluid

[8] Thus, originally labelled generalized wall functions (GWF).

https://doi.org/10.1017/9781108875400.010 Published online by Cambridge University Press

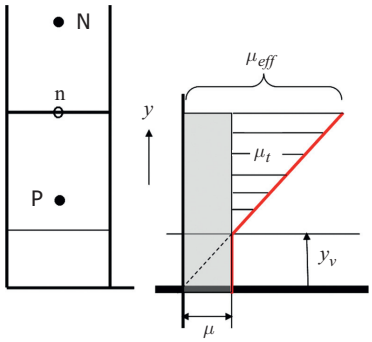

Fig. 8.13 Assumed turbulent viscosity distribution in the SAWF scheme.

properties), which allows a straightforward integration of Eq. (8.18) with a much simpler resulting velocity profile:

$$\frac{\mu_{eff}}{\mu} = \begin{cases} 1 & y^* < y_v^* \\ \kappa^* y^* & y^* \geq y_v^*. \end{cases} \tag{8.28}$$

It is readily seen that the turbulent viscosity can be written as $\mu_t/\mu = \kappa^* y^* - 1$, to which Eq. (8.17) of the AWF reduces if the thickness of the zero-μ_t sublayer is assumed fixed, i.e. $y_v^* = 1/\kappa^* \approx 4.45$. While this assumption for μ_t is less widely applicable than allowing for a variable y_v^* adopted by the AWF approach,[9] it offers advantages in greatly simplifying the integration, making it possible to formulate the wall functions for velocity and temperature in the form of conventional standard logarithmic expressions, so that they can be implemented more easily in existing in-house or commercial CFD codes.

With the above assumed distribution of μ_{eff}, Eq. (8.18) can be integrated twice over the two parts of the near-wall cell, following the same steps as in deriving AWFs. The two integration constants, appearing after the double integration of (8.18), are deduced by imposing equal values and gradients of U at the edge of the viscous sublayer, y_v. Because at this interface $\mu_{eff} = \mu$, equal velocity gradients on both sides of the interface guarantee continuity of the shear stress. After some rearrangement, the final integration from the wall to the point P at the cell-centre node leads to:

$$\frac{U_P k_P^{1/2}}{(\tau_w/\rho)} - \frac{C_U \mu}{\kappa^* \rho k_P^{1/2} \tau_w}(y_P^* - 1/2 y_v^*) = y_v^* + \frac{1}{\kappa^*} \ln\left(\frac{y_P^*}{y_v^*}\right). \tag{8.29}$$

The left-hand side of Eq. (8.29) can be conveniently rearranged into a product of the dimensionless velocity and a function containing the non-equilibrium effects

[9] It is noted that neither holds universally, especially in and around singularities such as stagnation, separation and reattachment; for some illustration based on *a posteriori* tests, see Popovac (2006).

https://doi.org/10.1017/9781108875400.010 Published online by Cambridge University Press

represented by C_U. For convenience (though not a necessary step) one can neglect $\frac{1}{2}y_{\mathrm{v}}^*$ compared with y_{P}^*, leading to

$$\frac{U_{\mathsf{P}}k_{\mathsf{P}}^{1/2}}{(\tau_w/\rho)} - \frac{C_U\mu y_{\mathsf{P}}^*}{\kappa^*\rho k_{\mathsf{P}}^{1/2}\tau_w} = U_{\mathsf{P}}^* - \frac{C_U^* y_{\mathsf{P}}^*}{\kappa^*} = U_{\mathsf{P}}^*\left(1 - \frac{C_U^* y_{\mathsf{P}}^*}{U_{\mathsf{P}}^*\kappa^*}\right) = U_{\mathsf{P}}^*\psi \tag{8.30}$$

where

$$\psi = 1 - \frac{C_U y_{\mathsf{P}}}{\rho\kappa c_\mu^{1/4}k_{\mathsf{P}}^{1/2}U_{\mathsf{P}}} = 1 - \frac{C_U^* y_{\mathsf{P}}^*}{\kappa^* U_{\mathsf{P}}^*} \tag{8.31}$$

and

$$C_U^* = \frac{C_U\mu}{\rho k_{\mathsf{P}}^{1/2}\tau_w} = \frac{\mu}{\rho k_{\mathsf{P}}^{1/2}\tau_w}\left(\rho\frac{\partial U}{\partial t} + \rho U\frac{\partial U}{\partial x} + \rho V\frac{\partial U}{\partial y} + \frac{dP}{dx}\right)_{\mathsf{P}}. \tag{8.32}$$

As before, the above integration is based on the assumption that C_U is constant over the cell and known from the previous time step or iteration[10]. The 'non-equilibrium' function ψ is thus a correction to the velocity distribution accounting for convection and pressure gradient in the wall-adjacent cell. The terms on the right-hand side of (8.29) can be grouped to give

$$y_{\mathrm{v}}^* + \frac{1}{\kappa^*}\ln\left(\frac{y_{\mathsf{P}}^*}{y_{\mathrm{v}}^*}\right) = \frac{1}{\kappa^*}\ln\left(\frac{e^{\kappa^* y_{\mathrm{v}}^*}y_{\mathsf{P}}^*}{y_{\mathrm{v}}^*}\right) = \frac{1}{\kappa^*}\ln(E^* y_{\mathsf{P}}^*) \tag{8.33}$$

where $E^* \equiv e^{\kappa^* y_{\mathrm{v}}^*}/y_{\mathrm{v}}^*$ remains to be determined. The right-hand side of Eq. (8.33) has the form of the conventional logarithmic velocity distribution. In an equilibrium turbulent wall layer when C_U can be set to zero, Eq. (8.29) gives the standard logarithmic law, Eq. (8.2) or (8.7), in which the integration constant has been determined empirically. One can also argue that the logarithmic expression on the right-hand side of Eq. (8.33) is valid only in the turbulent wall region, and here y_{v}^* (incorporated in E^*) can be interpreted as the lower bound of y^* below which the logarithmic velocity is not valid. This means that y_{v}^* here represents the thickness of the complete viscosity-affected near-wall layer and not just the zero-μ_t sublayer.[11] The lower limit of the logarithmic law is usually taken as the intersection of the linear and logarithmic velocity laws, Fig. 8.1, which occurs at $y^+ \approx 11$. This corresponds to $y^* \approx 20$, which gives $E^* = e^{\kappa^* y_{\mathrm{v}}^*}/y_{\mathrm{v}}^* \approx 4.8$ (consistent with the standard value $E = 8.4$, see definitions after Eq. (8.7)).

[10] The SAWF has also been used in an unsteady RANS mode (some examples appear in Chapter 9); then the non-equilibrium functions ψ and ψ_Θ also include the time derivatives of the mean velocity and scalar.

[11] This apparent inconsistency in interpreting and assigning different values to y_{v}^* on the two sides of equation should be regarded as approximations associated with different terms. The region between the edge of the zero μ_t sublayer and the lower bound of the logarithmic expression is the 'buffer' zone in which both the viscous and turbulent contributions to the shear stress are influential.

https://doi.org/10.1017/9781108875400.010 Published online by Cambridge University Press

Replacing the left- and right-hand sides of Eq. (8.29) by Eqs. (8.30) and (8.33) gives

$$U_{\mathsf{P}}^{*} = \frac{1}{\psi\kappa^{*}} \ln(E^{*} y_{\mathsf{P}}^{*}) \tag{8.34}$$

which has the standard form of the semi-logarithmic velocity law, apart from the non-equilibrium function ψ, defined by Eq. (8.31).

For practical implementation into a CFD code, one can again express the wall stress in the convenient form

$$\tau_w = \mu_w^{eff} \frac{U_{\mathsf{P}} - U_w}{y_{\mathsf{P}}} \psi_{\mathsf{P}} \tag{8.35}$$

where μ_w^{eff} is the effective 'wall viscosity' introduced earlier, Eq. (8.12), which can now be written as:

$$\mu_w^{eff} = \frac{\rho\kappa^{*} k_{\mathsf{P}}^{1/2} y_{\mathsf{P}}}{\ln(E^{*} y_{\mathsf{P}}^{*})} = \mu \frac{y_{\mathsf{P}}^{*}}{U_{\mathsf{P}}^{*}} \tag{8.36}$$

where, it is recalled,

$$\kappa^{*} = \kappa c_{\mu}^{1/4}, \quad U_{\mathsf{P}}^{*} = \frac{1}{\kappa^{*}} \ln(E^{*} y_{\mathsf{P}}^{*}), \quad y_{\mathsf{P}}^{*} = \frac{\rho k_{\mathsf{P}}^{1/2} y_{\mathsf{P}}}{\mu}$$

and, as before, P denotes values at the wall-adjacent node.

As expected, for flows in local equilibrium, $C_U = 0$, $\psi = 1$ and the equations reduce to the standard wall functions. The effect of introducing the non-equilibrium function ψ to modify the velocity distribution in boundary layers with moderate adverse and favourable pressure gradients is illustrated in §8.5 in conjunction with a combined WF+WIN treatment.

One can follow an analogous approach to derive the corresponding wall function for the temperature (or other mean scalar) and approximate the effects of convection and the source terms through corresponding C and ψ parameters by integrating the mean energy equation twice:

$$\frac{\partial}{\partial y}\left[\left(\frac{\mu}{\mathrm{Pr}} + \frac{\mu_t}{\sigma_\Theta}\right)\frac{\partial \Theta}{\partial y}\right] = \rho c_v \frac{\partial \Theta}{\partial t} + \rho c_p U \frac{\partial \Theta}{\partial x} + \rho c_p V \frac{\partial \Theta}{\partial y} + \dot{q} = C_\Theta \tag{8.37}$$

where $\dot{q}$ denotes any internal heat source. The equation can be integrated to give

$$\Theta_{\mathsf{P}}^{*} = \sigma_\Theta \left[\frac{1}{\kappa\psi_\Theta} \ln(E y_{\mathsf{P}}^{*}) + J\right] = \sigma_\Theta \left[\frac{\psi}{\psi_\Theta} U_{\mathsf{P}}^{*} + J\right] \tag{8.38}$$

$$\psi_\Theta \equiv 1 - \frac{\sigma_\Theta C_\Theta y_{\mathsf{P}}}{\rho c_p \kappa \sqrt{\tau_w/\rho}(\Theta_{\mathsf{P}} - \Theta_w)} = 1 - \frac{\sigma_\Theta C_\Theta^{*} y_{\mathsf{P}}^{*}}{\kappa \Theta_{\mathsf{P}}^{*}} \tag{8.39}$$

https://doi.org/10.1017/9781108875400.010 Published online by Cambridge University Press

where

$$\Theta^*_{\mathsf{P}} \equiv \frac{\rho c_p k_{\mathsf{P}}^{1/2}(\Theta_{\mathsf{P}} - \Theta_w)}{q''_w} \text{ and}$$

$$C^*_{\Theta} \equiv \frac{\mu}{\rho c_\mu^{1/4} k_{\mathsf{P}}^{1/2} q''_w}\left[\rho c_v \frac{\partial \Theta}{\partial t} + \rho c_p U \frac{\partial \Theta}{\partial x} + \rho c_p V \frac{\partial \Theta}{\partial y} + \dot{q}\right]_{\mathsf{P}}. \tag{8.40}$$

In flows with significant effects of *buoyancy*, Eqs. (8.34)–(8.40) can also be used, but in that case C^*_U, Eq. (8.32), should include the buoyancy force (here assumed to act in the x direction) $\beta\rho g_x(\Theta - \Theta_0)$, where β is the volumetric expansion factor and Θ_0 is the reference temperature. Moreover, for passive scalars without any internal heat source and with only a mild pressure variation one can assume that the time rate of change and convective transport of momentum and energy are similar, allowing the assumption that $\psi_\Theta \approx \psi$.

However, in cases where buoyancy plays a dominant role, the question arises whether, instead of $U_k \equiv c_\mu^{1/4} k^{1/2}$, the velocity and temperature should be scaled by the buoyancy velocity $U_q \equiv (\beta g q_w \alpha^2/\nu)^{1/4}$ (where $q_w \equiv q''_w/(\rho c_p)$ denotes the kinematic heat flux) commonly used for the mean temperature, especially for thermal convection over horizontal heated surfaces (Adrian *et al.*, 1986; Chung *et al.*, 1992). Indeed, in Chapter 9, Fig. 9.19 shows that the time-averaged temperature profiles in Rayleigh-Bénard convection, obtained from DNS and unsteady RANS (in Fig. 9.19 labelled 'TRANS') over a wide range of Rayleigh numbers ($10^5 - 10^9$), collapse onto a single curve in the wall-adjacent region when scaled with U_q. However, since the velocity averaged over the whole domain is zero, that scaling makes sense only for the ensemble-averaged value (see §9) when resolving the 'wind' velocity in time and space. Hanjalić and Hrebtov (2016) examined the scaling of both the velocity and temperature within a single convective roll in Rayleigh−Bénard and penetrative convection (the experiment of Deardorff *et al.*, 1969) using three different velocity scales: U_q, U_τ and U_k. The short-time filtered results (over about a quarter of the roll-over time) from the TRANS computations using the WIN (low-Re) $k - \varepsilon - \overline{\theta^2}$ algebraic flux-stress model (§7.3.2, verified in Fig. 7.10) showed that the best scaling in the near-wall region in both flow cases was achieved from using U_k. This is illustrated in Fig. 8.14 for the penetrative convection case by the velocity and temperature profiles versus the wall distance z on several vertical cross-sections through a single convective cell. Similar results are obtained for the case of Rayleigh−Bénard convection, where the temperature and, in particular, the velocity also scale better with U_k than with U_q.

To provide boundary conditions for the transport equations for turbulence quantities (and to supply the velocity scale, U_k) one follows the usual approach of

https://doi.org/10.1017/9781108875400.010 Published online by Cambridge University Press

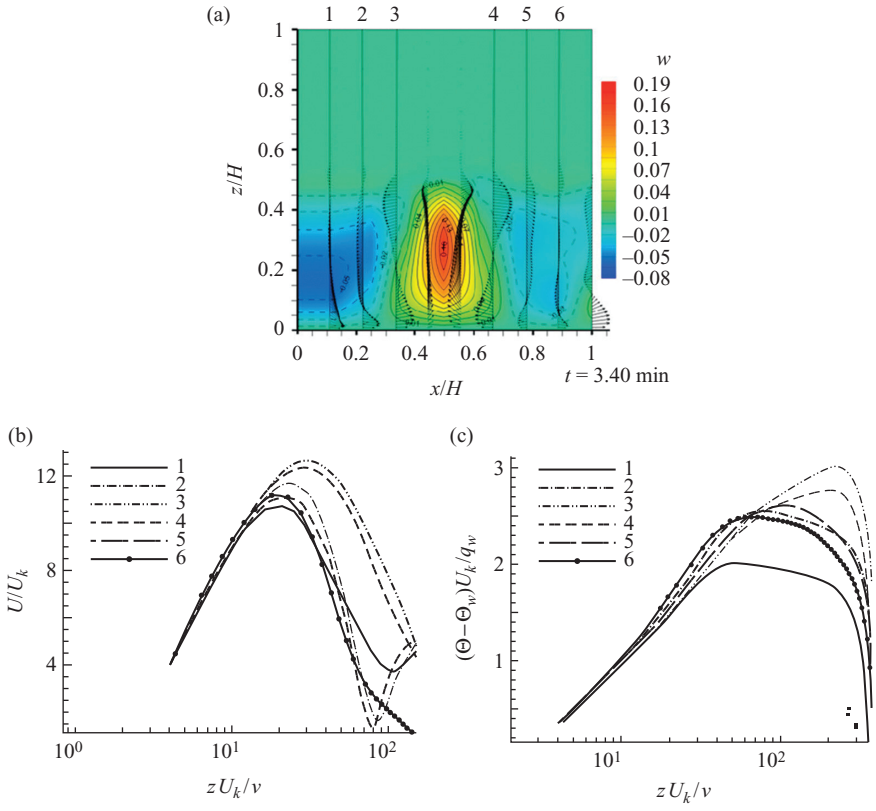

Fig. 8.14 Scaling the ensemble-averaged horizontal ('wind') velocity and temperature within a single convective roll in penetrative convection over a heated wall. (z denotes the vertical distance from the bottom wall, W is the velocity in the z direction). From Hanjalić and Hrebtov (2016), reprinted by permission from Springer Nature.

solving the equations over the wall-adjacent grid cells for k and $\overline{\theta^2}$ (with $k|_w = 0$ and $\overline{\theta^2}|_w = 0$ for a wall at constant temperature or $\partial\overline{\theta^2}/\partial x_n|_w = 0$ for an adiabatic wall, or the appropriate value for an imposed wall heat flux) and prescribing their production and destruction in terms of the SAWF. For the strain-rate production in the k-equation, one can simply use Eq. (8.13), but now including the non-equilibrium function ψ for velocity. However, in real-scale industrial and environmental flows at high Ra (and Re), the first grid node in coarse meshes may be expected to be located quite far from the wall (or the ground in environmental situations). Then, as argued in §8.1, it is rational to associate the stress at this node with the local kinetic energy in addition to the wall/ground shear stress. Thus, while U_τ enters the production through the velocity gradient, for the shear stress one can use $-\overline{u_x u_z} \approx c_\mu^{1/2} k$, in which case the usual expression, Eq. (8.13), at node P becomes (with z denoting the vertical direction)

https://doi.org/10.1017/9781108875400.010 Published online by Cambridge University Press

$$\mathcal{P}_{k,\mathsf{P}} = \frac{U_\tau^2 c_\mu^{1/2} k_\mathsf{P}^{1/2}}{\psi \kappa z_\mathsf{P}}. \tag{8.41}$$

Likewise, assuming that the wall-normal turbulent heat flux at node P equals the kinematic wall heat flux, i.e. $-\overline{\theta u_i} \approx q_{w,i}$, the body-force production of k, $\mathcal{G}_{k,\mathsf{P}} \equiv -\beta g_i (\overline{\theta u_i})_\mathsf{P}$, could be taken simply as $\mathcal{G}_{k,\mathsf{P}} = \beta g_i q_{w,i}$. However, as noted above, for the first grid node placed well into the fully turbulent region in the mixed layer (and thus not necessarily complying with the equilibrium assumption), it is again more reasonable to relate the flux to the local k and the temperature variance. An analysis of several LES and DNS data for Rayleigh–Bénard convection (e.g. Peng *et al.*, 2006) suggests that the flux correlation coefficient[12], $-\overline{\theta u_z}/\sqrt{\overline{\theta^2} k} = c_{\mu,\theta}^{1/2}$, reaches a value of about 0.3–0.4 at the base of the mixed layer and remains reasonably constant throughout the layer. Adopting the above, the buoyant production of k at node P over a horizontal wall can alternatively be written as $\mathcal{G}_{k,\mathsf{P}} = \beta g_z c_{\mu,\theta}^{1/2} \sqrt{\overline{\theta_\mathsf{P}^2} k_\mathsf{P}}$. This expression, however, may not be fully adequate for non-equilibrium situations as it is independent of the wall heat flux. By analogy with the formulation of the strain-rate production, Eq. (8.41), one can combine the two approximations for the wall heat flux and take the buoyant production at P as:

$$\mathcal{G}_{k,\mathsf{P}} = \beta g_i \sqrt{q_{w,\,i}} \left(c_{\mu,\theta}^{1/2} \sqrt{\overline{\theta_\mathsf{P}^2} k_\mathsf{P}} \right)^{1/2} \tag{8.42}$$

which accounts for the direction of the wall heat flux with respect to the gravitation vector and thus should hopefully be applicable to any orientation of the heated/cooled wall or ground.

The usual way of specifying the dissipation rate ε_P in the k-equation follows from the similarity arguments and definition of turbulence scales, with the empirical coefficient chosen to match the production $\mathcal{P}_{k,\mathsf{P}}$ in an equilibrium wall boundary layer (as in Eq. (8.13) right):

$$\varepsilon_\mathsf{P} = \frac{c_\mu^{3/4} k_\mathsf{P}^{3/2}}{\kappa z_\mathsf{P}} = \frac{k_\mathsf{P}^{3/2}}{c_l z_\mathsf{P}}. \tag{8.43}$$

Here the effects of buoyancy do not appear directly, but are accounted for through the kinetic energy k_P.

The above procedure is also followed in specifying the boundary conditions at the ground via wall functions for the ε-equation, which is solved over the wall-adjacent grid cell with the boundary condition at the surface itself: $\partial\varepsilon/\partial z|_w = 0$ and the pre-specified source terms defined by Eqs. (8.41)–(8.43).

[12] Analogous to the local-equilibrium limit for shear stress: $-\overline{u_x u_z}/k = c_\mu^{1/2} \approx 0.3$ (where subscript x denotes the wall-parallel and z the wall normal direction).

https://doi.org/10.1017/9781108875400.010 Published online by Cambridge University Press

The above arguments for the k-equation are also used for the scalar variance equation. The production at node P is modelled by again assuming that $-\overline{\theta u_z} = c_{\mu,\theta}^{1/2}\sqrt{\overline{\theta^2}k}$ and using the temperature gradient obtained from Eq. (8.38), resulting in

$$\mathcal{P}_{\theta\theta,\mathsf{P}} = \frac{q_w c_{\mu,\theta}^{1/2}\sqrt{\overline{\theta_\mathsf{P}^2}}}{\psi_\Theta \tilde{\kappa}^* z_\mathsf{P}}. \tag{8.44}$$

Finally, the destruction term is modelled as:

$$\varepsilon_{\theta\theta,\mathsf{P}} = 2\varepsilon_\mathsf{P}\frac{\overline{\theta_\mathsf{P}^2}}{k_\mathsf{P}}. \tag{8.45}$$

The performance of the above SAWF in buoyancy-driven flows is illustrated in Fig. 8.15 by the unsteady RANS (TRANS) simulation of the same penetrative convection of the mixed layer above a horizontal, heated wall mimicking the experiment of Deardorff *et al.* (1969). The computations were generated on a coarse grid of only ($10 \times 10 \times 20$) cells. The temperature evolution as well as the vertical turbulent heat flux (shown here for the lapse time $t = 7.40$ minutes) exhibit very good agreement with experiments as well as with the fine-grid one-dimensional computation ($1 \times 1 \times 100$ cells) with the WIN model shown earlier in Fig. 7.10. Moreover, the time evolution of the mixed-layer depth (the inversion elevation) defined as the height of the maximum negative heat flux (right figure) computed with 1D and 3D approaches using different grids was shown to follow closely the ½-power law i.e. $Z_{inv}/H \propto t^{1/2}$ (Fedorovich *et al.*, 2004).

8.5 Blended wall treatment (BWT)

The SAWF scheme, summarized in Fig. 8.13, attempts to take account of turbulent transport through the molecular sublayer but, like most other wall-function strategies,[13] requires that the wall-adjacent grid node should lie in the fully turbulent region as it employs a high-Reynolds-number model. As already noted in §8.2, with the steady increase in computer power there is a trend among industrial users to employ finer meshes. There is thus a high probability that, at least in some regions of complex flows, the wall-adjacent grid nodes will lie in the 'buffer zone' (the region between the viscous sublayer and the fully turbulent region) or even in the viscous sublayer itself (though still insufficiently close to the wall to satisfy the grid-density requirements for a WIN scheme). Thus, in such situations neither a conventional WIN nor a WF approach is strictly applicable.

We consider here an approach that provides approximate boundary conditions for situations where it is difficult to forecast where the wall-adjacent nodes will lie

[13] But not the AWF scheme considered above nor the NWF approach considered later.

https://doi.org/10.1017/9781108875400.010 Published online by Cambridge University Press

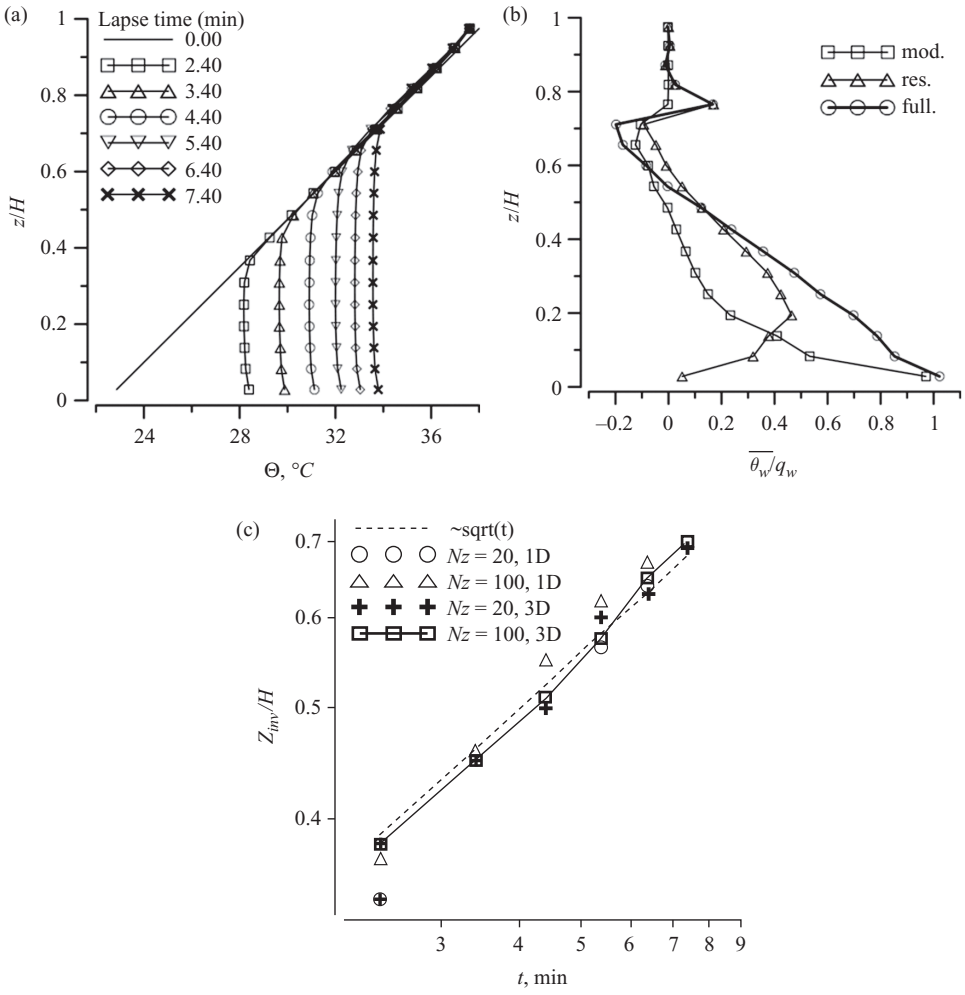

Fig. 8.15 Coarse-grid (10 × 10 × 20) URANS (TRANS) +SAWF computations of penetrative convection of a mixed layer into a stably stratified fluid (Deardorff *et al.*, 1969): top left: temperature evolution in time (compare with WIN solutions in Fig. 7.10); top right: vertical heat flux (resolved, modelled and total) at $t = 7.40$ min.; bottom: time evolution of the mixed-layer height computed with different grids; Nz denotes number of vertical nodes. From Hanjalić and Hrebtov (2016), reprinted by permission from Springer Nature.

(a situation that may commonly arise when using automatic gridding). Essentially it applies a *blending* of two estimates of the wall friction (heat flux, etc.), one based on the laminar flow limit and the other on a turbulent flow estimate. The method should reduce to one of the above two procedures (WIN or WF) when the wall-adjacent grid node happens to lie in the region appropriate to each approach. Of

https://doi.org/10.1017/9781108875400.010 Published online by Cambridge University Press

course, in contrast to the WF approach, the BWT requires a WIN model in which wall-proximity and viscous effects (that would be negligible if the first grid node were in the fully turbulent region) are included. If the cell-centre lies in this low-Re region, all the elements in the WIN model will be significant, but the boundary conditions are provided in the form of wall functions, though also modified for the viscous/molecular and other (inviscid) wall effects. The quantities for which these boundary conditions ought to be specified with a BWT depend, as in any WF approach, on the turbulence model used.

To illustrate the strategy, we consider the wall boundary condition for velocity which needs to provide the connection between the velocity at the wall-adjacent grid point P and the wall shear stress. The purely viscous and SWF schemes give the following expressions for the wall stress:

$$\tau_w^{\nu} = \mu(U_{\mathsf{P}}/y_{\mathsf{P}}) \quad \text{and} \quad \tau_w^{t} = \rho[\kappa U_{\mathsf{P}}/\ln(E y_{\mathsf{P}}^{+})]^2. \tag{8.46}$$

Let us explore the proposition that by blending these alternative formulae in some appropriate way one can obtain the correct value of wall stress irrespective of the value of y_{P}^{+}. As a preliminary test of this idea Fig. 8.16 shows the variation of the wall shear stress versus the location of the wall-adjacent grid point evaluated from the above expressions for τ_w^{ν} and for τ_w^{t} using DNS data for a plane channel flow at $\mathrm{Re}_t = 800$ (Tanahashi *et al.*, 2004). The plots are presented in normalized form for $\tau_w^{+} \equiv \tau_w/\tau_{wDNS}$ versus the normalized wall distance of the wall-nearest grid point, y_{P}^{+}. In determining these values the DNS data for U_{P} and the corresponding wall distance y_{P} are used to evaluate the wall shear stress using the above two formulae.[14]

The ideal blended model would always give $\tau_w^{+} = 1$ irrespective of the grid-node location. Such a result would be achieved if an expression for U^{+} was used that fitted perfectly the complete sublayer and logarithmic region.[15] However, the above-listed expressions for τ_w^{ν} and τ_w^{t} reproduce wall shear stress only over segments of the flow. As expected, the viscous definition τ_w^{ν} reproduces the exact boundary value of τ_w at the wall and fits the DNS profile for values of $y^{+} < 5$; but it falls off rapidly when moving further away from the wall. The fully turbulent definition τ_w^{t} on the other hand is very unrealistic in the viscous region and reproduces the proper value of τ_w only in the fully turbulent logarithmic region,

[14] For illustration we consider the standard log-law expressions using the friction velocity U_τ as the characteristic velocity scale. Of course, for the purpose of deriving a more general compound wall treatment one should use $k_{\mathsf{P}}^{1/2}$ as the velocity scale and employ the analytical wall functions, AWF or SAWF, instead.

[15] A number of expressions are available in the literature for the velocity profile in equilibrium wall boundary layers, which closely fit the experimental data from the wall to the outer turbulent region (e.g. Reichardt, 1951; Spalding, 1961; Musker, 1979; Liakopoulos, 1984; Shih *et al.*, 2002). However, none of them accounts for any non-equilibrium effects. Moreover, all these expressions are empirical, designed to fit only the velocity (and, in some cases, temperature) profiles and cannot be easily generalized to provide wall functions for other turbulence variables for which further empirical (curve-fitted) expressions would need to be invented.

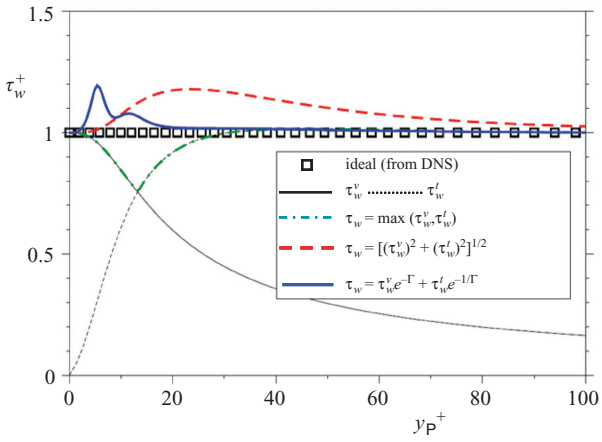

Fig. 8.16 Dependence of wall shear stress in a plane channel flow at $\mathrm{Re}_\tau = 800$ on the location of the wall-adjacent grid node, evaluated by different blending of the viscous and turbulent stress using DNS data of Tanahashi *et al.* (2004). From Popovac and Hanjalić (2007).

which, in this case, is reasonably recovered for $y^+ > 30$. In the buffer region ($5 < y^+ < 30$) both expressions give erroneous values for the wall shear stress. However, if one adopts a simple blending that entails choosing the maximum of the two:

$$\tau_w = \max(\tau_w^v, \tau_w^t) \tag{8.47}$$

while it will give a large departure ($\sim 25\%$) for $y_P^+ \approx 12$ in the channel flow considered, it returns only small errors for much larger or much smaller values of y_P^+.

In fact, one can generalize this 'blending' idea to any dependent variable for which wall boundary conditions are needed, provided expressions for the wall limit and the outer turbulent values are known (or can be provided from, say, standard or more advanced wall functions). These would take the form $\varphi_P = \max(\varphi_v, \varphi_t)$, where φ is the variable in question, and the subscripts 'v' and 't' denote the viscous (wall-limiting) and fully turbulent values of the variable. Other, indeed better, types of blending can be chosen than the simple example considered above; for example, the quadratic mean proposed by Esch and Menter (2003): $\varphi_P = \sqrt{\varphi_v^2 + \varphi_t^2}$, or a more general formulation $\varphi_P = (\varphi_v^n + \varphi_t^n)^{1/n}$. None of these expressions has any physical basis, but they all give the correct limiting behaviour: they reduce to the viscous or the fully turbulent limit deep into their respective regions. This is confirmed in Fig. 8.16, where two further blending strategies are shown. The quadratic mean produces higher values than the target τ_w^+ over most of the flow, leading to significant errors in computing friction and heat transfer. In order to

https://doi.org/10.1017/9781108875400.010 Published online by Cambridge University Press

achieve a better fit in the buffer region one can combine the viscous and fully turbulent values by means of a suitably chosen smoothing function in terms of some local flow quantities. Popovac and Hanjalić (2007) adopted the simple exponential blending of Kader (1981), which can be organized in a general form as

$$\varphi_{\mathsf{P}} = \varphi_v e^{-\Gamma_\varphi} + \varphi_t e^{-1/\Gamma_\varphi} \tag{8.48}$$

where Γ_φ is a function of the normalized distance from the wall, y^+, and molecular Prandtl number, Pr.[16] Equation (8.48) offers a convenient and simple way to provide 'blended' boundary conditions for all variables of interest. A straightforward application of this scheme to the wall shear stress gives:

$$\tau_w = \tau_w^v e^{-\Gamma} + \tau_w^t e^{-1/\Gamma} = (\mu e^{-\Gamma} + \mu_w^{\mathit{eff}} \psi e^{-1/\Gamma})_{\mathsf{P}} \frac{U_{\mathsf{P}}}{y_{\mathsf{P}}} \tag{8.49}$$

where the subscript P indicates that all variables are evaluated at the wall-adjacent grid node and μ_w^{eff} denotes the 'wall' effective viscosity, defined by Eqs. (8.12) and (8.36). A plot of Eq. (8.49) in Fig. 8.16 shows that it mimics the wall shear stress better than the other blending options discussed above, although a significant departure occurs in a narrow region around $y^+ \approx 7$. Of course, some other blending could be devised that performed even better throughout the buffer region but at the expense of simplicity. Moreover, achieving better tuning for a channel flow gives no guarantee that the method will perform better in non-equilibrium flows.

Figure 8.17 provides a further, perhaps more convincing, application of the blended wall treatment (BWT) based (for the turbulent limit) on the SAWF approach. The velocity profiles have been computed from the blended expression:

$$U^+ = y^+ e^{-\Gamma} + \left[\frac{1}{\kappa\psi}\ln(Ey^+)\right] e^{-1/\Gamma}, \quad \Gamma = 0.01 y^{+4}/(1+5y^+) \tag{8.50}$$

for boundary layers over a range of different values of the pressure-gradient parameter $P^+ \equiv \nu(dP/dx)/\rho U_\tau^3$ corresponding to strong adverse and favourable pressure gradients. The comparison with the experimental data of Nagano *et al.* (1998) (for $P^+ > 0$) and Fernholz and Warnack (1998) (for $P^+ < 0$) shows that Eq. (8.50) successfully reproduces the experimental results in all cases for $0 < y^+ < 60$. This result suggests that the BWT approach for the velocity allows the wall-adjacent grid node to lie anywhere in this region, at least for attached flows.

[16] In fact, Kader (1981) proposed a single expression for the temperature profile throughout the whole wall boundary layer for various Pr: $\Theta^+ = \mathrm{Pr} y^+ e^{-\Gamma_\Theta} + \left[\alpha \ln(y^+) + \beta(\mathrm{Pr})\right] e^{-1/\Gamma_\Theta}$, where $\alpha = 2.12$ and $\beta(\mathrm{Pr}) = (3.85\,\mathrm{Pr}^{1/3} - 1.3)^2 + 2.12\ln(\mathrm{Pr})$ are the thermal boundary-layer parameters, and the blending coefficient Γ_Θ is a function of the normalized distance from the wall y^+ and the molecular Prandtl number: $\Gamma_\Theta = 0.01(\mathrm{Pr}y^+)^4/(1 + 5\mathrm{Pr}^3 y^+)$. It is readily seen that by inserting $\mathrm{Pr} = 1$, the above equations reduce to the expression for the velocity profile $U^+ = y^+ e^{-\Gamma} + \left[\ln(Ey^+)/\kappa\right] e^{-1/\Gamma}$, where $\Gamma = 0.01 y^{+4}/(1+5y^+)$.

https://doi.org/10.1017/9781108875400.010 Published online by Cambridge University Press

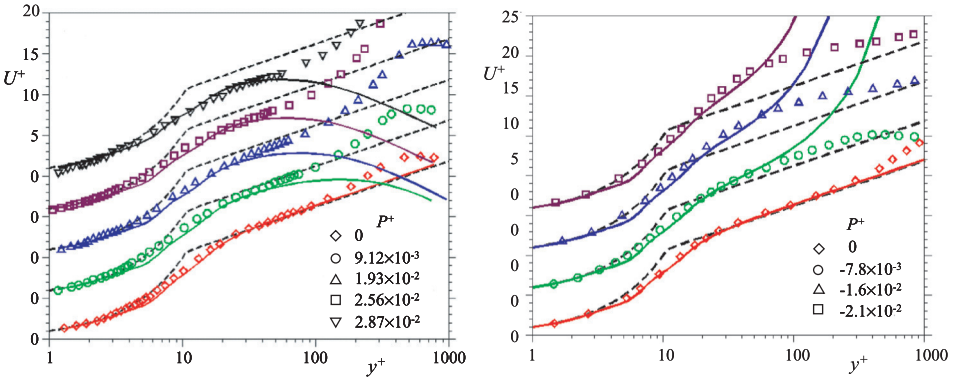

Fig. 8.17 Velocity distribution in a boundary layer subjected to adverse (left) and favourable (right) pressure gradients: *a priori* test of SAWF-based BWT. From Popovac and Hanjalić (2007).

Similar validation for flows over a backward-facing step and in a round, impinging jet reported by Popovac and Hanjalić (2007) also suggests that the BWT strategy provides a reasonable account of wall boundary conditions. With the wall-adjacent node placed in the buffer region, it achieves results close to those obtained with a much finer mesh and much superior to those from using standard wall functions.

As noted earlier, a practical advantage of Kader's exponential blending is that it can be applied in the same form to other variables for which wall boundary conditions are required. The blending can be applied to any turbulence model, but of course the specific formulation for turbulence properties depends on the model chosen, i.e. on the dependent variables that are to be obtained in the main flow region from the solution of turbulence-model equations. As most models solve the kinetic energy equation (or the normal-stress components), the application of this blending principle to the kinetic energy production $\mathcal{P}_k$ and dissipation rates ε are considered. The expressions below are given for the BWT approach when the elliptic relaxation (ζ–f) eddy-viscosity model is used (for details see Chapter 7) as the WIN limit (the latter version being adopted when the wall-adjacent grid node takes a value of $y^+ < 5$).

It is recalled first that computations with a sufficiently fine mesh in the near-wall region should correctly reproduce both the turbulent stress and the velocity gradient, which in turn should give a correct profile of $\mathcal{P}_k$. When a coarse mesh is used, however, neither the turbulent stress nor the velocity gradient is obtained correctly. In the SWF approach the values of $\mathcal{P}_k$ and ε are imposed assuming local-equilibrium conditions: a uniform shear stress and the velocity gradient obtained from the standard log-law expression, Eq. (8.13). Once an analytical expression for

https://doi.org/10.1017/9781108875400.010 Published online by Cambridge University Press

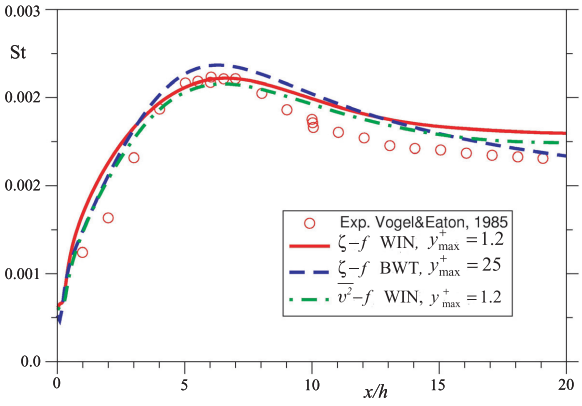

Fig. 8.18 Illustration of the blended wall treatment (BWT): the Stanton number along the wall behind a backward-facing step computed with a coarse grid, $(y_{\mathsf{P}}^{+})_{\max} = 25$, compared with fine-grid integration up to the wall with v^2–f and ζ–f models with $(y_{\mathsf{P}}^{+})_{\max} = 1.2$. From Popovac and Hanjalić (2007).

the velocity distribution across the near-wall region is available, however, one can derive an expression for $\mathcal{P}_k$ by taking $(\partial U/\partial y)$ in combination with the near-wall and fully turbulent expressions for the turbulent stress. This, basically, reduces to the blending according to Eq. (8.48), where φ_ν here is the fine-resolved $\mathcal{P}_k$ value from the WIN model, and φ_t is the coarse-mesh $\mathcal{P}_k$ from the SAWF approach:

$$\mathcal{P}_{k,\mathsf{P}} = -\overline{uv}\frac{\partial U}{\partial y} = c_\mu^\zeta \frac{\zeta_{\mathsf{P}} k_{\mathsf{P}}^2}{\varepsilon_{\mathsf{P}}} \left(\frac{\partial U}{\partial y}\right)_{\mathsf{P}}^2 e^{-\Gamma} + \frac{c_\mu^{3/4} k_{\mathsf{P}}^{3/2}}{\psi_{\mathsf{P}} \kappa y_{\mathsf{P}}} e^{-1/\Gamma}. \tag{8.51}$$

Note that $c_\mu^\zeta = 0.22$ and $c_\mu = 0.07$.

Likewise, a blending of the expression for ε in the viscous wall limit, $\varepsilon_\nu = 2\nu k/y^2$, i.e. Eq. (6.10), with that obtained by assuming a universal fully turbulent near-wall length scale (as adopted in SWF) leads to

$$\varepsilon_{\mathsf{P}} = \frac{2\nu k_{\mathsf{P}}}{y_{\mathsf{P}}^2} e^{-\Gamma_\varepsilon} + \frac{c_\mu^{3/4} k_{\mathsf{P}}^{3/2}}{\kappa y_{\mathsf{P}}} e^{-1/\Gamma_\varepsilon}. \tag{8.52}$$

As noted in §8.3, in connection with Eq. (8.26), because the viscous–turbulent interface for the dissipation rate is substantially closer to the wall than the edge of the viscous sublayer, it is advantageous to adopt a modified form of the expression for the damping parameter, Γ_ε, the form chosen being $\Gamma_\varepsilon = 0.01 y^{+4}/(1 + y^+)$.

It is recalled that in the usual finite-volume approach it is not the local point values of $\mathcal{P}_k$ and ε, but their averages over the cell, which are effectively needed in the k budget for the cell containing node P. In general, these averaged values tend to be less sensitive to the size of the wall-adjacent control volume and the actual

https://doi.org/10.1017/9781108875400.010 Published online by Cambridge University Press

position of the grid node than the local values. More details and illustrations can be found in Popovac and Hanjalić (2007).

Figure 8.18 illustrates the potential of the BWT approach by comparing the Stanton number along the wall downstream of a backward-facing step at $\mathrm{Re}_H = 28{,}000$ computed with a relatively coarse grid (with the maximum height of the wall-adjacent grid node $y^+_{\max}$ being 25), with results obtained from integration to the wall (WIN) using a much finer mesh with $y^+_{\max} = 1.2$. A slight deviation from the experimental data exhibited by both solutions is possibly a consequence of linear EVMs being unable to account for the strong streamline curvature. However, what matters here is that the BWT predictions are in close agreement with the WIN results.

The most important benefits from using a blended scheme such as BWT come to prominence when dealing with complex industrial flows. As remarked earlier, with the ever increasing computing power, industry tends to use finer and finer grids in its CFD applications, but for the very large Reynolds numbers that commonly arise it is still neither practicable nor economically justifiable to integrate the equations up to the wall.

Yet, it is highly probable that in some flow regions the wall-adjacent grid node will fall within the viscous buffer region where neither the viscous layer nor the fully turbulent boundary conditions are applicable. Figure 8.19 illustrates such a case relating to the external aerodynamics of a road vehicle. The figure shows predictions (obtained with the $\zeta - f$ model used with BWT) of the pressure distribution (in terms of the pressure coefficient $C_P \equiv 2(P - P_\infty)/\rho U^2_\infty$) on the central plane around a 1:2.5 scale model of a real automobile. The values of the wall-adjacent y^+_{P} for two meshes (with 2.85 and 4 million cells), Fig. 8.19a (upper right), show very strong variations around the vehicle ranging from typical viscous values of about 5 to fully turbulent values (around 30 for the finer mesh and up to 60 for the coarser mesh). The predictions with the coarser mesh (for which almost all the points lie in the fully turbulent region) show, by virtue of the BWT strategy, fair agreement with experiments (but are not included here). The results with the finer mesh (where most points lie in the buffer zone) show the predicted C_P in very satisfactory agreement with the measurements, Fig. 8.19b.

A further successful application of the BWT approach to a very complex industrial flow is that through the cooling jacket of an IC engine (Tatschl *et al.*, 2006). In this case, as in the car body study, current automatic-gridding software leads to a wide variation of near-wall values of y^+ or y^*. Although detailed experimental data were not available for this case, the mean temperature rise of the water in passing through the cooling passages agreed well with experiment when the model used for the previous example was applied.

https://doi.org/10.1017/9781108875400.010 Published online by Cambridge University Press

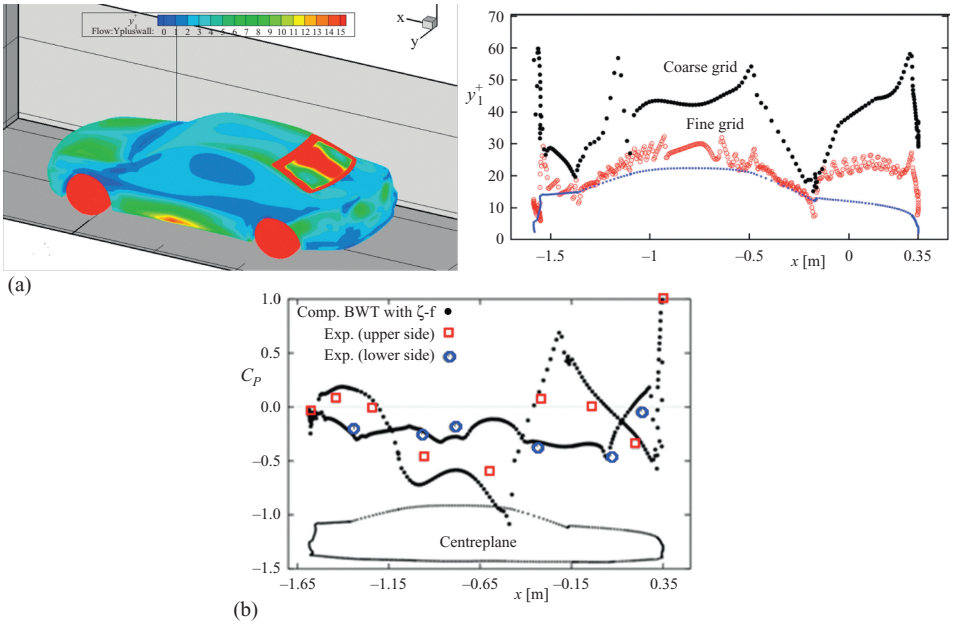

Fig. 8.19 Computation of flow around a 1:2.5 scale model of a BMW automobile with the BWT. (a) Vehicle examined (upper left); distribution of y^+ for the wall-adjacent grid nodes for two grids, 2.85×10^6 and 4×10^6 cells (upper right). (b) Predicted surface pressure distribution around the centre-plane obtained with the fine grid compared with measurements. From Basara *et al.* (2007).

8.6 Numerical wall functions (NWFs)

To conclude the chapter a further quite different wall-function approach is presented which can be applied irrespective of the variation of y^* at the wall-adjacent nodes. It is especially suited to flows where the structure of near-wall turbulence is too far from its equilibrium state for the types of wall function described so far to provide a reliable basis for capturing the actual flow behaviour. Then it may seem that the only viable route is to use the WIN approach with a low-Reynolds number model (whether with a stress-transport closure or some simpler scheme) integrated right up to the wall – with all the associated penalties. This section explains how, for many situations – probably the great majority – such a computationally costly treatment can be avoided. The strategy is to adopt what have become known as *numerical wall functions* (Gant, 2002; Craft *et al.*, 2004a).

The essential idea is illustrated in Fig. 8.20. Within the main grid one adopts a mesh spacing suitable for resolving the gradients of dependent variables and source terms applicable to the problem in question except that the wall-adjacent control volumes would usually be sufficiently large that they would cover all of the

https://doi.org/10.1017/9781108875400.010 Published online by Cambridge University Press

region where viscous effects are significant.[17] However, the near-wall cell for node P is itself divided into numerous 'slices' or sub-grid control volumes each with a sub-node at the centre. Depending on the low-Re turbulence model to be adopted and the flow under study, one can expect to employ between 10 and 35 sub-grid control volumes. The numerical wall-function approach consists of exchanging information between the main and sub-grids as described below.

We start at the point where an iteration on the main grid has just been completed (including node P and all such wall-adjacent nodes), returning provisional (unconverged) values for all the dependent variables. Attention then shifts to the sub-grid. A low-Re model must be used for this sub-region, of course, even though a high-Re form would ordinarily be used for the main grid. For the cells of the sub-grid (covering the control volume for node P, say) one normally takes the pressure gradient in the direction parallel to the wall as uniform over all the sub-grid, equal to that obtained from the main-grid iteration, i.e. $(P_e - P_w)/\Delta x$. Where the surface is highly curved, however, one may alternatively take account of the variation of static pressure across the primary cell by evaluating the pressure variation assuming radial equilibrium. Since the pressure gradient is thus known, the variation of velocity normal to the wall, V, may be obtained from the continuity equation (using sub-grid velocity components in directions parallel to the wall from the previous iteration). Starting from the wall, where the normal velocity will be zero for an impermeable surface, one may then work cell by cell out to the top

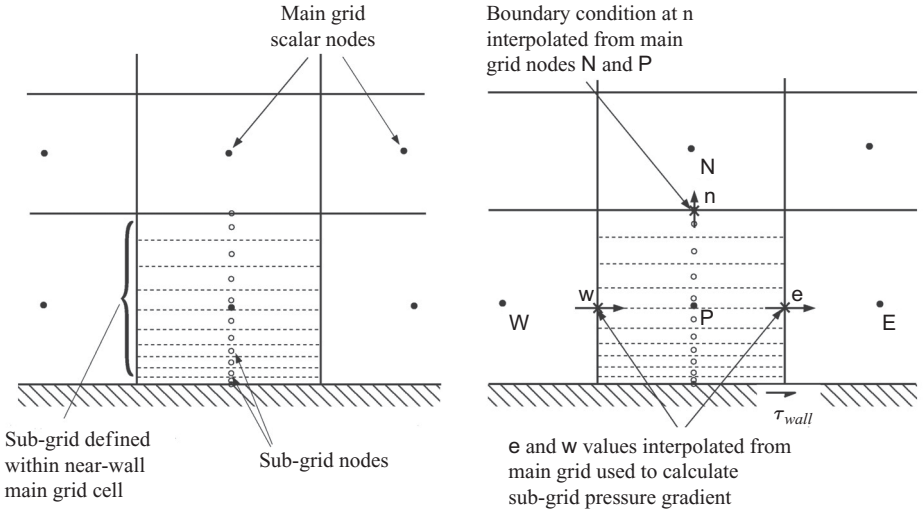

Fig. 8.20 Main and sub-grids used for the numerical wall-function approach.

[17] This is not a requirement, however. If automatic gridding creates near-wall primary-grid cells within the low-Re sublayer, the approach is still equally applicable provided the transport equations used in the main part of the flow contain appropriate low-Re and other wall-proximity terms.

https://doi.org/10.1017/9781108875400.010 Published online by Cambridge University Press

edge of the sub-grid column. This approach is similar to that of a boundary-layer solver though, in the present case, it may be applied, quite generally, to separating or reattaching flows. However, the normal velocity is also obtained independently on the main grid by solving the wall-normal momentum equation and, from the values thus obtained at P and N, one can obtain the value at n by interpolation. Because these two routes to obtaining the wall-normal velocity at n are not identical, small differences will generally exist between the values obtained. The practice advocated by Craft *et al.* (2004a) is to adopt the value returned by the main-grid computation and to scale linearly the normal velocities at all the internal sub-grid nodes in correction. The sub-grid momentum equation(s) can then be solved for the flow component(s) parallel to the wall and for any dependent variables of the turbulence and mean-scalar fields. Coding of the sub-grid transport equations is straightforward though Craft *et al.* (2004a) advise that stability is enhanced by handling convection in the *non*-conservative form: $\rho U(\partial\phi/\partial x) + \rho V(\partial\phi/\partial y)$, where ϕ denotes any of the dependent variables, U, W, k, ε, etc.

Having obtained profiles of the dependent variables across the sub-grid one can then work out the mean turbulence-energy dissipation and generation rates (or stress-component generation and dissipation rates, if a second-moment closure is employed up to the wall) across this region and the corresponding source and sink terms in the equations for other dependent variables. Such vital information as the wall shear stress and heat flux is also determined from normal velocity and temperature gradients at the near-wall sub-cell having completed the sub-grid iteration. Then, on switching attention to the main grid, one employs all the above quantities derived from the sub-grid computation as source terms in the various budget equations for control volume P. One proceeds in this way, successively switching from the main grid to the sub-grid, until the convergence criteria for the main grid are satisfied. The above account may seem an awfully long-winded way of carrying out the computation. However, as will shortly be seen, uncoupling the handling of the low-Re region from the main grid and treating the former in a somewhat simplified way enables the iteration to proceed to convergence far more rapidly, leading to a major reduction in computer time.

As an application of this approach, the case of the normal impingement of an axisymmetric jet onto a heated plane surface is considered. As discussed in §7.3.4 in connection with Fig. 7.14, this is a flow where assuming a linear eddy-viscosity stress–strain law leads to highly erroneous results. However, Fig. 7.14 has shown that a cubic eddy-viscosity model returns a behaviour in close accord with experiment when applied within a low Reynolds number model across the whole flow. First, Fig. 8.21 shows the variation of the Nusselt number along the heated plate from the stagnation point radially outwards. The complete low-Reynolds number cubic EVM captures reasonably well the double peak in Nusselt number shown

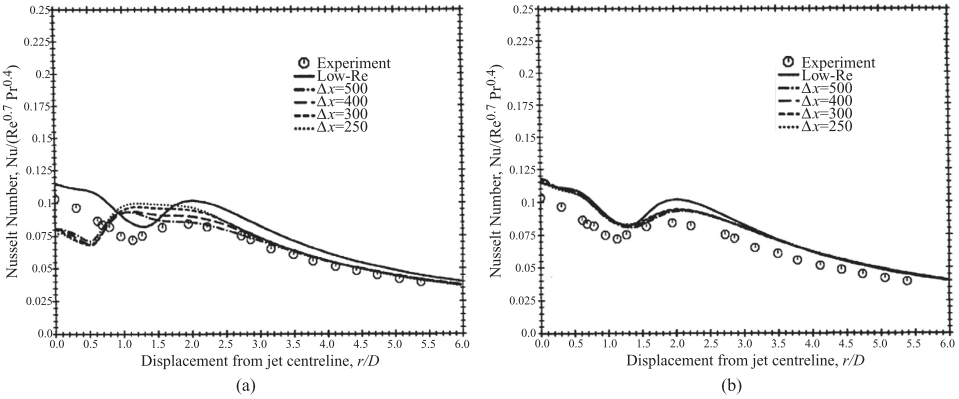

Fig. 8.21 Variation in Nusselt number with radius for an axisymmetric impinging jet. Jet discharge 4 diameters above plate, Re = 70,000 (Craft *et al.*, 2004a). (a) Heavy solid line, low-Re cubic EVM; other lines, log-law wall function with high-Re cubic EVM; symbols, experiment (Baughn *et al.*, 1991). (b) As for (a) except numerical WFs replace log-law WFs. Δx denotes the distance from the wall to the near-wall node on the primary grid.

by the experimental data of Baughn *et al.* (1991) albeit at a level about 12% higher than the measurements. If, however, the cubic EVM is used only in the fully turbulent region and is matched to standard log-law wall functions to bridge the sublayer a quite different behaviour is returned, Fig. 8.21a. Moreover, it is seen that the actual distribution of Nusselt number is quite sensitive to the thickness of the region over which the wall function is applied.[18] This behaviour may be contrasted with that obtained when, instead, the numerical wall functions (employing the cubic EVM) are applied to the wall-adjacent cells with the cubic EVM in the fully turbulent region, Fig. 8.21b. In this case, the computed Nusselt number agrees closely with that obtained with the complete low-Re cubic EVM and, as would be expected, is insensitive to the thickness of the region over which the NWF is applied. Figure 8.22 shows the associated temperature profiles across the radial wall jet at two radial positions downstream from the impingement point. This brings out both how different the temperature profile near the stagnation point is from the standard log-law result and how closely the profiles from the numerical wall function match those of the complete low-Reynolds number computation. Indeed, the only major difference between the two approaches is seen in Table 8.1. The CPU time per *iteration* with numerical wall functions is 20% less than for the complete low-Re treatment, while more than six times as many iterations were needed to achieve convergence with the low-Re approach. Thus, overall, the numerical wall-function strategy requires only about 12% of the computer budget needed for the full low-Re cubic EVM.

[18] In this computation the independent variables were x and r, where x is the direction of jet discharge normal to the wall. The symbol Δx on the figure thus indicates the dimensionless thickness of the region (in terms of wall units) where the wall function is applied.

https://doi.org/10.1017/9781108875400.010 Published online by Cambridge University Press

Table 8.1 *Comparative performance of alternative wall treatments for axisymmetric jet impingement, from Craft et al. (2004b)*

Wall treatment	Log-law WFs	Numerical WFs	Low-Re cubic EVM
Number of nodes	70 × 45	70 × 45(+40)	70 × 90
CPU per iteration(s)	0.158	0.260	0.324
Number of iterations	1426	1380	9116
Total CPU (s)	226	359	2955
Relative CPU time	1	1.6	13.1

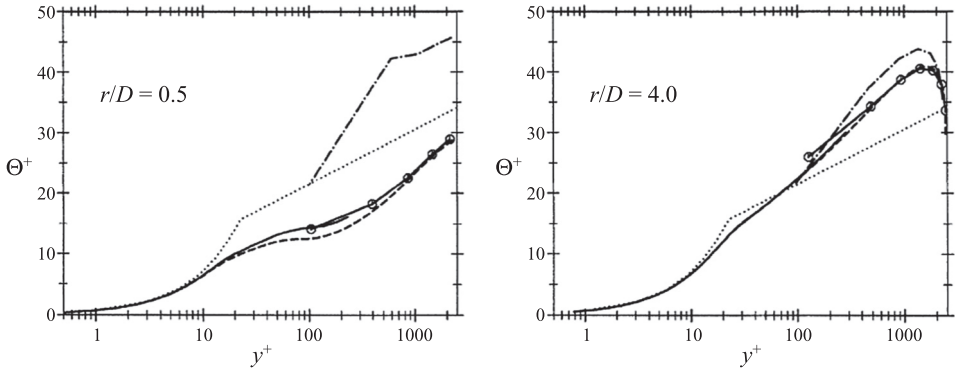

Fig. 8.22 Dimensionless temperature profiles in the impinging jet flow at two radial positions: —— cubic EVM across sub-grid matched to: —o—o— cubic EVM on main grid; - - - cubic EVM across whole flow; ·-·-· cubic EVM matched to SWF; · · · · · · standard log-law and sublayer profiles.

The approach has also been successfully applied to the case of flow induced in the vicinity of a spinning disc (Craft *et al.*, 2004a). This is a flow where it has long been known that WIN eddy-viscosity schemes can successfully capture the primary (circumferential) and secondary (radial) flow. The challenge, if one wishes to economize on computer time through the use of wall functions, is associated with the strong velocity skewing that occurs across the sublayer adjacent to the disc. Wall functions that presume that the resultant wall shear stress at the disc points in the same direction as the mean velocity at the last main-grid node (i.e. node P in Fig. 8.20) will be seriously in error. However, because the NWF solves (on the secondary grid) the velocity and turbulent flow equations down to the wall, the correct behaviour is captured. While for that case the NWF required twice the computer time of the standard log-law treatment, more than a 90% saving in computer time was achieved from using the NWF rather than the complete low-Re treatment!

https://doi.org/10.1017/9781108875400.010 Published online by Cambridge University Press

9

RANS modelling of unsteady flows (URANS)

9.1 Feasibility of URANS for inherently unsteady turbulent flows

The common perception of unsteady RANS (URANS) among the CFD community is the straightforward application of a RANS model in time-dependent mode (Eqs. (2.13, 2.14 and 2.16)) to solve flows that are unsteady in the mean. In most cases the externally imposed time scale of the mean-flow unsteadiness is much greater than the characteristic turbulence time scale, thus ensuring a sufficient separation of scales for the time-averaged equations still to be valid. As already introduced in §2.2.1, in such cases the time-averaging defined by Eqs. (2.5)–(2.7) implies the integration over a finite time period which should be much shorter than the time scale of the imposed mean-flow unsteadiness, but still sufficiently long to capture the turbulence statistics embedded in the common (stochastic) Reynolds turbulent stress. Under such conditions, the URANS computations can be expected to return the main flow features; but the credibility of the results will depend on the nature and dynamics of the flow unsteadiness and on the RANS turbulence model that is employed.

However, a controversy still surrounds the question of whether the URANS strategy can legitimately be applied to flows which are commonly regarded as steady (or slowly varying) in the mean, but yet which are inherently unstable and, in important respects, unsteady. The vortex shedding behind bluff bodies is the most common such example, though, in fact, following separation, most shear flows exhibit some overall unsteadiness. In some flows, however, especially those dominated by body forces (e.g. those over curved surfaces, buoyancy-driven flows heated from below or subjected to system rotation or electromagnetic forces), the flow remains steady in the bulk but the internal instabilities generate unsteady motion in the form of closed circulating structures. These features are found not only in turbulent flows but also frequently in the laminar regime (e.g. Taylor–Görtler vortices, the already noted von Karman vortex street or Bénard cells/rolls) and are regarded by some

https://doi.org/10.1017/9781108875400.011 Published online by Cambridge University Press

as a *mode of mean motion.* Some of these flows can still be averaged over a time period much larger than the time scale of the periodic motion to provide an integral, statistically steady field, which may have some practical relevance (e.g. in providing a reasonable estimate of total drag and heat transfer). However, as noted in §2.2.1, in some flows such as those driven solely by thermal or concentration buoyancy (Rayleigh–Bénard and penetrative convection into a stably stratified medium) where the fluid motion consists *only* of large recirculating structures without external flow, the long-time averaging makes no sense as the mean velocity is zero over the whole domain.

In turbulent flows, however, the large periodic structures are turbulent, whether the turbulence is generated by internal shear or by body forces within the structures, or entrained from the underlying surrounding stochastic turbulence field. In fact, in most complex flows the turbulence can be regarded as comprising *coherent (organized)* and *incoherent (phase-random, broadband, stochastic)* motions. According to Hussain (1983), the coherent structures can be defined as 'a connected, large-scale turbulent fluid mass with a phase-correlated vorticity over its spatial extent'. As such, the coherent vortical structures can indeed be regarded as the flow itself; but that does not necessarily exclude them from being treated by a turbulence model applied in URANS mode. In most cases the large coherent structures are three-dimensional, quasi-deterministic and periodic (though not necessarily regular), and act as the main carrier of momentum and heat, whereas the stochastic turbulence often acts almost as a passive scalar. In other words, the *resolved* stress and scalar flux associated with these coherent structures, if present (the coherent Reynolds stress/flux), usually make a much larger contribution to the total second-moment values than the stochastic constituents, $\overline{u_i u_j}$ and $\overline{\theta u_i}$, at least in separated and body-force driven flows remote from a solid wall. Thus, the solution of the usual RANS equations in a steady mode (i.e. without time and space resolution of the large-scale structures) would require incorporating some additional turbulence model for the large-scale coherent contribution to the stress and scalar-flux field in addition to the usual modelling of the stochastic correlations. Despite some early ideas for additional models of this type, the provision of such models did not appear feasible as, unlike stochastic turbulence, large-scale coherent structures usually depend on the flow configuration and thus differ from one flow type to another. A more promising approach for treating turbulent flows containing large organized structures (even if the flow is stationary in the mean) is to apply the URANS approach, i.e. to solve the RANS equations in time and 3D space and *resolve* the large structures in a manner akin to large eddy simulations (LES) to account for their contribution to the total stress and scalar flux. However, such an approach has limitations subject to the nature and properties of the organized structures. In that respect, a note of caution is warranted here. In turbulent

flows, coherent motion at scales considerably smaller than the local characteristic flow length scale are also found in many flows, especially wall-attached flows (e.g. hairpins vortices, vortical pockets or streaks), which Hussain (1983) termed *coherent substructures*. Unlike the large-scale coherent motion, resolving these coherent substructures is beyond the reach of the common URANS approach; such structures can be satisfactorily resolved only by the proper scale-resolving methods, such as LES or DNS.

As the RANS strategy is likely to remain the mainstay of industrial CFD (e.g. Slotnick *et al.*, 2014), either on its own or in combination with LES (as covered in Chapter 10), further in-depth (re)assessments of advanced RANS models and their limitations or potential when used in URANS mode is warranted. This is especially the case when targeting complex engineering and environmental flows at high Re or Ra for which well-resolved large eddy simulations are not obtainable or, at least, not practicable, and where one is thus faced with a choice between a URANS computation, a coarse LES or a hybrid RANS/LES approach using an affordable (usually a RANS-type) mesh. These will be the main themes of the present chapter.

In the next section we discuss first the mathematical rationale of applying the Reynolds-averaging concept to unsteady turbulent flows in general, and then focus on the URANS application to flows dominated by large organized structures where the approach seems broadly feasible, though with some snares and limitations.

9.2 Mathematical formalism

9.2.1 General remarks

We note first that Osborne Reynolds considered neither unsteady nor three-dimensional flows but, curiously enough, in his original time-averaged Navier–Stokes equation (Reynolds, 1895) he retained the time derivative of the mean velocity and all (three-dimensional) velocity and stress components, perhaps subconsciously allowing for the extension of his concept to more general non-stationary turbulent flows.

Let us consider again the common Reynolds time averaging (see §2.2.1) by redefining the Reynolds decomposition, Eq. (2.4), to handle unsteady flows. For this purpose, as illustrated in Fig. 9.1, we replace the long-term averaged variable $\bar{\Phi}(x_i)$ by $\tilde{\Phi}(x_i, t)$, the latter now itself time-dependent, representing the same variable but averaged over a finite time period, τ, much shorter that the time scale of the unsteady mean flow (if non-stationary) and also shorter than that of the large-scale coherent structures if present, i.e.

$$\hat{\Phi} = \tilde{\Phi} + \varphi, \text{ where } \tilde{\Phi}(x_i, t) = \frac{1}{\tau} \int_{t-\tau/2}^{t+\tau/2} \hat{\Phi}(x_i, t) dt. \tag{9.1}$$

https://doi.org/10.1017/9781108875400.011 Published online by Cambridge University Press

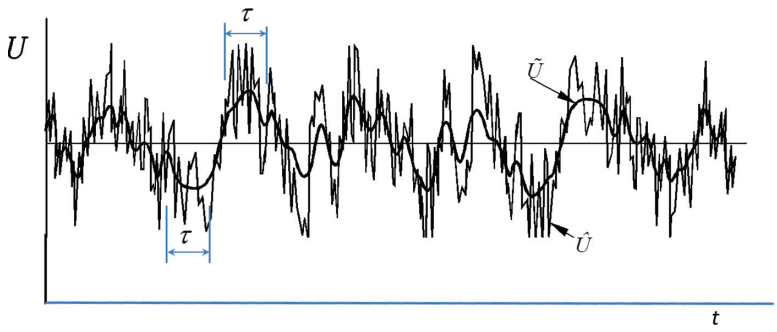

Fig. 9.1 A sketch of a typical time record of the instantaneous and locally time-averaged velocity in a flow with organized (quasi-periodic) large-scale structures evaluated using Eq. (9.1).

The implications of using this approach are illustrated by considering the momentum equation. Inserting the instantaneous velocity decomposed as in Eq. (9.1) into the instantaneous momentum Eq. (2.2) and averaging over the same time period τ (assuming that the averaging operator commutes with time and space derivatives) gives:

$$\frac{\partial \tilde{U}_i}{\partial t} + \frac{\partial (\tilde{U}_i \tilde{U}_j)}{\partial x_j} = \sum_n F_i^n - \frac{1}{\rho}\frac{\partial \tilde{P}}{\partial x_i} + \frac{\partial}{\partial x_j}\left[\nu \frac{\partial}{\partial x_j}\left(\frac{\partial \tilde{U}_i}{\partial x_j} + \frac{\partial \tilde{U}_j}{\partial x_i}\right)\right] - \frac{\partial}{\partial x_j}\left(\widetilde{\tilde{U}_i \tilde{U}_j} - \tilde{U}_i \tilde{U}_j + \widetilde{\tilde{U}_i u_j} + \widetilde{\tilde{U}_j u_i} + \widetilde{u_i u_j}\right). \quad (9.2)$$

Compared with the usual Reynolds momentum equation (Eq. (2.14)), Eq. (9.2) contains, in addition to the stochastic Reynolds stress, $\widetilde{u_i u_j}$, four new non-linear terms representing additional constituents of the stress tensor. The first two terms $\widetilde{\tilde{U}_i \tilde{U}_j} - \tilde{U}_i \tilde{U}_j$[1] originate from the large-scale coherent-structures' mutual interactions, whereas the next two terms, $\widetilde{\tilde{U}_i u_j} + \widetilde{\tilde{U}_j u_i}$ are the mixed (or cross) stresses resulting from interactions of the large-scale coherent and small-scale incoherent (stochastic) motions. The first and second terms, $\widetilde{\tilde{U}_i \tilde{U}_j}$ and $\tilde{U}_i \tilde{U}_j$, can in principle be evaluated from the time-resolved solution of Eq. (9.2) (*a posteriori*, or in the course of solution using values at earlier time instants). However, since in URANS the stochastic motion is not resolved (and is thus inaccessible), to close and solve Eq. (9.2) the other terms must be provided from separate turbulence models or some other approximations.[2] Such a task is neither feasible nor practical

[1] In LES, this term is known as the Leonard stress (see §10.2.1).

[2] For solving steady (long-term-averaged) equations for a flow with strong internal unsteadiness, the first two terms also need to be approximated by a separate model.

https://doi.org/10.1017/9781108875400.011 Published online by Cambridge University Press

as it involves a number of uncertainties. Unlike small-scale, stochastic turbulent motions that follow some general pattern in most turbulent flows and obey certain similarity laws (and are thus representable by a relatively general statistical turbulence model following the usual RANS approach), the large-scale structures retain memories of their origin and an awareness of their surroundings. They thus differ in form, pattern and intensity from one flow to another. Moreover, all these correlations will depend on the time-integration interval, τ, in the definition of $\tilde{U}_i$, whose choice is difficult to identify *a priori* on rational physical grounds.

9.2.2 Triple decomposition

For flows exhibiting distinct large-scale organized structures that are *repetitive*, a more appropriate approach is the *triple decomposition* of the instantaneous motion, which explicitly accounts for the periodic flow component:

$$\hat{U}_i = \underbrace{\overline{U}_i}_{mean} + \underbrace{u_i^c}_{periodic} + \underbrace{u_i^s}_{stochastic} = \underbrace{\widetilde{U}_i}_{phase-averaged} + \underbrace{u_i^s}_{stochastic} . \qquad (9.3)$$

The periodic component (relative to the time mean) is here denoted by u^c, the superscript c used to indicate its coherent character, while the stochastic fluctuations (relative to the periodic motion) are denoted by u^s. As indicated in Eq. (9.3), the sum of the first two terms, $\widetilde{U}_i = \overline{U}_i + u_i^c$, constitutes the *phase-averaged* motion, defined by Eq. (2.8)[3] and illustrated in Fig. 2.2 (right). (Note that the phase-averaged velocity $\widetilde{U}_i$ is different from the local short time-averaged $\tilde{U}_i$ defined by Eq. 9.1).

Substituting Eq. (9.3) into Eq. (2.2) and performing first the phase averaging and then the time averaging, Hussain (1983) derived separate equations for each of the three components, which in principle could serve for solving the time-averaged momentum equation for flows that are stationary in the mean but contain both periodic coherent structures and stochastic turbulence. However, here again we are confronted with the fact that such a set of equations contains a number of self- and cross-correlations involving all three components from Eq. (9.3). All these correlations are unknown, and to close and solve the equations the correlations must be approximated in terms of the available (solved) variables, as in RANS turbulence models, for the stochastic stress. As already noted in §9.1, such a route is not tenable, and the concept of triple decomposition does not really assist in the statistical approach to solving unsteady turbulent flows. However, triple decomposition can be useful in the analysis of turbulence and, as will be shown below, for gaining

[3] Valid strictly for a regular periodic flow; for general irregular periodicity, ensemble averaging at a particular phase of the structure is the more appropriate, see next section, §9.3.

https://doi.org/10.1017/9781108875400.011 Published online by Cambridge University Press

insight into the capabilities and limitations of conventional RANS when applied to solving inherently unsteady flows.

Hence, we are left at present with the only viable option: to follow the standard Reynolds-averaging approach, but with the need to ensure the satisfactory resolution of large-scale coherent structures to provide the resolved (coherent) contribution to the stress and scalar flux. In practice, the remaining unknown correlations, especially the mixed correlations, are then presumed negligible on the grounds of large-scale separation (and thus a lack of correlation) between the coherent and stochastic motion.

Thus, when one wishes or needs to extract what amounts to the effective turbulent second-moments of any flow variables Φ and Ψ from a URANS computation, one follows the above route in which, as in Eq. (9.3), the instantaneous fluid motion is decomposed into its (long-term-averaged) time mean, a coherent (deterministic) motion and the incoherent (stochastic) turbulence:

$$\hat{\Phi}(x_i,t)=\bar{\Phi}(x_i)+\varphi^c(x_i,t)+\varphi^s(x_i,t);\;\; \hat{\Psi}(x_i,t)=\bar{\Psi}(x_i)+\psi^c(x_i,t)+\psi^s(x_i,t). \tag{9.4}$$

Performing a long-term averaging of their product at a point in space gives:

$$\overline{\hat{\Phi}\hat{\Psi}}=\overline{\bar{\Phi}\bar{\Psi}}+\overline{\varphi^c\psi^c}+\overline{\varphi^c\psi^s}+\overline{\varphi^s\psi^c}+\overline{\varphi^s\psi^s}. \tag{9.5}$$

By assuming that the deterministic structures and the incoherent turbulence are not directly interacting ($\overline{\varphi^c\psi^s}=\overline{\varphi^s\psi^c}=0$), the *effective* turbulent second-moments are obtained as the sum of the deterministic (resolved, 'apparent') stress/flux and the modelled turbulence:

$$\overline{\hat{\Phi}\hat{\Psi}}-\bar{\Phi}\bar{\Psi}=\overline{\varphi^c\psi^c}+\overline{\varphi^s\psi^s}. \tag{9.6}$$

In the next section, the justification for such an assumption is examined by way of an *a posteriori* scrutiny of flow over an infinite round cylinder, which may be regarded as a paradigm of separated flows over bluff bodies.

9.3 The role of the URANS model: EVM versus RSM in flow over a cylinder

The challenges and uncertainties discussed above have nurtured a widespread view that conventional RANS models are incapable of predicting accurately turbulent flows dominated by inherent unsteadiness, especially those with significant regions of separation. Besides the conceptual inadequacy of the Reynolds time-averaging for treating internally unsteady flows, this negative perception has been reinforced by unsatisfactory outcomes in using linear eddy-viscosity models (LEVM). However, ample evidence exists that higher order models – especially those capable of reproducing reasonably well the stress anisotropy and phase shift between

https://doi.org/10.1017/9781108875400.011 Published online by Cambridge University Press

the stress and rate-of-strain eigenvectors when run in unsteady mode (URANS) – can perform satisfactorily, at least for practical purposes, even in challenging unsteady separating flows. This has been demonstrated for both generic as well as more complex flows, e.g. a periodic synthetic jet (Carpy and Manceau, 2006), a backward-facing step (Fadai-Ghotbi *et al.*, 2008), a triangular cylinder (Johansson *et al.*, 1993; Durbin, 1995) and flow over tube bundles (Benhamadouche and Laurence, 2003) to name but a few. Moreover, URANS computations with standard RANS models are widely used in solving complex flows in industrial practice. However, the open literature generally lacks any insightful analysis of the limitations of such an approach and their origin, and equally any explanation of why only some URANS models perform successfully in such flows.

As will be demonstrated in the following sections, for real-scale problems where only relatively coarse meshes are available (whether for speed, economy or resource limitations), second-moment (Reynolds-stress) closures and rationally simplified versions thereof can offer sufficient sensitivity and receptivity to inherent (absolute and convective) instabilities to capture the most salient unsteady features. These include laminar-to-turbulent transition induced by separation and/or body force, in flows with strong internal forcing. Capturing such flows is commonly regarded as inaccessible to RANS.

9.3.1 Flow modulation

In order to unravel some of the intricacies of applying the URANS strategy to separated flows, Palkin *et al.* (2016) assessed the performance of two wall-integration (WIN) RANS closure levels: the linear elliptic-relaxation eddy-viscosity $\zeta - f$ model (EVM), (§7.4.4), and the second-moment HJ model (RSM §6.4.1), in a canonical, zero-turbulence flow normal to an infinite cylinder, with reference to their LES data and the available DNS and experiments for $\mathrm{Re} = 3.9 \times 10^3$ and 1.4×10^5. Both the Reynolds numbers fall within the sub-critical regime with laminar separation. A particular challenge for URANS (and a sensitive performance indicator) is the well-known low-frequency flow modulation, detected experimentally and by DNS and LES in flows separating from bluff bodies, but also in many other periodic flows, such as in internal combustion engines. The modulation, repetitive at irregular time intervals, thus with its own time scale, and with a varying amplitude, has been detected not only in the detailed dynamics of the flow (separation location, the size and shape of the recirculation zone), but also in its integral parameters. The latter is illustrated in Fig. 9.2 by the time records of the drag (C_D) and lift (C_L) coefficients behind a cylinder, obtained from *a posteriori* processing of the LES results. Palkin *et al.* found that while both models satisfactorily predict the dominant frequency of vortex shedding (the Strouhal number,

https://doi.org/10.1017/9781108875400.011 Published online by Cambridge University Press

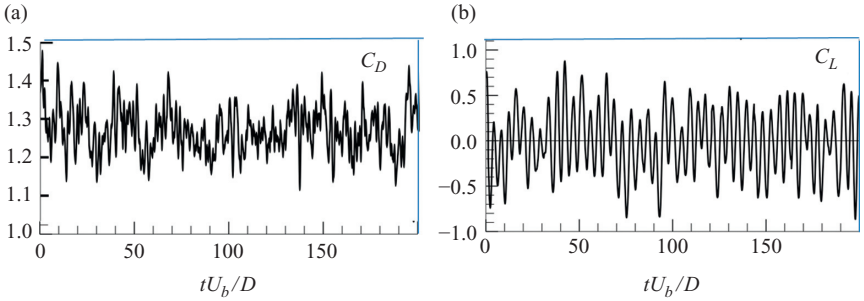

Fig. 9.2 Time records of the drag (C_D) and lift (C_L) coefficients on an infinite cylinder in a sub-critical cross-flow at Re $= 1.4 \times 10^5$ from LES, both revealing low-frequency modulations. From Palkin *et al.* (2016). Reprinted by permission from Springer Nature.

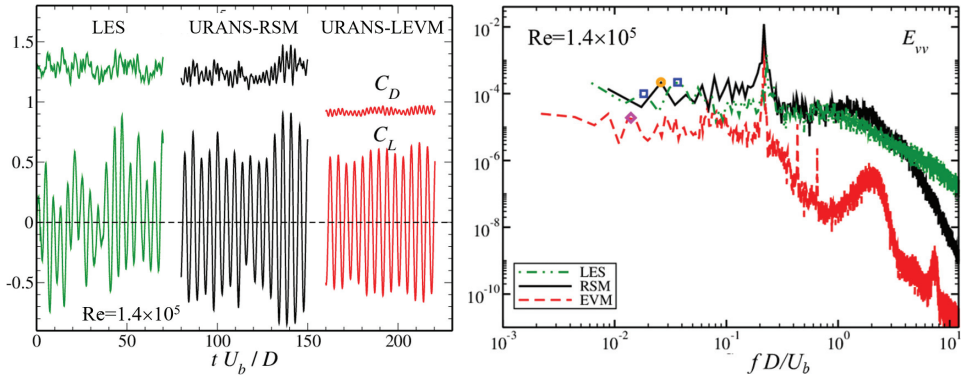

Fig. 9.3 Left: Portions of the time record of the drag (C_D) and lift (C_L) coefficients from LES and URANS (RSM and EVM) at Re $= 1.4 \times 10^5$. Right: power spectra of flow-normal velocity at $x/D = 0.71$, $y/D = 0.66$. From Palkin *et al.* (2016). Reprinted by permission from Springer Nature.

Sr $= 0.217$), the low-frequency modulations are reproduced only by the RSM, Fig. 9.3 (left), which also predicts the power spectrum in much closer agreement with the LES than achieved with the EVM, Fig. 9.3 (right).

9.3.2 *Modelled, resolved and mixed second-moments:* **a posteriori** *evaluation from LES*

We consider again the general momentum equation for unsteady turbulent flows, Eq. (9.2), derived by implementing the triple decomposition of the instantaneous velocity, Eq. (9.3), but now for the *conditional* phase-average velocity $\widetilde{U}_i$ defined as the ensemble average at a particular phase of the structure:

https://doi.org/10.1017/9781108875400.011 Published online by Cambridge University Press

$$\widetilde{U}\,(x_i, t) = \lim_{N\to\infty} \frac{1}{N} \sum_{n=1}^{N} U(x_i, t + t_n). \tag{9.7}$$

Here t is the time of the reference phase and t_n is the instant of occurrence of a characteristic repeatable ensemble pattern or event. (In a regular, periodic flow, $t_n = n\tau_p$, τ_p being the time period, and Eq. (9.7) then reduces to the strictly periodic phase averaging, defined by Eq. (2.8).)

With a focus on the stress term, Eq. (9.2) is recast as:

$$\frac{D\widetilde{U}_i}{Dt} = \cdots - \frac{\partial}{\partial x_j}\left(\underbrace{\widetilde{\widetilde{U}_i\widetilde{U}_j} - \widetilde{U}_i\widetilde{U}_j}_{L_{ij}} + \underbrace{\widetilde{\widetilde{U}_i u_j^s} + \widetilde{\widetilde{U}_j u_i^s}}_{C_{ij}} + \underbrace{\widetilde{u_i^s u_j^s}}_{R_{ij}} \right) \tag{9.8}$$

where, by analogy with LES practice, the five constituents of the stress tensor are grouped into the three terms labelled the Leonard stress, L_{ij}, the cross (or mixed) stress, C_{ij}, and the stochastic Reynolds stress R_{ij}.

Replacing the phase-average velocity by the sum of its components, $\widetilde{U}_i = \overline{U_i} + u_i^c$, and omitting the correlations involving the mean velocity $\overline{U}_i$, the terms L_{ij} and C_{ij} can be recast in terms of the periodic (coherent) and stochastic velocity, i.e.

$$L_{ij} = \widetilde{\widetilde{U}_i\widetilde{U}_j} - \widetilde{U}_i\widetilde{U}_j = \widetilde{u_i^c u_j^c} - u_i^c u_j^c;\;\; C_{ij} = \widetilde{\widetilde{U}_i u_j^s} + \widetilde{\widetilde{U}_j u_i^s} = \widetilde{u_i^c u_j^s} - \widetilde{u_i^s u_j^c}. \tag{9.9}$$

In the usual URANS approach it is presumed that $L_{ij} = C_{ij} = 0$ and Eq. (9.8) is closed by a RANS model for R_{ij} and solved for the time-dependent $\widetilde{U}_i$. Subject to sensitivity of the applied RANS model to flow instabilities, the solution in unsteady mode may be expected to resolve the large-scale coherent structures and thus to generate itself the coherent stress. It is this *resolved* contribution which, in principle, justifies the application of 3D URANS in complex flows irrespective of the true nature (or interpretation) of the distinct (quasi-)deterministic large-scale motion, whether considered as a mode of mean motion or as coherent turbulent structures. However, the trustworthiness of the solutions will depend, in addition to the choice of numerical scheme, greatly on the model for R_{ij}. As will be shown below, in the flow over a cylinder, the appropriate ratio of the resolved and modelled stresses is particularly important for correctly reproducing via URANS the initial turbulence levels in the shear layer right after the laminar separation.

To provide some verification of the above common URANS practice, Palkin *et al.* (2016) made a quantitative evaluation of the magnitude of the unaccounted terms compared with the total Reynolds stresses in the above flow over a cylinder using the well-resolved LES data; what matters in the end are the time-averaged values. The 'total' (RANS) Reynolds-stress tensor can now be written as:

https://doi.org/10.1017/9781108875400.011 Published online by Cambridge University Press

$$\overline{U_i U_j} - \overline{U_i}\,\overline{U_j} = \overline{u_i^c u_j^c} + \left(\overline{u_i^c u_j^s} + \overline{u_i^s u_j^c}\right) + \overline{u_i^s u_j^s} \tag{9.10}$$

where, as noted above, the first term on the right-hand side comes from the resolved URANS solution, while the last term is provided by the model. The mixed terms, intractable using a RANS approach, are disregarded in the literature, considered negligible due to scale separation, with little or no discussion of their importance or relevance.

The *a posteriori* processing of the LES data was carried out from conditional averaging of the LES signal by adopting a well-defined characteristic periodic state when the lift force (or the lift coefficient C_L) is minimum or zero, though any other identifiable state or event could have been used. Note, however, that because of flow modulation, the local minimum and maximum values of C_L vary from phase to phase. Also, the time elapse between periods is not constant, though the variation is only minor.

Figure 9.4 compares the coherent, stochastic and cross-correlations $\widetilde{u_i^c u_j^c}$, $\widetilde{u_i^s u_j^s}$ and $\widetilde{u_i^c u_j^s}$ normalized with the inflow velocity U_∞ for two Reynolds numbers. The coherent and stochastic parts are extracted from LES data using conditional averaging based on the trigger value of the lift coefficient, C_L, and then the cross-correlations are computed. The modelled sub-grid-scale stresses are not accounted for in $\widetilde{u_i^s u_j^s}$ as they are negligible for $\mathrm{Re} = 3.9 \times 10^3$ and also not significant for $\mathrm{Re} = 1.4 \times 10^5$.

As shown in Fig. 9.4, the non-dimensional correlations $\widetilde{u_i^c u_j^c}$ for the two Reynolds numbers have very similar amplitudes and spatial distributions. In contrast, the $\widetilde{u_i^s u_j^s}$ stress is considerably higher at high Re with the peak values moving closer to the cylinder as the recirculation bubble shrinks. Very similar non-dimensional coherent and stochastic stresses are recovered from the experimental data of Cantwell and Coles (1983).

Interestingly, the cross-term, $\widetilde{u_i^c u_j^s}$, although significantly smaller than the stochastic stress, $\widetilde{u_i^s u_j^s}$, reaches up to 30% of its (stochastic) values at some locations for the lower Reynolds number. However, for the case at higher Re, the ratio of the peak value of $\widetilde{u_i^c u_j^s}/\widetilde{u_i^s u_j^s}$ is around 5%, thus indicating a progressive decrease with increase in Re, arguably justifying the neglect of the mixed correlations for high-Reynolds-number flows. The percentage would be even smaller at high Re if the stochastic fluctuations appearing in the denominator had included the sub-grid-scale contribution.

The above LES-like scrutiny of the stress constituents provides at least some justification for the application of the standard URANS approach with its commonly applied assumptions not only for computing high-Reynolds-number vortex shedding over bluff bodies, but also in separating flows and other cases dominated by quasi-deterministic, periodic structures. As shown, the coherent correlations, resolved by URANS, are of the same order of magnitude as the stochastic stress

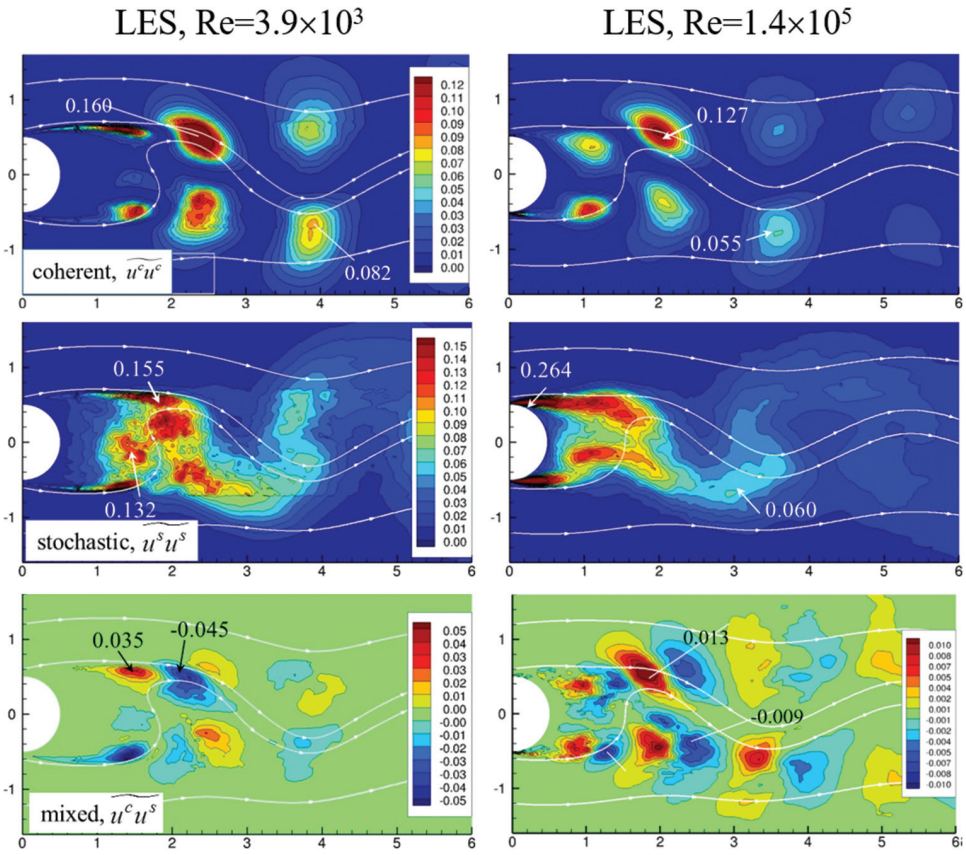

Fig. 9.4 Coherent, stochastic and mixed correlations normalized with the incoming velocity U_∞ calculated from LES averaged at a constant phase corresponding to the minimum lift force. Left: Re$= 3.9 \times 10^3$, right: Re$= 1.4 \times 10^5$. From Palkin *et al.* (2016). Reprinted by permission from Springer Nature.

provided by a RANS turbulence model. On the other hand, the mixed (cross) correlations, while non-negligible at low Re, steadily diminish relative to the stochastic ones with increasing Reynolds number and, on the whole, their omission does not undermine the URANS concept or its applicability to high-Re engineering and environmental flows. However, as shown below, the predicted flow dynamics may not accurately capture reality if the applied RANS model is too dissipative or otherwise inadequate.

9.3.3 Mean and dynamic flow properties

In flows with strong inherent instabilities, most RANS models respond to flow destabilization and reproduce unsteadiness when run in a 3D unsteady mode with a sufficiently fine computational grid. The resulting velocity field is determined

https://doi.org/10.1017/9781108875400.011 Published online by Cambridge University Press

by the total stress which, in addition to the stochastic component provided by the RANS model, also includes the contribution from the resolved large-scale structures, in the spirit of LES. However, in contrast to LES where, for a sufficiently fine numerical grid, the model of the fine sub-grid-scale stress becomes virtually uninfluential, with a URANS treatment the stochastic model is always important. Its role is not only to provide realistic stochastic (Reynolds) stresses, but also to *ensure sufficient sensitivity* to instabilities to enable the initiation and development of realistic large-scale coherent structures and, thus, the associated coherent (resolved) stress. Second-moment-closure models, because they account naturally for an anisotropic stress field and its non-coincidence in time with the strain rate, are generally more sensitive and receptive to internal instabilities and more successful in reproducing such phenomena, as shown in the URANS results considered below.

Palkin *et al.* (2016) reported a detailed comparison of mean and dynamic parameters obtained from URANS computations employing both a representative RSM and EVM, and from their own LES (as well as with other DNS, LES and experimental results from the literature). All computations were performed for a domain of $25D \times 20D \times$ (2–4)D with 13.4×10^6 cells employed for the LES over a span width of $2D$, and two coarser, typical WIN RANS grids with 3×10^6 (for $3D$) and 0.94×10^6 cells (for $4D$) for the RSM and EVM. Without going into fine-scale detail, we focus on certain key features which illustrate the URANS capabilities in vortex-shedding flows and the differences in performance between the two RANS modelling levels.

First, it is noted that both models capture the flow unsteadiness for both Reynolds numbers and accurately reproduce the shedding frequency. But, as noted in Fig. 9.3, only the RSM captures the low-frequency modulations. At high Reynolds numbers, the RSM is markedly superior to the EVM showing for all significant flow parameters good agreement with the LES and experimental data. A general impression of the mean velocity field at the higher Re is given in Fig. 9.5, showing the streamwise and cross-flow velocity profiles at different locations within the wake recirculation zone. Note that the RSM results for both the fine and the coarse computational grids are quite similar, both being in closer agreement with the reference LES and experimental data than the EVM results. Some difference between the fine and coarse RSMs (the latter labelled RSMc) appears in the V-velocity profiles at $x/D = 1.3$ due to a too short bubble length returned by the RSMc.

The failure of the EVM in this case and, indeed, in similar flows can be attributed to an excessive eddy viscosity, which in turn can be traced to the inaccurate modelling of the energy exchange between the modelled (stochastic) and resolved motion. This is represented by the production of the modelled turbulent kinetic

https://doi.org/10.1017/9781108875400.011 Published online by Cambridge University Press

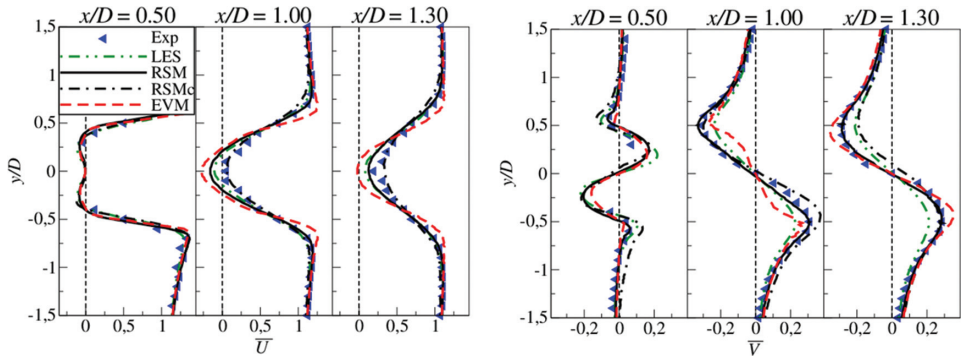

Fig. 9.5 Mean streamwise and cross-flow velocity profiles for Re $= 1.4 \times 10^5$ at different locations in the cylinder wake from LES ($13.4 \times 10^{6)}$), RSM (3.0×10^6), RSMc and EVM (0.94×10^6 cells). From Palkin *et al.* (2016). Reprinted by permission from Springer Nature.

energy, which for periodic flows for a particular phase is $\widetilde{\mathcal{P}}_k = -\widetilde{u_i u_j}(\partial \widetilde{U}_i/\partial x_j)$. In complex flows, some of the constituent terms in $\widetilde{\mathcal{P}}_k$ can be locally negative depending on the sign of the strain-rate components (especially the normal strains). Moreover, in such flows, the local stress and strain rates are usually not aligned but, in addition, in unsteady separating flows, the stress may exhibit a time lag or lead relative to the strain (Palkin *et al.*, 2016), which can further reduce the value of their product and thus their contribution to $\widetilde{\mathcal{P}}_k$. Indeed, regions of very low and even negative production $\widetilde{\mathcal{P}}_k$ have been detected in many flows, including the flow over a cylinder considered here (Franke *et al.*, 1989). But, as noted earlier (§1.3, §7.4.2), linear eddy-viscosity models, by virtue of their constitutive equation, always produce unconditionally positive production. Even if the turbulence energy production in a particular complex flow is never actually negative, modelling the flow with an EVM often leads to excessive and unrealistic production rates. In contrast, with the RSM computation, the exact definition of $\widetilde{\mathcal{P}}_k$ reproduces accurately the energy exchange between the stochastic and resolved fields and thus has a clear advantage, especially in capturing the initial stages in the development of internal instabilities. That is the key to capturing the consequent flow development and its dynamics!

The accurate modelling of the kinetic energy production is also very important for reproducing the growth rate of the turbulent kinetic energy in the initial shear layer, a feature that has proved to be crucial for the accurate prediction of separation-induced transition. It also affects the level and distribution of the kinetic energy and, consequently, the effective eddy viscosity throughout the whole flow domain. Thus, the proper capturing of the dynamics in unsteady turbulent flows depends greatly on the RANS model for the stochastic turbulence, in particular on the model's receptivity to internal instabilities. The requirements boil down

https://doi.org/10.1017/9781108875400.011 Published online by Cambridge University Press

to reproducing the proper intensity and distribution of the effective viscosity,[4] a prerequisite not only for reproducing accurately the stochastic stress, but also for generating realistic coherent structures and the associated resolved stress. A too high turbulent viscosity provided by the RANS model can supress perturbations and instabilities; that may lead to a steady solution if the internal forcing is insufficiently strong, or at least to incorrect unsteady solutions capturing only the strongest, time-smoothed, coherent structures. Such solutions have been reported in a number of EVM computations both for flow over a cylinder and for certain other flows with quasi-deterministic structures. This is especially the case when using a computational mesh that is too coarse to resolve large-scale structures (see Fig. 9.10), or a too diffusive numerical scheme (e.g. Eça *et al.*, 2014).

The above arguments are illustrated in Fig. 9.6 by comparing the modelled and resolved kinetic energy in flow over a cylinder computed by representative RSMs and EVMs. The k-ε-ζ-f elliptic-relaxation EVM, by virtue of the variable ζ, accounts partially for the near-wall stress anisotropy and models the near-wall eddy viscosity better than the standard k-ε or k-ω models in stagnation and separating flows. Nevertheless, Fig. 9.6 clearly shows that the EVM returns a much higher modelled and a lower resolved kinetic energy than the RSM, over the whole wake region.

The success of different RANS models in reproducing inherently unsteady flow features is illustrated in Fig. 9.7, which gives an impression of the vortical structures on and behind a cylinder at a selected phase at $\mathrm{Re} = 1.4 \times 10^5$, resolved by different simulation approaches. The vortex structures are visualized by the isosurfaces of the Q-criterion defined as $Q \equiv -(S_{ij}S_{ij} - W_{ij}W_{ij})/2$, where S_{ij} and W_{ij} are the strain and rotation rates.

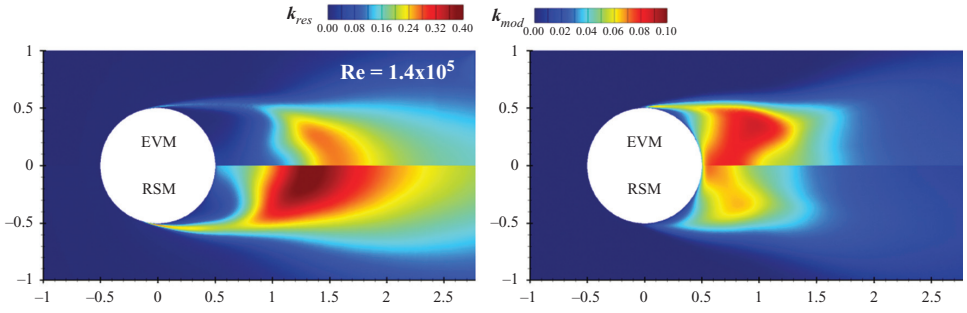

Fig. 9.6 Comparison of the resolved (left) and modelled (right) turbulent kinetic energy from the URANS models. $\mathrm{Re} = 1.4 \times 10^5$. From Palkin *et al.* (2016). Reprinted by permission from Springer Nature.

[4] Recall that, in the elliptic-relaxation linear EVM applied here, the eddy viscosity is defined as $\nu_t = c'_\mu \zeta k^2/\varepsilon$, whereas the RSM 'effective' eddy viscosity is evaluated from $\nu_t = \mathcal{P}_k/(2S_{ij}S_{ij})$.

https://doi.org/10.1017/9781108875400.011 Published online by Cambridge University Press

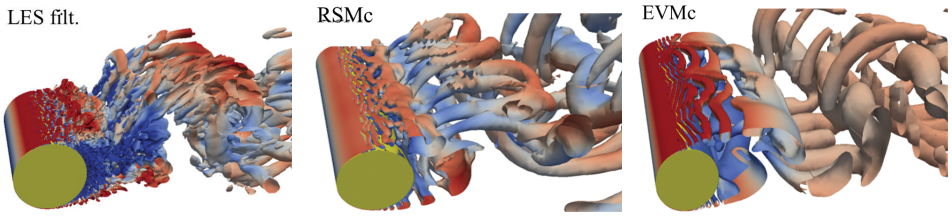

Fig. 9.7 Comparison of vortical structures educted by isosurfaces of $Q = 0.5$ coloured by axial velocity at $\mathrm{Re} = 1.4 \times 10^5$. Left: LES filtered to the RANS mesh; centre: RSM, right: EVM (both for the coarse grid). From Palkin *et al.* (2016). Reprinted by permission from Springer Nature.

For a fair comparison, the fine-mesh (13.4 M cells) LES results (not shown here) have been *a posteriori* filtered onto the RANS mesh of 3M cells used for the URANS solutions. All figures show similar overall structure patterns with a clear indication of the dominant shed vortices, but with varying levels of detail in their 3D evolution and embedded smaller scales. As expected, the URANS resolved fewer smaller structures than LES. However, there is also a difference in the number and size of the identifiable vortices resolved by the two methods. The Q-criterion reveals that the RSM resolved a broader spectrum, including some smaller eddies, than the EVM. This feature is also evident in the power spectrum in Fig. 9.3, right.

There is also a visible difference in the size and population density of the structures in the initial shear layer where, compared with the EVM, the RSM displayed some distinct small-scale vortices. These vortices contain energy, so their appearance is in line with the previously noted higher resolved kinetic energy in the RSM compared with that of the EVM. Thus, the lower modelled kinetic energy in the RSM is compensated by a larger resolved contribution, which makes it possible for finer structures to be resolved and identified. Their existence seems important for reproducing certain subtle dynamical features of the flow such as the low-frequency modulation of the flow as a whole.

Further insight into the capability of URANS for reproducing the subtle dynamics of separation on the cylinder and other curved surfaces is provided by a closer examination of the flow in the immediate vicinity of the cylinder upstream of the separation-induced transition. As indicated in the previous section, the correct reproduction of this region is important for the accurate prediction of the length of the recirculation bubble and, consequently, of the flow as a whole. As shown in Fig. 9.8 (left), the LES reveals the formation of near-wall eddy structures that roll up on the wall surface to form an array of vortical structures embedded in the initial phase of the separation shear layer, resulting in multiple local separations and reattachments. Figure 9.8 (right) shows that the RSM resolved this feature rather well,

https://doi.org/10.1017/9781108875400.011 Published online by Cambridge University Press

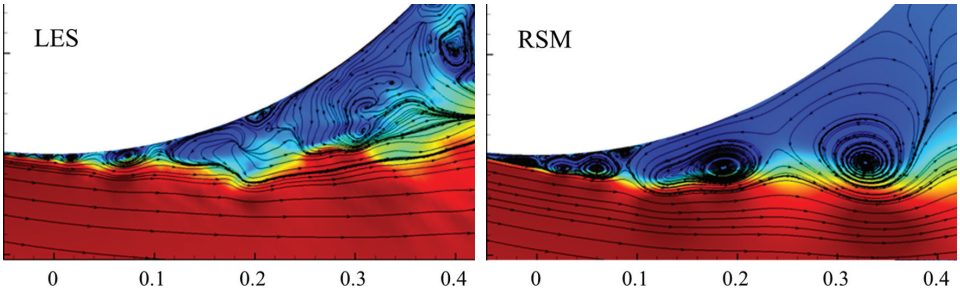

Fig. 9.8 A blow-up of the instantaneous streamlines after flow separation on the cylinder. Obtained from LES and URANS-RSM at the same phase based on the lift coefficient. From Palkin *et al.* (2016). Reprinted by permission from Springer Nature.

reproducing wall vortices, their growth and the associated periodic variation of the angle of separation/reattachment (for details see Palkin *et al.*, 2016). In contrast, the linear EVM (not shown) failed to resolve this process due to its strong diffusivity and consequent insensitivity to inherent instabilities, resulting in a notable absence of small-scale near-wall structures.

9.3.4 A note on the URANS prediction of separation-induced laminar-to-turbulent transition

The comparison above shows that, for successful URANS computations of the flow around a cylinder in cross-flow in the sub-critical regime, it is crucial to reproduce the origin of the laminar-turbulent transition and the rate of turbulence growth in the initial shear layer. As is well known, no RANS model can predict natural transition through all its stages in smooth, non-separating flows without sufficiently strong externally imposed perturbations or inflow turbulence. However, contrary to most EVMs, the low-Re RSM employed in the above computations had been shown earlier to reproduce accurately a number of cases of by-pass and separation-induced transition without any artificial triggering or use of integral flow parameters or any inflow turbulence (Hadžić and Hanjalić, 1999). The success can be attributed to the low 'effective' viscosity generated by the RSM, which, in contrast to an EVM, enables the laminar separating shear to respond strongly to instabilities, more or less in a natural manner similar to an LES.[5] This is clearly seen in Fig. 9.8, which shows the shear layer instability, the formation of

[5] Both RANS models applied here account for purely viscous and related near-wall effects. The EVM does that by imposing the Kolmogorov scale as the lower scale bound, which is known to be insufficient for treating transitional flows. The RSM does that in a more comprehensive, though still semi-empirical way, using model-adapting functions in terms of the turbulent Reynolds number and the stress and dissipation-rate anisotropy invariants (Jakirlić and Hanjalić, 2002).

https://doi.org/10.1017/9781108875400.011 Published online by Cambridge University Press

the subsequent vortices and transition to 3D turbulence closely in accord with the LES on a much finer mesh.

It is also confirmed by good agreement of the energy spectra of the resolved motion for values of the Strouhal number, Sr, up to Sr $\sim$ 5.0, though with some mild overshooting in the RSM spectrum around Sr $\sim$ 1.0−2.0 (Fig. 9.3). Of course, the numerical resolution also plays a role, especially in locating the separation and the subsequent rapid spread of turbulence through the shear layer. At and immediately after the point of separation the turbulence model is dormant, the flow being non-turbulent.

However, as noted above, the RSM shows the development of instability akin to that in LES (Fig. 9.8). An initial, temporarily imposed 'background' turbulence triggers the turbulence model in the shear layer and transition follows (and the background turbulence is then removed). While the results do not necessarily imply that the unsteady RSM applied here reproduces the real and complete transition mechanism, the instantaneous velocity field does not look unrealistic and is not very different from that obtained by LES. This result supports the claim that a sensitive and receptive URANS model can be applied to reproduce the separation-induced transition as encountered in flows over bluff bodies at sub-critical Reynolds numbers.

9.4 URANS modelling of swirling flows and vortex precessing

A class of flows where the URANS approach has been broadly seen as a viable option is swirling flows in hydraulic turbomachinery, especially for the analysis of operation under off-design and transient conditions. The increasing proportion of intermittent wind and solar power in electricity generation brings into focus the flexibility of operation and rapid load-adjustment capability of the load-smoothing hydropower plants over a wide range of operating conditions. Under such operation, however, the hydrodynamic instabilities in hydropower systems can cause not only a loss of efficiency but also, more importantly, mechanical damage, material fatigue and, ultimately, system failure. The intrinsic unsteadiness of swirling flows in the diffusor (or 'draft tube') behind the turbine impeller at suboptimal conditions often leads to the formation of complex unsteady vortical structures, characterized by a vortex breakdown and a precessing vortex core which causes intense pressure pulsations and vibrations of the turbine rotor, posing a serious threat to the system reliability and safety.

While the subtleties of unsteady flow physics in turbine components can best be captured by properly resolved LES (or hybrid LES-RANS), because of the high Reynolds numbers and complex geometry of fluid passages, the (U)RANS approach still prevails in design, analysis and optimization of the operating conditions, especially when considering the whole turbine installation. However, as in

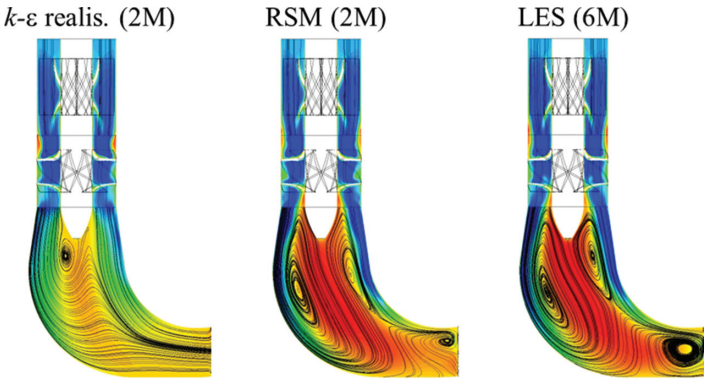

Fig. 9.9 Time-averaged streamlines coloured by axial velocity magnitude in a laboratory model of a Kaplan hydroturbine in an off-design regime (a load of 40% of the best efficiency point, BEP). Note that the circular cross-section evolves into rectangular at the exit of the draft-tube bend. From Minakov *et al.* (2017). Reprinted by permission of the publisher (Taylor & Francis, Ltd, www.tandfonline.com).

other complex flows, the choice of an adequate RANS model poses a challenge. In §4.3.8 and §6.4.1, it was shown that in contrast to a second-moment closure the standard k-ε and other popular linear EVMs fail to reproduce the basic features of several generic swirling flows even for steady and stable conditions. As shown below, the same conclusions emerge when the goal is to capture the internal flow unsteadiness and its dynamics in flows arising in hydroturbines and other devices with strongly swirling motion.

We note first that the flow in hydroturbines is characterized by different physical phenomena from those in flows separating from bluff bodies considered in §9.3. Under off-design conditions the flow usually separates from the turbine cone with the formation of a recirculation zone in the cone wake. However, the dominant effects come from the runner's rotation resulting in a strong swirl behind it. The resultant flow is largely governed by the pressure field and radial force balance determined by the ratio of the circumferential and axial flow momentum, usually characterized in term of the swirl number S_w. A stable swirl at a low S_w will destabilize and become unsteady in otherwise stationary flows when S_w increases beyond the threshold value for vortex breakdown to occur ($S_w \sim$ 05–0.6). Especially critical and challenging for a URANS simulation are the conditions when the swirl breaks down and evolves into unsteady, precessing, single or multiple helical vortices (Litvinov *et al.*, 2018).

As an illustration of the potential and limitations of URANS applications to this class of flows, we show some results of computations of flow in the draft tube of a laboratory model of a Kaplan hydroturbine at a part load of 40% of the design flow rate, reported by Minakov *et al.* (2017). Two linear EVMs and the Basic SMC

https://doi.org/10.1017/9781108875400.011 Published online by Cambridge University Press

from §4.3 were used, all on 2M and 6M grids.[6] The results were compared with LES on 6M and 19M grids and dedicated experiments. Figures 9.9–9.12 illustrate the major findings.

First, a general impression of the capabilities of the tested models to reproduce the bulk flow may be drawn from Fig. 9.9, which shows the time-averaged streamline patterns and the intensity of the axial velocity denoted by colour shades. The EVMs on a typical RANS grid of 2M nodes predicts the flow incorrectly, whereas the RSM on the same 2M grid and LES on 6M give very similar results in accord with observations. This is further substantiated by a quantitative comparison with the experiments, Fig. 9.11.

It is recalled that precession of the vortex core occurs under part load when the flow has a considerable residual swirl. Vortex breakdown in such a flow leads to the formation of a free recirculation zone at the flow axis and rotation of the corkscrew-shaped vortex ropes (often visible by local evaporation and/or dissolved air) around it. Figure 9.10 shows selected snapshots of the typical twin vortex ropes downstream from the impeller, captured by different models and compared with the experimental visualization of Skripkin *et al.* (2016).[7] The ropes in Fig. 9.10, consisting of two precessing helical vortices with somewhat different frequencies, are identified by the instantaneous isosurfaces of selected values of pressure.

As seen in Fig. 9.10(a) and (b), the LES and experiments show strikingly similar vortex structures in the form of a twin corkscrew rope. The formation of these structures influences the whole flow field, creating a strong back-flow in the central region of the draft tube as indicated by the mean axial velocity profiles in Fig. 9.11. It is interesting that the Basic RSM captures the vortex pattern reasonably well, albeit with smoothed fine-scale structures, Fig. 9.10(c). However, the EVM URANS computations on a 2M grid (not shown) did not maintain an unsteady solution, though they did so on a finer grid of 6M nodes, resulting in somewhat improved mean-flow patterns, but still failing to capture the multiple helices and the associated pressure pulsations. Specifically, despite resolving the unsteadiness, neither of the tested EVM URANS treatments – even on the 6M grid – reproduced the twin-rope structure, as seen in Fig. 9.10(d) and (e). The k-ε realizable model returns a single thick vortical bulb (Fig. 9.10 (d)), and the SST model (Fig. 9.10(e)) gives only a hint of a possible double vortex initiation, but with only one, irregularly shaped structure with no indication of a spiralling helix.

Profiles of the mean axial and tangential velocity components on a cross-section immediately behind the turbine cone in Fig. 9.11 provide quantitative information

[6] The realizable $k-\epsilon$ and the $k-\omega$ SST EVMs were considered as well as the detached eddy simulations (discussed in Chapter 10) based on the SST model (DES SST).

[7] The inflow conditions to the draft tube were generated from a precursor computation of the flow in the turbine in a rotating reference frame by what is known as the 'frozen rotor' method.

https://doi.org/10.1017/9781108875400.011 Published online by Cambridge University Press

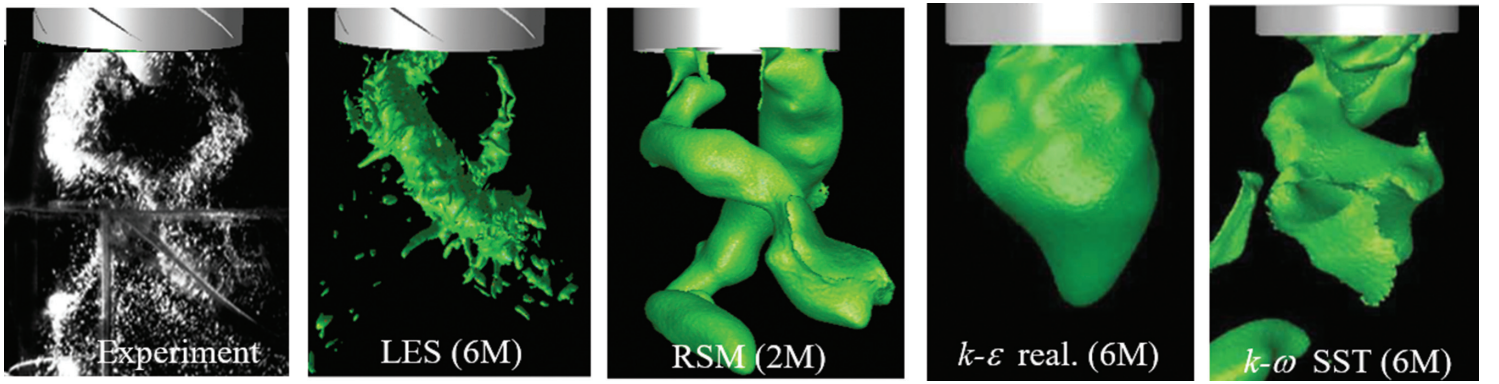

Fig. 9.10 Twin vortex ropes in the draft tube of a laboratory model of a Kaplan hydroturbine at low load (as in Fig. 9.9), computed by LES and URANS-RSM and two EVMs, with meshes of 2M and 6M cells. Note: the EVMs reproduced unsteadiness only on themuch finer (6M) mesh. From Minakov *et al.* (2017). Reprinted by permission of the publisher (Taylor & Francis, Ltd, www.tandfonline.com).

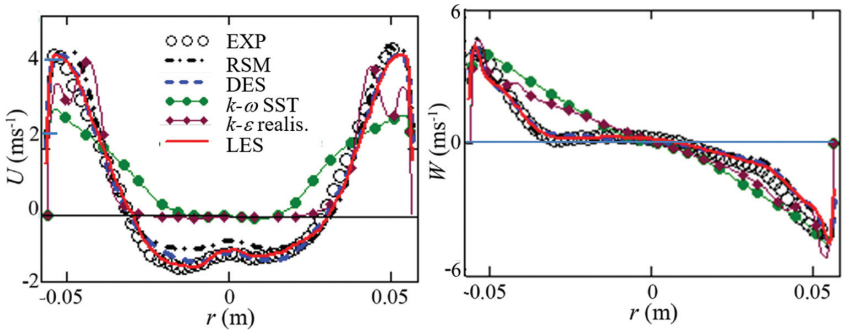

Fig. 9.11 Axial (left) and tangential (right) mean velocity profiles on a draft-tube cross-section right behind the rotor cone, obtained by different turbulence models. Grids: URANS and DES: 2M; LES: 6M. From Minakov *et al.* (2017). Reprinted by permission of the publisher (Taylor & Francis, Ltd, www.tandfonline.com).

about the flow field captured by different models. As shown, the RSM and DES[8] (both on a 2M grid) and LES (on a 6M grid) reproduced the experimental data very well for both velocity components. In contrast, both EVMs notably fail, as shown by typical (inappropriate) solid-body-rotation profiles of the tangential velocity, as well as unrealistic distributions of the axial velocity. The latter, being positive over the entire cross-section, indicates the absence of any recirculation in striking disagreement with the experiments.

Minakov *et al.* (2017) also presented the profiles of the turbulent kinetic energy (not shown here), as a sum of the (much larger) resolved and the (smaller but important) modelled contributions. Again, the RSM showed notably closer agreement with experiments and LES than the two EVMs, in accord with the findings on vortex shedding behind a cylinder discussed in §9.3.

The most important outcome from the formation of the precessing helical ropes is the pressure pulsations in the draft tube that propagate throughout the whole turbine and its system. In practice, it is important to know the character and parameters of the pressure pulsations – their intensity (especially their maximum amplitude) and frequency. The experimental pressure recordings are obtained from measurements at a discrete point on a cross-section roughly half-way down the turbine cone, flush-mounted with the interior wall surface. Figure 9.12 compares the calculated and measured pressure time records (left) and the frequency spectra (right). The LES results on the 6M grid and the RSM (as well as the DES, not shown here) on a 2M grid return the experimentally recorded character of pulsations rather well, with two slightly different characteristic frequencies identifiable (at about 14 and 17 Hz) corresponding to the two ropes, and the maximum peak-to-peak amplitudes of about 10 Pa. The LES signal is very close to the

[8] Detached Eddy Simulation. A detailed coverage of this and other hybrid RANS-LES modelling strategies appears in Chapter 10.

https://doi.org/10.1017/9781108875400.011 Published online by Cambridge University Press

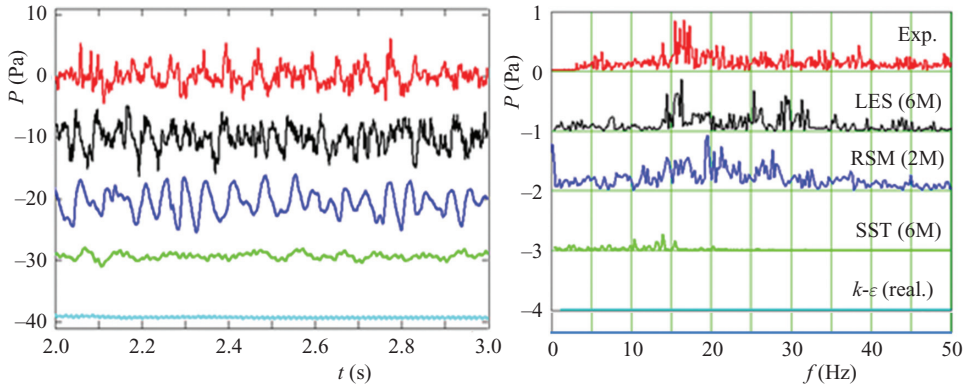

Fig. 9.12 Time variation (left) and spectra (right) of pressure pulsation recorded on the draft tube wall at the same cross-section as in Fig. 9.11. The vertical scale corresponds to the experiments; other curves shifted down in steps of 10 and 1.0 Pa, respectively. From Minakov *et al.* (2017). Reprinted by permission of the publisher (Taylor & Francis, Ltd, www.tandfonline.com).

experimental one with almost identical peak-to-peak amplitudes. The RSM also reproduces the pulsations very well, though showing a somewhat smoother record, but with almost the same amplitude maxima. In contrast, the EVMs on a finer grid (6 M), despite capturing some unsteadiness, showed only very mild pressure variations with a grossly underestimated intensity. Interestingly, neither the experiment nor any of the computations detected the frequency corresponding to the impeller blades' rotation speed of 40.5 Hz.

In summary, the results shown above provide considerable evidence that the RSM, even at the basic level (i.e. the linear model of the pressure-strain correlation, §4.3), is sufficiently sensitive to the strong flow unsteadiness associated with the vortex ropes and precessing vortex cores and can be used to estimate the level of the pressure pulsations in the hydroturbine draft tubes. Admittedly, for low Reynolds numbers, as in the laboratory model examined above, and focusing only on the draft tube, LES and, especially, hybrid RANS-LES schemes, such as DES, could be affordable and computationally even more accurate than the RSM. But the real advantage of URANS emerges when targeting real-scale applications at much higher Reynolds numbers and in complex configurations. One should keep in mind, however, that, in general, capturing unsteadiness with a URANS approach depends on the intensity of the internal instabilities, the strength of the forcing (often provided by a body force), and on the type of RANS model used, as well as on the discretization scheme, grid resolution and time-step adopted.

9.5 Capabilities of EVMs and ASM/AFMs within URANS

The previous sections have revealed gross failures of linear eddy-viscosity-type models (including some improved versions such as the realizable k-ε, the SST-k-ω

https://doi.org/10.1017/9781108875400.011 Published online by Cambridge University Press

and the elliptic-relaxation k-ε-ζ-f) when applied in unsteady mode to flows dominated by large-scale vortical structures. Chapter 7, on the other hand, has confirmed that turbulence models simpler than complete second-moment closure can lead to satisfactory predictions of a diversity of turbulent flows. However, the range of flows over which the simpler models are appropriate progressively reduces as each successive level of simplification is applied. In the case of linear eddy-viscosity models the range is narrowed to two-dimensional flows (or weakly three-dimensional flows driven by pressure gradients) where transport and force-field effects on the second-moments are unimportant. Moreover, all cases were considered stationary and computed by solving the equations in steady-state mode even though some of the flows may have had hidden internal unsteadiness and periodic deterministic structures. The question thus arises whether such simplified models, resolved in a URANS framework, might still perform successfully in flows with some internal unsteadiness where steady solutions with the same model fail.

To conclude this chapter, a brief outline is provided of some flow classes where linear eddy-viscosity models and other truncated second-moment closures return acceptably accurate simulations of highly complex flows that would ordinarily be seen as outside the scope of EVMs and, in some cases, beyond the capabilities of steady-state RANS resolution.

EVMs applied to separated flows

The earliest examples of forerunners of the URANS approach appeared in the papers by Celenligil and Mellor (1985), Ha Minh and Kourta (1993) and Johansson *et al.* (1993). The first two examined the steady flow behind (different) backward-facing steps but resolved the flow in a time-dependent manner. The former adopted a rudimentary second-moment closure, while the latter employed a linear k-ε EVM. Both sets of computational results showed that a succession of roller eddies were shed from the lip of the step which lengthened the mean reattachment length (compared with a strictly steady-flow computation) to values close to those measured. In the case of the k-ε computations, however, this desirable outcome was only achieved by reducing the coefficient, c_μ, from its conventional value of 0.09 to 0.02.[9] Moreover, while both these studies treated the momentum equations as unsteady, the flow was still handled as though it were two-dimensional (no momentum equation was solved in the direction parallel to the step), so there was no scope for stretching or bending of the shed vortices to occur. A similar approach was taken by Kato and Launder (1993) to study the vibration of a square-sectioned bridge spar induced by the wind flowing normal to it and the associated vortex shedding on the downwind side. As noted in §7.4.3, they modified the turbulence

[9] Of course, the model, thus adjusted, would then evidently give very poor predictions for turbulent flows not dominated by such deterministic structures such as channel flow.

https://doi.org/10.1017/9781108875400.011 Published online by Cambridge University Press

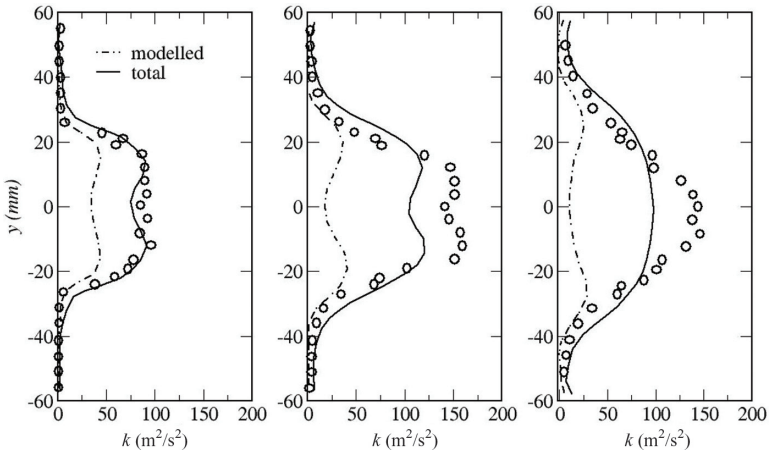

Fig. 9.13 Turbulent kinetic energy (modelled and total) behind a triangular cylinder. Symbols: experiments, lines: computations with URANS $k-\varepsilon$+WF. Adapted from Johansson *et al.* (1993).

energy production term in the standard k-ε EVM by replacing the square of the strain-rate tensor ($S_{ij}S_{ij}$) by the product of the strain and vorticity tensors ($S_{ij}W_{ij}$). This avoided the spurious excessive k-levels around the front stagnation point of the beam (since the flow there was essentially irrotational) which would have grossly attenuated the vortex street shed on the downstream side. The study found that, over a limited range, the vortex-shedding frequency 'locked-on' to the natural frequency of the spar, while the onset of 'galloping' oscillations was broadly in accord with experiment.

A further two-dimensional unsteady computation of flow normal to a triangular cylinder (a 'flameholder') by Johansson *et al.* (1993) using the standard k-ε model (with the standard value for c_μ) appeared more successful. The periodic vortex shedding and the mean velocity in the wake was in almost as good agreement with the experimental data as those reported later by Durbin (1995) with the more elaborate $\overline{v^2} - f$ model. Johansson *et al*. also showed, probably for the first time, tolerably good agreement between the measured and computed time-averaged turbulent kinetic energy after adding the (significantly larger) computed periodic component to the stochastic part obtained from the turbulence model, Fig. 9.13.

The successful performance of the standard k-ε model for this flameholder example (with just a two-dimensional computation) is initially surprising. It sharply contrasts with its notable failure in flow around a circular cylinder discussed in §9.3. There are, however, important differences. First, in flows around a triangular cylinder (or other sharp-edged body) the separation points (or lines) are fixed and symmetrical, whereas in flows over shaped bodies with a curved rear

https://doi.org/10.1017/9781108875400.011 Published online by Cambridge University Press

surface such as a cylinder, the separation location periodically moves over the body surface and its dynamic behaviour is very dependent on the inflow conditions as shown in Fig. 9.8. Second, in the flameholder flow, the incoming flow is turbulent with a relatively high imposed turbulence intensity (5%), whereas in the case examined earlier of flow around a cylinder, the incoming flow was non-turbulent and subject to transition in the shear layer behind the body, as shown in Fig. 9.8 and discussed in §9.3.4.

One should note, however, that both the flows considered above are unconfined. The presence of a solid wall in the close vicinity of (or even attached to) a bluff body, such as flows over a backward- or forward-facing steps, wall-mounted objects or similar configurations, will inevitably tend to suppress the separation-induced instabilities, posing challenges to URANS predictions even when using more advanced RANS models.

The first fully three-dimensional URANS explorations were those of Tatsumi *et al.* (1999) and Kenjereš and Hanjalić (1999), the former examining a backward-facing-step flow using the cubic NLEVM of Craft *et al.* (1996b) summarized in §7.3.4. In that case, as in all the examples examined later in this section, the computations have been made with precisely the model for the unresolved turbulent transport originally proposed for steady-flow applications.[10]

Rotating disc flows

The next class of flows considered comprises those formed within the narrow, enclosed cylindrical space between coaxial circular discs a short distance apart, one or both of which rotate. The flow configuration is an idealization of that which occurs in turbine-disc cavities or a stack of rotating computer discs. Conventionally, these flows have been examined assuming the flow to be steady and axisymmetric. The three-dimensional time-dependent results shown below are drawn from the computations of Zacharos (2010). The effects of the unresolved turbulence have been accounted for with the standard high-Reynolds-number k-ε EVM using the Yap correction, Eq. (5.12). Instead of resolving the low-Re sublayer, analytical wall functions (AWFs) have been used (§8.3) to enable an economical yet reasonably comprehensive modelling of the sublayer region where the mean velocity vector undergoes strong skewing.

The first example is of co-rotating discs at a spin Reynolds number of 1.46×10^5. The shroud is stationary and this induces a radially outward motion near the two rotating discs (the Ekman layer) with a return flow in the central region. Figure 9.14, left, provides a pictorial view for the case where the disc spacing is half the radius; it shows the flow surface where the circumferential velocity is half the

[10] Though, apparently for purposes of economy, the computations of Tatsumi *et al.* were made for a bulk Reynolds number less than one-fifth of that prevailing in the experiment.

https://doi.org/10.1017/9781108875400.011 Published online by Cambridge University Press

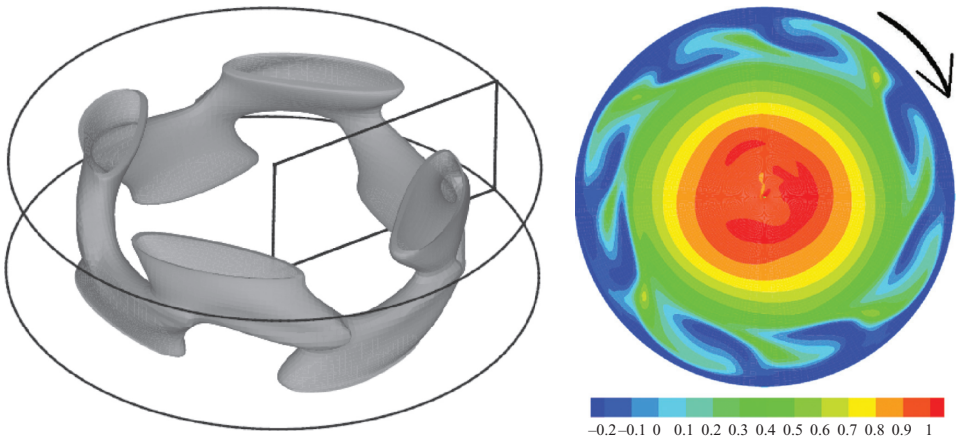

Fig. 9.14 Flow in a co-rotating disc cavity, $H/R = 0.5$, $\mathrm{Re}_\Omega = 1.46 \times 10^5$. Left: surface of circumferential velocity equal to half disc spin velocity (from Zacharos, 2010). Right: normalized axial vorticity contours on geometric symmetry plane (from Iacovides *et al.*, 2009).

disc speed. In this case, the time-dependent examination has revealed four large eddies in both the upper and lower halves of the cavity. While the flow is globally symmetric about the mid-plane, the four 'eddies' in the upper half are displaced by 45° relative to those in the lower half. The axial vorticity on the geometric symmetry plane, Fig. 9.14, right, thus exhibits eight trailing 'tails'.

Quite different large-scale structures appear in the case where one of the discs is stationary (the so-called rotor-stator cavity). The number of separate lobes in this case is known to depend on the disc spacing and the Reynolds number, Czarny *et al.* (2002), though the most commonly arising structure is a double lobe as seen in the flow visualization photograph in Fig. 9.15 (left). The vortical structure was made visible by dye, which had been carefully injected into the cavity. The three-dimensional, time-dependent calculation by Zacharos (2010) also predicts such a two-eddy form for the same values of H/R and Re_Ω (the Reynolds number based on the spin velocity of the outer rim of the disc and the disc radius). In fact, the computational contours show different levels of $k^{1/2}/\Omega R$ rather than dye concentration. The comparison is relevant, however, since the dark regions (in the left-hand figure) where the dye remains concentrated indicate areas where turbulent agitation is minimal and thus where the modelled k-levels are very low (which appear as the darkest blue zones in the right-hand figure). In fact, when the discs are brought closer and closer together, the large-scale vortices (that occupy the mid-height region between the discs) disappear and are replaced by spiral vortex structures within the near-wall radially outward and inward flowing layers near the rotating and stationary discs (the Ekman and Bødewadt layers, respectively). These very different

https://doi.org/10.1017/9781108875400.011 Published online by Cambridge University Press

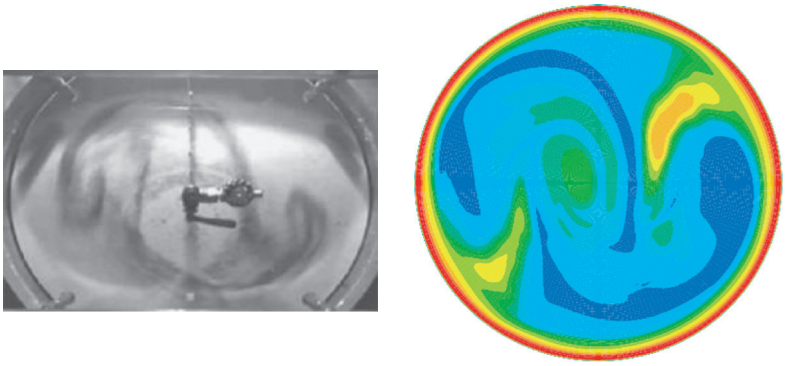

Fig. 9.15 Flow within a rotor-stator cavity. $H/R = 0.195$, $\mathrm{Re}_\Omega = 0.9 \times 10^6$. Left: streak-line flow visualization, Czarny *et al.* (2002); Right: computations showing contours of $k^{1/2}/\Omega R$, Zacharos (2010).

coherent structures are also well-resolved with precisely the same methodology, an example of which appeared in Fig. 8.10(a) in connexion with economical wall treatments.

As a third example on rotating flows, Fig. 9.16 considers the case of flow between *contra*-rotating discs, a case which is further complicated by the fact that one disc rotates at twice the speed of the other. Iacovides *et al.* (1996) had earlier examined this flow using a variety of turbulence models ranging from two-equation eddy-viscosity schemes up to second-moment closure but assuming the flow to be axisymmetric and steady. Their results achieved at best indifferent agreement with the experimental data of Gan *et al.* (1995), the greatest discrepancy occurring at $r = 0.85R$ close to the slower disc where the computed radial velocity was towards the disc centre, whereas the measurements showed an outward flow. Moreover, near the faster disc the boundary-layer thickness was more than twice as thick as measured. The flow predicted by the unsteady three-dimensional computations, Fig. 9.16a, shows major improvements in resolving the Ekman layers near each disc and, overall, a significantly closer agreement with the experiment. There were comparable improvements also in the tangential velocity profiles (not shown). Figure 9.16b provides a snapshot of the spiral flow structure present in this case near the slower moving disc (the dark and light surfaces show contours of two different values of axial velocity towards and away from the upper surface).

Buoyancy-driven flows

Kenjereš and Hanjalić (1999) (see also Hanjalić and Kenjereš, 2000, 2001) have applied the URANS concept to Rayleigh–Bénard convection where a fluid confined within infinite horizontal parallel planes is heated from below. In this case, long-term time averaging results in zero mean velocity, and the fluid motion

https://doi.org/10.1017/9781108875400.011 Published online by Cambridge University Press

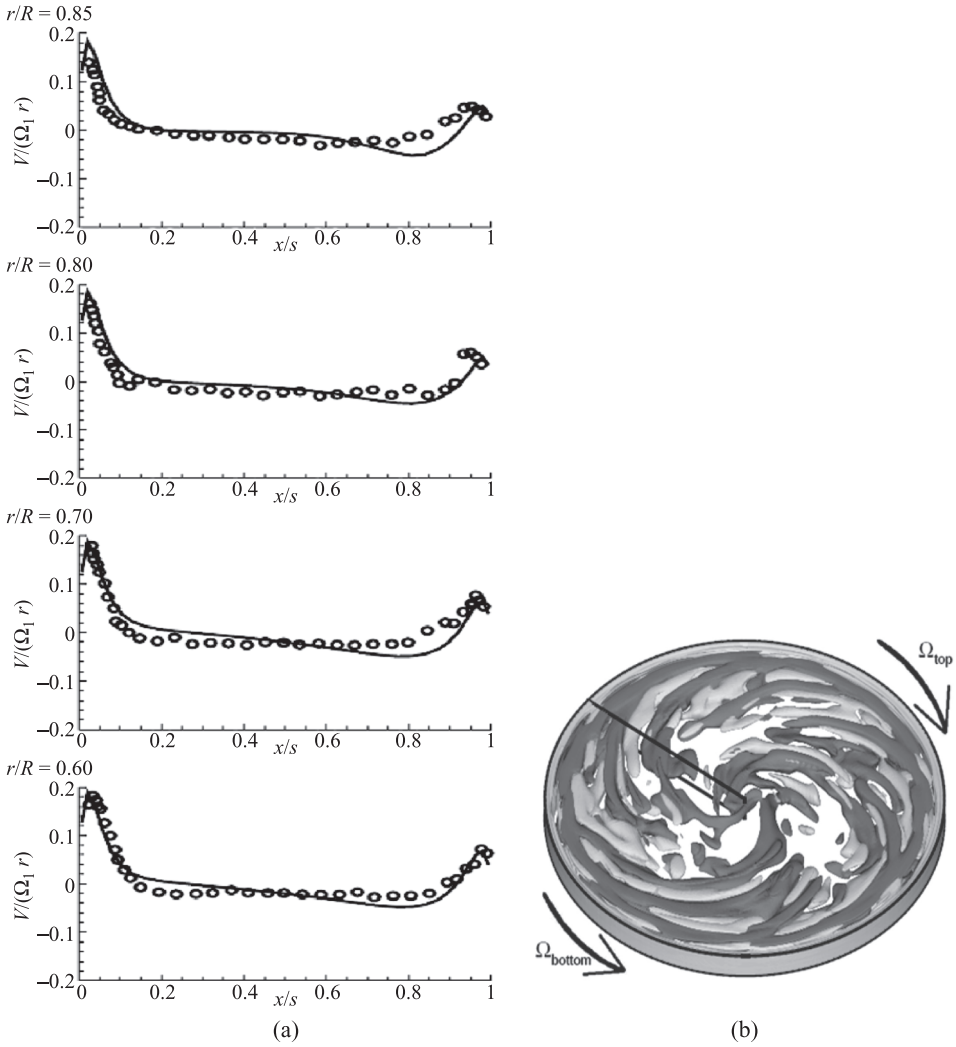

Fig. 9.16 Flow in a counter-rotating disc cavity with the faster disc (at $x/s = 0$) rotating at twice the speed of the slower disc. (a) Profiles of radial velocity at different radial locations. Symbols: experiments, Gan *et al.* (1995); —— URANS k-ε EVM with analytical wall functions, Iacovides *et al.* (2009); (b) Visualization of coherent vortex structure via isocontours of axial velocity towards and away from the slower disc with velocity $\pm 0.005\Omega_{fast}R$, Zacharos (2010).

takes the form of self-organized, unsteady convective roll structures (sometimes referred to as the 'wind'), which fill the whole flow domain and provide the mechanism for turbulent heat transport. For this reason Rayleigh–Bénard convection has always posed a challenge for conventional steady RANS solvers.[11] Later, the

[11] Though, as reported in Chapter 4, second-moment closure has been successfully applied to related mixed-layer problems.

https://doi.org/10.1017/9781108875400.011 Published online by Cambridge University Press

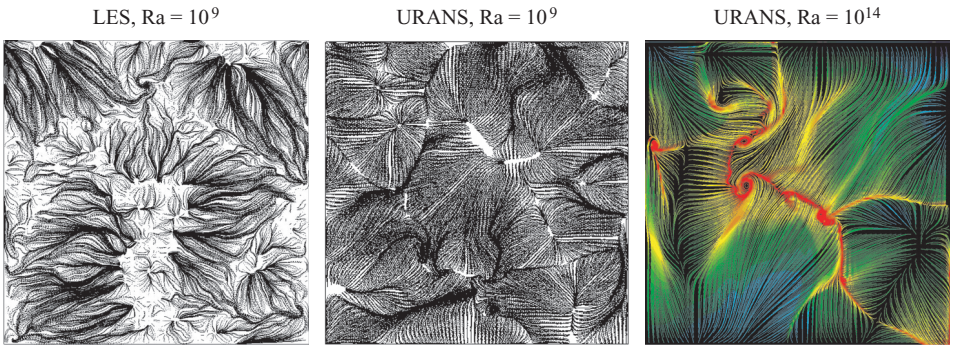

Fig. 9.17 Instantaneous streamlines in Rayleigh–Bénard convection seen on a horizontal plane very close to the bottom-heated wall, $z/D = 0.01$ (left and centre) and $z/D = 0.05$ (right) for high Ra (from Kenjereš and Hanjalić, 2006). D denotes height of computational domain.

same workers extended the approach to more general cases of thermal convection in different configurations, including the effects of a magnetic field (Hanjalić and Kenjereš, 2000, 2001, 2002), and to both indoor and external environmental flows dominated by thermal buoyancy (Kenjereš and Hanjalić, 2002; Kenjereš *et al.*, 2002). The method employs a three-dimensional time-resolved solution of the ensemble-averaged momentum and energy equations, closed by the algebraic flux model (§7.3.2, Eq. 7.12) together with the $\overline{\theta^2}$, k and ε equations (the AFM $k - \varepsilon - \overline{\theta^2}$ model) for the ensemble-averaged turbulence properties.[12]

Figure 9.17 compares the instantaneous streamlines on a horizontal plane very close to the bottom-heated wall in an open-ended 4:4:1 Rayleigh–Bénard domain obtained with a finely resolved LES ($256 \times 256 \times 128$ grid cells) and with URANS on a much coarser grid ($82 \times 82 \times 72$) for Ra $= 10^9$ (left and centre figures) (Kenjereš and Hanjalić, 2006). Of course, the patterns are not identical and, as would be expected, LES captures finer structures that are inaccessible to URANS on a coarse mesh; but the large-scale, organized structures (Bénard convective cells with bounding sheet plumes) certainly look similar. Indeed, both methods returned very similar Nusselt numbers (see Fig. 9.20), confirming that the small-scale turbulence that remains unresolved with URANS plays only a minor role in heat (and momentum) transfer. These findings provide confidence in applying the URANS approach to much higher Rayleigh numbers beyond the present reach of LES, as shown in Fig. 9.17, right, as well as to complex configurations of engineering and environmental relevance.

Figure 9.18 shows the breakdown between the resolved and stochastic (modelled) contributions, as in Eq. (9.6), to the vertical heat flux for a Rayleigh

[12] To distinguish the physical situation modelled here from situations where URANS is applied to flows where the mean-flow time scale is much longer than that for the turbulence, Kenjeres and Hanjalic labelled the approach T-RANS implying Triple-decomposition (or Time-dependent) RANS.

https://doi.org/10.1017/9781108875400.011 Published online by Cambridge University Press

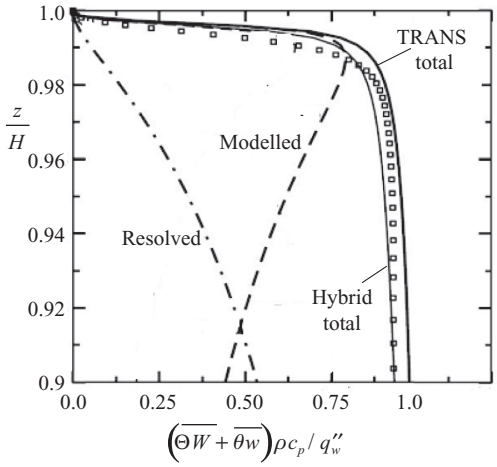

Fig. 9.18 Near-wall long-term-averaged turbulent heat flux for $\mathrm{Ra} = 10^9$ with the URANS modelled and resolved contributions, compared with the LES (Symbols) and hybrid RANS-LES simulations. From Kenjereš and Hanjalić (2006).

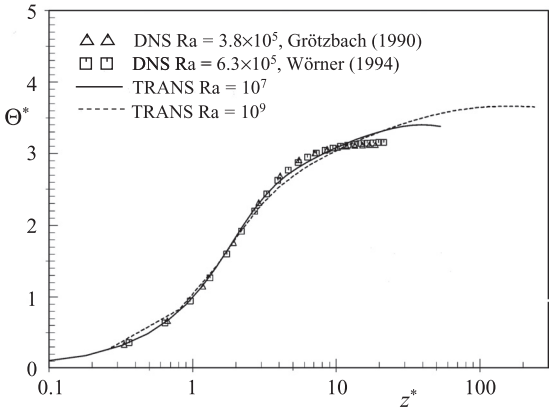

Fig. 9.19 Near-wall long-term-averaged temperature $\Theta^* = (\Theta_w - \Theta)U_q/q_w$ for RB convection at different Ra; URANS compared with DNS. From Kenjereš and Hanjalić (1999).

number of 10^9. The total turbulent heat flux thus computed agrees well with the LES (and also with a hybrid RANS-LES approach discussed in Chapter 10). The resultant time-averaged temperature $\Theta^* = (\Theta_w - \Theta)U_q/q_w$ (where $q_w = q_w''/\rho c_p$ is the bottom wall kinematic heat flux and $U_q = (\beta g q_w \alpha^2/\nu)^{1/4}$ the 'buoyancy' velocity) is plotted versus the non-dimensional height $z^* = zU_q/\alpha$ (where α is the thermal diffusivity and β the thermal expansion coefficient) in Fig. 9.19. For $\mathrm{Ra} = 10^7$ and 10^9, the two results collapse onto a single curve close to the wall in close agreement with the DNS results for $\mathrm{Ra} = 6.3 \times 10^5$.

https://doi.org/10.1017/9781108875400.011 Published online by Cambridge University Press

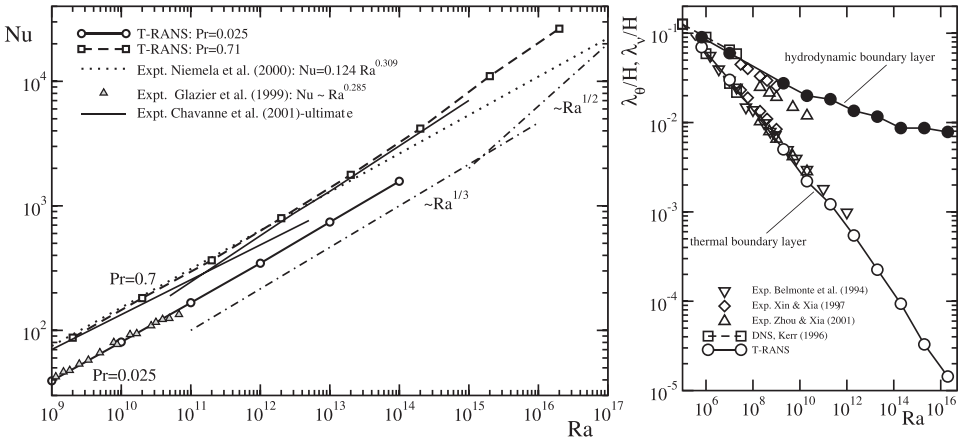

Fig. 9.20 Nusselt number for Pr = 0.7 and 0.025 (left) and thicknesses of the thermal and hydrodynamic boundary-layer, λ_θ and λ_υ, for Pr = 0.71 (right) over a range of Rayleigh numbers, indicating a change from Nu $\propto$ Ra$^{1/3}$ towards the ultimate Nu $\propto$ Ra$^{1/2}$ regime, computed by URANS. From Kenjereš and Hanjalić (2009).

As mentioned above, a major benefit of the URANS approach is its ability to resolve the behaviour at very high Ra, far beyond the present reach of LES. Figure 9.20 shows the Nusselt number obtained with URANS for Ra approaching 10^{17}. At much lower Rayleigh numbers the URANS results agree well with the available experiments and DNS data both for air (Pr = 0.71) and for mercury (Pr = 0.025) and with the accepted dependence of Nusselt number on Ra: Nu $\propto$ Ra$^{1/3}$. Moreover, the URANS results indicate a change in the regime at Ra $\approx 10^{12}$ for Pr $= \mathcal{O}(1)$ (apparently associated with the laminar-to-turbulent transition in the hydrodynamic wall boundary layer, Chavanne *et al.*, 1996), and a trend towards Kraichnan's (1962) 'ultimate' turbulence state characterized by the asymptotic solution Nu $\propto$ Ra$^{1/2}$ for Ra approaching infinity. The URANS computations of the thicknesses of the hydrodynamic and thermal wall boundary layer, shown in Fig. 9.20 (right), not only agree well with several experimental and DNS data for lower Rayleigh numbers but also, Fig. 9.20 (left), show a steepening slope of the Nu dependency from Ra $\approx 10^{13}$, arguably supporting Kraichnan's proposal.

Environmental flows

As an illustration of the potential of the URANS approach for predicting large-scale, unsteady phenomena in the environment, we consider the diurnal variation of air movement and pollutant dispersal over a medium-sized city situated in a valley during a critical windless period capped by an inversion layer.[13] A slight increase

[13] The terrain configuration and the meteorological scenarios mimic typical winter episodes in and around the city of Sarajevo, Bosnia and Herzegovina.

https://doi.org/10.1017/9781108875400.011 Published online by Cambridge University Press

in the ground temperature during the day, with a somewhat elevated heating over the distinct residential and industrial zones due to daily activities, representing heat islands, is the only generator of air movements that adjust to the terrain orography forming complex patterns of unsteady convective structures. In the absence of any field data, Kenjereš and Hanjalić (2002) adopted a hypothetical scenario in which the ground over the whole domain was uniformly heated and cooled over a daily cycle in a sinusoidal manner with the diurnal and nocturnal temperature amplitudes of $\pm 1°$C. In addition, on the ground in the 'residential' and 'industrial' areas, additional cyclic heating and cooling was superimposed. This comprised a sinusoidal variation in time within the subdomain areas, with mid-day and midnight temperature extrema of $\pm 2°$C and $\pm 1°$C, respectively, at the centre of the two zones. The amplitude of this local temperature variation reduced smoothly to zero at the subdomain edges. The two zones were also assumed to emit pollutants during the day with 50% and 100% of the maximum non-dimensional emission flux (defined as unity) for the two zones. The external conditions are defined by a uniform potential temperature of dry air in the lower atmosphere, capped by an inversion layer in which the temperature increases linearly with height at a rate of 4°C/km. Two scenarios of thermal stratification were considered differing in the height of the base of the inversion layer: for 'weak' stratification, the inversion layer begins at $z/H = 2/3 (\approx 1600$ m) from the deepest point in the valley, and for the 'strong' stratification at $z/H = 1/3 (\approx 800$ m), where H is the domain height. The situation is characterized by a very high Ra, $\mathcal{O}(10^{17})$. The terrain configuration and the boundary conditions for the considered scenarios are indicated in Fig. 9.21.

The complex flow patterns and their evolution over the cycle for the two stratification scenarios (reflecting the terrain orography) are illustrated in Fig. 9.22. For the weak stratification, at the peak ground heating at noon, the plumes and the convective structures show a significant degree of self-organization and strong vorticity concentration, with a tendency to erode the inversion layer (the region between the dotted horizontal lines); but during the subsequent ground cooling period this motion gets notably suppressed. In contrast, under a strong stratification, the convective structures are weaker and remain confined within the lower atmosphere below the inversion layer.

Naturally, the above difference in the flow patterns has direct repercussions on the dispersion of pollutants, as illustrated in Fig. 9.23. A comparison of the pollutant front, defined by 1% of the maximum emission concentration at the same time (corresponding to early evening), shows that under weak stratification the pollutant is being lifted above the ground, reaching and, in fact, locally penetrating the base of the inversion layer. In contrast, for a strong stratification, much of the pollutant remains close to the ground and spreads laterally. Although the imposed

https://doi.org/10.1017/9781108875400.011 Published online by Cambridge University Press

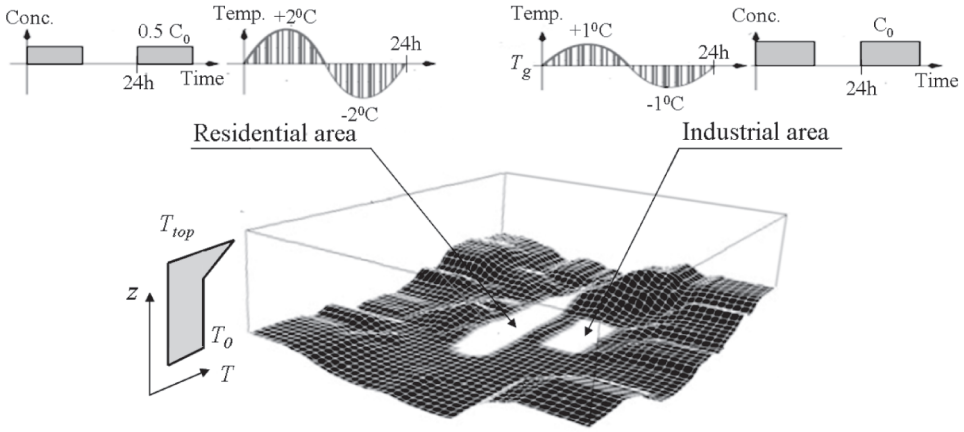

Fig. 9.21 Terrain orography of a medium-sized city valley capped by an inversion layer with diurnal variation of the ground temperature and pollutant emission from the two heat islands (residential and industrial areas). From Kenjereš and Hanjalić (2002).

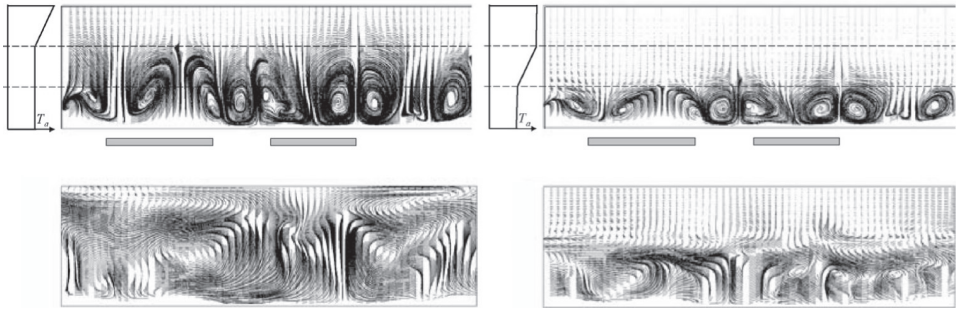

Fig. 9.22 URANS-computed streamlines projected on a vertical plane cutting through heat islands. Top figures correspond to heating during the first daytime cycle (at 12.00 hr) and the bottom to nocturnal cooling during the second cycle (at 24.00 hr). Left: weak stratification; right: strong stratification. From Kenjereš and Hanjalić (2002).

boundary conditions are purely hypothetical in an attempt to mimic a real environmental problem, the results suggest that the URANS strategy can be usefully applied to diagnosing urban pollution in situations which are inaccessible to other computational approaches.

To close this section, we consider the URANS simulation of another case of a windless diurnal cycle, this time a weakly stratified atmospheric boundary layer topped by an inversion over an urban terrain with a large river, reported by Hrebtov and Hanjalić (2017). With some simplification, the case mimics the real winter environment of the city of Krasnoyarsk in Russia where the non-freezing River

https://doi.org/10.1017/9781108875400.011 Published online by Cambridge University Press

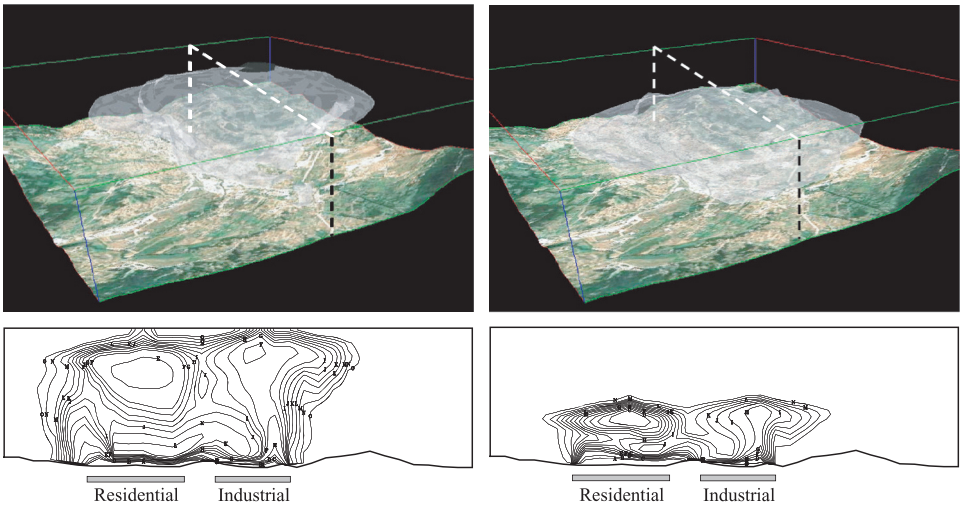

Fig. 9.23 Upper: URANS predictions of the pollutant front (1% of maximum concentration) in the early evening for weak (left) and strong (right) stratification. Lower: concentration contours at 6.00 pm of the first day, corresponding roughly to the top figures. From Kenjereš and Hanjalić (2002).

Yenisei (downstream from a hydropower water reservoir) acts as a thermal and humidity source. The river width is about 1 km at its widest part, which is comparable with the inversion height. In such situations some rare natural phenomena have been observed, featuring an undulating fog pattern along the river accompanied by scattered vortical columnar structures ('steam devils') topped by vortex rings.

An idealized full diurnal cycle was simulated over a domain of 32 km × 17 km × 2 km meshed with a 322 × 172 × 102 grid (i.e. about 5.64×10^6 grid cells). The same three-equation $k - \varepsilon - \overline{\theta^2}$ algebraic flux RANS model was used as in the previous example. Now, however, it employs the Simplified Analytical Wall Function strategy (SAWF, §8.4) for applying the ground boundary conditions, extended to account for stratification effects and typical ground roughness in different zones (Hanjalić and Hrebtov, 2016).

A realistic ground topography was generated from the Geographic Information System (GIS) data. The reference potential temperature was specified from precursor simulations of the evolution of the mixed layer over uniformly heated ground into a stably stratified environment with a lapse rate of 4°C/km until it reached the targeted inversion base at a height of 1 km. The temperature above the inversion layer (at 1.6 km) was assumed to be −3°C. To simulate the running river surface, a separate precursor simulation was conducted on a 2D finer mesh to determine approximately the free-surface water velocity, which was then projected onto the bottom boundary of the actual mesh. The on-site temperature measurements at 2 m

https://doi.org/10.1017/9781108875400.011 Published online by Cambridge University Press

above the ground for two weather stations showed the strength of the heat-island effect of about 3°C at its peak on windless days in winter. The spatial distribution of the ground temperature was estimated from the diurnal cycle of human activity and traffic intensity, accounting for building density and the location of the main industrial facilities. The resulting normalized distribution was used to estimate the urban heat-island temperature.

A generic, uniform, sinusoidal, diurnal temperature cycle (marginally different from the measured one) was set for the ground ranging from −6°C to −4°C. In the city area a heat-island temperature variation was added with amplitude of 2°C. The coldest time in the diurnal cycle corresponds to 06:00 and the warmest to 18:00. The temperature of the river water was assumed constant and equal to 0°C. The ground and the river were treated as rough surfaces defined in terms of the equivalent roughness for the city centre, the surrounding scarcely populated area and the river surface.

The strong heat transfer from the river throughout the whole diurnal cycle creates the main plumes over the river that, in turn, largely govern the air movement over the whole area. During the night phase the river is virtually the only source of heat and the air motion is concentrated around the river. Over that period (Fig. 9.24, left), the largest convective roll structures appear in the form of a pair of long, counter-rotating convective rolls with axes aligned with the river, especially evident in the straightest section of the river. Moreover, a number of concentrated vortices and vortex rings are clearly visible along the river, superimposed on the two main river-parallel rolls. Far enough from the river (though still above the city) the air is stagnant. In the morning the solar irradiation and the increasing human activity begin to heat the nearby ground, generating convective motion. As the heating progresses these rolls grow and begin to interact, intensifying the vertical heat transfer and reinforcing the creation of new plumes.

The non-uniform ground heat flux and the warming of the adjacent air within the ground layer create a horizontal temperature gradient towards the river, which interacts with the gravitational vector acting as a baroclinic source of vorticity, $\nabla(\beta T) \times \mathbf{g}$, with its axes normal to ∇T. In turn, this generates air movement in the direction of the gradient, entraining air from the suburbs towards the river and then into the plume rising above the warm water surface. The inversion layer acts as a barrier to the vertical motion, however, turning the flow and inducing horizontal spreading of the warm air away from the river at higher altitudes, thus creating a horizontal circulation to and away from the river, as shown by velocity vectors on planes normal to the river in Fig. 9.26.

The horizontal temperature gradient and the flow towards and away from the river interacting with shear and buoyancy can also be linked with the horizontal, counter-rotating roll pairs normal to the river over the city terrain. These are

https://doi.org/10.1017/9781108875400.011 Published online by Cambridge University Press

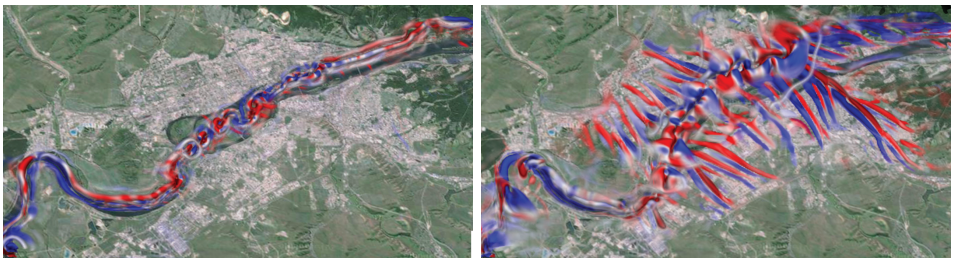

Fig. 9.24 A bird's-eye view of vortical structure visualized by the Q-criterion, coloured by helicity density $\overline{\omega_i u_i}$ (red: positive; blue: negative). Left: 06:00; right:18:00. From Hrebtov and Hanjalić (2017). Reprinted by permission from Springer Nature.

especially evident at peak heating (Fig. 9.24, right), though disappearing at night (Fig. 9.24, left). The width of the lineal vortex pairs is largest around and above the river, but their diameter, vorticity and identity reduce with distance from the heat source (provided by the river); hence their specific 'trumpet'- or 'carrot'-like shapes, with roots pointing outward from the river. The pattern is well reflected in the temperature and humidity distributions, especially at low elevations, as shown in Fig. 9.26.

The interplay of several distinct large-scale vortex systems leads to a complex flow picture, displaying a wavy pattern of moisture plumes over the river and a chain of swirling columns topped by toroidal rings along the river. A bird's-eye view of the vortex structure over the terrain at two different times in the diurnal cycle shown in Fig. 9.24 reveals such concentrated vertical vortex columns as well as vortex rings superimposed on the two main river-parallel rolls in the horizontal plane at higher elevations. This is in particular visible at peak cooling when the river-normal 'trumpet' vortices are absent, Fig. 9.24, left.

Swirling columnar structures have long been observed in Nature above lakes and large rivers when the temperature of the water surface is above the ambient, as shown in Fig. 9.25 (left). Their origin and formation are discussed in detail in Hrebtov and Hanjalić (2017). Suffice it to state here that the concentrated vertical vortex columns, believed to be the precursors of the swirling 'steam devils', are initiated by the interaction of some of the opposing river-normal longitudinal rolls over the river surface, creating another distinct vortex system in the form of concentrated vertically oriented counter-rotating vortices on and around the river. The toroidal rings on the top of swirling columns, however, seem to be created by a roll-up instability in the vertical shear layers around the edge and near the top of the columnar plume beneath the inversion layer. Presumably, they are also affected by shear at the moving water surface, which seems to be the prevailing mechanism during the night when the river plume is weak. As illustrated in Fig. 9.25 (right),

https://doi.org/10.1017/9781108875400.011 Published online by Cambridge University Press

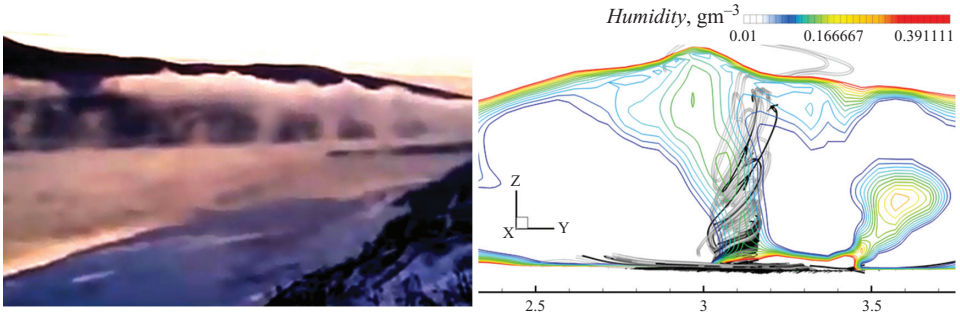

Fig. 9.25 Observed and computed columnar structures over the river at elevated temperature relative to the ambient in winter. Left: `https://youtu.be/hWOP3u_m9xQ`; Right: URANS computations, from Hrebtov and Hanjalić (2017). Reprinted by permission from Springer Nature.

the URANS computation reported by Hrebtov and Hanjalić (2017) reproduced the overall shape and swirling pattern of the columnar structures, closely resembling their natural appearance, Fig. 9.25 (left).

The velocity, temperature and humidity distributions shown in Fig. 9.26 reflect, to a large degree, the vortical structures and flow patterns discussed above. The left figure shows the temperature contours at peak heating with superimposed horizontal velocity-vector projections for two cross-sections roughly perpendicular to the river, just before and across the main island (the river surface is at the ordinate height of zero, while the area below it shows temperatures on the river and ground surfaces upstream from the plane). The temperature contours show an irregular field with, as expected, the strongest disturbances over and around the river. In both cases the inversion layer is clearly visible; it is noticeably eroded by upward air movements at locations directly above the river. The stable stratification above the inversion top is generally undisturbed. The velocity field is consistent with the above pattern, i.e. air moves towards the river within the ground layer and away from it at higher elevations. The typical sign reversal occurs at about one-third of the inversion height, but at some locations this happens at higher altitudes, as for example in the upper right figure. The inversion layer remains unbroken in all cases considered, though with a distinct erosion above the main plume, manifested by a bumpy pattern of the top temperature contours and a visible local depletion of the inversion layer thickness.

Unlike thermal plumes driven by buoyancy, the humidity, modelled as a passive scalar, is completely governed by the convection and vortical structures. The humidity distributions, together with the local velocity vectors, appear in Fig. 9.26, right for the same time instant in the diurnal cycle as the temperature, but at somewhat different cross-sectional planes. From the river, the vapour is transported

https://doi.org/10.1017/9781108875400.011 Published online by Cambridge University Press

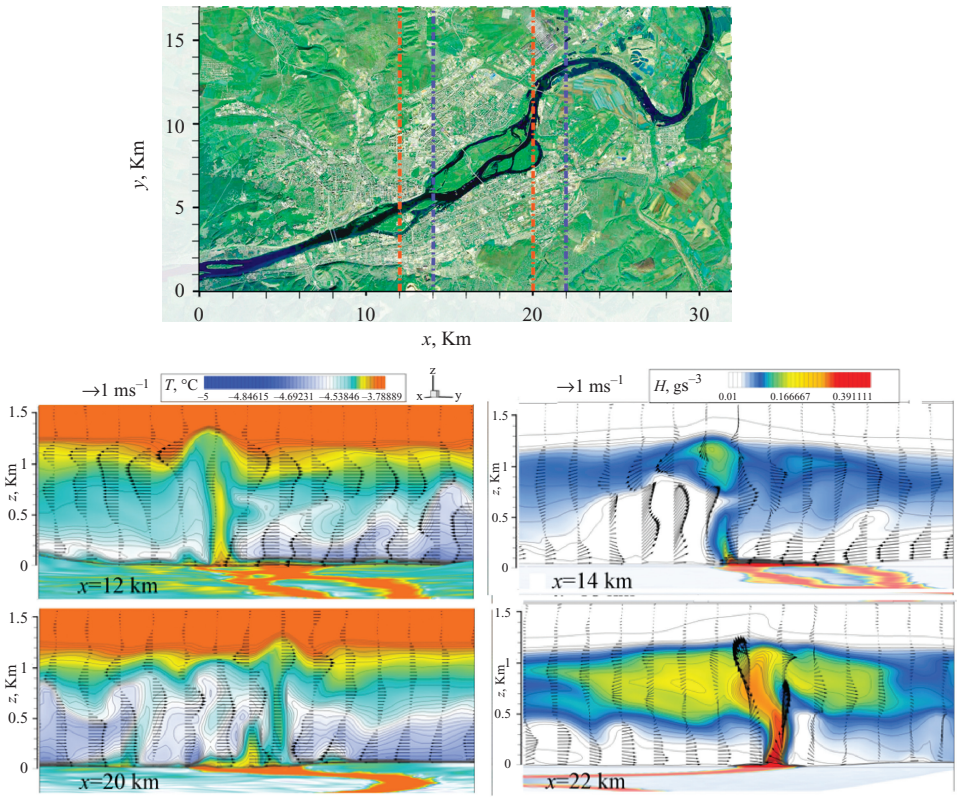

Fig. 9.26 Horizontal velocity vectors and temperature projections (left) and vapour concentration (right) on river-normal cross-sections (indicated in the plan view at the top) at 18:00 hr. A segment of the local ground coloured in the same temperature and humidity colour scales as the air above, depicts the river (orange) and its branching around an island. From Hrebtov and Hanjalić (2017). Reprinted by permission from Springer Nature.

almost vertically to the inversion base in the form of a condensed plume where the local maximum of humidity concentration occurs, and then spreads horizontally by convection. The overall mean-flow pattern shows that this spreading of moisture is most intense in the direction away from the river, convected by the flow at upper altitudes. During this process some of the moisture, entrained by the lower-altitude flow, is transported backwards towards the river. At some locations the spreading to left and right is almost equal while at other cross-sections one direction dominates over the other.

It is further noted that the humidity distribution along the river exhibits a relatively regular periodicity, reflecting the vortex structures in Fig. 9.24 (right). A bird's-eye view of the moisture concentration over the city, obtained by volume

https://doi.org/10.1017/9781108875400.011 Published online by Cambridge University Press

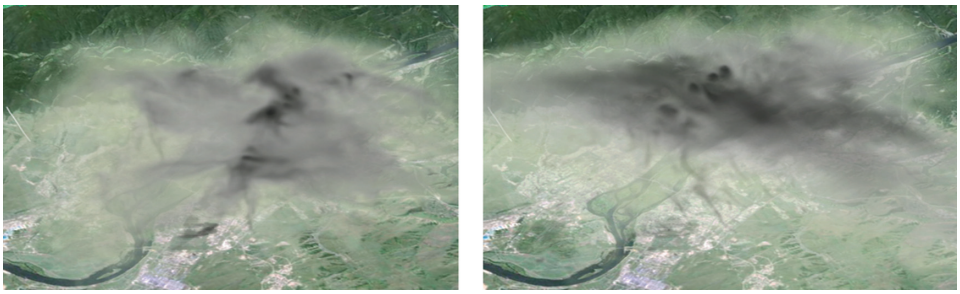

Fig. 9.27 Snapshots of instantaneous CO concentration distribution at 18:00 via volume rendering. Left: summer; right: winter. The grey shades range from zero concentration (fully transparent) to its maximum (fully opaque). From Hrebtov and Hanjalić (2019).

rendering,[14] indeed displays an undulating fog pattern along the river that qualitatively resembles the observation in the natural setting, as shown in Figs. 1 and 14 in Hrebtov and Hanjalić (2017).

Readers interested in microclimate impacts on pollution in the urban environment may also wish to consult the detailed follow-on explorations by Hrebtov and Hanjalić (2019) of air quality for Krasnoyarsk using the same URANS model for the same setting. This study focused on analyzing the origin of the seasonal variation in the carbon monoxide levels in winter and summer observed at different locations around the city despite a fairly similar emission from road traffic throughout the year. Their predictions broadly captured the sometimes major recorded differences in CO concentrations between winter and summer conditions, attributed to a different role of the river on the local microclimate, acting as heat source or heat sink depending on the season.

The instantaneous snapshots of volume rendering of the CO concentration at 18:00 in Fig. 9.27 give an impression of a typical late afternoon pollutant dispersion over the city in summer (left) and winter (right). Note that the greyscales in the two figures, ranging from full transparency for zero concentration to full opacity for its maximum, differ in absolute values, but they both show the maximum concentration in the same central downtown region, though with markedly different distributions.

[14] Volume rendering is a visualization method (widely used in medical diagnostics) now increasingly entering non-medical areas, particularly in the atmospheric and environmental sciences. It aims to convey what the human eye actually sees by assigning a value of the 'transparency' or 'opacity' of a variable in any computational cell, thus enabling the viewer to see fog or smoke in natural grey shades.

https://doi.org/10.1017/9781108875400.011 Published online by Cambridge University Press

10

Hybrid RANS-LES (HRL)

Co-authored with Alistair J. Revell

10.1 Introduction and overview

The focus of this book so far has been on the provision of turbulence modelling closures purely within the framework of RANS or URANS methodologies. This chapter provides an introduction and overview of a different class of approaches for predicting turbulent flow, often referred to as Hybrid RANS-LES (HRL) methods. As implied by its name, these approaches result from the direct combination of two stand-alone frameworks, giving rise to something altogether new. Hybrid methods seek to combine the robustness and favourable economic cost of RANS schemes with the ability of Large-Eddy Simulation (LES) to capture the influential large, energy-containing scales of turbulence.

Despite the established successes of engineering turbulence models presented in earlier chapters, there is a continual demand for greater reliability in modelling turbulent flows, driven by the goal of achieving *assuredly* accurate predictions of flows in arbitrarily complex flows. Sacrificing the practicality and economy of a time-averaged framework in favour of a time-dependent approach has become an increasing trend since the start of the twenty-first century. The previous chapter has shown that running a RANS solver in time-dependent (URANS) mode may bring out new features of organized turbulence structures in the flow, which on time-averaging the output produces a mean flow in much closer accord with experiment than a computation in steady-state mode with the same model of turbulence. Moreover, as demonstrated in Chapter 9, just as in steady-flow computations, the success of these time-dependent solutions can be significantly improved by using more advanced RANS treatments that better capture the turbulent stress field and the response of the model to flow instabilities.

This desirable outcome can by no means always be guaranteed, however. Moreover, since the reliability of a RANS treatment is recognized to be lowest in regions of separated flows, the idea emerged of employing a RANS model where the flow

https://doi.org/10.1017/9781108875400.012 Published online by Cambridge University Press

remains attached but LES in regions where the flow approaches separation and any separated-flow region itself. The advantage provided by such scale-resolving methods had been apparent from the early days of turbulence modelling. In 1979, Dean R. Chapman, the then director of the NASA Ames Research Centre, in a keynote address to the 17th AIAA Aerospace Sciences Meeting, took stock of the rate of advance in computational power and predicted that LES would be in regular use for full-aircraft simulation by the 1990s (Chapman, 1979). By the end of the 1990s, and in spite of Moore's[1] law, it had become apparent that the requisite computational resource still limited LES to low-to-moderate Reynolds numbers for flow around, within or through objects of relatively simple geometry. Arguably, it was from this recognition that hybrid methods were born. This was a time when the advantages of scale-resolving methods were clear but where their applicability to flows of practical engineering interest was, at best, of limited scope. Nearly two decades later, in an article for *Scientific American*, Moin and Kim (1997), reporting the opportunities and challenges of predicting turbulence with supercomputers, concluded that 'it will probably be many decades before computers are powerful enough to simulate in a detailed manner the flow over an entire airplane'. Indeed, in 2014, in a NASA white paper setting out the computational challenges up to 2030 (Slotnick *et al.*, 2014), LES was assessed as having only a medium likelihood of being technically ready for full-aircraft simulation by that end point. Hybrid RANS-LES was identified therein as becoming the primary workhorse over that period (see Fig. 10.1).

In the great majority of cases where CFD is employed, RANS will continue to be used alone to guide design or diagnose the origin of faults on account of its ease of application and relative economy (particularly for plainly steady, two-dimensional or axisymmetric flows). When, however, for industrial cases, particularly complex flow features are encountered or where there is a requirement for assuredly great accuracy, regardless of cost, Hybrid RANS-LES will be the preferred route. Interestingly, the NASA 2030 roadmap recognizes the potential for improved accuracy from computations with Reynolds-stress transport models (indicated as RST in Fig. 10.1) but makes reference to a decision point around the year 2020, when efforts to yield high-accuracy predictions with these methods may instead be directed to hybrid approaches. This foreseen shift in focus resulted from repeated indicators that to capture the frequency content required for the computation of instantaneous effects (such as three-dimensional separation and transient loading), some degree of scale resolution would be needed. Given that LES will remain beyond reach for complex industrial applications for many decades to come, HRL methods offer a promising way forward, aimed at bringing

[1] Moore's law rests on the observation that the rate of computational power, based on the number of microchips one can accommodate on a dense integrated circuit, doubles roughly every two years (Schaller *et al.*, 1997).

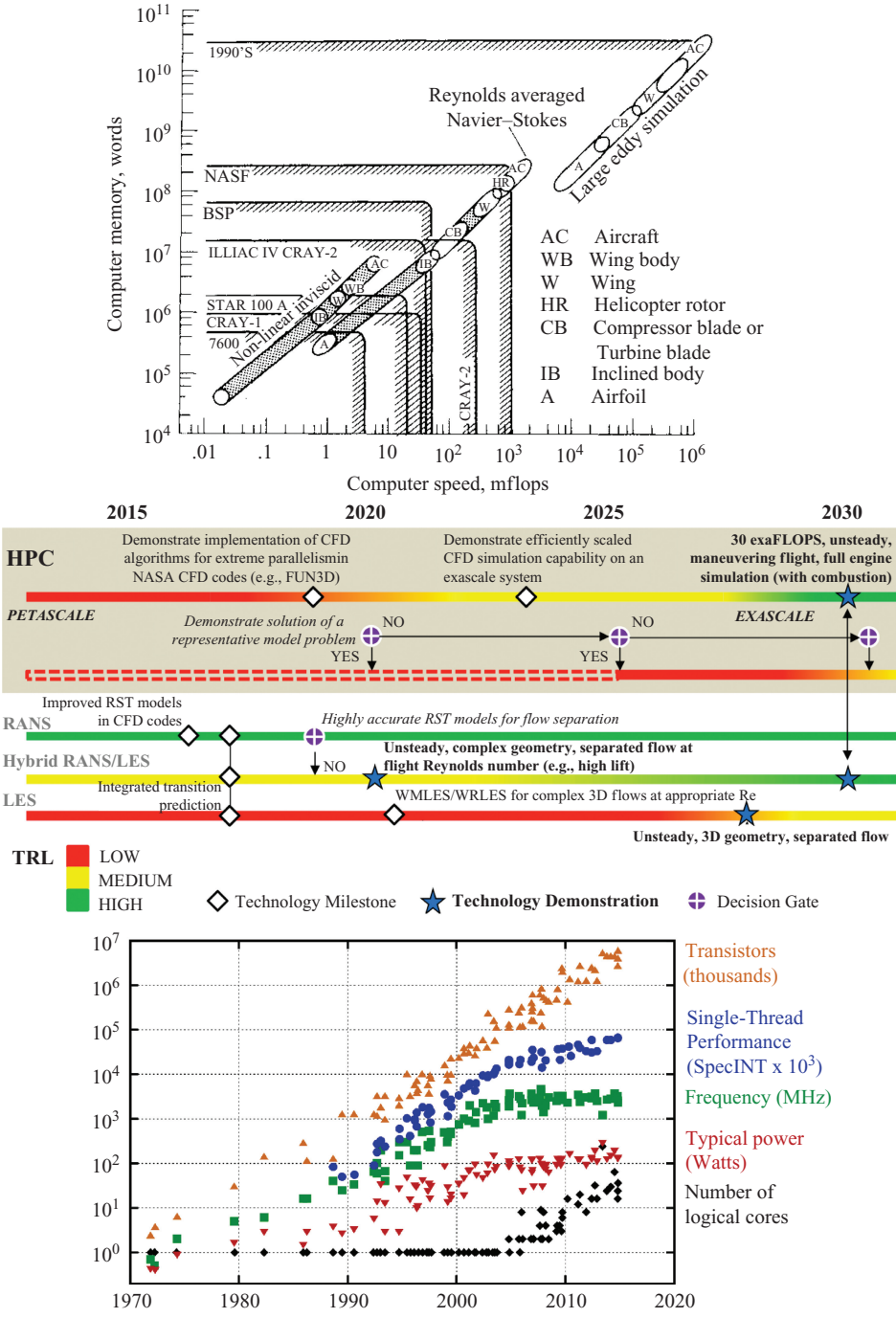

Fig. 10.1 Predictions of the readiness of Large-Eddy Simulation over the past 40 years (Top) from Chapman (1979). (Middle) Adapted from the NASA 2030 CFD Roadmap (Slotnick *et al.*, 2014). (Bottom) The trend in microprocessor power over this period. The top figure predicted full-aircraft LES to be feasible by the 1990s on computers using 10^6 megaflops (10^{12} flops), while the middle figure predicts medium readiness by the year 2030, with computational power estimate of 30 exaflops (10^{19} flops). The bottom figure demonstrates that growth rate has been more or less constant (Rupp, 2015).

https://doi.org/10.1017/9781108875400.012 Published online by Cambridge University Press

the majority of the benefits of LES at a much lower computational cost. The manner in which these approaches integrate and interface RANS modelling with LES methods is the subject of this final chapter.

An overview is first provided of the computational requirements for full resolution before introducing the main classification of different methods in this category. From there the LES rationale is briefly reviewed before moving sequentially through a series of approximations entailing the need for progressively greater modelling. A historical overview is provided of the principal methods in each category with examples of their use, before bringing together key findings, ideas and likely future developments.

10.1.1 General concepts of scale-resolving methods

The designation 'scale-resolving methods' includes any approach which aims to resolve at least part of the unsteady content of a turbulent flow. Here, the word 'scale' refers to the energy spectrum, as introduced in Section 3.3. Direct numerical simulation (DNS) and LES introduced in §1.1 and §1.2, along with hybrid methods and unsteady RANS, can all be considered to be scale-resolving methods, to a greater or lesser extent. In steady flow RANS the state of the fluid at any point depends on the mean and turbulent flow properties at that point and their spatial gradients. In contrast, scale-resolving methods include non-local effects via the continual interaction of intermittent turbulent structures around the point in question. Figure 10.2 showing flow over a hill, illustrates this distinction. A steady RANS scheme provides a single solution for all time while scale-resolution provides a continually changing flow field. The separation 'point' changes from a single location in the former case to a range of positions in the latter, made possible by this non-local accounting of turbulence. The ability to track the dynamics of coherent eddies is what produces this non-locality, a feature beyond time-averaged approaches. Note, however, that URANS, considered in Chapter 9, retains at least some of this scale-reolution capability. The classical way to represent and interpret the range of turbulent scales or eddies present in a flow is via the turbulence energy spectrum. This is essentially a map of the distribution of energy across the complete range of eddy sizes, or length scales, at a single point in space and time. Usually, as introduced in §3.3, the wave number is adopted rather than length, with dimensions L^{-1}. The turbulent kinetic energy at any given point in space and time is the sum of the motion of eddies of all scales at that point; it is thus the integral of the full energy spectrum. Often the majority of turbulent kinetic energy at any given location arises from eddies of a narrow range of sizes whose scale is closely linked to some geometric or flow feature from which the turbulence was created in the first place. Since it contains such a large proportion of

https://doi.org/10.1017/9781108875400.012 Published online by Cambridge University Press

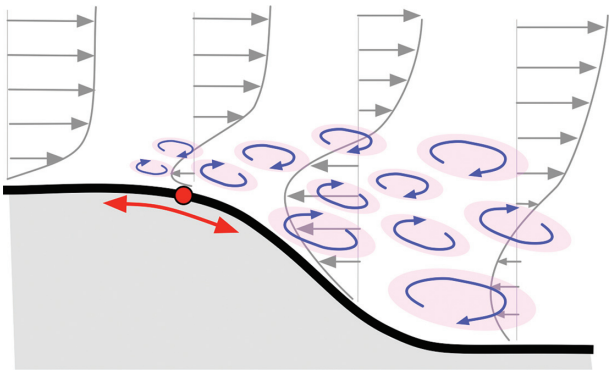

Fig. 10.2 Conceptual diagram showing separated flow over a hill. Grey lines show boundary-layer profiles of mean-flow field, while blue quasi-ellipses represent turbulent fluctuations. The red circle indicates the time-averaged point of flow separation, while the red line terminating in arrow heads indicates the range of the instantaneous point of separation.

the energy, it is called the integral length scale L. Turbulent scales interact with each other and, in so doing, break down into progressively smaller eddies. The smallest scales of motion, those in which the turbulence is finally dissipated, have a representative size known as the Kolmogorov length scale, η, after the pioneering Russian theoretician, A. N. Kolmogorov, who made fundamental discoveries about the universal nature of turbulence (e.g. Kolmogorov, 1941). This scenario is illustrated in Fig. 10.3 for the case of flow around a wall-mounted cube. As suggested by the sketch, the largest vortical structures in the wake, the integral length scales, L, are of the same order of size as the cube height, H. Eddies of many sizes (created by self-inter-tangling) are also shown but, while large in number, they contribute a diminishing fraction of the total turbulence energy as the wave number increases. When, by such self-interaction these fine-scale turbulent structures are broken down to the Kolmogorov scale, they have reached the smallest possible size before being dissipated.[2] The Reynolds number of these smallest scales (based on the velocity gradient across them and their dimension) is of order unity.

A final scale of note is the Taylor length scale, introduced in §3.3, p.38. As presented in that section, as the large, energy-containing eddies are broken down into successively smaller eddies, these finer-scale motions progressively lose their 'memory' of the mean-flow features from which they originated. Indeed, in many circumstances, away from the constraints imposed by a wall (§6.2.1), the finest-scale eddies become essentially isotropic. The Taylor length scale, λ

[2] The Kolmogorov length scale is formally defined in terms of ν and ε in §3.4, p.43.

https://doi.org/10.1017/9781108875400.012 Published online by Cambridge University Press

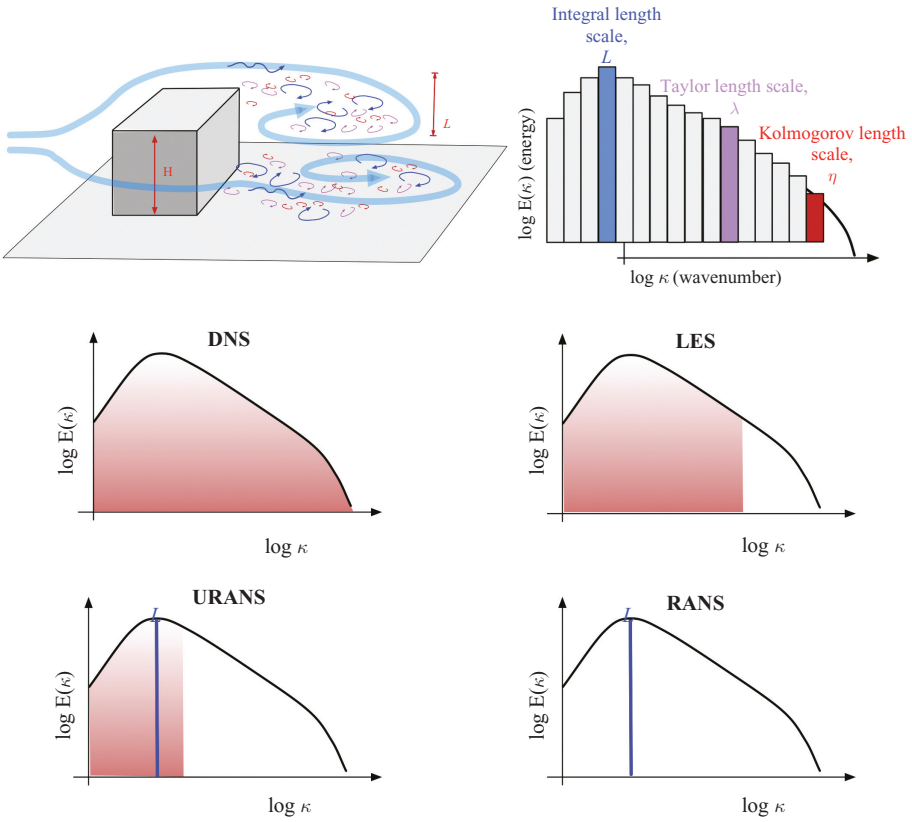

Fig. 10.3 Conceptual diagram showing: (top left) the flow around a wall-mounted cubic obstacle and the resulting turbulent flow field in its wake; (top right) the related turbulent kinetic energy spectrum for a point in the wake of the cubic obstacle; (middle and bottom rows) comparative representation of the trade-off between direct resolution (in red) and modelling for DNS, LES and RANS approaches to prediction of turbulence at a particular point. (The cut-off wave number in LES depends on the filter size, i.e. the size of the grid cells, whereas in URANS it depends on the type and level of the RANS model.)

(which is larger than the Kolmogorov length scale), is sometimes held to be the approximate scale at which the turbulent eddies becomes isotropic.

A conceptual distinction between DNS, LES, URANS and RANS is suggested in the lower rows of Fig. 10.3, where red-toned regions indicate wave numbers over which scales are directly simulated, while, over the blank regions, an attempt must be made to account for the energy contained therein using models. In a true DNS, all scales of motion are simulated numerically. That is to say, the numerically imposed spatial and temporal scales are sufficient to resolve directly the motion of all scales of turbulent motion. In contrast to DNS, RANS methods employ only modelling, while LES and URANS employ both modelling and simulation. Note that the modelling of small-scale turbulence becomes simpler when the motion is

https://doi.org/10.1017/9781108875400.012 Published online by Cambridge University Press

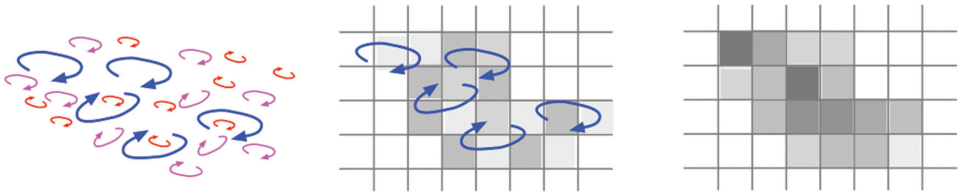

Fig. 10.4 Conceptual diagram showing comparison between (left) resolution of all turbulent scales as in DNS, (right) modelling of all scales as in RANS and (middle) combined resolution and modelling as in LES. (See also Fig. 1.1 for the case of flow in a channel.)

isotropic. It is for this reason that many scale-resolving methods aim to resolve scales as small as the Taylor length scale. Nevertheless, for high-Reynolds-number flow this is a challenging target and modelling is commonly introduced in LES treatments at scales substantially larger than this.

As a final point of note here, we recall from §3.3 that the integral of the energy spectrum across all scales gives the turbulent kinetic energy, k:

$$k = \int_0^{\kappa_\infty} E(\kappa) d\kappa. \tag{10.1}$$

For DNS, this quantity is readily available since all scales are resolved, $k = k_{res}$, while for RANS the value is modelled, $k = k_{mod}$.

For LES, we note that the situation is a little more complex, involving the sum of both a resolved component and a modelled component:

$$k = \int_{\kappa=0}^{\kappa=\kappa_{\max}} E(\kappa) d\kappa + k_{sgs} \tag{10.2}$$

where $\kappa_{\max}$ is the largest directly resolved wave number and k_{sgs} is the turbulence energy contained in scales too fine to be directly resolved (and which thus requires modelling), known as the 'sub-grid-scale' (sgs) turbulence. These scenarios are represented in Fig. 10.4. There are two particular challenges to computing the total energy for LES that, in turn, are highly relevant to HRL methods. First, we need to know the location in spectral space at which the turbulent structures switch from being resolved to being modelled. With that decided, one can arrange an appropriate numerical strategy for the former and the correct physical representation of the latter. Without careful accounting of this location, it is possible (and indeed likely) that part of the turbulence energy will either be double-counted or missed altogether. The second issue is the transfer of information across the resolved/modelled interface; most of the time energy moves from larger to smaller eddies, but not always. For example, a flow with mean unsteadiness will include energy transfer in both directions, and so we must include a means of moving energy both from resolved to modelled scales *and* from modelled to resolved scales (known as back-scatter).

https://doi.org/10.1017/9781108875400.012 Published online by Cambridge University Press

10.1.2 The scales of turbulent motion

A significant contribution by Kolmogorov (1941) was the recognition that turbulence, a wholly complex phenomenon, could be represented and interpreted with simple observations. Investigating the parametric dependence of turbulence across different scales of the turbulence kinetic energy spectrum provides an example of this. Kolmogorov demonstrated that the largest and smallest scales could be approximated using simple dimensional arguments. While knowledge of the rate of turbulence dissipation, ε, with dimensions $[\mathsf{L}^2\ \mathsf{T}^{-3}]$ is important across all scales, approximation of the largest scales also requires the turbulent kinetic energy, k $[\mathsf{L}^2\ \mathsf{T}^{-2}]$, to be known while, in the smallest scales, the key additional parametric dependence is on viscosity, $\nu[\mathsf{L}^2\ \mathsf{T}^{-1}]$. The situation has been discussed in §3.3; to paraphrase the text following Fig. 3.4, we may regard the spectrum as comprising three distinct regions: the largest scales (relating to energy and stress production), the smallest scales (relating to energy dissipation) and a mid-range of scales known as the *inertial subrange*. Kolmogorov recognized that, at high Reynolds number, the mid-range scales become independent of both the largest and smallest scales they bridge, achieving a universal state that holds true for all flows in energy equilibrium. Dimensional arguments can be used to infer that the variation of the spectrum in this region has the form:

$$E(\kappa) = C_\kappa \varepsilon^{2/3} \kappa^{-5/3} \tag{10.3}$$

which implies that a graph of $\log E(\kappa)$ versus $\log(\kappa)$ will be a straight line of gradient $-5/3$, a result that is widely confirmed by experiment (see, for example, Fig. 3.5).

10.1.3 Approximating the cost of full resolution

It is common to make use of the scaling approximations presented in Table 10.1 to estimate the computational cost of a simulation. While the precise nature of the computational domain and grid topology will vary from one case to the next, some impression of the cost can be obtained by considering the simplest possible situation: a box of homogeneous turbulence at a given Reynolds number.

Table 10.1 *Summary of scales*

	Length	Time	Velocity	Reynolds No.
Integral	$L = k^{3/2}/\varepsilon$	$\mathcal{T} = k/\varepsilon$	$k^{1/2}$	$k^2/\nu\varepsilon$
Taylor	$\lambda = \sqrt{\frac{10k\nu}{\varepsilon}}$	$\mathcal{T}_\lambda = \sqrt{\frac{15\nu}{\varepsilon}}$	$\sqrt{\frac{2}{3}}k^{1/2}$	$\sqrt{\frac{20}{3}}\frac{k}{(\varepsilon\nu)^{1/2}}$
Kolmogorov	$\eta = \left(\frac{\nu^3}{\varepsilon}\right)^{1/4}$	$\mathcal{T}_\eta = \sqrt{\frac{\nu}{\varepsilon}}$	$(\nu\varepsilon)^{1/4}$	1

https://doi.org/10.1017/9781108875400.012 Published online by Cambridge University Press

Homogeneous isotropic turbulence (HIT) occurs in the absence of solid boundaries, mean-velocity gradients and external forces. Without such forcing, the turbulence will decay, and this decay process provides the basis for a detailed evaluation of how the turbulent kinetic energy spectrum evolves. Figure 10.5 provides an instantaneous snapshot taken from a DNS of a turbulent field in HIT at a Reynolds number, based on the integral length scale of roughly 90,000. This simulation, by Okamoto *et al.* (2007), employed a cubic box of 4096^3 points, i.e. almost 68 billion cells, which helps one appreciate the vast range of spatial scales to be accounted for.

Thus, to approximate the computational cost of simulating a HIT case, we consider a box capable of simultaneously resolving both the largest and the smallest scales of motion, as shown in Fig. 10.6. In this way we assume the maximum spatial dimension to be resolved is equal to the integral length scale L and the minimum grid spacing to be the Kolmogorov length scale, η. Then, the number of cells in each coordinate direction, and thus the total number of cells, can be determined as a function of the turbulent Reynolds number Re_t:

$$N_{cell}^{x} = L/\eta = \frac{k^{3/2}}{\varepsilon} \times \frac{\varepsilon^{1/2}}{\nu^{3/4}} = \frac{k^{3/2}}{(\varepsilon\nu)^{3/4}} = \mathrm{Re}_t^{3/4} \tag{10.4}$$

$$N_{cell}^{xyz} = (N_{cell}^{x})^3 = \mathrm{Re}_t^{9/4}. \tag{10.5}$$

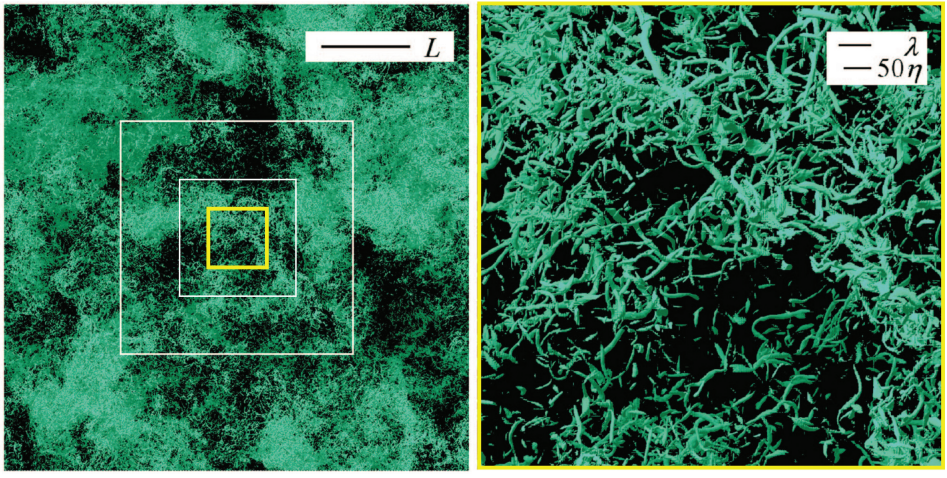

Fig. 10.5 Scales of turbulence in a DNS of homogeneous isotropic turbulence (HIT), showing vorticity isosurfaces (adapted from Okamoto *et al.*, 2007). Boxes within the left image have side dimensions of 1/2, 1/4 and 1/8 of the full image, and the inset scale indicates the size of the integral length, L, for this flow. A zoom view of the 1/4-size box appears on the right with the corresponding sizes of the Taylor length scale, λ, and the Kolmogorov length scale, η, shown in the inset.

https://doi.org/10.1017/9781108875400.012 Published online by Cambridge University Press

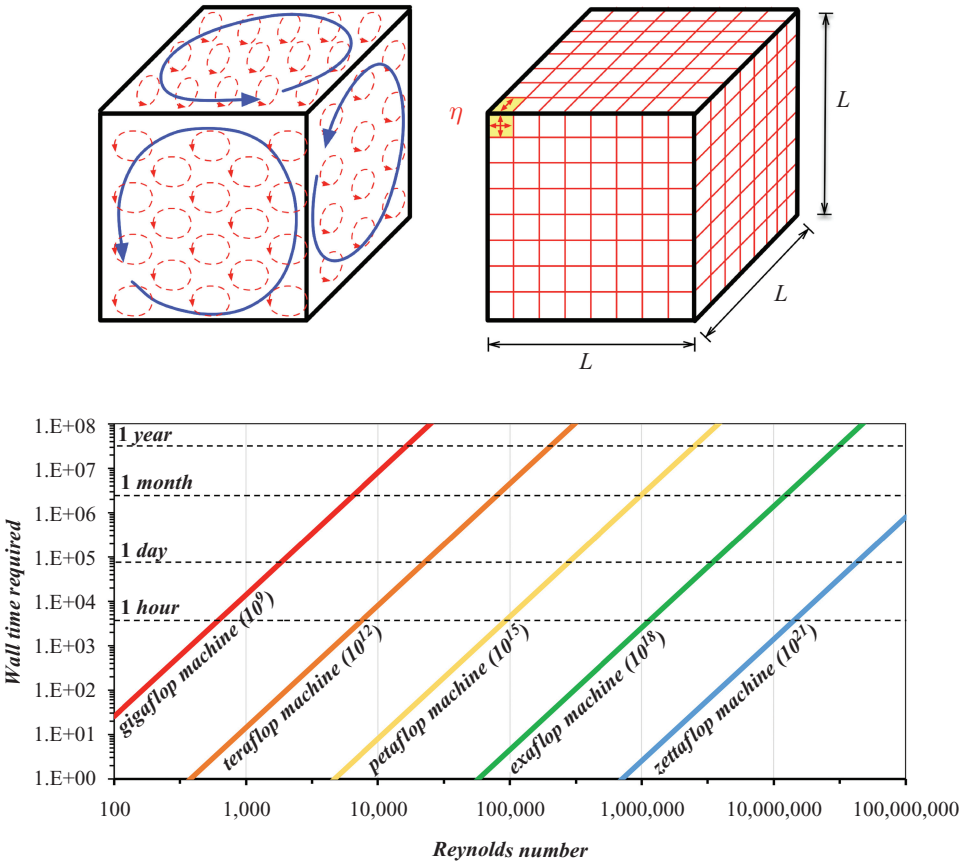

Fig. 10.6 Conceptual approach to approximating the cost of a DNS of homogeneous turbulence. Top left: domain size required to capture both the largest scales (blue) and smallest scales (red). Top right: the overall box dimension is approximated as a cube of side L, and mesh resolution η. Bottom: implications of Eq. 10.7 comparing wall time (in seconds) required to compute a simulation of varying Reynolds number, Re_t, on computational hardware of various speeds.

A similar argument can be made for the number of time steps, N_{dt}, required to capture accurately both the smallest scales as well as the largest scales:

$$N_{dt} = n_{cycle} n_{res} \mathcal{TT}_\eta = \frac{k}{\varepsilon} \times \left(\frac{\varepsilon}{\nu}\right)^{1/2} = \frac{k}{(\varepsilon\nu)^{1/2}} = 80\mathrm{Re}_t^{1/2} \tag{10.6}$$

where, typically, a simulation requires $n_{res} = 20$ time steps to resolve a single eddy motion and a typical simulation will need a factor of $n_{cycle} = 4$ times the integral time scale (hence the factor of 80 multiplying the turbulent Reynolds number above). From experience, we know that the numerical solution of the Navier–Stokes equations is dominated by a matrix inversion procedure, which itself scales with the size of the domain. A typical solution algorithm for matrix

https://doi.org/10.1017/9781108875400.012 Published online by Cambridge University Press

inversion requires $N_{matrix} = 10^3$ operations per cell at each time step (Pope, 2000). While this is only an approximation, this number may be used to estimate the total number of computational steps, or 'floating point operations' that are required to resolve all scales of turbulence.

An estimate of the computation time required to simulate a case of HIT can be obtained by dividing the output of Eq. (10.7) with the computational speed of a given High-Performance Computing (HPC) machine, measured in floating point operations per second (flops). While a modest desktop computer may, at the time of writing, offer a speed of the order of 1 giga-(10^9) flops, the state of the art in scientific computing facilities is currently measured in peta-(10^{15}) flops, with exa-(10^{18}) flops on the horizon. The lower figure of Fig. 10.6, where different diagonal lines represent different computational speeds, enables the cost of a DNS simulation to be appreciated in the context of computational power. The figure is best considered in conjunction with Fig. 10.1, introduced at the start of this section, relating to current objectives and trends in the growth of computational hardware. We can see that a computation on a petascale facility of a box of homogeneous turbulence with a turbulent Reynolds number of 10^6 will require months to compute. The implication is very clear: DNS for the simulation of turbulent flow at Reynolds numbers of practical engineering interest is far beyond the reach of general purpose CFD; for example, in the HIT case:

$$N_{total} = N_{cell}^{xyz} N_{dt} N_{matrix} = \mathrm{Re}_t^{9/4} \times 80\mathrm{Re}_t^{1/2} \times 10^3 = 8 \times 10^4 \mathrm{Re}^{2.75}. \qquad (10.7)$$

Thus, we are obliged to consider alternative methods that incorporate modelling. It may be remarked in passing that HPC is closely linked with the field of turbulence simulation because of the very high computational requirements that may be involved. (As an example beyond the field of engineering fluid dynamics, the task of weather prediction on a global scale may be cited.)

10.2 Large-eddy simulation

The aim of LES is to resolve only the larger and most energetic eddies with the impacts of the remaining smaller eddies being accounted for by modelling. This approach follows the common observation that 80% of the turbulent kinetic energy is carried by a relatively small number of larger energetic eddies, e.g. Pope (2000). An sgs model is employed to model the smaller eddies, which at this scale are dominated by dissipative effects. As discussed in §10.1, turbulent eddies at such small scales are less dependent on (indeed, are practically independent of) the geometry and mean flow, making them nearly isotropic in character, thus enabling their approximation by relatively simple models.

While in steady RANS approaches a time-averaging procedure is used, for LES the Navier–Stokes equations are instead *filtered* over a finite spatial range in order to separate the turbulence into eddies that are to be resolved from those that are

https://doi.org/10.1017/9781108875400.012 Published online by Cambridge University Press

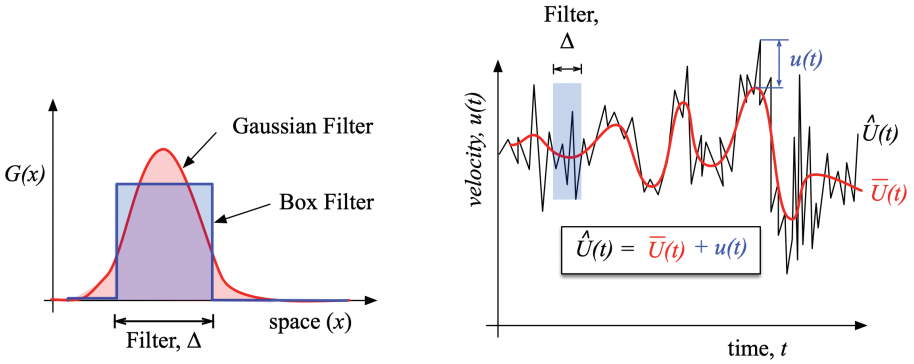

Fig. 10.7 Conceptual representation of the LES filtering operation. Left: the profile for a Gaussian and a box filter in space, with respect to grid size Δ. Right: the effect of filtering on the evolution of velocity. Comparison of instantaneous component $\hat{U}(t)$ and the filtered component $\overline{U}(t)$.

to be modelled. A low-pass filter, which allows lower wave numbers but removes higher ones, is used to decompose the instantaneous flow quantities, $\hat{\Phi}$, into the sum of a filtered component, $\overline{\Phi}$, and a residual component, φ. The residual component, $\hat{\Phi} - \overline{\Phi}$, requires modelling and its impacts on the flow are accounted for via the sgs model. The filtering operation, first introduced by Leonard (1975), is a convolution defined as follows:

$$\overline{\Phi}(x,t) = \int_{-\infty}^{+\infty} G(\Delta, x - x_1)\hat{\Phi}(x_1,t)dx_1 \tag{10.8}$$

where G is the spatial filter function with a width typically equal to the grid spacing, Δ, which satisfies the normalization condition:

$$\int_{-\infty}^{+\infty} G(x - x_i)dx_i = 1. \tag{10.9}$$

With finite-volume solvers, the filter for LES is usually chosen to be of box-type or Gaussian, while for spectral solvers, a sharp cut-off filter is applied, as illustrated in Fig. 10.7. It is important to note that, by virtue of the averaging applied by Eq. (10.8), these filtering operations behave quite differently from the RANS operator. The filtered Navier–Stokes equations may then be obtained for incompressible flow as:

$$\frac{\partial \overline{U}_i}{\partial t} + \frac{\partial \overline{U}_i \overline{U}_j}{\partial x_j} = -\frac{1}{\rho}\frac{\partial \overline{P}}{\partial x_i} + \frac{1}{\rho}\frac{\partial \tau_{ij}^{sgs}}{\partial x_j}; \quad \frac{\partial \overline{U}_i}{\partial x_i} = 0. \tag{10.10}$$

10.2.1 Sub-grid-scale modelling

In a similar manner to the RANS equations, the sgs stress tensor includes contributions from both the filtered and the instantaneous velocity fields, and since the contribution from instantaneous velocity is unknown, a closure is needed.

https://doi.org/10.1017/9781108875400.012 Published online by Cambridge University Press

$$\tau_{ij}^{sgs}/\rho = \overline{\hat{U}_i\hat{U}_j} - \overline{U}_i\overline{U}_j. \tag{10.11}$$

On substituting the definition, $\hat{U}_i = \overline{U}_i + u_i$, the full set of terms requiring closure (which for convenience are grouped into three sets) are as follows:

$$\begin{aligned}\tau_{ij}^{sgs}/\rho &= \overline{(U_i + u_i)(U_j + u_j)} - (\overline{U_i + u_i})(\overline{U_j + u_j}) \\ &= (\overline{U_iU_j + u_iU_j + U_iu_j + u_iu_j}) - \overline{U}_i\overline{U}_j \\ &= L_{ij} + C_{ij} + R_{ij}\end{aligned} \tag{10.12}$$

where

$L_{ij} = \overline{U_iU_j} - \overline{U}_i\overline{U}_j$ are the Leonard stresses which represent the resolved large-scale stresses and fluctuations resulting from the interactions between them;

$C_{ij} = \overline{u_i\overline{U}_j} + \overline{u_j\overline{U}_i}$ are the cross stresses which represent the cross-interactions between the resolved and the sub-grid stresses;

$R_{ij} = \overline{u_iu_j}$ are the sgs stresses.

All terms in Eq. (10.12) except for $\overline{U}_i\overline{U}_j$ require modelling via τ_{ij}^{sgs}. (In contrast, when the common time-averaged RANS operator is employed, terms corresponding to L_{ij} and C_{ij} are neglected. However, as noted in Chapter 9 (§9.2.1), in presenting the URANS approach using ensemble or phase averaging, the same type of terms, L_{ij} and C_{ij}, appear, with C_{ij} shown to be finite (in the URANS framework) but negligible, especially at higher Re numbers.

Superficially, the filtered Navier–Stokes equation, Eq. (10.10), and the Reynolds-averaged Navier–Stokes equation, as given in Eq. (2.14), appear identical in form, though the role of τ_{ij}^{sgs} is rather different from that of a RANS closure model. Nevertheless, a solver written for the RANS equations can be readily modified to solve the filtered Navier–Stokes equations instead. Indeed, it is possible to 'transform' a RANS solver to an LES solver with just a few lines of code, although more fundamental changes to numerical methods, boundary conditions and data output are also required.

In the following we introduce the most common sgs modelling approaches employed by LES users, but this is by no means intended to provide a comprehensive review of the topic. Readers interested in exploring in greater depth the further development and considerations of LES filtering and sgs modelling are referred to the several more comprehensive textbooks on this topic (e.g. Pope, 2000; Lesieur *et al.*, 2005; Sagaut, 2006; Schiestel, 2008).

The Smagorinsky model

The Smagorinsky model, the original sgs model proposed for LES (Smagorinsky, 1963), adopts the Boussinesq eddy-viscosity hypothesis. Its form closely follows the mixing-length hypothesis (MLH) of Prandtl (1925). While the MLH, discussed briefly in §7.4.7, is known to be extremely limited in its ability to represent the

https://doi.org/10.1017/9781108875400.012 Published online by Cambridge University Press

non-linear interactions governing large-scale motions in a turbulent flow, it remains well-suited to the isotropic and small-scale turbulence at unresolved scales in LES. In this context the form of the eddy-viscosity model is as follows:

$$\tau_{ij}^{sgs}/\rho = -2\nu_{sgs}\overline{S}_{ij} + \delta_{ij}\tau_{kk}^{sgs}/3\rho \tag{10.13}$$

where the sub-grid eddy viscosity, ν_{sgs}, is approximated as the product of representative length and time scales. The length scale is provided directly from the numerical grid, Δ, scaled by a constant, c_s, known as the Smagorinsky constant. The time scale is conveniently taken from the computed flow field via the invariant of the resolved velocity gradient tensor, $\left|\overline{S}\right| = \sqrt{2\overline{S}_{ij}\overline{S}_{ij}}$:

$$\nu_{sgs} = (c_s\Delta)^2\left|\overline{S}\right|. \tag{10.14}$$

The rudimentary nature of the scheme needs to be emphasized: there is no accounting for transport nor anisotropy, and no history effects are included. It seems evident that more comprehensive modelling would be needed unless the model is applied simply to the smallest scales of the spectrum. This is underlined by the fact that the value assigned to the constant c_s is case-dependent, and although a value of $c_s = 0.1$ is commonly used for many practical shear flow cases, quoted values range from $c_s = 0.065$ for turbulent channel flow (Moin and Kim, 1982) to $c_s = 0.2$ for HIT (Clark *et al.*, 1979). Moreover, the Smagorinsky constant needs to be reduced approaching a solid wall to reflect the reduction of turbulent stresses. This is generally achieved via a near-wall damping function, f_D, the most commonly adopted form of which being that proposed by Van Driest (1956) for use with Prandtl's MLH:

$$f_D = 1 - e^{-y^+/A^+} \tag{10.15}$$

with the damping constant A^+ taken as 25. This value is close to Van Driest's original proposal of 26, though none of the schemes for causing A^+ to vary, discussed in §7.4.7, appear to have been explored. Clearly, in laminar flows the sub-grid model should be switched off entirely, although this raises issues about the model's capacity to operate in cases exhibiting both laminar and turbulent flow, e.g. transition. It is also seen from Eq. (10.14) that the viscosity is positive; thus, there is no mechanism to allow a negative migration, or 'back-scatter' of energy from sgs to the resolved scales. Despite these drawbacks, the Smagorinsky model still enjoys a great deal of use on account of its simplicity, though users need to be aware of its shortcomings.

Part of the reason for the wide range in the values proposed for c_s stems from additional numerical diffusion arising from inadequacies of discretization schemes. Garnier *et al.* (1999) demonstrated that the numerical discretization error for a given code could be re-expressed in the form of a Smagorinsky model, where the equivalent 'extra' value of c_s is low for codes with low numerical diffusion and high for codes with high numerical diffusion. It was shown that in cases where the

https://doi.org/10.1017/9781108875400.012 Published online by Cambridge University Press

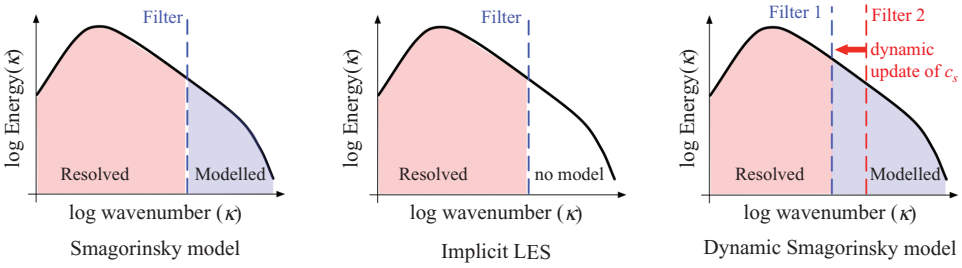

Fig. 10.8 Conceptual comparison of different sgs modelling approaches for LES, as represented by the turbulent kinetic energy spectrum. (Left) LES with a Smagorinsky or other sgs model. (Middle) Implicit LES, where no sgs model is used. (Right) A dynamic Smagorinsky model, where the constant c_s is updated in space and time based on the evaluation of two filtering operations.

equivalent false supplement to c_s was high, the underlying effect of the actual sgs model could be lost. In effect, the numerical error played the role of the sub-grid model, and a separate model for τ_{ij}^{sgs} was not required. While this may appear to be an unwelcome effect, it is actually the essence of a well-established and still quite widely used approach noted below.

Implicit filtering

The so-called *implicitly-filtered LES* (or simply Implicit LES) effectively provides sgs dissipation through the inherent numerical losses incurred from the mesh, and/or the particular numerical solving methods employed (see Fig. 10.8). Such methods are particularly useful where the complexity of the sub-grid physics exceeds the capabilities of the models available in the software, such as for compressibility effects due to combustion or shock-turbulence interactions (e.g. Lele, 1994). A popular strategy is the MILES (Monotonically Integrated Large-Eddy Simulation) strategy, a scheme proposed by Grinstein and Fureby (2002). While simplicity is a clear benefit of this family of models, the lack of direct control makes it difficult to fix the precise form of the filter, or to adjust the degree of filtering to the local mean-flow field. As a counter to these limitations, the level of numerical diffusion *can* be controlled by introducing higher-order schemes with specific numerical features. For further details on this topic the reader is referred to the comprehensive text by Grinstein *et al.* (2007).

Dynamic sub-grid-scale modelling

Dynamic sgs modelling seeks to overcome the weaknesses inherent in choosing a constant Smagorinsky coefficient throughout a domain. Germano *et al.* (1991) proposed the *dynamic Smagorinsky model* as a framework for automatically computing the required value of $c_s(x_i,\ t)$ as a function of space and time (see Fig. 10.8).

https://doi.org/10.1017/9781108875400.012 Published online by Cambridge University Press

The approach is based on the scale-similarity assumption, by relating the turbulent stresses at one scale Δ to those at a larger scale $n\Delta$, where $n > 1$ (commonly $n = 2$, which, with uniform mesh spacing, can be achieved by using a subset of the same grid). The assumption of scale similarity is used to define a value of c_s which satisfies both grid scales, i.e. $c_s|_\Delta = c_s|_{n\Delta}$. This is justified on the basis that both scales appear in the inertial range of turbulence and thus are likely to be 'scale-similar'. The model is now more suitable than the original for flows containing both laminar and turbulent regions, with the former corresponding to values of $c_s \simeq 0$. The constant can even take negative values, corresponding to the transfer of energy from smaller to larger scales, i.e. 'back-scatter' as introduced at the end of §10.1.1. These benefits come at a cost, however, in the form of reduced numerical stability and, possibly, the need for a finer mesh compared with the standard Smagorinsky model to ensure that both mesh sizes lie within the inertial subrange. Modifications proposed by Lilly (1992) and Meneveau *et al.* (1996) have helped to overcome these shortcomings though, conceptually, the scale-similarity assumption would not appear to be valid in regions where Δ approaches L or where either transition or laminarization is present. Despite these limitations, the scheme's undoubted success may be attributed to the fact that the procedure effectively identifies a value of c_s which reduces the sensitivity to the mesh at any point (Pope, 2004). These issues have been further addressed in the work by Bou-Zeid *et al.* (2005), which proposes a scale-dependent framework based on local averaging of the flow field.

More complex approaches

There are many other approaches for estimating the sgs stresses. Among them, we mention the Wall-Adapting Local Eddy-Viscosity (WALE) model of Nicoud and Ducros (1999) that has received considerable attention. The model was developed for wall-resolved LES of flows bounded by walls of complex configuration because it reproduces the near-wall scaling for the eddy viscosity without requiring any dynamic procedure or empirical damping. The WALE model is based on the square of the velocity gradient tensor.

$$\nu_{sgs} = (C_w\Delta)^2 \frac{(S^d_{ij}S^d_{ij})^{3/2}}{(\bar{S}_{ij}\bar{S}_{ij})^{5/2} + (S^d_{ij}S^d_{ij})^{5/4}} \quad \text{where } S^d_{ij} = \frac{1}{2}(\bar{g}_{ik}\bar{g}_{kj} + \bar{g}_{jk}\bar{g}_{ki}) - \frac{1}{3}\delta_{ij}(\bar{g}_{kk})^2 \text{ and, } \quad \bar{g}_{ij} = \partial\bar{U}_i/\partial x_j. \tag{10.16}$$

A mix of the local strain and rotation rates of the smallest resolved turbulent fluctuations in the sgs viscosity is designed to detect the near-wall dissipative structures, thus ensuring a proper near-wall behaviour by forcing the sgs eddy viscosity to diminish to zero when approaching a wall.

https://doi.org/10.1017/9781108875400.012 Published online by Cambridge University Press

Another popular choice (which overcomes some of the limitations of the Smagorinsky model) is the one-equation model for sub-grid kinetic energy, k_{sgs}, which takes the form:

$$\frac{\partial k_{sgs}}{\partial t} + \frac{\partial \overline{U}_j k_{sgs}}{\partial x_j} = -\tau_{ij}^{sgs}\overline{S}_{ij}/\rho - c_1\frac{k_{sgs}^{3/2}}{\Delta} + \frac{\partial}{\partial x_j}\left(\nu\frac{\partial k_{sgs}}{\partial x_j} + c_2 k_{sgs}^{1/2}\Delta\frac{\partial k_{sgs}}{\partial x_j}\right) \tag{10.17}$$

where terms on the right side are the readily recognized processes of generation by interaction of the sub-grid stresses with the strain field; dissipation by the fine-scale unresolved motion; and molecular and turbulent diffusion. Yoshizawa (1982) took the two empirical constants to be $c_1 = 1$ and $c_2 = 0.1$. The above approach introduces additional information about the sgs which, in principle, allows improved handling of non-equilibrium and time-history effects and spatial awareness into the sgs. It is found to offer improved stability over the dynamic sgs model and has the useful benefit of providing a means of directly computing the relative proportions of resolved to total turbulence energy at any point.

10.2.2 Resolution requirements of LES

Away from a wall, LES can be performed on coarser grids than those needed for DNS since this approach does not attempt to resolve the smallest scales of motion. However, as the wall is approached, the grid requirement becomes severe, particularly at high Reynolds numbers, since the local turbulence integral length scale is linearly dependent on wall distance, y. Even the largest eddies become small close to the wall since there $L \sim y$, requiring fine-grid resolution to completely resolve them. The region over which viscous stresses dominate turbulent stresses, i.e. the viscous sublayer, shrinks progressively as the Reynolds number increases, enabling turbulent eddies to persist closer to the wall. These structures cannot be readily ignored, since the near-wall region contributes substantially to turbulence energy dissipation.

An illustration of the grid sensitivity of LES in near-wall turbulent flows is provided in Fig. 10.9, from the work of Temmerman *et al.* (2005). The turbulent channel flow at a Reynolds number, based on wall units, of $\mathrm{Re}_\tau = 2,000$ is computed using LES on two grids for a periodic domain of $2\pi h \times 2h \times \pi h$. The 'coarse' grid is based on a typical grid resolution for a RANS approach of $64 \times 64 \times 32$ cells (in streamwise, wall-normal and spanwise directions, respectively) with necessary near-wall refinement for the low-Reynolds-number region, but high-aspect-ratio cells. The 'fine' grid resolution, of $512 \times 128 \times 128$, has

https://doi.org/10.1017/9781108875400.012 Published online by Cambridge University Press

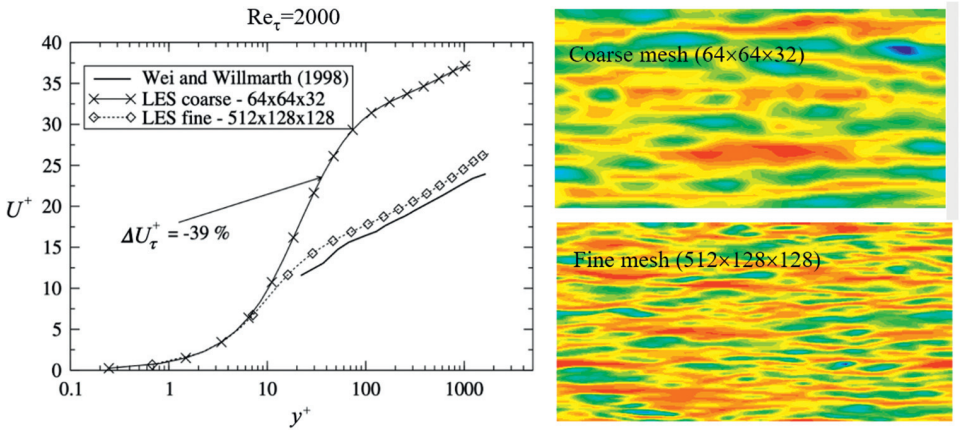

Fig. 10.9 Simulation results from LES at $\mathrm{Re}_\tau = 2,000$ for flow in a plane channel with a coarse and a fine mesh. Left: Time-averaged velocity profile scaled by wall units; Right: Instantaneous velocity contours from the two meshes on the plane $y^+ = 6$. Left: from Temmerman et al. (2005), reproduced by permission of Elsevier; right: from Hadžiabdić (2005), reproduced by permission of the author.

a total number of cells 64 times greater than the coarse mesh. These mesh scaling factors are indicative of the increased requirements when moving from RANS to LES, with cell count increasing by factors of 8 and 4 in the streamwise and spanwise directions, respectively, but only a factor of 2 in the wall-normal direction. With increased spatial resolution, an additional cost is necessarily incurred by the requirement to ensure a suitable temporal resolution. For a given local flow velocity, the requisite temporal resolution Δt is directly connected to the spatial resolution Δx by the condition proposed by Courant, Friedrichs and Lewy (1928). This condition, normally abbreviated to CFL, states that the local flow velocity U should be smaller than the smallest resolvable velocity $\Delta x/\Delta t$; or that the CFL number:

$$\mathrm{CFL} \equiv \frac{U\,\Delta t}{\Delta x} \tag{10.18}$$

should be a maximum of unity. As shown in the figure, the fine LES mesh provides reasonable agreement with the reference experimental data, but the prediction returned from the coarse mesh is poor, particularly when scaled by wall units, since the computed value of U_τ is under-predicted by almost 40%. Part of the reason for this error is the failure to resolve the near-wall turbulence correctly. The figure also shows contours of instantaneous velocity taken very near the wall surface ($y^+ = 6$) there is a striking difference between the flow structures predicted by the two meshes. The coarse mesh predicts a series of long streaks, many of which span the entire length of the domain. These so-called super-structures are not physical and are a tell-tale sign of under-resolution in scale-resolving methods.

https://doi.org/10.1017/9781108875400.012 Published online by Cambridge University Press

In contrast, the near-wall streaks from the fine mesh are shorter, thinner and more closely packed. This underlines the need for finer resolution of near-wall turbulent structures in LES and the erroneous results that may arise from not meeting that need. In the near-wall region it becomes impossible to define a clear separation between large and small scales, in the same way one does away from the wall. Thus, near-wall resolution requirements for LES are very high, essentially similar to those of DNS. Usually, the grid resolution needed means that the majority of the mesh nodes for the whole domain are in this region. These requirements are further explored in the following section.

Best-practice criteria for wall-resolved LES

In his landmark paper estimating the readiness of LES for application to actual problems in aerospace engineering, Chapman (1979) provided a detailed analysis of the number of cells required for wall-resolved LES applied to a turbulent boundary layer. He separated the flow into two regions: the inner and outer layers.

The outer layer of the boundary layer, beginning at about 0.1δ, where the mean velocity is effectively independent of viscosity, is populated by eddies that scale with the outer scales of the flow and is representative of the larger structures in the energy spectrum. That is, it is of the order of the boundary-layer thickness, δ, or, in the case of a simple internal flow, the channel half-height or pipe radius. Away from a wall, the main physical guidance for mesh resolution comes from the turbulent kinetic energy spectrum. Considering that the cut-off filter in LES should ideally be placed within the inertial cascade (beyond which scales can more readily be modelled), the grid resolution required to resolve scales is essentially independent of Reynolds number, since progression to higher Reynolds number simply extends the high-wave-number sgs-modelled region. Then the main concern is to ensure sufficient resolution quality wherever turbulent flow is expected. By using an idealized form of the energy spectrum, Chapman demonstrated that the number of cells required to resolve the eddies in a unit volume of the boundary layer was proportional only to the increasing volume of the boundary layer. An example is provided in Fig. 10.10 to illustrate this concept. Since experimental measurements show that in the absence of pressure gradients the turbulent boundary layer grows downstream at a rate proportional to $\mathrm{Re}^{0.2}$, an extra $\mathrm{Re}^{0.4}$ cells are needed since the streamwise resolution is unchanged. Chapman estimated the unit volume, δ^3, to require around 2500 cells. In practice, this value will depend on the particular choice of solver and the numerics employed. With the availability of more accurate experimental data, this number was more recently revised by Choi and Moin (2012) to $N_{cell}^{outer} \propto \mathrm{Re}^{0.29}$. These authors also surveyed a large number of previous studies and reported that requirements for $N_{cell}^{outer}/\delta^3$ fell in the range from 1,200 to 33,000. This very wide range resulted from a variation in N_x of more than six

https://doi.org/10.1017/9781108875400.012 Published online by Cambridge University Press

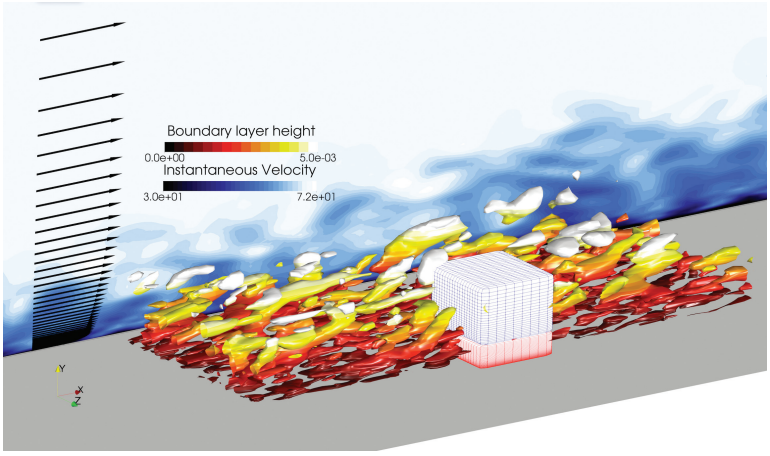

Fig. 10.10 Visualization of resolution requirement for a wall-modelled LES applied to the calculation of a flat-plate turbulent boundary layer. Instantaneous velocity contours are plotted at the back of the domain, along with a time-averaged velocity profile of the boundary layer. In the foreground, isosurfaces of vorticity are plotted and coloured with distance from the wall. The gridding arrangements are shown by way of a (non-physical and not to scale) white cube of side δ. Blue gridlines represent the outer layer comprising $8 \times 24 \times 24 = 4{,}608$ cells, while the red volume covers the inner layer, up to $y/\delta = 0.1$ with $8 \times 32 \times 24 = 6,144$ cells. (Revell and Mole, Personal Communication.)

with at least a twofold variation in the other directions. Beyond the outer layer, the flow may remain in an irrotational, inviscid state where the grid can be permitted to coarsen rapidly, especially when an unstructured mesh is used.

The inner region of the boundary layer incurs meshing requirements which are much more demanding, since here the effects of viscosity – and thus also of Reynolds number dependence – are much stronger. Indeed, here the mesh cells need to be scaled with wall units instead. If inner-layer eddies are to be adequately resolved, streamwise and spanwise grid spacings of $\Delta x^+ \simeq 100$, $\Delta z^+ \simeq 20$ are needed and with $\Delta y^+ \sim 1$. Chapman estimated the number of cells required to resolve a unit box to be proportional to $\mathrm{Re}^{1.8}$, subsequently revised by Choi and Moin (2012) to be $N_{cell}^{inner} \propto \mathrm{Re}^{1.86}$. In terms of specific cell dimensions for the inner layer, they propose $\Delta x^+ \equiv \Delta x U_\tau/\nu \cong 50 - 130$ and $\Delta z^+ \equiv \Delta z U_\tau/\nu \cong 15 - 30$, while the wall-normal mesh resolution should start with the first grid point or cell centre at $y^+ < 1$ and with 10–30 points in the wall-normal direction. Piomelli (2008) used the above recommendations to estimate the computational cost and time to simulate a turbulent boundary layer. He did this based on a standard workstation with a processing speed of 1 gigaflop. In

https://doi.org/10.1017/9781108875400.012 Published online by Cambridge University Press

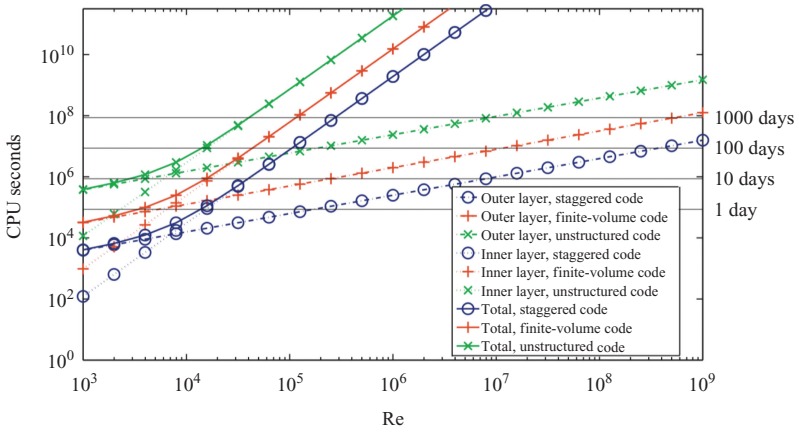

Fig. 10.11 Cost (in CPU seconds) of making an LES simulation of a flat-plate boundary layer. The calculations were performed on an AMD Opteron, using two in-house codes and an open-source code (from Piomelli, 2008).

his comparison, shown in Fig. 10.11, he plotted the inner and outer region times individually as well as their sum. The figure shows that even for a modest Reynolds number of around 10,000, some 50% of the computational effort is used to resolve the inner region, occupying around 10% of the flow. Doubling the Reynolds number to 20,000 leads to the inner share increasing to around 99%, clearly demonstrating the extremely high dependence of the resolution of the inner layer on Reynolds number. There is thus a strong motivation to find less time-consuming ways of resolving the inner region. Indeed, the options available for doing so are considered in §10.3 and subsequent sections. First, however, an important precursor issue is considered.

10.2.3 Interfacing LES and RANS strategies

If some alternative treatment, simpler and far less time-consuming than LES, is to be adopted for the inner region or 'zone', then issues arise as to how one handles the change in the representation of turbulence as fluid moves, or communicates by diffusion, between zones. Zonal methods which adopt separate RANS and LES regions, each treated with separate methodologies, must resolve this fundamental issue. On one side, the flow equations in the RANS zone adopt the RANS-averaging strategy (whether in steady or unsteady mode) used in earlier chapters while, in the LES zone, fluctuations are resolved directly at wave numbers far greater than resolved with a URANS resolution (or are accounted for only in their time-averaged effect in a steady RANS treatment). In the two-layer zonal approach the wall-adjacent region is, however, usually handled by URANS, i.e.

https://doi.org/10.1017/9781108875400.012 Published online by Cambridge University Press

solved in time simultaneously with the outer LES and thus excited by LES fluctuations across the interface. To a considerable extent that compensates for the limitations of natural URANS scale resolving. The issue is discussed in more detail in §10.5.2, where an *a priori* testing demonstrates satisfactory sensitivity and responsiveness of the URANS-computed velocity and wall shear stress to LES excitations.

However, in bulk zonal strategies where large flow regions (e.g. wall-attached flow regions upstream of separation) are handled by a steady RANS and only some or embedded zones are computed by LES, a representation of the turbulent fluctuations in the velocity field, $u_i(t)$, must be introduced. This is required to switch efficiently between a region of RANS solution and a region of LES, since the fluctuations are not present in the averaged flow field of the RANS region (or are only incompletely represented if a URANS treatment is adopted).

When 'pure' LES is applied to other than a fully developed flow,[3] one encounters an equivalent problem in assigning inlet boundary conditions to any fluctuating variable. One might suppose that a reasonable approach would be to superimpose a randomly fluctuating 'white-noise' velocity field onto the mean-flow profile to trigger the generation of turbulence downstream. However, this is insufficient and the flow quickly decays to a steady profile. The turbulent fluctuations themselves may appear to be random but, as we have seen in earlier chapters, they are shaped by a complex set of interacting physical processes. In fact, it is now appreciated that a well-prepared 'synthetic turbulence' approach *is* able to provide an inlet turbulence that is sustained as the flow develops downstream.

In this section, two principal methods for assigning inlet turbulence are considered: *precursor methods* and *synthesised methods*. An outline of both approaches follows while, for further details, the reader is referred to Tabor and Baba-Ahmadi (2010) and, more recently, Wu (2017), who provides a detailed review of LES inlet techniques that includes an outline of their application within an HRL framework.

Precursor methods

For simulations where all or almost all the physical scales are to be simulated directly, as in DNS or wall-resolved LES, defining the inlet boundary condition requires significant care and attention (far more so than is needed for RANS methods). The accuracy of the downstream simulation is directly dependent on the prescription of the inlet condition; without such careful definition, the value of expensive simulations can be greatly reduced. There are several inlet techniques specifically developed to achieve high-fidelity simulation, albeit at a cost.

[3] In the case of fully developed or periodically repeating flow, the inlet boundary conditions at any point may be successively updated by transferring values from the exit plane at the same (y, z) location and time (or even from the preceding time-step) to the inlet plane: $U(x_{in}, y, z, t) = U(x_{out}, y, z, t)$.

https://doi.org/10.1017/9781108875400.012 Published online by Cambridge University Press

Precursor or 'recycling' methods apply data from a separate, high-fidelity simulation to the inlet boundary of the target domain. There are two main categories of this approach. The first, sometimes referred to as 'strong' recycling methods, involves running a supplementary simulation in advance, to generate precise inlet data. The supplementary simulation is usually periodic, and will often require a significant computational effort to produce. Once completed, a velocity profile, U_{pre}, is extracted at the desired reference plane, x_{rp}, and applied at the inlet to the target domain, i.e.

$$U(x_{in}, y, z, t) = U_{pre}(x_{rp}, y, z, t). \tag{10.19}$$

For this method to work effectively, the geometry, mesh and Reynolds number of the supplementary simulation at the point $x_{rp}(t)$ should match those at the inlet location, $x_{in}(t)$, of the target simulation. The data storage requirement may be large, since data should cover a period in time equal to the required duration of the target simulation. The cost can be reduced by invoking Taylor's (frozen turbulence) hypothesis, in which the variation of turbulence in time is taken as equivalent to that in space. With that assumption one can instead sweep the location of the sampling plane in the streamwise direction at a rate equal to the bulk velocity, U_b, at a *single* instant of time thus, effectively, providing data for all required time.

While the above approach is only applicable to periodic precursor flows, a second category of methods is available for cases where the upstream flow evolves in a self-similar manner, such as the growth of a flat-plate turbulent boundary layer. In these cases, a 'recycling station' is used to develop fully turbulent boundary conditions from a mean-flow profile, within the same simulation as the target domain, i.e. no precursor simulation is required. These 'weak recycling' methods, originally proposed by Spalart (1988) and later extended by Lund *et al.* (1998) for the case of a zero-pressure-gradient turbulent boundary layer, require an iterative rescaling to take place between the domain inlet and a second location downstream. The fluctuating velocity component from the downstream location is extracted and rescaled according to the local Reynolds number of the turbulent boundary layer, before being superimposed on the mean inlet boundary-layer profile obtained from a theoretical model. The process is repeated until the desired boundary-layer Reynolds number is achieved at the downstream location. While limited to self-similar flows, the approach is relatively simple to implement and found to be quite efficient. Nevertheless, the technique remains inadequate in regions of strong pressure gradients and tends to suffer from issues of spurious periodicity introduced by the recycling process causing non-physical peaks in the spectra.

Synthetic methods – reconstructing the Reynolds stress tensor

Precursor methods are based on simulation data resulting from full solution of the Navier–Stokes equations, which are then transferred or manipulated onto the

https://doi.org/10.1017/9781108875400.012 Published online by Cambridge University Press

required inlet plane as needed. In contrast, for synthetic inlet methods the turbulent velocity fluctuations are synthesized artificially, without solving the Navier–Stokes equations, a strategy that poses a formidable challenge. A stochastically varying inlet condition must be created from a reduced set of low-order statistical data, such as the mean velocity and an approximate Reynolds stress tensor. While some knowledge of the low-order statistics may be available (or, at least, can be approximated from prior knowledge plus concepts such as local equilibrium), a full-time history of such data will almost certainly not be. The approach recognizes at the outset that a precise definition is not practical and instead aims to minimize the impact of the imperfect upstream boundary definition on the downstream domain. Synthetic methods provide a low-cost strategy and their success is often measured by the rate at which turbulent statistics return to expected levels downstream of the inlet. That is, an 'adjustment length' is anticipated downstream from the start of the domain where results are less reliable. While, unlike precursor methods, synthetic methods are not able to provide an exact replication of turbulence, they are considered the preferred option for more complex engineering applications and are also the predominant approach used in HRL methods.

In general, synthetic methods work on the basis of performing a Reynolds decomposition of the velocity field, in order to split the flow into mean and stochastic components. The mean component is required as an input to the method, while the stochastic component is synthetically generated so as to have a variance and co-variance consistent with a prescribed Reynolds stress tensor. From the user's perspective, the inflow problem is then reduced to the prescription of low-order statistical data over the inlet plane itself. In practice, these low-order statistics may be obtained by experiment, theoretical approximation or, as is perhaps the most common, by a separate or 'precursor' RANS study. Indeed, RANS statistics may be interpolated from an entirely independent calculation with different mesh, numerics and underlying code. As a natural evolution of this concept, it might then become useful to couple the RANS data generated in one mesh, with the generation of synthetic turbulence and subsequent turbulent simulation in another; such an approach can be termed embedded LES (ELES). This is described further in §10.4.

The simplest form of stochastically varying inflow condition is white noise. However, as reported above, this choice does not work even if one scales the fluctuations to match the magnitude of the Reynolds stress tensor. The missing ingredient is coherence: the length and time scales of white noise are of the order of the cell size and time-step size, respectively. Since the energy is evenly distributed between low- and high-wave-number ranges of the spectrum, the classical energy cascade is not established, and the fluctuations are quickly dissipated. It is thus apparent that practical synthetic turbulence generators must take into account some higher-order statistics, either explicitly or implicitly through the use of a length scale.

There are several classes of synthetic methods available in the literature. These include, but are not limited to, methods based on the following:

- *Digital filtering methods*: where statistical restrictions are placed on initially random data in order to mimic physical constraints (e.g. Klein *et al.*, 2003; Schmidt and Breuer, 2015);
- *Higher-order decomposition*: where they exist, detailed DNS data providing length-scale correlations in all coordinate directions can be reduced to provide an approximation for turbulence statistics (e.g. Druault *et al.*, 2004; Perret *et al.*, 2008);
- *Fourier modes*: fluctuations are generated based on the superposition of Fourier modes at the inlet, according to a prescribed representation of the turbulence energy spectrum (e.g. Smirnov *et al.*, 2001; Davidson and Billson, 2006; Shur *et al.*, 2014);
- *Synthetic methods*: a strategy in which 2D or 3D patches of fluctuations representing physical eddies are convected across the inlet boundary where fluctuations are sampled and superimposed on the mean flow.

It is beyond the scope of this book to discuss all the above methods in further detail, particularly as the first three are designed for use with DNS or LES methods. In the context of HRL methods, however, the fourth approach merits more extensive consideration.

Synthetic eddies

The creation of a field of synthetic turbulent eddies, or local spots of coherent fluctuations, provides a popular route for the generation of fluctuations. The first appearance of this Synthetic Eddy Method (SEM), proposed by Sergent (2002), introduced a random sequence of 2D vortices at different locations on the inlet plane, where they remained for short periods before disappearing and reappearing elsewhere on the same plane with a different intensity. In this way an attempt is made to mimic the passage of a field of turbulent eddies through the plane. Jarrin *et al.* (2006) extended this idea to 3D patches of motion. In this framework, synthetic eddies are generated with the intensity and sign of the fluctuations set to satisfy the prescribed first- and second-order statistics. The size of the synthetic eddies is a required user input, generally correlated to mean turbulence inlet data from a precursor RANS calculation.

The SEM has proved to be simple to implement, and provides a reasonable approximation to turbulent inflow at low computational cost. Since its inception several derivatives of it have been proposed, which have incrementally improved the performance. For external boundary layers Pamiès *et al.* (2009) split the inlet plane into discrete regions or modes. Within each region a different calibration of

the SEM was applied, in order to realize a specific arrangement of eddies with certain characteristic sizes and shapes. The eddy properties in each mode were set to match the local flow physics (e.g. streaks very close to a wall, with more isotropic eddies at modes away from the wall). In this approach, the selection of modes and corresponding eddy properties are described as suitable for a zero-pressure-gradient boundary layer. The adoption of the method for a significantly different flow type would involve identifying the appropriate eddy characteristics and recalibrating the modes; *that* assumes, however, the availability of relevant DNS or experimental data for this purpose. Another extension of the SEM, the Divergence-Free SEM (DFSEM), was proposed first for isotropic and, subsequently, for anisotropic turbulence by Poletto *et al.* (2013), with the aim of reducing non-negligible violations of mass conservation that had been found to cause numerical problems in the original method. Since the synthetic turbulence generated is then divergence-free, pressure fluctuations that would otherwise develop near the inlet are reduced. For a compressible solver, this has the advantage of reducing the spurious noise introduced at the inlet. For an incompressible solver, Poletto *et al.* (2013) report a reduction in the number of inner iterations required for their pressure solver to converge. Skillen *et al.* (2016) have proposed accuracy and efficiency improvements to the standard SEM as well as an alternate fluctuation normalization factor. Their scheme is based on a running average of the eddy concentration that guarantees the desired statistical properties, regardless of the spatial distribution or length scale of the eddies, thus correctly allowing for an inhomogeneous distribution of eddy size.

Figure 10.12 displays a comparison of the DFSEM with the vortex method of Sergent (2002), demonstrating that turbulent structures appear almost immediately downstream of the inlet in the former, when compared to the latter. The advantage of introducing additional information about the three-dimensional size and shape of the turbulent structures is clearly apparent also for the development of the Reynolds stresses. Figure 10.12c indicates an immediate convergence to the values of streamwise normal stress, obtained from a periodic channel for the DFSEM, whereas for the vortex method no correlation is present from the start of the domain, $x/\delta = 0$, and as such it requires a distance of almost 25δ to reach the correct levels.

10.3 The classification of hybrid methods

In the previous section the theory and framework for LES have been introduced. A means for approximating the cost of the approach was considered and the dramatic rise in these costs with increasing Reynolds number was noted. A clear conclusion was that without some further simplifying strategy, wall-resolved (WR)LES would not be usable for predicting high-Reynolds-number flows of industrial or environmental interest for many years to come. There is thus a strong motivation

https://doi.org/10.1017/9781108875400.012 Published online by Cambridge University Press

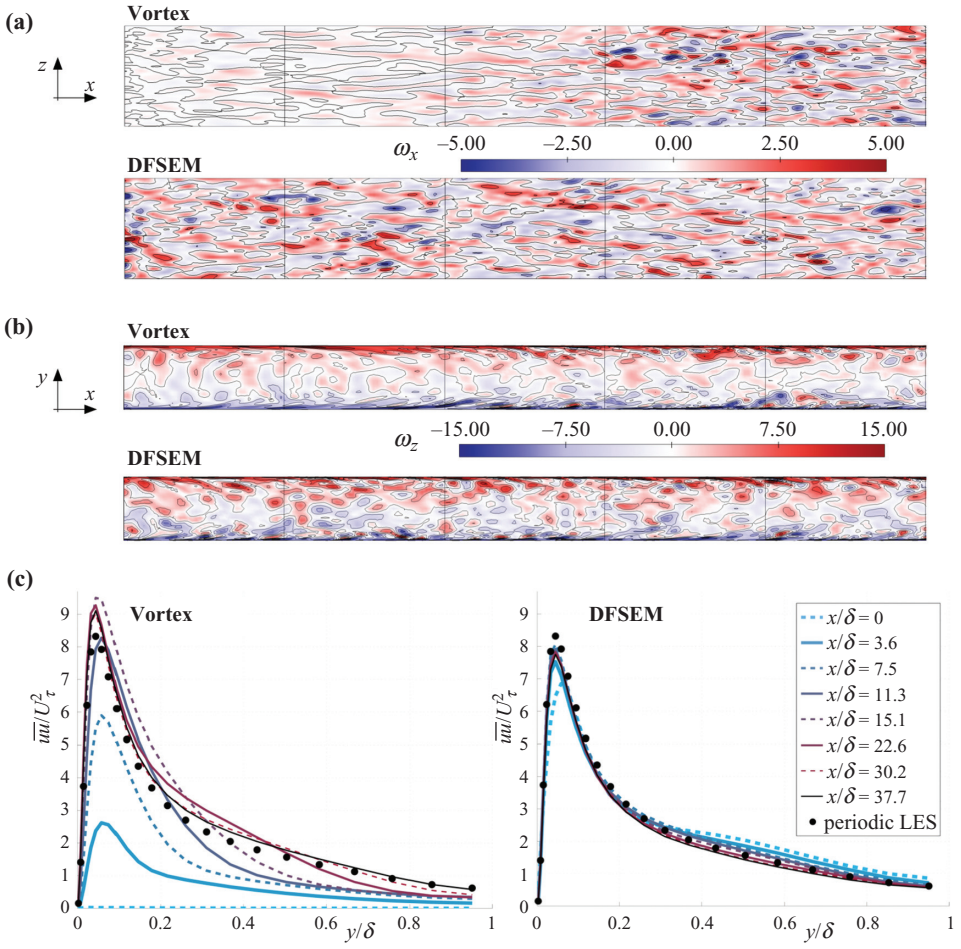

Fig. 10.12 Comparison of two synthetic eddy strategies applied at the inlet of a turbulent channel flow LES for $\mathrm{Re}_\tau = 395$: the vortex method of Sergent (2002) and DFSEM of Poletto *et al.* (2013). (a) contours of streamwise vorticity ω_x at the location $y/\delta = 0.05$. Faint vertical black lines denote intervals of 5δ, (b) contours of spanwise vorticity ω_z at the centre of the domain, (c) profiles of the streamwise normal component of Reynolds stress at different intervals downstream of the inlet.

to increase the role of modelling beyond that adopted in WRLES, essentially employing well-tested RANS models where it is known they reliably capture the turbulence behaviour and leaving LES to handle the remainder of the flow domain. It is from this standpoint that the main strategies for simplification are now explored in the context of HRL methods. After more than two decades of research, it is an area that has seen a large number of approaches and a sizeable community of model developers and industrial practitioners. These methods have been developed to address a wide range of different objectives and applications by researchers with

https://doi.org/10.1017/9781108875400.012 Published online by Cambridge University Press

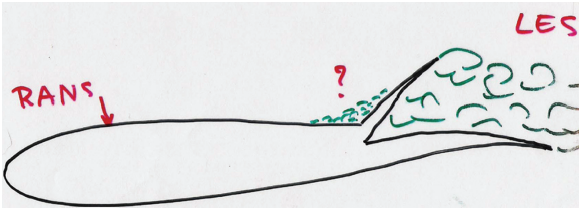

Fig. 10.13 A sketch by Philippe Spalart during early work on Detached Eddy Simulation, demonstrating the motivation for a methodology capable of operating in both RANS and LES modes, but identifying the 'grey area' problem in the region between the two (Spalart *et al.*, 1997).

diverse backgrounds and motivations. This diversity makes it difficult to classify approaches without exceptions, but in the following pages a framework is provided for organizing the different approaches.

Spalart, one of the originators of Hybrid RANS-LES, communicated these issues via a sketch during the early development of the seamless strategy for aerospace applications (Fig. 10.13). The existence of the transition zone and the associated challenges have come to be known as the 'grey area' problem, and a substantial body of research has appeared in recent years aimed at minimizing the extent and impact of its occurrence.

There are two main guiding principles that have broadly served to create a major difference between most proposed methods. The first is the idea that the separate strategies of RANS and LES are themselves mature and well understood; so, the best way forward is to combine these methods in the most efficient way. Such methods are generally known as 'zonal' or 'segregated' approaches. The second is the observation that both frameworks share commonality in their derivation and functional form (particularly for the *unsteady* RANS equations). This has motivated the development of 'seamless' (or 'global') frameworks which aim to adjust the function of a single baseline model, whether RANS or LES, to include the capability of the other.[4]

There is an exception to the classification above: *wall-modelled LES* methods which form a third category in Fig. 10.14. While these can be considered as zonal methods, in this presentation they are treated separately. Their motivation has been the adaptation of LES for high-Reynolds-number flows, and their development has, in large measure, been driven by the LES community. A brief account of the

[4] To avoid confusion, it is noted that throughout this chapter the acronyms RANS and URANS are not used interchangeably, but each with a specific meaning: the RANS refers to the *model* whether solved in steady or unsteady mode, whereas URANS refers to the (unsteady) mode of solution. Note also that the vast majority of HRL schemes apply URANS in the 'RANS region', i.e. a RANS model solved in unsteady mode simultaneously with a true LES or its surrogate in the 'LES region'.

https://doi.org/10.1017/9781108875400.012 Published online by Cambridge University Press

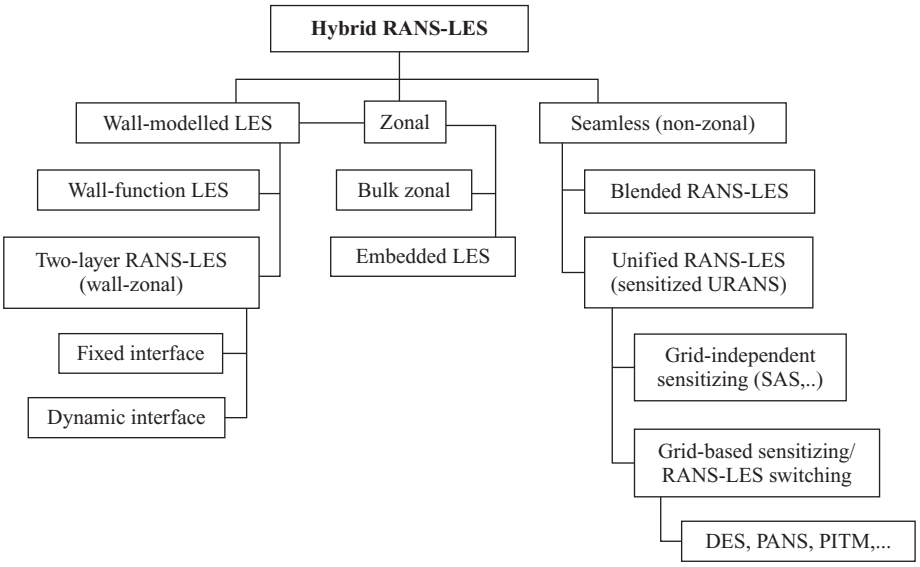

Fig. 10.14 A conceptual classification of Hybrid RANS-LES and their subclasses.

different strategies is provided below as a preliminary to further discussion. It is noted that each of the three categories of HRL contains a number of variants (submodels), which are difficult to classify in a clear-cut manner. The best known and popular methods are noted in Fig. 10.14.

Zonal methods. In these methods the prescription of RANS and LES regions is made in advance, based on knowledge or anticipation of the flow and the need to compromise between accuracy and cost. RANS regions are not limited to the near-wall as in WMLES but may be applied more extensively. These methods are more of a toolkit than a single approach, with different elements being interchangeable, thus bringing different solution strategies together effectively and without adversely impacting the prediction. A RANS treatment is used, where possible in steady mode (if the flow is stationary in the bulk) or solved in time (for unsteady flows without resolving any turbulence scales), while the LES-based treatment is here minimized or 'embedded' within the RANS zone in regions where scale resolution is deemed to be important. Usually, the LES is employed with an sgs viscosity defined with a length scale based on the grid size, Δ. Such methods are also known as segregated or 'bulk zonal' approaches to distinguish them from 'wall zonal'. The main challenge in their application lies at the interface where artificial/synthetic fluctuations need to be generated on the RANS side of the interface to match the LES. Determining how realistic, instantaneous fluctuations can be introduced at the inlet to the LES region is a crucial feature of these methods. In the other direction, from LES to RANS, obtaining time-averaged quantities for use

https://doi.org/10.1017/9781108875400.012 Published online by Cambridge University Press

in the RANS equations is straightforward, although care must be taken to ensure that the averaging window is sufficient. Overall, zonal methods provide the flexibility to employ separate equations, separate grids, separate numerical settings and in some cases entirely separate solvers!

Wall-modelled LES (*WMLES*). As a natural evolution from wall-resolved LES, these methods employ approximations in the near-wall viscosity-affected region in order to avoid the need to resolve this costly inner region of the boundary layer. Away from the wall, these methods are no different from wall-resolved LES. The level of approximation varies greatly, ranging from imposing energy equilibrium and the omission of pressure-gradient effects to the inclusion of a stand-alone RANS model in the near-wall region. Thus, the use of LES in this wall layer is replaced by a less expensive strategy for computing the (time-dependent) wall shear stress or by using transport equations solved in unsteady mode (URANS) for different turbulence variables. Clearly, these methods are 'zonal' ('wall zonal') since they switch from one approach to another close to the wall; but they differ from the more general (bulk) zonal methods in that WMLES methods are generally based on using RANS to support the LES region, whereas bulk zonal methods introduce regions of LES to overcome limitations of RANS. Much of the effort and focus is placed on overcoming issues which arise at the interface between the two regions.

Seamless methods. Where an approach is capable of switching automatically between URANS and LES operation, it is generally referred to as a 'seamless' or 'global' method (also termed 'non-zonal' or 'unified'). Seamless approaches are based on the continuous treatment of flow variables whether they act in URANS (usually in wall-adjacent areas) or LES mode. In the latter, the RANS solver acts as an sgs model. Thus, the same equations are solved in time-dependent mode over the whole domain (i.e. they encompass both regions) usually with the same numerical solution algorithm.

Seamless methods exploit the intrinsic similarities of the RANS and LES equations and invoke criteria and frameworks to initiate switching between the two. The mode of operation, RANS or LES, and consequently the location of the interface is prescribed as a function of the solution and/or the grid spacing. Some schemes effectively seek to extend LES frameworks to provide a reasonable approximation on coarse meshes, while others take the opposite approach, extending RANS methods to offer scale resolution, thus named as 'sensitized' RANS. In some approaches, authentic RANS and LES are blended via a continuous function in terms of local grid size. In principle, all such approaches offer practicality since the user does not need to know the flow in great detail in advance, i.e. one avoids the need to prescribe the regions of the flow to be treated in URANS and LES modes. However, on the down side, this can lead to situations where the switch between

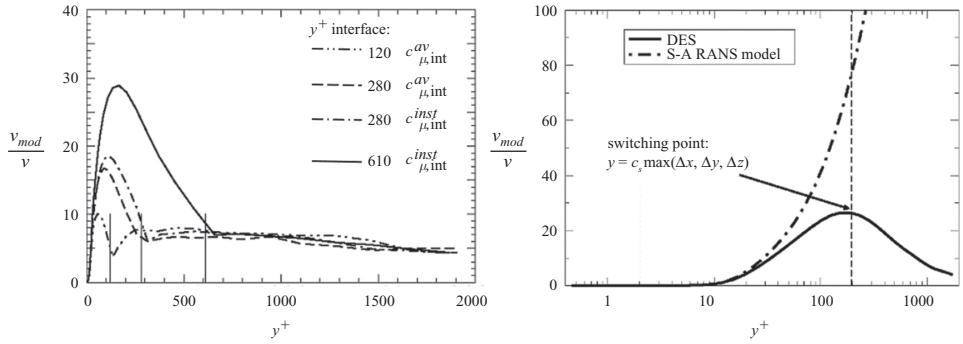

Fig. 10.15 Illustration of the conceptual difference between the two main approaches to Hybrid RANS-LES for a plane channel flow at $\mathrm{Re}_\tau = 2,000$. Left: Zonal two-layer method with a distinct interface between the wall-adjacent URANS region (low-Re k-ε model with adjusted coefficient to match the LES sgs viscosity at the interface), and a typical LES away from wall, for different predefined locations of the interface. Right: Seamless method (DES97) based on the Spalart–Allmaras one-equation RANS model modified by replacing the turbulence length scale with the representative grid size acting as a surrogate of the sgs model. From Hadžiabdić (2005), reproduced by permission of the author.

RANS and LES occurs in an unfavourable location, and there is less control of associated mesh and numerics, as there *can be* with zonal methods.

The conceptual difference between zonal and seamless methods is illustrated in Fig. 10.15 in terms of the effective (operational) eddy viscosity. The zonal approach (left) employs a two-layer model with a predefined interface (shown for three different locations); the LES region is clearly identifiable by a slowly varying Smagorinsky sgs viscosity, whereas in the RANS region the original model is active only very close to the wall but damped further away to match the sgs viscosity at the interface. In seamless methods (right) the eddy viscosity is continuous, obtained from the same RANS model, but damped gradually ('sensitized') away from the wall to serve as an sgs model (akin to one- or two-equation sgs models, §10.2) in the outer ('LES') region. The onset of this LES region cannot be identified by a clear-cut interface. The sgs viscosity is usually larger than with a conventional LES, as seen in Fig. 10.15 (right); and the 'true' LES is eventually recovered only very far away from the wall, if at all.

The grey area. As noted above, zonal methods require the user to identify in advance which regions should run in scale-resolving mode and which regions need only a time- or, more commonly, an ensemble-averaged solution. In doing so, the user must recognize that there will usually be an adjustment region on either side of the boundary where neither the RANS nor the LES solutions perform as would be expected if either were used alone.

https://doi.org/10.1017/9781108875400.012 Published online by Cambridge University Press

Seamless methods do not require the advance specification of which regions will be treated by which scheme; instead, there is a pre-assigned set of criteria that determine the location of the switching from one mode to the other. The automatic switchover is generally dependent on the evolution of the flow solution and is then liable to change continually over the course of the simulation. While the user may be able to deliberately steer a given region to be treated in either RANS or LES mode by coarsening or refining the mesh appropriately, there is generally no guarantee that the desired mode will always be applied in any given region.

A degree of uncertainty is associated with *all* the above approaches, whether zonal or seamless. In each case, the user is required to make choices and so must call on experience and knowledge of the simulation to decide which strategy is best. The feature common to all is that a finite adaptation region will occur from one strategy to the other. In the best case, the transition is achieved over a minimal distance and with minimal adverse impact on the prediction. At worst, an unintended transition may adversely alter the evolution of the whole solution, or errors arising at the interface may propagate throughout the domain and drastically corrupt the accuracy of the prediction.

10.4 Bulk zonal models and embedded LES

As discussed in previous chapters, when employed appropriately, the predictive capabilities of RANS models are capable of correctly predicting a wide range of complex flow phenomena. In such cases, the use of a scale-resolving method must be carefully considered. If an appropriate RANS method provides sufficient accuracy, the additional expense arising from the finer spatial and temporal resolution requirements of full domain LES may not be justified. Restricting LES to a specific portion of the domain, while maintaining a satisfactory RANS solution elsewhere, is thus pragmatic and offers potential for gains in computational efficiency.

In general, zonal approaches seek to use LES regions, or other scale-resolving methods, embedded within a RANS solution with an explicit, time-fixed, interface defined. Each subdomain is then solved individually with a separate set of transport equations. Unlike seamless (global) methods, there is a clear transitional boundary between RANS and LES regions. By introducing a general framework to incorporate RANS with LES in this way, one is able to select the level of closure that is particularly suited to the flow in question. This framework is then able to benefit from the extensive collection of modelling developments accumulated in recent decades in the domain of turbulence modelling. As described in §10.3, there are two main categories of approach which can be considered to be zonal. Bulk zonal is addressed in this section, while wall-modelled LES is addressed in the next section.

https://doi.org/10.1017/9781108875400.012 Published online by Cambridge University Press

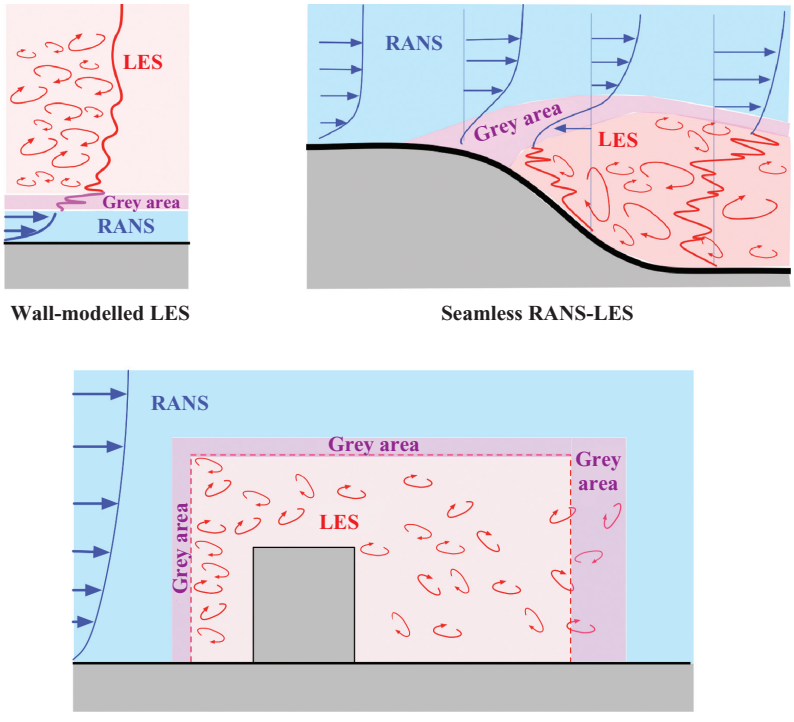

Fig. 10.16 A sketch of the three broad approaches adopted with Hybrid RANS-LES. (Top left): wall-modelled LES ascribes URANS (or, less frequently, steady RANS), or a wall-function model, to the near-wall, while the rest of the domain uses LES. (Top right): seamless methods adopt a single set of equations such that the solver switches automatically between RANS and LES. (Bottom): zonal methods prescribe in advance where the solution should be from RANS or LES. In each case, a region between the two modes, denoted the 'Grey Area', is marked, representing a region where careful consideration of results is needed. Note that the smooth line in the RANS region of WMLES (top left) does not necessarily imply a steady RANS; usually a URANS solution is adopted (see footnote in the introduction of §10.3).

In bulk zonal approaches, the RANS domain is used to provide boundary conditions to the LES region, and, as such, the method is often referred to as 'embedded LES' or ELES. In practice, the interfaces will be normal to the mean-flow direction, which can either be one-way-, i.e. transferring information in the direction of the mean flow only, or two-way-coupled, in which case there is continuous communication between the RANS and LES zones. Reducing the LES region delivers greater cost savings while the turbulence-resolving capability for specific features or physics that one identifies in advance is better handled by LES than RANS. An early implementation of ELES was presented by Cokljat *et al.* (2009), who

https://doi.org/10.1017/9781108875400.012 Published online by Cambridge University Press

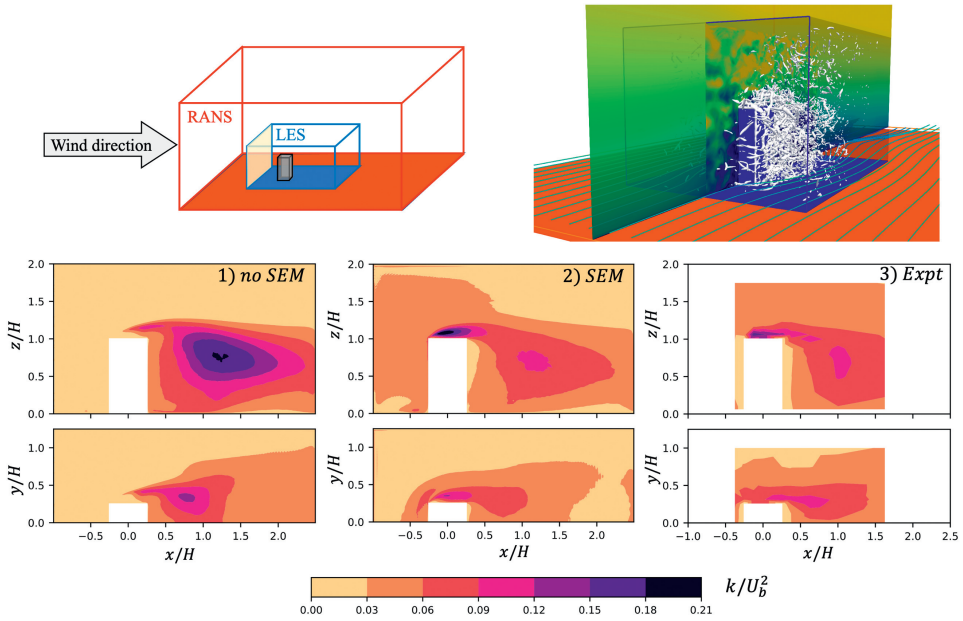

Fig. 10.17 Embedded LES applied to the flow around a simplified building, adapted from Santasmasas et al. (2022). Top Left: schematic of domain displaying blue LES region inside red RANS region; where synthetic turbulence (SEM) is applied on the pale orange shaded plane. Top right: 3D view of embedded region, showing streamlines at ground level and iso-contours of Q-criterion in white within LES domain. Bottom row: comparison of total turbulent kinetic energy, normalised by bulk velocity U_b, at symmetry plane (side view and top view) for three cases: 1) where no SEM is applied, 2) the case where SEM is applied, and 3) experimental results from Meng and Hibi (1998).

considered fully developed flow through both a pipe and a channel and flow over a backward-facing step. An interesting combination of both zonal and seamless hybrid methods is proposed by Deck and co-workers (e.g. Deck *et al.*, 2014) known as Zonal Detached Eddy Simulation (ZDES), particularly with external aerodynamics applications in mind. In ZDES, the user must define in advance where the RANS model should operate and where a scale-resolving approach is required. Figure 10.17 shows some recent results. A number of similar implementations have followed that approach, including the work of Anupindi and Sandberg (2017), who validated a two-region ELES solver that consisted of single RANS and implicit LES zones with the transfer of variables handled at the interface. A more comprehensive review of the developments in this category is provided by Holgate *et al.* (2019). Figure 10.17 shows recent results from Santasmasas et al (2022), for the application of embedded LES to the flow around a simplified building. The simulation passes from RANS to LES via the use of the Synthetic Eddy

https://doi.org/10.1017/9781108875400.012 Published online by Cambridge University Press

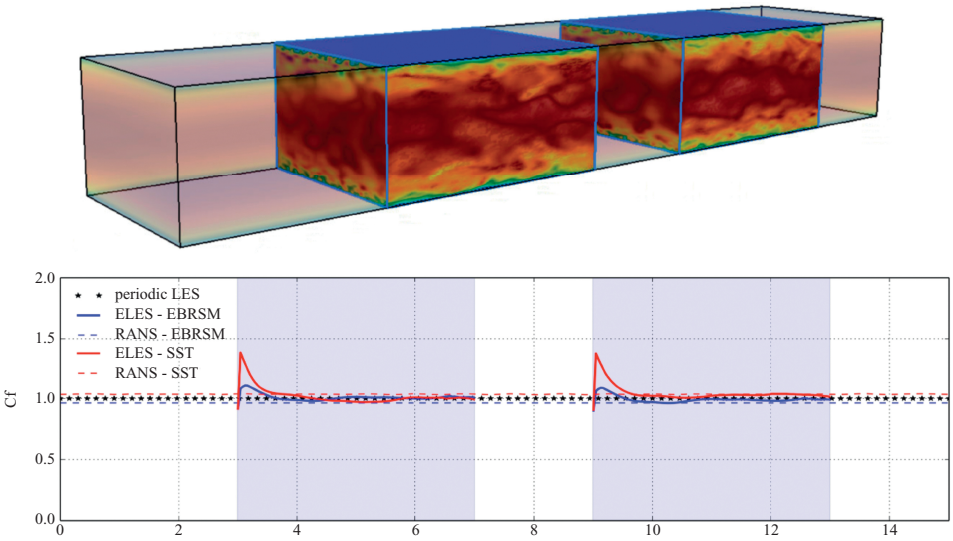

Fig. 10.18 Demonstration of embedded LES for a turbulent channel flow. Top: background simulation (transparent) is a RANS calculation, either $k-\omega$ SST or EBRSM, while two embedded regions of LES are included in the domain, from $3 < x/\delta < 7$ and $9 < x/\delta < 13$. Bottom: corresponding calculation of skin-friction coefficient for each combination, where shaded blue regions denote the location of embedded LES. The deviation from the periodic value (stars) at the inlet to each embedded region is indicative of the development length needed, $x/\delta \approx 1$. From Holgate and Revell, personal communication.

Method, introduced in the preceding section. The application of synthetic turbulence at the RANS-LES interface is required to correctly predict levels of turbulence arising over the top of the building. Without this, turbulence is observed to be under predicted at the separation point and subsequently over predicted in the wake.

The main challenge with ELES is the prescription of boundary conditions. Moving from a region of RANS, where quantities are time-averaged, to a region of LES requires knowledge of the turbulent fluctuations present in the flow. In the RANS region these quantities are represented by the Reynolds stress tensor, while in LES these values are time-dependent and result directly from the simulation. At the start of the LES domain, one must introduce turbulent fluctuations that are sufficiently realistic to minimize any adverse impact on the downstream solution. This has been described in §10.2.3. Such techniques necessarily incorporate significant approximation, and it is reasonable to expect that there will be an adjustment region downstream of the interface. An effective synthetic turbulence method will minimize this adjustment region. Figure 10.18 presents results from the case of a turbulent channel flow, where two successive embedded LES regions are coupled to

https://doi.org/10.1017/9781108875400.012 Published online by Cambridge University Press

a background RANS simulation. In both cases, the expected value of skin-friction coefficient, C_f, is recovered within one channel half-height, δ, of the interface, which is acceptably fast. The departure from the expected value of C_f can be reduced further by using a more advanced RANS closure – in this case, the elliptic-blending Reynolds stress model (EBRSM). This is an expected result since the accuracy of the synthetic turbulence depends on the predicted levels of turbulence anisotropy fed into the algorithm, and serves to underline the benefits of employing more capable RANS schemes in a zonal framework.

For a fully embedded region, one must also consider how flow moves from LES to RANS. In this scenario the degrees of freedom are reducing rather than increasing and, conceptually, at least, this is a more canonical problem. Often a moving time average is applied wherein fluctuating quantities at the edge of the LES region are averaged over a predefined time interval, or spatial region, so as to recover values suitable for matching with the RANS equations. More details of this can be found in Von Terzi and Fröhlich (2010). A number of more integrated approaches to zonal RANS-LES have been proposed, including the dual-mesh approach of Xiao and Jenny (2012), wherein two separate solvers, one for RANS and one for LES, are coupled together. As well as enabling mesh resolution to be targeted to specific regions of interest, this method allows the user to retain elements of the numerical solver and the mesh that are most suitable to the region in question, be it RANS or LES. For example, the RANS solver can retain a more stable numerical scheme on grids with higher aspect-ratio cells near the wall. Meanwhile, the LES mesh can be more directionally uniform; one can thus select numerical options that reduce artificial diffusion, that might otherwise adversely affect the stability in the RANS region.

10.5 Wall-modelled LES

In order to avoid the expensive resolution of fine near-wall structures at high Reynolds numbers, wall-modelled LES employs modelling approximations over the inner region of the boundary layer and switches to LES for the outer region and beyond. As discussed in §10.2.2, close to a wall it becomes impossible to define a clear separation between large and small scales, in the same way that one does well far from the wall. Thus, near-wall resolution requirements for LES and DNS are similar, with the cell count in the first few per cent of the flow nearest the wall often accounting for the vast majority of the overall grid numbers, even when the most important physical features occur well away from the wall. Resolving this issue has led to a great deal of effort in the LES community.

There are essentially two main approaches to approximating the wall shear stress: wall functions and two-layer methods, Fig. 10.19.

https://doi.org/10.1017/9781108875400.012 Published online by Cambridge University Press

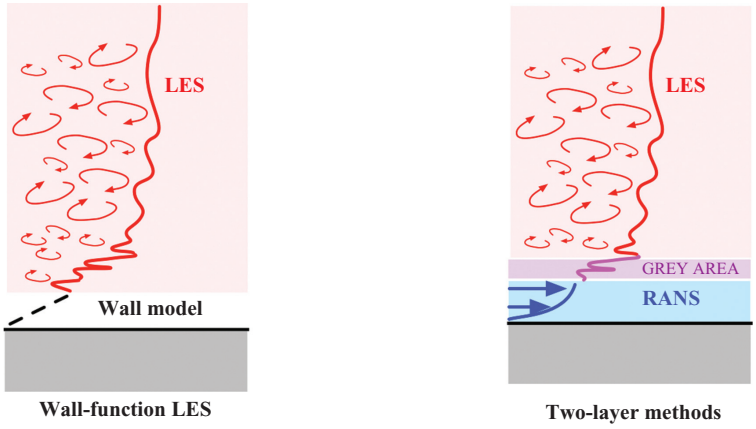

Fig. 10.19 The two main categories of wall-modelled LES approaches. (Left) Wall-function-based LES, where simple models are used for the inner region of the boundary layer. (Right) Two-layer methods, where full RANS approaches are employed next to the wall, offering a wider modelling capability and, possibly, the ability to cover a greater proportion of the near-wall region. Note that in both cases the near-wall properties, here for convenience denoted by continuous lines, are usually unsteady being excited by the LES solutions in the outer region.

Wall-function LES (WF-LES). These methods employ simple approximations to cover the near-wall zone that is assumed to be in local equilibrium, thus avoiding the need to resolve the costly innermost region of the boundary layer. Away from that region, the approach is conventional, no different from wall-resolved LES. Though the solution of a RANS model is not involved, many of the methods borrow heavily from the simpler wall-modelling strategies developed for RANS approaches and, as such, they are normally considered as an HRL approach. These schemes range in complexity from applying a rudimentary logarithmic velocity variation over the wall-adjacent cell, to the computation of a set of boundary-layer equations on a separate numerical mesh (rather in the manner of the numerical wall functions used with RANS closures discussed in Chapter 8). Near-wall turbulence energy is generally estimated from the wall shear stress rather than from a transport equation.

Two-layer methods. employ a stand-alone (U)RANS approach in the near-wall region, as opposed to the simpler approximations used in WF-LES. In principle, making a more complete modelling of the near-wall physics offers scope for capturing such non-equilibrium near-wall phenomena as laminarization and is especially beneficial in treating wall heat and mass transfer. They may likewise be applied over a greater region near the wall than would generally be possible with WF-LES methods, which, in turn, further reduces the computational burden of the

https://doi.org/10.1017/9781108875400.012 Published online by Cambridge University Press

LES. These methods are referred to as 'zonal' (or 'wall zonal') since they employ RANS and LES in separate, generally pre-determined, regions of the computational domain. Considerable effort is focused on overcoming issues that arise at the interface between the two regions, related to the fundamental differences between the RANS and LES rationales. Methods that automatically update the location of the interface are also available with the aim of avoiding the shortcomings arising from a user-defined choice; but they are currently less common.

These approaches are examined further in the following sub-sections.

10.5.1 Wall–function approaches

Equilibrium-based wall models

The primary goal of a wall function for LES is to provide a value for the wall shear stress (in both streamwise and spanwise directions, i.e. $\tau_{w,x}$ and $\tau_{w,z}$ with y the wall-normal direction) as well as, where appropriate, the wall heat or mass fluxes. Since their direct calculation would necessitate a fine near-wall mesh (which is not provided), their estimation will generally employ a combination of modelling and empirical approximations to account for turbulent mixing in the region from the wall to the first grid point; the strategy is similar in principle to that presented in Chapter 8 for RANS closures. Wall functions in LES are typically employed on meshes with dimensions $\Delta z^+ \simeq \Delta x^+ \simeq 100$ and $\Delta y^+ \simeq 50$. Thus, while the use of such a coarse grid across this near-wall zone leads to major computational savings, there is also a very large variation in the instantaneous flow properties within a single cell to be accounted for.

It is important to recognize that, when resolving eddies in a turbulent boundary layer via LES, one *simulates* the actual physical processes involved rather than modelling them. Indeed, certain physical processes must be correctly simulated to obtain accurate mean-flow statistics. With a RANS approach, the viscosity-affected layer and the fully turbulent region beyond may readily be treated separately, with distinctly different models. With scale-resolving approaches, however, there is a continuous sequence of physical interactions taking place between these two regions, as indicated in Fig. 10.20. A representation of the first near-wall cell in a wall-function approach is shown in the left figure, with the cell centre represented by a black dot, located at $y^+ \sim 50$. A wall function must attempt to approximate the motion in all these wall-adjacent cells. A view from above is provided on the right, where all of the visible structures lie within the region covered by the wall function.

As described in the textbook by Hinze (1975) (presenting ideas and photographs of the near-wall flow structure in a turbulent boundary layer reported by Kline *et al.*, 1967), a continuous cycle of non-linear interactions is present. Turbulent

https://doi.org/10.1017/9781108875400.012 Published online by Cambridge University Press

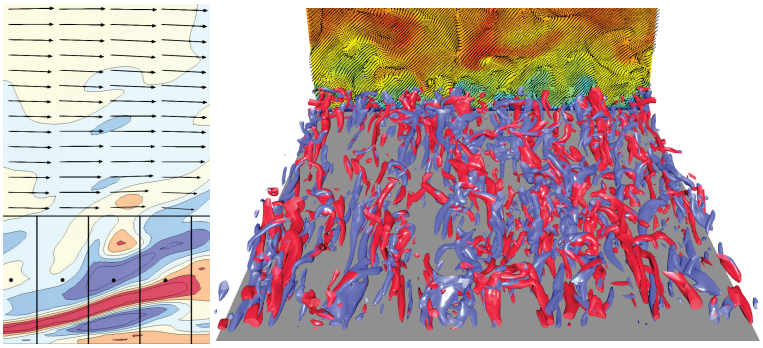

Fig. 10.20 DNS of a turbulent channel flow at $\mathrm{Re}_\tau = 395$, demonstrating the modelling challenge of a near-wall model (Revell and Santasmasas, Personal Communication). Left: a slice through the domain showing contours of vorticity representing turbulent sweep and ejection events, with a representative wall-function grid superimposed for reference. Right: a view from above (with flow direction now into the paper) of the turbulent structures in the same simulation, with streamwise streaks coloured red/blue to represent clockwise/counterclockwise rotation about the streamwise x-axis.

'bursts' bring high momentum fluid from the fully turbulent layer down through the inner layer ('sweeps'), impinging on the wall and displacing the low momentum fluid there upwards in the form of 'ejections'. These events introduce a continual variation in local values of wall shear stress, rising sharply during a sweep and dropping during an ejection.

Such interactions inevitably lead to large departures from the time-averaged form of the usual semi-logarithmic layer, Eq. (8.2), i.e.

$$U(y^+) = U_\tau \left[\frac{1}{\kappa} \ln y^+ + B \right]. \tag{10.20}$$

Moreover, the weaknesses of such a representation are even greater as one departs from the idealized flows where such a mean-velocity variation is found. Indeed, as discussed in Chapter 8, in the context of RANS modelling, such simplistic wall-function methods are generally not valid in the presence of substantial adverse pressure gradients, three-dimensional flow and flow separation, all of which are common in industrial configurations. For RANS methods, more advanced wall functions accounting for non-equilibrium effects have been developed (§8.3–8.6), but there is currently little sign in the literature of such models being used in or developed for WF-LES.

In fact, early research on LES was particularly constrained by computational resources and so wall modelling was the only option. Deardorff (1970) reported the first LES of a turbulent channel flow using a 3D domain of only 6,720 points

https://doi.org/10.1017/9781108875400.012 Published online by Cambridge University Press

($24 \times 20 \times 14$). Both the average velocity and the second derivative of the filtered velocity were assumed to obey the above log law, while the viscous contribution to wall shear stress was ignored; thus, the resulting framework was entirely insensitive to Reynolds number. Schumann (1975) developed a more general version, by calculating an effective viscosity from the definition of wall shear stress, essentially in the same way as the standard WF is applied in RANS software, Eqs. (8.10–8.12).

$$\frac{\tau_{xy}}{\rho} = (\nu + \nu_t)\,\frac{\partial U}{\partial y} \tag{10.21}$$

$$\frac{\tau_{xy}}{\rho}\int_0^{y_\mathsf{P}} \frac{1}{(\nu+\nu_t)}dy = \int_0^{y_\mathsf{P}} \frac{\partial U}{\partial y}dy \tag{10.22}$$

$$\frac{\tau_{xy}}{\rho} = \left[\frac{\int_0^{y_\mathsf{P}} 1/(\nu+\nu_t)dy}{y_\mathsf{P}}\right]^{-1}\frac{U_\mathsf{P}}{y_\mathsf{P}} \equiv \nu_{\mathit{eff}}\frac{U_\mathsf{P}}{y_\mathsf{P}} \tag{10.23}$$

where ν_{eff} represents the effective total viscosity in the first cell and subscript P denotes the location of the first node away from the wall. Schumann's approach required a statistical average (e.g. a spanwise average in a 2D flow or a time average) in order to apply the log-law to the filtered velocity field. It also required the mean wall shear stress to be prescribed *a priori*, which greatly limited its scope. In place of the log-law, Werner and Wengle (1993) proposed an approach based on a 1/7th power-law velocity profile, $U^+ \propto y^{+1/7}$ which provides a more convenient (albeit, not assuredly more accurate) formula for determining τ_{xy} directly from the velocity profile. However, these schemes, and a number of other similar approaches, are essentially all limited by the basic assumption that the law of the wall is applicable both locally and instantaneously, which is emphatically not the case. Indeed, Radhakrishnan *et al.* (2006) demonstrated for the case of flow separation over a contoured ramp, that while advanced WMLES methods provided a good representation of the flow (including separation and reattachment points), use of Schumann's wall-function approach entirely failed to identify any flow separation.

Improved analytical wall models

More complex formulations have been proposed to circumvent some of the more restrictive assumptions described in the previous section. They amount to analytical developments of the basic theory, made to incorporate the resolved turbulent structures in the outer layer. Here the motivation was provided by increasingly more detailed data from DNS and LES simulations. Piomelli *et al.* (1989) introduced modifications to account for the non-local nature of the near-wall structures. This was achieved by including a spatial offset in the streamwise direction between instantaneous velocity and wall shear stress, to account for tilted hairpin vortex

https://doi.org/10.1017/9781108875400.012 Published online by Cambridge University Press

structures. Marusic *et al.* (2001) extended this idea by separating the mean and fluctuating components of the wall shear stress, so that associated rises due to sweep events could be more directly scaled to available experimental data. These methods still inherited limitations from the assumptions made for the log. law though their dependence upon it was reduced through the use of the boundary-layer equations shown in Eq. (10.24):

$$\begin{aligned} &\frac{\partial}{\partial y}(\nu + \nu_t)\frac{\partial U_i}{\partial y} = F_i \quad \text{for } i = 1, 3 (\text{i.e. } x, z) \\ &F_i = \frac{1}{\rho}\frac{\partial P}{\partial x_i} + \frac{\partial U_i}{\partial t} + \frac{\partial}{\partial x_j}U_i U_j \end{aligned} \tag{10.24}$$

where U and P represent the near-wall unresolved values, and ν_t is often approximated using the MLH. This equation can be integrated from the wall, $y = 0$, to the first cell node, y_P as follows:

$$\frac{\tau_{yi}}{\rho} = \left[\int_0^{y_\mathrm{P}} \frac{1}{(\nu + \nu_t)} dy\right]^{-1} \left[U_{i,\mathrm{P}} - F_i \int_0^{y_\mathrm{P}} \frac{y dy}{(\nu + \nu_t)}\right]. \tag{10.25}$$

Setting F_i to zero recovers the equilibrium 'stress-balance model' and the log. law, Eq. (10.23). Wang and Moin (2002) compared the full-boundary-layer equations for a trailing-edge flow with simplified cases where $F_i = 0$ and $F_i = (1/\rho)\partial P/\partial x_i$, as shown in Fig. 10.21. When the pressure-gradient term is included, the location and discontinuous slope in skin friction is better predicted than with the standard equilibrium wall function. The deviation from the full LES around the trailing edge suggests convection terms play an important role there.

Hoffmann and Benocci (1995) developed a model based on the thin boundary-layer equations, Eq. (10.24), with a further simplification to relate the velocity gradient to the inviscid streamwise velocity gradient. That leads to an expression in terms of the boundary-layer displacement and momentum thicknesses, δ^* and θ. Manipulation of this form by Bose and Park (2018) showed that pressure-gradient effects can still be captured by resolving the outer layer, so long as the wall function does not cover more than 20% of the boundary layer. This has been shown to be practical and effective in several cases where the flow is attached, though it should be noted that these approximations are not applicable to the case where the flow becomes separated.

Numerical wall models

Regions of flow far from the wall can often be well predicted using wall-modelling LES with large near-wall cells; but for physical processes like boundary-layer

https://doi.org/10.1017/9781108875400.012 Published online by Cambridge University Press

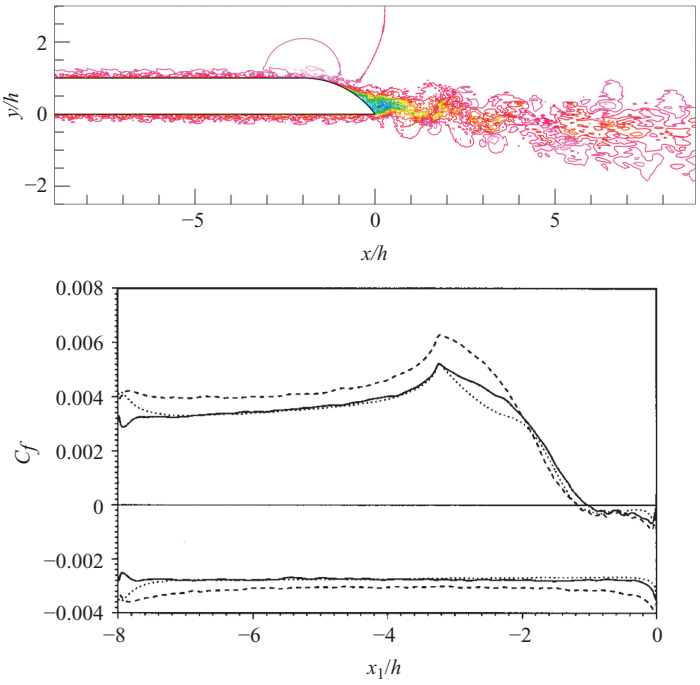

Fig. 10.21 Wall-modelled LES applied to the flow around the trailing edge of an airfoil. Top: contours of streamwise velocity U/U_∞ in a spanwise plane. Contour levels cover the range $U/U_\infty = -0.3$ (blue) to 1.2 (magenta) with increments of 0.1, (Wang, 2005). Bottom: corresponding prediction of skin-friction coefficient, C_f, for different versions of Eq. (10.24). Solid line: $F_i = 0.$; dashed line $F_i = (1/\rho)\partial P/\partial x_i$; dotted line: reference results from wall-resolved LES (Wang and Moin, 2002).

growth and separation that depend strongly on the character of the near-wall turbulence, these approaches are severely limited. Balaras and Benocci (1994) have proposed an extension of the above analytical approach. In place of the coarse wall-adjacent cells they applied a fine near-wall mesh over the inner region of the boundary layer, on which they solved the boundary-layer equations, Eq. (10.24), via a general framework based on the wall-normal component of velocity rather than specifically designating this as the y-component. (The approach has similarities with the 'numerical-wall-function' strategy for RANS solvers presented in §8.6.) Two-dimensional boundary-layer equations are solved, for both wall-parallel components, and so the cost of the method is slightly greater than wall-function versions such as that of Wang and Moin (2002) cited above. The approach has been found to work well for a range of flows, including high-Reynolds-number flow through a channel and square-duct flows, both stationary and rotating, with notable improvements over analytical treatments.

https://doi.org/10.1017/9781108875400.012 Published online by Cambridge University Press

The numerical wall model and its derivatives have also been applied to cases where the flow is driven by adverse pressure gradients producing flow separation. Two such examples are the backward-facing step and the trailing-edge case of the airfoil, which were considered by Cabot and Moin (2000). In their work they investigated a wall model based on the solution of Eq. (10.24) for these two cases: fully including F_i and the simplification, $F_i = 0$. A clear advantage of the former was found. Similarly, Diurno *et al.* (2001) demonstrated superior performance from a numerical-wall-function approach applied to a backward-facing step at Reynolds numbers based on step height of both 5,100 and 2,800, shown for the former in Fig. 10.22. The flow reversal is seen to be predicted on the inner mesh at the flow reattachment point. Accordingly, the prediction of skin-friction coefficient, C_f, is considerably improved compared with the algebraic model.

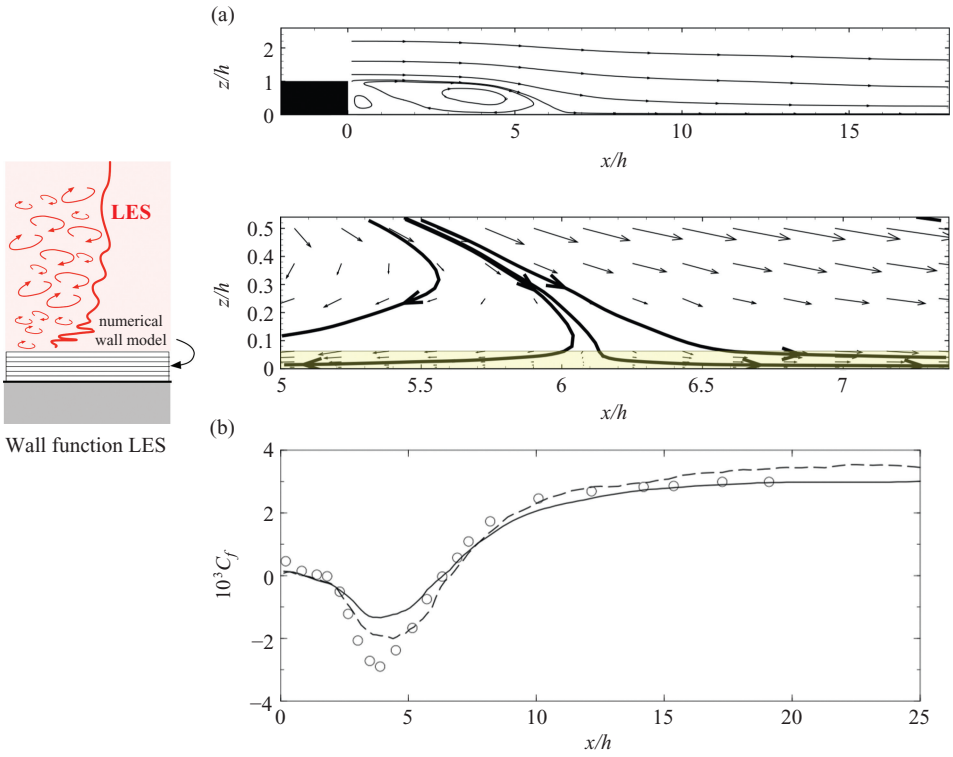

Fig. 10.22 Left: the concept of numerical wall functions with LES. Right: computations of flow over a backward-facing step from Diurno *et al.* (2001). Top: time-averaged flow field showing separation and recirculation. Middle: a zoom of the reattachment region, showing mean-flow vectors and streamlines as well as flow vectors from within the numerical WF. Bottom: skin-friction coefficient: Symbols: reference DNS data, Solid line: analytical WF + LES, Dashed line: numerical WF + LES.

https://doi.org/10.1017/9781108875400.012 Published online by Cambridge University Press

10.5.2 Two-layer RANS-LES

In 'two-layer' approaches the aim is to use the RANS solution to replace entirely the LES representation next to the wall. This practice permits a coarser near-wall mesh, especially in the streamwise and spanwise directions. RANS is applied from the wall surface up to an interface at a chosen wall-normal distance, beyond which LES is adopted. While the location of the interface and, thus, the thickness of the RANS layer can be chosen freely, the main modelling challenge is how to arrange the switchover, since conceptually the RANS and LES models remain unmodified away from the interface. Such methods are clearly zonal in nature. While the initial focus was on cases where the RANS–LES interface was parallel to the wall, schemes have subsequently been generalized to treat separated and other complex flows where the interface location may be freely chosen. Methods which introduce more general zonal frameworks are described in §10.4. In some methods the switch is imposed at a certain wall-normal distance, while in others the location of the interface is free to adapt to the solution. The former can be referred to as having a fixed (hard or static) interface, while the latter is termed a soft or dynamic interface. The manner in which RANS and LES quantities are matched at the interface also varies.

While a wall-function model will generally imply a local-equilibrium assumption and provide little information about turbulent near-wall scales, a full RANS approach can be significantly more capable and can therefore greatly improve the range of flows for which the modelling is appropriate. In their work on numerical wall models for LES, Cabot and Moin (2000) concluded that, despite the benefits of computing the full form of the boundary-layer equations, Eq. (10.24), more capable modelling of the near-wall structure would be necessary for complex flows typical of those arising in industry.

Response of the RANS layer to LES solutions across the interface

Two-layer or zonal schemes pose both fundamental and practical questions whatever approximation is adopted. The basic challenge is to reconcile the filtering operation underlying the LES representation with the RANS time/ensemble-averaged framework, especially in the vicinity of the RANS–LES interface, where both the LES and RANS solutions resolve the same range of turbulent scales. A major uncertainty in the use of a RANS near-wall model lies in its sensitivity and receptivity to the highly unsteady motion imposed on it by the LES solutions across the interface; i.e. will the RANS side of the interface respond adequately and return the proper dynamics to the LES?

To examine the response of RANS, Temmerman *et al.* (2005) conducted an *a priori* test in which flow in a plane channel at moderate Re (about 11,000 based on the channel half-width) was first solved by a wall-resolved, fine-grid LES. Then, an

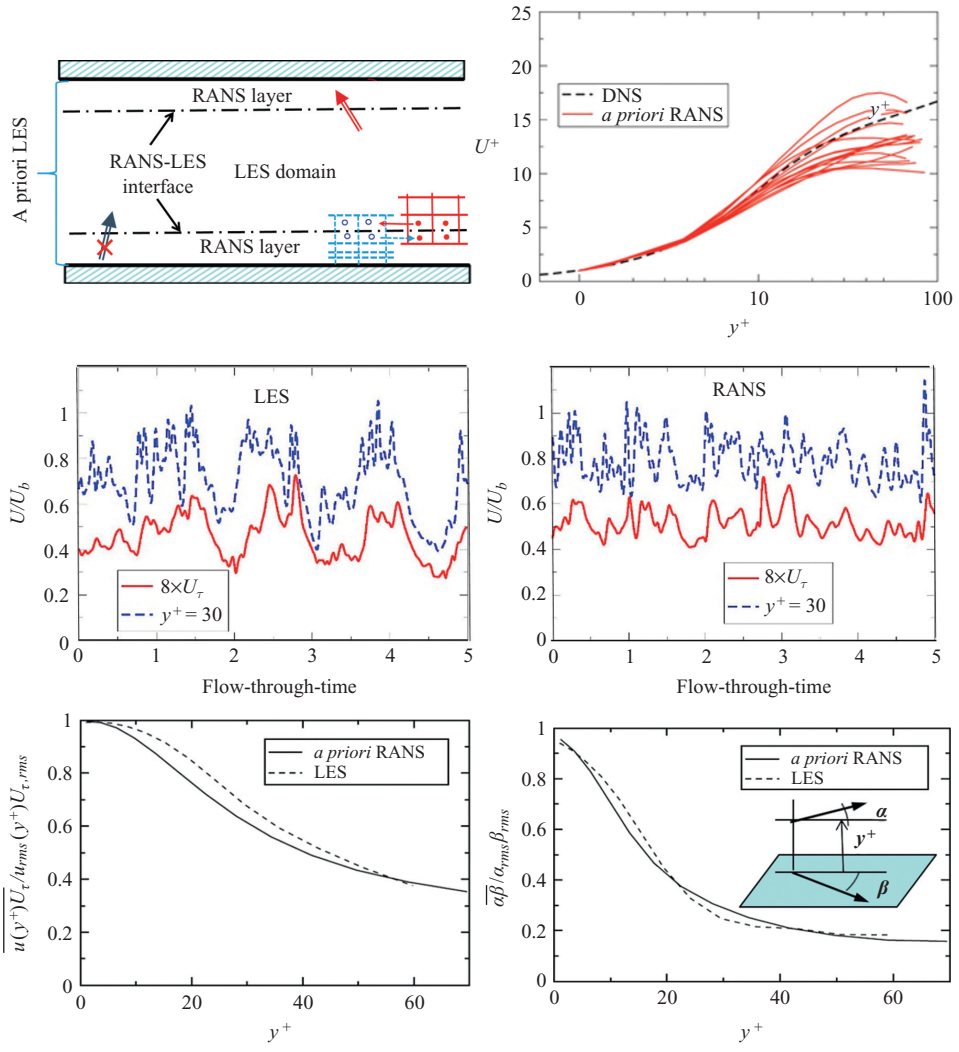

Fig. 10.23 *A priori* testing of the response of a RANS wall layer to an outer LES. Top left: schematic of flow configuration. Top right: instantaneous velocity plots for *a priori* RANS with LES data used as boundary conditions at the interface. Middle: histograms of wall-parallel velocity $\widehat{U}$ at $y^+ = 30$ and of friction velocity U_τ Bottom: wall-normal variations of the correlations of the instantaneous streamwise and friction velocities (left) and their angles with respect to the mean-flow direction (right). (Temmerman *et al.*, 2005.)

independent one-equation EVM/RANS model (solving a transport equation for k) was subsequently applied in unsteady mode in a predefined wall layer by feeding the LES solution at its outer edge at $y^+ \approx 65$, mimicking the RANS–LES interface, Fig. 10.23 (top left). A series of instantaneous velocity profiles in Fig. 10.23 (top right) obtained from the URANS computation shows a qualitatively similar set

https://doi.org/10.1017/9781108875400.012 Published online by Cambridge University Press

of realizations to those obtained from the fully wall-resolved LES. A quantitative confirmation of the satisfactory response of the RANS computation is provided in Fig. 10.23 (middle) comparing the time histograms of the fluid velocity at $y^+ = 30$ and the wall shear velocities obtained from LES and URANS. Finally, the bottom graphs of Fig. 10.23 compare the wall-normal variation of the two-point correlation coefficients $\overline{u(y^+)U_\tau}/u_{rms}(y^+)U_{\tau,rms}$ and $\overline{\alpha\beta}/\alpha_{rms}\beta_{rms}$, where both arise either from the LES or the RANS solution; U_τ is the friction velocity, α is the angle of the wall-parallel velocity, while β is the angle of the wall stress (all instantaneous), and the overbar indicates time averaging. These plots convey information on the extent to which the RANS model preserves key statistical parameters associated with the unsteady motion in the near-wall layer. The correlations are also of interest in relation to the use of wall laws in approximating the near-wall region; for, evidently, wall laws imply (inappropriately) a perfect correlation between the motion at the outer edge of the wall-law region and the wall shear stress (but see discussion re Fig. 8.10 drawn from Craft et al, 2008).

As is evident from Fig. 10.23, the RANS model captures (surprisingly well) the correlation levels predicted by the LES solution. These results suggest a substantial unsteady motion throughout the RANS region. Clearly, the unsteady LES motion imposed at the RANS-layer edge decays only slowly through the RANS region, and this has important implications for what should be the appropriate level of the modelled viscosity in the RANS layer, especially close to the interface.

Fixed interface methods

An early example of this approach is the work of Davidson and Peng (2003), who proposed a two-layer method where a RANS solver using a $k - \omega$ EVM was interfaced with a LES scheme using a one-equation sgs model. Unsteady velocities were matched at a pre-determined location, while RANS-determined k levels were converted to k_{sgs} (see Eq. (10.17)) and a zero-gradient condition was imposed on ω at the interface. The approach worked reasonably well, although the velocity indicated discontinuities across the interface; the authors also noted a lack of high-frequency content.

A different two-layer approach was employed in the study discussed above by Temmerman *et al.* (2005). They used both a one-equation EVM (Wolfshtein, 1969) and a k-ε model (Abe *et al.*, 1994), interfaced with an LES using either the dynamic Smagorinsky or one-equation sgs models. They also matched both velocity and turbulent kinetic energy in the same way as Davidson and Peng (2003) but improved continuity across the interface by matching also the turbulent viscosity. Their condition required that the sum of both modelled and resolved components on both sides be conserved, i.e.

https://doi.org/10.1017/9781108875400.012 Published online by Cambridge University Press

$$\nu_{LES}^{mod} + \nu_{LES}^{res} = \nu_{RANS}^{mod} + \nu_{RANS}^{res}. \tag{10.26}$$

Since the instantaneous strain rate should be the same on both sides of the interface, Eq. (10.26) should ensure continuity of the total turbulent stress.

A practical problem that occurs with virtually all forms of hybrid approach is that they lack a mechanism for constraining the level of turbulence activity that arises in the RANS layer. This arises from a combination of model-produced eddy viscosity and the resolved motion. It should be borne in mind that the eddy viscosity provided by a RANS turbulence model normally increases continuously away from the wall (in the absence of any constraint that imposes continuity in the turbulent/sgs viscosity and the associated stresses across the LES–RANS interface). The implication is that the time-averaged solution in the inner layer will not normally be compatible with the LES solution just beyond this layer. Thus, in practice, the most important point is to assign an equivalent value to the proportionality constant in the RANS eddy-viscosity model at the interface, i.e. to fix an equivalent turbulent viscosity coefficient, $c_{\mu,int}$, based on LES quantities, i.e.

$$c_{\mu,int} = \frac{\left\langle \nu_{LES}^{mod} \right\rangle}{\left\langle \nu_{RANS}^{mod}/c_\mu \right\rangle} \tag{10.27}$$

where angled brackets denote averaging over any homogeneous direction or over some predefined patch on both sides of the interface. In fact, ν_{LES}^{mod} is the conventional ν_{sgs} for LES, and $\nu_{LES}^{res} = \langle \overline{U_i U_j S_{ij}} \rangle / \langle \overline{S_{ij} S_{ij}} \rangle$, where U_i and S_{ij} refer to the resolved motion. The resulting value of $c_{\mu,int}$ is then blended with the standard value of c_μ on the RANS side, as a function of the mesh density Δy according to the following function:

$$c_\mu = 0.09 + (c_{\mu,int} - 0.09)\frac{1 - \exp(-y/\Delta y)}{1 - \exp(-y_{int}/\Delta y_{int})}. \tag{10.28}$$

The use of spatial averaging in this way requires there to be a homogeneous direction in the flow, which limits the general applicability of the method. However, Temmerman *et al.* (2005) showed that one can skip averaging by simply using the instantaneous values of $c_{\mu,int}^{inst}$, which also proved beneficial in reducing any unphysical inflection (termed the 'logarithmic mismatch') in the velocity profile in the grey area around the interface. This anomaly, observed in many methods, both zonal and seamless, has been attributed to insufficient effective (i.e. modelled plus 'resolved') viscosity in this region. Imposing instantaneous values of $c_{\mu,int}^{inst}$ introduces high-frequency fluctuations at and around the interface, similar in its effect to the randomly generated 'stochastic back-scatter' proposed by Piomelli *et al.* (2003) to cure the anomaly. Although this option cannot be claimed to generate realistic streaks and other missing small-scale structures that are inaccessible to URANS,

https://doi.org/10.1017/9781108875400.012 Published online by Cambridge University Press

it seems that the use of $c_{\mu,int}^{inst}$ provides some desirable extra unsteady forcing, thus injecting a proportion of the missing high-frequency components and improving the effective eddy viscosity.

The two-layer approach is observed to work especially well when using a two-equation model, achieving improved predictions of the velocity field relative to the one-equation model. This is primarily because the length-scale variable (here ε) is allowed to respond to external perturbations via its own transport equation. In comparison to a typical seamless approach, it demonstrates a cleaner switch between the RANS and LES regions, as already illustrated in Fig. 10.15. In this case, Temmerman *et al.* (2005) compared their strategy to the Detached Eddy Simulation (DES) approach (see §10.6.6 for further details). It can be seen from Fig. 10.24 that, for the case of channel flow at $\mathrm{Re}_\tau = 2{,}000$, the switch from RANS to LES occurs at a similar location (given by the vertical line), but the levels of turbulent (RANS) viscosity are far higher for the DES than for the zonal model. Corresponding plots

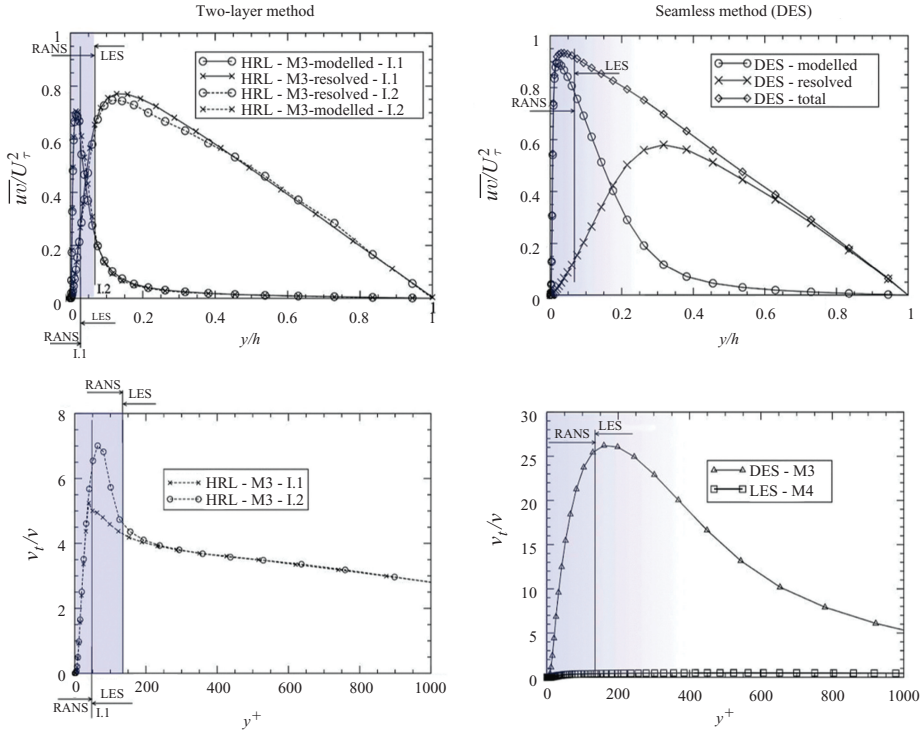

Fig. 10.24 Results from Temmerman *et al.* (2005) demonstrating the use of a two-layer model applied to a turbulent channel flow at $\mathrm{Re}_\tau = 2{,}000$; comparison of two-layer method (left) with a seamless DES method (right), showing: (top row) shear stress (modelled and resolved) and (lower row) viscosity ratio. The shaded blue region approximates the reach of the RANS modelling in each case.

https://doi.org/10.1017/9781108875400.012 Published online by Cambridge University Press

of shear stress in Fig. 10.24 show that for the zonal model, the modelled shear stress falls rapidly at the interface, to be replaced by the resolved shear stress. The distance between this switch location and the point at which the modelled and resolved stresses are equal is considered to be the transition region between the two. For the DES, this region is much longer, since the modelled shear stress is significantly larger than the resolved stress for some distance beyond the nominal switch from RANS to LES. This is significant since it impedes the impact of scale resolution in the LES region, because the high residual sub-grid viscosity acts to dampen the resolved eddies. Only beyond the transition region does the eddy content become sufficient to account for the majority of the shear stress. The delayed generation of resolved eddies in this region results in an upward displacement of the log-layer region mentioned above, reducing the predicted wall shear stress and the effective friction-velocity Reynolds number. Insufficient grid resolution in this region can further exacerbate the problem.

Despite the benefits indicated above, the need to define *a priori* the location of the interface presents some challenges. Temmerman *et al.* (2005) noted that the dependence of their results on this issue was more complex than they had expected. On the one hand, placing the interface closer to the wall resulted in an increase in the level of resolved relative to modelled turbulence, as expected. On the other hand, as the interface was moved towards the wall, the drop of eddy viscosity across it became more severe, resulting in a correspondingly high velocity gradient in the same region. In fact, their results improved as the interface was moved further from the wall. For example, an interface at $y^+ = 120$ resulted in an error in C_f of 9%, while moving the interface to $y^+ = 610$, i.e. well into the outer region, reduced the same error to just 3%. The model is more successful when the RANS solver is allowed to handle the inner layer entirely, and the LES is responsible only for the larger structures in the core region of the flow, as shown in Fig. 10.25. While one might rationally expect the accuracy to increase as the LES region resolves a progressively greater proportion of the domain, this example demonstrates that the optimum balance between RANS and LES is not so straightforward. An attached near-wall flow can be handled well with a RANS approach (with an appropriate level of model), but the introduction of a method which partially resolves this region instead introduces problems of compatibility between the two methods.

Dynamic interface methods

In cases where the flow is attached, or where the region of interest is away from the wall, the selection of an appropriate distance from the wall to locate the interface can be readily made; but in flows with a complex wall configuration it may not be immediately obvious where the RANS region should be replaced by

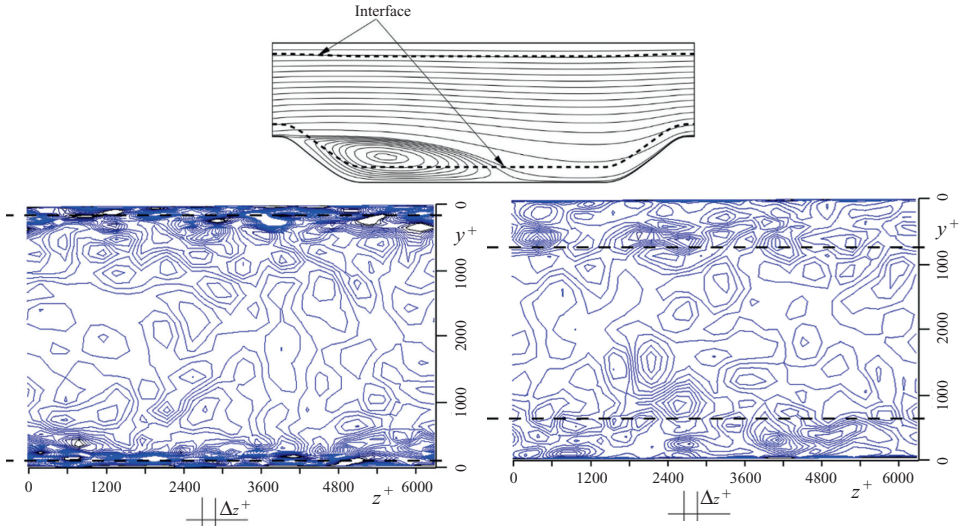

Fig. 10.25 Results from the application of the two-layer method (RANS $k-\varepsilon$ + dynamic sgs LES) to the flow over a periodic hill. Top: time-averaged flow field indicating the location of the interface. Bottom: contours of streamwise vorticity in planes normal to the flow where the interface is at $y^+ = 120$ (left) and $y^+ = 610$ (right), Temmerman *et al.* (2005).

the LES region. To address this issue, more general ways of defining the location of the RANS–LES interface have been proposed, based on physical criteria. These employ flow and turbulence parameters, possibly combined with the size of the local grid cells. Two approaches of this type have proved successful in reproducing a wide range of complex wall-bounded flows and heat transfer.

TU Darmstadt approach. The group of S. Jakirlić (see Kniesner *et al.*, 2007) proposed a version of the two-layer model which was able to dynamically self-adjust the location of the interface (hence the label dynamically interfaced HRL or Dynamic-interface hybrid two-layer (DIHRL)) as a function of a parameter which measures the ratio of the LES-modelled turbulent kinetic energy to the total turbulence energy in the LES region:

$$k^* = \left\langle \frac{k_{LES}^{mod}}{k_{LES}^{mod} + k_{LES}^{res}} \right\rangle \equiv \left\langle \frac{k_{sgs}}{k_{sgs} + k_{res}} \right\rangle \tag{10.29}$$

where k_{res} is calculated from on-line averaging over all grid cells at the interface on the LES side as indicated by the angled brackets, and $k_{LES}^{mod} (= k_{sgs})$ is obtained from the sub-grid model (the Smagorinsky model or an equation such as Eq. (10.17)). Where the value of k^* rises above a pre-determined level, the interface is moved further from wall; where it drops below the same value, the distance is decreased.

https://doi.org/10.1017/9781108875400.012 Published online by Cambridge University Press

Since the LES framework is developed on the basis that 80% of energy is resolved and 20% is modelled (see §10.1), it is sensible to set $k^* = 0.2$ in the first instance.

In the wall-adjacent region, a WIN eddy-viscosity RANS model (k-ε or ζ-f) is applied and matched with the LES computations at the interface by imposing the condition of equal total eddy viscosity on both sides, Eq. (10.26). This constraint ensures that the instantaneous stress and strain rates are continuous and the same equality applies for other modelled properties. Assuming that $\nu^{mod}_{RANS}|_{int} = c_\mu k^2_{sgs}/\varepsilon_{sgs}$, the kinetic energy and dissipation rates, needed for the boundary conditions in the RANS model at the interface, can be evaluated from the applied sgs model. For one-equation models such as Eq. (10.16), k_{sgs} and ε_{sgs} are readily available, while for the Smagorinsky model they can be obtained from presumed local energy equilibrium of the sgs motion, $k_{sgs} = (c_s\Delta)^2\overline{|S|}^2/\sqrt{c_\mu}$ and $\varepsilon_{sgs} = (c_s\Delta)^2|S|^3$ (Mason and Callen, 1986).

It is noted that despite a relatively fast transition from RANS to LES sgs eddy viscosity (which should promote fast generation of the resolved stress), the present model is not immune to anomalous behaviour in the grey area around the interface, particularly in attached equilibrium flows. This commonly leads to a notable velocity mismatch in the logarithmic region in a plane channel. To cure this anomaly, Kniesner *et al.* (2007) applied an artificial forcing by introducing correlated fluctuations using the digital filter-based method of Klein *et al.* (2003) for generating inflow turbulence for spatially developing LES or DNS. However, over the range of separating flows tested, this remedy appeared unnecessary as no anomaly was detected in flows where separation generated strong instabilities, particularly in the separated shear layer. These, apparently, compensated for an insufficient LES resolution of the broader-scale spectrum.

The above approach has been applied successfully to a number of flows, including both pressure- and geometry-induced separation and cases with heated walls.[5] Figure 10.26 shows some results for a flow characterized by shallow separation on a smoothly contoured, wall-mounted 2D hump from the NASA Langley Research database, Greenblatt *et al.* (2006), where the Reynolds number based on hump length is around 10^6. Two cases were considered, a baseline flow and one with steady suction through a slot at the hump crest immediately upstream of natural separation aimed at suppressing separation. As can be seen, when computed on similar meshes the prediction is improved with the two-layer model (denoted HRL in the figure) compared with the coarse LES. The interface between RANS and LES is represented by a black line, which begins smooth but becomes irregular in the separated-flow region. Analysis indicated that when $k^* = 0.2$, the interface

[5] Flows over a heated backward-facing step, a periodic 2D hill, a 2D hump, including separation control by flow suction, a 3D hill, a 3D separation in an asymmetric diffuser, swirling flows in an annular gas-turbine combustor (Jakirlić *et al.*, 2010).

https://doi.org/10.1017/9781108875400.012 Published online by Cambridge University Press

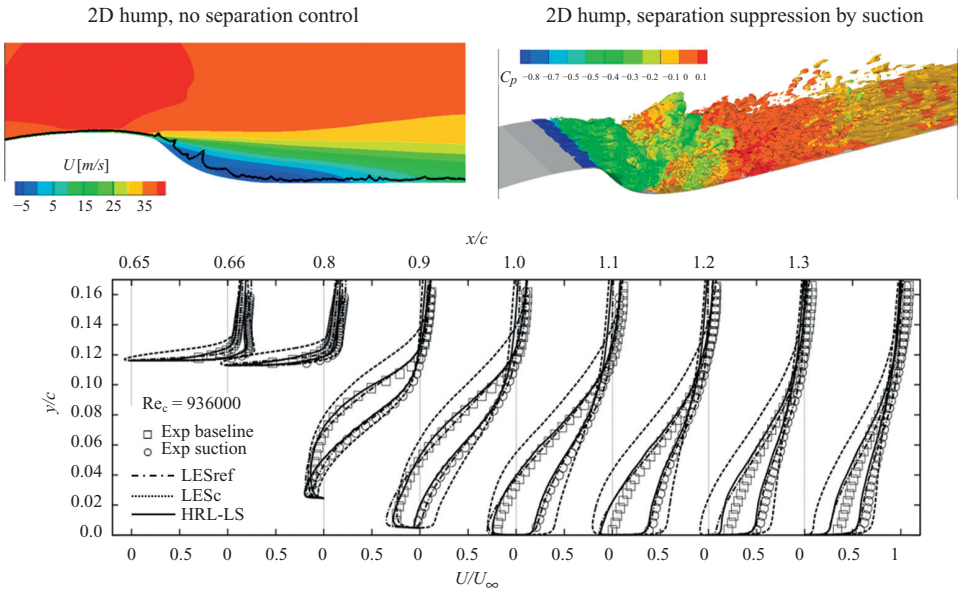

Fig. 10.26 Dynamic-interface hybrid two-layer method (DIHRL) applied to flow over a wall-mounted hump at Re = 936,000 (Kniesner *et al.*, 2007) without and with separation suppression by steady suction. Top left: mean-velocity field and the location of the automatic dynamic interface (solid black line). Top right: iso-surfaces of the spanwsie vorticity coloured by local pressure coefficient. Bottom: evolution of the mean axial velocity in both the baseline case and with a separation control for two LES (LESc: coarse grid with 2M cells as for HRL, LESref: finer grid with 4M cells). Reproduced with permission of ERCOFTAC.

self-located at $y^+ \sim 200$ upstream of the separation and in the range $10 - 100$ in the recirculation region, denoted by blue contour zones on the plot.

The method was also applied to some of the flows using different WIN RANS models in the wall-adjacent regions, i.e. the k-ε eddy-viscosity model (Launder and Sharma, 1974; Chien, 1982, §7.4.2) as well as with the elliptic-relaxation ζ-f model (Hanjalić, 2004a, §7.4.4). Contrary to expectation that the latter model, accounting for stress anisotropy and elliptic wall reflections, would perform better in separating flows (as it does when using a stand-alone RANS scheme for the whole flow), the comparison showed a relatively small effect, hardly justifying the increased computing time required by the more elaborate model. Presumably, this could be attributed to the LES stress anisotropy and pressure field imposed upon the RANS region across the interface compensating for the deficiency of the simpler RANS model. However, benefits from using a more advanced RANS model may be expected in situations involving walls of complex configurations and when, for computational economy, the RANS region is made thicker, e.g. by assigning a value to k^* greater than 0.2.

https://doi.org/10.1017/9781108875400.012 Published online by Cambridge University Press

TU Delft approach. An alternative way of defining the interface and switching dynamically between RANS and LES modes in a two-layer RANS-LES method is to introduce a 'grid-detection' parameter $\alpha = f(L, \Delta)$ (hence the label αHRL). This is akin to the DES practice, see §10.6.6[6] associated with the sink term in the equation for turbulent kinetic energy (a prime constituent of most popular RANS eddy-viscosity models). For this purpose, Hadžiabdić (2005) and Hanjalić (2005) proposed to modify the k-equation as follows:

$$\frac{Dk}{Dt} = \mathcal{D}_k + \mathcal{P}_k - \alpha\varepsilon \tag{10.30}$$

where

$$\alpha = \max(1, L_{RANS}/L_{LES}), \quad L_{RANS} = c_l k_{tot}^{3/2}/\varepsilon, \quad L_{LES} = 0.8(\Delta V)^{1/3}, \tag{10.31}$$

$k_{tot} = k_{res} + k_{mod}$ is the total turbulence energy, and $\Delta V = \Delta x \Delta y \Delta z$ is the local cell volume.

The switching parameter α is inactive close to the wall, but is activated when the turbulent length scale L_{RANS} becomes equal to the characteristic grid cell size, just as in the DES approach (see §10.6.6). Thereafter, the RANS model acts in the LES mode with L_{LES} as the characteristic length scale in the sink term, just as in Eq. (10.17) for the sgs kinetic energy, k_{sgs}. Moving further away from a wall, the RANS eddy viscosity ν_t^{RANS} continues to reduce until it reaches the value of the LES sgs viscosity ν_t^{LES} provided by the standard or dynamic Smagorinsky model. Thus, a distinct feature of this approach (compared with the common DES practice of switching the operating length scale from L_{RANS} to L_{LES} when transitioning from RANS to LES mode and vice versa) is an *additional* criterion that triggers the activation of the classic sgs viscosity based on the grid cell size. That ensures a full switching of the RANS model to the conventional LES, i.e.

$$\nu_t = \max(\nu_t^{RANS}, \ \nu_t^{LES}). \tag{10.32}$$

This method was first tested and tuned using a WIN k-ε model but, aiming at handling flows and heat/mass transfer over complex (ribbed, pinned, dimpled or similar) wall configurations, it was subsequently upgraded to the ζ-f elliptic-relaxation model (§7.4.4) with $\nu_t^{RANS} = c'_\mu \zeta k^2/\varepsilon$ (where $\zeta = \overline{v^2}/k$) in the RANS layer, and $\nu_t^{LES} \equiv \nu_{sgs} = (c_s\Delta)^2 \left|\bar{S}\right|$ in the LES region. A typical variation of the effective eddy viscosity with wall distance in a plane channel, Fig. 10.27, shows the 'buffer zone' between $\alpha = 1$ and $\nu_t^{RANS} = \nu_t^{LES}$, in which a continuous transition occurs from one region to another. The same figure shows the computed velocity profile in a plane channel for a very high Reynolds number ($\mathrm{Re}_t = 20,000$) using the ζ-f

[6] The grid detecting parameter α is identical (save for a possible empirical constant) to the function f_L used in unified/seamless methods, primarily in later versions of DES, though in different contexts (see Eqs. 10.43 and 10.53) but for consistency we use here the original notation.

https://doi.org/10.1017/9781108875400.012 Published online by Cambridge University Press

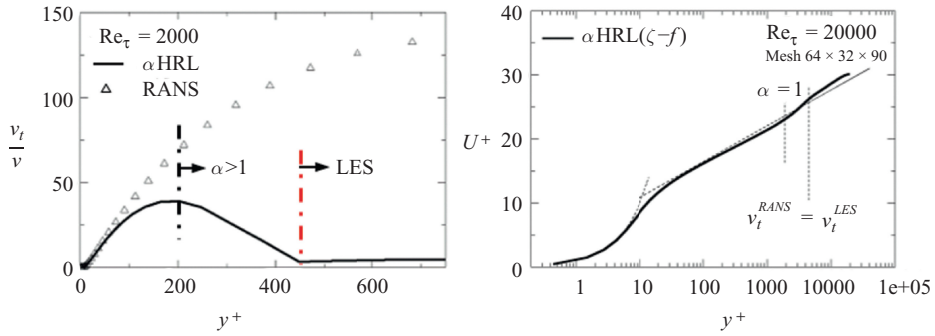

Fig. 10.27 Plane channel flow computed by the $\zeta - f$ HRL method. Left: effective viscosity compared with that in the stand-alone RANS $\zeta - f$ model. Right: mean-velocity profile for $\mathrm{Re}_t = 20,000$ with indicated buffer region where the grid-detecting parameter α is active. From Hadžiabdić (2005). Reproduced by permission of the author.

model in the RANS region with the dynamic Smagorinsky model in the LES zone, with the indicated location of the buffer zone from $\alpha = 1$ to the interface where turbulent viscosities on both sides are equal. A perfect log-law velocity is reproduced with the buffer zone at a quite large distance from the wall – a desirable feature for real flows at high Re. It is noted that a rapid fall of the effective viscosity in the buffer zone (presumably assisted in part by the back-scatter from the dynamic sgs in the Smagorinsky LES zone) excites the generation of the resolved stress sufficiently to show no sign of any log-law mismatch (grey area) – a feature achieved without employing any artificial forcing.

The performance of the model is illustrated by an internal flow with heat transfer in a complex configuration relating to the internal cooling of gas-turbine blades, Fig. 10.28. The blade trailing-edge region is cooled by relatively cool air[7] which passes over a matrix of staggered cylindrical pins, acting as promoters of vortex shedding and turbulence (and also providing additional heat-transfer surfaces). A generic set-up with parallel, differentially heated walls, mimicking the experiment of Ames *et al.* (2007) for two Reynolds numbers (10^4 and 3×10^4 based on pin diameter) was simulated by URANS, LES and HRL. The aim was to identify the optimum computational strategy for handling flows with challenging wall configurations (Delibra *et al.*, 2009, 2010).

The vortical structures that govern heat transfer and its enhancement computed by the αHRL model using a relatively coarse grid with 1.3×10^6 cells are shown in Fig. 10.28 (right). They agree qualitatively well with the LES results obtained on a much finer grid of 5×10^6 cells. Admittedly, the finer-scale structures captured by

[7] The air has by-passed the combustion chamber but has been heated significantly in passing through the compressor.

https://doi.org/10.1017/9781108875400.012 Published online by Cambridge University Press

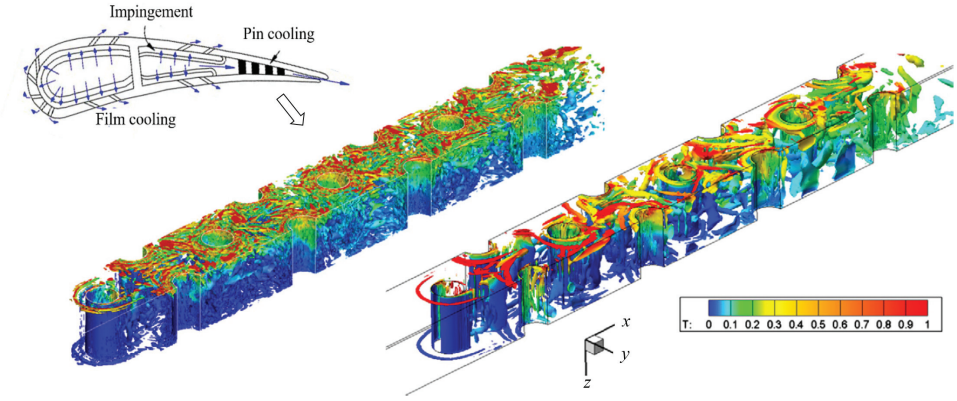

Fig. 10.28 Vortical structures educted by isosurfaces of the pressure Laplacian ($\nabla^2 p = 9$), coloured by temperature in a pinned passage (a periodic segment of an 8×8 pin matrix) between heated walls mimicking internal gas-turbine blade cooling, Re = 10,000. Left: LES (5×10^6 grid). Right: αHRL $\zeta - f$ (1.3×10^6 grid), top-wall heated. Reprinted from Delibra *et al.* (2010), with permission from Elsevier.

the LES are missing, but they do not appear to significantly affect heat transfer as indicated by the successful prediction of the end-wall Nusselt number, Fig. 10.30.

The functioning of the present LES-RANS hybridization is illustrated in Fig. 10.29 in terms of the active turbulent viscosities, shown by cuts taken horizontally and vertically through the bank of pins. The top figures show the ν_t^{RANS} field (blanked out where $\nu_t^{RANS} < \nu_t^{LES}$ to indicate the interface). It is clear that the RANS contribution is active only near the end walls and pins (near separation and in the near-wakes), whereas ν_t^{LES} (shown in the central figures) prevails away from the walls and in the pins' far wakes. In contrast to HRLs with a fixed interface based on a pre-specified wall distance, here the location of the RANS/LES boundary, defined in terms of physical flow properties obtained in the course of simulations, shows irregular shapes reflecting the flow solution rather than the wall contours. An impression of the αHRL prediction of convective heat transfer in this pinned passage can be gained from Fig. 10.30. The top figures show the computed distribution of the time-averaged Nusselt number over the end-wall surface, normalized with the area-averaged value, $\mathrm{Nu}/\mathrm{Nu}_{\mathrm{av}}$, for both the above-mentioned Reynolds numbers. The values compare reasonably well with the liquid-crystal data of Ames *et al.* (2007),[8] though with a somewhat larger non-uniformity in the upstream part of the domain. The wall imprints of the vortical structures shown in Fig. 10.28 are, however, reasonably reflected in the local Nusselt number distribution shown in Fig. 10.30.

[8] The colour scale of the computed results does not precisely match the liquid-crystal colour gradation due to the lack of precise information.

https://doi.org/10.1017/9781108875400.012 Published online by Cambridge University Press

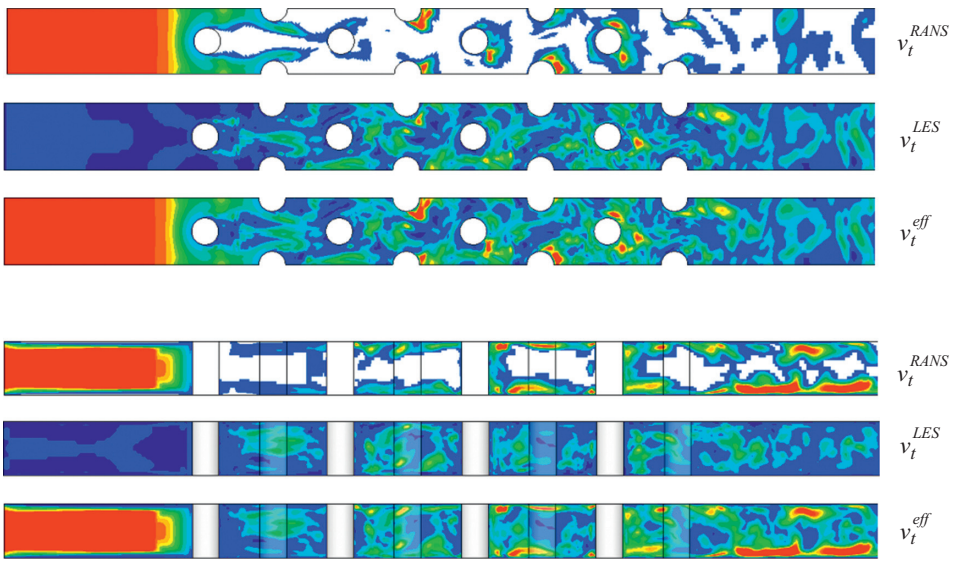

Fig. 10.29 The $\zeta - f$ αHRL turbulent viscosity fields in the horizontal mid-plane (top) and in the vertical cross-plane (bottom) cutting though pins 1, 3, 5 and 7. (The presence of pins 2, 4, 6 and 8 – laterally staggered – is also seen). Top row: ν_t^{RANS}, middle: $\nu_t^{LES} \equiv \nu_{sgs}$, bottom: effective viscosity $\nu_t^{eff} = \max(\nu_t^{RANS}, \nu_t^{LES})$. Reprinted from Delibra *et al.* (2010), with permission from Elsevier.

A further pointer that the end-wall heat transfer is well predicted is provided by the final part of Fig. 10.30. This shows the distribution of Nu/Nu_{av} on a plane that cuts pins 2, 4, 6 and 8. The agreement of the αHRL computations with the experiment is very good and notably superior to the URANS results using the same (stand-alone) $\zeta - f$ model and the same numerical grid. Admittedly, there is a penalty to pay: while the same grid and the same RANS model were employed in both, in comparison with a URANS solution, a hybrid approach resolves a larger part of the turbulence spectrum; thus, for physical reasons, it requires a smaller time step. Indeed, from a numerical viewpoint, the hybrid simulations are more sensitive to the CFL number (Eq. 10.18) and require a smaller time step to ensure CFL < 1 for numerical stability and a smooth convergence.

The αHRL was subsequently applied to some other internal flows, including tip leakage and secondary flows in an axial compressor cascade with both stagnant and moving casing (Borello *et al.*, 2009).

10.6 Seamless methods

Seamless Hybrid RANS-LES approaches adopt a continuous treatment of flow variables across a domain, using a single set of equations that is able to operate in both RANS and LES modes.[9] The popularity of these methods stems from the

[9] As noted by Fröhlich and Von Terzi (2008), in principle, any RANS model can be turned into an LES model by introducing the grid-cell size as a length scale of the model.

https://doi.org/10.1017/9781108875400.012 Published online by Cambridge University Press

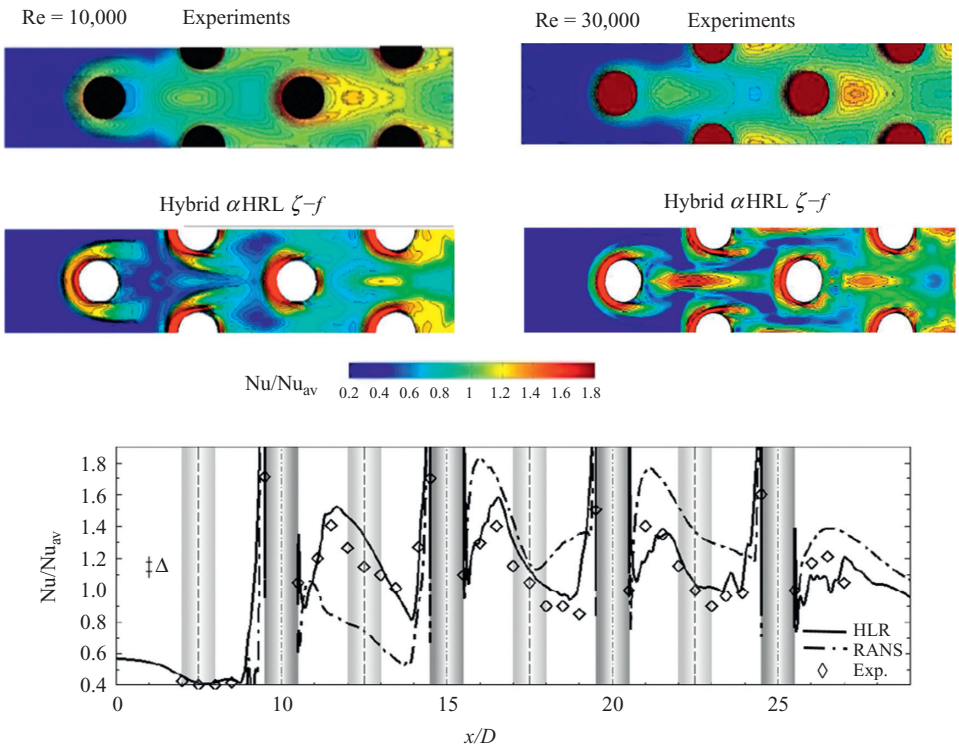

Fig. 10.30 Time-averaged Nusselt number, Nu/Nu_{av}, on the heated end-wall normalized with the area-averaged value, Nu_{av}. Liquid-crystal experiments of Ames *et al.* (2007) and αHLR simulations on grids 1.3×10^6 and 4.4×10^6 cells, respectively, for Re = 10,000 (left) and Re = 30,000 (right). Top: wall distribution around the first four pins. Bottom: distribution along the line cutting pins 2, 4, 6 and 8 for Re = 10,000. Comparison of computations using RANS and αHLR solving strategies with experimental data. Reprinted from Delibra *et al.* (2010), with permission from Elsevier.

direct way in which a baseline implementation (for either RANS or LES) can be extended to include the other.

In the following section, we start by considering the use of the unmodified (U)RANS or LES methodologies as a hybrid RANS-LES approach, as they often were before the currently more common schemes were established. Several commonly used seamless methods, derived from RANS models, are then examined, noting their differences, their shortcomings and proposals to mitigate them.

10.6.1 The need for a seamless framework

Before the advent of HRL methods in the late 1990s, a large number of studies explored the possibility of bridging the gap between URANS and LES without explicitly modifying the solution framework. Here, the main problems

https://doi.org/10.1017/9781108875400.012 Published online by Cambridge University Press

encountered from attempting to do so are briefly examined, in order to highlight the requirements for developing a functional seamless approach.

Very large eddy simulation

In the 1980s and early 1990s, the initial success of LES for simple cases, such as channel and pipe flows, motivated its application to more complex flow configurations at a time where computational resources were severely limited. Inevitably, the mesh resolution of studies at that time was far below current best-practice guidelines. Eddy resolution often fell short of the inertial scales and so the complex interaction between energetic modes was poorly captured or missed altogether. This unavoidable 'coarse LES' methodology, became known as Very Large Eddy Simulation (VLES),[10] Ferziger (1996).

One may recall from the discussion about length scales in §10.2 that turbulence remains anisotropic across most of the inertial subregion, where $E(\kappa)$ varies as $\kappa^{-5/3}$. Towards the high-wave-number end of this subregion, the turbulent eddies gradually lose any spatial bias they may have inherited from the mean-flow field and become nearly isotropic in form. For such wave numbers, with magnitude typical of the reciprocal of the Taylor length scale, it is reasonable to switch to a standard sgs model, even the simple Smagorinsky version. Resolution down to and beyond the Taylor length scale is computationally demanding, however, and, from an early point in the history of LES, it became clear that simple sgs models would be insufficient for complex geometries for all except quasi-DNS resolutions, as discussed in Hussaini *et al.* (1989).

VLES generally failed because the rudimentary sgs models that were invariably used could not take account of the complex interaction of non-local and strongly non-isotropic turbulent structures, with which they were simply not equipped to handle. When the cut-off frequency is placed in the vicinity of the turbulent stress-producing scales, the result is a decrease in k and an increase in ε, which results in a drop in viscosity while the small scales grow in a non-physical manner, as shown qualitatively in Fig. 10.31.

Unsteady RANS and scale resolution

Chapter 9 has provided an overview of the potential and limitations of unsteady RANS (URANS) for scale resolution via the inclusion of the time-dependent term within the transport equations of both the momentum equations and the chosen turbulence model. When compared to steady RANS, a URANS method is in many cases able to provide an improved prediction for flows with a dominant natural

[10] The acronym VLES had earlier been used in the literature (e.g. Ferziger, 1996) for certain other methods aimed at adapting the sgs model used in LES to better predict flows dominated by distinct large-scale structures; however, today the term VLES generally applies to coarse LES, as reported here.

https://doi.org/10.1017/9781108875400.012 Published online by Cambridge University Press

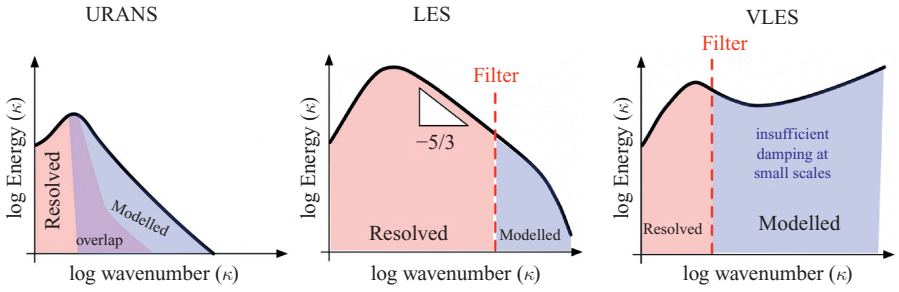

Fig. 10.31 Conceptual representation of the impact of applying either unmodified URANS or under-resolved LES (VLES).

instability; but the success depends greatly on the type and level of the RANS model adopted. Indeed, as demonstrated in Chapter 9, a key prerequisite is the ability of the RANS model to reproduce at least some features of stress anisotropy by which to ensure a realistic effective viscosity that would not damp the natural instabilities present. This is especially the case in the near-wall region of separated flows. Several examples of flows dominated by separation or a body force discussed in Chapter 9 showed that URANS can often be used to show how large coherent patches of fluid are periodically shed behind a bluff body or generated by buoyancy or rotation.

However, as commonly applied, URANS methods, especially when implemented with one- or two-equation linear EVMs, are limited in their ability to provide an accurate account of how turbulent structures interact with themselves, stretching and twisting each other apart in a non-linear fashion, characteristic of the turbulence energy cascade. The high levels of turbulent viscosity in regions of flow separation, produced by several of the early turbulence models, tend to dampen even the largest resolved structures, making it impossible to account accurately for even a small part of the energy cascade. Moreover, confusion can arise over how to account correctly for the overlap of both the turbulence energy and stresses provided by the model with the contributions resolved by the unsteady solution of the low-frequency motion. Without such careful accounting, this overlap can lead to an excessive production of turbulence energy, which in turn further increases the modelled viscosity and further dampens the resolved motion.

Where used correctly, a URANS solution describes the phase-averaged result for the flow: a series of cyclically repeating large-scale organized structures observed in Nature and detected in physical experiments by averaging data into discrete portions of an imposed periodic flow. This holds true for cases with either a strong externally imposed unsteadiness such as an oscillating channel flow or a geometry-induced flow instability with time and length scales far removed from

https://doi.org/10.1017/9781108875400.012 Published online by Cambridge University Press

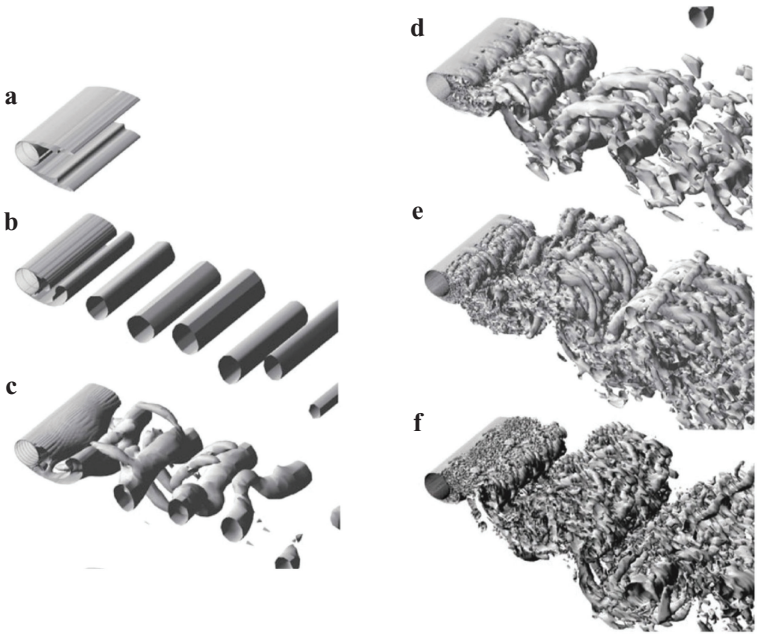

Fig. 10.32 Comparison of vorticity isosurfaces in the wake around a circular cylinder at $\mathrm{Re}_D = 50,000$. (a) SST 2D steady RANS, (b) SST 2D unsteady RANS, (c) SST 3D unsteady RANS, (d) coarse mesh SA-DES, (e) fine-mesh SA-DES, (f) fine-mesh SST-DES. Image from Travin, via Spalart (2009).

those of the turbulent scales of motion accounted for by the turbulence model. As discussed in Chapter 9, the latter is referred to as a 'separation of scales' and is commonly regarded as a condition for the appropriate use of a URANS approach.

Figure 10.32 from Spalart (2009) strikingly illustrates levels of turbulence resolution (represented by iso-vorticity surfaces) in the wake of a circular cylinder achieved with methods of increasing eddy-resolving potential. These range from RANS in different modes (2D, 3D, steady and unsteady) to DES with coarse and fine meshes. Obviously, the first two examples – the 2D steady and 2D unsteady RANS – make no sense here since turbulence structures, by their nature, are three-dimensional and unsteady. On the other hand, the three examples of DES, all show superior LES-like resolution, which improves with mesh refinement (parts d and e) and, still further, when applying the more capable two-equation SST compared to the one-equation SA RANS model (parts e and f). While the figure implies an undisputed advantage of DES over URANS, this is, to an extent, misleading as the applied RANS models (SA and SST) cannot be considered among the most

https://doi.org/10.1017/9781108875400.012 Published online by Cambridge University Press

capable representatives among the very wide range of RANS models.[11] When employed in a DES or other hybrid mode where RANS is applied only in limited (usually near-wall) regions, the weaknesses of simple RANS models may not be significant. Their deficiencies may, in part, be compensated by unsteady excitations and a pressure field propagating from the outer, more completely resolved LES solution. Highly resolved fine scales as provided by LES and hybrid methods, including DES, can be essential for some applications such as in aeroacoustics. But, as demonstrated in Chapter 9, capturing the dynamics of major integral parameters such as lift and drag coefficients in flows over bluff bodies, or dominant convective patterns and heat transfer in flows driven by buoyancy and rotation – where the physics is governed by large-scale structures – can also be achieved by more capable RANS models resolved in time on a typical RANS computational mesh.

Nevertheless, the labelling of URANS as a scale-resolving approach presents us with a conceptual challenge. A key tenet of RANS methods (and a practical advantage) is that they are independent of the mesh on which they are solved. That is, a grid-independent solution is possible, which, numerics aside, is the unequivocal solution for a given model. In this sense a fundamental difference exists between RANS and LES, since one is independent of the mesh while the other is strongly linked to it. For LES, a grid-independent solution is difficult to define, since in most LES formulations the grid acts also as the spatial filter and, instead, one tends towards a DNS solution in the limit of progressive refinement. On the other hand, accurate scale resolution with URANS is not guaranteed, even with a grid-independent solution, particularly where there is no clear separation of spatial scales between the dominant flow instability and the broadband turbulence.

10.6.2 Approaches which blend RANS and LES

Recognizing the shortfalls of VLES, Speziale proposed a methodology to bridge the gap between LES and RANS, based on 'state-of the-art Reynolds-Stress models', which automatically recovers a competent Reynolds-stress model (RSM) scheme in the coarse-mesh limit or DNS in the fine-mesh limit (Speziale, 1998a,b). The Flow Simulation Methodology (FSM) was developed further by Fasel *et al.* (2002), employing a function to blend between RANS and DNS by modifying the stress tensor according to the local grid size.

$$\tau_{ij}^{model} = f_\Delta \tau_{ij}^{RANS} \qquad (10.33)$$
$$f_\Delta = 1 - \exp(-\beta\Delta/\eta)$$

[11] As shown in Fig. 9.7, a more advanced, anisotropy-resolving RANS model at second-moment-closure level (or a simplified version thereof) when used in stand-alone mode, performs much better than the model shown in Fig. 10.32c.

https://doi.org/10.1017/9781108875400.012 Published online by Cambridge University Press

where the function f_Δ provides a simple blending between DNS (where there is no modelling, i.e. $f_\Delta = 0$) and RANS (where all scales are modelled, $f_\Delta = 1$). This function was sensitized to the mesh resolution, where $\eta \equiv \nu^{3/4}/\varepsilon^{1/4}$ is the Kolmogorov length scale and thus the 'damping ratio' Δ/η indicates the factor by which the mesh resolution is coarser than needed for DNS. The method has been used in a number of studies to good effect with particular focus on compressible turbulent flows, though it is not limited to such cases. However, there are some weaknesses in this approach, such as the calibration of the model constant β in Eq. (10.33) and the need for a reasonably accurate estimate of η.

Furthermore, Eq. (10.33) implies that the RANS and LES momentum equations are interchangeable although, since true RANS is only used when $f_\Delta = 1$, there is a need to provide an average of the 'blended' velocity field for regions where $0 < f_\Delta < 1$. In practice, this is achieved via an explicit averaging operation, which requires a homogeneous direction in space. This limits the general use of this formulation, since in more complex applications there will not be a homogeneous direction. Furthermore, where the flow moves from an area of low to high grid resolution, permitting a greater resolved content, turbulent fluctuations might need to be introduced artificially. The FSM was shown to perform well for a range of flows by Weinmann (2011), including the flow in a plane channel, around tandem circular cylinders and through a 3D diffuser. The last case is shown in Fig. 10.33 compared with experimental data from Cherry *et al.* (2008). The scale-resolving nature of the method is clearly demonstrated in the figure by the instantaneous contours of vorticity.

Also of note here is the Limited Numerical Scales method of Batten *et al.* (2002), which proposed a version of f_Δ from Eq. (10.33) based on the ratio of the kinematic viscosities computed for RANS and LES, rather than just the length scales.

10.6.3 Unified RANS-LES

A family of methods referred to variously as 'unified', 'bridging' RANS-LES, 'sensitized RANS' or even 'second-generation'[12] URANS models have attempted to transform the classical URANS model described in the previous chapter into a scale-resolving approach, i.e. one which moves from modelling the turbulence to simulating it. Essentially, the URANS models are sensitized to internal instabilities by *decreasing the effective eddy viscosity.* This is usually achieved by enhancing

[12] The label 'second-generation URANS', introduced by Fröhlich and Von Terzi (2008), can be misleading as modifications to a standard RANS model aimed at extending its applicability have been made in the past to account for various flow features that remain inaccessible to the basic model such as extra- (or irrotational) strain, swirl, stress anisotropy among others.

https://doi.org/10.1017/9781108875400.012 Published online by Cambridge University Press

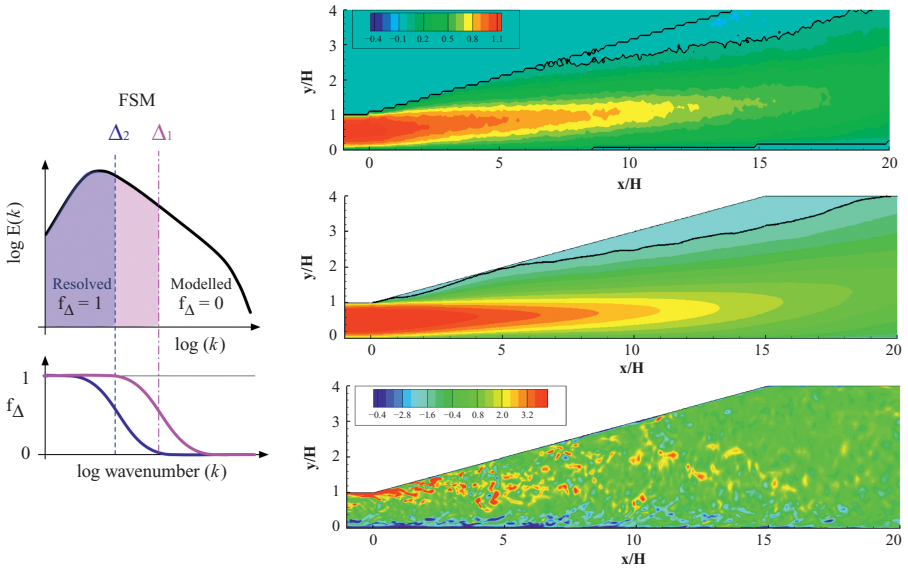

Fig. 10.33 (Left) Conceptual diagram of the Flow Simulation Methodology (FSM) approach, demonstrating how the blending function, f_Δ, adapts from a fine-mesh (1) to a coarse mesh (2). (Right) Performance of FSM for 3D diffuser case. (Top) Streamwise mean velocity from experiment (Cherry *et al.*, 2008). (Middle) Streamwise mean velocity from FSM. (Bottom) Spanwise instantaneous vorticity from FSM. Middle and Bottom images reproduced from Weinmann (2011).

the dissipation rate of the modelled turbulent kinetic energy either over the whole flow or in regions prone to instabilities, in a continuous and thus '*seamless*' manner.

Possible (albeit, not exclusive) modifications to the RANS models to expand their potential for scale resolution (beyond that achievable with the unmodified model when applied in unsteady mode) can be illustrated by way of the usual k-ε model, but noting that the principle is applicable to any scale-providing variable and equation:

$$\frac{Dk}{Dt} = \mathcal{P}_k - f_L\varepsilon + \frac{\partial}{\partial x_k}\left[\left(\nu + \frac{\nu_t}{\sigma_k}\right)\frac{\partial k}{\partial x_k}\right] \tag{10.34}$$

$$\frac{D\varepsilon}{Dt} = f_\varepsilon\left(c_{\varepsilon 1}\mathcal{P}_k\frac{\varepsilon}{k} - c^*_{\varepsilon 2}\frac{\varepsilon^2}{k}\right) + \mathcal{S}_{\varepsilon 3} + \frac{\partial}{\partial x_k}\left[\left(\nu + \frac{\nu_t}{\sigma_\varepsilon}\right)\frac{\partial \varepsilon}{\partial x_k}\right] \tag{10.35}$$

where $\nu_t = c_\mu k^2/\varepsilon$ and $f_L = \max(1, L_{RANS}/L_{LES})$ as in Eq. (10.43),[13]

[13] Also identical to α in Eq. (10.31) in two-layer HRL, §10.5.2.

https://doi.org/10.1017/9781108875400.012 Published online by Cambridge University Press

$f_\varepsilon > 1$ is a function that enhances the complete source of ε;
$c^*_{\varepsilon 2} < c_{\varepsilon 2}$, which reduces the sink of ε;
$\mathcal{S}_{\varepsilon 3}$ is an additional source that increases the energy dissipation rate.

Thus, the dissipation rate in Eq. (10.34) can be modified directly by multiplying it by a control parameter $f_L > 1$ (as in Eq. (10.30)), usually defined in terms of the ratio of the characteristic turbulence length scale and a representative grid cell size (already introduced in §10.5.2 in a two-layer HRL, Eqs. (10.30–10.31)). Alternatively, one may apply the same f_L or some similar parameter directly to the transport equation for turbulent eddy viscosity, as in the original DES of Spalart *et al.* (1997). For two-equation and higher-order RANS models, the dissipation rate can be modified through interventions in the scale-providing equations (ε, ω or some equivalent) as indicated in Eq. (10.35). A way to achieve this is by adding another source term (e.g. $\mathcal{S}_{\varepsilon 3}$ in Eq. (10.35)) defined in terms of the available flow and turbulence parameters. These are thus independent of the mesh (‘*grid-independent sensitizing*’), as in Menter and Egorov (2005) outlined below. Other routes focus on modifying the source terms in the scale-providing equation via a control (or ‘grid-detecting’) parameter akin to f_L (‘*grid-based sensitizing*’). The control parameter can be applied to the whole source term (e.g. through f_ε), or only to the source or sink (e.g. as $c^*_{\varepsilon 2}$ in Eq. (10.35)). Usually, only one of the above options is applied.

10.6.4 Grid-independent sensitizing of URANS

An example of a grid-independent method is the Scale-Adaptive Simulation (SAS) approach of Menter and Egorov (2005). This introduces another scale based on the second derivative of the velocity field via an additional term in the scale-determining equation. This additional information is used to reduce the characteristic length scale and, hence, the eddy viscosity in the RANS equations in which it is inserted. It thus provides a means of enabling scale resolution. A possible theoretical origin of this approach may be found in the form employed in Rotta’s length-scale (kL) equation (Rotta, 1951, 1972), which in its source terms contains higher mean-velocity derivatives. In the original SAS model the product $\sqrt{k}L$ was adopted as the scale-providing variable obtained by way of its transport equation that contained an additional source term $\mathcal{S}_3 \sim L/L_K$, where L_K is the von Karman length scale,

$$L_K = \kappa \left| \frac{U'}{U''} \right| \quad \text{with } U' = \sqrt{2 S_{ij} S_{ij}} \quad \text{and} \quad U'' = \sqrt{\frac{\partial^2 U_i}{\partial x_j^2} \frac{\partial^2 U_i}{\partial x_k^2}}. \qquad (10.36)$$

The authors claim that adding the length scale, L_K, in addition to L, expands the model’s scale-resolving potential beyond that of the single-scale parent model. One

https://doi.org/10.1017/9781108875400.012 Published online by Cambridge University Press

can argue, however, that the key addition is the second derivative of velocity that acts as an instability sensor (detecting inflection-point instabilities) which gives rise to inviscid instability modes (Saric *et al.*, 2003). Subsequently, Menter and Egorov (2010) extended the concept and offered SAS versions within the ε and ω modelling frameworks.

It is reiterated that the key feature of the above approaches is that the grid scale is not explicitly dependent on the mesh as it is with LES. However, it *does* require a good approximation of the second derivative (which itself imposes a restriction on the grid resolution), while, from a different standpoint, many would question whether the local second derivative of the resolved velocity should play such a key role in the modelling.

The above concept involving the second velocity derivative, reformulated and re-labelled as eddy-resolving (or instability-sensitized) URANS, has been further employed in the framework of the usual k-ε and k-ω models as well as in combination with the elliptic-relaxation ζ-f EVM approach (Jakirlić and Maduta, 2015; Krumbein *et al.*, 2020). It has also been employed in a second-moment (Reynolds-stress) closure (Maduta *et al.*, 2017), and applied to cases relevant to flow control, aeroacoustics (Köhler *et al.*, 2020) and bubble columns (Ullrich *et al.*, 2021) among others.

10.6.5 Approaches with a grid-based switch

In a seamless approach, the mode of operation, RANS or LES, and, consequently, the location of the interface are intrinsically defined as a function of both the predicted flow field and the grid spacing. By comparing the transport equations for both RANS and LES, it can be seen that the primary difference lies in the way in which the Reynolds stresses are estimated. The momentum equation, Eq. (2.14), rewritten as

$$\frac{\partial(\rho U_i)}{\partial t} + \frac{\partial(\rho U_j U_i)}{\partial x_j} = F_i - \frac{\partial P}{\partial x_i} + \frac{\partial\left(\tau_{ij}^{RANS}, \tau_{ij}^{LES}\right)}{\partial x_j} \tag{10.37}$$

can represent either RANS or LES, where U_i would be either a result of temporal or spatial averaging, or filtering, respectively. The stress tensor, τ_{ij}^{RANS}, τ_{ij}^{LES}, represents stresses which arise from the decomposition for either RANS or LES, and while, as described in §10.2.1, these terms represent different quantities, they may end up being approximated in exactly the same manner. This similarity is particularly strong where the RANS approach incorporates a time-dependent term (i.e. URANS), and where a linear eddy-viscosity model is used, since in that case the

https://doi.org/10.1017/9781108875400.012 Published online by Cambridge University Press

difference is reduced to the definition of the turbulent viscosity, ν_t. For example, where turbulent stresses are defined as:

$$\overline{u_i u_j} = -2\left[\nu_t^{RANS}, \nu_t^{LES}\right] S_{ij} + \frac{2}{3} k \delta_{ij} \tag{10.38}$$

the turbulent viscosity approximation for both RANS and LES, with a Smagorinsky model, Eq. (10.14), becomes

$$\nu_t^{RANS} \propto \mathsf{L}^2 \mathsf{T}^{-1} = c_\mu \left(\frac{k^{3/2}}{\varepsilon}\right)^2 \mathsf{T}^{-1} \quad \text{and} \quad \nu_t^{LES} = (c_S \Delta)^2 \mathsf{T}^{-1} \tag{10.39}$$

where the precise choice for T^{-1} could come from either modelled turbulence quantities (e.g. ε/k) or the mean-velocity field (e.g. S); at this stage this choice is not important, since they are both determined from the flow computation itself. The key difference between the two is the definition of the length scale, L. For LES it is based on the local grid size, while for RANS it is based on local macroscopic turbulence quantities. It is then logical for a global HRL approach to make use of this distinction by introducing a simple function to switch between the two different definitions of the length scale. Given that one seeks to improve the level of predictive accuracy by increasing the scale-resolved content, it makes sense to seek the minimum of these two scales as:

$$L_{\min}^{(R,L)} = \min\left[c_\mu \frac{k^{3/2}}{\varepsilon}, c_s \Delta\right] = \min\left[L_{RANS}, L_{LES}\right]. \tag{10.40}$$

Indeed, this argument is the basis for a number of seamless approaches, including one of the most popular Hybrid RANS-LES approaches, Detached Eddy Simulation, DES.[14]

10.6.6 Detached eddy simulation

Originally proposed by Spalart *et al.* (1997), DES is today a widely used scheme among HRL methods, particularly in flows linked with the aerospace industry. In DES, the objective is for the near-wall flow region, where turbulent length scales are small, to be solved by a RANS treatment, while the field away from the wall is computed via LES.[15] The popularity of DES is due in part to its simplicity and its practicality, since the work required to extend an existing RANS solver to handle

[14] In fact, the principle of RANS–LES hybridization, outlined above and through Eqs. (10.37)–(10.40), applies also to zonal approaches, apart from the fact that then there is a clear interface between the two schemes, which is, of course, absent with seamless methods.

[15] Such a general objective and the rationale of merging RANS and LES into a single algorithm (via a length-scale/grid-size ratio control) may qualify the label DES to include the whole family of eddy-resolving schemes between stand-alone URANS and LES. Nevertheless, in line with practice, and to acknowledge the method's originators, here we associate the acronym DES with the specific method introduced by Spalart *et al.* (1997) (also termed DES97) and its subsequent versions.

https://doi.org/10.1017/9781108875400.012 Published online by Cambridge University Press

DES is straightforward. A simple switch in length scale is required, following the principle set out in Eq. (10.40). It was originally developed for aerospace applications in largely attached, boundary-layer flows, and based around the one-equation model for effective turbulent viscosity, ν_t, proposed by Spalart and Allmaras (1992) (SA). As noted in §7.4.6, this is an empirically based model tuned to predict aerodynamic boundary layers at moderate to high Reynolds numbers. It takes the form:

$$\frac{\partial \tilde{\nu}}{\partial t} + \frac{\partial}{\partial x_j}\left(U_j \tilde{\nu}\right) = c_{b1}\tilde{\nu}\tilde{\omega} - c_{w1} f_w \frac{\tilde{\nu}^2}{d_w^2} + \frac{1}{\sigma_\nu}\left[\frac{\partial}{\partial x_j}(\nu + \tilde{\nu})\left(\frac{\partial \tilde{\nu}}{\partial x_j}\right) + c_{b2}\frac{\partial \tilde{\nu}}{\partial x_j}\frac{\partial \tilde{\nu}}{\partial x_j}\right] \tag{10.41}$$

where on the right-hand side are production, sink and diffusion terms. The invariant $\tilde{\omega}$ is the vorticity magnitude, d_w is the near-wall distance and turbulent viscosity $\nu_t = \tilde{\nu} f_{\nu 1}$, so as to ensure that $\tilde{\nu} = \kappa y U_\tau$ in the log-layer. The damping function $f_{\nu 1}$ is defined as $\chi^3/(\chi^3 + c^3)$, where χ is the viscosity ratio $\tilde{\nu}/\nu$, and c denotes a model coefficient. To extend this model to work within DES, the quantity d_w in Eq. (10.41) is replaced by $\tilde{d}$, defined as:

$$\tilde{d} = \min(d_w, C_{DES}\Delta). \tag{10.42}$$

It is noted that, for the SA model, d_w is the distance to the nearest wall since the model does not solve a separate length-scale-determining equation such as ε. Clearly, this definition requires a wall to be present, which for most practical applications is indeed the case. Note that when DES is used with two-equation RANS models, such as k-ε or k-ω, the RANS length scale L naturally arises without dependence on wall distance, and directly replaces d_w in Eq. (10.42). The grid filter Δ is generally based on either the maximum dimension of the local grid cell, $\Delta_{max} = \max(\Delta x, \Delta y, \Delta z)$, or the cube root of the cell volume, $\Delta_{vol} = (\Delta x \Delta y \Delta z)^{1/3}$. In regions of fine mesh, Eq. (10.42) allows $\tilde{d}$ to take a lower value than returned by the SA model. This in turn allows for a larger dissipation term, as seen in Eq. (10.41), which leads to a local reduction in turbulent viscosity.

Calibration of DES

Calibration of the constant C_{DES} appearing in Eq. (10.42) is code-dependent and is usually achieved via the simulation of decaying homogeneous turbulence, with the constant chosen to achieve a balance of RANS and LES activity while matching the measured rate of turbulence energy decay. For illustration, example results from a

https://doi.org/10.1017/9781108875400.012 Published online by Cambridge University Press

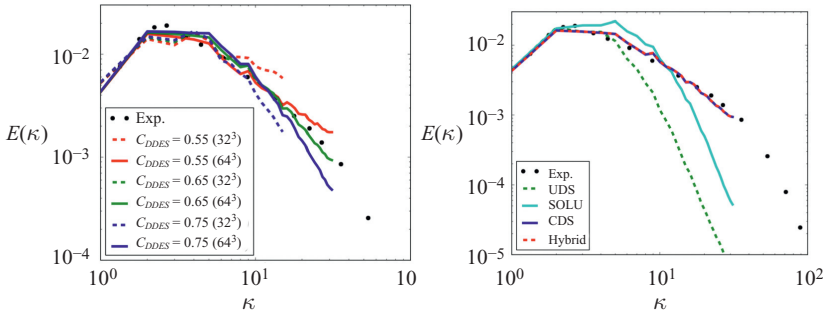

Fig. 10.34 Calibration of the SST-DES constant C_{DDES} based on decaying homogeneous, isotropic turbulence, from Ashton *et al.* (2013). (Left) Sensitivity to different values of C_{DDES} for two grid resolutions: 32^3 and 64^3. (Right) Sensitivity to different numerical schemes: UDS: first-order upwind, SOLU: second-order linear upwind, CDS: central-difference scheme, Hybrid: see main text. (Note that in the right figure the CDS (blue) and Hybrid (red) lines virtually coincide, creating the impression of a purple line.)

calibration exercise are presented in Fig. 10.34.[16] Increasing this constant effectively increases the Delayed Detached Eddy Simulation (DDES) cut-off scale as follows from Eq. (10.42) and thus extends the coverage of the RANS model to progressively lower values of wave number. Decreasing C_{DDES} has the opposite effect, reducing the role of the RANS model, which results in too little damping at higher wave numbers (i.e. smaller structures). This situation is reminiscent of the scenarios presented in Fig. 10.31 and demonstrates the careful balancing act required to maintain an appropriate representation of the energy spectra. Note that Fig. 10.34 presents results for two different grid resolutions, 32^3 and 64^3, each resulting in a slightly different optimal value for C_{DDES} as a consequence of compensating for each model's natural dissipation in this flow. The dependence of this constant on the local grid resolution places a significant limitation on the generality of the method.

The situation is further complicated when considering the artificial dissipation that can be introduced by the code numerics, especially for codes originally designed for solving the RANS equations rather than LES (as is generally the case for DES applications). Figure 10.34 demonstrates the impact of different numerical schemes following calibration using the least dissipative scheme. The use of a central-differencing scheme is seen to be vital since, when an upwind scheme is used (whether of first- or second order), a significant broadband damping of turbulence structures occurs.

Strictly, a central-differencing scheme is needed only where the model operates in LES mode, bringing additional stability in the case where turbulent fluctuations result in the continual change in local flow direction across a given cell from

[16] Note that here the later version, *DDES* – i.e. *delayed* DES, is used as introduced in §10.6.7, hence labelled C_{DDES}.

https://doi.org/10.1017/9781108875400.012 Published online by Cambridge University Press

one time step to the next. This is a common feature of LES due to the passage of fine-scale turbulent fluctuations through the domain. However, applying central differencing across the full domain is undesirable, since it introduces stability problems for RANS models, particularly for high-aspect-ratio cells in the boundary layer. Recognizing this, Travin *et al.* (2002) introduced a 'hybrid' numerical convection scheme which allows the code to switch the convective scheme depending upon whether the model is operating in RANS or LES modes (i.e. as determined from Eq. (10.42), deploying an upwind scheme for RANS and a central-difference scheme for LES).

Sensitivity of DES to the RANS model

The role of the RANS model is not trivial and it should be remembered that a seamless method inherits many of the characteristics of the model embodied in it, both its strengths and its weaknesses. This is particularly true where limitations on mesh size are imposed as a consequence of the computational resources available. Recall that while DES is not a zonal approach, the regions where it will act in either mode can indirectly be 'prescribed' as a consequence of selective mesh refinement or coarsening within a domain. This issue becomes more pertinent in the region of a coarser mesh, where RANS is expected to play a greater role, and differences due to the inherent capability of the RANS model employed will be amplified in the overall DES approach. DES variants have been proposed based on a range of turbulence models. We note, for example, two-equation models such as k-ω-SST-DES proposed by Travin *et al.* (2002), non-linear eddy-viscosity models (e.g. Greschner *et al.*, 2008), elliptic-blending-based models (e.g. Ashton *et al.*, 2013) and full Reynolds-stress-transport models (e.g. Probst *et al.*, 2011).

Indeed, the principle for DES may be generalized as outlined by Eqs. (10.34) and (10.35), where the sensitivity to mesh resolution now enters via the term F_{DES}, defined as:

$$f_L \equiv F_{DES} = \max\left(1, \frac{L_{RANS}}{L_{LES}}\right) = \max\left(1, \frac{k^{3/2}/\varepsilon}{C_{DES}\Delta}\right). \tag{10.43}$$

In an aeroacoustics study of a wake flow from a cylinder placed upstream of and interacting with an airfoil, Greschner *et al.* (2008) compared several such models, demonstrating significant dependence of the results on the underlying RANS model (see Fig. 10.35). In this case improved prediction of both the mean and turbulent flow fields was obtained from DES variants based on more capable RANS modelling. The figure also shows the extent to which RANS and LES modes vary throughout the wake via the plotting of the following function:

$$F^* = \log(L_{RANS}/C_{DES}\Delta) \tag{10.44}$$

https://doi.org/10.1017/9781108875400.012 Published online by Cambridge University Press

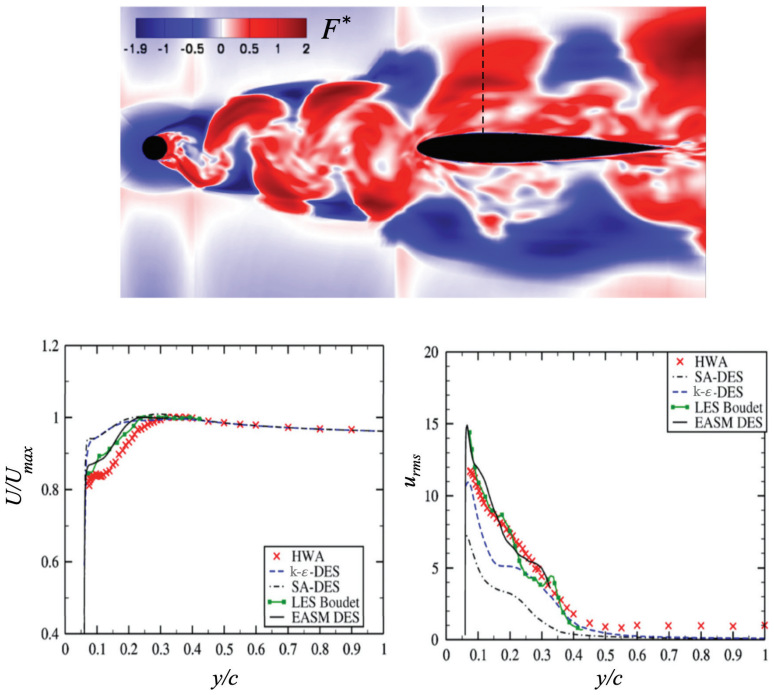

Fig. 10.35 Turbulent flow over a rod-airfoil configuration, where Re based on cylinder diameter is 48,000 (Greschner *et al.*, 2008). Top: instantaneous variation of RANS and LES zones, represented via the function F^* (defined in Eq. (10.44). Bottom: comparison of predicted mean and turbulent flow field around the airfoil of chord length c, along the dashed black line in the top figure.

for which a negative value corresponds to a region where RANS is used and a positive value to where LES is active. The figure clearly demonstrates the highly unsteady variation of the two modes, which is a characteristic of seamless models applied to separated flows, including bluff-body wakes. The selection of RANS or LES is strongly dependent on the mesh resolution and, as a given mesh is refined, a greater extent of the domain can be expected to operate in LES mode.

While the foregoing examples have been directed at predicting the dynamic field, applications focused on the thermal field, often within internal passages, are equally important. Dr D. Tafti and his team at Virginia Tech were one of the first groups to apply DES to the heat-transfer performance of such complex internal flows. The focus of their research was the internal cooling passages within gas-turbine blades where the cooling potential was enhanced by the use of square-sectioned ribs applied to opposite walls (Fig. 10.36). The sequence of publications suggests that they had examined both LES (Sewall and Tafti, 2004; Sewall *et al.*, 2006) and DES studies in parallel. After examining fully developed flow in stationary and rotating passages (Viswanathan and Tafti, 2005, 2006a), they

https://doi.org/10.1017/9781108875400.012 Published online by Cambridge University Press

undertook with DES the much larger computational study of flow along two lengths of cooling channel connected by a sharp, square-ended U-bend, as indicated in Fig. (10.36, left), Viswanathan and Tafti (2006b). It is from the last of these that results presented here are drawn.

Their version of DES adopted a non-zonal strategy, employing as the RANS model the original k-ω eddy-viscosity model of Wilcox (1988b) which resolved the viscous sublayer. The near-wall node was located at $y^+ < 1$ with three to four nodes covering the sublayer region $y^+ < 10$. The same k-ω model with the RANS-generated length scale $L_{k\text{-}\omega}$, replaced by the largest of a cell's dimensions, Δ, was used as the sgs model in the LES mode. The switchover from RANS to LES modelling occurred when $C_{DES}\Delta < L_{k\text{-}\omega}$ and, following Strelets (2001), the value of C_{DES} was taken as 0.61. The grid around each of the ribs is shown in Fig. 10.36 (right). The total solution domain was resolved by 7.7×10^6 cells, modest by today's standards but, at the time, requiring parallel processing to achieve acceptable run times. The forward time-step (non-dimensionalized by the bulk velocity and hydraulic diameter of the channel) was 1×10^{-4} in all cases. The thermal boundary condition imposed at the walls, including the three faces of the ribs exposed to the flow, was that of uniform heat flux. Figure 10.36 (bottom) shows, for the centre plane of the entry section upstream of the U-bend, the proportion of time that is spent in LES, DES and mixed mode, i.e. each cell is assigned a value of 0 or 1 at each time step depending on whether RANS or LES is used in that cell. The time

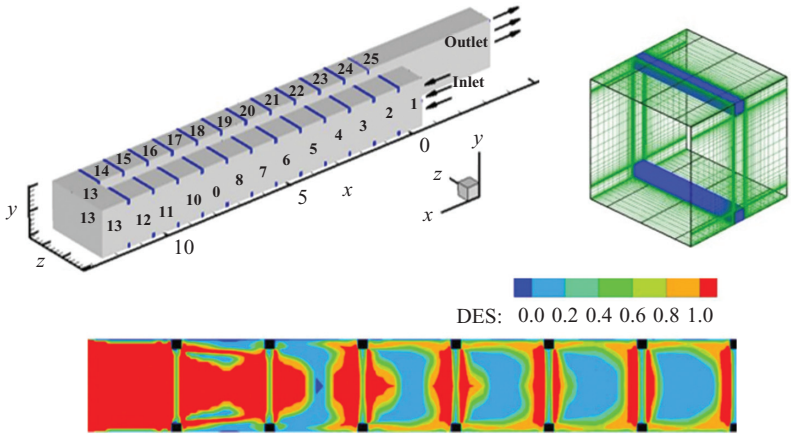

Fig. 10.36 Modelling flow in an internal gas-turbine blade-cooling passage. Top left: complete DES solution domain. Top right: details of the numerical grid around a single rib. Bottom: LES (red), DES (blue) and mixed-mode regions on the centre plane of the domain. Reprinted from Viswanathan and Tafti (2006b), with permission from Elsevier.

https://doi.org/10.1017/9781108875400.012 Published online by Cambridge University Press

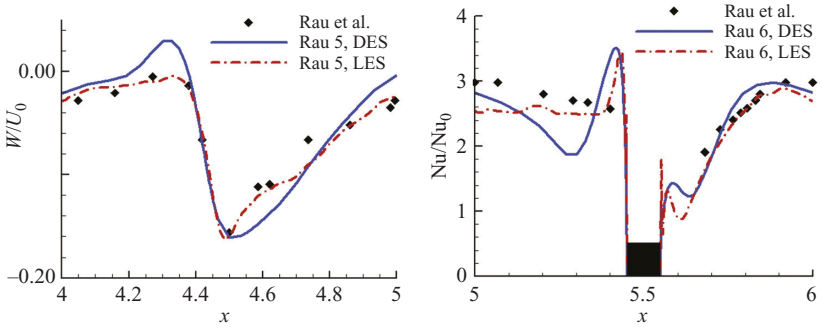

Fig. 10.37 Left: Comparison of the spanwise velocities above the fifth rib (y/e = 1.5) near the smooth side wall ($z/D_h = 0.05$). Right: heat-transfer augmentation ratios at the centre of the ribbed wall upstream and downstream of the sixth rib. Symbols: Experiments (Rau *et al.*, 1998); LES results (Sewall *et al.*, 2006). From Viswanathan and Tafti (2006b). Reprinted with permission from Elsevier.

average of this quantity is plotted. The RANS/LES distinction is based on comparison between the turbulent scale and the grid scale which is fundamental to the DES model. Thus, a value of 0.0 corresponds to a purely RANS mode, while 1.0 represents a completely LES operation. At inlet (on the left) the entering flow is treated by LES but, as the flow develops downstream, the RANS mode becomes increasingly used. By the sixth rib the flow treatment has become fully repeating from rib to rib, with the LES mode being predominantly applied in the separated shear layer and the recirculating region behind each rib.

Figure 10.37 (left) shows lateral velocities around the fifth rib close to the smooth side wall compared with the fully developed LES of Sewall and Tafti (2004) and the earlier experimental values by Rau *et al.* (1998). The DES results agree reasonably well with both experiment and the LES computations – far closer, Viswanathan and Tafti report, than when the same k-ω model is used in a purely RANS mode. These secondary velocities are reported to be particularly influential on the levels of heat-transfer coefficient. In fact, the computed Nusselt number augmentation (relative to the Dittus-Boelter correlation for fully developed flow in a smooth straight duct) is compared with experiment and LES data in Fig. 10.37 (Right) along the centre plane of the duct, upstream and downstream of the sixth rib. Evidently, there is again reasonable agreement among the computations and experiments.

Figures 10.38–10.39 present corresponding comparisons in the square-ended turning section of the U-bend. The LES computations had begun only three hydraulic diameters upstream of the turn, using the earlier LES data (Sewall and Tafti, 2004) to provide appropriate initial conditions. Both sets of LES data had been generated on a substantially finer grid than the DES computations with, as an example,

https://doi.org/10.1017/9781108875400.012 Published online by Cambridge University Press

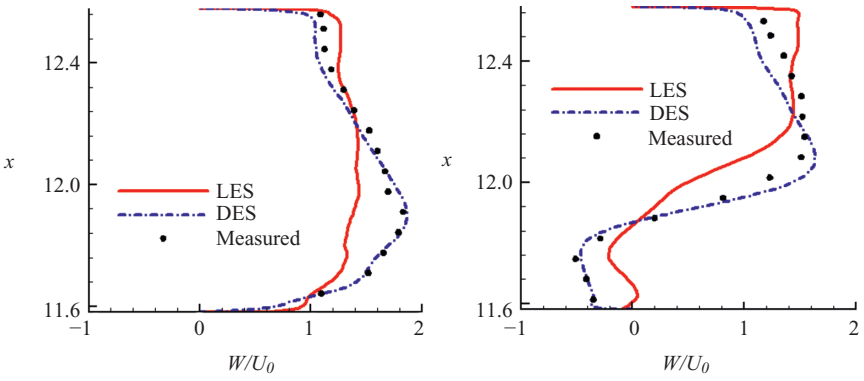

Fig. 10.38 Streamwise velocities halfway around turning section of U-Bend. Left: y/D_h= 0. 02; Right y/D_h= 0.57. From Viswanathan and Tafti (2006b). Reprinted with permission from Elsevier.

the elemental domain around each rib shown in Fig. 10.36 (top right) being mapped by a 96^3 mesh rather than the 64^3 mesh adopted for the DES computations. The distribution of streamwise mean velocity halfway around the turn is shown in Fig. 10.38 along two lines. Clearly, the DES computations are in close accord with the experiments but the LES show substantial differences.[17] Viswanathan and Tafti (2006b), commenting on this unexpected result, suggested that it 'could be a consequence of the inlet boundary conditions applied to the LES calculation upstream of the bend'. The normalized Nusselt number within the smooth, square-ended section of the U-bend and parts of the ribbed ducts immediately upstream and downstream thereof is shown for both LES and DES computations in isometric contour form in Fig. 10.39. The surface contour patterns of Nu are similar for both though, in most regions somewhat lower levels of Nusselt number are returned by the DES than the LES. This disparity is probably linked with the anomalous velocity profiles generated by the LES shown in Fig. 10.38, i.e. the thinner boundary layers given by the LES would be expected to lead to higher heat-transfer coefficients. Overall, the complete mapping of Nu around the U-bend given by the DES results provides invaluable guidelines to the designer in detecting likely hot spots.

The original DES method has been improved and refined over the years in order to address commonly observed, anomalous behaviour for certain configurations. Further details of these improvements are provided in the sections that follow.

[17] Viswanathan and Tafti (2006b) provide comparative profiles at six positions (rather than the two included here) which consistently show that closer agreement with the experiment is achieved by the DES computations.

https://doi.org/10.1017/9781108875400.012 Published online by Cambridge University Press

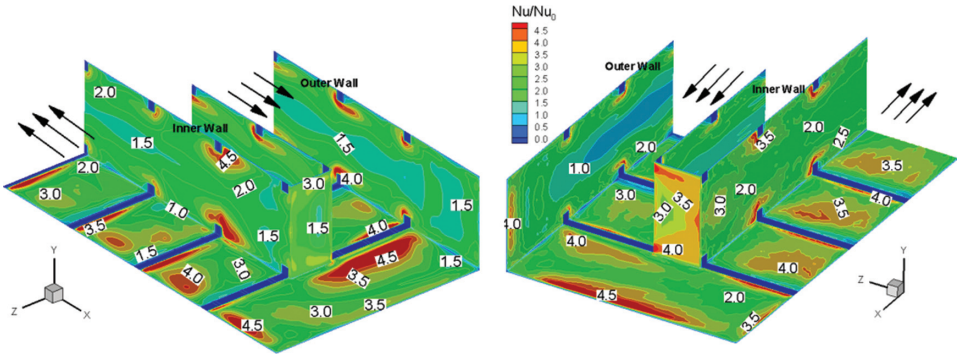

Fig. 10.39 Nusselt number augmentation ratios in the vicinity of the 180° bend. Left: DES Viswanathan and Tafti (2006b). Right: LES. Sewall *et al.* (2006), Reprinted with permission from Elsevier.

10.6.7 Issues and improvements for DES: DDES and IDDES

Stress depletion, turbulent transition and grid-induced separation

In the first few years after its first appearance, DES was applied to a range of flows of varying application area and degree of complexity. Its reputation grew on account of the ease of conversion of existing solvers. However, a common shortfall of the method was also soon identified. In areas of the boundary layer that, for various reasons, resulted in a finer mesh resolution than intended,[18] the method exhibited a tendency to switch unexpectedly to LES mode within a region of attached flow. These areas were characterized by regions in which $L \approx \Delta$ due to inadequate grid refinement or boundary-layer thickening. This sudden switching of modes (from RANS to LES) meant that the shear stress was no longer determined from the RANS model but by the LES which, in turn meant that, in that region, the mesh would need to be particularly fine in order to correctly account for the turbulence via scale resolution alone (i.e. tending to wall-resolved LES). Since this would usually not be the case, the total level of shear stress from the simulation (i.e. modelled plus resolved) is reduced, an effect known as *Modelled-stress depletion* (MSD), which results in the reduction of eddy viscosity far below what the RANS model would have provided were it still applied in this region (Spalart *et al.*, 2006). While not always the case, this reduction of wall shear stress can, in an adverse pressure gradient, lead to an entirely spurious separation of the boundary layer, referred to by Menter and Kuntz (2004) as *grid-induced separation.* This adverse feature was corrected by introducing a shielding function by way of a straightforward modification to the original formulation, leading to DDES.

[18] For example, for structured meshes with block refinement where refinement zones encroached on the meshing of the boundary layers.

https://doi.org/10.1017/9781108875400.012 Published online by Cambridge University Press

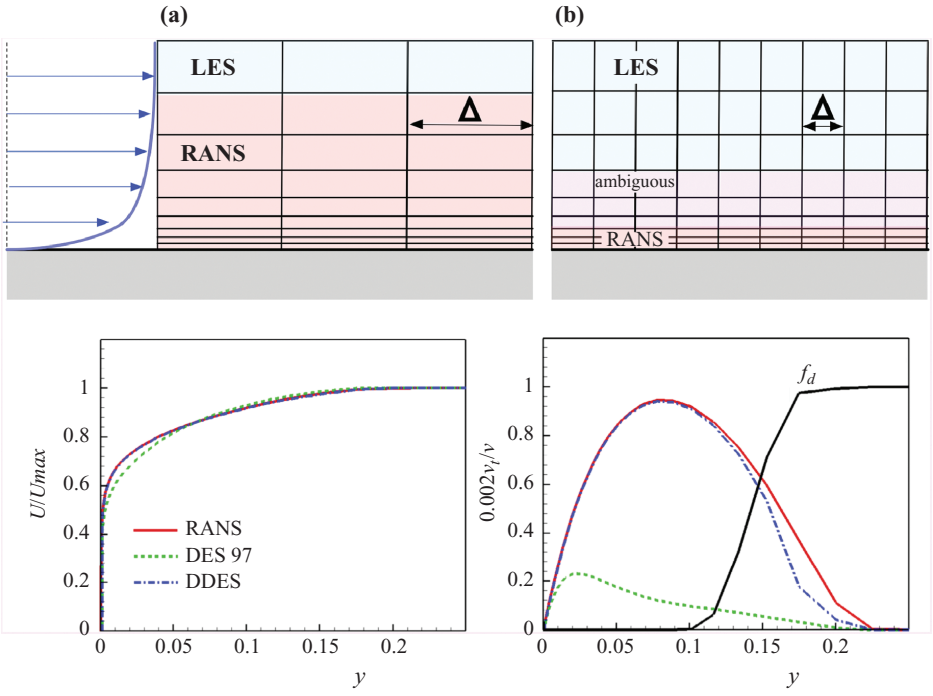

Fig. 10.40 (Top): different types of meshes for a boundary layer: (a) intended operation of DES, (b) ambiguous definition of LES region due to finer mesh. (Bottom): comparison of behaviour for a turbulent boundary layer. Left: mean velocity; right: viscosity ratio. The shielding function f_d, defined in Eq. (10.46), is also plotted for reference. (Bottom figures from Haase *et al.*, 2009.)

As shown in Fig. 10.40, the Type (a) mesh represents a common DES boundary mesh design with relatively large grid spacing in the mean-flow direction. The large space ensures the LES mode, $C_{DES}\Delta$, is too large to be triggered in Eq. (10.42). Meanwhile, for the Type (b) mesh, its spacing is sufficiently small to trigger the LES mode in the outer part of the boundary layer, while RANS is limited to a far narrower region than intended. A region exists in between the two, where $C_{DES}\Delta = L$, which gives rise to an ambiguous switching back and forth between the two modes. This causes the 'MSD' problem since the turbulence length scale at this point is not large enough to be captured by the mesh. In some cases, as indicated above, the MSD will lead to grid-induced separation.

Various attempts were made to overcome the issues of MSD and grid-induced separation, but most schemes introduced an arbitrary limiter to the DES length scale, $C_{DES}\Delta$ and, as such, were not general. The first step towards a practical and generally applicable solution was proposed by Menter and Kuntz (2004), who made use of the F_2 function of the SST model for shielding the RANS region. This

https://doi.org/10.1017/9781108875400.012 Published online by Cambridge University Press

correction proved to be successful across a broad range of flows though, since it was shaped specifically for use with the SST model, a more general version of the same strategy was proposed by Spalart *et al.* (2006) which could be used with any baseline RANS model. They applied the model to several external aerodynamic flows, including a multi-element airfoil, a cylinder and a backward-facing step. These showed that 'MSD' could be reliably suppressed without severe dependency on the mesh design. This approach was styled DDES; its implementation requires a modification to the length scale $L_{DES} = \tilde{d}$ as shown in Eq. (10.45). It is noted that the switch depends not only on the grid, but also on the eddy-viscosity field. Note that the SA model uses the distance to the wall as the turbulent length scale and so, in the original paper,

$$L_{DDES} = L - f_d \max(0, L - C_{DES}\Delta) \tag{10.45}$$

$$f_d = 1 - tanh\left(|8r_d|^3\right) \tag{10.46}$$

$$r_d = (\nu_t + \nu)\,/L^2 \left[\left(\partial U_i/\partial x_j\right)^2\right]^{1/2}. \tag{10.47}$$

The 'shielding' function f_d is set to unity in the LES region outside the boundary layer and gradually transitions to unity within the boundary layer. The function r_d is a modified version of the ratio of the model length scale to the wall distance.

DDES has been increasingly used instead of the original DES, especially in aerospace applications. An example of such applications is shown in Fig. 10.41, illustrating simulation of flows over a generic transport aircraft (the NASA Common Research Model, CRM) that has also been studied experimentally at flight Reynolds numbers in the pressurized cryogenic European Transonic Windtunnel (ETW) (Probst *et al.*, 2019). The simulations with the SA-based DDES were performed for low-speed stall conditions at $\mathrm{Re} = 11.6 \times 10^6$, $\mathrm{Ma} = 0.25$ and angle of attack, $\alpha = 18°$ on a hybrid mesh of the aircraft half-model with around 50×10^6 grid points containing a structured block downstream of the wing to resolve the wake region for which PIV measurements were available. For these conditions the flow on the wing separates close to the leading edge and the models operate in LES mode over a large zone between the wing and the horizontal tail plane, Fig. 10.41 (left). The performance of DDES simulations is illustrated in Fig. 10.41 (right) by the vertical mean-velocity profiles at two streamwise positions in the wing wake. The DDES velocity averaged over about a dozen flow-through times compares well with the ETW PIV measurements, notably superior to the RANS predictions with the same base k-ω model.

A further elaboration of DES has been proposed by Shur *et al.* (2008) which they termed *Improved* DDES (IDDES), for application where scale resolution was required in regions of wall-bounded turbulent flow. They had observed that due to the shielding offered by DDES, a wall-bounded flow would often remain in RANS

https://doi.org/10.1017/9781108875400.012 Published online by Cambridge University Press

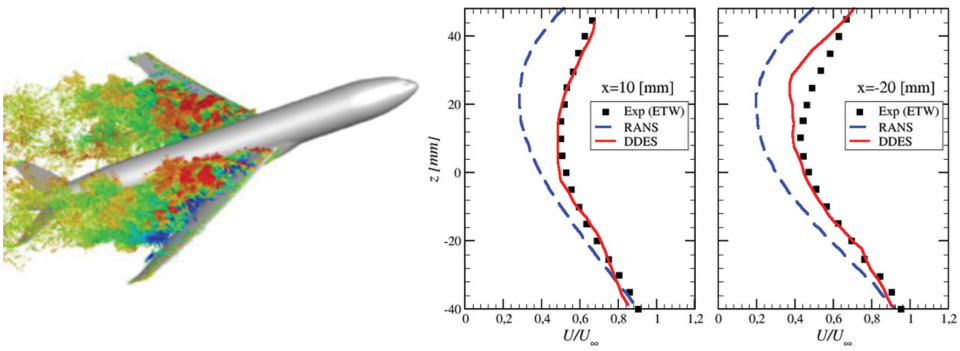

Fig. 10.41 DDES-SA of flow over a generic transport aircraft (The NASA Common Research Model). Left: resolved turbulence (Q-criterion). Right: mean-velocity profiles at two positions in the wing wake compared with measurements and the base (SA) RANS, from Probst *et al.* (2019).

mode when no external forcing or geometry-related instabilities were present. This problem can be partly overcome by introducing a fluctuating boundary condition at the inlet, e.g. by applying synthetic turbulence at the inlet as described in §10.4. Furthermore, the extent of the RANS region should be further reduced compared to DDES so as to reduce the dissipative effects of larger length scales introduced by the RANS model via the momentum equations.

Compared to DDES, IDDES employs RANS over a much smaller near-wall region. The length scale is defined as:

$$L_{IDDES} = f_B(1 + f_e)L_{RANS} + (1 - f_B)C_{DES}\Delta \tag{10.48}$$

where a blending function f_B is introduced to ensure a rapid switch between RANS ($f_B = 1$) and LES ($f_B = 0$) methods, while the function f_e is used to smooth the Reynolds stress change in the interface region of RANS and LES. IDDES can be interpreted as a two-layer wall-modelled LES approach, as introduced in §10.5.2, and so, in comparison to DDES, it generally requires a significantly higher grid resolution. While, as demonstrated here, IDDES may provide an effective means of obtaining superior accuracy for flows around simple geometries at moderate Reynolds number, the practical utility of IDDES for high-Reynolds-number industrial applications is limited.

Grey area mitigation

More recently, significant research and development activity has focussed on reducing the 'grey area' issue in seamless methods. As a reminder of the discussion in §10.3, the 'grey area' refers to regions of the domain where there is an ambiguous split between turbulent scales accounted for by RANS modelling, and scales resolved by LES. In this context, further improvements have been brought

https://doi.org/10.1017/9781108875400.012 Published online by Cambridge University Press

to both DDES and IDDES via the consideration of the LES sgs model. In the vast majority of cases and, in particular, those prior to 2015, DES, DDES and IDDES have employed a grid-size-based length scale as in the standard Smagorinsky or one-equation models to account for sgs effects. This practice exhibits a number of well-documented shortcomings, as discussed in §10.2. Of primary relevance in this context is the inability of the Smagorinsky model to handle correctly low levels of turbulence or the transition from laminar to fully turbulent regions of flow. The simple and direct link employed with this model between sgs stresses and the filtered velocity gradient generally leads to excessive levels of sgs viscosity in regions of transition. In turn, this acts to hinder the resolution of scales relevant to the transition process. In the context of seamless methods, the inherent weakness in handling transitional flows hinders the ability of the flow to adapt from a RANS region to an LES region. More advanced LES-sgs models have subsequently been incorporated into a DDES framework with some success; one such example is the WALE model, Eq. (10.16).

The LES length scale, originally based either on the volume, $\Delta_{vol}=(\Delta x\Delta y\Delta z)^{1/3}$, or the maximum coordinate dimension of the grid cell, $\Delta_{max} = \max(\Delta x, \Delta y, \Delta z)$ has also been the subject of further innovation. One emerging option of note is the vorticity-sensitized definition of Δ based on work by Chauvet *et al.* (2007), where the LES length scale is adjusted to the local direction of the vorticity vector in each cell, with centre $\mathbf{r}$ and cell vertices at $\mathbf{r_n}$ is defined as:

$$\widetilde{\Delta}_{\omega} = \frac{1}{\sqrt{3}} \max(\mathbf{I}_n - \mathbf{I}_m), \quad n, m = 1 \text{ to } 8 \tag{10.49}$$

where $\mathbf{I}_n = \mathbf{n}_{\omega} \times (\mathbf{r}_n - \mathbf{r})$ and $\mathbf{n}_{\omega}$ is the unit vector aligned with the vorticity vector, with $n = 1 \ldots 8$ defined as the general case for hexahedral cells.

Work by Mockett *et al.* (2015) considered a range of different combinations of LES length-scale and sgs models applied to a range of flows. Figure 10.42 presents a comparison of model performance for the case of a plane shear layer, where a high velocity flow mixes with a lower velocity stream downstream of a splitter plate. A stark difference is observed between the results, demonstrating that the standard DDES combination of the Smagorinsky model and $L_{LES} = \Delta_{max}$ leads to a significant delay in the development of resolved turbulent structures downstream of the end of the splitter plate, particularly when compared to the case where a WALE sgs model is used with $L_{LES} = \widetilde{\Delta}_{\omega}$, as defined in Eq. (10.49).

10.6.8 Partially integrated transport modelling (PITM)

The PITM, proposed by Schiestel and co-workers, is another example of a formal scheme to develop a hybrid approach from the concept of the turbulence kinetic energy cascade (Chaouat and Schiestel, 2005; Schiestel and Dejoan, 2005).

https://doi.org/10.1017/9781108875400.012 Published online by Cambridge University Press

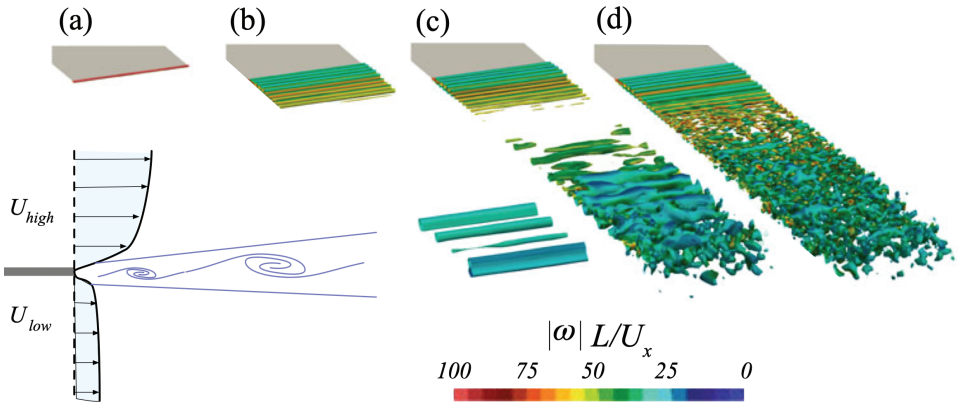

Fig. 10.42 Results for the plane shear layer case, described by sketch (bottom left) of flow topology. Top: iso-contours of the Q-criterion, coloured by vorticity, are displayed for four different combinations of sgs model and filter width: (a) standard DDES using Δ_{max}, (b) DDES using $\tilde{\Delta}_\omega$, (c) WALE-DDES using Δ, (d) WALE-DDES using $\tilde{\Delta}_\omega$. Figure adapted from Mockett *et al.* (2015).

The method is inspired by the concept of multi-scale turbulence modelling (§5.3), wherein the model accounts for energy transfer between multiple scales covering different wave-number ranges of the spectrum (instead of the standard approach with a single integral length scale). A standard RANS formulation is recast in terms of the cut-off wave number, κ_c, so that the interval $0 < \kappa < \kappa_c$ is resolved and the interval $\kappa_c < \kappa < \infty$ is modelled. A complex formal derivation leads to a set of equations which resemble those derived for the partially averaged Navier–Stokes (PANS) framework, §10.6.9, presented in Eqs. (10.54)–(10.58), the constants σ_k, and σ_ε are here unmodified, so in the end the sole change with respect to the original k-ε model is via a modified $c_{\varepsilon 2}$:

$$c^*_{\varepsilon 2} = c_{\varepsilon 1} + r(c_{\varepsilon 2} - c_{\varepsilon 1}) \tag{10.50}$$

where r is defined as the ratio k_{sgs}/k_{total}, i.e. equivalent to the quantity f_k in PANS (see below). The κ concept has been extended by incorporating a model form of the energy spectrum known as the von Karman spectrum, an analytical form for $E(\kappa)$, which can be integrated for $\kappa_c < \kappa < \infty$ to obtain a functional solution where κ_c relates to the grid size:

$$c^*_{\varepsilon 2}(\eta_c) = c_{\varepsilon 1} + \frac{c_{\varepsilon 2} - c_{\varepsilon 1}}{1 + \beta_c \eta_c^{2/3}} \tag{10.51}$$

where η_c is the familiar ratio L_{RANS}/L_{LES} defined here as $\kappa_c L_{RANS}$ with $\kappa_c = \pi/\Delta$, and $\beta_c \approx 3.0$ is a model constant.

https://doi.org/10.1017/9781108875400.012 Published online by Cambridge University Press

Subsequent application of a more widely applicable model for the energy spectrum that better describes the spectrum at low wave numbers (Chaouat and Schiestel, 2009) led to the more general expression:

$$c^*_{\varepsilon 2}(\eta_c) = c_{\varepsilon 1} + \frac{c_{\varepsilon 2} - c_{\varepsilon 1}}{(1 + \beta_c \eta_c^3)^{2/9}}. \tag{10.52}$$

Originally developed within the k-ε framework, the PITM was subsequently elevated to second-moment closure level with an elaborate stress- and dissipation-rate sgs ('sub-filter') model. The new PITM was tested in a plane channel flow, including cases of spanwise rotation and fluid injection through one of the walls, as well as in a flow over periodic hills. In all cases satisfactory agreements with the reference data were achieved using relatively coarse computational grids (Chaouat, 2017).

It is noted, however, that the sub-filter stress model requires solving equations for the six stress component and for the corresponding sub-filter dissipation rate, which inevitably increases the computational time. Chaouat and Schiestel (2013) estimated that roughly 30–50% more CPU is required than for conventional LES (presumably on the same or similar grid) even when using the more costly dynamic Smagorinsky eddy-viscosity model for the LES. In view of a potential reduction in the number of grid points by a factor 5 to 10 compared with the properly resolved LES, the authors argue that the estimated additional cost of about 50% still brings the saving time of roughly 60–80%. Yet, the use of such an elaborate model might pose computational challenges in handling real-life flows of complex configurations. As shown in the previous chapters, second-moment closures have proved in numerous cases to capture better the turbulence physics than the simpler linear eddy-viscosity models when both are used in stand-alone (U)RANS mode. However, when blended with an LES in a hybrid approach, some of the RANS shortcomings are compensated by the LES solutions in the adjacent or outer flow region feeding the resolved velocity and pressure into the RANS field through the fixed or floating interface. Thus, while the use of a more capable RANS model, especially in flow over complex wall configurations, is always useful, one may question the justification for employing such a highly elaborate model option in most circumstances.

In line with the above rationale, some researches, aiming at the application of HRL to complex flows, explored options to simplify further the earlier two-equation PITM, while preserving its basic concept. Even then, in some complex flows the use of the original formulation of Eq. (10.51) with the k-ε EVM was found to cause some numerical instabilities, that led Kenjereš and Hanjalić (2005) to suggest still further simplification of Eq. (10.51), similar to those shown in Eq. (10.35):

https://doi.org/10.1017/9781108875400.012 Published online by Cambridge University Press

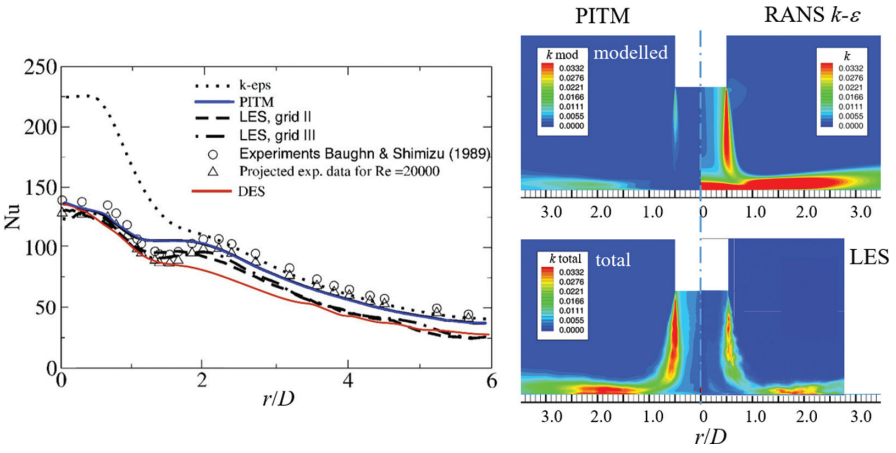

Fig. 10.43 Cold round jet impinging on a heated flat wall at Re = 23,000: comparison of PITMα with RANS k-ε, LES and experiments. Left: Nusselt number distribution. Right: modelled and resolved turbulent kinetic energy. From Hadžiabdić (2005).

$$c^*_{\varepsilon 2}(\eta_c) = c_{\varepsilon 1} + \frac{c_{\varepsilon 2} - c_{\varepsilon 1}}{\alpha} \tag{10.53}$$

where $\alpha = \max(1, c_l \eta_c) = \max[1, c_l(L_{RANS}/L_{LES}]$ as in Eq. (10.31).

The performance of the above simplified PITMα model is illustrated for the case of a cold round jet impinging on a heated plane surface. Figure 10.43 compares Nusselt numbers and the turbulent kinetic energy with the RANS low-Re k-ε model of Abe *et al.* (1994) and wall-resolved LES.

Figure 10.43 (right) shows that the excessive levels of turbulence energy created in a stagnation flow with the standard k-ε EVM (as discussed in §7.4.2) are avoided with the PITM scheme. These computations were made with a computational mesh of 1.5 M cells achieving an accuracy comparable with wall-resolved LES made on a mesh of $\sim$ 10 M cells.[19] We may note, however, that, as shown in Chapter 7, the heat-transfer coefficient for this test case has been reproduced at least as accurately by more refined RANS schemes.

The same simplified PITM was verified in an ERCOFTAC benchmark test case of the flow over the Askervein Hill in Scotland, Fig. 10.44, for which a rich collection of wind-field measurements is available. Figure 10.44 (left) shows the terrain topography with locations of two measurement towers, CP and HT, as well as the two lines, A and AA, along which the wind speed was measured at a height of 10 m above the ground using cup anemometers, indicated by open circles. The figure on the right shows the fractional speed-up ratio ΔS along line

[19] It is recalled though that the anomaly can be eliminated when imposing scale limiters from realizability constraints, §7.4.2, and especially when accounting for the elliptic relaxation, as shown in Fig. 7.26.

https://doi.org/10.1017/9781108875400.012 Published online by Cambridge University Press

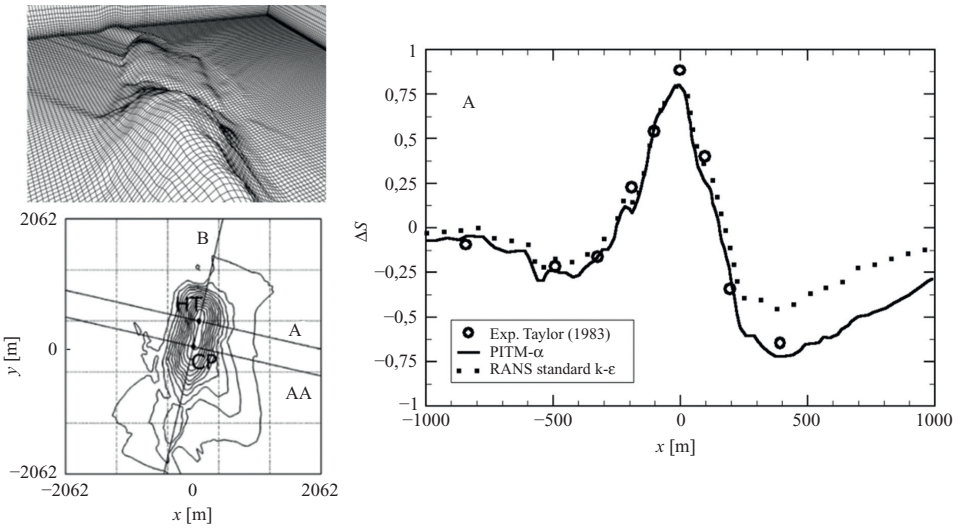

Fig. 10.44 Comparison of the PITM (Kenjereš *et al.*, 2006a) and RANS computations (Abe *et al.*, 1994) with measured velocity over the Askervein Hill, illustrated by the distribution of the fractional speed-up ratio, ΔS, at 10 m above the surface along line A.

A, defined as the normalized relative speed increase or decrease with respect to the incoming wind mean velocity at the same height above the ground, i.e. $\Delta S = \left[U(x, y, \Delta z) - U_0(\Delta z)\right] / U_0(\Delta z)$.

10.6.9 The partially averaged Navier–Stokes approach (PANS)

The PANS method, proposed by Girimaji (2006), is a popular alternative to DES, with many similarities, though the framework is obtained by way of a quite different rationale. The original approach is based on the idea that the fraction of the energy spectrum to be resolved by the sub-grid model is fixed from the outset, i.e. it is *not* a function of the ratio of the RANS and LES grid scales as proposed by Eq. (10.45). Thus, the PANS method implies a decomposition of the velocity field based on kinetic energy content rather than on cut-off wave number. The ratios of modelled (i.e. unresolved) quantities to total quantities, termed *resolution control parameters*, are introduced for the turbulence energy, $f_k = k_u/k$, and energy dissipation rate, $f_\varepsilon = \varepsilon_u/\varepsilon$. These ratios are then bounded between a minimum of zero, implying no energy is left unresolved (as in DNS), and a maximum of one, which indicates that all scales are modelled as in RANS. The new transport equations for the unresolved k and ε are obtained from the substitution $Dk_u/Dt = f_k Dk/Dt$ and $D\varepsilon_u/Dt = f_\varepsilon D\varepsilon/Dt$, resulting in

$$\frac{Dk_u}{Dt} = \mathcal{P}_u - \varepsilon_u + \frac{\partial}{\partial x_k}\left[\left(\nu + \frac{\nu_u}{\sigma_{ku}}\right)\frac{\partial k_u}{\partial x_k}\right] \tag{10.54}$$

https://doi.org/10.1017/9781108875400.012 Published online by Cambridge University Press

$$\frac{D\varepsilon_u}{Dt} = c_{\varepsilon 1}\mathcal{P}_u\frac{\varepsilon_u}{k_u} - c^*_{\varepsilon 2}\frac{\varepsilon_u^2}{k_u} + \frac{\partial}{\partial x_k}\left[\left(\nu + \frac{\nu_u}{\sigma_{\varepsilon u}}\right)\frac{\partial \varepsilon_u}{\partial x_k}\right] \tag{10.55}$$

$$\nu_u = c_\mu \frac{k_u^2}{\varepsilon_u}$$

where, apart from the replacement of k and ε by k_u and ε_u, respectively, the difference between this and the original form of the parent $k-\varepsilon$ model can be summarized as follows:

$$c^*_{\varepsilon 2} = c_{\varepsilon 1} + \frac{f_k}{f_\varepsilon}(c_{\varepsilon 2} - c_{\varepsilon 1}) \tag{10.56}$$

$$\sigma_{ku} = \sigma_k \frac{f_k^2}{f_\varepsilon}, \quad \sigma_{\varepsilon u} = \sigma_\varepsilon \frac{f_k^2}{f_\varepsilon}. \tag{10.57}$$

Assuming that a clear separation between energy-containing and dissipation scales is achieved (high-Reynolds-number flow), ε_u is not expected to differ much, if at all, from ε thus the model is simplified by assuming that $\varepsilon_u \approx \varepsilon$, so f_ε is taken as unity for most implementations of PANS. This leaves f_k as the main variable to be chosen. In the original version of PANS, during the model development and testing, a fixed, intuitively chosen value of f_k was prescribed, with reported values in the literature commonly in the range $0.4 < f_k < 0.7$. The coefficients $c_{\varepsilon 1} = 1.44$, $c_{\varepsilon 2} = 1.92$, $\sigma_k = 1.0$ and $\sigma_\varepsilon = 1.3$ are those of the parent RANS model, which in this case is the standard two-equation $k-\varepsilon$ closure. The same applies to c_μ, which retains the standard value of 0.09. The latter choice is based on the argument that with common values of f_k in the range 0.4–0.7 and $f_\varepsilon = 1$, the desired reduction in the turbulent viscosity for the unresolved motion, ν_u, is achieved by ensuring that k_u is sufficiently smaller than the total k, thus dispensing with the need for modifying c_μ (Girimaji, 2006; Basara and Girimaji, 2019).

The above modification can, to some extent, also be interpreted as an effective reduction in c_μ in the parent model, as follows:

$$\nu_t^{PANS} = c_\mu \frac{k_u^2}{\varepsilon_u} = c_\mu \frac{f_k^2}{f_\varepsilon}\frac{k^2}{\varepsilon} = c_\mu^{PANS}\frac{k^2}{\varepsilon}. \tag{10.58}$$

For the usual values of f_k in the range 0.4–0.7 and with $f_\varepsilon = 1$, we obtain an equivalent viscosity constant $c_\mu^{PANS} = c_\mu f_k^2/f_\varepsilon$ in the range $0.014 < c_\mu^{PANS} < 0.044$, representing reductions from the standard value by 50–80%. The proposal for a reduced c_μ resonates with the idea behind Organized Eddy Simulation (OES), an approach proposed by Ha Minh and Kourta (1993) applied to flow over a backward-facing step in which the constant c_μ was reduced from its standard value of 0.09 to 0.02, in order to permit a greater range of turbulent scales to be resolved. In the case of OES this reduction was justified on the basis of *a priori* calculation of the flow with a Reynolds-stress-transport model, which indicated that the effective viscosity

https://doi.org/10.1017/9781108875400.012 Published online by Cambridge University Press

was substantially lower in the wake region of a bluff body. (Further examples of applications adopting this framework are given in Martinat *et al.*, 2008.) However, the PANS approach can by no means be reduced simply to the modification of c_μ while retaining the original model (here the k-ε model) as the equations for k_u and ε_u (if $f_\varepsilon \neq 1$) with some other coefficients (primarily $c^*_{\varepsilon 2}$) significantly different.

In order to enhance the fidelity of modelling near-wall flows and scalar transport, especially in complex geometrical configurations, Basara *et al.* (2011) adapted the PANS approach to the elliptic-relaxation concept (see §7.4.4). They derived a PANS version of the k–ε–ζ–f model, which, in addition to k_u and ε_u, involves solution of the transport equation for the unresolved velocity scale ratio $\zeta_u = \overline{v_u^2}/k_u$ and the elliptic function f_u analogous to Eqs. (7.48) and (7.49).

$$\frac{D\zeta_u}{Dt} = f_u - \frac{\zeta_u}{k_u}\mathcal{P}_u + \frac{\zeta_u}{k_u}\varepsilon_u(1-f_k) + \frac{\partial}{\partial x_k}\left[\left(\nu + \frac{\nu_u}{\sigma_{\zeta_u}}\right)\frac{\partial \zeta_u}{\partial x_k}\right] \tag{10.59}$$

$$f_u - L_u^2\frac{\partial^2 f_u}{\partial x_k^2} = \left(c_1 - 1 + c_2'\frac{\mathcal{P}_k}{\varepsilon}\right)\frac{(2/3-\zeta_u)}{\mathcal{T}_u} \tag{10.60}$$

$$\mathcal{T}_u = \max\left[\frac{k_u}{\varepsilon},\ c_\mathcal{T}\left(\frac{\nu}{\varepsilon}\right)^{1/2}\right] \text{ and } L_u = c_L \max\left[\frac{k_u^{3/2}}{\varepsilon},\ c_\eta\left(\frac{\nu^3}{\varepsilon}\right)^{1/4}\right] \tag{10.61}$$

where $\mathcal{T}_u$ and L_u are the simplified, unresolved equivalents of the time and length scale defined by Eqs. (7.44) and (7.45), and the coefficients take the same values as in the parent model.

The wall boundary conditions, originally provided from the standard wall functions (WF), §8.1, were subsequently advanced by employing a blended wall treatment (BWT), §8.5, which combines the WF with wall integration (WIN) to accommodate different near-wall grid resolutions. As discussed in §8.5, the scheme applies WF, WIN or a blend of both depending on the position of the wall-adjacent grid point, whether in the viscous, buffer or fully turbulent wall zone. The BWT is particularly suited to the framework of the $\zeta - f$ model (either RANS or PANS) because it ensures trustworthy and robust integration up to the wall when using a wall-clustered or dynamically adapted meshes, as discussed below.

Extensions to the original PANS framework consider variations in spatial and temporal values of the functions f_k and f_ε, as well as specific calibrations in certain flows. A key aspect of the original PANS with prescribed values of f_k and f_ε is that there is no reference to the grid resolution; thus it *is* able to provide a grid-independent solution. In this sense the model may be considered to resemble a URANS approach with a modified coefficient c_μ. However, lack of any dependency on grid also removes the opportunity for the user to refine regions of the mesh further where more complex flow physics are to be resolved, enabling the model to switch to a scale-resolving mode. The assumption that a constant proportion of

https://doi.org/10.1017/9781108875400.012 Published online by Cambridge University Press

the spectrum is resolved at each point in the flow may also give rise to instabilities, since regions of the domain where the mesh has been intentionally coarsened are likely to be under-resolved. One way around this is to allow f_k to vary as a function of the mesh, as proposed by Girimaji and Abdol-Hamid (2005). They recommended that a precursor RANS calculation should be run in order to fix the value of f_k in the domain as follows:

$$f_k(x_i) \geq \frac{1}{\sqrt{c_\mu}} \left(\frac{\Delta_i}{L_i} \right)^{2/3} \approx 3.0 \left(\frac{\Delta_i}{L_i} \right)^{2/3} \tag{10.62}$$

where Δ_i is the representative grid size, usually $(\Delta x \Delta y \Delta z)^{1/3}$, $L = k^{3/2}/\varepsilon$. Condition (10.62) stipulates the smallest f_k a grid can support at a given location. This helps circumvent some of the limitations mentioned above, as it offers the potential for such dynamic updates of f_k and grid adjustments in the course of simulations as might be desired, in particular for flows with unsteady mean motion in complex geometries with moving boundaries. However, Eq. (10.62) employs the total kinetic energy k for the length scale L, which requires an averaging of the resolved velocity field in the course of the computation. That process is computationally intensive and generally impractical. In subsequent developments, Basara *et al.* (2018) proposed solving a separate modelled equation for the resolved kinetic energy, k_{ssv}, termed the scale-supplying variable (SSV),

$$\frac{Dk_{ssv}}{Dt} = \frac{k_{ssv}}{k_u} \left(\mathcal{P}_u - \varepsilon_u \right) + \frac{\partial}{\partial x_k} \left[\left(\nu + \frac{\nu_u}{\sigma_{ku}} \right) \frac{\partial k_{ssv}}{\partial x_k} \right] \tag{10.63}$$

which together with the unresolved kinetic energy, k_u, provides the total turbulence energy, $k = k_{ssv} + k_u$. It is noted that the sole purpose of Eq. (10.63) and the variable k_{ssv} is to obviate the need for expensive averaging operations.

In addition to a range of canonical benchmark flows, the PANS approach has also been verified in and applied to a number of more complex, 'real-life' cases. The scheme has been gaining in popularity, particularly in the automotive industries both for external car aerodynamics and for IC engines. An example of car aerodynamics is the flow over a 1:2.5 scale BMW car model with full design details, including mirrors, underbody configuration with an asymmetric exhaust system, differential gear and (here non-rotating) wheels, including brake discs and rim details (Jakirlić *et al.*, 2014). Figures 10.45 and 10.46 compare some results obtained by PANS as well as with steady and unsteady RANS[20] using the same k-ε-ζ-f RANS model. The oncoming air velocity is 140 km/hr ($\mathrm{Re} = 9 \times 10^5$)

[20] Computed sequentially, starting with a steady RANS until a converged solution is reached (about 50,000 iterations), then switching to URANS and eventually to PANS, run over 15 and 10 flow-through times (FTT), respectively.

https://doi.org/10.1017/9781108875400.012 Published online by Cambridge University Press

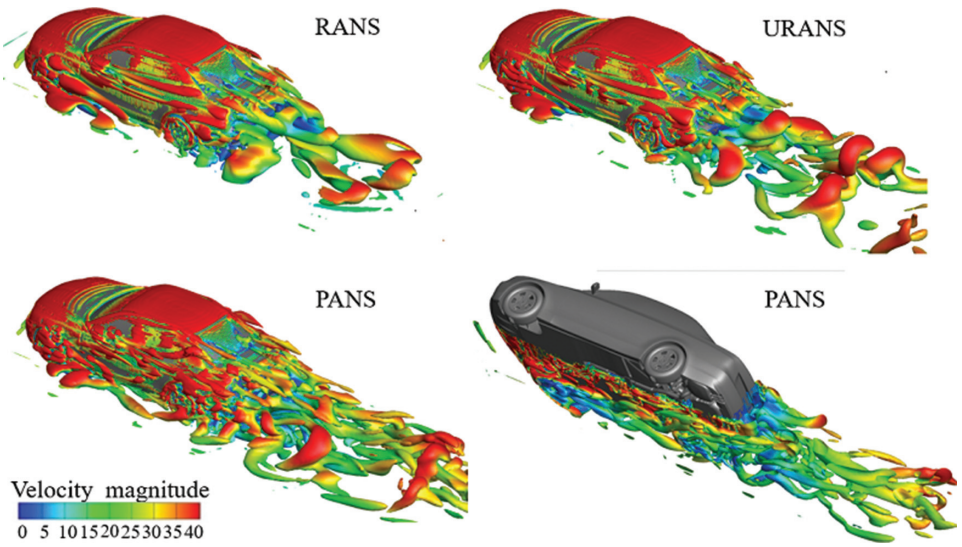

Fig. 10.45 Vortical structures educted by the Q-criterion ($Q = 5,000\ s^{-2}$) around a real car computed by steady RANS ($\partial/\partial t = 0$) (top left), URANS (top right), PANS (bottom left) for the upper surface, and bottom right for underbody, using the same k-ε-ζ-f RANS model as the base. Courtesy S. Jakirlić and L. Kutej.

and the domain is meshed by 24–28 million polyhedral grids with regular hexahedral cells clustered towards the solid surfaces to ensure that the maximum value of y^+ at the wall-adjacent cell centre was less than 20. Figure 10.45 illustrates a rich variety of organized structures generated by separation from the car body and various protrusions with a clear identification of dominant horseshoe vortices in the car wake, which are well captured by the PANS, but also, to a large extent, by both URANS and even steady 3D RANS. The PANS results for the time-averaged integral properties (pressure, drag and lift coefficients) agree well with the available windtunnel measurements on the same car model. This is illustrated in Fig. 10.46 by the mean pressure coefficients along the reference lines ($y = \pm 0.14$m on both sides of the central line) on the upper surface and along the central line on the underneath surface. The pressure coefficient is plotted for each wall-adjacent grid cell (hence an impression of continuous lines) along the reference lines on all sides of the car body. It is interesting that the computations show sharp peaks in the pressure coefficients at some x-locations around design elements with sharp edges on the car underbody, reflecting local complex flow patterns.

We note in passing that the vortex structures shown in Fig. 10.45 over the upper car surface (compared with those of Spalart (2009) for flow over a circular cylinder, Fig. 10.32) give quite a different impression of the comparative ability of RANS, URANS and the scale-resolving methods, DES and PANS, although all deal with

https://doi.org/10.1017/9781108875400.012 Published online by Cambridge University Press

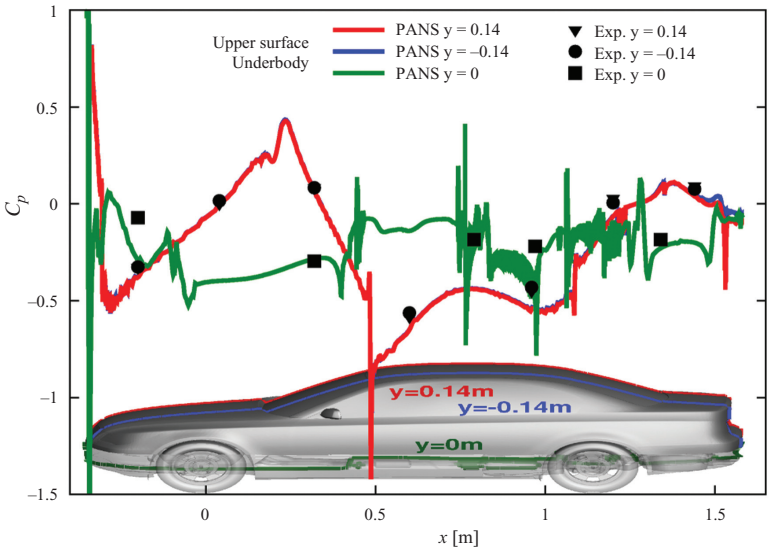

Fig. 10.46 Mean pressure coefficient on the upper surface and underbody on the car model obtained by the PANS method. Courtesy S. Jakirlić and L. Kutej.

flow over bluff bodies. The resolved scales in Fig. 10.45 show much less difference between the performances of the three modelling levels than those in Fig. 10.32. This could partly be due to the complex shape of the car body with multiple sharp edges fixing the locations of flow separations compared with the infinite smooth cylinder surface in Fig. 10.32. However, the principal difference is that Spalart compared RANS and DES solutions that all use the S-A and SST as the base RANS models, whereas here, in all cases, the more advanced near-wall k-ε-ζ-f model was employed. This, yet again, illustrates the important role of the RANS model, especially when treating flows over solid boundaries of complex configuration.

The next example is a combusting flow in a single-cylinder AVL research IC engine (Basara *et al.*, 2020). The focus is on predicting cycle-to-cycle variations in a practically relevant periodic flow (that also involves relevant thermal and concentration properties) under design operating conditions. For this purpose, a PANS computation (in parallel with a URANS scheme using the same base k-ε-ζ-f model) was combined with the AVL default models for treating spray and combustion. The PANS solution was shown to reproduce the cylinder pressure, temperature, heat release and concentration of emitted gases – including their cycle-to-cycle variation – closely in accord with the laboratory measurements. Interestingly, the authors reported that the URANS results also returned a behaviour in reasonable agreement for most properties. Figure 10.47 shows a selection of PANS results illustrating its potential for application in IC engines with all major design features, including flow details through the valve port and the

https://doi.org/10.1017/9781108875400.012 Published online by Cambridge University Press

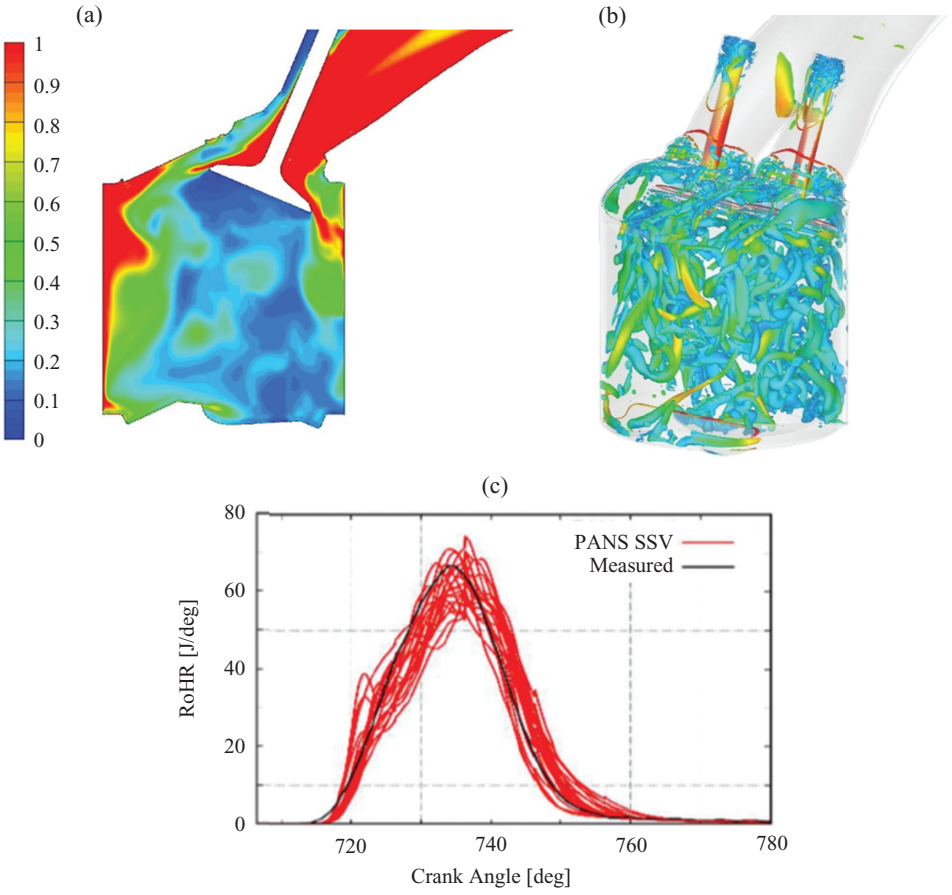

Fig. 10.47 PANS-ssv k-ε-ζ-f simulation of the AVL single-cylinder research engine operating at 4,000 rpm. a) resolution parameter f_k; and (b) vortex structures educted by the Q criterion at 480 deg. crank angle; (c) heat release cycle-to-cycle variation compared with measurements; Courtesy B. Basara and Z. Pavlović.

time variation of the flow domain due to moving piston boundaries. The stretchable computational mesh was refined in the wall vicinity and continuously adjusted throughout the cycles to the corresponding resolution parameter f_k using Eq. (10.62). An impression of the parameter f_k and scale resolution is provided by their snapshot for a particular crank angle in Fig. 10.47 (a) and (b). The cycle-to-cycle heat release (Fig. 10.4c) averaged over a large number of cycles agrees well with the measurements.

10.6.10 Links and similarities between different seamless HRL

The field of seamless HRL methods has evolved from several quite different directions over the past two decades. It is thus interesting to note how the ideas

https://doi.org/10.1017/9781108875400.012 Published online by Cambridge University Press

have converged. Consider the strong similarities between Eq. (10.42) for DES, Eq. (10.51) for PITM and Eq. (10.56) for PANS. They all have very similar functional forms and although they may enter the equations at slightly different points, it is possible to manipulate the equations to allow direct comparison. Friess *et al.* (2015) noted this trend and proposed a general theory for these methods, known as H-Equivalence. In a follow-up work, Davidson and Friess (2019) reflected on the possibilities that a unified theory could offer. While DES and, to some extent, PANS were proposed on an intuitive basis, PITM has a more rigorous derivation. While the task is not trivial, the PITM framework may be able to be expanded to overcome some of the limitations of DES, such as the treatment of length scales over highly non-uniform grids which habitually arise with industrial CFD. More details about the links between DES, PITM and PANS can be found in Chaouat (2017).

10.7 Hybrid RANS-LES models: summary and outlook

This chapter has provided an overview of the main HRL methods introduced since the origination of this strategy, explaining their origin and demonstrating their intended application. The chapter began by underlining the challenge posed by the direct resolution of turbulent scales, before describing approaches which incorporate progressively more modelling. We first introduced LES, before exploring wall-modelled LES and bulk zonal methods, finally arriving at the rich field of seamless methods. In doing so, we have attempted to include a selection of the most-widely used approaches: those most likely to be encountered in the current application of industrial simulation strategies for turbulent flow. There are undoubtedly many more methods that have not been included here, because they remain, at present, less widely used, or are very novel and still in the early stages of development, or because they are very similar to other approaches already described. The intention has been to chart the main milestones in this field, as opposed to an exhaustive summary.

The overarching motivation for HRL methods is the opportunity to provide resolution of the relevant turbulence scales at a more affordable cost than is possible with LES alone. The non-local interaction of multi-scale turbulent structures is particularly challenging to model in a general manner. It is undeniably the case that the unsteady resolution of large, energy-containing, turbulent eddies achieved by HRL methods can provide predictive accuracy superior to the use of URANS modelling alone. Nevertheless, the role of the RANS component is also shown to be significant, particularly given that it is usually required to account for important near-wall processes. Although a broad range of RANS-modelling levels in HRL methods has

https://doi.org/10.1017/9781108875400.012 Published online by Cambridge University Press

been explored, ranging from one-equation models (as in DES97) to full second-moment closure (as in the new PITM), there is a notable tendency among users to underemphasize the role of the RANS model. Most HRL methods, irrespective of whether of zonal, seamless or other type, employ the standard one- or two-equation ($k-\omega$ or $k-\varepsilon$) eddy-viscosity models, presuming that the scale-resolving nature of the results obtained are the dominant feature of the solution. While, in a correctly implemented LES region, it is indeed true that large-scale structures will account for the majority of the kinetic energy of the turbulence (notionally 80% or greater), it is still the case that where the RANS mode is active, the HRL approach retains all the characteristics of the particular RANS model upon which it is based, i.e. both its strengths and its weaknesses. This is especially important where one is looking to reduce the cost of the HRL solver by ascribing more of the domain to the far less expensive RANS component.

However, the increased development and testing of HRL has demonstrated that the choice of RANS model is very important, in particular when dealing with flows over walls of complex topology and involving heat and mass transfer and other surface phenomena. Such challenging features are encountered in many areas of engineering and the environment. As broad examples we cite turbomachinery (pinned, ribbed, grooved or dimpled internal blade-cooling passages, blade-tip gaps, labyrinth seals), internal combustion engines (valves, cooling jackets), thermal equipment (compact heat exchangers), electronic packages, as well as in environmental flows over complex terrain and built/urban structures. If a substantial flow portion is entrusted to RANS mode, whether intentionally (for economy) or uncontrolled (due to the seamless RANS–LES interface and automatic gridding), the (U)RANS region may include local separation, multiple vortex systems and interactions, secondary flows, strong stress anisotropy, local transition and laminarization. Capturing most of these and other phenomena requires a RANS model free from topological parameters and capable of reproducing the basic near-wall physics as well as ensuring sufficient receptivity to the LES forcing at the interface. These requirements usually go beyond the capabilities of the common eddy-viscosity models.

Second-moment closures, despite their well-established superiority in purely RANS schemes, do not seem a rational option in this role in view of their substantially higher computational costs. Moreover, the need for seamless HRL to operate both in the RANS and LES (as well as in mixed) modes further militates against their use. A rational compromise seems to be in using advanced eddy-viscosity models that account in a physically sounder and transparent manner for the overall wall effects which, besides providing an effective viscosity, includes inviscid wall-blocking and stress anisotropy, as offered, e.g. by the elliptic-relaxation eddy-viscosity concept, or algebraic stress and flux models.

As for the choice of the optimal HRL method, from the large range currently available in the literature, it is not possible to give unambiguous recommendations or absolute advice on which approach to use for any given scenario. Nevertheless, some general observations and conclusions emerge, and are summarized in the following paragraphs.

Zonal methods, which aim to employ separately the component parts of the approach, i.e. RANS and LES, in their native format, are appealing where one has already realized a certain level of understanding of the flow in question. For instance, a RANS model can be applied in regions where it is known to perform well, while the LES component can be restricted to regions where one expects to encounter more challenging flow features, such as unsteady three-dimensional separation, to be influential. Or, alternatively, the LES component can be restricted to locations where knowledge of the turbulent fluctuations is required for a different purpose, e.g. for prediction of noise or thermal/structural fatigue. These methods are, on the whole, more reliable at predicting such phenomena, although in this case the major challenge is in generating an appropriate representation of turbulent fluctuations, when moving from time-averaged (or coarse time-dependent) regions to properly scale-resolving regions of the domain. Once these challenges have been adequately resolved, zonal methods tend to be reliable in application to the majority of flows, whether statistically steady, as in fully developed flow through a channel of complex cross-section, or globally unstable, as in the case of the flow around a circular cylinder. While zonal methods are therefore often understood to offer a greater level of accuracy overall, they also often lead to greater computational requirements than seamless methods, since in most cases they seek to use LES over a greater proportion of the flow domain.

Seamless methods offer a more general framework, in which the method itself is largely able to decide whether to operate in either RANS or LES mode, dependent on local comparison of the turbulent scales, usually in relation to the local mesh resolution. Seamless approaches benefit from a more flexible framework which requires less advance knowledge of the flow. However, the decision to allow the switching between RANS and LES to be more automatic can lead to less certainty and several common shortfalls have been identified. For instance, small changes in local grid density can have unintended impacts on the behaviour, resulting in an ambiguous selection of either RANS or LES. Although, in more recent work, these shortcomings have been addressed by modelling improvements, seamless methods may in general be used with more confidence for flows where there is a global instability present in the flow. For example, the case where a boundary layer is fully separated as a consequence of a specific geometry, such as a wing at high incidence or a deployed landing gear. The use of seamless methods for flows where small local instabilities grow to dictate large-scale changes downstream,

such as the pressure-induced separation from a smooth surface, tends to have a less assured success.

As methods evolve further, it is likely that the number of HRL variants in regular use will reduce as improvements developed in one sub-group of methods are applied to others and where the margins for further improvement become smaller. Similarly, while there are still some active developments in the field, the number of *entirely* new HRL approaches has reduced in recent years, as the community converges towards a greater understanding of the common best-practice elements to follow and the main pitfalls to avoid. On the other hand, the improved reliability of HRL approaches has, in recent years, led to their use over a broader range of applications than originally envisaged. Once restricted mainly to the domain of aerospace, it is now common for HRL approaches to be used to good effect in a diverse range of sectors, such as automotive, energy, environmental and even cardiovascular flows. Furthermore, these methods have been developed to incorporate various additional physical modelling, such as fluid-structure interaction, acoustics, heat and mass transport, multiphase flow, combustion and other chemical reactions.

While accumulated experience and know-how will often lead to a narrower range of methods used by the majority, there will most likely remain a need for approaches which offer a different balance between cost and accuracy. In much the same manner as for RANS models, there will likely remain a need for faster approximations that can cover a broader region of parameter space at the expense of some accuracy in order to gain a greater understanding of the operational range of a system than can be garnered from a few isolated design points alone. A carefully selected combination of higher- and lower-fidelity methods can, in this context, offer even greater efficiency in the exploration of a broad range of parameters. The higher-order methods, used sparingly, can provide continual feedback and correction to the lower order methods and, in doing so, provide greater accuracy overall. This is the basis for uncertainty quantification methods, which seek to quantify the effect on predicted outcomes of different initial conditions. In most practical scenarios a precise definition of the initial conditions, or indeed boundary conditions, is impossible to provide. Small discrepancies can be amplified over time, and eventually lead to an unexpectedly broad range of possible predicted outcomes. Ensemble approaches, which combine large numbers of low-fidelity methods with fewer high-fidelity runs, each with slightly different initial conditions, can offer the basis for a more statistical prediction of the most likely outcome. In the outlook of future developments in HRL sketched above, Artificial Intelligence and Machine Learning are also likely to play an increasingly important role.

We expect the research field of Hybrid RANS-LES to remain a fertile area for further innovation for many years to come, and for the employment of these approaches in industry and the environment to continue far beyond. Until such time

as the readily available computational resource is so great as to obviate the need for modelling altogether, there will always be a need for a compromise between cost and accuracy. In many cases we expect the use of turbulence models to provide a suitably accurate solution in their own right, as described in the preceding chapters of this book. However, in certain cases where higher accuracy is required or where a more complex unsteady phenomenon is known to dominate, it is likely that a Hybrid RANS-LES approach will be favoured.

References

Abe, K. and Suga, K., 1998, Large-eddy simulation of passive scalar fields under several strain conditions, *Proc. 2nd Engineering Foundation Conf. on Turbulent Heat Transfer*, Manchester, UK, 8.15–8.30.

Abe, K. and Suga, K., 2001, Towards the development of a Reynolds-averaged turbulent scalar-flux model, *Int. J. Heat Fluid Flow* **22**, 19–29.

Abe, K., Kondoh, T. and Nagano, Y., 1994, A new turbulence model for predicting fluid flow and heat transfer in separating and reattaching flows – I. Flow field calculations, *Int. J. Heat Mass Transfer* **37**(1), 139–151.

Abrahamsson, H., Johansson, B. and Löfdahl, L., 1997, An investigation of the turbulence field in the fully-developed three-dimensional wall jet, Internal Report 97/1, Chalmers University of Technology, Göteborg, Sweden.

Acharya, M. and Reynolds, W. C., 1975, Measurements and predictions of a fully-developed turbulent channel flow with imposed controlled oscillations, Report TF-8, Department of Mechanical Engineering, Stanford University, Stanford, CA.

Ackerman, J. W., 1970, Pseudo-boiling heat transfer to supercritical-pressure water in smooth and ribbed tubes, *ASME J. Heat Transfer* **92**, 490–498.

Addad, Y., Benhamadouche, S. and Laurence, D., 2004, The negatively buoyant wall jet: LES results, *Int. J. Heat Fluid Flow* **25**, 795–808.

Adrian, R. J., Ferreira, R. T. D. S. and Boberg, T., 1986, Turbulent thermal convection in wide horizontal fluid layers, *Exp. Fluids* **4**, 121–141.

Alam, M. and Sandham, N. D., 2000, Direct numerical simulations of short laminar separation bubbles, *J. Fluid Mech.* **403**, 223–250.

Ames, F. E., Dvorak, L. A. and Morrow, M. J., 2005, Turbulent augmentation of internal convection over pins in staggered pin-fin arrays, *ASME J. Turbomachinery* **127**, 183–190.

Ames, F. E., Nordquist, C. A. and Dvorak, L. A., 2007, Endwall heat transfer measurements in a staggered pin-fin array with an adiabatic pin, *Proc. GT-2007 ASME Turbo Expo*, Montreal, Canada.

André, J. C., de Moor, G., Lacarrère, P. and du Vachat, R., 1976, Turbulence approximation for inhomogeneous flows: Part II. The numerical simulation of a penetrative convection experiment, *J. Atmos. Sci.* **33**, 482–491.

André, J. C., de Moor, G., Lacarrère, P., Thierry, G. and du Vachat, R., 1978, Modelling the 24-hour evolution of the mean and turbulent structures of the planetary boundary layer, *J. Atmos. Sci.* **35**, 1861–1883.

André, J. C., de Moor, G., Lacarrère, P., Thierry, G. and du Vachat, R., 1979, The clipping approximation and inhomogeneous turbulence simulations, in *Turbulent Shear Flows* 1 (Ed. F. J. Durst *et al.*), 307–318, Springer Verlag, Heidelberg.

Anupindi, K. and Sandberg, R. D., 2017, Implementation and evaluation of an embedded LES-RANS solver, *Flow, Turbulence Combust.* **98**(3), 697–724.

Aris, R., 1962, *Vectors, Tensors and the Basic Equations of Fluid Mechanics*, Prentice Hall, Englewood Cliffs, NJ.

Armitage, C. A., 2001, *Computational modelling of double-diffusive flows in stratified media*, PhD Thesis, Department of Mechanical Engineering, UMIST, Manchester, UK.

Armitage, C. A., Launder, B. E. and Leschziner, M. A., 1998, Second-moment modelling of combined turbulent and species transfer in multiply stratified fluid bodies, *Proc. 2nd Engineering Foundation Conf. on Turbulent Heat Transfer*, Manchester, UK, 5.36–5.47.

Ashton, N., 2013, *Development, implementation and testing of an alternative DDES formulation based on elliptic relaxation*, PhD Thesis, University of Manchester, Manchester, UK.

Ashton, N., Revell, A., Prosser, R. and Uribe, J., 2013, Development of an alternative delayed detached-eddy simulation formulation based on elliptic relaxation, *AIAA J.* **51**(2), 513–519.

Bachalo, W. D. and Johnson, D. A., 1986, Transonic turbulent boundary layer separation generated on an axisymmetric flow model, *AIAA J.* **33**, 2026–2031.

Badri Narayanan, M. A. and Ramjee, V., 1969, On the criteria for reverse transition in a two dimensional boundary layer flow, *J. Fluid Mech.* **35**, 225–241.

Baggett, J. S., 1998, On the feasibility of merging LES with RANS for the near-wall region of attached turbulent flows, Annual Research Briefs 1998, Center for Turbulence Research, Stanford University, Stanford, CA, 267–277.

Baker, R. J. and Launder, B. E., 1974, The turbulent boundary layer with foreign gas injection: 1. Measurements in zero pressure gradient, *Int. J. Heat Mass Transfer* **17**, 275–291.

Balaras, E. and Benocci, C., 1994, Subgrid-scale models in finite-difference simulations of complex wall bounded flows, *AGARD CP* 551, SEE N95-21061 06–34.

Barberis, D. and Molton, P., 1995, Shock-wave/turbulent boundary-layer interaction in a three-dimensional turbulent flow, AIAA Paper 95-0227, Reno, Nevada.

Basara, B., 2015, PANS method as a computational framework from an industrial perspective, in *Progress in Hybrid RANS-LES Modelling*, Series: Notes on Numerical Fluid Mechanics and Multidisciplinary Design (NNFM), Vol. 30 (Ed. S. Girimaji *et al.*), 3–17, Springer, Switzerland.

Basara, B. and Girimaji, S. S., 2019, Partially averaged Navier-Stokes (PANS) scale resolving simulations: from fundamentals to engineering applications, *ERCOFTAC Bull.* **121**, 25–32.

Basara, B. and Jakirlić, S., 2003, A new hybrid turbulence modelling strategy for industrial CFD, *Int. J. Num. Meth. Fluids* **42**, 89–116.

Basara, B., Aldudak, F., Jakirlić, S., Tropea, C., Schrefl, F., Mayer, J. and Hanjalić, K., 2007, Experimental investigations and computations of unsteady flow past a real car using a robust elliptic-relaxation closure with a universal wall treatment, *SAE Trans.* **116**, 22–32.

Basara, B., Krajnovic, S., Girimaji, S. and Pavlovic, Z., 2011, Near wall formulation of the Partially Averaged Navier Stokes (PANS) turbulence model, *AIAA J.* **49**(12), 2627–2636.

Basara, B., Pavlovic, Z. and Girimaji, S. S., 2018, A new approach for the calculation of the cut-off resolution parameter in bridging methods for turbulent flow simulation, *Int. J. Heat Fluid Flow* **74**, 76–88.

Basara, B., Pavlovic, Z. and Girimaji, S. S., 2020, The prospects and benefits of using the Partial-Averaged Navier-Stokes method for engine flows, Technical Paper 2020-01-1107, SAE International.

Batchelor, G. K. and Townsend, A. A., 1948, Decay of turbulence in the final period, *Proc. R. Soc. London A* **194**, 527–543.

Batten, P., Craft, T. J., Leschziner, M. A. and Loyau, H., 1999, Reynolds-stress transport modeling for compressible aerodynamic flows, *AIAA J.* **37**, 785–796.

Batten, P., Goldberg, U. and Chakravarthy, S., 2002, LNS – an approach towards embedded LES, AIAA Paper 2002-0427, *40th AIAA Aerospace Sciences Meeting and Exhibit*, Reno, Nevada, 427.

Baughn, J. W. and Shimizu, S., 1989, Heat transfer measurements from a surface with uniform heat transfer and an impinging jet, *ASME J. Heat Transfer* **111**, 1096–1098.

Baughn, J. W. and Yan, X., 1992, Local heat transfer measurements in square ducts with transverse ribs, *28th National Heat Transfer Conf. ASME HTD*, Vol. 202, San Diego, CA.

Baughn, J. W., Hechanova, A. E. and Yan, X., 1991, An experimental study of entrainment effects on the heat transfer from a flat surface to a heated circular impinging jet, *J. Heat Transfer* **113**, 1023–1025.

Baughn, J. W., Yan, X. J. and Mesbah, M., 1992, The effects of Reynolds number on the heat transfer distribution from a flat plate to a turbulent impinging jet, *ASME HTD vol. 226*, 1–7.

Behnia, M., Parneix, S. and Durbin, P. A., 1998, Prediction of heat transfer in an axi-symmetric turbulent jet impinging on a flat plate, *Int. J. Heat Mass Transfer* **41**, 1845–1899.

Benhamadouche, S. and Laurence, D., 2003, LES, coarse LES, and transient RANS comparisons on the flow across a tube bundle, *Int. J. Heat Fluid Flow* **24**, 470–479.

Bennett, J. C. and Corrsin, S. C., 1978, Small Reynolds number nearly isotropic turbulence in a straight duct and in a contraction, *Phys. Fluids* **21**, 2129–2140.

Bergman, T. L., Incropera, F. P. and Viskanta, R., 1985, A differential model for salt-stratified, double-diffusive systems heated from below, *Int. J. Heat Mass Transfer* **28**, 779–788.

Bernard, P. S., 1990, Turbulent vorticity transport in three dimensions, *Theor. Comput. Fluid Dyn.* **2**, 165–183.

Bertoglio, J.-P., Charnay, G. and Mathieu, J., 1980, Effets de la rotation sur un champ turbulent cisaillé: application au cas des turbomachines, *J. Méc*. **4**, 421–443.

Borello, D., Hanjalić, K. and Rispoli, F., 2005, Prediction of cascade flows with innovative second-moment closures, *ASME J. Fluids Eng.* **127**, 1059–1070.

Borello, D., Delibra, G., Hanjalić, K. and Rispoli, F., 2009, Large-eddy simulations of tip leakage and secondary flows in an axial compressor cascade using a near-wall turbulence model, *Proc. IMechE Part A: J. Power Energy* **223**, 645–655.

Bose, S. T. and Park, G. I., 2018, Wall-modeled large-eddy simulation for complex turbulent flows, *Ann. Rev. Fluid Mech.* **50**, 535–561.

Boudjemadi, R., Maupu, V., Laurence, D. and Le Quéré, P., 1997, Budgets of turbulent stresses and fluxes in a vertical slot natural convection at Rayleigh Ra = 10^5 and 5.4 $\times$ 10^5, *Int. J. Heat Fluid Flow* **18**, 70–79.

Bou-Zeid, E., Meneveau, C. and Parlange, M., 2005, A scale-dependent Lagrangian dynamic model for large eddy simulation of complex turbulent flows, *Phys. Fluids* **17**(2), 025105.

Bradshaw, P., 1967, The turbulence structure of equilibrium boundary layers, *J. Fluid Mech.* **29**, 625–645.

Bradshaw, P., 1971, *An Introduction to Turbulence and its Measurements*, Pergamon Press, Oxford.

Bradshaw, P., 1973, Effect of streamline curvature on turbulent flow, AGARDograph 169.

Bradshaw, P., 1976, Introduction, in *Turbulence*, Topics in Applied Physics, Vol. 12 (Ed. P. Bradshaw), 1–44, Springer Verlag, Berlin.

Bradshaw, P., Ferriss, D. H. and Atwell, N. P., 1967, Calculation of boundary layer development using the turbulent energy equation, *J. Fluid Mech.* **28**, 593–616.

Bradshaw, P., Mansour, N. N. and Piomelli, U., 1987, On local approximations of the pressure-strain term in turbulence models, Report CTR-S87, *Studying Turbulence using Numerical Simulation Data Bases*, Proc. 1987 Summer Program, Center for Turbulence Research, Stanford University, Stanford, CA, 159–164.

Branover, H., 1978, *Magnetohydrodynamic Flow in Ducts*, Wiley, New York.

Brasseur, J. M. and Lee, M., 1987, Local structure of intercomponent energy transfer in homogeneous turbulent shear flow, Report CTR-S87, *Studying Turbulence using Numerical Simulation Data Bases, Proc. 1987 Summer Program*, Center for Turbulence Research, Stanford University, Stanford, CA, 165–178.

Bremhorst, K. and Gehrke, P. J., 2000, Measured Reynolds stress distributions and energy budgets of a fully-pulsed round air jet, *Exp. Fluids* **28**, 519–531.

Bremhorst, K., Craft, T. J. and Launder, B. E., 2003, Two-time-scale turbulence modelling of a fully-pulsed axisymmetric air jet, *Proc. 3rd Int. Symp. on Turbulence & Shear Flow Phenomena*, Sendai, Japan, 711–716.

Brouillette, E. C. and Lykoudis, P. S., 1967, Magneto-fluid-mechanic channel flow. I. Experiment, *Phys. Fluids* **10**, 995–1001.

Businger, J. A., Wyngaard, J. C., Izumi, Y. and Bradley, E. F., 1971, Flux-profile relationships in the atmospheric surface layer, *J. Atmos. Sci.* **28**, 181–189.

Cabot, W. and Moin, P., 2000, Approximate wall boundary conditions in the large- eddy simulation of high Reynolds number flow, *Flow, Turbulence Combust*. **63**, 269–291.

Cadiou, A., Hanjalić, K. and Starwiaski, K., 2004, A two-scale second-moment turbulence closure based on weighted spectrum integration, *Theor. Comput. Fluid Dyn.* **18**, 1–26.

Cantwell, B. and Coles, D., 1983, An experimental study of entrainment and transport in the turbulent near wake of a circular cylinder, *J. Fluid Mech.* **136**, 321–374.

Carpy, S. and Manceau, R., 2006, Turbulence modelling of statistically periodic flows: synthetic jet into quiescent air, *Int. J. Heat Fluid Flow* **27**(5), 756–767.

Carr, A. D., Connor, M. A. and Buhr, H. O., 1973, Velocity, temperature and turbulence measurements in air for pipe flow with combined free and forced convection, *Trans. ASME J. Heat Transfer* **95**, 445–452.

Castro, I. and Bradshaw, P., 1976, The turbulence structure of a highly curved mixing layer, *J. Fluid Mech.* **73**, 265–304.

Cebeci, T., 1999, *An Engineering Approach to the Calculation of Aerodynamic Flows*, Springer, New York.

Cebeci, T. and Mosinskis, G. J., 1971, The calculation of incompressible turbulent boundary layers with mass transfer including highly accelerated flows, *ASME J. Heat Transfer* **93**, 271–280.

Cebeci, T. and Smith, A. M. O., 1974, *Analysis of Turbulent Boundary Layers*, Academic Press, New York.

Celenligil, M. C. and Mellor, G. L., 1985, Numerical solution of two-dimensional separated flows using a Reynolds-stress closure model, *ASME J. Fluids Eng.* **107**, 467–476.

Champagne, F., Harris, V. and Corrsin, S. C., 1970, Experiments on nearly homogeneous shear flows, *J. Fluid Mech.* **41**, 81–139.

Chaouat, B., 2010, Sub-filter-scale transport model for Hybrid RANS/LES simulations applied to a complex bounded flow, *J. Turbulence* **11**, 1–30.

Chaouat, B., 2017, The state of the art of Hybrid RANS/LES modeling for the simulation of turbulent flows, *Flow, Turbulence Combust*. **99**, 279–327.

Chaouat, B. and Schiestel, R., 2005, A new partially integrated transport model for subgrid-scale stresses and dissipation rate for turbulent developing flows, *Phys. Fluids* **17**, 065106.

Chaouat, B. and Schiestel, R., 2007, From single-scale turbulence models to multiple scale and sub-grid-scale models by Fourier transform, *Theor. Comput. Fluid Dyn.* **21**, 201–229.

Chaouat, B. and Schiestel, R., 2009, Progress in sub-grid-scale transport modelling for continuous hybrid non-zonal RANS/LES simulations, *Int. J. Heat Fluid Flow* **30**, 602–616.

Chaouat, B. and Schiestel, R., 2013, Hybrid RANS/LES simulations of the turbulent flow over periodic hills at high Reynolds number using the PITM method, *Comput. Fluids* **84**, 279–300.

Chapman, D. R., 1979, Computational aerodynamics development and outlook, *AIAA J.* **17**(12), 1293–1313.

Chauvet, N., Deck, S. and Jacquin, L., 2007, Zonal detached eddy simulation of a controlled propulsive jet, *AIAA J*. **45**(10), 2458–2473.

Chavanne, X., Chillà, F., Chabaud, B., Castaign, B., Chaussy, J. and Hébral, B., 1996, High Rayleigh number convection with gaseous helium at low temperature, *J. Low Temp. Phys.* **104**, 109–129.

Cheah, S. C., Iacovides, H., Jackson, D. C., Ji, H.-H. and Launder, B. E., 1996, LDA investigation of the flow development through rotating U-ducts, *J. Turbomachinery* **118**, 590–596.

Chen, C. J. and Rodi, W., 1980, *Vertical Turbulent Buoyant Jets: A Review of Experimental Data*, Pergamon Press, Oxford.

Cherry, E. M., Elkins, C. J. and Eaton, J. K., 2008, Geometric sensitivity of three-dimensional separated flows, *Int. J. Heat Fluid Flow* **29**(3), 803–811.

Chien, K.-Y., 1982, Prediction of channel and boundary layer flows with a low-Reynolds number turbulence model, *AIAA J*. **20**, 33–38.

Chieng, C. C. and Launder, B. E., 1980, On the calculation of turbulent heat transport downstream from an abrupt pipe expansion, *Numerical Heat Transfer* 3, 189–207.

Choi, H. and Moin, P., 2012, Grid-point requirements for large eddy simulation: Chapman's estimates revisited, *Phys. Fluids* **24**(1), 011702.

Choi, Y. D., Iacovides, H. and Launder, B. E., 1989, Numerical computation of turbulent flow in a square-sectioned 180° bend, *J. Fluids Eng*. **111**, 59–68.

Chou, P.-Y., 1945, On the velocity correlations and the solutions of the equations of turbulent fluctuation, *Q. J. Appl. Math.* **3**, 38–54.

Chow, J. S., Zilliac, G. G. and Bradshaw, P., 1997, Mean and turbulence measurements in the near field of a wingtip vortex, *AIAA J.* **35**, 1561–1567 (see also NASA TM 110418).

Chu, V. E. and Baddour, R. E., 1984, Turbulent gravity-stratified shear flows, *J. Fluid Mech*. **138**, 353–378.

Chung, M. K., Yun, H. C. and Adrian, R. J., 1992, Scale analysis and wall-layer model for the temperature profile in a turbulent thermal convection, *Int. J. Heat Mass Transfer* **35**, 43–51.

Ciofalo, M. and Collins, M. W., 1989, The $k - \varepsilon$ predictions of heat transfer in turbulent recirculating flows using an improved wall treatment, *Numerical Heat Transfer, B Fundamentals* **15**, 21–47.

Clark, R. A., Ferziger, J. H. and Reynolds, W. C., 1979, Evaluation of sub-grid-scale models using an accurately simulated turbulent flow, *J. Fluid Mech.* **91**(1), 1–16.

Clark, T. T. and Zemach, C., 1995, A spectral model applied to homogeneous turbulence, *Phys. Fluids* **7**, 1674–1694.

Cokljat, D., Caridi, D., Link, G., Lechner, R. and Menter, F. R., 2009, Embedded LES methodology for general-purpose CFD solvers, *Proc. 6th Int. Symp. on Turbulence & Shear Flow Phenomena*, Seoul, Korea, 1191–1196.

Coles, D., 1956, The law of the wake in the turbulent boundary layer, *J. Fluid Mech.* **1**, 191–226.

Comte-Bellot, G. and Corrsin, S., 1966, The use of a contraction to improve the isotropy of grid-generated turbulence, *J. Fluid Mech.* **25**, 657–682.

Cooper, D., Jackson, D. C., Launder, B. E. and Liao, G.-X., 1993, Impinging jet studies for turbulence model assessment, *Int. J. Heat Mass Transfer* **36**, 2675–2684.

Cormack, D. E., Leal, L. G. and Seinfeld, J. H., 1978, An evaluation of Reynolds stress turbulence models: the triple velocity correlations, *ASME J. Fluids Eng.* **100**, 47–54.

Corrsin, S., 1952, Heat transfer in isotropic turbulence, *J. Appl. Phys.* **23**, 113–118.

Cotton, M. A. and Ismael, J. O., 1998, A strain parameter turbulence model and its application to homogeneous and thin shear flows, *Int. J. Heat Fluid Flow* **19**, 326–337.

Cotton, M. A. and Jackson, J. D., 1987, Calculation of turbulent mixed convection in vertical tubes using a low-Reynolds-number $k - \varepsilon$ turbulence model, Paper 9.6, *Proc. 6th Symp. on Turbulent Shear Flows*, Toulouse, France.

Cotton, M. A. and Jackson, J. D., 1990, Vertical tube air flows in the turbulent mixed convection regime calculated using a low-Reynolds-number $k - \varepsilon$ model, *Int. J. Heat Mass Transfer* **33**, 275–286.

Courant, R., Friedrichs, K. and Lewy, H., 1928, Über die partiellen Differenzengleichungen der mathematischen Physik, *Mathematischen Annalen* **100**, 32–74.

Cousteix, J. and Aupoix, B., 1981, Reynolds stress equations modeling in a rotating reference frame, Recherche Aérospatiale No 1981–4, CERT, ONERA.

Cousteix, J., Desopper, A. and Houdeville, R., 1979, Structure and development of a turbulent boundary layer in an oscillatory external flow, in *Turbulent Shear Flows 1* (Ed. F. J. Durst *et al.*), 154–171, Springer Verlag, Berlin.

Craft, T. J., 1991, *Second-moment modelling of turbulent scalar transport*, PhD Thesis, Faculty of Technology, University of Manchester, Manchester, UK.

Craft, T. J., 1998, Developments in a low-Reynolds-number second-moment closure and its application to separating and reattaching flows, *Int. J. Heat Fluid Flow* **19**, 541–548.

Craft, T. J., 2002, Modelling of separating and impinging flows, in *Closure Strategies for Turbulent and Transitional Flows* (Ed. B. E. Launder and N. D. Sandham), 341–360, Cambridge University Press, Cambridge.

Craft, T. J. and Launder, B. E., 1989, A new model for the pressure/scalar-gradient correlation and its application to homogeneous and inhomogeneous free shear flows, Paper 17.1, *Proc. 7th Symp. on Turbulent Shear Flows*, Stanford University, Stanford, CA.

Craft, T. J. and Launder, B. E., 1991, Computation of impinging flows using second-moment closures, Paper 8.5, *Proc. 8th Symp. on Turbulent Shear Flows*, Technical University of Munich, Germany.

Craft, T. J. and Launder, B. E., 1992, New wall-reflection model applied to the turbulent impinging jet, *AIAA J*. **30**, 2970–2972.

Craft, T. J. and Launder, B. E., 1996, A Reynolds-stress closure designed for complex geometries, *Int. J. Heat Fluid Flow* **17**, 245–254.

Craft, T. J. and Launder, B. E., 2002a, Application of TCL modelling to stratified flows, in *Closure Strategies for Turbulent and Transitional Flows* (Ed. B. E. Launder and N. D. Sandham), 407–423, Cambridge University Press, Cambridge.

Craft, T. J. and Launder, B. E., 2002b, Closure modelling near the two-component limit, in *Closure Strategies for Turbulent and Transitional Flows* (Ed. B. E. Launder and N. D. Sandham), 102–126, Cambridge University Press, Cambridge.

Craft, T. J. and Launder, B. E., 2002c, On the spreading mechanism of the three-dimensional turbulent wall jet, *J. Fluid Mech.* **435**, 305–326.

Craft, T. J., Graham, L. J. and Launder, B. E., 1993, Impinging jet studies for turbulence model assessment: 2. An examination of the performance of four turbulence models, *Int. J. Heat Mass Transfer* **36**, 2685–2697.

Craft, T. J., Ince, N. Z. and Launder, B. E., 1996a, Recent developments in second-moment closure for buoyancy-affected flows, *Dyn. Atmos. Oceans* **23**, 99–114.

Craft, T. J., Launder, B. E. and Suga, K., 1996b, Development and application of a cubic eddy-viscosity model of turbulence, *Int. J. Heat Fluid Flow* **17**, 108–115.

Craft, T. J., Kidger, J. W. and Launder, B. E., 1997a, Importance of 3rd-moment modelling in horizontal, stably stratified flow, *Proc. 11th Symp. on Turbulent Shear Flows*, Grenoble, France, 20.13–20.18.

Craft, T. J., Launder, B. E. and Suga, K., 1997b, Prediction of turbulent transitional phenomena with a nonlinear eddy-viscosity model, *Int. J. Heat Fluid Flow* **18**, 15–28.

Craft, T. J., Kidger, J. W. and Launder, B. E., 2000, Second-moment modeling of developing and self-similar turbulent three-dimensional free-surface jets, *Int. J. Heat Fluid Flow* **21**, 338–344.

Craft, T. J., Gerasimov, A. V., Iacovides, H. and Launder, B. E., 2002, Progress in the generalization of wall-function treatments, *Int. J. Heat Fluid Flow* **23**, 148–160.

Craft, T. J., Gant, S. E., Iacovides, H. and Launder, B. E., 2004a, A new wall-function strategy for complex turbulent flows, *Numerical Heat Transfer, B Fundamentals* **45**, 301–318.

Craft, T. J., Gerasimov, A. V., Iacovides, H. and Launder, B. E., 2004b, The negatively buoyant turbulent wall jet: performance of alternative options in RANS modelling, *Int. J. Heat Fluid Flow* **25**, 809–823.

Craft, T. J., Gant, S. E., Gerasimov, A. V., Iacovides, H. and Launder, B. E., 2006a, Numerical modelling of wall heat transfer in wall-adjacent turbulent flows, in *Handbook of Numerical Heat Transfer*, 2nd ed. (Ed. W. J. Minkowycz, E. M. Sparrow and J. Y. Murthy), 369–388, Wiley, Hoboken, NJ.

Craft, T. J., Gerasimov, A. V., Launder, B. E. and Robinson, C. M., 2006b, A computational study of the near-field generation and decay of wingtip vortices, *Int. J. Heat Fluid Flow* **27**, 684–695.

Craft, T. J., Iacovides, H., Launder, B. E. and Zacharos, A., 2008, Some swirling-flow challenges for turbulent CFD, *Flow, Turbulence Combust*. **80**, 419–434.

Crow, S. C., 1968, Visco-elastic properties of fine-grained incompressible turbulence, *J. Fluid Mech.* **33**, 1–20.

Czarny, O., Iacovides, H. and Launder, B. E., 2002, Precessing vortex structures within rotor-stator disc cavities, *Flow, Turbulence Combust.* **69**, 51–61.

Dakos, T. and Gibson, M. M., 1985, On modelling the pressure terms of the scalar-flux equations, *Proc. 5th Symp. on Turbulent Shear Flow*, Cornell University, Ithaca, NY, 12.1–12.6.

Daly, B. J. and Harlow, F. H., 1970, Transport equations in turbulence, *Phys. Fluids* **13**, 2634–2649.

Davidov, B. I., 1959, On the statistical dynamics of an incompressible turbulent fluid, *Dokl. Akad. Nauk SSSR* **127**, 768 (translated in *Soviet Physics–Doklady* **4**, 769).

Davidov, B. I., 1961, On the statistical dynamics of an incompressible turbulent fluid, *Dokl. Akad. Nauk SSSR* **136**, 47–50 (translated in *Soviet Physics–Doklady* **6**, 10).

Davidson, L. and Billson, M., 2006, Hybrid LES-RANS using synthesized turbulent fluctuations for forcing in the interface region, *Int. J. Heat Fluid Flow* **27**(6), 1028–1042.

Davidson, L. and Friess, C., 2019, A new formulation of f_k for the PANS model, *J. Turbulence* **20**(5), 322–336.

Davidson, L. and Peng, S.-H., 2003, Hybrid LES-RANS modelling: a one-equation sgs model combined with a $k - \omega$ model for predicting recirculating flows, *Int. J. Num. Meth. Fluids* **43**(9), 1003–1018.

Davidson, P. A., 2004, *Turbulence*, Oxford University Press, Oxford.

Deardorff, J. W., 1970, A numerical study of three-dimensional turbulent channel flow at large Reynolds numbers, *J. Fluid Mech.* **41**(2), 453–480.

Deardorff, J. W., Willis, G. E. and Lilly, D. K., 1969, Laboratory investigation of non-steady penetrative convection, *J. Fluid Mech.* **35**, 7–31.

Deck, S., 2005, Zonal-detached-eddy simulation of the flow around a high-lift configuration, *AIAA J*. **43**(11), 2372–2384.

Deck, S., Weiss, P. É., Pamiès, M. and Garnier, E., 2011, Zonal detached eddy simulation of a spatially developing flat plate turbulent boundary layer, *Comput. Fluids* **48**(1), 1–15.

Deck, S., Gand, F., Brunet, V. and Ben Khelil, S., 2014, High-fidelity simulations of unsteady civil aircraft aerodynamics: stakes and perspectives. Application of zonal detached eddy simulation, *Phil. Trans. Roy. Soc. A* **372**(2022), 20130325.

Dekeyser, I., 1982, *Etude d'un jet plan dissymmetrique chauffé en regime turbulent incompressible*, Thèse Docteur-es-Sciences, Université d'Aix-Marseille II, France.

Dekeyser, I. and Launder, B. E., 1985, A comparison of triple-moment temperature-velocity correlations in the asymmetric heated jet with alternative closure models, in *Turbulent Shear Flows 4* (Ed. L. J. S. Bradbury *et al.*), 102–117, Springer Verlag, Heidelberg.

Delibra, G., Borello, D., Hanjalić, K. and Rispoli, F., 2009, URANS of flow and endwall heat transfer in a pinned passage relevant to gas-turbine blade cooling, *Int. J. Heat Fluid Flow* **30**, 545–560.

Delibra, G., Hanjalić, K., Borello, D. and Rispoli, F., 2010, Vortex structures and heat transfer in a wall-bounded pin matrix: LES with a RANS wall-treatment, *Int. J. Heat Fluid Flow* **31**, 740–753.

Demuren, A. O., Rogers, M. M., Durbin, P. and Lele, S. K., 1996, On modeling pressure diffusion in non-homogeneous shear flows, *Proc. Summer Program*, Center for Turbulence Research, NASA Ames/Stanford University, 63–72.

Diurno, G. V., Balaras, E. and Piomelli, U., 2001, Wall-layer models for LES of separated flows, in *Modern Simulation Strategies for Turbulent Flows* (Ed. B. G. Geurts), 157–174, R. T. Edwards, Philadelphia.

Dol, H. S., 1998, *Turbulence models for natural convection in side-heated enclosures*, PhD Thesis, Delft University of Technology, Delft, The Netherlands.

Dol, H. S. and Hanjalić, K., 2001, Computational study of turbulent natural convection in a side-heated near-cubic enclosure at a high Rayleigh number, *Int. J. Heat Mass Transfer* **44**, 2323–2344.

Dol, H. S., Hanjalić, K. and Kenjereš, S., 1997, A comparative assessment of the second-moment differential and algebraic models in turbulent natural convection, *Int. J. Heat Fluid Flow* **18**, 4–14.

Dol, H. S., Hanjalić, K. and Versteegh, T. A. M., 1999, A DNS-based thermal second-moment closure for buoyant convection at vertical walls, *J. Fluid Mech*. **391**, 211–247.

Donaldson, C. du P., 1971, A progress report on an attempt to construct an invariant model of turbulent shear flows, Paper B-1, *Proc. AGARD Conf. on Turbulent Shear Flows*, London.

Donaldson, C. du P., Sullivan, R. D. and Rosenbaum, H., 1972, A theoretical study of the generation of atmospheric clear-air turbulence, *AIAA J.* **10**, 162–170.

Druault, P., Lardeau, S., Bonnet, J.-P., Coiffet, F., Delville, J., Lamballais, E., Largeau, J.-F. and Perret, L., 2004, Generation of three-dimensional turbulent inlet conditions for large-eddy simulation, *AIAA J*. **42**(3), 447–456.

Durbin, P. A., 1991, Near-wall turbulence closure modelling without damping functions, *Theor. Comput. Fluid Dyn.* **3**, 1–13.

Durbin, P. A., 1993, A Reynolds stress model for near-wall turbulence, *J. Fluid Mech.* **249**, 465–498.

Durbin, P. A., 1995, Separated flow computations with the $k-\varepsilon-\overline{v}^2$ model, *AIAA J*. **33**, 659–664.

Durbin, P. A., 1996, On the $k-\varepsilon$ stagnation point anomaly, *Int. J. Heat Fluid Flow* **17**, 89–90.

Eça, L., Vaz, G., Rosetti, G. and Pereira, F., 2014, On the numerical prediction of the flow around smooth circular cylinders, OMAE2014-23230, *Proc. ASME 33rd Int. Conf. on Offshore Mechanics and Arctic Eng'ing*, San Francisco, CA.

Eckelmann, H., 1970, Experimentelle Untersuchungen in einer turbulenten Kanalströmung mit starken viscosen Wandschichten, Mitt. Max Planck Inst. f. Strömungsforschung, No. 48, Göttingen, Germany.

Egorov, Y., Menter, F. R., Lechner, R. and Cokljat, D., 2010, The scale-adaptive simulation method for unsteady turbulent flow predictions. Part 2: application to complex flows, *Flow, Turbulence Combust*. **85**, 139–165.

El Baz, A. M., Launder, B. E. and Nemouchi, Z., 1989, On the prediction of memory effects in plane turbulent wakes, Paper T-4, *Proc. 7th Symp. on Turbulent Shear Flows*, Stanford University, Stanford, CA.

El Baz, A. M., Craft, T. J., Ince, N. Z. and Launder, B. E., 1993, On the adequacy of the thin-shear-flow equations for computing turbulent jets in stagnant surroundings, *Int. J. Heat Fluid Flow* **14**, 164–169.

Elena, L., 1994, *Modelisation de la turbulence inhomogène en présence de rotation*, Thèse Doctoral, Université d'Aix-Marseille II, France.

Elena, L. and Schiestel, R., 1996, Turbulence modelling of rotating confined flows, *Int. J. Heat Fluid Flow* **17**, 283–289.

Elghobashi, S. and Launder, B. E., 1983, Turbulent time scales and the dissipation rate of temperature variance in the turbulent mixing layer, *Phys. Fluids* **26**, 2415–2419.

Eringen, A. C., 1962, *Non-Linear Theory of Continuous Media*, 93, McGraw Hill, New York.

Esch, T. and Menter, F. R., 2003, Heat transfer predictions based on two-equation turbulence models with advanced wall treatment, in *Turbulence, Heat and Mass Transfer*, Vol. 4 (Ed. K. Hanjalić, Y. Nagano and M. Tummers), 633–640, Begell House, New York.

Fadai-Ghotbi, A., Manceau, R. and Borée, J., 2008, Revisiting URANS computations of the backward-facing step flow using second moment closures. Influence of the numerics, *Flow, Turbulence Combust*. **81**, 395–414.

Fasel, H. F., Seidel, J. and Wernz, S., 2002, A methodology for simulations of complex turbulent flows, *J. Fluids Eng.* **124**(4), 933–942.

Favre, A., 1965, Equations des gaz turbulents compressibles: formes générales, *J. Méc*. **4**, 361–390.

Fedorovich, E., Conzemius, R. and Mironov, D., 2004, Convective entrainment into a shear-free linearly stratified atmosphere: bulk models re-evaluated through large-eddy simulation, *J. Atmos. Sci.* **61**, 281–295.

Fernholz, H. H. and Warnack, D., 1998, The effects of a favorable pressure gradient and of Reynolds number on an incompressible axisymmetric boundary layer, *J. Fluid Mech.* **359**, 329–356.

Ferziger, J. H., 1996, Large eddy simulations, in *Simulation and Modelling of Turbulent Flows*, ICASE/LaRC Series in Computational Science and Engineering (Ed. M. Y. Hussain and T. Gatski) (also Oxford Scholarship Online, 2020).

Forstall, W. and Shapiro, A. H., 1950, Momentum and mass transfer in coaxial gas jets, *ASME J. Appl. Mech.* **17**, 399.

Franke, R., Rodi, W. and Schönung, B., 1989, Analysis of experimental vortex-shedding data with respect to turbulence modelling, *Proc. 7th Symp. on Turbulent Shear Flows*, Stanford, CA, 24.4.1–24.4.6.

Freymuth, P. and Uberoi, M. S., 1973, Temperature fluctuations in a turbulent wake behind an optically heated sphere, *Phys. Fluids* **16**, 161–168.

Friess, C., Manceau, R. and Gatski, T., 2015, Toward an equivalence criterion for Hybrid RANS/LES methods, *Comput. Fluids* **122**, 233–246.

Fröhlich, J. and Von Terzi, D., 2008, Hybrid LES/RANS methods for the simulation of turbulent flows, *Prog. Aerosp. Sci.* **44**, 349– 377.

Fu, S., 1988, *Computational modelling of turbulent swirling flows with second-moment closures*, PhD Thesis, Faculty of Engineering, University of Manchester, Manchester, UK.

Fu, S. and Wang, C., 1997, Second-moment closure modelling of turbulence in a non-inertial frame, *Fluid Dyn. Res.* **20**, 43–65.

Fu, S., Launder, B. E. and Leschziner, M. A., 1987a, Modelling strongly swirling recirculating jet flows with Reynolds stress transport closures, Paper 1.5, *Proc. 6th Symp. on Turbulent Shear Flows*, Toulouse, France.

Fu, S., Launder, B. E. and Tselepidakis, D. P., 1987b, Accommodating the effects of high strain rates in modelling the pressure-strain correlation, Technical Report FD/87/5, Department of Mechanical Engineering, UMIST, Manchester, UK.

Fu, S., Huang, P. G., Launder, B. E. and Leschziner, M. A., 1988, A comparison of algebraic and differential second-moment closures for axisymmetric free shear flows with and without swirl, *J. Fluids Eng.* **110**, 216–221.

Gan, X., Kilic, M. and Owen, J. M., 1995, Flow between contra-rotating discs, *J. Turbomachinery* **117**, 298–305.

Gant, S. E., 2002, *Development and application of a new wall function for complex turbulent flows*, PhD Thesis, Department of Mechanical, Aerospace and Manufacturing Engineering, UMIST, Manchester, UK.

Gardner, R. A. and Lykoudis, P. S., 1971, Magneto-fluid-mechanic pipe flow in a transverse magnetic field. 1. Isothermal flow, *J. Fluid Mech.* **47**, 737–764.

Garnier, E., Mossi, M., Sagaut, P., Comte, P. and Deville, M., 1999, On the use of shock-capturing schemes for large-eddy simulation, *J. Comput. Phys.* **153**(2), 273–311.

Gatski, T. B. and Bonnet, J.-P., 2009, *Compressibility, Turbulence and High-Speed Flow*, Elsevier, Oxford.

Gatski, T. B. and Rumsey, C. L., 2002, Linear and non-linear eddy viscosity models, in *Closure Strategies for Turbulent and Transitional Flows* (Ed. B. E. Launder and N. D. Sandham), 9–46, Cambridge University Press, Cambridge.

Gatski, T. B. and Speziale, C., 1993, On explicit algebraic stress models for complex turbulent flows, *J. Fluid Mech.* **254**, 59–78.

Geers, L. F. G., 2004, *Multiple-impinging jet arrays: an experimental study on flow and heat transfer*, PhD Thesis, Delft University of Technology, Delft, The Netherlands.

Gence, J. N. and Mathieu, J., 1979, Application of successive plane strains to grid-generated turbulence, *J. Fluid Mech.* **93**, 501–513.

Gerasimov, A. V., 2003, *Development and application of an analytical wall-function strategy for modelling forced, mixed and natural convection phenomena*, PhD Thesis, UMIST, Manchester, UK.

Germano, M., Piomelli, U., Moin, P. and Cabot, W. H., 1991, A dynamic subgrid-scale eddy viscosity model, *Phys. Fluids A* **3**(7), 1760–1765.

Gibson, M. M. and Launder, B. E., 1976, On the calculation of horizontal, turbulent, free shear flows under gravitational influence, *ASME J. Heat Transfer C* **98**, 379–386.

Gibson, M. M. and Launder, B. E., 1978, Ground effects on pressure fluctuations in the atmospheric boundary layer, *J. Fluid Mech.* **86**, 491–511.

Gibson, M. M. and Rodi, W., 1981, A Reynolds stress closure model of turbulence applied to the calculation of a highly curved mixing layer, *J. Fluid Mech.* **101**, 161–182.

Gibson, M. M. and Younis, B. A., 1986, The calculation of swirling jets with a Reynolds-stress closure, *Phys. Fluids* **29**, 38–48.

Gibson, M. M., Jones, W. P. and Kanellopoulos, V. E., 1987, Turbulent temperature mixing layer: measurement and modelling, Paper 9–5, *Proc. 6th Symp. on Turbulent Shear Flows*, Toulouse, France.

Gilbert, N. and Kleiser, L., 1991, Turbulence model testing with the aid of direct numerical simulation results, Paper 26.1, *Proc. 8th Symp. on Turbulent Shear Flows*, Munich, Germany.

Girimaji, S. S., 1996, Fully explicit and self-consistent algebraic Reynolds stress model, *Theor. Comput. Fluid Dyn.* **8**, 387–402.

Girimaji, S. S., 2006, Partially-averaged Navier–Stokes model for turbulence: a Reynolds-averaged Navier–Stokes to direct numerical simulation bridging method, *J. Appl. Mech.* **73**, 413–421.

Girimaji, S. S. and Abdol-Hamid, K. S., 2005, Partially-averaged Navier Stokes model for turbulence: implementation and validation, AIAA Paper 2005-502, *43rd AIAA Aerospace Sciences Meeting and Exhibit*, Reno, Nevada, 10–13 January.

Girimaji, S. S., Jeong, E. and Srinivasan, R., 2006, Partially-averaged Navier–Stokes model for turbulence: fixed point analysis and comparison with unsteady partially-averaged Navier–Stokes, *J. Appl. Mech.* **73**, 422–429.

Gleize, V., Schiestel, R. and Couaillier, V., 1996, Multiple scale modelling of turbulent non-equilibrium boundary layers, *Phys. Fluids* **8**, 2716–2732.

Gorski, J. J. and Bernard, P. S., 1996, Modeling of the turbulent enstrophy equation, *Int. J. Eng. Sci.* **34**, 699–714.

Gosse, J. and Schiestel, R., 1974, The prediction of turbulent forced convection with a new model, Paper FC4.1, *5th Int. Heat Transfer Conf.*, Tokyo, Japan.

Greenblatt, D., Paschal, K. B., Yao, C.-S., Harris, J., Schaeffler, N. W. and Washburn, A. E., 2006, Experimental investigation of separation control Part 1: baseline and steady suction, *AIAA J.* **44**(12), 2820–2830.

Greenspan, H. P., 1962, *The Theory of Rotating Fluids*, Cambridge University Press, Cambridge.

Greschner, B., Thiele, F., Jacob, M. C. and Casalino, D., 2008, Prediction of sound generated by a rod–airfoil configuration using EASM DES and the generalised Lighthill/FW-H analogy, *Comput. Fluids* **37**(4), 402–413.

Grinstein, F. F. and Fureby, C., 2002, Recent progress on MILES for high Reynolds number flows, *J. Fluids Eng.* **124**(4), 848–861.

Grinstein, F. F., Margolin, L. G. and Rider, W. J., 2007, *Implicit Large Eddy Simulation: Computing Turbulent Fluid Dynamics*, Cambridge University Press, Cambridge.

Groth, J., 1991, Description of the pressure effects in the Reynolds stress transport equations, *Phys. Fluids A* **3**(9), 2276–2277.

Grundestam, O., Wallin, S. and Johansson, A. V., 2005, An explicit algebraic Reynolds stress model based on a non-linear pressure strain rate model, *Int. J. Heat Fluid Flow* **26**, 232–745.

Ha Minh, H. and Kourta, A., 1993, Semi-deterministic turbulence modelling for flows dominated by strong organized structures, *Proc. 9th Symp. on Turbulent Shear Flows*, Kyoto, Japan, 10.5-1–10.5-6.

Haase, W., Braza, M. and Revell, A. (Eds.), 2009, *DESider – A European Effort on Hybrid RANS-LES Modelling: Results of the European-Union Funded Project, 2004–2007*, NNFM, Vol. **103**, Springer Science & Business Media.

Hadžiabdić, M., 2005, *LES, RANS and combined simulation of impinging flows and heat transfer*, PhD Thesis, Delft University of Technology, Delft, The Netherlands.

Hadžić, I., 1999, *Second-moment closure modelling of transitional and unsteady turbulent flows*, PhD Thesis, Delft University of Technology, Delft, The Netherlands.

Hadžić, I. and Hanjalić, K., 1999, Separation-induced transition to turbulence: second-moment closure modelling, *Flow, Turbulence Combust*. **63**, 153–173.

Hadžić, I., Hanjalić, K. and Laurence, D., 2001, Modeling the response of turbulence subjected to cyclic irrotational strain, *Phys. Fluids* **13**, 1739–1747.

Hall, W. B. and Jackson, J. D., 1969, Laminarization of a turbulent pipe flow by buoyancy, ASME Paper 69-HT-55.

Hallbäck, M., Groth, J. and Johansson, A. V., 1990, An algebraic model for nonisotropic turbulent dissipation rate in Reynolds stress closures, *Phys. Fluids A* **2**, 1859–1866.

Hanjalić, K., 1970, *Two-dimensional asymmetric turbulent flow in ducts*, PhD Thesis, Imperial College, University of London, UK.

Hanjalić, K., 1994, Advanced turbulence closure models: a view of current status and future prospects, *Int. J. Heat Fluid Flow* **15**, 178–203.

Hanjalić, K., 1996, Some resolved and unresolved issues in modeling non-equilibrium and unsteady turbulent flows, in *Engineering Turbulence Modelling and Experiments 3* (Ed. W. Rodi and G. Bergeles), 3–18, Elsevier, Amsterdam.

Hanjalić, K., 1999, Second-moment turbulence closures for CFD: need and prospects, *Int. J. Comput. Fluid Dyn.* **12**, 67–97.

Hanjalić, K., 2002, One-point closure models for buoyancy-driven turbulent flows, *Ann. Rev. Fluid Mech.* **34**, 21–47.

Hanjalić, K., 2004, Closure models for incompressible turbulent flows, in *Introduction to the Modelling of Turbulence*, Lecture Series 2004–06 (also 2002–04), Von Karman Institute, Rhode St Genèse, Belgium.

Hanjalić, K., 2005, Will RANS survive LES? A view of perspectives, *J. Fluids Eng.* **127**, 831–839.

Hanjalić, K. and Hrebtov, M., 2016, Ground boundary conditions for thermal convection over horizontal surfaces at high Rayleigh numbers, *Boundary Layer Meteorol.* **160**(1), 41–61.

Hanjalić, K. and Jakirlić, S., 1993, A model of stress dissipation in second-moment closures, *Appl. Sci. Res.* **51**, 513–518.

Hanjalić, K. and Jakirlić, S., 1998, Contribution towards the second-moment closure modelling of separating turbulent flows, *Comput. Fluids* **27**, 137–156.

Hanjalić, K. and Jakirlić, S., 2002, Second-moment turbulence closure modelling, in *Closure Strategies for Turbulent and Transitional Flows* (Ed. B. E. Launder and N. D. Sandham), 47–101, Cambridge University Press, Cambridge.

Hanjalić, K. and Kenjereš, S., 2000, Reorganization of turbulence structure in magnetic Rayleigh–Bénard convection: A T-RANS study, *J. Turbulence*, http://jot.iop.org/S1468–5248(00)17901–9.

Hanjalić, K. and Kenjereš, S., 2001, T-RANS simulation of deterministic eddy structure in flows driven by thermal buoyancy and Lorentz force, *Flow, Turbulence Combust.* **66**, 427–451.

Hanjalić, K. and Kenjereš, S., 2002, Simulations of coherent eddy structures in buoyancy-driven flows with single point turbulence closure models, in *Closure Strategies for Turbulent and Transitional Flows*(Ed. B. E. Launder and N. D. Sandham), 659–684, Cambridge University Press, Cambridge.

Hanjalić, K. and Kenjereš, S., 2008, Some developments in turbulence modeling for wind and environmental engineering, *J. Wind Eng. Ind. Aerodyn.* **96**, 1537–1570.

Hanjalić, K. and Launder, B. E., 1972a, Fully developed asymmetric flow in a plane channel, *J. Fluid Mech.* **51**, 301–335.

Hanjalić, K. and Launder, B. E., 1972b, A Reynolds stress model of turbulence and its application to thin shear flows, *J. Fluid Mech.* **52**, 609–638.

Hanjalić, K. and Launder, B. E., 1976, Contribution towards a Reynolds-stress closure for low-Reynolds-number turbulence, *J. Fluid Mech.* **74**, 593–610.

Hanjalić, K. and Launder, B. E., 1980, Sensitizing the dissipation equation to irrotational strains, *ASME J. Fluids Eng.* **102**, 34–40.

Hanjalić, K. and Musemić, R., 1997, Modelling the dynamics of double-diffusive scalar fields at various stability conditions, *Int. J. Heat Fluid Flow* **18**, 360–367.

Hanjalić, K. and Stošić, N., 1985, Hysteresis of turbulent stresses in wall flows subjected to periodic disturbances, in *Turbulent Shear Flows 4* (Ed. F. Durst *et al.*), 287–300, Springer Verlag, Berlin.

Hanjalić, K. and Vasić, S., 1993, Some further exploration of turbulence models for buoyancy driven flows, in *Turbulent Shear Flows 8* (Ed. F. Durst *et al.*), 319–341, Springer Verlag, Heidelberg.

Hanjalić, K., Launder, B. E. and Schiestel, R., 1980, Multiple-time-scale concepts in turbulent transport modelling, in *Turbulent Shear Flows 2* (Ed. L. J. S. Bradbury *et al.*), 36–49, Springer Verlag, Heidelberg.

Hanjalić, K., Jakirlić, S. and Durst, F., 1994, A computational study of joint effects of transverse shear and streamwise acceleration on three-dimensional boundary layers, *Int. J. Heat Fluid Flow* **15**, 269–282.

Hanjalić, K., Jakirlić, S. and Hadžić, I., 1995, Computation of oscillating turbulent flows at transitional Re-numbers, in *Turbulent Shear Flows 9* (Ed. F. Durst *et al.*), 323–342, Springer-Verlag, Berlin.

Hanjalić, K., Jakirlić, S. and Hadžić, I., 1997, Expanding the limits of 'equilibrium' second-moment turbulence closures, *Fluid Dyn. Res.* **20**, 25–41.

Hanjalić, K., Hadžić, I. and Jakirlić, S., 1999, Modeling turbulent wall flows subjected to strong pressure variations, *ASME J. Fluids Eng.* **12**, 57–64.

Hanjalić, K., Hadžiabdić, M., Temmerman, L. and Leschziner, M., 2004a, Merging LES and RANS strategies: zonal or seamless coupling? in *Direct and Large-Eddy Simulations* (Ed. R. Friedrich *et al.*), 451–464, Kluwer Academic, The Netherlands.

Hanjalić, K., Popovac, M. and Hadžiabdić, M., 2004b, A robust near-wall elliptic-relaxation eddy-viscosity turbulence model for CFD, *Int. J. Heat Fluid Flow* **25**, 1047–1051.

Hanjalić, K., Laurence, D., Popovac, M. and Uribe, C., 2005, Turbulence model and its application to forced and natural convection, in *Engineering Turbulence Modelling and Experiments*, Vol. 6 (Ed. W. Rodi and M. Mulas), 67–76, Elsevier, Amsterdam.

Hanjalić, K., Borello, D., Delibra, G. and Rispoli, F., 2015, Hybrid LES/RANS of internal flows: a case for more advanced RANS, in *Progress in Hybrid RANS-LES Modelling*, NNFM, Vol. 130 (Ed. S. Girimaji *et al.*), 19–35, Springer, Switzerland.

Harris, V. G., Graham, J. A. and Corrsin, S., 1977, Further experiments on a nearly homogeneous turbulent shear flow, *J. Fluid Mech.* **81**, 657–687.

Heinz, S., 2020, A review of Hybrid RANS-LES methods for turbulent flows: concepts and applications, *Prog. Aerosp. Sci.* **114**(100597), 1–25.

Hino, M., Kashiwayanagi, M., Nakayama, A. and Hara, T., 1983, Experiments on the turbulence statistics and the structure of a reciprocating oscillatory flow, *J. Fluid Mech.* **131**, 364–400.

Hinze, J. O., 1973, Experimental investigation on secondary currents in turbulent flow through a straight conduit, *Appl. Sci. Res.* **28**, 453–465.

Hinze, J. O., 1975, *Turbulence*, 2nd ed., McGraw Hill, New York.

Hoffmann, G. and Benocci, C., 1995, Approximate wall boundary conditions for large eddy simulations, in *Advances in Turbulence V* (Ed. R. Benzi), 222–228, Springer.

Hogg, S. and Leschziner, M., 1989, Computation of highly swirling confined flow with a Reynolds stress turbulence model, *AIAA J.* **27**, 57–63.

Holgate, J., Skillen, A., Craft, T. and Revell, A., 2019, A review of embedded large eddy simulation for internal flows, *Arch. Comput. Meth. Eng.* **26**(4), 865–882.

Hossain, M. S. and Rodi, W., 1982, A turbulence model for buoyant flows and its application to vertical buoyant jets, in *Turbulent Buoyant Jets and Plumes*, HMT Series, Vol. 6 (Ed. W. Rodi), 122–178, Pergamon Press, Oxford.

Hoyas, S. and Jimenez, J., 2006, Scaling of velocity fluctuations in turbulent channels up to $\mathrm{Re}_t = 2003$, *Phys. Fluids* **18**, 0011702, http://torroja.dmt.upm.es/ftp/channels/data/.

Hoyas, S. and Jimenez, J., 2008, Reynolds number effects on the Reynolds-stress budgets in turbulent channels, *Phys. Fluids* **20**, 101511.

Hrebtov, M. and Hanjalić, K., 2017, Numerical study of winter diurnal convection over the city of Krasnoyarsk: effects of non-freezing river, undulating fog and steam devils, *Boundary Layer Meteorol.* **3**, 469–495.

Hrebtov, M. and Hanjalić, K., 2019, River-induced anomalies in seasonal variation of traffic-emitted CO distribution over the City of Krasnoyarsk, *Atmosphere* **10**(7), 407.

Huang, P. G., 1986, *The computation of elliptic turbulent flows with second-moment-closure models*, PhD Thesis, Faculty of Technology, University of Manchester, Manchester, UK.

Hussain, A. K. M. F., 1983, Coherent structures – reality and myth, *Phys. Fluids* **26**, 2816–2850.

Hussain, A. K. M. F., 1986, Coherent structures and turbulence, *J. Fluid Mech.* **173**, 303–356.

Hussain, A. K. M. F. and Reynolds, W. C., 1972, The mechanics of an organized wave in turbulent shear flow. Part 3. Theoretical models and comparisons with experiments, *J. Fluid Mech.* **54**, 263–288.

Hussaini, M. Y., Speziale, C. G. and Zang, T. A., 1989, Discussion of the potential and limitations of direct and large-eddy simulations, NASA CR-181892, ICASE Report 89-61.

Hussein, J. H., Capp, S. and George, W. K., 1994, Velocity measurements in a high-Reynolds-number momentum-conserving axisymmetric turbulent jet, *J. Fluid Mech.* **258**, 31–75.

Iacovides, H. and Launder, B. E., 1985, ASM predictions of turbulent momentum and heat transfer in coils and U-bends, in *Numerical Methods in Laminar and Turbulent Flow* (Ed. C. Taylor *et al.*), 1023–1045, Pineridge Press, Swansea.

Iacovides, H. and Raisee, M., 1997, Computation of flow and heat transfer in 2D rib-roughened passages, in *Turbulence, Heat and Mass Transfer 2*, Supplement (Ed. K. Hanjalić and T. Peeters), Delft University Press, Delft, The Netherlands (see also *Int. J. Num. Meth. Heat Fluid Flow* **11**, 138–155, 2001).

Iacovides, H. and Raisee, M., 1999, Recent progress in the computation of flow and heat transfer in internal cooling passages of turbine blades, *Int. J. Heat Fluid Flow* **20**, 320–328.

Iacovides, H. and Toumpanakis, P., 1993, A turbulence modeling of flow in axisymmetric rotor-stator systems, *Proc. IAHR Int. Symp. on Refined Flow Modelling and Turbulence Measurements*, Paris, France.

Iacovides, H., Launder, B. E. and Loizou, P. A., 1987, Numerical computation of flow through a 90° bend, *Int. J. Heat Fluid Flow* **8**, 320–325.

Iacovides, H., Nikas, K. S. and Te Braak, M., 1996, Turbulent flow computations in rotating cavities using Low-Reynolds-number models, Paper 96-GT-159, *ASME Int. Gas Turbine Congress*, Birmingham, UK.

Iacovides, H., Launder, B. E. and Zacharos, A., 2009, The economical computation of unsteady flow structures in rotating cavities, *Proc. 6th Int. Symp. on Turbulence & Shear Flow Phenomena*, 797–802.

Ilyushin, B. B., 2002, Higher moment diffusion in stable stratification, in *Closure Strategies for Turbulent and Transitional Flows* (Ed. B. E. Launder and N. D. Sandham), 424–448, Cambridge University Press, Cambridge.

Ince, N. Z. and Launder, B. E., 1989, On the computation of buoyancy-driven turbulent flows in rectangular enclosures, *Int. J. Heat Fluid Flow* **10**, 110–117.

Ince, N. Z. and Launder, B. E., 1995, Three-dimensional and heat-loss effects on turbulent flow in a nominally two-dimensional cavity, *Int. J. Heat Fluid Flow* **16**, 171–177.

Itoh, M., Yamada, Y., Imao, S. and Gonda, M., 1990, Experiments on turbulent flow due to an enclosed rotating disk, in *Proc. 1st Conf. on Engineering Turbulence Modelling & Measurements* (Ed. W. Rodi and E. N. Ganić), 659–668, Elsevier Science, New York.

Jackson, J. D., Cotton, M. A. and Axcell, B. P., 1989, Studies of mixed convection in vertical tubes, *Int. J. Heat Fluid Flow* **10**, 2–15.

Jackson, J. D., He, S., Xu, Z. and Wu, T., 2002, CFD quality and trust: generic studies of thermal convection, Technical Report HTH/GNSR/5029, University of Manchester, Manchester, UK.

Jakirlić, S., 1997, *Reynolds-Spannungs-Modellierung komplexer turbulenter Strömungen*, Doktor Arbeit, Universität Erlangen-Nürnberg, Germany; Herbert Utz Verlag, Munich.

Jakirlić, S., 2004, *A DNS-based scrutiny of RANS approaches and their potential for predicting turbulent flows*, Habilitation Thesis, Technishe Universität Darmstadt, Germany.

Jakirlić, S. and Hanjalić, K., 1995, A second-moment closure for non-equilibrium separating high and low Re-number flows, *Proc. 10th Symp. on Turbulent Shear Flows*, Vol. 3, Pennsylvania State University, Pennsylvania, 23.25–23.30.

Jakirlić, S. and Hanjalić, K., 2002, A new approach to modelling near-wall turbulence energy and stress dissipation, *J. Fluid Mech.* **459**, 139–166.

Jakirlić, S. and Maduta, R., 2015, Extending the bounds of 'steady' RANS-closures: toward an instability-sensitive Reynolds stress model, *Int. J. Heat Fluid Flow* **51**, 175–194.

Jakirlić, S., Volkert, J., Pascal, H., Hanjalić, K. and Tropea, C., 2000, DNS, experimental and modelling study of axially compressed in-cylinder swirling flow, *Int. J. Heat Fluid Flow* **21**, 627–639.

Jakirlić, S., Hanjalić, K. and Tropea, C., 2002, Modeling rotating and swirling flows: a perpetual challenge, *AIAA J.* **40**, 1984–1996.

Jakirlić, S., Kniesner, B., Kadavelil, G., Gnirß, M. and Tropea, C., 2009, Experimental and computational investigations of flow and mixing in a single-annular combustor configuration, *Flow, Turbulence Combust.* **83**(3), 425–448.

Jakirlić, S., Kadavelil, G., Kornhaas, M., Schäfer, M., Sternel, D. C. and Tropea, C., 2010, Numerical and physical aspects in LES and Hybrid LES/RANS of turbulent flow separation in a 3-D diffuser, *Int. J. Heat Fluid Flow* **31**(5), 820–832.

Jakirlić, S., Kutej, L., Basara, B. and Tropea, C., 2014, Computational study of the aerodynamics of a realistic car model by means of RANS and Hybrid RANS/LES approaches, *SAE Int. J. Passeng. Cars – Mech. Syst.* **7**(2), 559–574.

Jakirlić, S., Kutej, L., Basara, B. and Tropea, C., 2018, Scale-resolving simulation of an 'on-road' overtaking maneuver involving model vehicles, Technical Paper 2018-01-0706, SAE International.

Jakirlić, S., Kutej, L., Basara, B. and Tropea, C., 2020, On PANS ζ-f model assessment by reference to car aerodynamics, in *Progress in Hybrid RANS-LES Modelling*, NNFM, Vol. 143 (Ed. Y. Hoarau *et al.*), 143–156, Springer Nature, Switzerland.

Jarrin, N., Benhamadouche, S., Laurence, D. and Prosser, R., 2006, A synthetic- eddy method for generating inflow conditions for large-eddy simulations, *Int. J. Heat Fluid Flow* **27**(4), 585–593.

Jayatilleke, C. L. V., 1969, The influence of Prandtl number and surface roughness on the resistance of the laminar sub-layer to momentum and heat transfer, *Prog. Heat Transfer* **1**, 193–199.

Ji, H. C. and Gardner, R. A., 1997, Numerical analysis of turbulent pipe flow in a transverse magnetic field, *Int. J. Heat Mass Transfer* **40**, 1839–1851.

Johansson, A. V. and Hällback, M., 1994, Modelling of rapid pressure strain in Reynolds stress closures, *J. Fluid Mech.* **269**, 143–168.

Johansson, S. H., Davidson, L. and Olsson, E., 1993, Numerical simulation of vortex shedding past triangular cylinder at high Reynolds number using a $k-\varepsilon$ turbulence model, *Int. J. Num. Meth. Fluids* **16**, 859–878.

Johnston, J. P., Halleen, R. M. and Lezius, D. K., 1972, Effects of spanwise rotation on the structure of two-dimensional, fully-developed channel flow, *J. Fluid Mech.* **56**, 533.

Jones, W. P., 1971, *Laminarization in strongly accelerated boundary layers*, PhD Thesis, Faculty of Engineering, University of London, UK.

Jones, W. P. and Launder, B. E., 1972a, The prediction of laminarization with a two-equation model of turbulence, *Int. J. Heat Mass Transfer* **15**, 301–314.

Jones, W. P. and Launder, B. E., 1972b, Some properties of sink flow turbulent boundary layers, *J. Fluid Mech.* **56**, 337–351.

Jones, W. P. and Manners, A., 1989, The calculation of the flow through a two-dimensional faired diffuser, in *Turbulent Shear Flows 6* (Ed. J. C. André *et al.*), 18–31, Springer Verlag, Heidelberg.

Jones, W. P. and Musonge, P., 1988, Closure of the Reynolds stress and scalar flux equation, *Phys. Fluids* **31**, 3589–3604.

Jovanović, J., 2004, *The Statistical Dynamics of Turbulence*, Springer, Berlin Heidelberg.

Jovanović, J., Ye, Q. Y. and Durst, F., 1995, Statistical interpretation of the turbulent dissipation rate in wall-bounded flows, *J. Fluid Mech.* **293**, 321–347.

Jović, S. and Driver, D. M., 1994, Backward-facing step measurements at low Reynolds number, $\mathrm{Re_H} = 5000$, NASA Report TM 108807.

Kader, B. A., 1981, Temperature and concentration profiles in fully turbulent boundary layers, *Int. J. Heat Mass Transfer* **24**, 1541–1544.

Kasagi, N. and Matsunaga, A., 1995, Three-dimensional particle-tracking velocimetry of turbulence statistics and energy budget in a backward-facing step flow, *Int. J. Heat Fluid Flow* **16**, 477–485.

Kato, M. and Launder, B. E., 1993, The modelling of turbulent flow around stationary and vibrating square cylinders, Paper 10.4, *Proc. 9th Symp. on Turbulent Shear Flows*, Kyoto, Japan.

Kawamura, H., Sasaki, J. and Kobayashi, K., 1995, Budget and modelling of triple-moment velocity correlations in a turbulent channel flow based on DNS, *Proc. 10th Symp. on Turbulent Shear Flows*, Pennsylvania State University, Pennsylvania.

Kays, W. M. and Moffat, R. J., 1975, The behaviour of transpired turbulent boundary layers, in *Studies in Convection 1* (Ed. B. E. Launder), 223–319, Academic Press, London.

Kays, W. M., Crawford, M. E. and Weigand, G., 2004, *Convective Heat and Mass Transfer*, McGraw Hill, New York.

Keating, A. and Piomelli, U., 2006, A dynamic stochastic forcing method as a wall- layer model for large-eddy simulation, *J. Turbulence* **7**(12), 1–24.

Kebede, W., Launder, B. E. and Younis, B. A., 1985, Large-amplitude periodic pipe flow: a second-moment closure study, *Proc. 5th Symp. on Turbulent Shear Flows*, Cornell University, Ithaca, NY, 16.23–16.28.

Kenjereš, S., 1999, *Numerical modelling of complex buoyancy-driven flows*, PhD Thesis, Delft University of Technology, Delft, The Netherlands.

Kenjereš, S. and Hanjalić, K., 1996, Prediction of turbulent thermal convection in concentric and eccentric horizontal annuli, *Int. J. Heat Fluid Flow* **15**, 430–439.

Kenjereš, K. and Hanjalić, K., 1999, Transient analysis of Rayleigh–Bénard convection with a RANS model, *Int. J. Heat Fluid Flow* **20**, 329–340.

Kenjereš, S. and Hanjalić, K., 2000a, Convective rolls and heat transfer in finite-length Rayleigh–Bénard convection: a two-dimensional numerical study, *Phys. Rev. E* **62**, 1–12.

Kenjereš, S. and Hanjalić, K., 2000b, On the implementation of effects of Lorentz force in turbulence closure models, *Int. J. Heat Fluid Flow* **21**, 329–337.

Kenjereš, K. and Hanjalić, K., 2002, Combined effects of terrain orography and thermal stratification on pollutant dispersion in a town valley: a T-RANS simulation, *J. Turbulence* **3**, 1–21, http://jot.iop.org/ S1468-5248(02)3599-1.

Kenjereš, S. and Hanjalić, K., 2004, Numerical simulation of magnetic control of heat transfer in thermal convection, *Int. J. Heat Fluid Flow* **25**, 559–568.

Kenjereš, K. and Hanjalić, K., 2006, LES, T-RANS and hybrid simulations of thermal convection at high Ra numbers, *Int. J. Heat Fluid Flow* **27**, 800–810.

Kenjereš, S. and Hanjalić, K., 2007, Numerical insight into magnetic dynamo action in a turbulent regime, *New J. Phys.* **9**, 1–29.

Kenjereš, K. and Hanjalić, K., 2009, Tackling complex turbulent flows with transient RANS, *Fluid Dyn. Res.* **41**, 1–32.

Kenjereš, K., Hanjalić, K. and Gunarjo, S. B., 2002, A T-RANS/VLES approach to indoor climate simulations, FEDSM2002–31400, *Proc. ASME FEDSM'02*, Montreal, Canada.

Kenjereš, S., Hanjalić, K. and Bal, D., 2004, A direct-numerical-simulation-based second-moment closure for turbulent magnetohydrodynamic flows, *Phys. Fluids* **16**, 1229–1241.

Kenjereš, S., Gunarjo, S. B. and Hanjalić, K., 2005, Contribution to elliptic relaxation modelling of turbulent natural and mixed convection, *Int. J. Heat Fluid Flow* **26**, 569–586.

Kenjereš, S., Hagenzieker, R. and Hanjalić, K., 2006a, Numerical simulations of turbulent flows over hill and complex urban areas with dispersion of pollutants, *Proc. 13th Int. Conf. Fluid Flow Technology (CMFF'06)*, Budapest, Hungary.

Kenjereš, S., Hanjalić, K. and Renaudier, S., 2006b, Coupled fluid-flow and magnetic-field simulation of the Riga dynamo experiment, *Phys. Plasma* **13**, 1–13.

Kidger, J. W., 1999, *Turbulence modelling for stably stratified flows and free-surface jets*, PhD Thesis, Department of Mechanical, Aeronautical and Manufacturing Engineering, UMIST, Manchester, UK.

J. Kim, 1989, Personal communication.

Kim, J., Moin, P. and Moser, R. D., 1987, Turbulence statistics in fully-developed channel flow at low Reynolds number, *J. Fluid Mech.* **177**, 133.

Kim, K. R., Cotton, M. A., Craft, T. J. and Heynes, O. R., 2008, On the dynamics and frequency response of fully-pulsed turbulent round jets: computations using two-time-scale/strain sensitized eddy viscosity models, *Int. J. Heat Fluid Flow* **29**, 1650–1669.

Kitoh, O., 1991, Experimental study of turbulent swirling flow in a straight pipe, *J. Fluid Mech.* **225**, 445–479.

Klein, M., Sadiki, A. and Janicka, J., 2003, A digital filter based generation of inflow data for spatially developing direct numerical or large eddy simulations, *J. Comput. Phys.* **186**(2), 652–665.

Kline, S. J., Reynolds, W. C., Schraub, F. A. and Runstadler, P. W., 1967, The structure of turbulent boundary layers, *J. Fluid Mech.* **30**, 741–773.

Kline, S. J., Morkovin, M. V., Sovran, G. and Cockrell, D. J., 1969, *Proc. Computation of Turbulent Boundary Layers, AFOSR-IFP-Stanford Conference*, Stanford University, Stanford, CA.

Kline, S. J., Cantwell, B. J. and Lilley, G. M., 1981, *Proc. AFOSR-HTTM-Stanford Conf. on Complex Turbulent Flows: Comparison of Computations and Experiments, Vol. 1, Objectives, Evaluation of Data, Specification of Test Cases*, Thermosciences Division, Stanford University, Stanford, CA.

Kline, S. J., Cantwell, B. J. and Lilley, G. M., 1982, *Proc. AFOSR-HTTM-Stanford Conf. on Complex Turbulent Flows: Comparison of Computations and Experiments, Vol. 2, Taxonomies, Reporters' Summaries Evaluation and Conclusions*, Thermosciences Division, Stanford University, Stanford, CA.

Kniesner, B., Šaric, S., Mehdizadeh, A., Jakirlic, S., Hanjalić, K., Tropea, C., Sternel, D., Gauß, F. and Schäfer, M., 2007, Wall treatment in LES by RANS models: method development and application to aerodynamic flows and swirl combustors, *ERCOFTAC Bull.* **72**, 33–40.

Köhler, F., Maduta, R., Krumbein, B. and Jakirlic, S., 2020, Scrutinizing conventional and eddy-resolving unsteady RANS approaches in computing the flow and aeroacoustics past a tandem cylinder, in *New Results in Numerical and Experimental Fluid Mechanics XII*, NNFM, Vol. 142 (Ed. A. Dillmann *et al.*), 586–596, Springer.

Kolmogorov, A. N., 1941, The local structure of turbulence in an incompressible viscous fluid for very large Reynolds numbers, *Dokl. Akad. Nauk SSSR* **30**, 299–303.

Kolmogorov, A. N., 1942, Equations of motion of an incompressible fluid, *Dokl. Akad. Nauk SSSR* **30**, 299–303.

Kolovandin, B. A. and Vatutin, I. A., 1972, On the statistical theory of non-uniform turbulence, *Int. J. Heat Mass Transfer* **15**, 2371–2383.

Kourta, A. and Ha Minh, H., 1991, Modified turbulence model to predict unsteady separated flow, *Proc. 7th Int. Conf. on Numerical Methods in Laminar and Turbulent Flow*, Vol. **7**, Part 1, Pineridge Press, Stanford, CA, 469–479.

Kovasznay, L. S. G. and Ali, S. F., 1974, Structure of turbulence in the wake of a heated flat plate, *Proc. 5th Int. Heat Transfer Conf.*, Tokyo, Japan, 99–103.

Kraichnan, R. H., 1962, Turbulent thermal convection at arbitrary Prandtl number, *Phys. Fluids* **5**, 1374–1389.

Kristoffersen, R. and Andersson, H., 1993, Direct simulations of low-Reynolds-number turbulent flow in a rotating channel, *J. Fluid Mech.* **256**, 163–197.

Kristoffersen, R., Nilsen, P. J. and Andersson, H. I., 1990, Validation of Reynolds stress closures for rotating channel flows by means of direct numerical simulations, in *Engineering Turbulence Modelling and Experiments* (Ed. W. Rodi and E. N. Ganic), 55–64, Elsevier.

Krumbein, B., Maduta, R., Jakirlić, S. and Tropea, C., 2020, A scale-resolving elliptic-relaxation-based eddy-viscosity model: development and validation, in *New Results in Numerical and Experimental Fluid Mechanics XII*, NNFM, Vol. 142 (Ed. A. Dillmann *et al.*), 90–100, Springer.

Lai, Y. G. and So, R. M. C., 1990, On near-wall turbulent flow modelling, *J. Fluid Mech.* **221**, 641–673.

Lam, C. K. G. and Bremhorst, K. A., 1981, Modified form of the $k-\varepsilon$ model for predicting wall turbulence, *J. Fluids Eng.* **103**, 456–460.

Lamballais, O., Métais, O. and Lesieur, M., 1998, Spectral dynamic model for large-eddy simulations of turbulent rotating channel flow, *Theor. Comput. Fluid Dyn.* **12**, 149–177.

Laraufie, R., Deck, S. and Sagaut, P., 2011, A dynamic forcing method for unsteady turbulent inflow conditions, *J. Comput. Phys.* **230**(23), 8647–8663.

Launder, B. E., 1964a, Laminarization of the turbulent boundary layer by acceleration, Gas Turbine Lab Report #77 (also Sc.D. Thesis, 1965), Massachusetts Institute of Technology, Cambridge, MA.

Launder, B. E., 1964b, Laminarization of the turbulent boundary layer in a severe acceleration, *ASME J. Appl. Mech.* **31**, 707–709.

Launder, B. E., 1973, Scalar property transport by turbulence, Report HTS/73/26, Department of Mechanical Engineering, Imperial College, London.

Launder, B. E., 1975a, On the effects of a gravitational field on the turbulent transport of heat and momentum, *J. Fluid Mech.* **67**, 569–581.

Launder, B. E., 1975b, Progress in the modelling of turbulent transport, in *Prediction Methods for Turbulent Flow*, Lecture Series 76, Von Karman Institute for Fluid Dynamics, Rhode St Genèse, Belgium.

Launder, B. E., 1976, Heat and mass transport, in *Topics in Applied Physics: Turbulence*, Vol. 12 (Ed. P. Bradshaw), 231, Springer Verlag, Berlin.

Launder, B. E., 1982, A generalized algebraic stress transport hypothesis, *AIAA J.* **20**, 436–437.

Launder, B. E., 1986, Low-Reynolds-number turbulence near walls, Report TFD/86/4, Department of Mechanical Engineering, UMIST, Manchester, UK.

Launder, B. E., 1988, On the computation of convective heat transfer in complex turbulent flows, *ASME J. Heat Trans.* **110**, 1112–1128.

Launder, B. E., 1989, Second-moment closure: present... and future?, *Int. J. Heat Fluid Flow* **10**, 282–300.

Launder, B. E., 1993, An introduction to single-point closure methodology, in *Les Houches Summer School – 59 on Computational Fluid Dynamics* (Ed. M. Lesieur, P. Comte and J. Zinn-Justin), 257–325, Elsevier Science, Oxford.

Launder, B. E., 1996, An introduction to single-point closure methodology, in *Les Houches, Session LIX, 1993, Mécanique des Fluides Numérique/Computational Fluid Mechanics* (Ed. M. Lesieur, P. Comte and J. Zinn-Justin), 315, Elsevier Science, Amsterdam.

Launder, B. E., 2005, RANS modelling of turbulent flows affected by buoyancy or stratification, in *Prediction of Turbulent Flows* (Ed. G. F. Hewitt and J. C. Vassilicos), 50–127, Cambridge University Press, Cambridge.

Launder, B. E. and Jones, W. P., 1969, Sink flow turbulent boundary layers, *J. Fluid Mech.* **38**, 817–831.

Launder, B. E. and Li, S.-P., 1994, On the elimination of wall-topography parameters from second-moment closure, *Phys. Fluids* **6**, 999–1006.

Launder, B. E. and Morse, A. P., 1979, Numerical prediction of axisymmetric free shear flows with a Reynolds stress closure, in *Turbulent Shear Flows 1* (Ed. F. Durst *et al.*), 279–294, Springer Verlag, Heidelberg.

Launder, B. E. and Reynolds, W. C., 1983, Asymptotic near-wall stress dissipation rates in a turbulent flow, *Phys. Fluids* **26**, 1157–1158.

Launder, B. E. and Samaraweera, D. S. A., 1979, Application of a second-moment turbulence closure to heat and mass transport in thin shear flows – 1. Two-dimensional transport, *Int. J. Heat Mass Transfer* **22**, 1631–1643.

Launder, B. E. and Sandham, N. (Eds.), 2002, *Closure Strategies for Turbulent and Transitional Flows*, Cambridge University Press, Cambridge.

Launder, B. E. and Sharma, B. I., 1974, Application of the energy-dissipation model of turbulence to the calculation of flow near a spinning disc, *Lett. in Heat Mass Transfer* **1**, 131–138.
Launder, B. E. and Shima, N., 1989, Second-moment closure for the near-wall sublayer: development and application, *AIAA J.* **27**, 1319–1325.
Launder, B. E. and Spalding, D. B., 1972, *Mathematical Models of Turbulence*, Academic Press, London.
Launder, B. E. and Spalding, D. B., 1974, The numerical computation of turbulent flows, *Comput. Meth. Appl. Mech. Eng.* **3**, 269–289.
Launder, B. E. and Tselepidakis, D. P., 1993, Contribution to the modelling of near-wall turbulence, in *Turbulent Shear Flows 8* (Ed. F. Durst *et al.*), 81–96, Springer, Berlin.
Launder, B. E. and Tselepidakis, D. P., 1994, Application of a new second-moment closure to turbulent channel flow rotating in orthogonal mode, *Int. J. Heat Fluid Flow* **15**, 2–10.
Launder, B. E., Morse, A., Rodi, W. and Spalding, D. B., 1973, Prediction of free shear flows: a comparison of the performance of six turbulence models, *Free Turbulent Shear Flows, Vol. 1, Conference Proceedings*, NASA SP-321, Langley Research Center, Hampton, VA, 321–426.
Launder, B. E., Reece, G. J. and Rodi, W., 1975, Progress in the development of a Reynolds stress turbulence closure, *J. Fluid Mech.* **68**, 537–566.
Launder, B. E., Priddin, C. H. and Sharma, B. I., 1977, The calculation of turbulent boundary layer on spinning and curved surfaces, *J. Fluids Eng.* **99**, 231–239.
Launder, B. E., Tselepidakis, D. P. and Younis, B. A., 1987, A second-moment study of rotating channel flow, *J. Fluid Mech.* **183**, 63–75.
Launder, B. E., Poncet, S. and Serre, E., 2010, Laminar, transitional and turbulent flow in rotating disk cavities, *Ann. Rev. Fluid Mech.* **42**, 229–248.
Laurence, D. R., Uribe, J. C. and Utyuzhnikov, S. V., 2004, A robust formulation of the model, *Flow, Turbulence Combust*. **73**, 169–185.
Le, H., Moin, P. and Kim, J., 1997, Direct numerical simulation of flow over a backward-facing step, *J. Fluid Mech.* **330**, 349–374.
Lee, D, 1984, *Measurement of the turbulent transport downstream of an abrupt expansion in a circular duct with a constant wall temperature*. MS Thesis, Mech. Eng. Dept., University of Davis., CA.
Leslie, D. C., 1973, *Developments in the Theory of Turbulence*, Clarendon Press, Oxford.
Levchenya, A. M., Smirnov, E. M. and Goryachev, V. D., 2010, RANS-based numerical simulation and visualization of the horseshoe vortex system in the leading-edge endwall region of a symmetric body, *Int. J. Heat Fluid Flow* **31**, 1107–1112.
Li, S.-P., 1992, *Predicting riblet performance with engineering turbulence models*, PhD Thesis, Faculty of Technology, University of Manchester, Manchester, UK.
Liakopoulos, A., 1984, Explicit representations of the complete velocity profile in a turbulent boundary layer, *AIAA J.* **22**, 844–846.
Libby, P. A., 1975, Prediction of intermittent turbulent flows, *J. Fluid Mech.* **68**, 273–295.
Lien, F. S., and Kalitzin, G., 2001, Computations of transonic flow with the turbulence model, *Int. J. Heat Fluid Flow* **22**, 53–61.
Lien, F. S., Kalitzin, G. and Durbin, P. A., 1998, RANS modelling for compressible and transitional flows, *CTR Proc. Summer Program*, Stanford, CA, 267–286.
Lilly, D. K., 1992, A proposed modification of the Germano subgrid-scale closure method, *Phys. Fluids A* **4**(3), 633–635.

Lin, A. and Wolfshtein, M., 1979, Theoretical study of the Reynolds stress equations, in *Turbulent Shear Flows 1* (Ed. F. J. Durst *et al.*), 327–343, Springer Verlag, Heidelberg.

Lin, S. C. and Lin, S. C., 1973, Study of strong temperature mixing in subsonic grid-generated turbulence, *Phys. Fluids* **16**, 1587–1598.

Litvinov, I., Shtork, S., Gorelikov, E., Mitryakov, A. and Hanjalić, K., 2018, Unsteady regimes and pressure pulsations in draft tube of a model hydro-turbine in a range of off-design conditions, *Exp. Therm. Fluid Sci.* **91**, 410–422.

Liu, N.-S. and Shih, T.-H., 2006, Turbulence modeling for very large-eddy simulation, *AIAA J.* **44**(4), 687–697.

Lumley, J. L., 1967, Similarity and the turbulent energy spectrum, *Phys. Fluids* **10**, 855–858.

Lumley, J. L., 1975a, Introduction, in *Prediction Methods for Turbulent Flow*, Lecture Series 76, Von Karman Institute for Fluid Dynamics, Rhode St Genèse, Belgium.

Lumley, J. L., 1975b, Pressure-strain correlation, *Phys. Fluids* **18**, 750.

Lumley, J. L., 1978, Computational modeling of turbulent flows, *Adv. Appl. Mech.* **18**, 123–176.

Lumley, J. L. and Khajeh-Nouri, B., 1973, Modeling homogeneous deformation of turbulence, Sibley School of Mechanical and Aerospace Engineering, Cornell University, Ithaca, NY.

Lumley, J. L. and Khajeh Nouri, B., 1974, Computational modeling of turbulent transport, *Proc. 2nd IUGG-IUTAM Symp. on Atmospheric Diffusion in Environmental Pollution*, Academic Press, London.

Lumley, J. L. and Newman, G. R., 1977, The return to isotropy of homogeneous turbulence, *J. Fluid Mech.* **82**, 162–178.

Lund, T. S., Wu, X. and Squires, K. D., 1998, Generation of turbulent inflow data for spatially-developing boundary layer simulations, *J. Comput. Phys.* **140**(2), 233–258.

Lykoudis, P. S. and Brouillette, E. C., 1967, Magneto-fluid-mechanic channel flow. II. Theory, *Phys. Fluids* **10**, 1002–1007.

Maden, I., Maduta, R., Kriegseis, J., Jakirlić, S., Grundmann, S. and Tropea, C., 2015, Plasma-actuated manipulation of secondary flow towards pressure recovery enhancement in a 3D diffuser: modelled by an eddy-resolving second-moment closure, *Flow, Turbulence Combust.* **95**, 377–398.

Maduta, R. and Jakirlić, S., 2018, On the von Karman length scale as a triggering parameter in eddy-resolving simulations of turbulent flows, in *Progress in Hybrid RANS-LES Modelling 6*, NNFM, Vol. **137** (Ed. Y. Hoarau *et al.*), 179–193, Springer.

Maduta, R., Urlich, M. and Jakirlić, S., 2017, Reynolds-stress modelling of wake interference of two-cylinders in tandem: conventional vs eddy-resolving closure, *Int. J. Heat Fluid Flow* **67**, 139–148.

Magnaudet, J., 1992, The modelling of inhomogeneous turbulence in the absence of mean velocity gradients, *4th Eur. Turbulence Conf.*, Delft, The Netherlands.

Malecki, P., 1994, *Etude de modèles de turbulence pour les couches limites tridimensionelles*, PhD Thesis, ONERA-CERT, Toulouse, France.

Manceau, R., 2005, An improved version of the elliptic blending model application to non-rotating and rotating channel flows, *Proc. 4th Int. Symp. on Turbulence & Shear Flow Phenomena*, Williamsburg, VA, 259–264.

Manceau, R. and Hanjalić, K., 2000, A new form of the elliptic relaxation equation to account for wall effects in RANS modelling, *Phys. Fluids* **12**, 2345–2351.

Manceau, R. and Hanjalić, K., 2002, The elliptic blending model: a new near-wall Reynolds-stress closure, *Phys. Fluids* **14**, 744–754.

Manceau, R., Wang, M. and Laurence, D., 2001, Inhomogeneity and anisotropy effects on the redistribution term in RANS modelling, *J. Fluid Mech.* **438**, 307–338.

Mansour, N. N., Kim, J. and Moin, P., 1988, Reynolds-stress and dissipation-rate budgets in a turbulent channel flow, *J. Fluid Mech.* **194**, 15–44.

Martinat, G., Braza, M., Hoarau, Y. and Harran, G., 2008, Turbulence modelling of the flow past a pitching NACA0012 airfoil at 10^5 and 10^6 Reynolds numbers, *J. Fluid Struct.* **24**(8), 1294–1303.

Marusic, I., Kunkel, G. J. and Porté-Agel, F., 2001, Experimental study of wall boundary conditions for large-eddy simulation, *J. Fluid Mech*. **446**, 309–320.

Mason, P. J. and Callen, N. S., 1986, On the magnitude of the subgrid-scale eddy coefficient in large-eddy simulations of turbulent channel flow, *J. Fluid Mech.* **162**, 439–462.

Mathieu, J. and Jeandel, D., 1984, Turbulence et approche spectrale, in *Turbulence Models and their Applications*, Vol. 1, 1–213, Eyrolles, Paris.

McGuirk, J. J. and Papadimitriou, C., 1988, Stably stratified free-surface shear layers with internal hydraulic jumps, in *Stably Stratified Flows and Dense Gas Dispersion*, IMA Conference Series (Ed. J. S. Puttock), 385–407, Oxford University Press, Oxford.

Medić, G. D. and Durbin, P., 2002, Towards improved heat transfer on turbine blades, *J. Turbomachinery* **124**, 187–192.

Mellor, G. L., 1973, Analytical prediction of the properties of stratified planetary surface layers, *J. Atmos. Sci.* **30**, 1061–1069.

Mellor, G. L. and Herring, H. J., 1973, A survey of the mean turbulent field closure models, *AIAA J*. **11**, 590–599.

Mellor, G. L. and Yamada, T., 1974, A hierarchy of turbulence closure models for planetary boundary layers, *J. Atmos. Sci.* **31**, 1791–1806.

Meneveau, C., Lund, T. S. and Cabot, W. H., 1996, A Lagrangian dynamic sub-grid-scale model of turbulence, *J. Fluid Mech.* **319**, 353–385.

Menter, F. R., 1994, Two-equation eddy-viscosity turbulence models for engineering applications, *AIAA J*. **32**, 1598–1605.

Menter, F. R., 2003, Zonal two-equation $k - \omega$ turbulence model for aerodynamic flows, AIAA Paper 1993-2906.

Menter, F. R. and Egorov, Y., 2005, A scale adaptive simulation model using two- equation models, AIAA Paper 2005-1095, *43rd AIAA Aerospace Sciences Meeting and Exhibit*.

Menter, F. R. and Egorov, Y., 2010, The scale-adaptive simulation method for unsteady turbulent flows predictions, Part 1: theory and model description, *Flow, Turbulence Combust*. **85**, 113–138.

Menter, F. R. and Kuntz, M., 2004, Adaptation of eddy-viscosity turbulence models to unsteady separated flow behind vehicles, in *The Aerodynamics of Heavy Vehicles: Trucks, Busses and Trains*, Lecture Notes in Applied and Computational Mechanics, Vol. 19 (Ed. R. McCallen *et al*.), 339–352, Springer, Berlin Heidelberg.

Menter, F. R., Langtry, R. and Kuntz, M., 2003, Ten years of industrial experience with the SST turbulence model, in *Turbulence Heat and Mass Transfer 4* (Ed. K. Hanjalić, Y. Nagano and M. Tummers), 625–632, Begell House, New York.

Millionshtchikov, M. D., 1941, On the theory of homogeneous isotropic turbulence, *C. R. Acad. Sci. SSSR* **32**, 615–619.

Minakov, A., Platonov, D., Litvinov, I., Shtork, S. and Hanjalić, K., 2017, Vortex ropes in draft tube of a laboratory Kaplan hydroturbine at low load: an experimental and LES scrutiny of RANS and DES computational models, *J. Hydraul. Res.* **55**(5), 668–685.

Mockett, C., Fuchs, M., Garbaruk, A., Shur, M., Spalart, P., Strelets, M., Thiele, F. and Travin, A., 2015, Two non-zonal approaches to accelerate RANS to LES transition of free shear layers in DES, in *Progress in Hybrid RANS-LES Modelling*, NNFM, Vol. 130 (Ed. S. Girimaji *et al.*), 19–35, Springer, Switzerland.

Moin, P. and Kim, J., 1982, Numerical investigation of turbulent channel flow, *J. Fluid Mech.* **118**, 341–377.

Moin, P. and Kim, J., 1997, Tackling turbulence with supercomputers, *Sci. Am.* **276**(1), 62–68.

Monin, A. S., 1965, On the symmetry of turbulence in the surface layer of air, *Izv. Atm. Oceanic Phys.* **1**, 45.

Monin, A. S. and Yaglom, A. M., 1975, *Statistical Fluid Mechanics*, Vol. 2, MIT Press, Cambridge, MA.

Moreau, R., 1990, *Magnetohydrodynamics* (translated from French), Kluwer Academic, Dordrecht.

Moretti, P. M. and Kays, W. M., 1965, Heat transfer to a turbulent boundary layer with varying surface temperature – an experimental study, *Int. J. Heat Mass Transfer* **8**, 1187–1202.

Morse, A. P., 1980, *Axisymmetric free shear flows with and without swirl*, PhD Thesis, Faculty of Engineering, University of London, UK.

Moser, D., Kim, J. and Mansour, N. N., 1999, Direct numerical simulation of turbulent channel flow up to $\mathrm{Re}_t = 590$, *Phys. Fluids* **11**, 943–945.

Musker, A. J., 1979, Explicit expression for the smooth wall velocity distribution in a turbulent boundary layer, *AIAA J*. **17**, 655–657.

Myong, H. K. and Kasagi, N., 1990, Prediction of anisotropy of the near wall turbulence with an anisotropic low-Reynolds-number model of turbulence, *J. Fluids Eng.* **112**, 521–524.

Nagano, Y., 2002, Modelling heat transfer in near-wall flows, in *Closure Strategies for Turbulent and Transitional Flows* (Ed. B. E. Launder and N. D. Sandham), 188–247, Cambridge University Press, Cambridge.

Nagano, Y. and Tagawa, M., 1991, Turbulence model for triple velocity and scalar correlations, in *Turbulent Shear Flows 7* (Ed. F. Durst *et al.*), 47–62, Springer, Berlin.

Nagano, Y., Tagawa, M. and Tsuji, T., 1993, Effects of adverse pressure gradients on mean flows and turbulence statistics in a boundary layer, in *Turbulent Shear Flows 8* (Ed. F. Durst *et al.*), 7–21, Springer, Berlin.

Nagano, Y., Tsuji, T. and Houra, T., 1998, Structure of turbulent boundary layer subjected to adverse pressure gradient, *Int. J. Heat Fluid Flow* **19**, 563–572.

Naot, D., 1994, Response of shear flow turbulence to diffusional electromagnetic fluctuations: transverse magnet, *Appl. Math. Modelling* **18**, 23–31.

Naot, D. and Rodi, W., 1982a, Calculation of secondary currents in channel flow, *J. Hydraulics* **108**, 948–968.

Naot, D. and Rodi, W., 1982b, Numerical simulation of secondary currents in channel flow, *Trans. ASCE J. Hydr. Div.* **108**, 948–968.

Naot, D., Shavit, A. and Wolfshtein, M., 1970, Interactions between components of the turbulent correlation tensor, *Isr. J. Technol.* **8**, 259–269.

Naot, D., Shavit, A. and Wolfshtein, M., 1973, Two-point correlation model and the redistribution of Reynolds stress, *Phys. Fluids* **16**, 738.

Naot, D., Peled, A. and Tanny, J., 1990, Response of shear flow turbulence to diffusional electromagnetic fluctuations, *Appl. Math. Modelling* **14**, 226–236.
Nee, V. W. and Kovasznay, L. S. G., 1969, Simple phenomenological theory of turbulent shear flows, *Phys. Fluids* **12**, 473–484.
Nejad, A. S., Favaloro, S. C., Vanka, S. P., Samimy, M. and Langenfeld, C., 1989, Application of laser velocimetry for characteristics of confined swirling flows, *ASME J. Eng. Gas Turbines Power* **111**, 36–45.
Newman, B. G., Patel, R. P., Savage, S. B. and Tjio, H. K., 1972, Three-dimensional wall jet originating from a circular orifice, *Aero. Q.* **23**, 693–698.
Newman, G. R., Launder, B. E. and Lumley, J. L., 1981, Modelling the behaviour of homogeneous scalar turbulence, *J. Fluid Mech.* **111**, 217–232.
Ng, K. H. and Spalding, D. B., 1972, Turbulence model for boundary layers near walls, *Phys. Fluids* **15**, 20–30.
Ng, E. Y. K., Tan, H. Y., Lim, H. N. and Choi, D., 2002, Near-wall function for turbulence closure models, *Comput. Mech.* **29**, 178–181.
Nicoud, F. and Ducros, F., 1999, Sub-grid-scale stress modelling based on the square of the velocity gradient tensor, *Flow, Turbulence and Combust*. **62**, 183–200.
Nishibori, K., Kikuyama, K. and Murakami, M., 1987, Laminarization of turbulent flow in the inlet region of an axially rotating pipe, *JSME Int. J.* **30**, 255–262.
Nisizimi, S. and Yoshizawa, A., 1987, Turbulent channel and Couette flows using an anisotropic $k - \varepsilon$ model, *AIAA J.* **25**, 414–420.
Noguchi, H., Ohtsubo, Y. and Kasagi, N., 1998, Personal communication, DNS database, ftp.thlab.t.u-tokyo.ac.jp.
Obi, S., Aoki, K. and Madsuda, S., 1993, Experimental and computational study of flow in an asymmetric plane diffuser, *Proc. 9th Symp. on Turbulent Shear Flows*, Kyoto, Japan.
Okamoto, N., Yoshimatsu, K., Schneider, K., Farge, M. and Kaneda, Y., 2007, Coherent vortices in high resolution direct numerical simulation of homogeneous isotropic turbulence: a wavelet viewpoint, *Phys. Fluids* **19**(11), 115109.
Orlandi, P. and Fatica, M., 1997, Direct simulations of turbulent flow in a pipe rotating about its axis, *J. Fluid Mech.* **343**, 43–72.
Page, F., Corcoran, W. H., Schlinger, W. G. and Sage, B. H., 1952, Temperature and velocity distributions in uniform flow between parallel plates, *Ind. Eng'g. Chem.* **44**, 419–424.
Palkin, E., Mullyadzhanov, R., Hadžiabdić, M. and Hanjalič, K., 2016, Scrutinizing URANS in shedding flows: the case of cylinder in cross-flows in the subcritical regime, *Flow, Turbulence Combust.* **97**, 1017–1046.
Pamiès, M., Weiss, P. E., Garnier, E., Deck, S. and Sagaut, P., 2009, Generation of synthetic turbulent inflow data for large eddy simulation of spatially evolving wall-bounded flows, *Phys. Fluids* **21**, 045103.
Panchapakesan, N. R. and Lumley, J. L., 1993, Turbulence measurements in axisymmetric jets of air and helium. Part 1: air jets, *J. Fluid Mech.* **246**, 197–223.
Patankar, S. V. and Spalding, D. B., 1967, *Heat and Mass Transfer in Boundary Layers*, Morgan-Grampian Press, London.
Patankar, S. V. and Spalding, D. B., 1970, *Heat and Mass Transfer in Boundary Layers*, 2nd ed., International Textbook Co., London.
Patel, V. C. and Head, M. R., 1969, Some observations on skin friction and velocity profiles in fully-developed pipe and channel flows, *J. Fluid Mech.* **38**, 161–201.
Patel, V. C., Rodi, W. and Scheuerer, G., 1985, Turbulence models for near-wall and low Reynolds number flows, *AIAA J*. **23**, 1308–1319.

Peng, S.-H., Hanjalić, K. and Davidson, L., 2006, Large-eddy simulation and deduced scaling analysis of Rayleigh–Bénard convection up to Ra = 10^9, *J. Turbulence* **7**(66), 1–29.

Perkins, K. R. and McEligot, D. M., 1975, Mean temperature profiles in heated laminarizing air flows, *ASME J. Heat Transfer* **97**, 589–593.

Perot, B. and Moin, P., 1995, Shear-free turbulent boundary layers, *J. Fluid Mech.* **295**, 199–245.

Perret, L., Delville, J., Manceau, R. and Bonnet, J.-P., 2008, Turbulent inflow conditions for large-eddy simulation based on low-order empirical model, *Phys. Fluids* **20**(7), 075107.

Pettersson Reif, B. A., 2006, Towards a nonlinear eddy-viscosity model based on elliptic relaxation, *Flow, Turbulence Combust*. **76**, 241–256.

Piomelli, U., 2008, Wall-layer models for large-eddy simulations, *Prog. Aerosp. Sci.* **44**(6), 437–446.

Piomelli, U., Ferziger, J., Moin, P. and Kim, J., 1989, New approximate boundary conditions for large eddy simulations of wall-bounded flows, *Phys. Fluids A* **1**(6), 1061–1068.

Piomelli, U., Balaras, E., Pasinato, H., Squires, K. D. and Spalart, P. R., 2003, The inner–outer layer interface in large-eddy simulations with wall-layer models, *Int. J. Heat Fluid Flow* **24**(4), 538–550.

Piquet, J., 1999, *Turbulent Flows*, Springer, Berlin.

Poletto, R., Revell, A., Craft, T. and Jarrin, N., 2011, Divergence free synthetic eddy method for embedded LES inflow boundary conditions, *Proc. 7th Int. Symp. on Turbulence & Shear Flow Phenomena*, Ottawa.

Poletto, R., Craft, T. and Revell, A., 2013, A new divergence-free synthetic eddy method for the reproduction of inlet flow conditions for LES, *Flow, Turbulence Combust*. **91**(3), 519–539.

Pope, S. B., 1975, A more general effective viscosity hypothesis, *J. Fluid Mech.* **72**, 331–340.

Pope, S. B., 1978, An explanation of the round-jet/plane-jet anomaly, *AIAA J*. **16**, 279–281.

Pope, S. B., 1983, Consistent modelling of scalars in turbulent flows, *Phys. Fluids* **26**, 404.

Pope, S. B., 2000, *Turbulent Flows*, Cambridge University Press, Cambridge.

Pope, S. B., 2004, Ten questions concerning the large-eddy simulation of turbulent flows, *New J. Phys.***6**(1), 35.

Popovac, M., 2006, Modelling and simulation of turbulence and heat transfer in wall-bounded flows, Compound wall treatment for RANS computations of complex turbulent flows and heat transfer, *Flow, Turbulence Combust.* **78**, 177–202.

Praisner, T. J. and Smith, C. R., 2006a, The dynamics of the horseshoe vortex and the associated end-wall heat transfer – 1. Temporal behaviour, *J. Turbomachinery* **128**, 747–754.

Praisner, T. J. and Smith, C. R., 2006b, The dynamics of the horseshoe vortex and the associated end-wall heat transfer – 2. Time-mean results, *J. Turbomachinery* **128**, 755–762.

Prandtl, L., 1925, Bericht über Untersuchungen zur ausgebildeten Turbulenz, *ZAMM* **5**, 136.

Probst, A., Radespiel, R. and Knopp, T., 2011, Detached-eddy simulation of aerodynamic flows using a Reynolds-stress background model and algebraic RANS/LES sensors, AIAA Paper 2011–3206, *20th AIAA Computational Fluid Dynamics Conf*., Honolulu, Hawaii, 3206.

Probst, A., Probst, S. and Francois, D. G., 2019, Hybrid RANS/LES methodologies for external aircraft aerodynamics, *ERCOFTAC Bull.* **120**, 20–25.

Prud'homme, M. and Elghobashi, S., 1986, Turbulent heat transfer near the reattachment point of flow downstream from a sudden pipe expansion, *Num. Heat Trans.* **10**, 349–368.

Radhakrishnan, S., Piomelli, U., Keating, A. and Lopes, A. S., 2006, Reynolds-averaged and large-eddy simulations of turbulent non-equilibrium flows, *J. Turbulence* **7**(63), 1–30.

Rau, G., Cakan, M., Moeller, D. and Arts, T., 1998, The effect of periodic ribs on local aerodynamic and heat transfer performance of a straight cooling channel, *ASME J. Turbomachinery* **120**, 368–375.

Reichardt, H., 1951, Vollstaendige Darstellung der turbulenten Geschwindigkeitsverteilung in glatten Leitungen, *ZAMM* **31**, 208–219.

Revell, A., Craft, T. and Laurence, D., 2011, Turbulence modelling of unsteady turbulent flows using the stress-strain-lag model, *Flow, Turbulence Combust.* **86**(1), 129–151.

Reynolds, O., 1895, On the dynamical theory of incompressible viscous fluids and the determination of the criterion, *Phil. Trans. R. Soc. London* **186**, 123–164.

Reynolds, W. C., 1984, Physical and analytical foundations, concepts and new directions in turbulence modelling and simulation, in *Turbulence Models and Their Applications*, Vol. 2, 149–294, Collection de la Direction des Études et Recherches d'Éléctricité de France, Eyrolles, Paris.

Reynolds, W. C. and Hussain, A. K. M. F., 1972, The mechanics of an organised wave in turbulent shear flow. Part 3: theoretical models and comparisons with experiments, *J. Fluid Mech.* **54**, 263–288.

Richardson, L. F., 1926, Atmospheric diffusion shown on a distance-neighbour graph, *Proc. R. Soc. London A* **110**, 709.

Ristorcelli, J. R., Lumley, J. L. and Abid, R., 1995, A rapid pressure covariance representation consistent with the Taylor–Proudman theorem, materially frame indifferent in the two-component limit, *J. Fluid Mech.* **292**, 111–152.

Rodi, W., 1972, *The prediction of free turbulent boundary layers by use of a two-equation model of turbulence*, PhD Thesis, University of London, UK.

Rodi, W., 1975, A review of experimental data of uniform-density, free turbulent boundary layers, in *Studies in Convection*, Vol. 1 (Ed. B. E. Launder), 79–165, Academic Press, London.

Rodi, W., 1976, A new algebraic stress relation for calculating Reynolds stresses, *ZAMM* **56**, T219–T221.

Rodi, W. and Scheuerer, G., 1983, Calculation of curved shear layer with 2-equation turbulence models, *Phys. Fluids* **26**, 1422–1436.

Rodi, W. and Scheuerer, G., 1986, Scrutinizing the $k - \varepsilon$ model under adverse pressure gradient conditions, *J. Fluids Eng.* **108**, 174–179.

Rodi, W. and Spalding, D. B., 1970, A two-parameter model of turbulence and its application to free jets, *Wärme Stoffübertragung* **3**, 85–95.

Rogers, M. M., Mansour, N. N. and Reynolds, W. C., 1989, An algebraic model for the turbulent flux of a passive scalar, *J. Fluid Mech.* **203**, 77–101.

Rotta, J. C., 1951, Statistische Theorie nichthomogener Turbulenz, *Z. Phys.* **129**, 547–572 Pt 1; 131, 51–77 Pt 2.

Rotta, J. C., 1968, Über eine Methode zur Berechnung turbulenter Scherströmungen, Report 69 A 14, Aerodynamische Versuchanstalt, Göttingen.

Rotta, J. C., 1972, *Turbulente Strömungen*, B. G. Teubner, Stuttgart.

Rubel, A., 1985, On the vortex-stretching modification of the $k-\varepsilon$ turbulence model: radial jets, *AIAA J*. **23**, 1129–1130.

Rubinstein, R. and Barton, J. M., 1990, Nonlinear Reynolds stress models and the renormalization group, *Phys. Fluids A* **2**, 1472–1476.

Rupp, K., 2015, www.karlrupp.net/2015/06/40-years-of-microprocessor-trend-data.

Saddoughi, S. G. and Veeravalli, S. V., 1994, Local isotropy in turbulent boundary layers at high Reynolds numbers, *J. Fluid Mech.* **268**, 333–372.

Saffman, P. G., 1970, A model for inhomogeneous turbulent flow, *Proc. R. Soc. London A* **317**, 417–433.

Sagaut, P., 2006, *Large Eddy Simulation for Incompressible Flows: An Introduction*, Springer Science & Business Media, Berlin Heidelberg.

Samuel, A. E. and Joubert, P. N., 1974, Boundary layer developing in an increasingly adverse pressure gradient, *J. Fluid Mech.* **66**, 481–505.

Saric, W. S., Reed, H. L. and White, E. B., 2003, Stability and transition of three-dimensional boundary layers, *Ann. Rev. Fluid Mech.* **35**(1), 413–440.

Šaric, S., Kniesner, A., Mehdizadeh, A., Jakirlić, S., Hanjalić, K. and Tropea, C., 2008, Comparative assessment of Hybrid LES/RANS modes in turbulent flows separating from smooth surfaces, in *Advances in Hybrid RANS-LES Modelling*, NNFM, Vol. **97** (Ed. S.-H. Peng and W. Haase), 142–151, Springer, Corfu, Greece.

Savill, A. M., 2002a, By-pass transition using conventional closures, in *Closure Strategies for Turbulent and Transitional Flows* (Ed. B. E. Launder and N. D. Sandham), 464–492, Cambridge University Press, Cambridge.

Savill, A. M., 2002b, New strategies in modelling by-pass transition, in *Closure Strategies for Turbulent and Transitional Flows* (Ed. B. E. Launder and N. D. Sandham), 493–521, Cambridge University Press, Cambridge.

Schaller, R. R., 1997, Moore's law: past, present and future, *IEEE Spectrum* **34**(6), 52–59.

Scheuerer, G., 1983, *Entwicklung eines Verfahrens zur Berechnung zweidimensionaler Grenzschichten an Gasturbinenschauffeln*, Dr Ing Thesis, University of Karlsruhe, Germany.

Schiestel, R., 1974, *Sur un nouveau modèle de turbulence appliqué aux transferts de quantité de mouvement et de chaleur*, Thèse Doct. Ès Sciences Phys., Université de Nancy-1, France.

Schiestel, R., 1987, Multiple-time-scale modeling of turbulent flows in one-point closures, *Phys. Fluids* **30**, 722–731.

Schiestel, R., 2008, *Modeling and Simulation of Turbulent Flows*, ISTE-John Wiley, London.

Schiestel, R. and Dejoan, A., 2005, Towards a new partially integrated transport model for coarse grid and unsteady flow simulations, *Theor. Comput. Fluid Dyn.* **18**, 443–468.

Schlüter, J. U., Pitsch, H. and Moin, P., 2004, Large-eddy simulation inflow conditions for coupling with Reynolds-averaged flow solvers, *AIAA J*. **42**(3), 478–484.

Schmidt, H. and Schumann, U., 1989, Coherent structure of the convective boundary layer derived from large-eddy simulations, *J. Fluid Mech.* **200**, 511–562.

Schmidt, S. and Breuer, M., 2015, Extended synthetic turbulence inflow generator within a Hybrid LES–URANS methodology for the prediction of non–equilibrium wall–bounded flows, *Flow, Turbulence Combust*. **95**(4), 669–707.

Schmidt, S. and Breuer, M., 2017, Source term based synthetic turbulence inflow generator for eddy-resolving predictions of an airfoil flow including a laminar separation bubble, *Comput. Fluids* **146**, 1–22.

Schumann, U., 1975, Sub-grid-scale model for finite difference simulations of turbulent flows in plane channels and annuli, *J. Comput. Phys.* **18**, 376–404.

Schumann, U., 1976, Numerical simulation of the transition from three- to two-dimensional turbulence under a uniform magnetic field, *J. Fluid Mech.* **74**, 31–58.

Schumann, U., 1977, Realizability of Reynolds-stress turbulence models, *Phys. Fluids* **20**, 721–725.

Schwarz, W. R. and Bradshaw, P., 1994, Term-by-term tests of stress-transport turbulence models in a 3-dimensional boundary layer, *Phys. Fluids* **6**, 986–998.

Sergent, E., 2002, *Vers une méthodologie de couplage entre la simulation des grandes échelles et les modeles statistiques*, PhD Thesis, École Centrale de Lyon, Écully.

Sewall, E. A. and Tafti, D., 2004, Large eddy simulation of flow and heat transfer of the developing region of a stationary ribbed internal turbine blade cooling channel, Paper GT2004-53832, *ASME Turbo Expo 2004*, Vienna, Austria.

Sewall, E. A., Tafti, D. K., Graham, A. and Thole, K. A., 2006, Experimental validation of large eddy simulation of flow and heat transfer in a stationary ribbed duct, *Int. J. Heat Fluid Flow* **27**, 243–258.

Shih, T.-H. and Lumley, J. L., 1985, Modeling of pressure correlation terms in Reynolds stress and scalar flux equations, Report FDA-85–3, Sibley School of Mechanical and Aerospace Engineering, Cornell University, Ithaca, NY.

Shih, T.-H., Lumley, J. L. and Chen, J.-Y., 1985, Second-order modelling of a passive scalar in a turbulent shear flow, Report FDA-85–15, Sibley School of Mechanical and Aerospace Engineering, Cornell University, Ithaca, NY.

Shih, T.-H., Lumley, J. L. and Chen, J.-Y., 1990, Second-order modelling of a passive scalar in a turbulent shear flow, *AIAA J.* **28**, 610–617.

Shih, T.-H., Zhu, J. and Lumley, J. L., 1995, A new Reynolds stress algebraic equation, *Comput. Meth. Appl. Mech. Eng.* **125**, 287–302.

Shih, T.-H., Povinelli, L. and Liu, N., 2002, Application of generalised wall functions for complex turbulent flows, in *Engineering Turbulence Modelling and Experiments 5* (Ed. W. Rodi and N. Fueyo), 177–186, Elsevier, Amsterdam.

Shima, N., 1993, Prediction of turbulent boundary layers with second-moment closure: Part 1. Effects of periodic pressure gradient, wall transpiration and free-stream turbulence, *J. Fluids Eng.* **115**, 56–63.

Shimomura, Y., 1991, Large eddy simulation of magnetohydrodynamic turbulent channel flows under a uniform magnetic field, *Phys. Fluids A* **3**, 3098.

Shir, C. C., 1973, A preliminary numerical study of atmospheric turbulent flows in the idealized turbulent boundary layer, *J. Atmos. Sci.* **30**, 1327–1339.

Shur, M. L., Spalart, P. R., Strelets, M. K. and Travin, A. K., 2008, A Hybrid RANS-LES approach with delayed-DES and wall-modelled LES capabilities, *Int. J. Heat Fluid Flow* **29**(6), 1638–1649.

Shur, M. L., Spalart, P. R., Strelets, M. K. and Travin, A. K., 2014, Synthetic turbulence generators for RANS-LES interfaces in zonal simulations of aerodynamic and aeroacoustic problems, *Flow, Turbulence Combust*. **93**(1), 63–92.

Simpson, R. L. and Wallace, D. B., 1975, Laminarescent turbulent boundary layers: experiments on sink flows, Project Squid Technical Report SMU-1-PU, Thermal Science and Propulsion Center, Purdue University.

Simpson, R. L., Kays, W. M. and Moffat, R. J., 1967, The turbulent boundary layer on a porous plate: an experimental study of the fluid dynamics with injection and suction, Thermosciences Division Report HMT-2, Stanford University, Stanford, CA.

Simpson, R. L., Moffat, R. and Kays, W. M., 1969, The turbulent boundary layer on a porous plate: experimental skin friction with variable injection and suction, *Int. J. Heat Mass Transfer* **12**, 771–789.

Skillen, A., Revell, A. and Craft, T., 2016, Accuracy and efficiency improvements in synthetic eddy methods. *Int. J. Heat Fluid Flow* **62**, 386– 394.

Skripkin, S. G., Tsoy, M. A., Shtork, S. and Hanjalić, K., 2016, Comparative analysis of twin vortex ropes in laboratory models of two hydro-turbine draft-tubes, *J. Hydraul. Res.* **54**, 450–460.

Slotnick, J., Khodadoust, A., Alonzo, J., Darmofal, D., Gropp, W., Lurie, E. and Mavriplis, D., 2014, CFD vision 2030 study: a path to revolutionary computational aerosciences, NASA/CR-2014-21878.

Smagorinsky, J., 1963, General circulation experiments with the primitive equations, *Mon. Weather Rev.* **91**(3), 99–164.

Smirnov, A., Shi, S. and Celik, I., 2001, Random flow generation technique for large eddy simulations and particle-dynamics modeling, *J. Fluids Eng.* **123**(2), 359–371.

Spalart, P. R., 1986, Numerical study of sink-flow boundary layers, *J. Fluid Mech.* **172**, 307–328.

Spalart, P. R., 1988, Direct simulation of a turbulent boundary layer up to Re_θ =1410, *J. Fluid Mech.* **187**, 61–98.

Spalart, P. R., 2009, Detached-eddy simulation, *Ann. Rev. Fluid Mech.* **41**, 181–202.

Spalart, P. R. and Allmaras, S. R., 1992, A one-equation turbulence model for aerodynamic flows, AIAA Paper 92-0439 (see also *Recherche Aérospatiale* **1**, 5–21, 1994).

Spalart, P. R. and Strelets, M. K., 1997, Direct and Reynolds-averaged numerical simulations of a transitional shear bubble, *Proc. 11th Symp. on Turbulent Shear Flows*, Joseph Fourier University, Grenoble, France, 30.13–30.18.

Spalart, P. R. and Strelets, M. K., 2000, Mechanism of transition and heat transfer in a separation bubble, *J. Fluid Mech.* **403**, 329–349.

Spalart, P. R., Jou, W.-H., Strelets, M. K. and Allmaras, S. R., 1997, Comments on the feasibility of LES for wings, and on a Hybrid RANS/LES approach, *Proc. 1st AFOSR Int. Conf. on DNS/LES*, Ruston, Louisiana, 137–147.

Spalart, P. R., Deck, S., Shur, M. L., Squires, K. D., Strelets, M. K. and Travin, A., 2006, A new version of detached-eddy simulation, resistant to ambiguous grid densities. *Theor. Comput. Fluid Dyn.* **20**(3), 181–195.

Spalding, D. B., 1961, A single formula for the law of the wall, *ASME J. Appl. Mech.* **28**, 444–458.

Spalding, D. B., 1967, Monograph on turbulent boundary layers, Report TWF/TN/33, Department of Mechanical Engineering, Imperial College, London.

Spalding, D. B., 1971, Concentration fluctuations in a round turbulent free jet, *Chem. Eng. Sci.* **26**, 95–107.

Speziale, C. G., 1987a, On the decomposition of turbulent flow fields for the analysis of coherent structures, *Acta Mech*. **70**, 243–250.

Speziale, C., 1987b, On non-linear *k–l* and $k-\varepsilon$ models of turbulence, *J. Fluid Mech.* **178**, 459–478.

Speziale, C. G., 1991, Analytical methods for the development of Reynolds stress closures in turbulence, *Ann. Rev. Fluid Mech.* **23**, 107–157.

Speziale, C. G., 1998a, A combined large-eddy simulation and time-dependent RANS capability for high-speed compressible flows, *J. Sci. Comput.* **13**(3), 253–274.

Speziale, C. G., 1998b, Turbulence modeling for time-dependent RANS and VLES: a review, *AIAA J*. **36**(2), 173–184.

Speziale, C. G. and Gatski, T. B., 1997, Analysis and modeling of anisotropies in the dissipation rate of turbulence, *J. Fluid Mech.* **344**, 155–189.

Speziale, C. G., Sarkar, S. and Gatski, T. B., 1991, Modelling the pressure-strain correlation of turbulence: an invariant dynamical systems approach, *J. Fluid Mech.* **227**, 245–272.

Stawiarski, K. and Hanjalić, K., 2002, A two-scale second-moment one-point turbulence closure, in *Engineering Turbulence Modelling and Measurements 5* (Ed. W. Rodi and N. Fueyo), 97–106, Elsevier Science, Amsterdam.

Stawiarski, K. and Hanjalić, K., 2005, On physical constraints for multi-scale turbulence closure models, *Prog. Comput. Fluid Dyn.* **5**, 120–135.

Steenberger, W., 1995, *Turbulent pipe flow with swirl*, PhD Thesis, Eindhoven University of Technology, The Netherlands.

Stevens, S. J. and Fry, P., 1973, Measurements of the boundary-layer growth in annular diffusers, *J. Aircraft* **10**, 73–80.

Strelets, M., 2001, Detached eddy simulation of massively separated flows, AIAA Paper 2001-0879, *39th AIAA Aerospace Sciences Meeting and Exhibit*, Reno, Nevada.

Suga, K., 1995, *Development and application of a non-linear eddy viscosity model sensitized to stress and strain invariants*., PhD Thesis, UMIST, Manchester, UK.

Suga, K., 2001, Application of a TCL second-moment closure to turbulent duct flows, *Proc. UEF Conf. on Turbulent Heat Transfer – 3*, Anchorage, AL.

Suga, K., 2004a, Improvement of second-moment closure for turbulent obstacle flow and heat transfer, *Int. J. Heat Fluid Flow* **25**, 776–784.

Suga, K., 2004b, Modeling the rapid part of the pressure-diffusion process in the Reynolds stress transport equation, *ASME J. Fluids Eng.* **126**, 634–641.

Suga, K., 2007, Computation of high Prandtl number turbulent thermal field by the analytical wall-function, *Int. J. Heat Mass Transfer* **50**, 4967–4974.

Suga, K. and Abe, K., 2000, Non-linear eddy viscosity modelling for turbulence and heat transfer near wall and shear-free boundaries, *Int. J. Heat Fluid Flow* **21**, 37–48.

Suga, K. and Kubo, M., 2010, Modelling turbulent high Schmidt number mass transfer across undeformable gas-liquid interfaces, *Int. J. Heat Mass Transfer* **53**, 2989–2995.

Suga, K., Nagaoka, M., Horinouchi, N., Abe, K. and Kondo, Y., 2001, Application of a three-equation cubic eddy viscosity model to 3-D turbulent flows by the unstructured grid method, *Int. J. Heat Fluid Flow* **22**, 259–271.

Suga, K., Craft, T. J. and Iacovides, H., 2006, An analytical wall function for turbulent flow and heat transfer over rough walls, *Int. J. Heat Fluid Flow* **27**, 852–866.

Suga, K., Ishibashi, Y. and Kuwata, Y., 2013, An analytical wall-function for recirculating and impinging turbulent heat transfer, *Int. J. Heat Fluid Flow* **41**, 45–54.

Tabor, G. R. and Baba-Ahmadi, M., 2010, Inlet conditions for large eddy simulation: a review, *Comput. Fluids* **39**(4), 553–567.

Tailland, A. and Mathieu, J., 1967, Jet pariétal, *J. Mécanique* **6**, 103–131.

Tanahashi, M., Kang, S.-J., Miyamoto, S., Shiokawa, S. and Miyauchi, T., 2004, Scaling law of fine scale eddies in turbulent channel flows up to $\mathrm{Re}_\tau = 800$, *Int. J. Heat Fluid Flow* **25**, 331–340.

Tatschl, R., Basara, B., Schneider, J., Hanjalić, K., Popovac, M., Brohmer, A. and Mehring, J., 2006, Advanced turbulent heat transfer modeling for IC-engine applications using AVL FIRE, *International Multidimensional Engine Modelling, User's Group Meeting*, Detroit, MI.

Tatsumi, K., Iwai, H., Neo, E. C., Inaoka, K. and Suzuki, K., 1999, Prediction of time-mean characteristics and periodical fluctuation of velocity and thermal fields of a

backward-facing step, in *Proc. 1st Int. Symp. on Turbulence & Shear Flows* (Ed. S. Banerjee and J. K. Eaton), 1167–1172, Begell House, New York.
Taulbee, D., 1992, An improved algebraic Reynolds stress model and corresponding nonlinear stress model, *Phys. Fluids A* **4**, 2555–2561.
Taulbee, D. and Tran, L., 1988, Stagnation streamline turbulence, *AIAA J.* **26**, 1011–1013.
Tavoularis, S. and Corrsin, S. C., 1981, Experiments in nearly homogeneous turbulent shear flow with a uniform mean temperature gradient: Part 1, *J. Fluid Mech.* **104**, 311–347.
Tavoularis, S. and Corrsin, S. C., 1985, Effects of shear on the turbulent diffusivity tensor, *Int. J. Heat Mass Transfer* **28**, 265–276.
Taylor, A. M. K., Whitelaw, J. H. and Yianneskis, M. J., 1982, Curved ducts with strong secondary motion – velocity measurements of developing laminar and turbulent flow, *J. Fluids Eng.* **104**, 350–359.
Taylor, G. I., 1915, Eddy motion in the atmosphere, *Phil. Trans. Roy. Soc. A* **215**, 1–25.
Taylor, G. I., 1932, The transport of vorticity and heat through fluids in turbulent motion, *Proc. Roy. Soc.* **135**, 685–702.
Taylor, G. I., 1935, Statistical theory of turbulence: Parts I–III, *Proc. R. Soc. London A* **151**, 421–464.
Temmerman, L., Hadžiabdić, M., Leschziner, M. and Hanjalić, K., 2005, A hybrid two-layer URANS–LES approach for large eddy simulation at high Reynolds numbers, *Int. J. Heat Fluid Flow* **26**(2), 173–190.
Tennekes, H. and Lumley, J. L., 1972, *A First Course in Turbulence*, MIT Press, Cambridge, MA.
Thielen, L., Hanjalić, K. and Jonker, H., 2003, Symmetry breaking of flow and heat transfer in multiple impinging jets, *Int. J. Heat Fluid Flow* **24**, 444–457.
Thielen, L., Hanjalić, K., Jonker, H. and Manceau, R., 2005, Predictions of flow and heat transfer in multiple impinging jets with an elliptic-blending second-moment closure, *Int. J. Heat Mass Transfer* **48**, 1583–1598.
Thomas, T. G. and Takhar, H. S., 1988, Frame invariance of turbulence constitutive relations, *Astrophys. Space Sci.* **141**, 159–168.
Townsend, A. A., 1956, *The Structure of Turbulent Shear Flow*, Cambridge University Press, Cambridge.
Travin, A., Shur, M., Strelets, M. and Spalart, P., 2002, Physical and numerical upgrades in the detached-eddy simulation of complex turbulent flows, in *Advances in LES of Complex Flows, Fluid Mechanics and its Application*, Vol. 65 (Ed. R. Friedrich and W. Rodi), 239–254, Kluwer Academic, Dordrecht.
Tucker, H. J. and Reynolds, A. J., 1968, The distortion of turbulence by irrotational plane strain, *J. Fluid Mech.* **32**, 657–673.
Tunstall, R., Laurence, D., Prosser, R. and Skillen, A., 2017, Towards a generalised dual-mesh Hybrid LES/RANS framework with improved consistency, *Comput. Fluids* **157**, 73–83.
Uberoi, M. S., 1957, Equipartition of energy and local isotropy in turbulent flows, *J. Appl. Phys.* **28**, 1165–1170.
Uittenbogaard, R., 1988, Measurement of turbulence fluxes in a steady, stratified mixing layer, Proc. 3rd Int. Symp. on Refined Flow Modelling & Turbulence Measurements.
Van Driest, E. R., 1956, On turbulent flow near a wall, *J. Aero. Sci.* **23**, 1007–1011.
Van Reeuwijk, M., Jonker, H. J. J. and Hanjalić, K., 2005, Identification of the wind in Rayleigh–Bénard convection, *Phys. Fluids* **17**, 1–4.
Van Reeuwijk, M., Jonker, H. J. J. and Hanjalić, K., 2008, Wind and boundary layers in Rayleigh–Bénard convection. Pt. I. Analysis and modeling, *Phys. Rev. E* **77**, 036311-1-15.

Versteegh, T. A. M. and Nieuwstadt, F. T. M., 1998, Turbulent budgets of natural convection in an infinite, differentially heated vertical channel, *Int. J. Heat Fluid Flow* **19**, 135–149.

Viswanathan, A. and Tafti, D., 2005, Detached eddy simulation of turbulent flow and heat transfer in a duct, *J. Fluids Eng.* **127**, 888–896.

Viswanathan, A. and Tafti, D., 2006a, Detached eddy simulation of flow and heat transfer in fully-developed rotating internal coolant channel with normal ribs, *Int. J. Heat Fluid Flow* **27**, 351–370.

Viswanathan, A. and Tafti, D., 2006b, Detached eddy simulation of turbulent flow and heat transfer in a two-pass internal cooling duct, *Int. J. Heat Fluid Flow* **27**, 1–20.

Vogel, J. C. and Eaton, J. K., 1985, Combined heat transfer and fluid dynamic measurements downstream of a backward-facing step, *ASME J. Heat Transfer* **107**, 922–929.

Von Terzi, D. A. and Fröhlich, J., 2010, Segregated coupling of large-eddy simulations with downstream Reynolds-averaged Navier–Stokes calculations, *Comput. Fluids* **39**(8), 1314–1331.

Wallin, S. and Johansson, A. V., 2000, An explicit algebraic Reynolds stress model for incompressible and compressible turbulent flows, *J. Fluid Mech.* **403**, 89–132.

Wang, M., 2005, Computation of trailing-edge aeroacoustics with vortex shedding, *CTR Ann Research Briefs*, Center for Turbulence Research, Stanford University, Stanford, CA, 379–388.

Wang, M. and Moin, P., 2002, Dynamic wall modeling for large-eddy simulation of complex turbulent flows, *Phys. Fluids* **14**(7), 2043–2051.

Warhaft, Z., 2000, Passive scalars in turbulent flow, *Ann. Rev. Fluid Mech.* **32**, 203–240.

Warhaft, Z. and Lumley, J. L., 1978, An experimental study of the decay of temperature fluctuations in grid-generated turbulence, *J. Fluid Mech.* **88**, 659–684.

Webster, C. A. G., 1964, An experimental study of turbulence in a density-stratified shear flow, *J. Fluid Mech.* **19**, 221–245.

Wei, T. and Willmarth, W. W., 1989, Reynolds number effects on the structure of a turbulent channel flow, *J. Fluid Mech.* **204**, 57–95.

Weinmann, M., 2011, *Simulation strategies for complex turbulent flows*, PhD Thesis, University of Southampton, UK.

Werner, H. and Wengle, H., 1993, Large-eddy simulation of turbulent flow over and around a cube in a plate channel, in *Turbulent Shear Flows*, Vol. 8 (Ed. F. Durst *et al.*), 155–168, Springer, Heidelberg.

Wieghardt, K., 1943, Über die Wandschubspannung in turbulenten Reibungsschichten bei veränderlichem Aussendruck, Z.W.B., K.W.I., Göttingen, U. & M. 6603.

Wilcox, D. C., 1988a, Multiscale model of turbulent flows, *AIAA J.* **26**, 1311–1320.

Wilcox, D. C., 1988b, Reassessment of the scale determining equation for advanced turbulence models, *AIAA J.* **26**, 1299–1310.

Wilcox, D. C., 1993, Comparison of two-equation turbulence models for boundary layers with pressure gradient, *AIAA J.* **31**, 1414–1421.

Wilcox, D. C., 2000, *Turbulence Modeling for CFD*, 2nd ed., DCW Industries, La Cañada, CA.

Wilcox, D. C. and Rubesin, M. W., 1980, Progress in turbulence modelling for complex flow fields including effects of compressibility, NASA TP-1517.

Wizman, V., Laurence, D., Kanniche, M., Durbin, P. A. and Demuren, A., 1996, Modeling near-wall effects in second-moment closures by elliptic relaxation, *Int. J. Heat Fluid Flow* **17**, 255–266.

Wolfram, 1988, *Mathematica*^{TM}, Addison-Wesley.
Wolfshtein, M., 1969, The velocity and temperature distribution in one-dimensional flow with turbulence augmentation and pressure gradient, *Int. J. Heat Mass Transfer* **12**, 301–318.
Wörner, M., 1994, *Direkte Simulation turbulenter Rayleigh–Bénard Konvektion in flüssigem Natrium*, Dissertation, University of Karlsruhe, KfK 5228, Kernforschungszentrum Karlsruhe, Germany.
Wörner, M. and Grötzbach, G., 1997, Pressure transport in DNS of turbulent natural convection in horizontal fluid layers, in *Turbulence, Heat and Mass Transfer 2* (Ed. K. Hanjalić and T. W. J. Peeters), 351–360, Delft University Press, Delft, The Netherlands.
Wu, X., 2017, Inflow turbulence generation methods, *Ann. Rev. Fluid Mech.* **49**(1), 23–49.
Wygnanski, I., Champagne, F. and Marasli, B., 1986, On the large-scale structures in two-dimensional, small-deficit turbulent wakes, *J. Fluid Mech.* **168**, 31–71.
Wyngaard, J. C., Coté, O. R. and Izumi, Y., 1971, Local free convection, similarity, and the budgets of shear stress and heat flux, *J. Atmos. Sci.* **28**, 1171–1182.
Xiao, H. and Jenny, P., 2012, A consistent dual-mesh framework for Hybrid LES/RANS modelling, *J. Comp. Phys.* **231**(4), 1848–1865.
Yakhot, V. and Orszag, S. A., 1986, Renormalization group analysis of turbulence. 1. Basic theory, *J. Sci. Comput.* **1**, 3–51.
Yakhot, V., Orszag, S. A., Thangam, S., Gatski, T. B. and Speziale, C. G., 1992, Development of turbulence models for shear flows by a double expansion technique, *Phys. Fluids A* **4**, 1510–1520.
Yap, C. R., 1987, *Turbulent heat and momentum transfer in recirculating and impinging flows*, PhD Thesis, Faculty of Technology, University of Manchester, Manchester, UK.
Yoshizawa, A., 1982, A statistically-derived subgrid model for the large-eddy simulation of turbulence, *Phys. Fluids* **25**(9), 1532–1538.
Younis, B. A., 1984, *On modelling the effects of streamline curvature on turbulent shear flows*, PhD Thesis, Faculty of Engineering, University of London, UK.
Zacharos, A., 2010, *The use of unsteady RANS in the computation of 3-dimensional flow in rotating cavities*, PhD Thesis, Faculty of Engineering and Physical Sciences, University of Manchester, Manchester, UK.
Zeierman, S. and Wolfshtein, M., 1986, Turbulent time-scale for turbulent flow calculations, *AIAA J.* **24**, 1606–1610.
Zeman, O. and Lumley, J. L., 1976, Modeling buoyancy driven mixed layers, *J. Atmos. Sci.* **33**, 1974–1988.

Index

https://doi.org/10.1017/9781108875400.014 Published online by Cambridge University Press

https://doi.org/10.1017/9781108875400.014 Published online by Cambridge University Press

https://doi.org/10.1017/9781108875400.014 Published online by Cambridge University Press

https://doi.org/10.1017/9781108875400.014 Published online by Cambridge University Press